Scientific Computing in Chemical Engineering II

Computational Fluid Dynamics, Reaction Engineering, and Molecular Properties

Keil · Mackens · Voß · Werther (Eds.)

Scientific Computing
in Chemical Engineering II

Computational Fluid Dynamics,
Reaction Engineering, and Molecular Properties

With 189 Figures and 29 Tables

Springer

Preface

The present proceedings assemble the contributions to the second workshop on "Scientific Computing in Chemical Engineering". The two volumed edition covers the wide spectrum of computational activities in chemical process engineering encompassing tasks from process development, process design and optimization to process operations and control. The increasing performance of computers and the rapid advancement of numerical techniques encourages the employment of more sophisticated models. Quantum chemical approaches, molecular dynamics and Monte Carlo methods penetrate engineering design of catalysts and the calculation of phase transfer phenomena. Computational fluid dynamics of multi-phase flow is now a standard tool in chemical plant design. Numerical simulations replace time consuming and, therefore, expensive experiments to an ever increasing extent. The present workshop reflects these developments.

The large number of contributions made it necessary to split the proceedings into two volumes. We grouped the contributions into ten sections with the headings *Simulation of Reactive Flows, Reaction Engineering, Reaction Diffusion Problems, Molecular Properties, Computer Aided Process Design, Combustion and Flame, Image Processing, Optimization, Control* and *Neural Networks*. The present volume deals with the first four of them including the invited presentations related to these topics. The companion volume deals with the remaining six.

The workshop was organized by the Collaborative Research Center (Sonderforschungsbereich) 238 of the Deutsche Forschungsgemeinschaft "In-situ measuring techniques and dynamic modelling of multiphase flow systems" at the Technical University of Hamburg-Harburg in cooperation with the German Society for Chemical Apparatus, Chemical Engineering and Biotechnology e.V. (DECHEMA), the special interest groups "Scientific Computing" and "Industrial Mathematics" of the Deutsche Mathematiker Vereinigung (DMV), the joint special interest group "Numerical Software" of the DMV, the Gesellschaft für Angewandte Mathematik und Mechanik (GAMM), and the Gesellschaft für Informatik (GI), as well as the GAMM special interest group "Scientific Computing".

We thank all the people from these societies and groups who helped to realize both these proceedings and the workshop. We are grateful to our large number of referees for their careful inspection of the contributed papers and their valuable comments which increased the quality of the proceedings considerably.

Last but not least it is a pleasure for us to thank Dipl.-Phys. Ing. Vera Lochmann and Margitta Janssen for their untiring efforts in collecting all contributions and adapting them to the Springer LaTeX conventions.

The Editors

Contents

Contents of Complementary Volume

Part I

Invited Presentations

Molecular Simulation:
Phase equilibria and confined systems

Keith E. Gubbins

North Carolina State University, Department of Chemical Engineering
Raleigh, North Carolina 27695 - 7905, USA

Abstract. Recent advances in direct and indirect methods of molecular simulation for studying fluid phase equilibria are reviewed. For bulk fluids and mixtures, the emphasis is on phase equilibria for fluids of nonspherical molecules, including ionic fluids, aqueous mixtures, hydrocarbons and chain molecules. The application of these methods to adsorption is also discussed, with emphasis on phase separation in porous media.

1 Introduction

The use of Molecular Dynamics (MD) or Monte Carlo (MC) simulation methods to calculate the so-called "mechanical" properties, such as internal energy or pressure, is straightforward. The situation is considerably more difficult for the "statistical" properties - free energy, chemical potential or entropy. The difficulty is that conventional methods sample parts of phase space where the Boltzmann factor exp(-U/kT) is large (here U is configurational energy), whereas for the statistical properties other regions of phase space make major contributions [1]. Various ways around this problem have been devised, including special sampling techniques and integration over a range of thermodynamic states. Reviews are given in refs. [1-6] and references therein. Recently, methods for simulating fluid phase equilibria directly have been developed, and are fast and convenient where they can be applied [5].

An important application of such simulations is to the prediction of phase equilibria in cases where experimental measurements are difficult or impossible; examples include bulk systems at extreme temperatures or pressures, or fluids confined within porous media. Simulations of this sort also find other applications, e.g.: (a) testing statistical mechanical theories, where identical models for the molecules (and any surfaces present) are used in both simulation and theory, so that the comparison tests only the statistical mechanical approximations in the theory; (b) comparisons with experiment, which give information about the suitability of the assumed intermolecular potential.

The main limitation of the simulations is usually the reliability of the intermolecular potentials used. Since computers are still too slow to calculate reliable *ab initio* potentials for any but the simplest molecules, most workers use semi-empirical potentials, developed by using a combination of knowledge from theory (quantum mechanics, electrostatics) and experimental data. Such

models [7] include universal force fields, transferable isotropic site-site models (e.g. the OPLS model, or optimized potentials for liquid simulations), and more sophisticated models [8] involving anisotropic site-site potentials and distributed multipoles.

In the remainder of this paper a brief survey is given of some developments in this area over the last ten years. Both direct and indirect (via calculation of the chemical potential) methods for calculating phase equilibria are considered, with an emphasis on applications to fluids of complex molecules and on confined systems.

2   Bulk Fluids

2.1   Direct Method: Gibbs Ensemble Monte Carlo

The Gibbs Ensemble Monte Carlo (GEMC) method, first proposed by Panagiotopoulos in 1987 [9], involves setting up boxes representing the two coexisting phases (I and II) that are in equilibrium with each other; however, these phases are not in physical contact. The two boxes representing the phases have volumes V_I and V_{II} and contain N_I and N_{II} molecules, respectively. The system of two boxes is at a uniform temperature T, and the usual periodic boundaries are used with each box to minimize surface effects. The simulation requires three kinds of trial moves [9], which are designed to achieve (a) internal thermal equilibrium in each box through the usual Monte Carlo molecular moves, (b) mechanical equilibrium through equality of pressures between the two phases, by changing the volumes of the two phases (keeping the total volume of the two phases constant), and (c) chemical equilibrium via equality of chemical potential between phases, through molecule exchange between the two boxes. The derivation of the GEMC method is given in detail by Smit et al. [10], and the implementation of the method, programming considerations and applications have been recently reviewed [5,6]. The merit of the method is its directness and resulting speed of computation; in particular it is not necessary to calculate the chemical potentials, and the molecules do not have to diffuse across a physical interface in order for the system to reach equilibrium. The method is particularly attractive for mixture phase equilibria, where the indirect methods become tedious. The main limitation is the difficulty in making the molecule transfer step at high densities; this problem becomes more pronounced if the molecules are highly nonspherical in their interactions, and is acute for polymers. This limitation is shared by many of the other methods for calculating phase equilibria described below. The difficulty can be largely overcome by various biased sampling methods for liquids, but so far the method has not been successfully applied to solids or liquid crystals.

Applications of the method to pure fluids and mixtures up to 1995 have been reviewed [5,6]. Studies of vapor-liquid equilibria in pure fluids of more

complex molecules have included the restricted primitive model of a 1:1 electrolyte (charged hard spheres of equal diameter and unit charge) [11], and chain molecules [12,13]. The usual sampling methods fail for chain molecules, and it is necessary to bias the sampling in a way that 'looks' for available space (see section below).

For mixtures, the method has been applied to high pressure fluid phase equilibria in hydrogen-helium mixtures [14]. Further calculations for this system have been made to 2500 K and 700 kbar [15]. Agreement with the existing experimental data is good. These studies provide a further example of the use of these methods to extrapolate existing data into regions that are difficult to reach experimentally. An application to a more complex mixture has been made for water with methanol [16]. The SPC (simple point charge) model was used for water, and OPLS (optimized potential for liquid state) for methanol with potential parameters taken from the literature and used without adjustment. The compositions of the two phases agree with experimental data within a few percent.

2.2   Indirect Methods

An alternative to the Gibbs ensemble MC method is to calculate the free energy or chemical potentials for a range of state conditions. The phase transition conditions can then be determined by the usual methods of Gibbs thermodynamics. Such methods are called indirect ones; they involve more computational effort than the Gibbs method, in general. However, they are useful because: (a) one often wants to know the values of the chemical potentials, e.g. in studying surface phase transitions or conformational changes (the Gibbs method does not yield the chemical potential unless special steps are taken in coding), and (b) the Gibbs method (and some of the indirect methods) fails for high densities because of the molecule insertion step. This is particularly the case for liquid crystals and solids.

These indirect methods include the test particle method, Grand Canonical Monte Carlo (GCMC), modified sampling methods, and thermodynamic integration over states. They have been reviewed elsewhere [2-6]. Both the test particle and GCMC methods involve attempts to insert a molecule into the fluid, and so suffer from the same difficulty as the Gibbs ensemble MC method at high densities. In the modified sampling methods an attempt is made to overcome this problem by modifying the MC sampling procedure, so that the probability of successful insertion attempts is greatly increased. The aim of these methods is to try to find the 'holes' in the fluid and put the molecule there.

Of particular importance is the use of histogram reweighting methods. This method, due to Ferrenberg and Swendsen [17], can be applied in a variety of ensembles, but is most often used in the Grand Canonical Monte Carlo (GCMC) method, in which chemical potential, volume and temperature (μ, V and T) are the independent variables that are fixed in the simu-

lation. In this ensemble, the number of molecules, N, and the energy of the system, U, fluctuate. The essence of Ferrenberg and Swendsen's method is to construct a histogram of the distribution of N and U during the course of the simulation, and thus determine the distribution function $f(N,U)$ at the state condition (μ, V, T). From this distribution function it is possible to calculate the thermodynamic average of any property $X(N,U)$, including the grand partition function itself, and hence the grand free energy. Moreover, once $f(N,U)$ is known at a given state condition (μ, V, T), it is possible to calculate any property $X(N,U)$, including free energy, at all other state conditions (μ', V, T') [17,18]. Thus, in principle, one long GCMC run should be sufficient to obtain the complete phase diagram for the system. In practice it is usually necessary to carry out several runs at different (μ, V, T) values in order to obtain $f(N,U)$ with sufficient accuracy over the range of N and U needed. Weighting or biasing is frequently used in order to improve the statistics in regions of phase space that are important in the desired averages. Histogram reweighting has been used to determine the vapor-liquid coexistence curve for polarizable Stockmayer fluids [18], polarizable water models [19,20], and carbon dioxide-water mixtures [19]. It can also be applied in other MC ensembles, including the Gibbs [19] and semi-grand ensemble [21].

For the most difficult systems, e.g. liquid crystals and solids, thermodynamic integration may be necessary. This involves making a series of simulations for a range of thermodynamic temperatures, densities or intermolecular potentials, and then integrating over thermodynamic states using standard thermodynamic or statistical mechanical equations to obtain the chemical potential [4,6]. An alternative procedure is to calculate the Landau free energy as a function of some order parameter, Φ [22,23]. The probability $P(\Phi)$ of observing the system with an order parameter value between Φ and $\Phi + d\Phi$ is determined in the simulation, and assumes a bi-modal distribution when two phases are in coexistence. The Landau free energy is obtained from this probability distribution, and subsequent integration of this over the order parameter gives the grand free energy. The success of this method hinges on an appropriate choice of order parameter; the order parameter is a density variable or rotational invariant that takes on distinctly different values in different phases of the system. It has been used to study the fluid-solid phase transition for simple fluids and metals [24,25].

To obtain a complete phase diagram it is often necessary to employ several simulation techniques for different parts of the phase diagram. For the Gay-Berne model of a liquid crystal [26], for example, the vapor-liquid region was determined by the Gibbs ensemble MC method; isotropic liquid-nematic transitions were determined by thermodynamic integration and the remaining transitions were found approximately from order parameters (orientational correlation parameter P_2, tilt angle ϕ and heat capacity C_v).

The extension of some of these methods to chain molecules in the last few years has sparked particular interest. Two approaches have been put forward,

the *chain increment method* and the *configurational bias MC method*. The *chain increment method*, proposed by Kumar et al. [27], is based on a test particle equation that gives an exact expression for the incremental chemical potential for adding a monomer unit to a chain molecule. This increment is found to become essentially constant for chains longer than about 10-20 mers. If this limiting value is determined, and also the chemical potential for a relatively short chain, it is possible to calculate the chemical potential for long chains. The method has been applied [28] to obtain the phase diagram for a polymer melt of chains of length up to 100 mers. The chain increment method has the advantage that it can be applied to arbitrarily long chains.

The configurational bias MC method [29-31] involves the insertion of a short chain into the fluid, followed by the addition of other segments to the end of the chain until a chain of the desired length has been grown. The chain configuration is chosen by a suitable weighting process, using another modified test particle equation. The method can be used in Gibbs ensemble simulations to obtain phase equilibria directly. It has been used to study alkanes [30], and also alkanes dissolved in polyethylene and in supercritical solvents [29].

3   Confined fluids and solids

A fluid confined within a porous material can exhibit a variety of phase transitions. Such transitions are of two general types, those that also occur in the bulk phase but are modified in the pore by finite size effects and the strong fluid-wall forces (e.g. melting, condensation, liquid-liquid equilibria, etc.), and new transitions that arise solely from the fluid-wall forces (e.g. wetting, layering transitions). The methods used to study phase transitions in bulk fluids are, with little modification, suitable for investigation of phase transitions in pores. However, long-lived metastable states are often a more serious problem in confined systems. These lead to hysteresis effects in many cases, the state condition at which the transition occurs being different depending on the direction from which the transition is approached. The determination of the true thermodynamic transition point will often require the calculation of the free energy or chemical potential. Phase transitions that have been studied rather extensively by simulation are capillary condensation (condensation from vapor to liquid inside the pore; this usually occurs at a pressure much below the normal vapor pressure), wetting (the point at which the liquid just wets the surface, i.e. the contact angle becomes zero), and layering transitions (transitions between low coverage and a full monolayer, between a full monolayer and two full layers, and so on). The melting transition, liquid-liquid separation for mixtures, and solubility of dilute components in a solvent have received less attention from the simulation community, but are the subject of current investigations.

Care is needed in defining exactly what is meant by a 'phase transition' in a pore. In cylindrical pores, for example, the molecular correlation length can grow to infinity along the axis of the cylinder, but is restricted to the pore diameter in the other two dimensions. Such a fluid does not have a true critical point in the usual sense. Nevertheless, in such a system there are often two states of distinctly different density and structure having the same free energy or chemical potential, and sharp changes occur between these two states.

We first briefly consider the most commonly used methods, followed by a brief discussion of the main types of transition. More extensive reviews of phase separation in porous materials are available [32,33]

3.1 Methods

Phase equilibria in pores, and also the equilibrium between the porous medium and the bulk phase, are governed by equality of temperature and the chemical potential of each component between the various phases. Pressure equality is not a requirement since pressure in confined systems is a tensor.

The GCMC method has been widely used to determine adsorption isotherms, heats of adsorption, and phase transitions in pores. The method (like the GEMC method) runs into difficulties with the molecule insertion step at high densities. This difficulty, which is more pronounced for significantly non-spherical molecules, can be overcome by using a biased sampling method [2-6], which attempts to insert the molecules into 'holes' in the fluid, thus improving the chance of successful insertion; the effects of such biasing on the statistical sampling is removed at a later stage. A further difficulty with GCMC (and some other methods) is that hysteresis is found in the calculation of adsorption isotherms where phase transitions occur. Thermodynamic integration can be used to determine the true transition point [34,35]. This method has been used by Peterson et al. [34,35] to determine capillary condensation lines.

Molecular dynamics (MD) simulations can be used to observe the interfaces in the pore between coexisting phases, and so have this advantage over the GCMC method. One procedure that has proved successful [34,36] involves first equilibrating the fluid in the pore at a high temperature, above the critical point in the case of gas-liquid or liquid-liquid transitions (or above the range in which the transition of interest occurs in other cases). The simulation is then stopped, the velocities of all the molecules scaled back by a constant factor (chosen to correspond to a suitably lower temperature), and then restarted. The new molecular velocities correspond to a temperature inside the spinodal region for the two phase region of interest. The fluid in the pore will then separate into the two phases. In general, mechanical equilibrium is quickly reached, whereas chemical equilibrium takes at least one order of magnitude longer, because of the slow diffusion in the dense phases. This quench MD method has the advantage of providing dynamic information about diffusion in the pore and the kinetics associated with the

phase separation. Moreover it provides a clear picture of the interface itself, something that cannot be easily studied in the laboratory.

Other methods have proved valuable for special cases. For example, the semi-grand ensemble MC method is useful for the study of phase equilibria in dense fluid mixtures [21]; in this method there is no particle insertion step, but rather a species exchange, which is tolerated more easily at high densities. Thermodynamic integration methods for studying fluid-solid transitions usually fail for confined systems, because adsorbed layers near the wall of the pore freeze at a different point than the adsorbate in the pore interior. Order parameter methods are usually preferable for such studies [37].

3.2   Capillary Condensation and Layering Transitions

Since about 1986 there have been numerous simulation studies of capillary condensation in pores of simple geometry, e.g. slits and cylinders, and several studies of layering transitions. More recently, there have also been studies of capillary condensation in more complex and realistic pore structures [e.g. 38,39]. These are too numerous to review here, but a cross-section of examples of studies of this type can be found in the proceedings of the International Conferences on the Fundamentals of Adsorption, held every few years [40]. Most of these simulations have employed the GCMC method, but several use either Gibbs Ensemble MC or Quench MD.

Studies of the gas-liquid coexistence behavior (temperature vs. density) in narrow pores show that the coexistence curve is considerably narrower than for bulk fluids, and the critical point is lowered. The narrowing of the coexistence region occurs because the 'gas' phase in the pore usually consists of several layers of adsorbed fluid molecules on the pore walls, with a gas-like phase in the interior of the pore; since the adsorbed layers have a liquid-like density, the overall density in the pore is relatively high. The liquid side of the coexistence curve has a density similar (usually somewhat higher) to that of the bulk liquid. The lowering of the critical temperature in the pore is expected since the average coordination number, Z, of fluid molecules in the pore will be lower than that of the bulk liquid (because an appreciable fraction of molecules are near the wall). Mean field theory predicts that the critical temperature is proportional to Z.

3.3   Liquid-Liquid Equilibria

Simulation studies of liquid-liquid separation in pores have been reported for a simple Lennard-Jones mixture in which the unlike pair interaction is weak [21,41-43]. This is the simplest model for such phase separation. Recent simulations have been made using semi-grand ensemble MC with histogram reweighting to obtain the liquid-liquid coexistence curves [21]. The critical mixing temperature is lowered as for the vapor-liquid case, and the coexistence curve (temperature vs. composition) is shifted towards the side of the

component that more strongly wets the pore walls. These qualitative features agree with experiment. In addition to these equilibrium studies, the kinetics of phase separation has been studied using quench MD simulations [43], and the power laws governing the growth of the phases has been determined for simple geometries.

3.4 Melting/Freezing Transitions

Freezing and melting transitions in pores are of importance in frost heaving, in the distribution of pollutants in soils, in the manufacture of nanomaterials, and in several other manufacturing processes. Simulation studies, using GCMC and MD, have been made to study the melting and freezing of Lennard-Jones methane in both slit [37,44,45] and cylindrical [46] pores. Large hysteresis loops are found on heating or cooling, and it is necessary to calculate the free energies in order to determine the true melting point. Since adsorbed layers near the wall melt at different temperatures to adsorbed material in the inner parts of the pore, the usual thermodynamic integration methods cannot be used. Instead, order parameter methods have proved successful [37]. The freezing transition is found to be first order. For weakly adsorbing walls, such as silicas and oxides, the melting temperature in the pore is lower than that in the bulk. For carbons, however, the melting temperature is generally higher than the bulk value, and this effect is particularly marked for slit pores, since the molecules can more readily form the necessary lattice.

4 Conclusions

For fluid phase transitions the Gibbs ensemble MC and histogram reweighting methods are particularly useful. For transitions involving solid phases the order parameter method for obtaining free energies is likely to emerge as an important technique. Current research is likely to focus on applying and extending these methods to difficult systems such as ionic fluids, associating and reacting liquids, liquid crystals, polymers and surfactants. In the case of confined systems, applications to more realistic and complex pore geometries will be emphasized. A persistent problem in such work remains the determination of sufficiently accurate intermolecular potentials for prediction of phase equilibria in real systems.

References

1. Allen, M.P. and Tildesley, D.J., "Computer Simulation of Liquids", p. 49, Clarendon Press, Oxford (1987).

2. Mezei, M. and Beveridge, D.L., *Ann. New York Acad. Sc.*, vol. 482 (1987), p. 1.
3. Gubbins, K.E., *Mol. Simulation*, vol. 2 (1989), p. 223.
4. Frenkel, D. and Smit, B., "Understanding Molecular Simulation", Academic Press, San Diego (1996).
5. Panagiotopoulos, A.Z., in "Observation, Prediction and Simulation of Phase Transitions in Complex Fluids", ed. M. Baus et al., p. 463, Kluwer Academic (1995).
6. Gubbins, K.E., in "Models for Thermodynamic and Phase Equilibrium Calculations", ed. S.I. Sandler, Dekker, New York, pp. 507–600 (1994).
7. Gubbins, K.E. and Quirke, N., in "Molecular Simulation and Industrial Applications", ed. K.E. Gubbins and N. Quirke, pp. 1–70, Gordon and Breach, Amsterdam (1996).
8. Price, S.L. in "Computer Simulation in Materials Science", eds. M. Meyer and V. Pontikis, Kluwer Academic, Dordrecht (1991).
9. Panagiotopoulos, A.Z., *Mol. Phys.*, vol. 61 (1987), p. 813; a more detailed derivation is given in A.Z. Panagiotopoulos, N. Quirke, M. Stapleton and D.J. Tildesley, *Mol. Phys.*, vol. 63 (1988), p. 527.
10. Smit, B., de Smedt, Ph. and Frenkel, D., *Mol. Phys.*, vol. 68 (1989), p. 931.
11. Panagiotopoulos, A.Z., *Fluid Phase Equilibria*, vol. 76 (1992), p. 97; Orkoulas, G. and Panagiotopoulos, A.Z., *J. Chem. Phys.*, vol. 101 (1994), p. 1452; Calliol, J.M., *J. Chem. Phys.*, vol. 100 (1994), p. 2161.
12. Mooij, G.C.A.M., Frenkel, D. and Smit, B., J. Phys.: *Cond. Matter*, vol. 4 (1992), p. L255; Siepmann, J.I., Karaborni, S. and Smit, B., *Nature*, vol. 365 (1993), p. 330.
13. Laso, M., de Pablo, J.J. and Suter, U.W., *J. Chem. Phys.*, vol. 97 (1992), p. 2817.
14. De Kuijper, A., Smit, B., Schouten, J.P. and Michels, J.P.J., *Europhysics Lett.*, vol. 13 (1990), p. 679.
15. Schouten, J.A., de Kuijper, A. and Michels, J.P.J., *Phys. Rev. B: Cond. Matter*, vol. 44 (1991), p. 6630.
16. Strauch, H.J. and Cummings, P.T., *Fluid Phase Equilibria*, vol. 83 (1993), p. 213.
17. 17. Ferrenberg, A.M. and Swendsen, R.H.: *Phys. Rev. Lett.*, vol. 61 (1988), p. 2635.
18. Kiyohara, K., Gubbins, K.E. and Panagiotopoulos, A.Z.: *J. Chem. Phys.*, vol. 106 (1997), pp. 3338–3347.
19. Errington, J.R., Kiyohara, K., Gubbins, K.E. and Panagiotopoulos, A.Z.: *Internat. J. Thermophys.*, in press (1998).
20. Kiyohara, K., Gubbins, K.E. and Panagiotopoulos, A.Z.: *Molec. Phys.*, vol. 94 (1998), pp. 803–808.
21. Gelb, L.D. and Gubbins, K.E.: *Physica*, vol. 244 (1997), pp. 112–123.
22. Landau, L.D. and Lifshitz, E.M.: *Statistical Physics*, 3rd edn., Pergamon Press, London (1980).
23. Chaikin, P.M. and Lubensky, T.C.: *Principles of Condensed Matter Physics*, Cambridge University Press, Cambridge (1995).
24. Van Duijneveldt, J.S. and Frenkel, D.: *J. Chem. Phys.*, vol. 96 (1993), p.4655.
25. Lynden-Bell, R.M., van Duijneveldt, J.S. and Frenkel, D.: *Mol. Phys.*, vol. 80 (1993), p. 801.
26. De Miguel, E., Rull, L.F., Chalam, M.K. and Gubbins, K.E.: *Mol. Phys.*, vol. 74 (1991), p. 405.

27. Kumar, S.K., Szleifer, I. and Panagiotopoulos, A.Z.: *Phys. Rev. Lett.*, vol. 66 (1991), p. 2935; Kumar, S.K., *J. Chem. Phys.*, vol. 96 (1992), p. 1490; Szleifer, I. and Panagiotopoulos, A.Z.: *J. Chem. Phys.*, vol. 97 (1992), p. 6666.
28. Panagiotopoulos, A.Z. and Szleifer, I.: *Polymer Preprints*, vol. 33 (1992), p. 547; Sheng, Y.-J., Panagiotopoulos, A.Z., Kumar, S. and Szleifer, I.: *Macromolecules*, vol. 27 (1994), p. 400.
29. De Pablo, J.J., Laso, M. and Suter, U.W.: *J. Chem. Phys.*, vol. 96 (1992), p. 2395, 6157; de Pablo, J.J., Laso, M., Suter, U.W. and Cochran, H.D.: *Fluid Phase Eqba.*, vol. 83 (1993), p. 323.
30. Siepmann, J.I. and Frenkel, D.: *Mol. Phys.*, vol. 75 (1992), p. 59; Frenkel, D. and Smit, B.: *Mol. Phys.*, vol. 75 (1992), p. 983.
31. Frenkel, D., Mooij, G.C.A.M. and Smit, B.: *J. Phys.: Cond. Matter*, vol. 4 (1992), p. 3053.
32. Gubbins, K.E., Sliwinska-Bartkowiak, M. and Suh, S.-H.: *Molec. Simulation*, vol. 17 (1996), p. 333.
33. Gelb, L.D., Gubbins, K.E., Radhakrishnan, R. and Sliwinska-Bartkowiak, M.: *Reports Progr. Phys.*, submitted (1998).
34. Peterson, B.K., Gubbins, K.E., Heffelfinger, G.S., Marini Bettolo Marconi, U. and van Swol, F.: *J. Chem. Phys.*, vol. 88 (1988), p. 6487.
35. Peterson, B.K. and Gubbins, K.E.: *Mol. Phys.*, vol. 62 (1987), p. 215.
36. Heffelfinger, G.S., van Swol, F. and Gubbins, K.E.: *Mol. Phys.*, vol. 61 (1987), p. 1381.
37. Radhakrishnan, R. and Gubbins, K.E.: *Mol. Phys.*, in press (1999).
38. Page, K.S. and Monson, P.A.: *Phys. Rev. E*, vol. 54 (1996), p. 6557.
39. Gelb, L.D. and Gubbins, K.E.: *Langmuir*, vol. 14 (1998), pp. 2097-2111.
40. See *Fundamentals of Adsorption: Proceedings of the Sixth International Conference on Fundamentals of Adsorption*, ed. F. Meunier, Elsevier, Paris (1998).
41. Gózdz, W.T., Gubbins, K.E. and Panagiotopoulos, A.Z.: *Mol. Phys.*, vol. 84 (1995), p. 825.
42. Kierlik, E., Fan, Y., Monson, P.A. and Rosinberg, M.L.: *J. Chem. Phys.*, vol. 102 (1995), p. 3712.
43. Gelb, L.D. and Gubbins, K.E.: *Phys. Rev. E*, vol. 56 (1997), p. 3185-3196.
44. M. Miyahara and K.E. Gubbins: *J. Chem. Phys.*, vol. 106 (1997), p. 2865-2880.
45. H. Dominguez and R. Evans: *Mol. Phys.*, vol. 96, 209–229 (1999).
46. M.W. Maddox and K.E. Gubbins: *J. Chem. Phys.*, vol. 107 (1997), pp. 9659-9667.

Efficient Bifurcation Analysis of Forced Periodic Processes

Dan Luss[1] and Johannes Khinast[2]

[1] Department of Chemical Engineering,University of Houston, Houston, TX 77204-4792, USA, dluss@uh.edu
[2] Department of Chemical and Biochemical Engineering, Rutgers University, Piscataway, NJ 08854-8058, USA, khinast@sol.rutgers.edu

Abstract. A numerically efficient procedure is described for computing the loci of bifurcation points separating parameter regions with qualitatively different dynamics and bifurcation diagrams of spatially distributed and periodically forced processes. The numerical method combines shooting, Broyden's Jacobian update, continuation and direct Fréchet differentiation of the PDEs describing the system. The reverse-flow reactor is used to illustrate the application of the numerical procedure.

1   Introduction

In several chemical processes, reactors are operated periodically to exploit the improved performance during transient operation. Typically, the feed conditions (flow rate, concentration, pressure, etc.) are periodically changed. In some cases the periodic operation is achieved only by reversing the flow direction of a constant feed source at fixed intervals, i.e., by using a *reverse-flow* operation. In pressure and temperature swing adsorption (PSA, TSA) [20]; [2]; [12], different steps (adsorption, desorption, purge, etc,) are used to separate gases with different adsorption affinities and/or kinetics. In a reverse-flow reactor (RFR) the slow motion of the temperature wave (relative to that of the gas) is used to trap a hot zone within the reactor. [14] reviewed various industrial applications of the RFR.

   Early studies of periodically forced operations used dynamic simulations to determine the periodic states. These methods are numerically inefficient as the (pseudo-steady) periodic states are typically attained only after several hundreds to thousands of cycle periods. To overcome this deficiency, *direct determination* of these states may be used, i.e., requiring the state variables at the end and beginning of a cycle to be identical, i.e., $u(0) = u(t_c)$, where u denotes the state variables and t_c is the cycle period. This transforms the initial value problem solved by dynamic simulation into a temporal boundary-value problem solvable by Newton-based methods. A special feature of reverse-flow reactors is the fact that the temperature profiles at the beginning and the end of a flowing period are symmetric. [5] suggested to directly determine the periodic states by forcing the temperature profiles at the beginning and

end of each semi-cycle (half cycle) to be mirror images of each other, i.e., $u(0, x) = u(t_c/2, L - x)$, where x is the spatial variable and L the length of the fixed bed. This requires integration of the model equations only over half a cycle (semi-cycle).

In practice, it is important to know the various types of qualitatively different dynamics and the possible coexistence of multiple periodic states. In addition, it is important to know the bifurcation loci, at which qualitative changes in the dynamic features occur. We describe here the mathematical and numerical techniques, which enable a detailed bifurcation analysis and prediction of these transitions.

A *bifurcation diagram* shows the dependence of a state variable on a parameter. Bifurcation diagrams are qualitatively similar when the number, order, and orientation of the solution is changed in an identical way upon a continuous change in the bifurcation variable λ. We consider a system $g(u, \lambda, p) = 0$, in which p is a vector of parameters and restrict the treatment to cases in which g is a single-valued function of u and λ within the feasible region and the branches of the solution neither intersect nor have limit points on the u and λ boundaries. For convenience we omit p in the future notation. A typical bifurcation diagram of the maximum reactor temperature in a cycle versus the cooling capacity is shown in Fig.1. The model used to generate the diagram is presented in section 5.
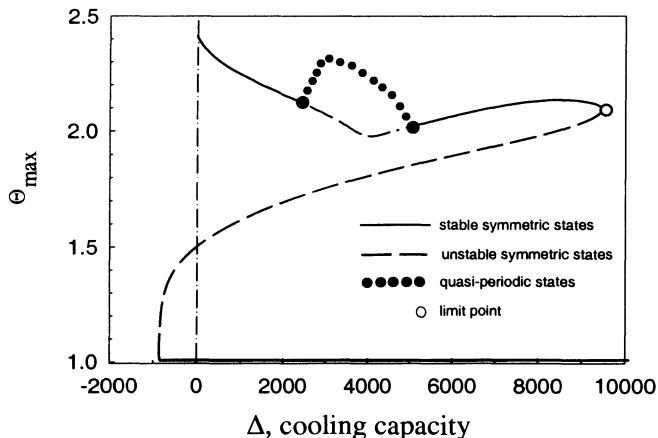
Fig. 1. Typical dependence of the maximum RFR temperature Θ_{max} on the cooling capacity Δ.

2   Transitions between qualitatively different multiplicity features

Multiple periodic states are frequently encountered in periodic operations, e.g., in PSA and reverse flow operation. The boundaries of parameter regions containing bifurcation diagrams with qualitatively different multiplicity features may be determined by application of the singularity theory with a distinguished parameter, developed by [4]. We follow the scheme used by [19] of solving simultaneously the model equations and the defining conditions obtained by a Liapunov-Schmidt reduction [4].

Regions with qualitatively different multiplicity features are separated by three surfaces (*varieties*). Typically, two limit points coalesce upon crossing a *hysteresis variety*, at which a transition between n and n+2 periodic states occurs. An isolated branch of solutions appears (or disappears) upon crossing an isola variety. Crossing of either the hysteresis or the *isola variety* typically changes by two the number of limit points of the bifurcation diagrams. Crossing a *double limit variety* typically changes the relative positions of two limit points in the bifurcation diagrams. In Fig.2 a schematic of these three varieties are shown. For example, the defining conditions of a hysteresis variety of $g(u, \lambda) = 0$ are:
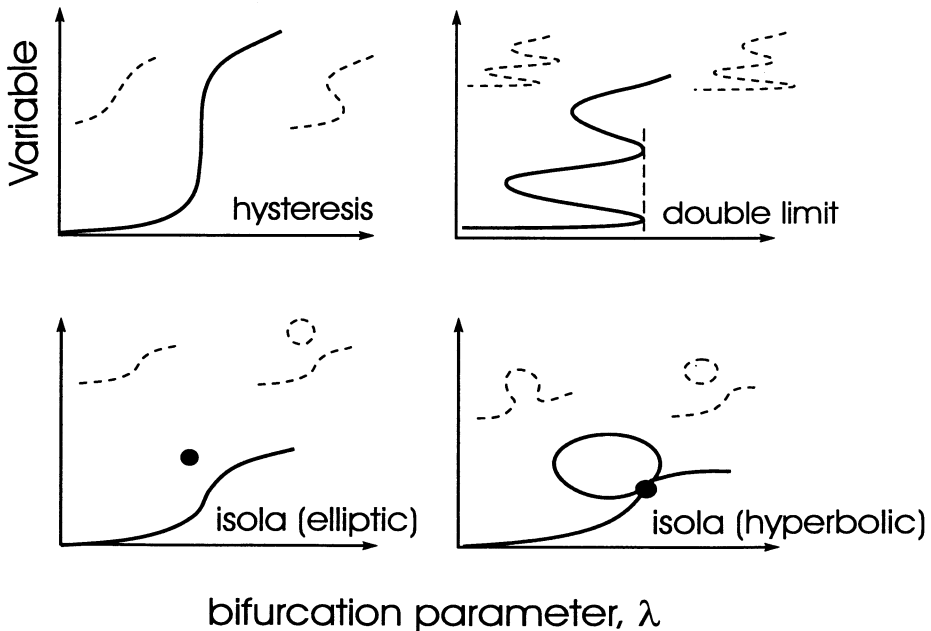
Fig. 2. The bifurcation diagrams (solid lines) and their unfoldings (dashed lines) for a set of parameters on the hysteresis, double limit and isola variety.

$$g(u, \lambda) = 0 \tag{1}$$

$$Lv = D_u g \cdot v = 0 \tag{2}$$

$$L^* y = 0 \tag{3}$$

$$< y, D_{uu}^2 g \cdot (v, v) >= 0, \tag{4}$$

where $D_u g \cdot v$ and $D_{uu}^2 g \cdot (v, v)$ are the first and second Fréchet derivatives of g, u is the vector of the state variables, v and y are the eigenvector and adjoint eigenvector corresponding to the zero eigenvalue of the linearization operator $D_u g$. Eq. (4) defines the second derivative of the branching equation, which has to vanish at the hysteresis variety.

The linearization Lv can be determined by computing the Jacobian matrix J of the discretized model equations g followed by a numerical estimation of eigenvectors and eigenvalues. However, we circumvent this tedious computational task by direct Fréchet differentiation of $g(u, \lambda)$, which yields a set of equations similar in structure to the model equations. Thus, we do not compute J but only the product of J v, which is equal to $D_u g$ v. This direct linearization by Fréchet differentiation significantly reduces the numerical effort associated with determining the different varieties. The details of this procedure are presented in a separate paper [10].

Since the eigenvectors are defined except for a multiplicative constant, we have to specify a norm of the eigenvector. We use

$$\langle v, y \rangle = 1. \tag{5}$$

This normalization condition avoids obtaining the trivial solution $v = y = 0$ for both eigenvectors. The adjoint problem $L^* y$ may be determined by the Lagrangian identity

$$\langle Lv, y \rangle = \langle v, L^* y \rangle. \tag{6}$$

The above set of $3n + 2$ equations determines the $3n$ variables, (u, y, v), λ and a parameter p_1 in p. The hysteresis can then be continued with respect to a third parameter p_2. The defining conditions of the isola and double-limit variety are reported by [4], [19] and [8].

3   Numerical bifurcation analysis

We consider here cases in which $g(u, \lambda)$ is a set of periodically forced, coupled, non-linear PDEs. Then, the linearization and the adjoint problem are a set of linear PDEs and Eqs. (4) and (5) are integral conditions. The set of defining conditions may be solved by various numerical schemes, such as a *shooting* technique or discretization of both the spatial and temporal derivatives (*relaxation* method). We describe here a numerical method, which is

based on the shooting technique, using Broyden's method and Fréchet differentiation to avoid the numerically expensive calculations of the Jacobian matrix and its eigenvalues.

As an example the conditions of the hysteresis point are used. We discretize the spatial derivatives by finite differences (100 node points on a symmetric grid) and compute the integral terms in the defining conditions by a Gaussian quadrature. After spatial discretization the defining conditions form a differential-algebraic (DA) system of first order. Since the conditions are periodic they may be solved by requiring the solutions to be identical after one period (cycle). If U is the vector of all the discretized variables, e.g. (u, v, y), we define an algebraic set of *residual function* as

$$f(U, \lambda) = U_0(t = 0) - U(t = t_c) = 0, \tag{7}$$

where t_c is the cycle period. In order to evaluate $U(t_c)$ the differential-algebraic system has to be integrated over one cycle using U_0 as the initial condition. We use LIMEX [3] with a relative tolerance of $5 \cdot 10^{-7}$ to integrate the DA system in time (shooting in time). If the residual function and Eqs. (4) and (5) vanish, the defining conditions of a singular point or variety are satisfied. Usually, a Newton-based method is used to iteratively determine these solutions. For an RFR the mirror symmetry over a half cycle may be used as the defining condition rather than integrating over a full cycle.

We use *pseudo-arc length continuation* to track the loci of the singularities as a function of a parameter p_2 [18]. If U is the vector of all spatially discretized variables, e.g. (u, v, y), the set of defining conditions, i.e., Eqs. (4), (5) and (7) are augmented by the single equation

$$|U - U_{old}|^2 + (\lambda - \lambda_{old})^2 + \sum_i^2 (p_i - p_{i,old})^2 = s^2, \tag{8}$$

where λ is the bifurcation parameter and p_2 the continuation parameter. In Eq. (8) s is a user-defined step size and the subscript "old" denotes the previous continuation step. For example, the final set of algebraic equations defining the hysteresis variety are:

$$G(X) = \begin{pmatrix} g(u, \lambda) \\ Lv \\ L^*y \\ \langle y, D_{uu}^2 g \cdot (v, v) \rangle \\ \langle v, y \rangle - 1 \\ s^2 - |U - U_{old}|^2 - (\lambda - \lambda_{old})^2 - \sum_{i=1}^2 (p_i - p_{i,old})^2 \end{pmatrix} = 0 \tag{9}$$

$$U = (u, v, y)^T, X = (U, \lambda, p_1, p_2)^T.$$

Note, that u, v, and y are spatially discretized. Eq. (9) is a nonlinear problem in X. It may be solved by a Newton method. In our calculations we use $N = 100$ node points and the maximum number of state variables M is 12, so that we have at most $(N \cdot M + 3) = 1203$ residual equations. Thus, inverting of the Jacobian matrix of G needed in the Newton method is inexpensive. Since no analytical solution of the Jacobian matrix exists, a finite-difference method may be used for its numerical approximation. However, this is very expensive since it requires integration of the defining conditions 1203 times over one cycle. To avoid the need for repeated calculations of the Jacobian we use Broyden's method [15], which updates the Jacobian matrix by

$$J_{[k]} = J_{[k-1]} + \frac{[(G_k - G_{k-1}) - J_{[k-1]} \cdot dX_k] \cdot dX_k^T}{dX_k^T dX_k}. \tag{10}$$

The use of Broyden's method requires two to three times more iteration steps than Newton's method to converge to the solution. However, it requires only *one* integration (function evaluation) per step, while Newton's method requires 1203 integrations. In general, for the start-up step the Jacobian matrix has to be determined. When the update strategy is embedded in the continuation scheme the Jacobian matrix of the preceding step may be used for the first iteration in the actual continuation step. Thus, the Jacobian matrix is estimated only once for the whole solution branch at the beginning of the continuation procedure. It should be noted that other quasi-Newton methods exist, e.g., the Davidson-Fletcher-Powell [15] or the Zontendijk formula, which may give better convergence for a specific problem.

The shooting method is more efficient than the relaxation method (discretization of temporal *and* spatial derivatives) since relaxation results in very large matrices that have to be inverted. For 80 node points in time, $M \cdot N \cdot 80 + 3 = 96,003$. Thus a sparse $96,003 \times 96,003$ matrix has to be inverted for each iteration step, which is very time consuming. The shooting method results in a matrix size of 1203×1203, and the computation of the Jacobian matrix is fast since Broyden's method is used. Additionally, accurate time integration may be obtained by using a standard IVP-solver. The relative numerical advantage of our numerical approach increases as the number of state variables in the model and/or the number of spatial node points increases. For example, when the various varieties of the RFR were computed a speed-up of at least 5 was obtained by using the shooting method.

4   Dynamic Bifurcations of Periodic Processes

Bifurcations from the periodic states may occur for critical parameter values. Examples are *stability loss*, a *bifurcation to period-n states, quasi-periodic* or even *chaotic* states. The stability of a periodic state is characterized by the spectrum of the eigenvalues of its *monodromy matrix* M, i.e., the matrix, which reflects the propagation of small perturbations over one cycle [1], [6].

Generically, a periodic state is stable, when the absolute value of every eigen-value (*Floquet multiplier*) of the monodromy matrix is smaller than unity. A periodic solution becomes unstable when at least one eigenvalue crosses the unit circle in the complex plane. Different bifurcations occur depend-ing on the angle, at which the eigenvalues cross the unit circle. In principle, it is possible to track the various bifurcations by repeatedly computing the monodromy matrix and its eigenvalues. The computation of the monodromy matrix may be implemented by perturbing each variable or by integration of the sensitivity equations [13]. Repeated computation of the monodromy matrix requires extensive computer capacity and time. This motivated us to develop an alternative method for tracking the dynamic bifurcations.

We define the periodic residual function of the state variables u (temper-atures, concentrations, etc.) as

$$F(u_o, \lambda) = u_0(t = 0) - u(t = t_c). \tag{11}$$

Eq. (11) has to vanish at a periodic orbit. The monodromy matrix and the Jacobian matrix of Eq. (11) are related by

$$M(u_0, \lambda_o) = \frac{\delta u_{k+1}}{\delta u_k} = I - J(u_0, \lambda_0) \tag{12}$$

Here δu_k denotes a small perturbation vector at the beginning of cycle k. Eq. (12) establishes a relation between the monodromy matrix and the Jacobian (linearization) of the residual equations. These relations are essen-tial for tracking the dynamic singular points, since the linearization may be determined by Fréchet differentiation.

We now discuss the individual bifurcations from the periodic states. At a limit point of a periodic state (saddle node bifurcation) one eigenvalue of M crosses the unit circle at $\mu = +1$. A period-1 solution undergoes a period doubling bifurcation when M has a $\mu = -1$ eigenvalue. When a conjugate complex pair of eigenvalues crosses the unit circle a quasi-periodic (two-torus) state is usually obtained. We denote this as a bifurcation to quasi-periodic solutions. Each of the described bifurcations satisfies the condition

$$Mv_0 = (I - J)v_0 = \mu v_0 \tag{13}$$

where

$$Re(\mu)^2 + Im(\mu)^2 = 1. \tag{14}$$

An eigenvector v_0 satisfying Eq. (13) can be found only at the bifurcation point under consideration. We rewrite Eq. (13) as

$$Jv_0 = (1 - \mu) \cdot v_0 \tag{15}$$

[8] proposed to use the fact that the product of the Jacobian matrix with its eigenvector can be determined by direct Fréchet differentiation of the residual equation, Eq. (11),

$$\boldsymbol{D_u F(u_0, \lambda) \cdot v_0 = J \cdot v_0 = v_0 - v}(t = t_c) \qquad (16)$$

Substitution of Eqs. (16) into (15) gives the final condition for a bifurcation from periodic states

$$\mu \boldsymbol{v_0 = v}(t = t_c). \qquad (17)$$

Additionally, a norm of $\boldsymbol{v_0}$ has to chosen, e.g. $\langle \boldsymbol{v_0, v_0} \rangle = 1$. $\boldsymbol{v}(t_c)$ can be obtained by integrating the linearized equations (Fréchet derivative of $\boldsymbol{g}$) in time using $\boldsymbol{v_0}$ as initial conditions. We iterate the solution until we find a $\boldsymbol{v_0}$, which satisfies Eq. (17) for the specific μ value of the corresponding bifurcation ($\mu = +1$ at limit point, -1 at period-doubling, $\mu_r + i \cdot \mu_i$ at a bifurcation to quasi-periodic solutions). This relation leads to significant computational saving in computing the loci of the various dynamic bifurcations. In order to find the bifurcation varieties we first compute a bifurcation diagram and the monodromy matrix at every n^{th} (n = about 20) continuation step in order to identify an approximate locus of the bifurcation. This information is then used to start-up a continuation procedure with Eq. (17) as a constraint. This procedure enables us to circumvent the extensive calculation of the monodromy matrix and its eigenvectors. The continuation procedure is much faster and requires less memory storage than one based on repeated computation of the monodromy matrix. In the examples reported later the speed up was at least one to two orders of magnitude.

In case of the RFR the symmetry within one half of the cycle leads to special bifurcations. Here the monodromy matrix may be defined for only half of the cycle and an eigenvalue of $\mu = -1$ corresponds to symmetry loss, i.e., a bifurcation to asymmetric solutions. (The profile at the end of a semi-cycle is not a mirror of that at the beginning of the semi-cycle, see Fig. 3b). Details are given in [9].

5   Example: The RFR

A reverse-flow reactor (RFR) is a forced periodic system in which the flow direction is periodically reversed to trap a hot zone within a packed-bed reactor. Heat losses frequently occur and if temperature limitations exist, the reactor has to be cooled. The RFR operates under conditions for which multiple periodic, asymmetric, quasi-periodic and chaotic states exist. The dimensionless energy and species balances and boundary conditions describing a single exothermic, first-order reaction occurring in a cooled RFR are [10]:
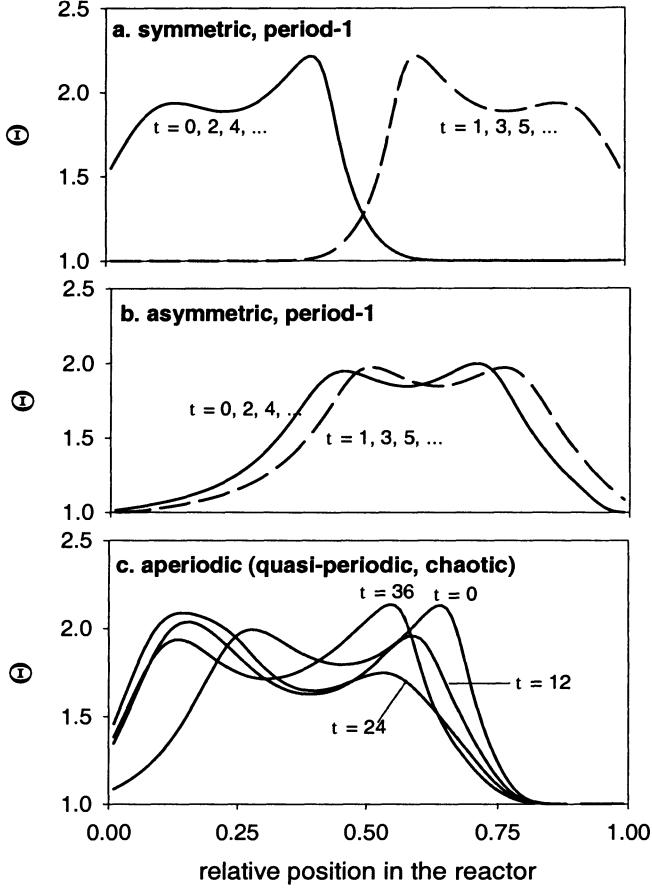
Fig. 3. Termperature profiles in the catalytic bed just before the flow direction is switched from the left to the right. a. Symmetric period-1 state, b. Asymmetric period-1 state, b. Aperiodic state (quasi-periodic, chaotic).

$$g(u) = \begin{pmatrix} \frac{1}{\zeta}\frac{\partial\Theta}{\partial\tau} - \frac{1}{Pe_h}\frac{\partial^2\Theta}{\partial\xi^2} + f\frac{\partial\Theta}{\partial\xi} - Da \cdot \beta \cdot B(\Theta) \cdot (1-x) + \Delta(\Theta - \Theta_c) \\ \frac{1}{Le}\frac{\partial x}{\partial\tau} - \frac{1}{Pe_m}\frac{\partial^2 x}{\partial\xi^2} + f\frac{\partial x}{\partial\xi} - Da \cdot B(\Theta) \cdot (1-x) \end{pmatrix} = 0 \tag{18}$$

The boundary conditions are:

$$\frac{\partial u}{\partial\xi} = Pe \cdot u \quad at \quad \xi = 0; \quad \frac{\partial u}{\partial\xi} = 0 \quad at \quad \xi = 1 \tag{19}$$

$$u(\tau = 0, \xi) = u(\tau = 1, 1 - \xi) \tag{20}$$

for the right flowing period. For the left flowing period the boundary conditions in space are flipped. At constant intervals, i.e., $\tau = 1, 2, 3 \ldots$, the flow direction is reversed. In Eqs. (18) - (20)

$$\boldsymbol{u} = \begin{pmatrix} \varTheta - 1 \\ x \end{pmatrix}, \boldsymbol{Pe} = \begin{pmatrix} Pe_h & 0 \\ 0 & Pe_m \end{pmatrix}, B(\varTheta) = \frac{a_\nu k_c exp\left\{\gamma \frac{\varTheta-1}{\varTheta}\right\}}{a_\nu k_c + k_\infty exp\left\{-\frac{\gamma}{\varTheta}\right\}}, \quad (21)$$

where $\varTheta$ and x are the dimensionless temperature and conversion, respectively. Pe_i are the Peclet numbers, k_c the mass transfer coefficient, k_∞ the rate constant, γ the dimensionless activation energy, β the dimensionless adiabatic temperature rise, and a_ν the specific surface area of the catalytic packing per m^3 reactor volume. A full cycle t_c consists of two flowing periods t_f. In dimensionless coordinates, $\tau = 1$ corresponds to $t = t_f$. The parameter values are the same as those used by [9]. Fréchet differentiation yields the linearized system:

$$\boldsymbol{Lv} = \begin{pmatrix} \frac{1}{\zeta}\frac{\partial v_1}{\partial \tau} - \frac{1}{Pe_h}\frac{\partial^2 v_1}{\partial \xi^2} + \frac{\partial v_1}{\partial \xi} - Da\beta \left[\frac{\partial B}{\partial \varTheta}v_1(1-x) - Bv_2\right] + \Delta v_1 \\ \frac{1}{Le}\frac{\partial v_2}{\partial \tau} - \frac{1}{Pe_m}\frac{\partial^2 v_2}{\partial \xi^2} + \frac{\partial v_2}{\partial \xi} - Da \left[\frac{\partial B}{\partial \varTheta}v_1(1-x) - Bv_2\right] \end{pmatrix} \quad (22)$$

$$\frac{\partial \boldsymbol{v}}{\partial \xi} = \boldsymbol{Pe} \cdot \boldsymbol{v} \quad at \quad \xi = 0; \quad \frac{\partial \boldsymbol{v}}{\partial \xi} = \boldsymbol{0} \quad at \quad \xi = 1. \quad \boldsymbol{v} = (v_1, v_2)^T \quad (23)$$

$$\boldsymbol{v}(\tau = 0, \xi) = \boldsymbol{v}(\tau = 1, 1 - \xi) \quad (24)$$

Both [16,17] and [8] found that for an adiabatic RFR a stability exchange occurs only at the limit points of the solution branches. The cooled RFR exhibits more interesting dynamic features, such as the existence of asymmetric states in which the profiles at the end of a semi-cycle are not mirror images of those at its beginning, and of quasi-periodic and chaotic states as shown in Fig. 3.

The bifurcation diagram of the dependence of the maximum RFR temperature on the cooling capacity Δ (Fig.1) describes such a stability change. The branch of the extinguished states emanates from a bifurcation point, with a negative cooling capacity so that an extinguished state exists for all $\Delta \geq 0$ values. An ignited state exists for all Δ smaller than that of the limit point. All states with negative Δ values have no physical meaning. Quasi-periodic states emanate from the ignited solution branch and exist in a bounded range of Δ-values.

The methods described in section 2, 3 and 4 were used to construct a map (Fig.4) of regions with qualitatively different dynamic states.
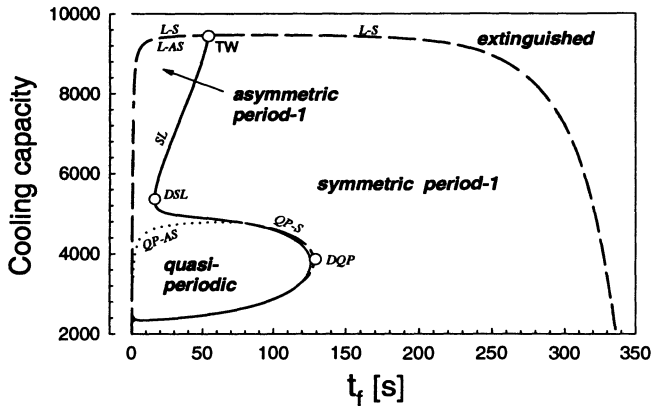
Fig. 4. Map of regions with qualitatively different dynamic behavior of an RFR. Boundaries are loci of codimension-0 singularities in the $\Delta - t_f$ plane. (SL = symmetric-loss, L-S = limit point of the symmetric solution, L-AS = limit point of the asymmetric solution, QP-S = quasi-periodic bifurcation of the symmetric solution, DQP = degenerate quasi-periodic bifurcation, DSL = degenerate symmetry-loss bifurcation, TW = twist bifurcation.

The boundaries separating regions with qualitatively different dynamic features are the loci of various codimension-1 singularities. The relevant bifurcations are:

(1) Limit points of symmetric states (L-S),
(2) bifurcation from symmetric to quasi-periodic states (QP-S),
(3) bifurcation from symmetric to asymmetric states (symmetry loss = SL),
(4) limit points of asymmetric states (L-AS), and
(5) bifurcation from asymmetric to quasi-periodic states (QP-AS).

In the case shown in Fig.4 an extinguished state exists for any t_f and cooling capacity. However, only an extinguished state is attained when either the cooling capacity exceeds a critical value or the flow reversal time is either very long or very short (extinguished region). The loci of the limit points of the symmetric (L-S) and asymmetric (L-AS) period-1 states bound a region in which the RFR has ignited states in addition to the extinguished ones. The period-1 symmetric states occupy the largest part of this region of feasible operation and are the only ignited states that exist when the cooling and heat loss are insignificant. However, when the reactor is cooled complex periodic and asymmetric states exist when the flow-reversal period is short relative to the time the temperature front needs to propagate through the reactor.

Asymmetric states exist for relatively high cooling capacities and short flow-reversal periods. The transition from symmetric to asymmetric states upon a decrease in t_f occurs via symmetry loss (SL) bifurcation. Quasi-periodic states exist for intermediate flow-reversal times and an intermediate level of cooling capacity. The symmetric period-1 states transform to quasi-periodic states usually via a quasi-periodic symmetric (QP-S) bifurcation. The asymmetric period-1 states transform to quasi-periodic states at a quasi-periodic-asymmetric (QP-AS) bifurcation. However, in some cases this transition is more intricate and consists of a sequence of several bifurcations [9].

Our calculations reveal a rather moderate change in the behavior of the RFR following a SL bifurcation. However, crossing the QP-S loci causes a rapid change in the qualitative dynamic features. The time series of the reactor center temperature (Fig. 5) illustrates such a sharp transition. While a period-1 symmetric state exists for t_f of 129 s, a complex quasi-periodic state is obtained for t_f of 127 s. Additional simulations show that for a limited range of parameters, chaotic states exist within the "quasi-periodic" window. The time series and Poincaré map of a chaotic attractor of a cooled RFR are shown in Fig. 6 [11]. We could not predict these transitions, as we do not know which bifurcation led to these transitions.
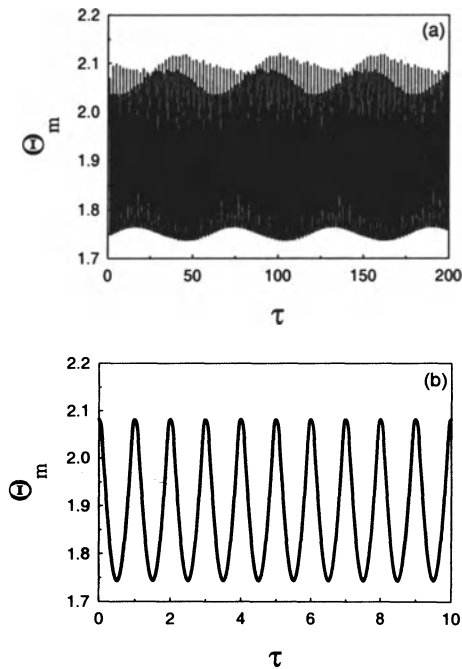
Fig. 5. Changes between symmetric period-1 to quasi-periodic behavior of the temperature at the center of the RFR upon crossing the QP-S bifurcation.
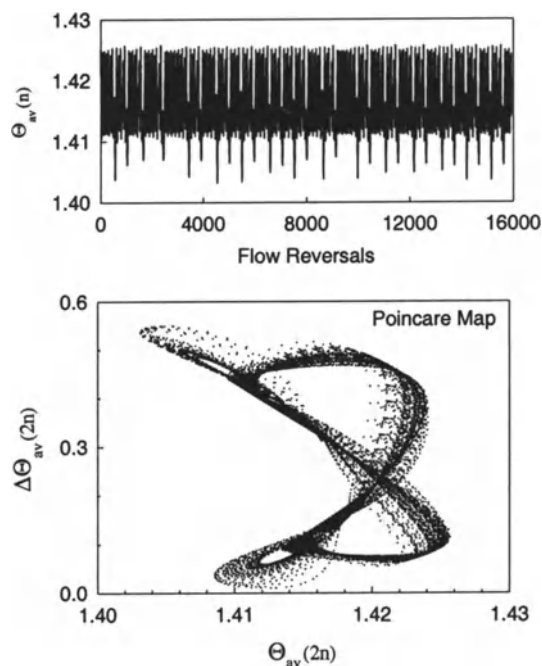
Fig. 6. Chaotic temporal reactor center temperature and corresponding Poincaré map of the RFR model.

6   Conclusions

The combination of direct Fréchet differentiation, continuation techniques, quasi-Newton and the shooting method was found to be an efficient technique in the numerical determination of the various varieties and dynamic bifurcations of periodic distributed parameter systems. The main numerical savings are due to the use of the Fréchet differentiation of the PDEs to avoid the lengthy computation of either the Jacobian or the monodromy matrix and its eigenvectors and the use of the Broyden update of the Jacobian matrix in the shooting method. While the technique was illustrated for the RFR, it may be applied to many other forced periodic processes.

References

1. Coddington, E. and Levinson, N., "Theory of Ordinary Differential Equations", Mc Graw-Hill, New York (1955)
2. Croft, D.T. and Levan, M.D., Chem. Eng. Sci., 49, 1821, 1831 (1994)
3. Deuflhard, P., Hairer E., Zugck J., "One-step and Extrapolation Methods for Differential-Algebraic Systems", Numer. Math 51, 1 (1987)
4. Golubitsky, M. and Schaeffer, D.G., "Singularities and Groups in Bifurcation Theory", Vol. 1. Springer, New York (1985)
5. Gupta, V. K. and Bhatia, S. K., "Solution of Cyclic Profiles in Catalytic Reactor Operation with Periodic Flow Reversal", Computers Chem. Engng. 15, 229–237 (1991)
6. Iooss, G. and Joseph, D.D., "Elementary Stability and Bifurcation Theory", Springer-Verlag, New York (1981)
7. Keller, H.B., "Numerical Solutions of Bifurcation and Nonlinear Eigenvalue Problems", Applications of Bifurcation Theory (ed. P.H. Rabinowitz), Academic Press, New York, 159–385 (1977)
8. Khinast, J., Luss, D., Mapping Regions with Different Bifurcation Diagrams of a Reverse Flow Reactor, AIChEJ., 43, 8, p.2034, (1997)
9. Khinast, J., Gurumoorthy, A., Luss, D., Complex Dynamic Features of a Cooled Reverse-Flow Reactor, AIChEJ.,44,5, p.1128, (1998b)
10. Khinast, J. and Luss, D., Efficient Computation of Singularities of High-Dimensional Models, Scientific Computing in Chemical Engineering, Hamburg, Springer Verlag, (1999)
11. Khinast, J., Jeong Y.O., Luss, D., Dependence of Cooled Reverse-Flow Dynamics on Reactor Model, AIChEJ., in press, (1999)
12. Kikkinides, E.S., Sikavitsas, V.I., Yang, R.T., Ind. Eng. Chem. Res. 34 255 (1995)
13. Leis J.R. and Kramer M.A., "Odessa - An Ordinary Differential Equation Solver with Explicit Simultaneously Sensitivity Analysis", ACM Trans. Math Software, 14(1), 61–67 (1988)
14. Matros, Yu.Sh. and Bunimovich, G.A., "Reverse-Flow Operation in Fixed Bed Catalytic Reactors", Cat. Rev. Sci. Eng. 38, 1 (1996)
15. Press, W.H., Teukolsky, S.A., Vetterling W.T., Flannery B.P., "Numerical Recipes in Fortran", Cambridge University Press Cambridge (1992)
16. Salinger, A. G. and Eigenberger, G., "The Direct Calculation of Periodic States of the Reverse-flow Reactor: 1. Methodology and Propane Combustion Results", Chem. Eng. Sci. 51, 4903–4913 (1996a)
17. Salinger, A. G. and Eigenberger, G., "The Direct Calculation of Periodic States of the Reverse Flow Reactor: 2. Multiplicity and Instability", Chem. Engng Sci. 51, 4915–4922 (1996b)
18. Seydel, R. and Hlavacek, V., "Role of Continuation in Engineering Analysis", Chem. Engng Sci. 42, 1281–1295 (1987)
19. Subramanian S. and Balakotaiah, V., "Classification of steady-state and dynamic behavior of distributed reactor models", Chem. Engng Sci. 51, 401–421 (1996)
20. Yang, R.T., Gas Separation by Adsorption Processes, Butterworth Press, 1987;

Mathematical Modeling of the Coupling of Chemical Kinetics With Flow and Molecular Transport

Ulrich Maas[1]

Institut für Technische Verbrennung, Universität Stuttgart, Pfaffenwaldring 12, 70569 Stuttgart, Germany

Abstract. Mathematical modeling of chemically reacting flows is complicated by the fact that the chemical kinetics typically involves a large number of chemical species leading to a high dimension of the governing equation system. We present methods which allow a simplification of the description of the chemical kinetics and its coupling with molecular transport and turbulent mixing. The methods are based on the observation that the chemical kinetics does not access the whole composition space, but it is confined to low-dimensional subspaces, the so-called intrinsic low-dimensional manifolds (ILDM). The reason is that the fast chemical processes introduce correlations between the species concentrations. These correlations can be extracted either by a direct mathematical analysis of the system of chemical rate equations or by an analysis of direct numerical simulation (DNS) data. Several examples of laminar and turbulent flame calculations which verify the approach are shown and discussed.

1   Introduction

The interest in mathematical modeling of reacting flows has grown considerably during the last years. One particular example is mathematical modeling of combustion processes. In this case the underlying chemical kinetics is (at least for the combustion of aliphatic hydrocarbons) well understood [1], and numerical simulations of laminar flames in simple one- or two-dimensional configurations have become a standard research tool. Furthermore, direct numerical simulations (DNS), originally developed to investigate turbulent non-reactive flows, have found important applications in the simulation of turbulent combustion processes [2,3]. For general turbulent three-dimensional flows a detailed treatment of the chemical and physical processes by DNS is, and will remain in the near future, computationally prohibitive [4]. Thus, simplified models for the turbulence (see, e.g. [5]) as well as for the chemical kinetics have to be devised.

   The need of simplified models for the chemistry stems from the fact that one species conservation equation has to be solved for each chemical species. This is computationally prohibitive for complex reacting flow systems. Moreover, it is desirable not to perform the time-consuming evaluation of all the

chemical source terms during the computation of a reacting flow, but to evaluate them beforehand, store the functional dependence on the thermochemical state variables (e.g., based on table look-up procedures [4,6] or polynomial representations [7]) and then use the results in the computational fluid dynamics code. In the past various methods have been developed to generate reduced reaction mechanisms for combustion systems. Examples are systematically reduced reaction mechanisms [8,9], the constrained equilibrium approach [10], repro-modeling [11], computational singular perturbation [12,13], the method of intrinsic low-dimensional manifolds [14,6,15,16], and dynamic dimension reduction [17,18] (surveys of the work can be found in [8,9,19]). In principle all these methods are based on the fact that the chemical kinetics does not access the whole composition space, but is restricted to small subspaces of lower dimension. This is caused by the dynamic nature of the chemical kinetics, but also by the fact that the physical processes like diffusion, heat conduction, or turbulent mixing introduce correlations between the thermochemical state variables, too.

Summarizing, we can state that the thermokinetic state space of reacting flows is characterized by two important properties:

- The state space accessed in a reacting flow is only a small subset of the allowed space (i. e., of the space which is in principle accessible and whose states do not violate physical laws).
- After a short relaxation time the thermokinetic state is restricted to a small neighborhood of low-dimensional attractors (intrinsic low-dimensional manifolds, ILDMs).

These observations can be used to simplify mathematical modeling of reacting flows, as will be shown in the following.

2 Dynamics of reacting flows

The dynamics of reacting flows is governed by the system of conservation equations for mass, momentum, energy, and species masses, which reads in its general form [20]

$$
\begin{aligned}
\frac{\partial \rho}{\partial t} &+ \mathrm{div}\,(\rho\,\boldsymbol{v}) &&= 0 \\
\frac{\partial \rho \boldsymbol{v}}{\partial t} &+ \mathrm{div}\,(\rho \boldsymbol{v} \otimes \boldsymbol{v} + \bar{\bar{p}}) &&= \rho \boldsymbol{g} \\
\frac{\partial \rho u}{\partial t} &+ \mathrm{div}\,(\rho u \boldsymbol{v} + \boldsymbol{j}_q) + \bar{\bar{p}} : \mathrm{grad}\,\boldsymbol{v} &&= q_r \\
\frac{\partial \rho w_i}{\partial t} &+ \mathrm{div}\,(\rho w_i \boldsymbol{v} + \mathrm{div}\,\boldsymbol{j}_i) &&= \hat{\omega}_i && i = 1, 2, \ldots, n_s ,
\end{aligned}
\tag{1}
$$

where t denotes the time, ρ the density, $\boldsymbol{v}$ the velocity, $\bar{\bar{p}}$ the pressure tensor, g the gravitational acceleration, u the specific enthalpy, $\boldsymbol{j}_q$ the heat

flux density, q_r a source term for energy (e. g. due to radiation), w_i the mass fraction of species i, $\boldsymbol{j_i}$ the diffusion flux density of species i, $\hat{\omega}_i$ the mass rate of production of species i per volume, and n_s the number of different chemical species. The chemical reaction rates $\hat{\omega}_i$ are complicated nonlinear functions of the thermokinetic state variables u, ρ, and w_i. The transport terms $\bar{\bar{p}}$, $\boldsymbol{j_i}$ and $\boldsymbol{j_q}$, which are needed to close the system, are functions of the thermokinetic state variables and, in addition, of the gradients of the primitive variables $\boldsymbol{v}$, T, $\boldsymbol{x}$, and p [20,21] ($\boldsymbol{x}$ = vector of mole fractions, $T=$ temperature, p = pressure) [20–22].

For the following analysis it is useful to separate the equations for the thermokinetic state variables from the equations for the flow field and to assume (for sake of simplicity) a low Mach number flow with constant thermodynamic pressure (a generalization to general flows is straight forward and shall not be considered here). Using the expressions for the molecular transport terms as given in [20–22] and reformulating them in terms of the dependent variables, the evolution equation for the $n = (n_s + 1)$-dimensional vector of thermokinetic variables $\boldsymbol{\psi} = (u, w_1, \ldots, w_{n_s})^T$ can be expressed as:

$$\frac{\partial \boldsymbol{\psi}}{\partial t} = \boldsymbol{F}(\boldsymbol{\psi}) + \boldsymbol{\Xi}\left(\boldsymbol{\psi}, \nabla\boldsymbol{\psi}, \nabla^2\boldsymbol{\psi}\right) \tag{2}$$

$$\boldsymbol{\Xi} = \boldsymbol{v}\,\mathrm{grad}\boldsymbol{\psi} + \frac{1}{\rho}\mathrm{div}\left(\overline{\overline{D}}\,\mathrm{grad}\boldsymbol{\psi}\right) , \tag{3}$$

where $\boldsymbol{F}(\boldsymbol{\psi})$ is the vector of source terms (e.g., chemical rates of production), $\boldsymbol{\Xi}(\boldsymbol{\psi}, \nabla\boldsymbol{\psi}, \nabla^2\boldsymbol{\psi})$ is a vector denoting all other physical processes (e.g., heat conduction, diffusion, etc.), and $\overline{\overline{D}}$ is the n by n matrix of transport coefficients (cf. [20,22])

Physical constraints like positiveness of temperature and mass fractions limit the allowed state space to a domain Σ, where

$$\Sigma = \left\{\boldsymbol{\psi} | T(\boldsymbol{\psi}) > 0, \rho(\boldsymbol{\psi}) > 0, w_i(\boldsymbol{\psi}) \geq 0, i = 1, \ldots, n_s, \sum_{j=1}^{n_s} w_j(\boldsymbol{\psi}) = 1\right\}. \tag{4}$$

Because (2) does not invoke any modeling procedure, it is valid for laminar as well as for turbulent flows. Furthermore it constitutes a reaction - convection - diffusion problem which has three important features: The eigenvalues of the Jacobian $\boldsymbol{F_\psi}$, $(F_\psi)_{ij} = \partial F_i/\partial \psi_j$ typically differ by several orders of magnitude, the molecular transport term $\mathrm{div}(\overline{\overline{D}}\,\mathrm{grad}\boldsymbol{\psi})$ is characterized by the fact that the eigenvalues of the matrix $\overline{\overline{D}}$ of transport coefficients have typically non-negative real parts [23] which causes the diffusion term to lead to a "contraction" of the accessed state with time, and the convective term can be eliminated by a transformation into Lagrangian coordinates [24].

The nature of the molecular transport operator causes the accessed space of a system to be only a small subset of the allowed domain Σ. This can be
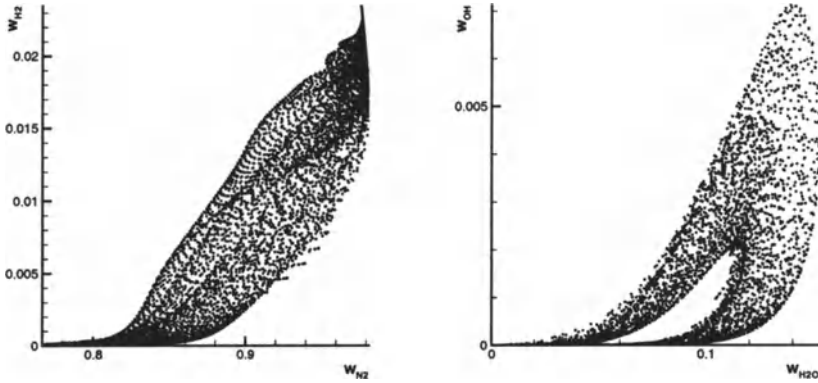
Fig. 1. Plot of DNS results [25] in the state space
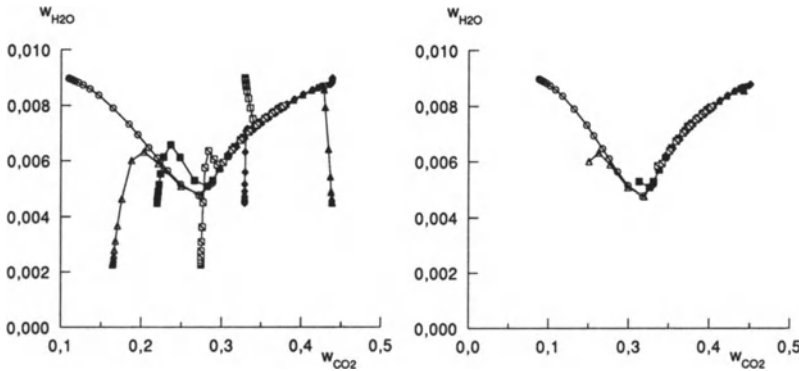
Fig. 2. Trajectories of the chemical reaction for a $CO-H_2$-air system, $\circ$ denotes the equilibrium; projection into the CO_2-H_2O-plane. Left: complete reaction process, Right: trajectories after a relaxation time of 100 μs.

seen from scatter plots of DNS-results for a non-premixed hydrogen-oxygen-nitrogen flame in the state space (Fig. 1). Shown are projections into the N_2 - H_2 and the H_2O - OH plane, respectively. The points in state space are sample points from a DNS-calculation [25].

Furthermore, the strongly differing time scales of the chemical kinetics cause the existence of attractors (intrinsic low-dimensional manifolds, ILDM) in the state space with the property that the chemical kinetics relaxes very fast to these attractors and that after a short initialization phase the chemical kinetics is governed by a movement along these attractors [14]. This can be seen from Fig. 2, where sample trajectories of chemical reactions in a $CO-H_2$-air combustion system [26] in the state space are shown. Plotted are projections into the CO_2-H_2O-plane. Different initial conditions were chosen.

It can be seen from Fig. 2 (left) that the chemical kinetics leads to a quite complicated dynamics in the state space. The reason is that the dynamics considered includes all chemical processes, i.e., also all the fast equilibration processes causing species to obtain quasi-steady states or reactions to be in partial equilibrium. On the other hand the dynamics after the first 100 μs shows a much simpler behavior. This is shown in the right part of Fig. 2, where the parts of the trajectories which correspond to the time interval $[0, 100\mu s]$ have been omitted. Within 100 μs all the trajectories have almost merged to a single curve (one-dimensional manifold) in the state space, and the state of the whole system can be described by one variable only. The reason is that the fast relaxation processes lead to species being in quasi-steady state or reactions in partial equilibrium, and thus introduce correlations among the various species.

3   Intrinsic low-dimensional manifolds of chemical reaction systems

It is well known that the molecular transport term introduces an infinite number of time scales into the system of governing equations (see, e.g., [27]). On the other hand the chemical kinetics, represented by the chemical source term $F(\psi)$ is governed by n time scales. The chemical time scales correspond to the eigenvalues of the Jacobian F_ψ and the characteristic directions of the reaction progress correspond to the eigenvectors of the Jacobian. It has been shown in [14] that a chemical system relaxes to low-dimensional manifolds in composition space such that after a short time the system can be approximated by a movement along these low-dimensional manifolds. They are defined by the requirement that the reaction rates in direction of the subspace corresponding to the fast relaxing processes vanish. This means that the low (m_s)-dimensional manifolds are defined according to:

$$L_m = \left\{ \psi \in \Sigma | \hat{Z}_f(\psi) F(\psi) = 0 \right\} \ , \tag{5}$$

where

$$F_\psi = (Z_s Z_f) \begin{pmatrix} N_s & 0 \\ 0 & N_f \end{pmatrix} \begin{pmatrix} \hat{Z}_s \\ \hat{Z}_f \end{pmatrix} , \tag{6}$$

and Z_s is the n by m_s-dimensional matrix which forms an invariant subspace associated with the m_s eigenvalues having the largest real parts, and Z_f the n by m_f-dimensional matrix which forms an invariant subspace associated with the m_f eigenvalues having the smallest real parts (degenerate eigenvalues are counted multiple) [14,25]. This equation system is an implicit definition of the correlations between the state variables of a reacting flow which are introduced by fast relaxing chemical processes (species in quasi-steady state, reactions in partial equilibrium).
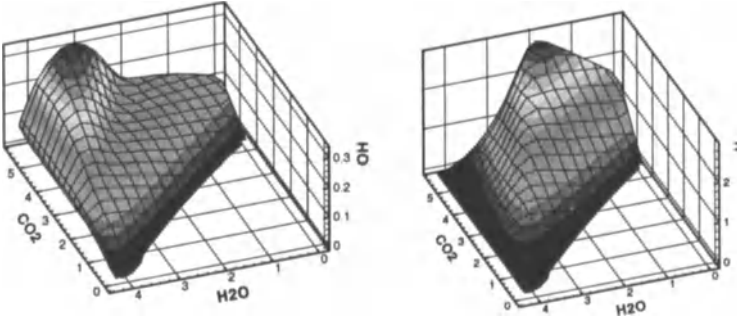
Fig. 3. Intrinsic low-dimensional manifolds of a syngas - air system [28]

An example for two-dimensional manifolds for a CO - H_2 - O_2 - N_2 system is shown in Fig. 3. Plotted are the manifolds of OH and H versus CO_2 and H_2O (the axis denote the mass fractions of the species divided by their molar masses). Similar figures (not shown here) are obtained for all other chemical species in the system. This means that if all chemical time scales except for the largest two can be decoupled from the system, then it is sufficient to describe the dynamics of the system by two variables (e.g., CO_2 and H_2O), and all other state variables are known from the correlations introduces by the fast relaxation processes.

After a suitable parametrization of the manifolds [25,29] by a vector $\boldsymbol{\theta}$ of m_s parameters θ_i, the state of a chemical system is completely determined by the values of these parameters ($\boldsymbol{\psi} = \boldsymbol{\psi}(\boldsymbol{\theta})$). Furthermore let us assume that a parametrization of the manifold is used such that $\boldsymbol{\theta_\psi} = P$, where P is an $m_s \times n$ parametrization matrix. Then (2) can be simplified to yield the reduced equation system [6]

$$\frac{\partial \boldsymbol{\theta}}{\partial t} = PZ_s\hat{Z}_s\boldsymbol{F}\left(\boldsymbol{\psi}\right) + PZ_s\hat{Z}_s\boldsymbol{\Xi}\left(\boldsymbol{\psi}, \nabla\boldsymbol{\psi}, \nabla^2\boldsymbol{\psi}\right) = \boldsymbol{S}\left(\boldsymbol{\theta}\right) + \boldsymbol{\Gamma}\left(\boldsymbol{\theta}, \nabla\boldsymbol{\theta}, \nabla^2\boldsymbol{\theta}\right),$$
$$(7)$$

where $S = PZ_s\hat{Z}_s\boldsymbol{F}$, and $\boldsymbol{\Gamma} = \boldsymbol{v}\mathrm{grad}\boldsymbol{\theta} + (1/\rho)PZ_s\hat{Z}_s\mathrm{div}\left(\overline{\overline{D}}\boldsymbol{\psi_\theta}\,\mathrm{grad}\boldsymbol{\theta}\right)$ [29].

This reduced equation system describes the dynamics of the scalar field of a reacting flow based on the assumption that for the whole physical domain Ω and for all times $t > t_0$ the time scales introduced by the physical processes are longer than those chemical time scales which have been decoupled from the system.

To summarize, the ILDM method, based on a local analysis of the chemical reaction system, consists of three steps [14,6,15,16]:

- the identification of the intrinsic low-dimensional manifolds [14,16,25].
- the storage of the information for subsequent use in reacting flow codes [15,7,29],

- and the solution of the projected equation system for the scalar field [14–16,29].

4   Coupling of the chemical kinetics with molecular transport

In the previous section it has been shown that fast relaxing chemical processes introduce correlations between the state variables. The number of correlations depends on how the chemistry is perturbed by the physical processes (molecular transport, turbulent mixing) that means on the characteristics of the reacting flow. The question arises how much the chemical kinetics is perturbed locally in a reacting flow, i. e. what the local ILDMs are. If the physical processes are slow compared to the chemical kinetics, then the dimensions of the ILDMs are small, whereas if the physical processes are fast and perturb the chemical kinetics considerably, then the dimensions of the ILDMs increase. Based on the results of reacting flow calculations, the local ILDMs of the system can be identified. Let us look at a given point r in physical space where we have the thermochemical state $\psi(r)$. The following question arises: What is the thermochemical state at point r if the n_f fastest chemical time scales are assumed to be infinitely fast and have already relaxed onto a local ILDM? In order to answer this question, we start from the governing equations for the chemical kinetics only (eq. (2) with $\Xi = 0$). Finding the point ψ^m on the local manifold to which the system relaxes corresponds to solving the equation

$$\frac{\partial \psi}{\partial t} = Z_f \hat{Z}_f F(\psi) \tag{8}$$

until the stationary solution is obtained [30].

The local dimension of the manifold can then be determined based on the local error as follows: Find the minimal m_s for which $|\psi^m - \psi^0| < \epsilon$, where $|\cdot|$ denotes a weighted norm of the difference between the values ψ^0 in the reacting flow and the corresponding values ψ^m on the manifold. In this way no physical time scale has to be identified, but the analysis is based on the local error.

Using this method, it is possible to calculate the local dimensions of the ILDM. The results for a free flat premixed syngas-air-flame (using a detailed transport model) are shown in Fig. 4. Plotted are the mass fractions of H_2, H_2O, H, and OH versus the mass fraction of CO_2, which characterizes the reaction progress, and is a more suitable coordinate than the spatial coordinate in this context. Furthermore, the number of relaxed modes is shown. The local dimension, i.e. the remaining number of reaction progress variables resulting after elimination of the relaxed modes, is based on an error $\epsilon = 10^{-2}$. This small error has been chosen to show that an arbitrary accuracy can be obtained if the dimension is adapted to the local time scale of the physical processes (if the dimension of the manifold equals the dimension of the state
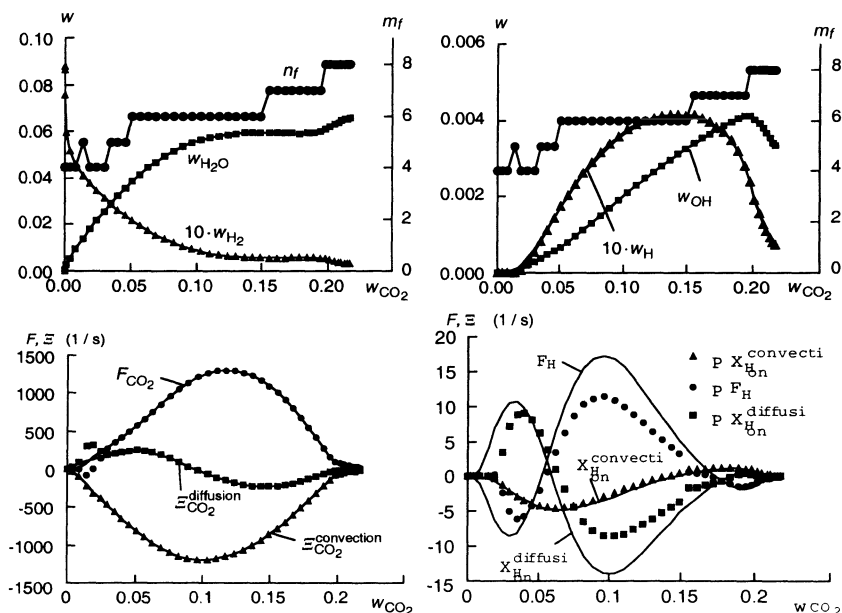
Fig. 4. Coupling of the chemical kinetics with the physical processes for a free flat premixed syngas-air-flame [30], plots versus w_{CO_2}, which characterizes the reaction progress. Upper part: species profiles and number of relaxed modes based on a local error of 1%. Lower part: Different terms in the species conservation equations for CO_2 (left) and H (right); lines denote the overall contributions, symbols denote the net contributions after eliminating the fast time scales.

space, we obtain the detailed mechanism and the error is zero). The predictions of the detailed (curves) and the reduced scheme (symbols) show barely any difference, because the dimension of the manifold has been adapted locally, taking into account the coupling with the physical processes. For large values of w_{CO_2} (near chemical equilibrium) the number of the relaxed modes is 8, corresponding to only one slow chemical process that has to be taken into account. The number of very fast, relaxed chemical processes decreases with increasing departure from the equilibrium. But even in the low temperature regime at least 4 chemical time scales can be decoupled while still guaranteeing an error of the reduced scheme of less than 1 %. If the allowed error is larger, then the number of relaxed modes is larger, too, and practically all of the domain can be described by two reaction progress variables only (see [26,15]). Because the required minimal dimension of the manifold is very low in most parts of the state space, a local adaptation of the dimension of the manifolds can lead to a large reduction of the storage needed for the tabulation of the manifolds. As already mentioned, Fig. 4 shows that in some parts of the domain almost all fast chemical processes have relaxed, whereas in oth-

ers (i.e. for low amounts of CO_2 in Fig. 4) a considerable number of chemical processes are slow. In these parts of the state space, however, the chemical kinetics in general is slow and the dynamics of the system is governed by the physical processes. If the chemistry is slow compared to the transport processes, then the transport itself causes the existence of attractors in the state space (cf. section 5).

In section 3 it has been shown that the coupling of the chemical kinetics with the molecular transport is accounted for by projecting the governing equation system onto the ILDM. This is necessary, because a physical perturbation can be decomposed into two parts: One part which is in direction of fast relaxing chemical processes and results in a zero net contribution, and another part which is tangential to the manifold and leads to a non-zero net contribution [6].

The coupling of molecular transport with the chemical kinetics is illustrated for the flat syngas - air flame in Fig. 4. The diffusion, reaction, and convection terms in the CO_2 and H species conservation equations are plotted against w_{CO_2}. Curves denote the terms that are obtained if a detailed reaction mechanism is used, symbols denote the values of the terms after projection onto the manifold, i.e. the net terms after relaxation of the fast modes. In the left part of the figure (CO_2) it can be seen that the terms are almost identical for both the detailed and the simplified kinetics. The reason is that CO_2 is a slowly changing variable, whose rate of formation is directly associated with a slow time scale. On the other hand H is a species which attains a steady state in large parts of the flame. This means that a perturbation caused by diffusion is relaxed back to the manifold very fast. Because the fast relaxation processes had been decoupled during the simplification of the chemical kinetics, the effective diffusion term has to be changed, too. This means that within the concept of ILDM the coupling of chemical kinetics with molecular transport is treated correctly: The decoupling of the fast time scales is not only performed for the chemical kinetics, but the information about the dynamics of the chemical kinetics is stored and used subsequently for the evaluation of the molecular transport terms (via the projection matrix $Z_s \hat{Z}_s$).
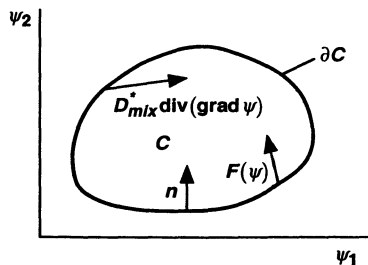
Fig. 5. Convex domains in the state space

One problem in the identification of the ILDMs based on an analysis of the chemical reaction system is that the ILDMs are identified within the whole state space. From typical combustion processes, however, we know that only a small subset of the state space is actually accessed, and it is desirable to restrict the computation of the ILDMs to this small subset [30]. This can be done if information about the transport processes is incorporated into the calculation of the manifolds. Let us assume for simplicity that the evolution of the scalar field is governed by the simplified equation

$$\frac{\partial \psi}{\partial t} = F(\psi) + v \mathrm{grad}\psi + D_{mix}^{\star} \mathrm{div}(\mathrm{grad}\psi) \ . \tag{9}$$

Furthermore the initial- and boundary conditions shall be contained in a convex subdomain C of the state space bounded by ∂C. Then it can be shown that no transport processes $(D_{mix}^{\star}\mathrm{div}(\mathrm{grad}\psi))$ can cause a state of the system to leave the domain C. Furthermore, if all chemical rates F are directed into the domain C, it can be shown that all states accessed in the further evolution of the scalar field will remain within C. For the reduced system (7) a similar behavior results with the difference that "convexity" has to be defined locally in terms of the tangent space of the manifold. Using this observation, a simple method to generate bounded subsets of the ILDMs can be developed [31], which reduces the storage requirement for the ILDMs considerably.

5   Correlation analysis of DNS data

Direct numerical simulations (DNS), which are based on a direct solution of the conservation equations without applying any modeling assumption, allow detailed studies of turbulent combustion, even taking into account detailed chemical kinetics [3,32–34]. Nevertheless, the cost of such simulations is still extremely high, which limits the physical domain that can be simulated (typical lengths of the computational domains are of the order of cm) and the number of computations that can be carried out. Nevertheless DNS provide a deep insight into the coupling of chemical kinetics with turbulence, and knowledge obtained through DNS can be used to improve statistical models for turbulent reacting flows. One major problem of DNS is the overwhelming amount of data that is obtained from each calculation, and methods are needed which allow to extract the information which one is really interested in and answer questions such as

- How does the turbulence perturb the chemical kinetics? Are some chemical processes so fast that they are not influenced by turbulent mixing?
- Are there correlations between the species concentrations that allow to reduce the dimension of the system (cf. section 3)?
- Are there correlations of the thermokinetic state variables with their gradients?
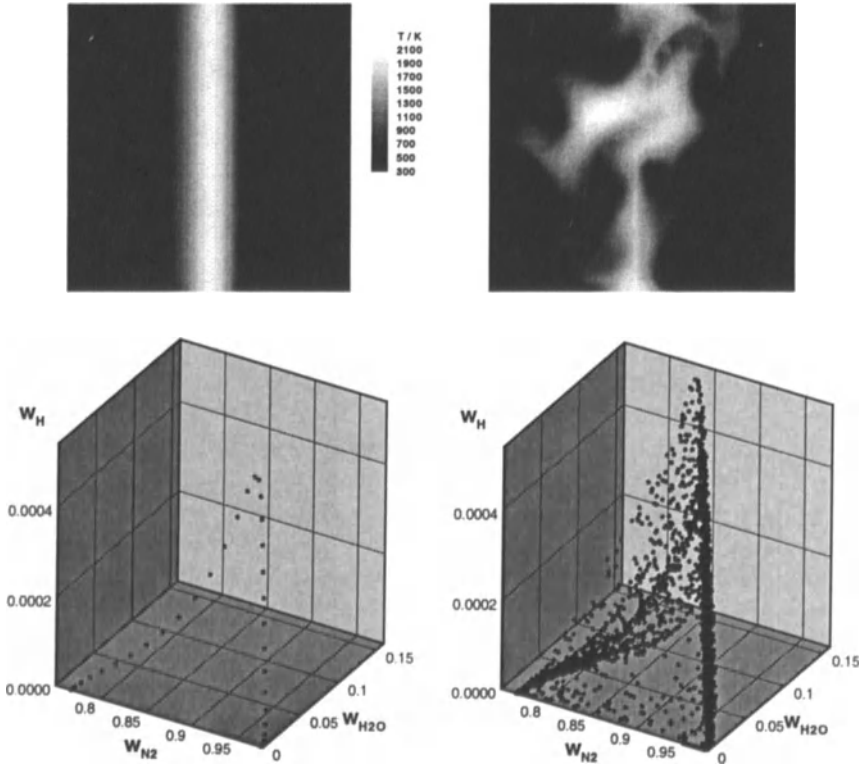
Fig. 6. Results of DNS of a hydrogen-oxygen-nitrogen non-premixed flame [25]. Upper figures: data plotted in the physical space (x-y-plots); Lower Figures: scatter plots in the composition space. The left figures correspond to the initial conditions, the right figures to the results after $t = 2.2\tau_t$.

In the previous sections it has been outlined that, indeed, the coupling of chemical kinetics with transport introduces correlations among the state variables and their gradients, and in the following we shall outline briefly how these correlations can be extracted from DNS data (see [25] for details).

DNS are typically initialized starting with laminar flame profiles and imposing a random turbulent flow field. Then the interaction of the turbulent flow field with the flame is calculated and can be analyzed. This is shown in Fig. 6, where results of a DNS for a non-premixed hydrogen-air flame (fuel: 25 Vol.% H_2, 75 Vol.% N_2) are plotted for an initial turbulent Reynolds number of 210 and a turbulent characteristic time τ_t of 0.536 ms [25]. In the upper left figure the initial temperature field is shown, whereas in the upper right figure the turbulent flame is shown after a a time $t = 2.2\tau_t$. It can be seen that the turbulent flow field perturbs the structure of the flame

considerably. Now it is interesting to look at the results in the state space. In the lower parts of Fig. 6 the results of the DNS (i.e. the states at the different nodes of the computational grid (301 by 301) have been represented as scatter plots in the state space (only about 5% of the points are shown for sake of clarity of the representation). In our example which consists of 9 species we have a 9-dimensional composition space, but in order to visualize the results we restrict to a 3-dimensional plot of the results with the mass fractions of N_2, H_2O, and H as coordinates. In the left figure it can be seen that there is a direct correlation between the different mass fractions. This is evident because the DNS has been initialized with the profiles of a one-dimensional flame, where all the mass fractions are unique functions of the mixture fraction which is represented by the mass fraction of N_2. After the turbulent flow field has had enough time to perturb the flame, some of the correlations cease to exist. But the figure shows that still not the whole composition space is accessed and that the accessed states seem to be in the neighborhood of intrinsic low-dimensional manifolds. In section 4 it has been shown that fast chemical processes lead to the relaxation to intrinsic low-dimensional manifolds and that the local dimensions of the ILDMs depend on the physical perturbation of the chemistry. The smaller the time scale of the physical perturbation the fewer chemical processes can be assumed to be in local equilibrium and be decoupled.

Recently a method has been reported [25] which allows to determine whether the points obtained from the DNS lie on low-dimensional manifolds and, if yes, what the local dimension is. The method is based on an analysis of clusters of neighboring points in the state space. For these clusters a local analysis is performed. If we assume that the low-dimensional manifolds can be linearized locally, this corresponds to determining whether the cluster of points can be approximated locally by m-dimensional hyperplanes. The quality of the approximation is then given by the root mean square ϵ_m of the distances of the points from the hyperplanes. It can be shown [25] that a simple analysis allows to specify the local error ϵ_0 which is made by approximating the cluster of points by their mean value, and the errors ϵ_m which are made by approximating the points by an m-dimensional hyperplane. A suitable measure for the quality of the m-dimensional approximation is given by calculating $\eta = \epsilon_m/\epsilon_0$. The analysis can be performed for any point in the composition space. In this way it is possible either to specify the maximum error resulting from an m-dimensional approximation or to calculate locally the minimum dimension that is necessary to keep the error below a certain threshold. Furthermore the analysis reveals the equation of the locally approximating hyperplanes and allows to characterize the low-dimensional manifold. For the example presented above it was shown that a maximum dimension of 4 is necessary to decrease the approximation error below 1.5% [25]. This means that the whole composition space is a function of 4 vari-

ables at most if the required accuracy is less than 1.5%. If a more accurate description is desired, then the dimension has to be increased.

As a consequence it is possible to determine approximate low-dimensional manifolds by a correlation analysis of DNS data. A major advantage of this method (in contrast to the calculation of the ILDM as outlined in section 3) is that not only the attractors caused by the chemistry, but also those caused by the transport processes can be identified. Furthermore correlations between the state variables ψ and their gradients $\mathrm{grad}\psi$ can be identified, which yields important information for the improvement of mixing models for turbulent reacting flows.

6   ILDM in the context of PDF models for turbulent reacting flows

In PDF-models for reacting flows, a transport equation for the joint probability density function f of velocity and scalars (PDF) is solved in order to model the coupling of chemical kinetics with the turbulent flow field. In this way the closure problem for the chemical kinetics is overcome, whereas the molecular transport still needs modeling. Typically the flow is represented by a large number of stochastic particles which mimic the PDF. A detailed description of the method can be found in [35].

The fast relaxing chemical processes cause the existence of ILDMs in the state space, and the question arises how this is reflected in the evolution of the joint PDF. First of all it is evident that the existence of correlations among the state variables causes the random variables of the reacting flow to be no longer independent. This has important consequences for the joint PDF.

In order to simplify the analysis let us restrict to a pure chemical reaction system neglecting all transport processes. Then the transport equation for the PDF is given by

$$\frac{\partial f(\psi; t)}{\partial t} + \sum_{\alpha=1}^{n} \frac{\partial}{\partial \psi_\alpha} \{F_\alpha f(\psi; t)\} = 0 \ , \tag{10}$$

and the corresponding characteristic system is

$$\frac{\mathrm{d}\psi}{\mathrm{d}s} = F(\psi) \tag{11}$$

$$\frac{\mathrm{d}f}{\mathrm{d}s} = -f \sum_{\alpha=1}^{n} \frac{\partial F_\alpha}{\partial \psi_\alpha} = -f \ \mathrm{trace}(F_\psi) \tag{12}$$

Analogous to the relaxation of a chemical system to the ILDM (8), the PDF relaxes according to

$$\frac{\mathrm{d}\psi}{\mathrm{d}s} = Z_f \hat{Z}_f F(\psi) \tag{13}$$

$$\frac{\mathrm{d}f}{\mathrm{d}s} = -f\,\mathrm{trace}(N_f) \tag{14}$$

Noting that the eigenvalues of N_f are smaller than zero (cf. section 3), it can be seen that, according to fast chemical relaxation processes, the PDF evolves such that $f(\psi) \to 0$ for $\psi \notin L_m$ and $f(\psi) \to \infty$ for $\psi \in L_m$.

This observation has important consequences for the use of statistical models for turbulent reacting flows. First it shows that the concept of ILDM can be used to reduce the number of independent variables in the PDF transport equation considerably. Furthermore it shows that if assumed shape PDF methods (cf. [5]) are used in connection with reduced kinetic schemes, the shape of the PDFs have to be chosen carefully such that the correlations among the state variables, introduced by the chemical kinetics, are not violated.

One further aspect of ILDMs in the context of PDF methods is the fact that correlations do not only exist among the state variables ψ, but also among $\nabla^2\psi$ (cf. section 5). Thus, an analysis of DNS-data can be used to extract information about correlations among the state variables and their gradients. This is an important issue in PDF-methods for turbulent flows [35], because it allows to gain information about the conditional expectations $\langle \mathrm{div}D\mathrm{grad}\phi|\phi = \psi\rangle$ of the molecular transport terms and to close, at least partially, the unclosed molecular transport terms.

7   Conclusions

In this paper we have outlined some aspects of modeling the coupling of chemical kinetics with flow and molecular transport. It has been shown that the chemical kinetics as well as molecular transport processes cause the existence of intrinsic low-dimensional manifolds (ILDMs) in the state space which act as attractors for the dynamics of the reacting flow. These ILDMs can be identified either by a time scale analysis of the chemical reaction system or by a correlation analysis of DNS data. The information obtained on the ILDMs can then be used to simplify the chemical kinetics and its coupling with molecular transport processes.

References

1. J. Warnatz. Resolution of gas phase and surface chemistry into elementary reactions. In *24*[th] *Symposium (International) on Combustion*, pages 553–579. The Combustion Institute, Pittsburgh, PA, 1992.
2. T. Poinsot. In *26*[th] *Symposium (International) on Combustion*, pages 219–232. The Combustion Institute, Pittsburgh, PA, 1996.
3. M. Baum. *Direct Numerical Simulation – A tool to study turbulent reacting flows*, volume V of *Annual Reviews of Computational Physics*. World Scientific Publishing Company, 1997.

4. S. B. Pope. Computations of turbulent combustion: Progress and challenges. In 23rd *Symposium (International) on Combustion*, page 591. The Combustion Institute, Pittsburgh, PA, 1990.

5. P. A. Libby and F. A. Williams (eds.). *Turbulent Reactive Flows*. Springer, New York, 1980.

6. U. Maas and S. B. Pope. Implementation of simplified chemical kinetics based on intrinsic low-dimensional manifolds. In 24th *Symposium (International) on Combustion*, page 103. The Combustion Institute, Pittsburgh, PA, 1992.

7. H. Niemann, D. Schmidt, and U. Maas. An efficient storage scheme for reduced chemical kinetics based on orthogonal polynomials. *Journal of Engineering Mathematics*, 31:131–142, 1997.

8. N. Peters and B. Rogg. *Reduced Kinetic Mechanisms for Applications in Combustion Systems*. Springer, Berlin, 1993.

9. M. D. Smooke (ed.). *Reduced Kinetic Mechanisms and Asymptotic Approximations for Methane-Air Flames*. Lecture Notes in Physics 384, Springer, Berlin, Heidelberg, New York, 1991.

10. R. Law, M. Metghalchi, and J. C. Keck. Rate-controlled constraint equilibrium calculations of ignition delay times in hydrogen-oxygen mixtures. In 22nd *Symposium (International) on Combustion*, pages 1705–1713. The Combustion Institute, Pittsburgh, PA, 1988.

11. T. Turanyi. Parameterization of reaction mechanisms using orthonormal polynomials. *Computers Chem.*, 18:45–54, 1994.

12. S. H. Lam and D. A. Goussis. Understanding complex chemical kinetics with computational singular perturbation. In 22nd *Symposium (International) on Combustion*, page 931. The Combustion Institute, Pittsburgh, PA, 1988.

13. S. H. Lam. Using CSP for complex chemical kinetics. Technical report, Princeton University, USA. Technical Report 1941-MAE, 1992.

14. U. Maas and S. B. Pope. Simplifying chemical kinetics: Intrinsic low-dimensional manifolds in composition space. *Combustion and Flame*, 88:239–264, 1992.

15. U. Maas and S. B. Pope. Laminar flame calculations using simplified chemical kinetics based on intrinsic low-dimensional manifolds. In 25th *Symposium (International) on Combustion*, pages 1349–1356. The Combustion Institute, Pittsburgh, PA, 1994.

16. U. Maas. Coupling of chemical reaction with flow and molecular transport. *Applications of Mathematics*, 3:249–266, 1995.

17. P. Deuflhard and J. Heroth. Dynamic dimension reduction in ODE models. In F. Keil, W. Mackens, Voß, and J. Werther (1996): Scientific Computing in Chemical Engineering, editors, *Scientific Computing in Chemical Engineering*, pages 29–43. Springer, 1996.

18. P. Deuflhard, J. Heroth, and U. Maas. Towards dynamic dimension reduction in reactive flow problems. In J. Warnatz and F. Behrendt, editors, *Modelling of Chemical Reaction Systems, Proceedings of an International Workshop, Heidelberg, Germany, July 24 - 26, 1996*. Springer, 1996. ISBN 3-932217-00-4.

19. A. S. Tomlin, T. Turanyi, and M. J. Pilling. Mathematical tools for the construction, investigation and reduction of combustion mechanisms. In M. J. Pilling, editor, *Oxidation Kinetics and Autoignition of Hydrocarbons*. Elsevier, in press.

20. J. O. Hirschfelder and C. F. Curtiss. *Molecular Theory of Gases and Liquids*. John Wiley & Sons, Inc., New York, 1964.

21. R.B. Bird, W.E. Stewart, and E.N. Lightfoot. *Transport Phenomena*. Wiley Interscience, New York, 1960.

22. A. Ern and V. Giovangigli. *Multicomponent Transport Algorithms*. Lecture Notes in Physics. Springer, Berlin, Heidelberg, New York, 1994.

23. V. Giovangigli. Mass conservation and singular multicomponent diffusion algorithms. *IMPACT Comp. Sci. Eng.*, 2:73–97, 1990.

24. R. D. Richtmyer and K. W. Morton. *Difference Methods for Initial Value Problems, 2*. John Wiley & Sons, Inc., New York London Sydney, 1967.

25. U. Maas and D. Thévenin. Correlation analysis of dns data of turbulent non-premixed flames. In 27th *Symposium (International) on Combustion*, page in print. The Combustion Institute, Pittsburgh, PA, 1999.

26. U. Maas. *Automatische Reduktion von Reaktionsmechanismen zur Simulation reaktiver Strömungen*. Habilitation thesis, Institut für Technische Verbrennung, Universität Stuttgart, 1993.

27. G. Grosche, E. Zeidler, D. Ziegler, and V. Ziegler (eds.). *Teubner-Taschenbuch der Mathematik*. Teubner, Leipzig, 1995.

28. U. Maas. Efficient calculation of intrinsic low-dimensional manifolds for the simplification of chemical kinetics. *Computing and Visualization in Science*, 1:69–82, 1998.

29. T. Blasenbrey, D. Schmidt, and U. Maas. Automatically simplified chemical kinetics and molecular transport and its application in premixed and non-premixed laminar flame calculations. In 27th *Symposium (International) on Combustion*, page in print. The Combustion Institute, Pittsburgh, PA, 1999.

30. D. Schmidt and U. Maas. Analysis of the intrinsic low-dimensional manifolds of strained and unstrained flames. In J. Warnatz and F. Behrendt, editors, *Modelling of Chemical Reaction Systems, Proceedings of an International Workshop, Heidelberg, Germany, July 24 - 26, 1996*. Springer, 1996. ISBN 3-932217-00-4.

31. T. Blasenbrey, D. Schmidt, and U. Maas. An improved tabulation strategy for reduced chemical kinetics based on ildm, 1999. submitted for presentation at the ICDERS conference, Heidelberg.

32. D. Thévenin, F. Behrendt, U. Maas, and J. Warnatz. *Comput. Fluids*, 25,5:485–496, 1996.

33. D. Thévenin, J. C. Rolon, P. H. Renard, D. W. Kendrick, D. Veynante, and S. Candel. In 26th *Symposium (International) on Combustion*, pages 1079–1086. The Combustion Institute, Pittsburgh, PA, 1996.

34. D. Thévenin, E. van Kalmthout, and S. Candel. In J. P. Chollet, P. R. Voke, and L. Kleiser, editors, *Direct and Large Eddy Simulation II*, pages 343–354. Kluwer Academic Publishers, 1997.

35. S. B. Pope. PDF methods for turbulent reactive flows. *Prog. Energy Combust. Sci.*, 11:119–192, 1985.

Non-Adiabatic Effects in Quantum-Classical Molecular Dynamics

Christof Schütte and Peter Nettesheim

Konrad-Zuse-Zentrum Berlin, Takustr. 7, 14195 Berlin, Germany

Abstract. In molecular dynamics applications there is a growing interest in mixed quantum-classical models. The article is concerned with the so-called QCMD model. This model describes most atoms of the molecular system by the means of classical mechanics but an important, small portion of the system by the means of a wavefunction. We review the conditions under which the QCMD model is known to approximate the full quantum dynamical evolution of the system.

   In most quantum-classical simulations the *Born-Oppenheimer model* (BO) is used. In this model, the wavefunction is adiabatically coupled to the classical motion which leads to serious approximation deficiencies with respect to non-adiabatic effects in the fully quantum dynamical description of the system. In contrast to the BO model, the QCMD model does include non-adiabatic processes, e.g., transitions between the energy levels of the quantum system. It is demonstrated that, in mildly non-adiabatic scenarios, so-called *surface hopping* extensions of QCMD simulations yield good approximations of the non-adiabatic effects in full quantum dynamics. The algorithmic strategy of such extensions of QCMD is explained and the crucial steps of its realization are discussed with special emphasis on the numerical problems caused by highly oscillatory phase effects.

1   Introduction

In molecular dynamics applications there is a growing interest in including specific quantum dynamical effects into the otherwise classical description of some large molecular system. Typical examples are proton transfer processes in the active site of an enzyme, electron diffusion in molten salts, or scattering effects on the electronic structure of the target molecule. Unfortunately, full quantum dynamical calculations for the entire molecule are beyond the scope of simulations, today and in the next decades. In the mixed quantum-classical approach to this problem, most atoms of the molecular system are described by the means of classical mechanics but important (and mostly small) portions of the system by the means of a wavefunction.

   A typical example of these models, the so-called QCMD model, consists of a *singularly perturbed* Schrödinger equation nonlinearly coupled to classical Newtonian equations, see §2. We will carefully review the assumptions under which this model is known to approximate the full quantum dynamical (QD) evolution of the system. One important insight is that both, the QCMD model and the full QD evolution, in fact have the same *adiabatic limit system*, the well-known time-dependent Born-Oppenheimer (BO) model, see §2.1.

It is well-known that BO simulations are sufficient approximations of the full QD evolution in many important situations but lead to entirely wrong descriptions in as many other "non-adiabatic" cases. In contrast to the BO model, the QCMD model includes non-adiabatic processes, e.g., transitions between the energy levels of the quantum system or resonance effects near level crossings, §2.2. The literature on this topic contains a significant number of specific examples in which QCMD simulations yield better approximations of QD than the simple BO approximation. But the literature also contains important examples in which QCMD fails entirely because it is a single-trajectory model while the full QD solution develops *multi-configuration* character [11]. In the present article, these observations will be illustrated by means of a certain simple example, see §2.3.

Subsequently, a specific *surface hopping* extension of QCMD will be introduced and compared with similar approaches, §3. The insights gained in the example will then allow to understand the algorithmic strategy of such QCMD-based surface hopping algorithms: to exploit the advantages of the non-adiabatic effects in QCMD while preventing the algorithm from behaving like QCMD in situations where multiply-branched classical paths are required for an accurate description.

For an efficient realization of QCMD simulations numerical integrators are required which allow to use time steps much larger than the fastest quantum time scales. Such long-step integrators have to reproduce correctly the highly oscillatory phase effects in the quantum part of the system. The basic problems related to this requirement are discussed with special emphasis on the particular aspects in the context of QCMD-based surface hopping simulations, see §4.

2 QCMD Model

To keep the notation simple we restrict our study to the case of a system with just two degrees of freedom $x \in \mathbb{R}^{d_1}$ and $q \in \mathbb{R}^{d_2}$ with significantly different associated masses, m and M. We suppose that the mass ratio $\epsilon^2 = m/M$ is a small parameter. After an appropriate rescaling [21], the time-dependent Schrödinger equation of this systems becomes

$$i\epsilon\, \partial_t \Psi \;=\; \left(-\tfrac{\epsilon^2}{2}\Delta_q \;-\; \tfrac{1}{2}\Delta_x \;+\; V(x,q) \right) \Psi. \tag{1}$$

The corresponding solution $\Psi = \Psi(x,q,t)$ describes what we call the full QD evolution of the system. Typically, a proper choice of the coordinate system allows the initial quantum state to be approximated by a product state (cf. [7], §IIb):

$$\Psi(x,q,t=0) \;=\; \phi_*(q) \cdot \psi_*(x). \tag{2}$$

We will throughout assume this initial condition to be given.

The equations of motion of the *QCMD model* are given by

$$i\epsilon\partial_t\psi_{QC} = H(q)\,\psi_{QC} \quad \text{and} \quad \ddot{q}_{QC} = -\text{grad}_q\langle\psi, V\psi\rangle(q_{QC}), \tag{3}$$

where $H = H(q)$ is the q-parametrized Hamiltonian

$$H(q) = -\tfrac{1}{2}\Delta_x + V(x, q).$$

The QCMD solution can be understood as an approximation of the full QD evolution if the initial wavefunction ϕ_* is an approximate δ-function, e.g.,

$$\phi_*(q) = \tfrac{1}{A_\epsilon}\exp\left(-\tfrac{1}{4\epsilon}(q - q_*)^2\right)\exp\left(\tfrac{i}{\epsilon}\dot{q}_* q\right). \tag{4}$$

If this is the case and some other conditions are satisfied,[1] the QD solution $\Psi = \Psi(x, q, t)$ is approximately given by $\Psi(x, q, t) \approx \phi(q, t)\psi(x, t)$ with ϕ remaining an approximate δ-function moving along the classical part $q_{QC} = q_{QC}(t)$ of the QCMD solution and $\psi \approx \psi_{QC}$ (for details compare [3]).

This approach, however, does not reveal the close connection between the QCMD and BO models. For establishing this connection, we will now summarize the approach of [4] showing that —under some non-resonance conditions— the BO model is the adiabatic limit of both, QD and QCMD.

2.1   Adiabatic Theory and BO Model

Subsequently, we will study the *limit equations* governing the QCMD solutions for the *adiabatic* limit $\epsilon \to 0$, in which the motions in the degree of freedom x are infinitely faster than the slow processes in the classical coordinate q. Therefore, we rewrite the QCMD system, Eqs. (3), by explicitly denoting the dependence of its solution $(q_\epsilon, \dot{q}_\epsilon, \psi_\epsilon)$ on the parameter ϵ:

$$\begin{aligned}
i\epsilon\partial_t\psi_\epsilon &= H(q_\epsilon)\,\psi_\epsilon, & \psi_\epsilon|_{t=0} &= \psi_*, \\
\ddot{q}_\epsilon &= -\text{grad}_q\langle\psi_\epsilon, H(q_\epsilon)\psi_\epsilon\rangle, & q_\epsilon(0) &= q_*,\ \dot{q}_\epsilon(0) = \dot{q}_*.
\end{aligned} \tag{5}$$

We restrict ourselves to finite-dimensional Hilbert spaces,[2] making H a Hermitian matrix. We denote the eigenvalues of $H(q)$ by $E_k(q)$ and consider the spectral decomposition

$$H(q) = \sum_k E_k(q)\,P_k(q), \tag{6}$$

where P_k is the orthogonal projection onto the eigenspace associated with E_k. With respect to a quantum state ψ, the number $\theta_k = \langle\psi, P_k\psi\rangle$ is the *population* of the *energy level* E_k.

---

[1] The main condition is the absence of caustics along the QCMD-solution, cf. [3].

[2] The reader may think of a finite dimensional subspace of the original state space. This subspace may, e.g., be associated with a suitable discretization in space. For a generalization of the results presented in this subsection to the infinitely dimensional case, see [2].

Adiabatic Limit of QCMD The limit equation governing $\lim_{\epsilon \to 0} q_\epsilon$ can be motivated by referring to the *quantum adiabatic theorem* which originates from work of BORN and FOCK [1,14]: The classical position q influences the Hamiltonian very slowly compared to the time scale of oscillations of ψ_ϵ, in fact, "infinitely slowly" in the limit $\epsilon \to 0$. Thus, in analogy to the quantum adiabatic theorem, one would expect that the populations of the energy levels remain *invariant* during the evolution:

$$\lim_{\epsilon \to 0} \theta_k^\epsilon(t) = \lim_{\epsilon \to 0} \langle \psi_\epsilon, P_k(q_\epsilon)\psi_\epsilon \rangle \; = \; \theta_k^0 = \langle \psi_*, P_k(q_*)\psi_* \rangle.$$

The *constant* θ_k^0 is the initial population of level E_k and thus computable from the initial data, Eq. (5). All this turns out to be true: According to [4], the limit solution $q_{\mathrm{BO}} = \lim_{\epsilon \to 0} q_\epsilon$ is given by:

$$\ddot{q}_{\mathrm{BO}} \; = \; -\mathrm{grad}_q \sum_k \theta_k^0 \, E_k(q_{\mathrm{BO}}), \qquad q_{\mathrm{BO}}(0) = q_*, \; \dot{q}_{\mathrm{BO}}(0) = \dot{q}_*. \qquad (7)$$

whenever the following assumption on the eigenspaces and eigenenergies of $H(q)$ is satisfied:

(A) The spectral decomposition Eq. (6) of H depends smoothly on q and the transversality condition $\frac{d}{dt}(E_k(q_{\mathrm{BO}}) - E_l(q_{\mathrm{BO}})) \neq 0$ holds.

We refer to equation (7) as to the *time-dependent Born-Oppenheimer* (BO) model of adiabatic motion. Notice that Assumption (A) does *not* exclude *energy level crossings* (i.e., positions q_c at which $E_k(q_c) = E_l(q_c)$ for some $k \neq l$).

For simplicity we will assume in the following that, for every position q, all the eigenspaces of $H(q)$ are one-dimensional, i.e., for every energy level $E_k(q)$ there exists a normalized eigenvector $\Phi_k(q)$ such that

$$H(q)\Phi_k(q) \; = \; E_k(q)\Phi_k(q), \quad \text{and} \quad P_k(q) \; = \; \Phi_k(q) \otimes \Phi_k(q).$$

Then, the population of the energy level $E_k(q)$ with respect to the quantum state ψ is given by $\theta_k(q) = |\langle \Phi_k(q), \psi \rangle|^2$.

Adiabatic Limit of QD The time-dependent BO model describes the adiabatic limit of QCMD. If QCMD is a valid approximation of full QD for sufficiently small ϵ, the BO model has to be the adiabatic limit of QD itself. Exactly this question has been addressed in different mathematical approaches, [5], [8], and [13]. We will follow HAGEDORN [8] whose results are based on the product state assumption Eq. (2) for the initial state with ϕ_* assumed to be given by (4) and on the "no-crossings" assumption

(B) Along the BO solution q_{BO}, crossings between initially occupied energy levels are excluded, i.e., for all pairs (E_k, E_l) of energy levels with $k \neq l$ and $\theta_k^0 + \theta_l^0 > 0$, we have $E_k(q_{\mathrm{BO}}(t)) \neq E_l(q_{\mathrm{BO}}(t))$ for all $t \in [0, T]$.

Using these conditions and the BO solution q_{BO}, a wavefunction Ψ_{BO} is constructed which comes out to be the limit of the sequence of QD solution Ψ_ϵ for $\epsilon \to 0$, [8]. In particular, for the position expectation

$$\langle q \rangle_\epsilon^{QD} = \langle \Psi_\epsilon, q\Psi_\epsilon \rangle(t),$$

the statement of HAGEDORN is:

THEOREM 1 (THM. 2.1 IN [8]) *Assume* $q_{BO} = q_{BO}(t)$ *to be the solution of the BO equation, Eq. (7), in a finite time interval* $[0,T]$ *and let assumption (B) be satisfied. Then, we have*

$$\lim_{\epsilon \to 0} \langle q \rangle_\epsilon^{QD} = q_{BO} \quad in \ [0,T].$$

That is, in the limit, the center of the QD wavepacket Ψ_ϵ moves along the BO-solution. Summarizing, QD and QCMD have the same adiabatic limit solution which is given by the BO model if the initial conditions are appropriate and if we exclude energy level crossings and discontinuities of the spectral decomposition. Consequently, QCMD is justified as an approximation of QD if only ϵ is small enough and these conditions are satisfied.

These are important results. However, the following question remains: Can QCMD describe anything beyond the correct adiabatic limit of QD? Can it describe *non-adiabatic effects*, i.e., deviations of the QD solution from its adiabatic limit for realistically small $\epsilon > 0$?

2.2   Non-Adiabaticity in QCMD

One can easily inspect the deviation of QCMD from its adiabatic limit if we reformulate its equation of motion in the coordinate system given by the eigenstate of the one-particle Hamiltonian H. In terms of the notation introduced above, we therefore make the following ansatz for the QCMD-wavepacket ψ_ϵ:

$$\psi_\epsilon(t) = \sum_k c_k^\epsilon(t)\, \Phi_k(q_\epsilon(t)).$$

Inserting this into the QCMD equations we find

$$i\epsilon\partial_t c_k^\epsilon = E_k(q_\epsilon)c_k^\epsilon - i\epsilon\dot{q}_\epsilon \sum_l d_{kl}(q_\epsilon)\, c_l^\epsilon,$$
$$\ddot{q}_\epsilon = -\nabla_q \sum_k |c_k^\epsilon|^2\, E_k(q_\epsilon) - \sum_{kl}(c_k^\epsilon)^* c_l^\epsilon\, \Delta E_{kl}(q_\epsilon)\, d_{kl}(q_\epsilon), \tag{8}$$

where the coupling matrix elements d_{kl} and energy gaps ΔE_{kl} are given by

$$d_{kl}(q) = (d_{kl}^j), \quad d_{kl}^j = \langle \Phi_k(q), \partial_{q_j}\Phi_l(q) \rangle \quad \text{and} \quad \Delta E_{kl}(q) = E_k(q) - E_l(q).$$

Thus, the non-adiabatic coupling between the energy levels in QCMD is governed by the coupling matrix (d_{kl}). Whenever assumption (B) from above is valid one can show [2] that the deviation from the adiabatic solution induced by this non-adiabatic coupling is of order $\mathcal{O}(\epsilon)$!

First Order Corrections Additionally, we are able to construct explicit expressions for the first order deviation terms: To this end, the coefficients c_k^ϵ must be represented in polar coordinates, i.e.,

$$c_k^\epsilon(t) = \sqrt{\theta_k^\epsilon(t)} \, \exp\left(-\frac{i}{\epsilon}\varphi_k^\epsilon(t)\right),$$

and one introduces the BO angle φ_k^{BO} as the solution of $\dot{\varphi}_k^{\mathrm{BO}} = E_k(q_{\mathrm{BO}})$ along the BO solution q_{BO} with $\varphi_k^{\mathrm{BO}}(0) = \varphi_k^\epsilon(0)$. In addition, we have to exclude all symmetric resonances of order four, i.e., to assume that in some neighborhood of $q_{\mathrm{BO}} = q_{\mathrm{BO}}(t)$:

$$E_k(q) + E_l(q) \neq E_j(q) + E_m(q) \quad \text{for} \quad k \neq j,\ k \neq m,\ l \neq j,\ l \neq m. \tag{9}$$

This condition allows to compute the non-adiabatic corrections to the adiabatic limit up to the leading orders in ϵ [2,18]:

$$q_\epsilon = q_{\mathrm{BO}} + \epsilon^2 \delta q^{2,\epsilon} + \mathcal{O}(\epsilon^3), \qquad\qquad \dot{q}_\epsilon = \dot{q}_{\mathrm{BO}} + \epsilon\,\delta \dot{q}_{1,\epsilon} + \mathcal{O}(\epsilon^2),$$

$$\theta_k^\epsilon = \theta_k^0 + \epsilon\,\delta\theta_k^{1,\epsilon} + \epsilon^2 \delta\theta_k^{2,\epsilon} + \mathcal{O}(\epsilon^3), \quad \varphi_k^\epsilon = \varphi_k^{\mathrm{BO}} + \mathcal{O}(\epsilon^2).$$

Under the assumption of (9), we have the following two theorems:

THEOREM 2 (APPENDIX C OF [2]) *The first order corrections are given by*

$$\delta\theta_{1,\epsilon}^k = 2\left(\Theta_{1,0}^k - \sum_{l \neq k, j} \frac{\dot{q}_{\mathrm{BO}}^j \sqrt{\theta_l^0 \theta_j^0}}{\Delta E_{kl}(q_{\mathrm{BO}})} \sin\left(\epsilon^{-1}(\varphi_k^{\mathrm{BO}} - \varphi_l^{\mathrm{BO}})\right) d_{kl}^j(q_{\mathrm{BO}})\right)$$

$$\Theta_{1,0}^k = \sum_{l \neq k, j} \frac{\dot{q}_\epsilon^j(0) \sqrt{\theta_l^0 \theta_j^0}}{\Delta E_{kl}(q_\epsilon(0))} \sin\left(\epsilon^{-1}(\varphi_k^\epsilon(0) - \varphi_l^\epsilon(0))\right) d_{kl}^j(q_\epsilon(0))$$

$$\delta\dot{q}_{1,\epsilon}^k = \sum_{l,j} \sqrt{\theta_l^0 \theta_j^0} \sin\left(\epsilon^{-1}(\varphi_k^{\mathrm{BO}} - \varphi_l^{\mathrm{BO}})\right) d_{kl}^j(q_{\mathrm{BO}}).$$

This result implies $c_k^\epsilon(t) = \sqrt{\theta_k^0}\,\exp(-\frac{i}{\epsilon}\varphi_k^{\mathrm{BO}}(t)) + \mathcal{O}(\epsilon)$. Moreover, in the particular case, that initially the wavepacket occupies only one of the eigenstates, say Φ_μ, this theorem states that the first order corrections vanish identically. Then, the following is valid for the second order corrections:

THEOREM 3 ([18]) *Whenever $\theta_l^0 = \delta_{\mu,l}$, the second order corrections for the populations in state l, $l \neq \mu$, are given by*

$$\delta\theta_{2,\epsilon}^l(t) = \left(\frac{B_{\mathrm{BO}}^{l\mu}(t)}{\Delta E_{l\mu}^{\mathrm{BO}}(t)}\right)^2 + \left(\frac{B_{\mathrm{BO}}^{l\mu}(0)}{\Delta E_{l\mu}^{\mathrm{BO}}(0)}\right)^2$$

$$- 2\,\frac{B_{\mathrm{BO}}^{l\mu}(t)}{\Delta E_{l\mu}^{\mathrm{BO}}(t)}\frac{B_{\mathrm{BO}}^{l\mu}(0)}{\Delta E_{l\mu}^{\mathrm{BO}}(0)} \cos\left(\frac{\varphi_l^{\mathrm{BO}}(t) - \varphi_\mu^{\mathrm{BO}}(t)}{\epsilon}\right) + \mathcal{O}(\epsilon) \tag{10}$$

with $B_{\mathrm{BO}}^{l\mu} := -\langle \Phi_l(q_{\mathrm{BO}}), \nabla_j \Phi_\mu(q_{\mathrm{BO}})\rangle \cdot \dot{q}_{\mathrm{BO}}$ and $\Delta E_{kl}^{\mathrm{BO}} = \Delta E_{kl}(q_{\mathrm{BO}})$.

2.3   An Avoided Crossing Example

In the subsequent, let us consider the particularly simple test case where the quantum subsystem can be described as a two state system and the classical subsystem is one-dimensional. Thus, $q \in \mathbb{R}^1$ and the full Schödinger equation has the form:

$$i\epsilon \dot{\Psi} = \left(-\tfrac{\epsilon^2}{2}\mathcal{T}_q + H(q)\right)\Psi, \qquad (11)$$

with $H = H(q)$ and $\mathcal{T}_q$ denoting 2×2 hermitian matrices:

$$\mathcal{T}_q = \begin{pmatrix} \Delta_q & 0 \\ 0 & \Delta_q \end{pmatrix} \quad \text{and} \quad H(q) = \begin{pmatrix} V_1(q) & c \\ c & V_2(q) \end{pmatrix}.$$

The wavefunction $\Psi \in L^2(\mathbb{R}) \times L^2(\mathbb{R})$ consists of two components $\Psi = (\Psi_1, \Psi_2)^T$, each of which a function in q and t.

Herein, we choose the potentials to be $V_1(q) = q^2$ and $V_2(q) = 1/q$. The interpretation is the following: V_1 describes a harmonic bond, V_2 a repulsive potential, and c a weak coupling between these two (electronic) configurations. We choose $\epsilon = 0.01$ which is a suitable scaling for electrons. In the following we set $c = 0.1$. For the choices made, Fig. 1 shows the energy eigenvalues $E_1 = E_1(q)$ and $E_2 = E_2(q) < E_1(q)$ of $H(q)$ and the corresponding off-diagonal entry of the non-adiabatic coupling matrix d_{12}. Notice that there
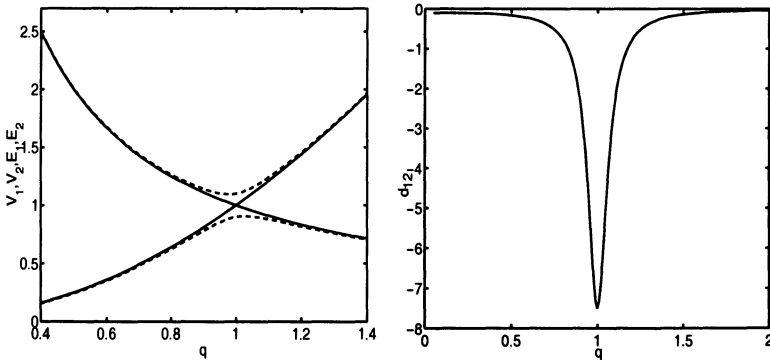
Fig. 1. (a) Potentials V_1 and V_2 (*solid lines*) and energy levels E_1 and E_2 (*dashed lines*) versus q. (b) Non-Adiabatic coupling matrix element d_{12} versus q

is some "transition zone" around $q = 1$ where the gap between the two energy levels is minimal and the coupling matrix entry significantly large.

We are interested in the following initial condition: Let $\Phi_1 = \Phi_1(q)$ be the eigenvector to E_1, $q_0 = 0.4$ and $p_0 = 1$. Then the initial wavefunction

is centered at q_0 with momentum expectation p_0 and the energy level E_1 is occupied only, i.e.,

$$\Psi(q, t = 0) = \tfrac{1}{A} \exp\left(-\tfrac{1}{4\epsilon}(q - q_0)^2 - \tfrac{i}{\epsilon}p_0 q\right) \cdot \Phi_1(q_0).$$

Figure 2 illustrates the true quantum dynamical solution of (11) for the initial condition given. We observe that the centers of the two components Ψ_1 and Ψ_2 of the wavefunction diverge when crossing the transition zone. The motion of each of these two centers is governed by the Born-Oppenheimer solutions on the corresponding[3] energy levels E_1 and E_2 (cf. Fig. 3 (b)). We can conclude that the non-adiabatic effect of the transition zone induces some significant population of the initially unoccupied energy level whereas the motion outside of the transition zone is governed by classical dynamics on the energy levels and induces the observed divergence. Obviously, a *single* QCMD trajectory – even when representing the correct population dynamics – cannot reproduce this divergence. Thus, we follow the idea of splitting QCMD trajectories leading to a specific variant of so-called surface hopping.
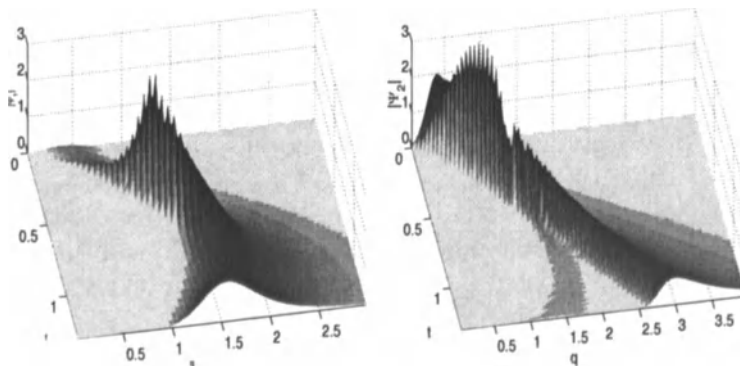
Fig. 2. Avoided Crossing Example: Evolution of the full QD wavepacket in q and t for parameter $\epsilon = 0.01$. Absolute value of (a) Ψ_1 and (b) Ψ_2

3 QCMD-based Surface Hopping

Due to the previous section, a single QCMD trajectory may reproduce the QD evolution if ϵ is small enough, resonances (level crossings) are avoided, and the initial QD wavepacket $\Psi(\cdot, \cdot, t = 0)$ is an approximate δ-function in the q-direction (cf. eqs. (2) and (4)). Since the full Schrödinger equation is linear, we may drop this last condition by decomposing the actual $\Psi(\cdot, \cdot, t = 0)$ into

---

[3] Away from the transition zone, the eigenvectors of H are approximately given by the two unit vectors.
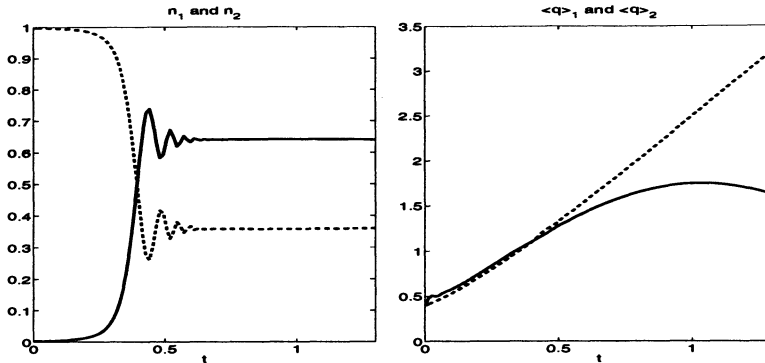
Fig. 3. Full QD for $\epsilon = 0.01$: **(a)** Statistical weights $n_1 = \|\Psi_1\|_2^2$ and $n_2 = \|\Psi_2\|_2^2$ of the two components versus t. **(b)** Position expectation values $\langle q \rangle_k = \langle \Psi_k, q \Psi_k \rangle / n_k$ of the components

finitely many approximate δ-functions at appropriately distributed locations q_0^j and momenta $\dot{q}_0^j$. Thus, we have to simulate the *QCMD trajectory bundle* starting at all the different $(q_0^j, \dot{q}_0^j)$ each with an initial x-wavefunction $\psi_0^j = \Psi(q_0^j, \cdot, t = 0)$. In a simulation of this kind, every QCMD-trajectory exhibits its own non-adiabaticity as discussed in §2.2, but any non-adiabatic effect mediated by coupling between different trajectories is excluded.

In [24], the "father" of the so-called *surface hopping* techniques [25,22], C.J. TULLY, shows that we can understand the non-adiabatic effects in full QD as a composition of two different contributions: the non-adiabatic effects along each QCMD trajectory given by the solution of (8) and the contribution of the coupling between the trajectories in the QCMD particle bundle constructed to represent the QD wavefunction.

In this section, a surface hopping algorithm is introduced which makes use of the QCMD solution in order to include non-adiabatic effects.

3.1   Surface Hopping Algorithm

Suppose that we start a trajectory at position q_0 with initial momentum $\dot{q}_0$ on the kth energy surface E_k, i.e., with initial QCMD-wavefunction $\psi_0 = \Phi_k(q_0)$. In the following we denote the QCMD trajectory, i.e., the solution of (5), by $(q(t), \dot{q}(t), \psi(t)) = \text{QCMD}(t \,|\, q(0), \dot{q}(0), \psi(0))$, omitting the ϵ-dependence since ϵ now is assumed to have a fixed value. The key assumption of surface hopping techniques is as follows: We can use the non-adiabatic effects along the QCMD trajectory as an indicator for the deviation of the full QD evolution from its adiabatic limit. In other words: Whenever the non-adiabatic effects along the QCMD trajectory induce populations on some level $l \neq k$ which are significantly larger than zero, i.e., whenever $\theta_l \geq tol > 0$, one should additionally follow the path which corresponds to the dynamics on

level E_l. But instead of starting a new trajectory on this level in every such case which would finally yield a combinatorial explosion, one stochastically decides whether or not to switch the energy level ("make a hop or not"). This algorithm should be constructed so that, at any instance in time for a large ensemble of particles, the fraction of trajectories assigned to any energy surface is approximately equal to the relative population of this energy level.

This idea leads to the following *QCMD-based surface hopping variant* of TULLY's surface hopping algorithm:

1. Start with a large ensemble of N independent QCMD-trajectories with states $(q_0^j, \dot{q}_0^j, \psi_0^j)$, $j = 1, \ldots, N$, where every ψ_0^j belongs to a certain energy level k_j, that is, satisfies $\psi_0^j = \Phi_{k_j}(q_0^j)$. This trajectory bundle has to represent the initial QD wavepacket $\Psi(\cdot, \cdot, t = 0)$ in the ensemble sense.

2. For every single trajectory $j = 1, \ldots, N$ repeat the following propagation:
   (a) Propagate the trajectory along the QCMD solution

   $$(q_{m+1}^j, \dot{q}_{m+1}^j, \psi_{m+1}^j) = \text{QCMD}(\Delta t \,|\, q_m^j, \dot{q}_m^j, \psi_m^j)$$

   for some large time span Δt.
   (b) Compute the transition zone indicator Ξ for the trajectory on level k_j:

   $$\Xi = \sum_{l \neq k_j} \left| \frac{\langle \Phi_l(q_{m+1}^j), \nabla_q \Phi_{k_j}(q_{m+1}^j) \rangle \, \dot{q}_{m+1}^j}{\Delta E_{l k_j}(q_{m+1}^j)} \right|$$

   (c) If the indicator Ξ exceeds a preset threshold value Ξ_0, decide whether to make a hop or not (Step 2d). Otherwise continue with the propagation (Step 2a).
   (d) Compute the level populations $\theta_l = |c_l^j|^2$ with $c_l^j = \langle \Phi_l(q_{m+1}^j), \psi_{m+1}^j \rangle$. In the last step the trajectory j started on the energy level E_{k_j}; the energy level for the next step is selected via the hopping probabilities $P(k_j \to l) = |c_l^j|^2$, $k = 1, \ldots, n$. If due to this random decision a hop onto the lth level is carried out, then set the wavefunction on energy level E_l and accordingly modify the momentum:

   $$\psi_{m+1}^j = \Phi_l(q_{m+1}^j), \quad \dot{q}_{m+1}^j = \mu(k_j \to l, q_{m+1}^j, \dot{q}_{m+1}^j), \quad \text{and} \quad k_j = l$$

   Otherwise – if the random decision is to stay on level k_j – do nothing.
   (e) Continue the propagation with Step 2a.

The reader might have noticed that the transition zone indicator Ξ is deduced from the second order correction (10) of the populations. In contrast to indicators used in other approaches, it is not highly oscillatory.

The momentum adjustment is standardly realized in form of a correction in the direction of the non-adiabatic coupling vector [12]:

$$p_{\text{new}} = \mu(k_j \to l, q, p_{\text{old}}) = p_{\text{old}} + \frac{\alpha}{\|d_{k_j l}(q)\|_2} d_{k_j l}(q),$$

where the scalar coefficient α is chosen such that energy conservation is achieved, i.e., such that

$$\tfrac{1}{2}\left(|p_{\text{new}}|^2 - |p_{\text{old}}|^2\right) = \sum_\eta |c_\eta^j|^2 E_\eta(q) - E_l(q).$$

The above version of the scheme can be improved by removing the populations on the energy levels E_l, $l \neq k_j$, of trajectories initially on the k_jth level when leaving the transition zone, i.e., the region where the indicator $\varXi$ exceeds the threshold $\varXi_0$. This ensures a Born-Oppenheimer-like motion outside of the transition zone.

Surface hopping algorithms vary mainly in the realization of the hopping procedure. In several aspects, the above proposed QCMD-based variant differs from typical realizations; the interested reader may compare the above algorithmic scheme with the detailed description of typical algorithmic steps in [12] or with the derivation of the standard realization [23].

3.2 Numerical Example

In this section, the performance of the proposed surface hopping algorithm is presented in application to the avoided crossing example from §2.3. For comparison, we solved the full Schrödinger equation (1) of the problem. Using $N = 2000$ trajectories with randomly distributed initial values sampling the initial wavefunction, we found an astonishingly good agreement between the purely quantum solution and the result of our surface hopping algorithm. The populations of the wavefunction components seem to be in accordance to the "exact" solution (cf., Figs. 4 and 5). But notice, just the absolute value of the components can be obtained by the surface hopping algorithm. The corresponding phase of $\Psi_1(q,t)$ and $\Psi_2(q,t)$ cannot be reconstructed.
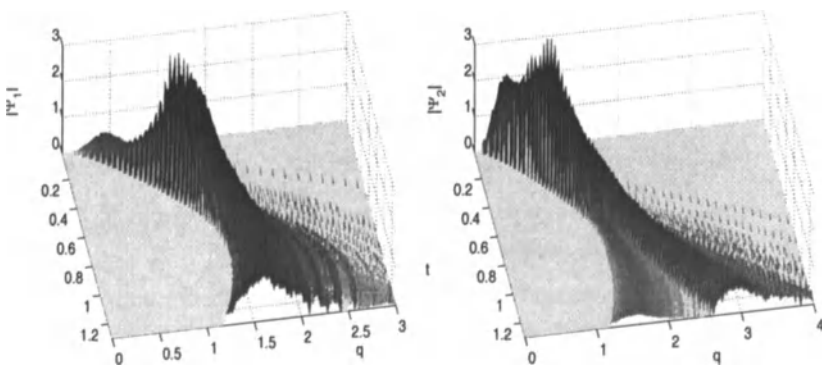
Fig. 4. QCMD-based surface hopping algorithm: Reconstructed wavepacket evolution in q and t . Absolute value of **(a)** Ψ_1 and **(b)** Ψ_2 for $\epsilon = 0.01$
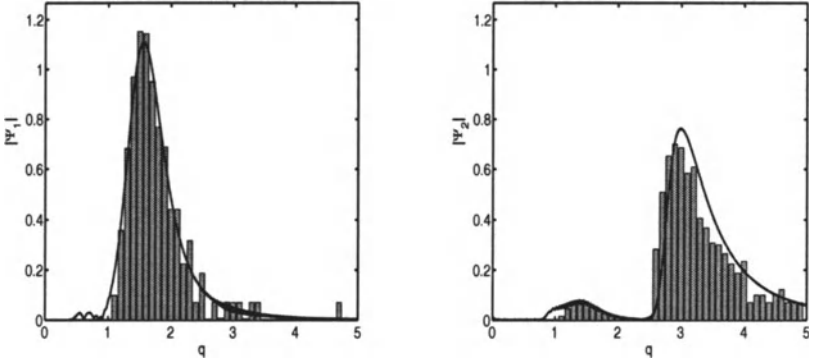
Fig. 5. Comparison of quantum dynamically calculated solution (*lines*) and solution of QCMD-based surface hopping algorithm (*bars*) at time $t = 1.3$. Absolute value of (**a**) $\Psi_1(q, t = 1.3)$ and (**b**) $\Psi_2(q, t = 1.3)$ vs. q for $\epsilon = 0.01$

Unfortunately, the results of our algorithm strongly depend on the parameters. Obviously, the number of sampling trajectories has a major influence on the accuracy of the computation. The algorithm reacts comparably sensitively on modifications of the transition zone threshold Ξ_0 and the size of the time interval Δt. The present authors think that only some careful mathematical analysis of the approximation properties may be able to cope with these difficulties – which are a common problem of surface hopping methods.
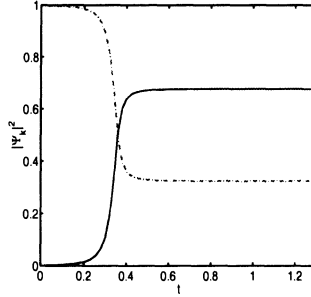
Fig. 6. QCMD-based surface hopping algorithm for $\epsilon = 0.01$: Statistical weights $\|\Psi_1\|_2^2$ (*solid line*) and $\|\Psi_2\|_2^2$ (*dashed dotted*) of the two components of the reconstructed wavefunction versus t

4   Numerical Integrators for QCMD

The numerical integration of the QCMD equations of motion includes the following crucial problem: the time scales of the quantum phase oscillations

are of order $\mathcal{O}(\epsilon)$ and are nonlinearly coupled to the slow classical motion. Thus, any numerical reproduction of these highly oscillatory behavior is a challenging problem whenever ϵ is small. In fact, most of the presently used QCMD integrators require discretization steps of order $\mathcal{O}(\epsilon)$ in time. Several quite different types of such integrators have been developed (cf. [20,16]); the results presented in Sec. 3 have been produced by means of the symplectic PICKABACK scheme [15].

However, for every QCMD simulation over an $\mathcal{O}(1)$ time span, such integrators require $\mathcal{O}(1/\epsilon)$ many time steps, which adds up to an undesirable numerical effort whenever light quantum particles as, e.g., electrons are concerned. Consequently, it is of outstanding interest to construct QCMD integrators that circumvent the pointwise resolution of the highly oscillatory quantum phases, but allow for $\mathcal{O}(1)$ time steps (adapted to the classical motion) while still propagating the quantum motion correctly. In order to summarize the present state of the discussion concerning such *long-stepsize integration schemes*, we have to distinguish between two different cases: (a) *essentially non-adiabatic* quantum processes for which the value of ϵ is significantly different from 0, and (b) *almost adiabatic* quantum processes where ϵ is close to 0 and the asymptotic scaling $\epsilon \to 0$ is of real interest. For the essentially non-adiabatic case, it is in fact possible to construct long-stepsize integration schemes by means of applying appropriate *exponential integrators* to the almost harmonic quantum phase oscillation, compare [17,9,10]. For almost adiabatic situations, however, it seems to be impossible to realize any *exact* reproduction of the quantal phases (in any pointwise sense). Thus, we have to ask whether it might at least be possible to reproduce correctly the "essential" dynamics of the QCMD system, i.e., the classical location and momentum as well as the quantum state population dynamics, while taking (arbitrary) errors in the quantal phases into account. For surface-hopping-like algorithmic schemes such "essential" QCMD simulations would be sufficient. But notice that any error in the phase might have a devastating effect on the other degrees of freedom because of the nonlinear coupling. However, a precise asymptotic analysis [19] reveals that under certain conditions so-called *averaging* integration schemes allow to correctly approximate the dynamics up to a given order in ϵ thus preventing an ϵ^{-1} error growth. Due to the highly oscillatory character of the analytic solution "correct" is now meant with respect to an averaging norm but not to a "pointwise" evaluation in time. Consequently, a mathematical justification of the QCMD-based surface hopping as an approximation of the full quantum evolution should reveal whether some pointwise reproduction of the quantal phase is necessary or not.

References

1. M. Born and V. Fock (1928) Beweis des Adiabatensatzes. *Z. Phys.*, 51:165–180

2. F. A. Bornemann (1998) *Homogenization in Time of Singularly Perturbed Mechanical Systems*, Volume 1687 of *Lecture Notes in Mathematics, no. 1687*. Springer, Berlin, Heidelberg, New York

3. F. A. Bornemann, P. Nettesheim, and C. Schütte (1996) Quantum-classical molecular dynamics as an approximation to full quantum dynamics. *J. Chem. Phys.*, 105:1074–1083

4. F. A. Bornemann and C. Schütte (1998) On the singular limit of the quantum-classical molecular dynamics model. *To appear in SIAM J. Appl. Math.*

5. J. M. Combes (1977) The Born-Oppenheimer approximation. *Acta Phys. Austriaca*, 17:Suppl., 139–159, 1977.

6. P. Deuflhard, J. Hermans, B. Leimkuhler, A. Mark, B. Skeel, and S. Reich, editors (1998) *Computational Molecular Dynamics: Challenges, Methods, Ideas. Proceedings of the 2nd International Symposium "Algorithms for Macromolecular Modelling"*, Lecture Notes in Computational Science and Engineering, No. 4. Springer, Berlin, Heidelberg, New York

7. R.B. Gerber and M.A. Ratner (1988) Time–dependent self–consistent field approximation for intramolecular energy transfer. *Adv. Chem. Phys.*, 70:97–1323

8. G. A. Hagedorn (1980) A time dependent Born-Oppenheimer approximation. *Comm. Math. Phys.*, 77:1–19

9. M. Hochbruck and Ch. Lubich (1998) A bunch of time integrators for quantum/classical molecular dynamics. Published in collection [6], 421–432

10. M. Hochbruck and Ch. Lubich (1998) Exponential integrators for quantum/classical molecular dynamics. *Submitted to BIT*

11. P.J. Kuntz (1991) Classical path surface-hopping dynamics. I. General theory and illustrative trajectories. *J. Chem. Phys.*, 95:141

12. D. Laria, G. Ciccotti, D.F. Cooker, R. Kapral, and M. Ferrario (1998) Nonadiabatic molecular dynamics methods for diffusion. In B. Berne, G. Ciccotti, and D.F. Coker, editors, *Classical and Quantum Dynamics in Condensed Phase Simulations*, pages 700–720. World Scientific, Singapore, Hong Kong, London

13. V.P. Maslov and M.V. Fedoriuk (1981) *Semi-Classical Approximation in Quantum Mechanics*. D. Reidel Publishing Company, Dordrecht, Boston, London

14. A. Messiah (1962) *Quantum Mechanics. Vol. I & II*. North-Holland Publ. Co., Amsterdam, New York

15. P. Nettesheim, F. A. Bornemann, B. Schmidt, and Ch. Schütte (1996) An explicit and symplectic integrator for quantum-classical molecular dynamics. *Chem. Phys. Lett.*, 256:581–588

16. P. Nettesheim and S. Reich (1998) Symplectic multiple-time-stepping integrators for quantum-classical molecular dynamics. Published in collection [6], 412–420

17. P. Nettesheim and Ch. Schütte (1998) Numerical integrators for quantum-classical molecular dynamics. Published in collection [6], 396–411

18. P. Nettesheim (1998) Second order transitions in quantum-classical molecular dynamics. *Preprint*, SC98–37, Konrad-Zuse-Zentrum Berlin

19. P. Nettesheim (1999) Manuscript in preparation, Konrad-Zuse-Zentrum Berlin

20. U. Schmitt and J. Brickmann (1996) Discrete time-reversible propagation scheme for mixed quantum-classical dynamics. *J. Chem. Phys.*, 208:45

21. Ch. Schütte and F. A. Bornemann (1998) Approximation properties and limits of the quantum-classical molecular dynamics model. Published in collection [6], 380–395

22. J.C. Tully (1976) Nonadiabatic processes in molecular collisions. In W.H. Miller, editor, *Dynamics of Molecular Collisions, Part B*, page 217. Plenum, New York

23. J.C. Tully (1990) Molecular dynamics with electronic transitions. *J. Chem. Phys.*, 93(2):1061–1071

24. J.C. Tully (1998) Mixed quantum-classical dynamics: mean field and surface hopping. In B. Berne, G. Ciccotti, and D.F. Coker, editors, *Classical and Quantum Dynamics in Condensed Phase Simulations*, pages 700–720. World Scientific, Singapore, Hong Kong, London

25. J.C. Tully and R.K. Preston (1971) Trajectory Surface Hopping Approach to Nonadiabatic Molecular Collisions: The Reaction of H^+ with D_2. *J. Chem. Phys.*, 55(9):562–572

Part II

Molecular Properties

Molecular Dynamics Simulation of Penetrant Transport in Organic/Inorganic Composite Membrane Materials

Martin Böhning, Dieter Hofmann, and Dieter Paul

GKSS Research Centre, Institute of Chemistry
Kantstrasse 55, D - 14513 Teltow, Germany
e-mail: Martin.Boehning@gkss.de, Dieter.Hofmann@gkss.de

Abstract. Detailed atomistic Molecular Dynamics (MD) simulations are used to investigate the transport behaviour of small penetrant molecules in composites consisting of polymer and microporous inorganic materials. The two model components, an amorphously packed rubbery polymer (PDMS) with included gas molecules (N_2/O_2 and CH_4/CO_2 mixtures, respectively) and a surface modified fully siliceous type-A zeolite (ZK4) were constructed separately and then combined within a single simulation box with applied periodic boundary conditions. After interface formation between these components and thorough equilibration subsequent MD-simulation runs are analysed considering the trajectories of individual gas molecules as well as the polymer and zeolite phase.

1   Introduction

Membrane processes provide a cost effective and flexible way for separating a wide range of mixtures of gases, vapours and liquids in the chemical industry as well as in the environmental and the energy supply sector. In most cases amorphous polymers are used to form a dense separating membrane layer in which the transport of small penetrant molecules is described in terms of a solution diffusion mechanism [1,2]. Although a huge amount of new polymers was synthesised and characterised with respect to their gas transport properties within the last two decades, it was not possible to significantly overcome a limitation known as 'Robeson Upper Bound' [3,4] concerning the relation between selectivity and permeability of polymeric membrane materials. One promising way to distinctively improve the separation performance is the incorporation of microporous structures in a polymeric matrix [5] providing additional molecular sieving as well as adsorption effects influencing the transport processes in combination with the easy handling of polymer based membrane materials. Our molecular dynamics (MD) simulation study is intende to investigate the combination of a rigid microporous lattice structure with a flexible rubbery polymer especially in the interfacial region between these two phases on an atomistic level.

1.1   Gas transport in dense polymeric membranes

According to the solution-diffusion model the overall transport of small molecules through a dense polymer membrane, denoted as permeation, involves the sorption of the penetrant particles at the upstream surface (feed), the diffusion along the membrane cross section and the desorption at the downstream side (permeate). The concentration gradient as the driving force of the diffusive transport is determined by the sorption equilibria at the opposite boundaries of the dense membrane layer (Fig. 1: C_1, C_2).
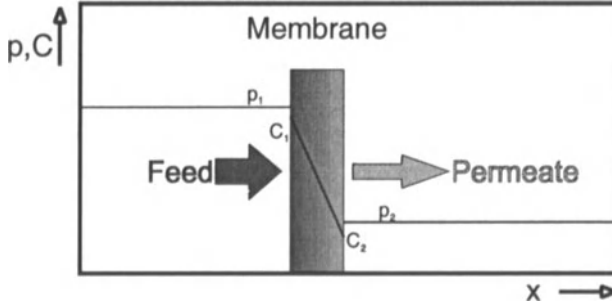
Fig. 1. Concentration profile along the membrane cross section

Generally the permeability (P) of a membrane is given by the product of diffusivity (D) and solubility (S) (equation 1) while the ideal selectivity (α^{id}) can be calculated from the permeability ratio according to equation 2.

$$P = D \cdot S \tag{1}$$

$$\alpha^{id}_{AB} = \frac{P_A}{P_B} = \left(\frac{D_A}{D_B}\right) \cdot \left(\frac{S_A}{S_B}\right) \tag{2}$$

The ideal selectivity can be further splitted into a diffusivity term (D_A/D_B) depending mainly on chain mobility, free volume fraction and penetrant size, and a solubility term (S_A/S_B) determined primarily by the chemical composition of penetrant molecule and polymer. With respect to MD simulations it has to be pointed out that a sufficient size of the model is necessary in order to represent the dynamic behaviour as well as the free volume distribution of an amorphously packed polymer determining its transport properties towards small molecules.

1.2   Gas transport in the interfacial region between polymer and zeolite

MD simulations of various amorphous polymers performed in our group [6] as well as reported in literature [7,8] have shown that the macroscopic diffusive

transport of gases is a result of certain molecular jump events which allow the penetrant molecule to move between two adjacent free volume elements within the polymer matrix. The occurrence and lifetime of temporary 'channels' between these holes depends strongly on the chain mobility affected by the stiffness of the polymer backbone as well as the local morphology which both are expected to be different in the vicinity of the very rigid inorganic lattice. Therefore, the gas transport in the interfacial regions is of considerable importance for the transition of gas molecules between the two phases of the composite and the overall performance of the membrane material. It has to be noted that our primary focus is on the polymer and penetrant behaviour near the interface.

2   Model and simulation details

The model used in our study is composed of an amorphous polymer packing and a surface modified zeolite lattice as described below. Our calculations were performed using the *InsightII / Discover* package of Molecular Simulations Inc. (MSI, San Diego) on a Silicon Graphics (SGI) *Octane SI* workstation with a MIPS R10000 CPU at 175MHz and 640MB RAM. For the construction of the zeolite the *Solids_ Builder* module was utilised while the polymer chain was created using the *Polymerizer* module. Amorphous packing of the polymer chain together with the appropriate amount of gas molecules was done with the *Amorphous_ Cell* module. All dynamics calculations and minimisations were performed with *Discover3/CDiscover* and the *PCFF* forcefield using the *InsightII* interface as well as the implemented *BTCL* scripting language [9].

2.1   Model components

For the zeolite phase a fully siliceous type-A (LTA) structure (ZK4) was chosen. The absence of Al-atoms in the framework implies that the structure contains no cations normally necessary for compensating the negative charge of AlO_4^-- framework units. In order to get at least a somewhat more realistic surface structure the unit cell of the zeolite was shifted by 1/4 in z-direction and the resulting surface Si atoms were terminated with hydroxyl groups. a and b dimensions of the zeolite structure were kept as in the unit cell (a= b= 24.61Å) whereas in c direction the size was doubled (c= 49.22Å). As polymer component a poly(dimethyl siloxane) (PDMS, Fig.2) with a degree of polymerisation of $P=$ 220 was chosen.

PDMS is a well characterised rubbery membrane material showing a high chain mobility due to a very flexible backbone structure. Therefore it was possible to start the packing procedure using the experimental value of $\rho = 0.95 g/cm^3$ [10,11] as initial density. The subsequent equilibration procedure consisted of several high temperature dynamic runs in combination

$$\left[\begin{array}{c} CH_3 \\ | \\ -Si-O- \\ | \\ CH_3 \end{array}\right]_n$$

Fig. 2. Repeat unit of poly(dimethyl siloxane) (PDMS)

with energy minimisation where the last equilibration/minimisation stage was performed at the intended simulation temperature of 303K. The a and b dimensions of the packing cell were predetermined by the zeolite size in order to allow the interface formation while the c dimension was adjusted during packing to meet the anticipated experimental density value. The high mobility of the chosen polymer should allow the mobility constraints which might be imposed by the rigid zeolite to be more easily observed. The gas mixtures under investigation so far (i.e. N_2/O_2 and CH_4/CO_2, respectively) were inserted into the polymer phase prior to the amorphous packing procedure. The number of gas particles was chosen according to calculated concentration values using experimentally determined solubility parameters taken from literature [12], based on a modified dual-mode sorption relation of Suwandi and Stern (also shortly described in [12]). In the case of the methane / carbon dioxide mixture 10 and 33 molecules, respectively, were included in the polymer packing which corresponds to the gas concentration of PDMS being in equilibrium with a gas phase pressure of about 15bar ($C_{CH4} = 7.8cm^3(STP)/cm^3$(polymer), $C_{CO2} = 25.6cm^3(STP)/cm^3$ (polymer) [1]). For nitrogen / oxygen 10 and 18 molecules, respectively, were in-
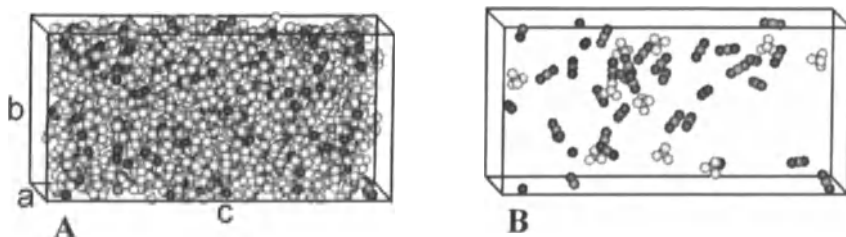
Fig. 3. A - Amorphously packed PDMS; **B** - Initial distribution of the gas molecules (CH_4/CO_2) within the packing (after equilibration; $a = b = 24.61\mathring{A}, c = 50.0\mathring{A}, r = 0.95g/cm^3$)

serted corresponding to a pressure of about 60bar in the gas phase ($C_{N2} = 7.8cm^3(STP)/cm^3$(polymer), $C_{O2} = 13.7cm^3(STP)/cm^3$(polymer)). Fig. 3

---

[1] Concentration are given in cm^3 of gas under STP conditions per cm^3 of polymer. STP denotes standard temperature and pressure ($p_0 = 1.013bar, T_0 = 273.15K$)

shows the initial distribution of gas molecules (CH_4/CO_2, B) within the packed polymer cell (A).

2.2   Composite model

The complete model was then created by placing the polymer/gas packing and the zeolite lattice with an additional empty volume into a single simulation cell as shown in Fig. 4. This resulted in a system size of about 3500 atoms.
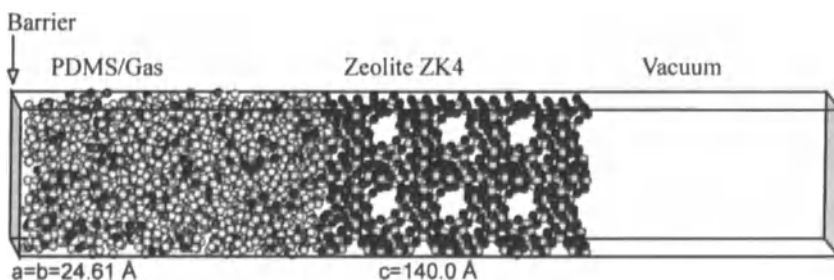
Fig. 4. Simulation cell (after interface formation and equilibration) containing the PDMS/gas packing and the zeolite structure used for MD calculations under periodic boundary conditions

The periodic boundary conditions (PBC) applied during the subsequent simulation runs were restricted to two dimensions by means of an energy barrier at the a-b cell surface in order to prevent the enclosed gas molecules from directly entering the empty volume within the simulation cell. The interface between the two components was formed by a cautious approach during an initial molecular dynamics run with extremely small simulation steps of 0.1 fs. Unlike the polymer packing the zeolite structure needs a special treatment under the applied PBC. Two different attempts were made to consider effects of cross boundary bonds in the zeolite lattice. First this can be achieved by fixing the lateral edge atoms of the lattice. A more sophisticated approach is to ensure that bonding information is retained across the cell boundaries. The latter is complicated by the fact that the three dimensional lattice symmetry of the zeolite is destroyed by the surface modification done before. The problem can, however, be solved by the introduction of translational symmetry for the zeolite in the lateral (x, y) directions only. Both approaches were tested in our study.

2.3   Simulation details

Molecular dynamics runs for data production were performed under NVT conditions, i.e. number of atoms and volume are held constant, at 303K with

a step-width of 1.0 fs. The temperature was controlled using the Berendsen heat-bath method. For our model special attention has to be paid to the treatment of nonbonding interactions. Coulombic interactions within infinite periodic lattice structures, such as the zeolite under PBC, cannot be calculated with sufficient accuracy using the usual atom- or group-based cutoff methods [9]. The Ewald summation technique [9,13] is best suited in those cases but associated with a high consumption of CPU time. As for the trajectory analysis of single penetrant molecules with respect to their diffusive movement within the polymer matrix as well as the zeolite rather long simulation times of several nanoseconds are necessary, we also performed calculations using the periodic cell multipole method (CMM) [9] implemented in MSI's *Discover* package which provides a reasonable accuracy level at 5 to 10 times higher computing speed.

2.4   Temperature differences

A general problem associated with interface MD-simulations is the occurrence of temperature differences between model components with very different atom mobilities. In the case of our model the arising temperature differences between the flexible polymer and the very rigid zeolite become as high as 300K during MD simulation runs. An attempt to overcome this behaviour was made by scaling the atom velocities of polymer and zeolite separately to meet the target temperature. Using the *BTCL* scripting language of the *Discover* software an appropriate procedure was included in every calculation step of the dynamics run.

2.5   Trajectory analysis

Trajectory data of individual gas molecules may be analysed using the Einstein relation which allows the calculation of diffusion coefficients (D) from the mean squared displacement (MSD) averaged over all possible time origins ($s(t)$, eq.4) according to equation 5.

$$r(t) = \left| \vec{R}(t) - \vec{R}(0) \right| \tag{3}$$

$$s(t) = \langle |r(t) - r(0)|^2 \rangle \tag{4}$$

$$D = s(t)/6t \tag{5}$$

The distance $r(t)$ can be calculated from the position vectors $\vec{R}$ (eq. 3) which are extracted from the time dependent cartesian atom coordinates stored during the dynamics run. The MSD of selected atoms within the lattice can also be used to compare the vibrational motion of the zeolite framework for the different methods of calculation of nonbonding interactions mentioned above as well as for comparison between the bulk and interface regions of the amorphous polymer. The trajectory of a single N_2 molecule within the

simulation box can be seen in Fig. 5. It has to be noted that the trajectory parts at the polymer/zeolite interface are connected by the outer surfaces of the box due to the applied periodic boundary conditions. The corresponding
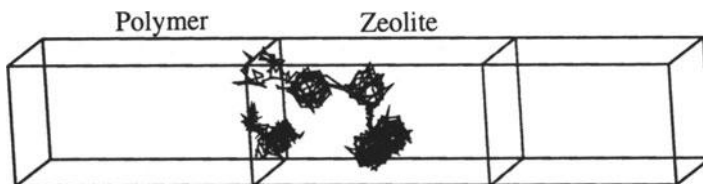
Fig. 5. Trajectory of a single N2 molecule within the simulation box

plot of $r(t)$ vs. simulated time t (Fig. 6A) together with the z-coordinate (Fig. 6B) allows a more detailed analysis of the molecules trajectory. The interface between polymer and zeolite is situated around $z = 50\text{Å}$.
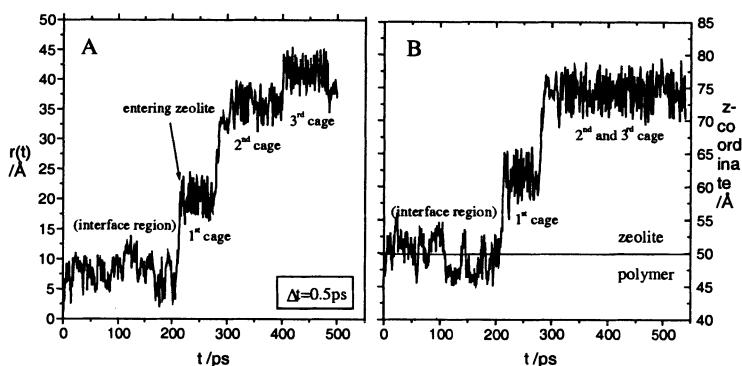
Fig. 6. Radial distance $r(t)$ (**A**) and z-coordinate (**B**) for the single molecule trajectory (shown in Fig.5) plotted vs. simulated time t

3   Conclusions

A detailed atomistic model combining an amorphously packed rubbery polymer and a rigid microporous lattice structure was constructed. Gas molecules were included within the polymer packing in order to investigate their transport behaviour within the two model phases as well as in the interface region using molecular dynamics calculations.

The very complex structure of the model implicates an extensive consideration of the calculation of nonbonding interactions with respect to accuracy and computing speed. Besides the Ewald summation technique for coulombic nonbond interactions, also the cell multipole method can be used to treat

the composite model with reasonable accuracy providing distinctively higher performance. The latter is particularly necessary considering long dynamics simulation runs up to several nanoseconds needed for detailed trajectory studies. Furthermore, the problem of temperature differences across a modelled interface arising during MD-simulation runs, which appeared drastically between the very rigid zeolite and the flexible polymer used in our model, was addressed by a velocity scaling procedure treating the atoms of the two phases separately.

The results obtained so far suggest further expansions of our study which may include sandwich models with two polymer/zeolite interfaces in the simulation box as well as the employment of latest, more sophisticated forcefields such as the *COMPASS* forcefield of MSI.

References

1. M. Mulder "Basic Principles of Membrane Technology", Kluwer Academic Publ., Dordrecht 1991
2. D.R. Paul, Y.P. Yampol'skii (eds) "Polymeric Gas Separation Membranes", CRC Press, Boca Raton 1994
3. L.M. Robeson 'Correlation of separation factor versus permeability for polymeric membranes' J. Membrane Sci. **62** (1991) 165–185
4. L.M. Robeson, W.F. Burgoyne, M. Langsam, A.C. Savoca, C.F. Tien 'High performance polymers for membrane separation' Polymer **35** (1994) 4970–4978
5. M. Moaddeb, W.J. Koros 'Gas transport properties of thin polymeric membranes in the presence of silicon dioxide particles' J. Membrane Sci. **125** (1997) 143–163
6. D. Hofmann, J. Ulbrich, D. Fritsch, D. Paul 'Molecular modelling simulation of gas transport in amorphous polyimide and poly(amide imide) membrane materials' Polymer **37** (1996) 4773–4785
7. A.A. Gusev, F. Müller-Plathe, W.F. van Gunsteren, U.W. Suter 'Dynamics of Small Molecules in Bulk Polymers' Adv. Polym. Sci. **116** (1994) 207–247
8. F. Müller-Plathe 'Permeation of polymers - A computational approach' Acta Polymer. **45** (1994) 259–293
9. Software documentation: "Simulation Tools: Discover" Molecular Simulations Inc., San Diego 1996 also on: http:// www.msi.com/doc/
10. "Silicones and Silicon containing polymers", ABCR catalogue 1994/95
11. L. Fritz, D. Hofmann 'Molecular dynamics simulations of the transport of water - ethanol mixtures through polydimethylsiloxane membranes' Polymer **38** (1997) 1035–1045
12. Y. Kamiya, Y. Naito, T. Hirose, K. Mizoguchi 'Sorption and Partial Molar Volume of Gases in Poly(dimethyl siloxane)' J. Polym. Sci. Part B: Polym. Phys. **28** (1990) 1297–1308
13. R. Haberlandt, S. Fritzsche, G. Peinel, K. Heinzinger "Molekulardynamik - Grundlagen und Anwendung" Vieweg, Braunschweig 1995

ParaGauss: A Density Functional Approach to Quantum Chemistry on Parallel Computers

Th. Belling[1], Th. Grauschopf[2], S. Krüger[1], F. Nörtemann[1], M. Staufer[1], M. Mayer[1], V. A. Nasluzov[1], U. Birkenheuer[1], and N. Rösch[1]

[1] Lehrstuhl für Theoretische Chemie, Technische Universität München, 85747 Garching
[2] Institut für Informatik, Technische Universität München, 80290 München

Abstract. A density functional method for electronic structure calculations of atoms, molecules and clusters has been parallelized and newly implemented in the program *ParaGauss*. Parallelization strategies and performance aspects are discussed. The capabilities of this new quantum chemical code, which includes an option for scalar-relativistic calculations, are demonstrated by all-electron results for large transition metal clusters (Pd_{309}, $Au_{38}(SH)_{24}$).

1 Introduction

The efficient development and optimization of many modern technological and scientific devices and processes hinges upon a detailed understanding of underlying structures and mechanisms at an atomic scale. Examples range from homogeneous and heterogeneous catalysis and drug design in pharmaceutical research to the areas of material sciences and semiconductor devices. Not every information desirable for a thorough understanding is directly available via experiment. Accurate theoretical calculations can provide complementary insight. Moreover, the interpretation of experimental results often strongly relies on comparison with theoretical models. Thus, there is a growing interest in an accurate theoretical description of systems on the molecular scale. Quantum chemistry, which is the appropriate approach for such a treatment, has become a powerful tool to deal with practical problems during the last two decades. On the one hand, this progress relies on the considerable increase in available computer power, on the other hand, also quantum chemical methodology has made noticeable progress. A wide spectrum of methods is available [1]. They range from empirical approaches, which can handle about several thousands of atoms up to highly sophisticated methods yielding very accurate results for small molecules. Parallel computers had a large impact on the capabilities of quantum chemistry. Quite a number of methods have been adapted to exploit parallel hardware architectures [2], relying mostly on the parallelization of existing serial codes.

Here we present a new implementation of a first-principles density functional approach to the electronic structure of molecular systems. The new

program *ParaGauss* has been developed for efficient use of parallel and vector-parallel architectures [3]. Nonrelativistic as well as relativistic variants of the method allow application to molecules and clusters composed of elements of the entire periodic table. After a brief introduction to the concepts of the underlying density functional methodology the parallelization strategy is described. Scaling properties and capabilities of the new code are illustrated by sample applications.

2   The LCGTO Approach and its Relativistic Extension

Quantum theory provides the proper framework for determining the electronic structure of molecules, clusters, and solids, which represents the basis for accessing further properties of these systems. Relativistic effects have to be accounted for when heavy elements are present. First the solution of a non-relativistic electronic many-body problem will be considered.

Conventional wave function based methods of quantum chemistry which start with a solution of the Hartree-Fock problem aim at a direct determination of the many-particle wave function as a solution of the Schrödinger equation. Density functional theory [4] pursues a different approach: The total energy is viewed as a functional of the electron density ρ, which is expressed by the so-called Kohn-Sham orbitals ψ_i. Variation of the total energy with respect to these orbitals leads to the Kohn-Sham equations

$$\hat{h}_{KS}\psi_i = \epsilon_i\psi_i \tag{1}$$

with the one-electron Kohn-Sham operator

$$\hat{h}_{KS} = \hat{h}_{kin} + v_{nuc} + v_{coul} + v_{xc}. \tag{2}$$

In analogy to the Schrödinger equation the first term represents the kinetic energy operator, the second term the nuclear potential and the last two terms account for the electron-electron interaction. Since the latter two potentials depend on the electron density via the one-particle orbitals, the above operator pseudo-eigenvalue equation has to be solved self-consistently (self-consistent field procedure, SCF). The exchange-correlation potential v_{xc} is defined as a functional derivative of the exchange-correlation energy $E_{xc}\left[\rho\left(r\right)\right]$ with respect to the density ρ, which is not known in general as a functional of the density. However, good approximations are available for E_{xc} and thus for v_{xc}.

In order to transform the effective one-particle equation (1) into an algebraic problem, the Kohn-Sham orbitals ψ_i are expanded in a finite set of basis functions χ_μ with coefficients c^i_μ. The LCGTO approach (Linear Combination of Gaussian-Type Orbitals) [5] applies Gaussian functions to model the radial dependence and harmonic polynomials $r^l Y^m_l\left(\vartheta, \varphi\right)$ to describe the angular

part. Expressing the Kohn-Sham orbitals by means of basis functions leads to the following symmetric generalized matrix eigenvalue problem

$$\mathbf{h}_{KS}\mathbf{c}^i = \epsilon_i \mathbf{S}\mathbf{c}^i \quad \text{with} \quad \mathbf{h}_{KS}^{\mu\nu} = \langle \mu | \hat{h}_{KS} | \nu \rangle \text{ and } \mathbf{S}_{\mu\nu} = \langle \mu | \mathbf{1} | \nu \rangle. \quad (3)$$

$\mathbf{h}_{KS}$ is the Kohn-Sham matrix and $\mathbf{S}_{\mu\nu}$ is the so-called overlap matrix which contains the unity operator $\mathbf{1}$. For brevity we introduce a shorthand notation for integrals:

$$\langle \mu | \mathcal{O} | \nu \rangle = \int \chi_\mu(\mathbf{r})\, \mathcal{O}(\mathbf{r})\, \chi_\nu(\mathbf{r})\, d\mathbf{r}\,, \quad [\mu|\nu] = \int \int \frac{\chi_\mu(\mathbf{r})\, \chi_\nu(\mathbf{r}')}{|\mathbf{r} - \mathbf{r}'|}\, d\mathbf{r}\, d\mathbf{r}' \quad (4)$$

Apart from the overlap matrix $\mathbf{S}_{\mu\nu}$ the construction of the Hamilton matrix requires further integrals which can be classified according to the number of basis functions involved as "n-center" integrals.

The classical electron-electron interaction yields four-center integrals, since the electron density is proportional to the (absolute) square of the orbitals,

$$\mathbf{h}_{coul}^{\mu\nu} \propto [\mu\nu|\rho] \to [\mu\nu|\kappa\lambda]\,. \quad (5)$$

Introduction of an approximate variational expansion of the electron density via an auxiliary set of Gaussian basis functions f_k ("fitting" functions),

$$\rho(\mathbf{r}) \simeq \bar{\rho}(\mathbf{r}) = \sum_k a_k f_k(\mathbf{r})\,, \quad (6)$$

reduces the computational effort for the electron Coulomb interaction term to three-center integrals [5]

$$\mathbf{h}_{coul}^{\mu\nu} \simeq \sum_k a_k\, [\mu\nu|f_k]\,. \quad (7)$$

Due to its complex form, the exchange-correlation term is integrated numerically while all other integrals are determined analytically.

If an automatic optimization of the molecular geometry is desired, the forces acting on the nuclei have to be calculated. They are given as the negative gradients of the total energy expression with respect to the atomic positions [6].

In a relativistic density functional treatment one has to solve a four-component Kohn-Sham-Dirac equation [6]:

$$\hat{h}_{\mathrm{DKS}}^{(4)}\psi_i^{(4)} = \left(\beta c^2 + c\boldsymbol{\alpha}\boldsymbol{\pi}_i + v_{eff}\right)\psi_i^{(4)} = \epsilon_i \psi_i^{(4)} \quad (8)$$

$$v_{eff} = v_{nuc} + v_{coul} + v_{xc}. \quad (9)$$

The four-component spinors $\psi_i^{(4)}$ comprise two electronic and two positronic components which can be decoupled to second order in the effective potential v_{eff} by means of a unitary Douglas-Kroll (DK) transformation U:

$$\hat{h}_{\mathrm{DKS}}^{(2)} = U^\dagger \hat{h}_{\mathrm{DKS}}^{(4)} U \quad (10)$$

The electronic operator $\hat{h}_{\mathrm{DKS}}^{(2)}$ still includes all relativistic effects of chemical relevance. It can be further simplified to a single-component, scalar-relativistic form by neglecting spin-orbit interaction. Since the Douglas-Kroll transformation depends on the effective potential v_{eff}, it has to be carried out in every cycle of the SCF procedure when the relativistic Hamilton matrix is constructed. The repeated transformation can be avoided when only the nuclear potential is taken into account for the DK transformation and relativistic effects are restricted to the kinetic and nuclear potential terms of the Hamilton operator. Then the latter terms can be transformed before entering the SCF procedure while the electron-electron interaction is treated nonrelativistically. This efficient and accurate approximation of the relativistic Dirac-Kohn-Sham Hamilton operator is implemented in *ParaGauss* in the scalar-relativistic as well as in the two-component version that includes spin-orbit interaction. In *ParaGauss* forces are so far available for the scalar-relativistic variant of the method. For more details on the relativistic Kohn-Sham approach see Ref. [6].

   With respect to its structure, *ParaGauss* is a typical density functional program. At the beginning of an electronic structure calculation the input is processed and information for symmetry adaption of orbitals and operators is provided. In the subsequent "integral" part the analytical integrals needed for the SCF procedure are precalculated and stored. The dominating amount of data are the three-center integrals, which may accumulate to several giga-bytes for larger applications. For relativistic calculations, two-center integrals only are needed in addition. Also the grid for numerical integration of the exchange-correlation potential is set up before the SCF procedure is started. The core of the algorithm is the SCF part, where the Kohn-Sham equations are solved iteratively. This part is repeated until the electron density and the total energy are converged to the desired accuracy. In case of a geometry optimization, the density is used subsequently to calculate the forces on all nuclei. Together with the total energy these data are passed to an external optimization package which searches a local mimimum of the energy hypersurface (ground state) or a saddle point ("transition state"). At the end, various modules for analysis of the results and for calculating properties can be invoked. The computational demand of the different parts depends crucially on the system under study, but in general the SCF part dominates.

3   Parallelization and Performance

Each of the various steps of a molecular density functional calculation with a Gaussian-type basis set features a different data structure; thus, no overall strategy for parallelization may be invoked. On the other hand, a fine grain parallelization at the level of the basic linear algebra operations would not be effective due to a low ratio of computation-to-communication effort [7]. For this reason a coarse grain parallelization was chosen, applying suitable

parallelization strategies for each specific task. The structure of the parallel implementation has been designed as a controlling master process which executes serial parts and distributes the parallelized tasks to slave processes [3]. To exemplify this approach, we discuss in the following the implementation for the dominating SCF part in more detail.

Within each loop of the SCF part, several steps, each involving a different data structur, are performed as depicted in Fig. 1. The four dominanting steps which account for over 98% of computational cost have been parallelized.
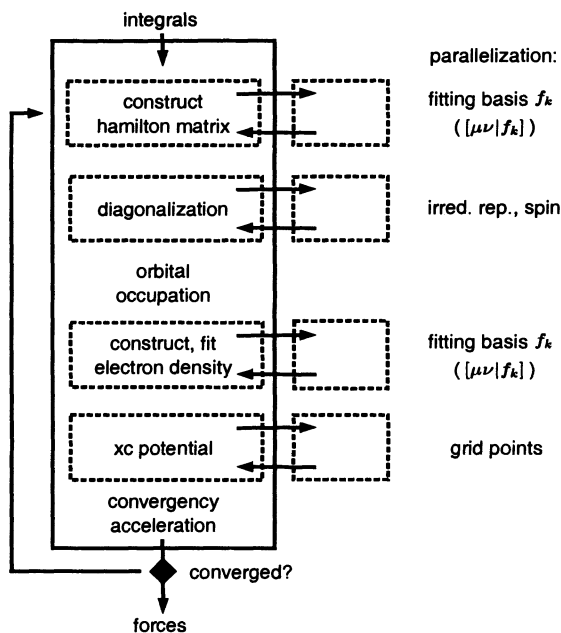
Fig. 1. Structure and parallelization of the SCF part. Parallelized tasks are indicated by dashed boxes.

First, the Hamilton matrix is constructed using the three-center integrals which are distributed according to the index of the fitting basis. Each processor calculates a certain contribution to the elements of the Hamilton matrix; these contributions are then summed up in a binary cascade and the final result is sent to the master. Next, the Hamilton matrix is diagonalized. In the present implementation, this step is parallelized exploiting the block-diagonal form of the Hamilton matrix according to the irreducible representations of the point group symmetry of the molecular structure. In a spin-polarized calculation, the duplication of blocks for spin-up and spin-down orbitals is also exploited. These independent eigenvalue problems are solved in parallel in the order of decreasing matrix dimension; application of a parallel eigensolver may be more efficient for large problem sizes. The following step

where the occupation numbers of the calculated orbitals are determined requires negligible computational effort and thus is not parallelized. Setting up the charge density matrix and subsequently fitting the density involves three-center integrals. The construction of the corresponding system of linear equations is thus parallelized over the index of the fitting functions. The numerical integration of the contribution of the exchange-correlation potential to the Hamilton matrix is carried out over a grid which typically comprises about 3000 points per atom. This task is parallelized by partitioning the grid in sections of equal size. Accordingly, for the various grid partitions the electron density and the exchange-correlation potential are evaluated in parallel. Finally, the contributions to the Hamilton matrix from the grid partition are summed in a cascade. The evaluation of the exchange-correlation related quantities is the computationally most demanding step of the SCF procedure. It is vectorized over the grid points in the innermost loops, which are partitioned further according to the optimal vector length of the hardware architecture used. At the end of the SCF procedure convergence checks and acceleration are performed; they involve negligible computational effort.
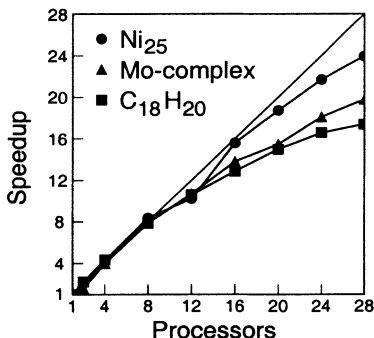
Fig. 2. Parallel performance of single geometry runs on an IBM SP2 computer.

In Fig. 2 the acceleration of electronic structure calculations including forces is shown, using up to 28 processors of an IBM SP2. Three test examples were selected which feature considerable variation with respect to the computational parameters: the surface cluster model Ni_{25}, the hydrocarbon $C_{18}H_{20}$, and the molybdenum complex $[(HOCHO)(SH)OMoS_2C_2H_2]^-$. Although the performance differs for the three examples, very good scaling is obtained for up to 16 processors. This demonstrates that most parts of the algorithm have been efficiently parallelized. For larger numbers of nodes the more demanding test system Ni_{25} exhibits better efficiency than the smaller ones. The program *ParaGauss* was developed on a cluster of HP workstations and ported to the shared-memory parallel hardware SGI PowerChallenge, to the scalar distributed-memory architecture IBM SP2, and to the high-performance distributed-memory vector-parallel computer Fujitsu VPP700.

The relative performance of the different parts of the program on various platforms depends on the relative weight of integer and floating-point operations as well as on the loop length available for vectorization. While the integral part features a higher fraction of integer operations and rather short loop lengths, the other parts are dominated by floating-point operations and, at least in the numerical parts, support very long loop lengths. This is corroborated by a comparison of computing times on an IBM SP2 computer and a Fujitsu VPP700 machine (vector length 2048). Efficient vectorization leads to an overall speed-up on a VPP700 by about a factor of ten relative to SP2.

Finally, to illustrate the efficiency of the parallel code *ParaGauss* and the possibilities it offers, we discuss recent applications, focusing on the computational aspects. Large transition metal clusters provide some of the most challenging computational problems in quantum chemistry. We studied gas-phase clusters in order to identify how various properties scale with cluster size. In this context, the average interatomic distance of the four-shell icosahedral cluster Pd_{309} has been optimized in an all-electron density functional calculation. The orbitals of the 14214 electrons of this clusters have been described by 13905 contracted (i.e. fixed linear combinations of) Gaussian basis functions leading to 2 GB background storage for the three-center integrals. The calculations were performed utilizing 20 thin nodes of an IBM SP2 in parallel; the wall clock time for the computation of one geometry was about 58 hours.
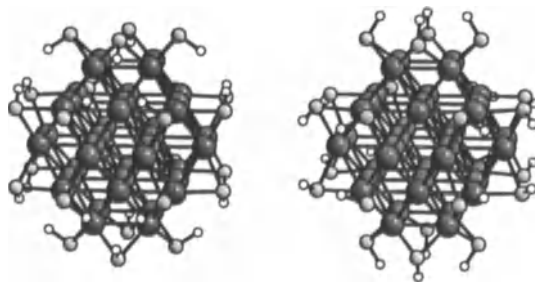
Fig. 3. Cluster $Au_{38}(SH)_{24}$: optimized ground state geometries of octahedral symmetry for different ligand orientations.

An even more demanding task is the determination of the equilibrium geometry of ligated clusters. As a model for the recently synthesized species $Au_{38}(SR)_{24}$ with $R = C_{15}H_{25}$ we studied the ligand orientation and the cluster deformation of $Au_{38}(SH)_{24}$ (Fig. 3). All 4598 electrons of the cluster were described utilizing 3410 contracted basis functions. Although the geometry was restricted to octahedral symmetry, eight degrees of freedom had to be optimized. With 8 processors of a Fujitsu VPP700, a single geometry (including forces) required 3.2 hours computing time for the scalar-relativistic

variant of the method. About 30 single-geometry calculations were necessary to determine the ground state geometry of a specific ligand orientation.

4   Summary and Outlook

The code *ParaGauss* presents a new implementation of a density functional method for carrying out first-principles calculations of the electronic structure of molecules and clusters. Both standard nonrelativistic as well as relativistic variants of the method are available. In the code *ParaGauss* the method is fully parallelized as well as adapted to high-performance vector-parallel architectures. For applications of moderate size up to 16 processors can be efficiently used. The good overall scaling behavior of the implemented algorithms permits employment of more nodes for more demanding problems. Electronic structure calculations on systems with more than 10000 electrons are now feasible with high accuracy. The strongly enhanced computational capability of *ParaGauss* allows one to tackle problems of considerably enhanced complexity, like complete geometry optimizations for a many degrees of freedom on systems that include heavy elements. Yet, there is considerable demand for further methodological development. For example, increased computational power of programs and hardware opens the path to a new goal of computational molecular science: the treatment of dynamical processes on a "first principles" level. Such problems require electronic structure determinations for at least 10^4 geometries, a demand that is within reach with *ParaGauss*, at least for smaller systems.

References

1. *Reviews in Computational Chemistry*, Eds. K.B. Libkowitz, D.B. Boyd, Vol. 1-11, Wiley-VCH, New York 1990-1997.
2. R.J. Harrison, R. Shepard, Ann. Rev. Phys. Chem. **45** (1994) 623.
3. N. Rösch, S. Krüger, Th. Belling, F. Nörtemann, M. Staufer, C. Zenger, Th. Grauschopf, in *Statustagung des BMBF HPSC97. Paralleles Höchstleistungsrechnen und seine Anwendungen*, Eds. R. Krahl, G. Wolf, p. 165.
4. R.G. Parr, W. Yang, *Density Functional Theory of Atoms and Molecules*, Oxford University Press, New York 1989.
5. B.I. Dunlap, N. Rösch, Adv. Quantum Chem. **21** (1990) 317.
6. N. Rösch, S. Krüger, M. Mayer, V.A. Nasluzov, in *Recent Developments and Applications of Modern Density Functional Theory*, Ed. J.M. Seminario, Elsevier, Amsterdam 1996. p. 497.
7. W. Thiel and D.G. Green, in *Methods and Techniques in Computational Chemistry: METECC-95*, Eds. E. Clementi, G. Corongiu, STEF, Cagliari 1995, p. 141.

Mathematics for Combinatorial Chemistry

Th. Grüner[1], A. Kerber[1], R. Laue[1], and M. Meringer[1]

Department of Mathematics, University of Bayreuth,D-95440 Bayreuth, Germany

Abstract. Some of the mathematical methods will be described which are implemented in the software package

$$MOLCOMB^1$$

that allows to simulate combinatorial chemistry by generating combinatorial libraries and to do screening according to geometric substructures.

1 Combinatorial Chemistry

To begin with, we consider the examples described in the prominent papers [1] and [2] on combinatorial chemistry. The authors introduce particular combinatorial libraries obtained by starting from the *central molecules*
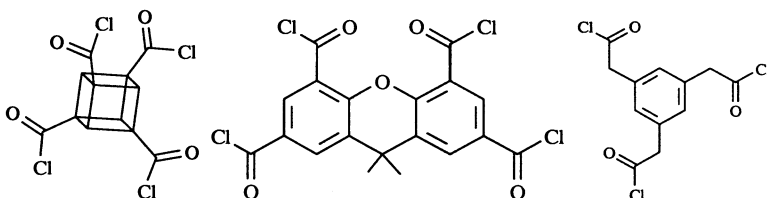
i.e. they start from cubane, xanthene, benzene triacid chlorine as central molecules to which they attach amino acids according to the *reaction scheme* that describes the reaction between the active sites
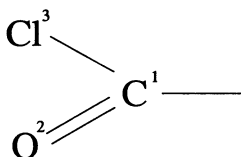
of the central molecule and the active parts of the aminoacids in question:
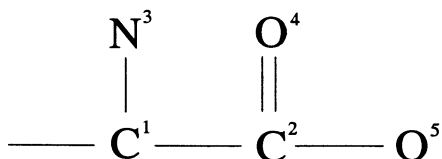
Here is the *reaction scheme:*

$$\rho = \begin{pmatrix} 0 & 0 & 1 & 0 & 0 \\ 0 & 0 & 0 & 0 & 0 \\ -\infty & -\infty & -\infty & -\infty & -\infty \end{pmatrix}.$$

Atom i of the central molecule's active site will be connected to atom j of the amino acid by a bond of multiplicity $\rho_{i,j}$.

It is a variation of the Ugi's be&r-matrices. The aim is to describe the combinatorial libraries that arise from the given central molecule by reaction with a prescribed set of amino acids.

2 A mathematical model

A mathematical model for that situation is well known since Pólya ([3]). It is in fact the very same model that applies to the description of *permutational isomers* corresponding to a given skeleton and a prescribed set of ligands. We introduce two sets:

- S, the set of *active sites* of the central molecule,
- A, the prescribed set of *building blocks* , which are in our example, a set of amino acids.

A reaction of the central molecule with the amino acids is, in mathematical terms, a mapping from S into A, i.e. an element of the following set of all such mappings:

$$A^S := \{f \colon S \to A\}.$$

For example, if we allow 20 amino acids to react, then there are $20^4 = 160000$ mappings in the case of the cubane as well as in the case of the xanthen or the benzene triacid chlorine.

These 160 000 molecules (better say: the corresponding molecular graphs) are easily generated, but we definitely should *not* put them into a big data bank and do screening immediately, since they are in fact too many, as *not all of them are essentially different* and we should definitely try to save space, since combinatorial libraries can be very big. The reason why not all of them are different is the *symmetry group* of the central molecule. In case of the cubane it is the group T_d, in case of the xanthen it is C_{2v} while the symmetry group of the triacid is C_{3v}.

Hence what we are really after is the set of *orbits* of these groups on the set of mappings. We indicate these sets by

$$T_d \backslash\backslash A^S, \ C_{2v} \backslash\backslash A^S, \ C_{3v} \backslash\backslash A^S.$$

Pólya's theory of enumeration under group action contains enough results to evaluate first of all the *size* of these sets, i.e. the size of the libraries of

molecules arising from the central molecules and the amino acids. We obtain the following formulae in terms of the order $|A|$ of the set of amino acids which we would like to take: In the cubane case we get that

$$|T_d\backslash A^S| = \frac{1}{24}\left(|A|^4 + 6\cdot|A|^3 + 11\cdot|A|^2 + 6\cdot|A|\right).$$

$|A| = 20$ yields the number 8 855. For the xanthen we obtain

$$|C_{2v}\backslash A^S| = \frac{1}{2}(|A|^4 + |A|^2).$$

$|Y| = 20$ gives 80 200, while for the triacid we find

$$|C_{3v}\backslash A^S| = \frac{1}{3}(|A|^3 + 2\cdot|A|),$$

which gives 2680 in the case when $|A| = 20$. Here is a table for different sizes of A :

$|A|$	cubane	xanthene	triacid
1	1	1	1
2	5	10	4
3	15	45	11
4	35	136	24
5	70	325	45
6	126	666	76
7	210	1225	119
8	330	2080	176
9	495	3321	249
10	715	5050	340
11	1001	7381	451
12	1365	10440	584
13	1820	14365	741
14	2380	19306	924
15	3060	25425	1135
16	3876	32896	1376
17	4845	41905	1649
18	5985	52650	1956
19	7315	65341	2299
20	8855	80200	2680

If you want to do further examples you may use the *online calculations* offered by the home page of MOLGEN

http://www.mathe2.uni-bayreuth.de/molgen4/

You simply enter a vector of permutations (in list notation) that generate the symmetry group together with the number of admissible different amino acids that you want to allow. For example, in case you want to allow proper rotations of the cubane only, then you enter the vector (after numbering the active sites from 1 to 4):

$$[[2, 3, 1, 4], [1, 3, 4, 2]]$$

as a vector of generators and the number 19 of admissible amino acids. You will obtain the following result:

```
no_orbits_arb
```

```
The input was
```

```
[[2,3,1,4],[1,3,4,2]]
```

```
and
```

```
19
```

```
The result of the computation is
```

```
11191
```

```
the computation was finished after 0.01 seconds
on a pentium 133 MHz
```

Pólya's theory allows a refinement, the enumeration of the libraries *by weight.* This means that we can derive a multivariate polynomial such that the coefficient of a monomial summand is the number of orbits the weight of the elements of which is just the sequence of exponents of the monomial. For example, in the case of the cubane, the polynomial

$$\frac{1}{24}((\sum_y y)^4 + 6(\sum_y y^2)(\sum_y y)^2 + 6(\sum_y y^4) + 3(\sum_y y^2)^2 + 8(\sum_y y^3))$$

is the desired generating function. For xanthen it is

$$\frac{1}{2}((\sum_y y)^4 + (\sum_y y^2)^2),$$

while for the triacid we obtain

$$\frac{1}{3}((\sum_y y)^4 + (\sum_y y^2)^2).$$

In order to get that in a more explicit form, we can use the *online calculations* offered by the home page of MOLGEN. It yields, for the xanthen case, say, and for 3 admissible amino acids the expression

`grf_arb`

```
The input was
```

```
[[2,1,4,3]]
```

```
and
```

```
3
```

```
The result of the computation is
```

```
1 [0,0,4]   2 [0,1,3]   4 [0,2,2]   2 [0,3,1]
```

```
1 [0,4]   2 [1,0,3]   6 [1,1,2]   6 [1,2,1]
```

```
2 [1,3]   4 [2,0,2]   6 [2,1,1]   4 [2,2]
```

```
2 [3,0,1]   2 [3,1]   1 [4]
```

```
the computation was finished after 0.01 seconds
```

```
on a pentium 133 MHz
```

It shows, for example, that there are exactly 6 elements of type $[1, 2, 1]$ in the library, i.e. which contain exactly one amino acid of type 1, 2 of type 2 and 1 of type 3.

3   The library

The most interesting problem is, of course, the *generation* of the elements in the library itself. In order to solve this we simply need to apply the connection between isomers and double cosets introduced by Ruch/Hässelbarth/Richter ([4], see also [5]) for the construction of permutational isomers of a given ligand partition. It says, for example, that the elements in the library that contain a_1 amino acids of type 1, a_2 amino acids of type 2 and so on are in one-to-one correspondence to the elements of the set of couble cosets

$$T_d \backslash S_4 / S_{a_1} \oplus S_{a_2} \oplus \ldots$$

in the cubane case, while we have for the xanthen case the corresponding bijection to the set of double cosets

$$C_{2v} \backslash S_4 / S_{a_1} \oplus S_{a_2} \oplus \ldots.$$

and for the triacid we get

$$C_{3v} \backslash S_3 / S_{a_1} \oplus S_{a_2} \oplus \ldots$$

This fact is used in the software package

MOLCOMB

which will be demonstrated. Here are 4 elements of the xanthen library for the case when 3 different amino acids are allowed (see the generating function given above):
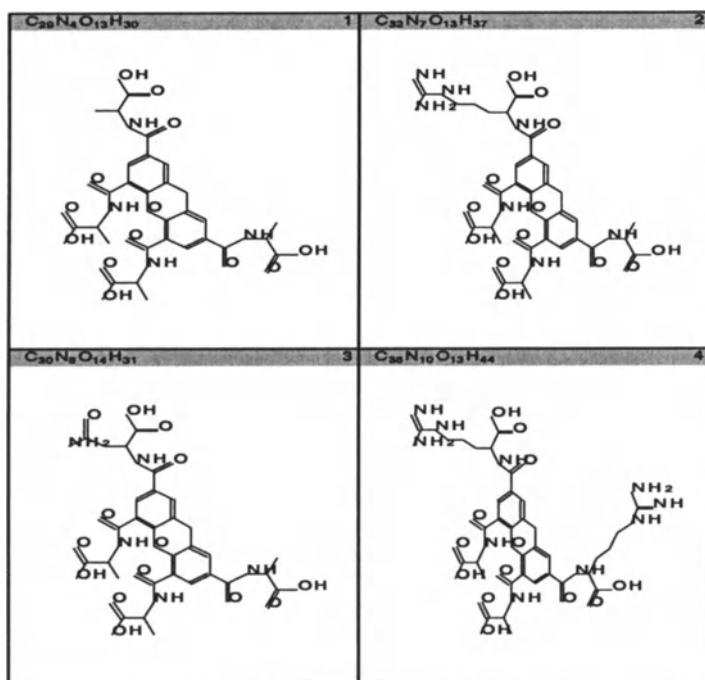
The method used is to go along a so-called *subgroup* ladder. It is in fact the very same method that can be used for the construction of permutational isomers. Here is, for example, the subgroup ladder that is used for the evaluation of the isomers of dioxin:

$$S_8$$

$$S_7 \oplus S_1$$

$$S_6 \oplus S_2$$

$$S_6 \oplus S_1 \oplus S_1$$

$$S_5 \oplus S_3$$

$$S_5 \oplus S_1 \oplus S_2$$

$$S_4 \oplus S_4$$

$$S_4 \oplus S_1 \oplus S_3$$
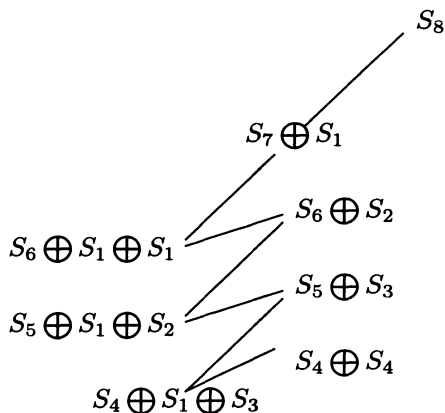
More detailed descriptions of the methods used can be found in [6], [7],[8].

4   Conformations

Having the library at hand we may want to do screening for a lead structure. Such a structure is mostly a geometric one, and so we need to evaluate *conformations* for the elements in the library. This is, of course, the most time consuming part of the process. For this purpose we have developed an object oriented way of classifying energy minima ([9]) and a mixture of conjugate gradient method of optimization together with an evolutionary approach to the evaluation of energetic minima ([10]). This software package is called MOLCLASS. The picture on the next page illustrates an example of several classes of conformations of norbornan which we obtained this way (starting from a random distribution of the atoms in space, so that, at least in principle, we can reach all the minima, and also using atomic tables for the approximate lengths of bonds and sizes of angles).

References

1. CARELL, T., E.A. WINTNER, A. BASHIR-HASHEMI, J. REBEK JR.. Neuartiges Verfahren zur Herstellung von Bibliotheken kleiner organischer Moleküle. *Angew. Chemie*, **106**, S. 2159-2161, 1994.
2. CARELL, T., E.A. WINTNER, A.J. SUTHERLAND, J. REBEK, JR., Y.M. DUNAYEVSKIY UND P. VOUROS. New promise in combinatorial chemistry: synthesis, characterization, and screening of small-molecule libraries in solution. *Chem. & Biol.*, **2**, S. 171–183, 1995.
3. G. PÓLYA. Kombinatorische Anzahlbestimmungen für Gruppen, Graphen und chemische Verbindungen. *Acta mathematica*, **68**, pp. 145–253, 1937.
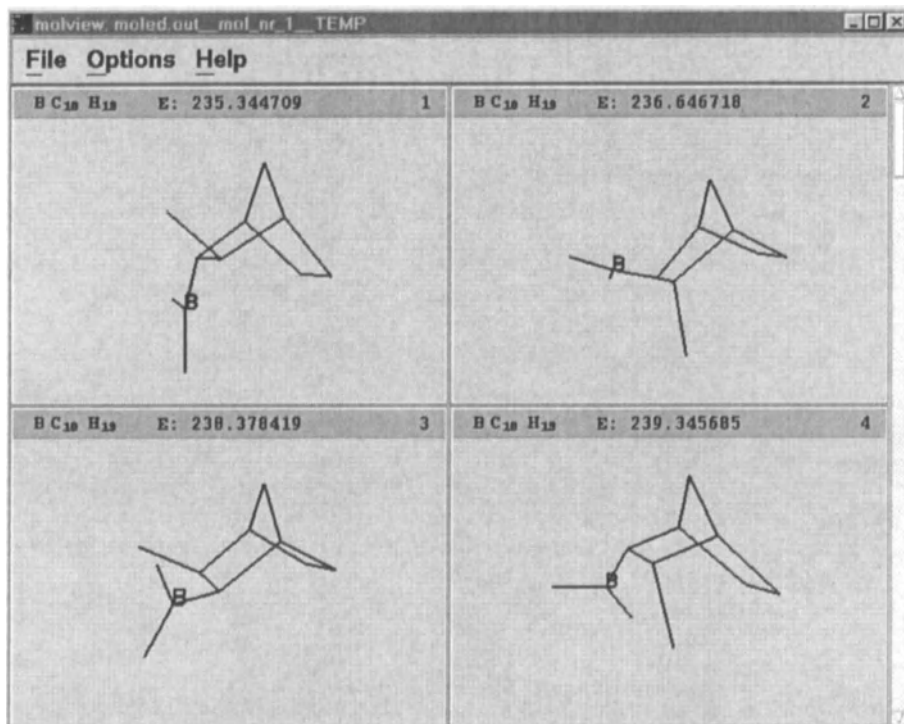
4. E. RUCH, W. HÄSSELBARTH, B. RICHTER. Doppelnebenklassen als Klassen-
   begriff und Nomenklaturprinzip für Isomere und ihre Abzählung. *Theoretica
   Chimica Acta*, **19** (1970), 288-300.

5. E. RUCH, D. J. KLEIN. Double cosets in chemistry and physics. *Theoretica
   Chimica Acta*, **63** (1983), 447-472.

6. T. WIELAND. Mathematical Simulations in Combinatorial Chemistry.
   MATCH, **34**, pp. 179–206, 1996.

7. T. WIELAND. Combinatorics of Combinatorial Chemistry. *J. Math. Chem.*,
   21, pp. 141–157, 1997.

8. T. WIELAND. Konstruktionsalgorithmen bei molekularen Graphen und deren
   Anwendung. *MATCH*, **36**, pp. 5–155, 1997.

9. CH. BENECKE. Objektorientierte Darstellung und Algorithmen zur Klassi-
   fizierung endlicher bewerteter Strukturen. *MATCH*, **37**, pp. 7–156, 1997.

10. C. FREY. An Evolutionary Algorithm with Local Search and Classification for
    Conformational Searching. *MATCH*, **38**, in print, 1998.

Monte Carlo simulation of diffusion within three-dimensional pores with irregular walls

Xiang-yun Guo[1] and Frerich J. Keil[2]

[1] State Key Laboratory of Coal Conversion, Institute of Coal Chemistry, Chinese Academy of Sciences, Taiyuan 030001, China

[2] Technical University of Hamburg-Harburg, Chemical Reaction Engineering, D-21073, Hamburg, Germany

Abstract. Diffusion within porous media modeled by three-dimensional networks containing pores with irregular walls is simulated by the Monte Carlo method. Lennard-Jones 12-6 potential is introduced to calculate the interaction between diffusing species and the pore walls. From the simulation, the diffusion within the irregular pores could be anomalous or normal depending on the molecular size and pore diameter. Moreover, the diffusivity in irregular pores is found to be more dependent on the porosity than in smooth pores.

1   Introduction

Porous media have been widely used in many industrial processes such as catalysis, adsorption, membrane separation etc. Most of these media are composed of small microporous particles which usually form into macroporous pellets [1]. Obviously, it is of great importance to fully characterize their structures and describe the transport phenomena within the media. The classic theories dealing with the problem are often based on some assumptions, by which pore space is uniform and surrounded by smooth walls. The diffusion is modeled by Fick's law or Maxwell-Stefan approach. Now, it is well known that most of the microporous particles can be regarded as fractal at molecular level [2-3]. Therefore, diffusion and reaction within the media formed by fractal particles have attracted much attention in recent years and a lot of theoretical work on diffusion and reaction over fractal substrates was executed [4]. However, the diffusion of gaseous molecules within porous media takes place in a void space separated by walls, and it is usually a combined bulk and Knudsen diffusion. In some cases, the surface diffusion is also significant. Therefore, it would be a challenge to develop a model for describing the process in detail. Moreover, computer experiments based on molecular dynamics (MD) and Monte Carlo (MC) simulations have been successfully employed to the problem of diffusion and reaction within porous media, and one of the authors has reviewed the advances of computer simulations in this field [5].

The present work will focus on Monte Carlo simulation of diffusion within a three-dimensional network model containing irregular pores, which is expected to resemble a realistic porous pellet. The aim of this work is to examine

the difference between the diffusion in irregular and smooth pores. Details of network models are given in [6].

2   Model and Algorithm

Monte Carlo models for investigating diffusion within porous media usually include two different sections: generation of porous pellets and the simulation of diffusion within the pellets. The porous pellets employed in the present work are like aggregates formed by fractal clusters which are similar to DLA clusters [7]. The procedure used to generate the pellets follows our previous work [8] with some improvement, and is briefly described as follows. Initially, some seeds are randomly placed in a simple cubic lattice with 100 x 100 x 100 sites, and fixed at lattice sites as growing centers of fractal clusters. The pellets are formed by aggregating particles on the seeds. A particle is deposited at a randomly chosen lattice site, and the particle then starts a random walk within the lattice until it visits one of the seeds where it adheres as a part of one growing cluster. A further particle is deposited after the previous one has been fixed in the lattice. The random walk is limited to the lattice, in other words, it is not permitted to move out of the lattice. The process continues until the particles fixed in the lattice reach a given total number. A two-dimensional pellet model is shown in Fig. 1.
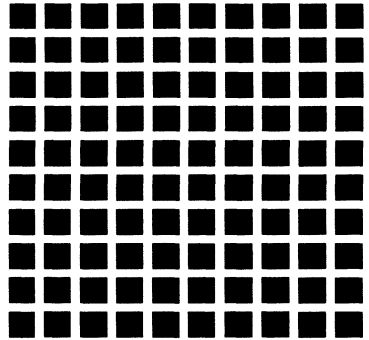
Fig. 1 Irregular pore-network (2-dim.)   Fig. 2 Smooth pore-network (2-dim.)

As can be seen, it is composed of many small clusters. Correspondingly, Fig. 2 is a two-dimensional model of a smooth pore structure which is uniformly formed by regular bricks.

The clusters forming the pellets are fractal when they contain a significant number of particles, and the fractal dimension calculated by the window box scaling method according to [9]

$$M(R) \sim R^{d_f} \tag{1}$$

gives values of $2 < d_f < 3$, where R is the window radius and $M(R)$ is the number of particles in the window box. By making a log-log plot of $M(R)$ vs R, the fractal dimension d_f is equal to the slope of the plot. For large three-dimensional clusters containing more than 5,000 particles, the fractal dimension is about 2.45 from the log-log plots shown in Fig. 3, and it is slightly dependent on the number of particles forming clusters.
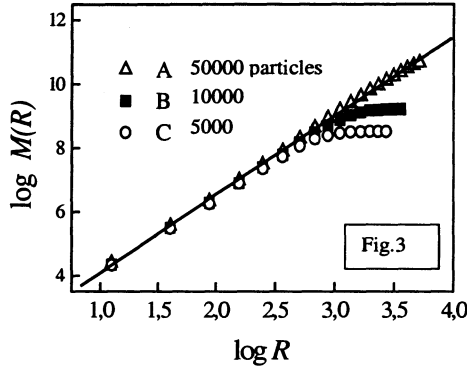
However, the clusters cannot be regarded as real fractals when they contain several hundreds of particles, because the plot-slope always changes with the particle number although the log-log plot is linear. To construct irregular pores, we have to place many seeds (usually 10^3) on the lattice, and, as a result, the clusters cannot grow to large size. Such small clusters can form pores with irregular walls. The given porosity is obtained by changing the total number of particles forming the pellet.

The diffusion of molecules is represented by a simple random walk, which makes one jump per unit time. In case of self-diffusion, the probability of jumping in one of the six axial directions is identical and equal to 1/6. In the simulation of transient experiments, the walk will be under the influence of a bias field, that is, the probability of moving along the field direction is increased by a pressure factor (α) and the probability of moving against the field direction is decreased correspondingly. A diffusing molecule is only permitted to adsorb at an empty lattice point. When a new direction is randomly chosen, the molecule can proceed along the chosen direction in one jump at most n lattice units, except it reaches at any of the clusters in the pellet. Whether a trial jump is accepted or not is determined by a random number (ζ) distributed uniformly over the interval (0,1). The number ζ is compared with a transition probability

$$P = exp(-\Delta E / kT) \tag{2}$$

where T is the temperature, k is Boltzmann's constant and ΔE is the energy difference between the two configurations. The jump is only successful when the random number ζ is less than the probability P, otherwise, the walker has to stay at its present place.

The interaction between a moving molecule and an atom in pore walls is calculated by the Lennard-Jones 12-6 potential.

In the simulation, only the nearest atoms in walls are taken into account for calculating the interaction. A moving molecule can at a certain time step only stay at one lattice site, so one can calculate the interaction energy (E) by taking into account the number of the wall atoms which are adjacent to the moving molecule

$$E = \sum_{i=1}^{N} \nu_i \tag{3}$$

where N is the number of nearest neighbors. It is assumed that the pore walls are formed of oxygen atoms.

In uniform Euclidean systems, the mean square displacement of a random walker, $< R(t)^2 >$, is proportional to time t

$$< R(t)^2 > = 6\,D\,t \tag{4}$$

The Equation (4) is well known as Einstein's relation. However, it is not valid in general for diffusion in disordered systems. Rather, the diffusion becomes anomalous, that is, the mean square displacement grows geometrically with time

$$< R(t)^2 > \sim t^{2/dw} \qquad (t > 0) \tag{5}$$

with $dw > 2$. In our simulation, it is noticed that the mean square displacement can be regarded to grow linearly with the time when the time of diffusion is sufficiently long. Therefore, the diffusivity in the present work is calculated by

$$D = lim < R(t)^2 > /6t \qquad (t \to \infty) \tag{6}$$

D in Eq.(4) and (6) is generally called self-diffusivity.

According to percolation theory [9], there exists a critical concentration P_c below which only finite clusters exist and above which a cluster extends over the entire lattice. When the particle concentration is greater than P_c, the "infinite" cluster is called a conductive phase, which is homogeneous in nature. Of course, the random walk on the cluster is also normal when the observation time is long enough. The present model is similar to the random walk in the void network of the percolation clusters. Therefore, some of the results from the present simulation are expected to be in agreement with those in the percolation theory.

3   Results and Discussion

3.1   Characteristic of the void network

If the void space (or pores) in our model is fractal, the fractal dimension should be obtained by Eq.(1). In this case, of course, $M(R)$ means the number of empty sites in the box with the radius of R. A series of pellets with the porosity from $\epsilon_p = 0.2$ to 0.6 are analyzed by the method, and all of them have the same dimension value of 3.00, as shown in Fig. 4. From the figure, all of the log-log plots have an identical slope, and it is same as obtained from an uniform three-dimensional void space, which is represented by the solid line in the figure. The results in the figure indicate that the pore void space is not fractal. As the porosity values of real porous media such as catalysts are usually in the range of $\epsilon_p = 0.4$ to 0.6, we conclude that the void space in pore networks in the present porous media are not fractal although the walls forming the pore networks may be fractal.

Fig. 4

Fig. 5
$\epsilon_p = 0.488$
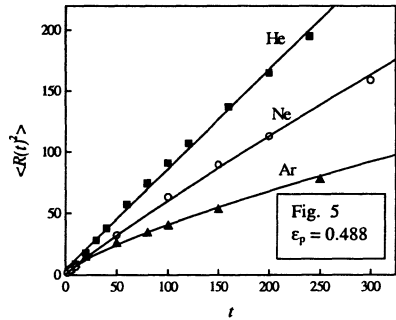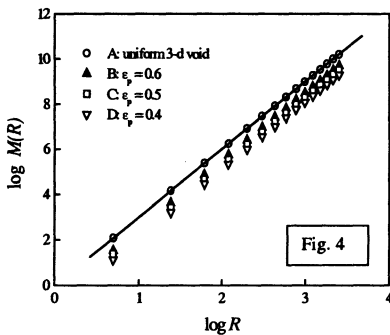
Three types of molecules He, Ne and Ar are used to investigate the effect of molecule sizes on diffusion. In each Monte Carlo (MC) experiment, a molecule is released at an empty site in the void space of the pellet, and the molecule then starts a random walk within the pellet. To obtain correct values for the mean square displacement, the experiment is generally repeated about 10^5 times. The simulation results of different types of molecules are shown in Fig. 5, in which the solid lines are curved for Ar and Ne, and linear for He. The figure reveals that the diffusion of He is normal, that is, the mean square displacement linearly increases with time. Within the same pellet, however, the diffusion of He and Ar is anomalous. It indicates that within the same pellets diffusion of molecules with different sizes have different dependence of the mean square displacement on time. Diffusion of molecules with a smaller size is normal, while on the other hand molecules with a larger size may reveal an anomalous diffusion.

Increasing the porosity leads to diffusivities for Ne and Ar as presented in Figs. 6 and 7. From Fig. 6, the diffusion of Ne in low porosity pellets is anomalous, and becomes normal when the porosity is increased. On the other

hand, when the porosity is increased from 0.488 to 0.657, the diffusion of Ar is still anomalous although the diffusivity increases obviously, as shown in Fig. 7. This effect can be explained by the larger van der Waals radius of argon compared to neon.
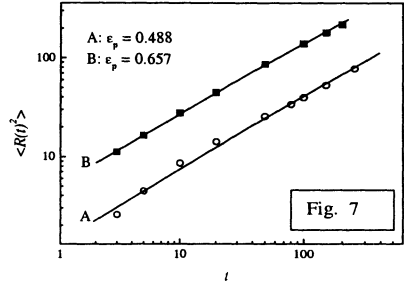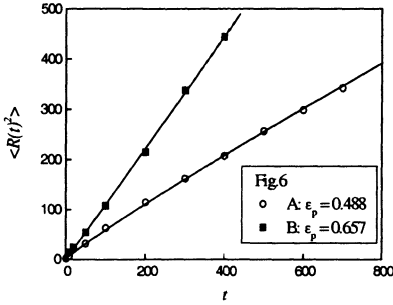
According to the Einstein relation diffusivities are independent of time. Moreover, it is also known that the diffusivity is directly proportional to the pore size in case of the Knudsen mechanism, in which the mean free path of diffusing molecules is comparable with or even greater than the pore diameter. Generally, the diffusivity for irregular pores can become smaller than for smooth pores, and the slowing down is caused by the delay of the diffusing species in the dangling ends, bottlenecks and backbends in irregular pores.

Our simulation corresponds to Knudsen diffusion, and the dependence of the diffusivities within irregular pores on the porosity is shown in Fig. 8. As can be seen, the diffusivities of He, Ne and Ar increase exponentially with the porosity, or, with the pore diameter because all of the pellets in the simulation are composed of the same number of clusters. Comparatively, the diffusion within a series of smooth pores is also simulated by the same model, however it is found that the diffusivity within smooth pores (shown in Fig. 2) increases slowly and linearly with the porosity. From the above results one can conclude that the diffusivity within irregular pores depends more strongly on the pore diameter than in smooth pores.

The present model can also be employed to simulate transient experiments. In transient experiments, the total quantity (Q_t) of the diffusing species that has passed through the porous membrane with a thickness of L in time t is related to the diffusivity D. For $t \to \infty$, the relation approaches the asymptote

$$Q_t = \frac{Dc_0}{L}\left(t - \frac{L^2}{6D}\right) \qquad (7)$$

which yields a straight line with intercept (time lag) $L^2/6D$ on the time axis. Therefore the diffusivity can be obtained by measuring the time lag [10].

A molecule pulse in the simulation is released at one of the parallel sides of pellets, and than the number of the passed molecules is measured at the

Fig. 8
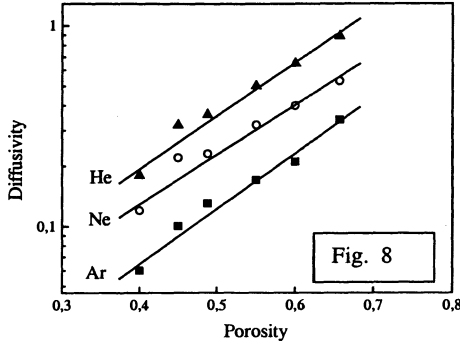
opposite side. The $Q_t \sim t$ curves for different pressure values are shown in Fig. 9. The different curves approach to nearly the same intercept regardless of pressure, and this indicates that the diffusivity is slightly dependent of gas pressure over the given range. It is noticed that the result is in agreement with that in Knudsen diffusion.

Fig. 9
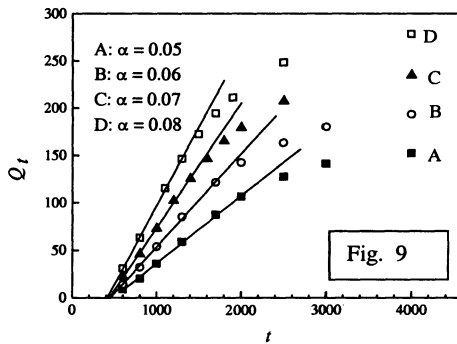
4   Conclusions

Porous media composed of small fractal particles were represented by a network model, and the network model was employed to investigate the diffusion within irregular pores. From the simulation, the diffusion within irregular pores is different from those both in uniform space and over fractals, and the results are:

4.1 Void space of porous media created by the present algorithm is not fractal. The diffusion within irregular pores could be anomalous or normal in finite observation time, and it depends on the molecular size and the pore diameter. However, the diffusion in smooth pores is always normal.

4.2 The diffusivity in irregular pores is found to grow exponentially with the

porosity. For diffusion in smooth pores, as it is expected, the diffusivity increases slowly and linearly with the porosity.

4.3 The simulation results of transient experiments show that the diffusivity is slightly dependent on the gaseous pressure, and indicates that the Knudsen diffusion is predominant. This is in agreement with the conditions in the simulation.

References

1. Ruthven D. M. (1984) Principles of adsorption and adsorption process, Wiley, New York
2. Rothschild W.D. (1991) Fractals in heterogeneous catalysis, Catal. Rev. -Sci. Eng. 33: 71
3. Pfeifer P., Avnir D.(1992) A discussion of some aspects of surface fractality and of its determination, New J. Chem. Phys. 16: 439
4. Rothschild W. (1998) Fractals in Chemistry. John Wiley, New York
5. Keil F. J.(1996) Modelling of phenomena within catalyst particles, Chem. Eng. Sci. 51: 1543
6. Rieckmann C., Keil F.J. (1997) Multicomponent diffusion and reaction in three dimensional networks: general kinetics, Ind. Eng. Chem. Res. 36: 3275
7. Witten T.A., Sander L.M.(1981) Diffusion-limited aggregation: a kinetic critical phenomenon, Phys. Rev. Lett. 47:1400
8. Guo X. Y., Zhong B., Peng S. Y. (1994) Monte Carlo simulation to study surface diffusion and reaction processes on a fractal catalyst, Surf. Sci. 321: L261
9. Bunde A., Havlin S. (1991) Fractals and Disordered Systems, Springer, Berlin
10. Kärger J., Ruthven D.M. (1992) Diffusion in Zeolites, John Wiley, New York

Molecular Modeling of Polymers

Reinhard Hentschke, Thomas Flebbe, and Ewald Aydt

Max-Planck Institute for Polymer Research
Ackermannweg 10, 55128 Mainz, Germany

Abstract. Computer simulations based on phenomenological interaction potentials have developed into a powerful tool aiding the understanding of materials properties on the molecular level. Here we discuss two applications of force field molecular modeling to polymers (for a broader overview see for instance [1] or [2]). These include structural and dynamic properties of two vinyl polymers in aqueous solutions, and adsorption/swelling phenomena in a model polymeric network.

1 Modeling of Polyvinylpyrrolidone and Polyvinylimidazole in Aqueous Solution

Polyvinylpyrrolidone (PVP) and polyvinylimidazole (PVI) are polymers of great technical importance for example in the context of the manufacturing of textiles, paper, adhesives, membranes, plastics, cosmetics, pharmaceutical products or as polymeric dye transfer inhibitor in laundry detergents [3]. The goal was a better understanding of the material properties of these polymers on the basis of microscopic simulations. Here we studied the polymer hydration and the conformation behavior in aqueous solution.

We employed a conventional Molecular Dynamics algorithm numerically solving Newton's equations of motion for all atoms $i = 1, ..., N$ in the molecular liquid. The potential energy U is given by

$$
\begin{aligned}
U(\boldsymbol{r}_1, \ldots, \boldsymbol{r}_N) = {} & \sum_{\text{bonds } i} k_b^{(i)} (b_i - b_0^{(i)})^2 + \sum_{\text{angles } i} k_\alpha^{(i)} (\alpha_i - \alpha_0^{(i)})^2 \\
& + \sum_{\text{dihedrals } i} \sum_{m=1}^{m_{max}} k_{d,m}^{(i)} [1 + \cos(n_m^{(i)} \phi_i - \gamma_m^{(i)})] \\
& + \sum_{\text{atom pairs } ij} \left(\frac{A_{ij}}{r_{ij}^{12}} - \frac{B_{ij}}{r_{ij}^6} + \frac{q_i q_j}{r_{ij}} \right) .
\end{aligned}
\tag{1}
$$

This is the AMBER (Assisted Model Building with Energy Refinement) description of the potential energy for a large molecular system [4] (and references therein). The first three sums encompass the valence potential energy contributions due to bond (b_i) and bond angle (α_i) deformations as well as bond rotations (ϕ_i). The last sum describes the inter-atomic overlap repulsion and dispersion attraction in terms of Lennard-Jones potentials and Coulomb

interactions between partial charge sites located on the nuclei. The summations include all atom pairs ij (i and j are separated by at least three covalent bonds if they do belong to the same molecule). In addition, the non-bonded (1-4)-interaction terms are scaled by a factor $1/2$ in the case of the Lennard-Jones potential and by a factor $1/1.2$ in the case of the Coulomb potential. Non-bonded interactions are calculated using a molecule based cutoff of 9Å. In addition, the Lorentz-Berthelot combining rules [5] are used to compute the dispersion interaction between unlike atoms. The atomic equations of motion were integrated via the leap-frog Verlet algorithm [5] with a time step of $2fs$ (using version 4.1 of the AMBER modeling package [6]). Temperature and pressure ($1bar$) were controlled via the weak coupling method due to Berendsen et al. [5]. All bond lengths were constrained using the SHAKE algorithm [5]. The water model used in this work was SPC/E (Simple Point Charge/Extended) [7] with a single Lennard-Jones center on the oxygen and three charge sites on the nuclei. The force field parameters were taken from the AMBER 4.1 data base [6] with the exception of the SPC/E parameters, the torsion parameters of the $C_\alpha - N$-bond, and the polymer partial charges located on the nuclei. The missing polymer parameters were obtained via a combination of quantum mechanical calculations, and separate simulations of liquid properties of the monomer-analogous compounds (see [3] for a complete listing).

We have investigated the hydration of oligo-VP and oligo-VI (isolated 20-mers in explicit water) in terms of the quantity $N(t, t_e)$. $N(t, t_e)$ is the average number of water molecules residing within a particular solvation shell of an oligomer atom A at time t under the condition that the same molecules were residing in the same solvation shell at time $t = 0$. Here we defined solvation shells in terms of the successive minima in the radial pair correlation function, $g_2(r_{A\ldots H_2O})$, where $r_{A\ldots H_2O}$ is the distance between atom A and the water oxygen. The above definition of $N(t, t_e)$ allows excursions from the solvation shell, under the additional condition that the particle is not absent from the solvation shell longer than t_e per excursion. Here we used $t_e = \infty$ (for a discussion see [3]), and defined $N(t) \equiv N(t, \infty)$. The example in Fig. 1 displays $N(t)$ calculated with respect to the carbonyl oxygen atom in i-PVP and s-PVP. In this case $N(0)$ is the average number of water molecules fulfilling the following criterion: (a) the water oxygen is inside the first hydration shell, and (b) the angle, α, between the direction of the angular bisector of the water molecule and the direction of the carbonyl bond does not exceed 77.5^o (cf. the sketch in Fig. 1). This geometric condition is motivated by the shape of the corresponding orientation-correlation function [3]. It roughly captures the hydrogen bonded water molecules together with a certain number of less strongly bonded, more mobile water molecules. $N(t)$ can be represented in terms of the fit function $N(t) = N_{fast} \exp(-t/\tau_{fast}) + N_{slow} \exp(-t/\tau_{slow})$ (cf. Fig. 1). The parameter values $\tau_{slow}^{i-PVP} = 112ps$ and $\tau_{slow}^{s-PVP} = 62ps$ can be considered as the approximate life time of the $C = O...H$-hydrogen bond

in the two cases. Note that $N_{slow}\exp(-t/\tau_{slow})$ extrapolates to ≈ 1 for $t \to 0$, i.e. one hydrogen bonded water molecule per $C = O$-group.
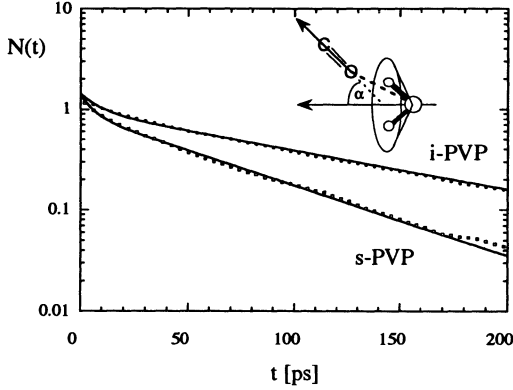
Fig. 1. Average residence time, $N(t)$, of molecules fulfilling the sketched distance-orientation criterion used to characterize the lifetime of the $C = O...H$-hydrogen bonds vs. time, t. The solid lines correspond to the fit functions explained in the text. In addition, i- and s- stand for the respective tacticities.

In order to characterize the polymer conformation globally as well as locally we calculated the characteristic ratio, $C_n = \langle R^2 \rangle / nb^2$, where $\langle R^2 \rangle$ is the mean square end-to-end distance for a polymer consisting of n bonds of length b, and the averaged scattering intensity, I, given by

$$\frac{I}{I_o} = \sum_l N_l f_l(q)^2 + \sum_{l,l'} N_{l'} f_l(q) f_{l'}(q) \langle \sum_{i=1}^{\infty} 4\pi \Delta r^2 \cdot i \frac{sin(q\Delta r \cdot i)}{q} \rho_{ll'}(i) \rangle . \quad (2)$$

I_o is a structure independent constant, N_l is the number of atoms of type l, $f_l(q)$ is the corresponding atomic form factor, and q is the magnitude of the scattering vector. In addition, $\rho_{ll'}(i)$ denotes the average number density of l-atoms in a spherical shell, $\Delta r \cdot i \pm \Delta r/2$, centered on the l'-atom ($\Delta r \approx 0.01$Å). The averages, $\langle ... \rangle$, should be calculated using a large number (typically > 100) of conformations. As an example Fig. 2 shows the intensity of polyethylene (PE) computed in this fashion as a function of N_{CH_2} (here $f_{CH_2} = 1$). Apparently there is only little difference between the 20-mer and the 1000-mer above $q \approx 0.5b^{-1}$. Because PE has the same backbone structure as PVP and PVI, we do expect the simulated 20-mers to yield a very similar reduced scattering intensity as the polymer in this q-regime. Detailed calculations of the scattering intensity for iso-, a-, and syndiotactic PVP as well as PVI are carried out in ref. [3]. Here we focus on C_n.

Independent of the details of the underlying chemical structure global polymer conformations are well understood based on scaling arguments [8] (with the exception of systems dominated by long range electrostatic interactions). On small and intermediate length scales, where the chemical structure governs the conformation behavior, the RIS/transfer matrix-model has
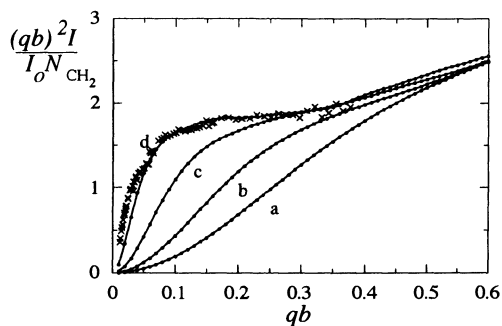
Fig. 2. Reduced intensity, $(qb)^2I/(I_oN_{CH_2})$, for PE vs. qb at $T = 413K$ generated via a RIS/transfer matrix-model [3]. N_{CH_2} is the number of methylene units ($f_{CH_2} = 1$) per chain ($N_{CH_2} = 20(a), 50(b), 200(c), 1000(d)$). The crosses are neutron scattering data.

proven to be immensely powerful in relating molecular structure to molecular conformations [9]. However, including solvent effects in the transfer matrix formalism requires effective statistical weights which are a priori unknown and difficult to obtain. Here we use a Monte Carlo construction based on the simulated oligomer conformations for sampling the conformation space of the polymers.

Our Monte Carlo construction of backbone conformations (cf. also [9]) utilizes the conditional probability, $p(\phi'|\phi) = p(\phi'\phi)/p(\phi)$, that a torsion angle ϕ is followed by ϕ' along the backbone. $p(\phi)$ is the probability of occurrence of the main chain torsion angle ϕ. Similarly, $p(\phi'\phi)$ is the probability of occurrence of the neighbor pair $\phi'\phi$. We directly extracted these probabilities from the simulation in terms of the normalized frequencies h_ϕ and $h_{\phi'\phi}$, i.e. $p(\phi) = h_\phi$ and $p(\phi'\phi) = h_{\phi'\phi}$. Thus, other than in the usual transfer matrix calculation of these probabilities molecular solvent effects are included on the length scale of the simulated oligomer in solution. A simple backbone construction algorithm appropriate for PE with three rotational isomeric states (t,g^-,g^+) consists of the two steps: (i) generate a random number z between 0 and 1; (ii) following the torsion angle ϕ, which can be either ϕ^t, ϕ^{g^-}, or ϕ^{g^+}, continue the backbone with ϕ^t if $z \leq p(\phi^t|\phi)$ or with ϕ^{g^-} if $p(\phi^t|\phi) \leq z \leq p(\phi^t|\phi) + p(\phi^{g^-}|\phi)$ or with ϕ^{g^+} if $p(\phi^t|\phi) + p(\phi^{g^-}|\phi) < z$. A new bond vector $\boldsymbol{b}_{i+1} = b\hat{\boldsymbol{b}}_{i+1}$ is added to an existing chain of backbone bond vectors via $\hat{\boldsymbol{b}}_{i+1} = -\hat{\boldsymbol{b}}_i \cos\alpha + \hat{\boldsymbol{b}}_i \times \hat{\boldsymbol{b}}_{i-1} \sin\phi' - (\hat{\boldsymbol{b}}_i \times \hat{\boldsymbol{b}}_{i-1}) \times \hat{\boldsymbol{b}}_i \cos\phi'$, where b is the bond length. The angles α and ϕ' are the fixed bond angle and the newly selected torsion angle, respectively. Note that the intensities shown in Fig. 2 are calculated from conformations generated in this fashion, except that h_ϕ and $h_{\phi\phi'}$ were calculated using the transfer matrix. The extension of the above algorithm to a larger number of possible RIS-values for ϕ is obvious. Note, however, that in general the polymer backbone is characterized by a periodic sequence of non-equivalent torsion angles, ϕ_A, ϕ_B, ϕ_C,..., ϕ_A, ϕ_B,... rather than by just one (type of) torsion angle ϕ as in the case of PE. For i-PVP and i-PVI there are two non-equivalent backbone torsion angles. Consequently the construction algorithm for these types of polymers

is based on the successive conditional probabilities $p(\phi_A|\phi_B)$ and $p(\phi_B|\phi_A)$. Fig. 3 shows the corresponding distributions $h_{\phi_A\phi_B}$ and $h_{\phi_B\phi_A}$ extracted from the simulation of i-PVP in SPC/E water, which can be used directly to calculate the conditional probabilities. Results for C_n obtained in this fashion are shown in Fig. 4. Also included are experimental measurements on atactic PVP obtained in an 9% NaCl solution. The overall correspondence between experimental and theoretical results is fairly close. It should be noted that C_n^{exp} diverges for large n due to excluded volume interactions which the MC-RIS construction neglects, i.e., in the former case $\langle R^2 \rangle \propto n^{2\nu}$ with $\nu \approx 0.63$ whereas in the latter case $\nu = 0.5$. Note that C_n is rather similar for i-PVP and i-PVI, whereas s-PVP is significantly stiffer than s-PVI. The corresponding persistence lengths a, where $a = (C_\infty + 1)b/2$, are 6.7Å(i-PVP), 8.6Å(a-PVP), 46Å(s-PVP), 8.5Å(i-PVI), and 19.3Å(s-PVI).
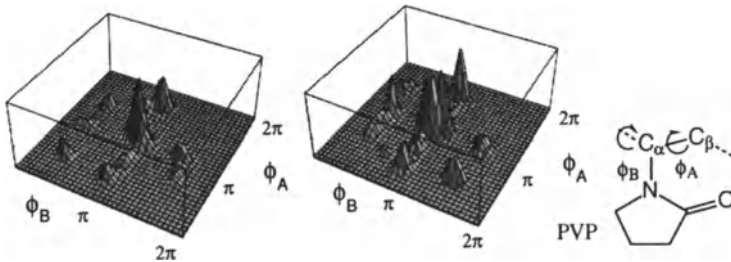
Fig. 3. Frequency histograms of the backbone torsion angle pairs $\phi_A\phi_B$ (top: $h_{\phi_A\phi_B}$) and $\phi_B\phi_A$ (bottom: $h_{\phi_B\phi_A}$) extracted from the simulation of i-OVP in water. Note that $\phi = 180^o$ corresponds to the trans-state.

2   Swelling of a model network

The swelling characteristics of polymer networks play a crucial role in many technical and hygienic (e.g. superabsorber) applications. Despite the industrial importance of swelling phenomena and the research activities in this field, our knowledge of the underlying mechanisms on an atomic level is still incomplete. Here we studied the swelling process in model networks by applying the Gibbs-Ensemble Molecular Dynamics (GEMD) technique [10] (and references therein). The method models the simultaneous chemical equilibrium of two (or more) bulk phases based on the molecular dynamics framework. Each phase is represented by a simulation box, which exchange particles in an unphysical but thermodynamically consistent fashion. This is achieved by introducing a dynamic transfer variable, $0 \le \xi_i \le 1$, for each molecule i,
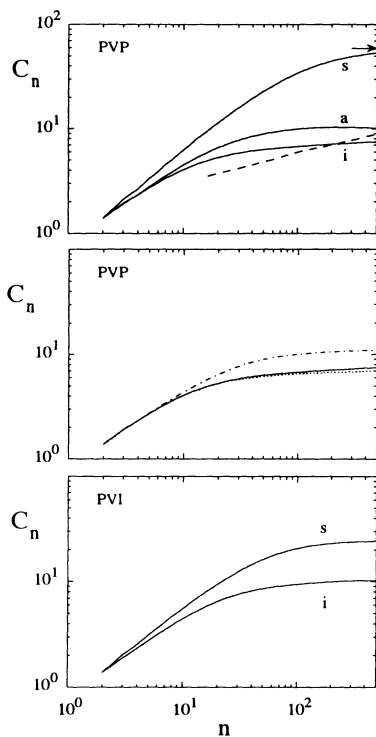
Fig. 4. Top: Characteristic ratio, C_n, vs. n for i-, a-, and s-PVP as obtained with the MC-RIS method compared to experimental values (dashed line) obtained in a 9% NaCl solution. The arrow indicates C_∞ for s-PVP. Middle: The minor influence of the bin width in the torsion histograms (solid line: 1° as in the upper panel; dashed line: 5°) as well as the effect of next-nearest neighbor coupling (dashed-dotted line) on C_n for i-PVP. Note that next-nearest neighbor coupling leads to significant stiffening. Bottom: Characteristic ratio, C_n, vs. n for i- and s-PVI as obtained with the MC-RIS method.

which obeys its own equation of motion. Values of ξ_i close to 0 or 1 correspond to "real" molecules residing in respective boxes. Intermediate values correspond to molecules in a transfer state. Note that each ξ_i is like a coupling parameter in thermodynamic cycle integration [11]. We have applied the GEMD method to analyze a model network in contact with an atomic as well as with a molecular Lennard–Jones fluid. The first box contained the model network, the second box represented the bulk fluid. The network nodes were connected through harmonic potentials, while long range interactions were of the Lennard–Jones type. Angle and torsion potentials within the network were not employed. The fluid–fluid and fluid–network interactions are also modeled via Lennard–Jones potentials. Furthermore we use the AMBER force field (cf. above) to model the internal degrees of freedom of the molecular species.

Fig. 5 shows a simulation snapshot for (united atom) dodecane in contact with the model network. Note that the number of transfer particles must be sufficiently small in order to not disturb the physically meaningful equilibrium distribution of molecules between the boxes. Fig. 6 illustrates the time evolution of selected quantities for methane in contact with the same model

network. Notice that the final number of transfer particles is indeed small. Fig. 7 finally shows different isobars in the T-q-plane, where q is the swelling ratio. Note the shrinkage of the network with increasing temperature. This behavior, which currently is under investigation, bears a certain analogy to the collapse transition observed in real gels [12].
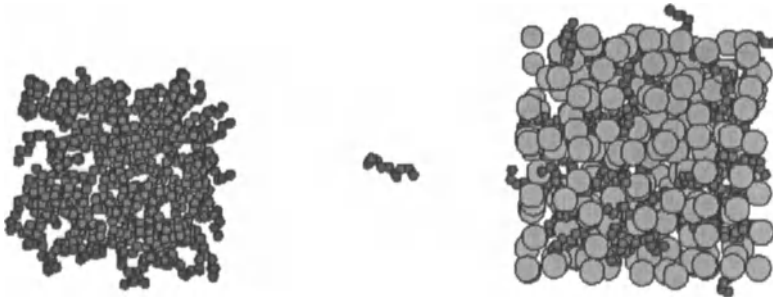
Fig. 5. Snapshot of the model polymeric network (right) containing dodecane molecules diffusing through the network. The dodecane molecules may transfer between the fluid phase (left) and the network cavities. The transferring molecule is positioned between the two boxes according to its instantaneous ξ-value.
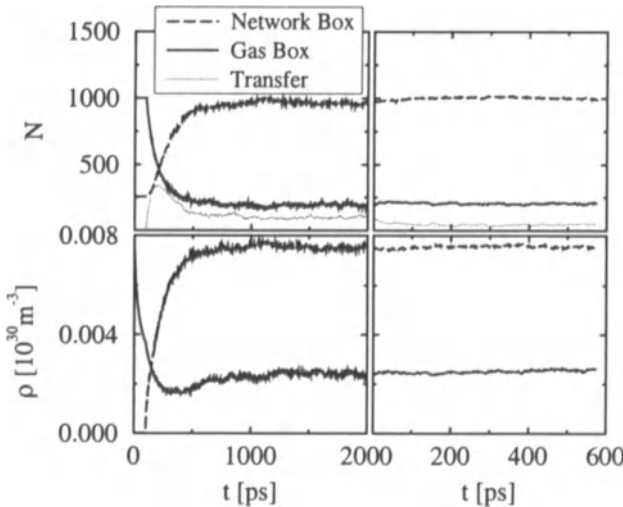
Fig. 6. Top: Time evolution of the number of real and transferring methane molecules. Bottom: Time evolution of the densities in the simulation volumes.
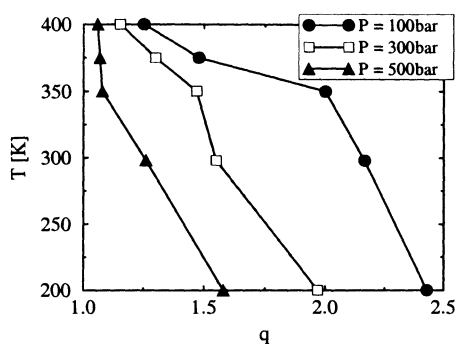
Fig. 7. Temperature vs. swelling ratio, $q = V_{swollen\ network}/V_{dry\ network}$. P is the hydrostatic pressure.

References

1. Gelin B.R. (1994) Molecular modeling of polymer structures and properties. Hanser Publishers, New York
2. Binder K. (Ed.) (1995) Monte Carlo and molecular dynamics simulations in polymer science. Oxford University Press, New York
3. Flebbe T., Hentschke R., Hädicke E., Schade Ch. (1998) Modeling of polyvinylpyrrolidone and polyvinylimidazole in aqueous solution. Macromol. Theory Simul. **7**, 567–577
4. Cornell W. D., Cieplak P., Bayly C. I., Gould I. R., Merz K. M., Ferguson D. M., Spellmeyer D. C., Fox T., Caldwell J. W., Kollman P. A. (1995) A second generation force field for the simulation of proteins, nucleic acids, and organic molecules. Am. Chem. Soc. **117** 5179–5197
5. Allen M. P., Tildesley D. J. (1990) Computer Simulation of Liquids Clarendon Press, Oxford
6. Pearlman D. A., Case D. A., Caldwell J. C. , Ross W. S., Cheatham T. E., Ferguson D. M., Seibel G. L., Singh U. C., Weiner P., Kollman P. A. (1995) AMBER 4.1: Molecular Dynamics Simulation Package. University of California, San Francisco, USA.
7. Berendsen H. J. C., Grigera J. R., Straatsma T. P. (1987) The missing term in effective pair potentials. J. Phys. Chem. **91**, 6269–6271.
8. de Gennes, P.-G. (1988) Scaling concepts in polymer physics. Cornell University Press, Ithaca
9. Mattice W. L., Suter U. W. (1994) Conformational theory of large molecules. John Wiley & Sons, New York
10. Hentschke R., Bast T., Aydt E. M., Kotelyanskii M. J. (1996) Gibbs-ensemble molecular dynamics: A new method for simulations involving particle exchange. J. Mol. Model. **2**, 319–326
11. van Gunsteren W. F., Berendsen H. J. C. (1987) Thermodynamic cycle integration by computer simulation as a tool for obtaining free energy differences in molecular chemistry. J. Comp.-Aided Mol. Design **1**, 171–176
12. Hirotsu S., Hirokawa Y., Tanaka T. (1987) Volume-phase transitions of ionized N-isopropylacrylamide gels. J. Chem. Phys. **87**, 1392–1395

Extension of Modified UNIFAC to Refrigerant Mixtures

Michael Kleiber[1] and Joachim K. Axmann[2]

[1] Aventis Research & Technologies GmbH & Co KG, PT / TTF, D-65926
   Frankfurt a. M.
[2] Studsvik Scandpower GmbH, Flotowstr. 41-43, D-22083 Hamburg

Abstract. The prediction of phase equilibria without using experimental data is
one of the most difficult things to do in thermodynamics. By the time, group con-
tribution methods generally yield the most trustworthy results. At the moment, the
Modified UNIFAC (Dortmund) method has become common standard for VLE, h^E
and LLE predictions. To apply this method to refrigerants, as it has already been
done for the original UNIFAC method, finally 386 adjustable parameters had to be
fitted simultaneously.
   For fitting the parameters, a conventional gradient method and an Evolutionary
Algorithm have been compared. The latter uses the mutation-selection-principle
which is well-known from biological evolution. The optimum interplay of different
strategies as well as the use of parallel computers resulted in levels well below the
local extremes found using a conventional search method.
   The results of genuine predictions using the new parameters are satisfactory.

1   Introduction

In chemical industry, information about multicomponent phase equilibria is
extremely important for the design of thermal separation processes like dis-
tillation, absorption, extraction, and its various combinations. Generally, cal-
culations on multicomponent phase equilibria are based on parameters de-
scribing the interactions of two different molecules. If these parameters are
unknown, the choice is to determine them by experiments or to estimate
them. The latter way is meaningful if qualitative statements about the phase
equilibria are sufficient, for instance for compounds that are not decisive for
the process or even for important binary mixtures in the concept evalua-
tion phase. The most popular tool for phase equilibrium estimations is the
UNIFAC group contribution method, which does not treat a system as a
mixture of components but of functional groups. Its foundations are in detail
explained in [5].
   During the last few years, the Modified UNIFAC (Dortmund) method [4]
has been recognized as the most powerful tool in predicting phase equilibria
by this time and has almost replaced the original version. The main differ-
ence between UNIFAC and Mod. UNIFAC is caused by an extension of the
UNIFAC group interaction parameters a_{mn} to a quadratic polynomial with
respect to temperature:

$$a_{mn} \longrightarrow \alpha_{mn} + \beta_{mn} * T + \delta_{mn} * T^2 \tag{1}$$

Furthermore, in Mod. UNIFAC the van-der-Waals-volume R_j and the van-der-Waals surface area Q_j of the groups are taken as adjustable to get a higher flexibility. In order to extend the application range of the method to refrigerant mixtures, it was decided to integrate the structural groups for the refrigerants developed in 1994 [2] and fit the involved parameters using the EVOBOX program, which was introduced in [2]. The groups are shown in Table 1.

Main group	Subgroups	Main group	Subgroups	Main group	Subgroups
CF_4	CF_4	CHF_3	CHF_3	$CHClF$	$CHClF_2$
CHF	CH_3F		$(CH_2-)CF_3$		$(CH_3-)CClF_2$
	CH_2F	$CClF$	CCl_3F		$CHClF$
	CHF		CCl_2F	$CHCl_2F$	$CHCl_2F$
CHF_2	CH_2F_2	$CClF_2$	CCl_2F_2		CH_3-CCl_2F
	CHF_2		$CClF_2$		$CHCl_2-CF_3$
	CH_3-CHF_2		$CBrF_3$	$C_2F_3Cl_3$	$CFCl_2-CF_2Cl$
	$(CF_3-)CH_2F$	$CClF_3$	$CClF_3$		
			$(CF_3-)CClF_2$		
			$CClBrF_2$		

Table 1. New UNIFAC structural groups for refrigerants

2   Data Base and Procedure

Table 2 shows the structure of the database for refrigerant mixtures. Data sets for Liquid-liquid Equilibria (LLE) had been converted into activity co-efficient data sets. For the VLE data sets, a sensitive consistency test has been performed, non-consistent data have already been removed from the data base.

	data sets	data points
VLE	510	4301
h^E	36	587
γ	42	145

Table 2. Structure of the data base

However, considering that 196 binary systems are available for fitting 122 pairs of interaction parameters a_{mn}, it must be stated that the data base is comparably small.

For the VLE calculations the PRSV equation [8] was used to determine the fugacity coefficients and the Poynting corrections in the phase equilibrium conditions. Details can be taken from [7].

The Modified UNIFAC interaction parameters and the R- and Q-values of the groups are adjusted by minimizing the objective function

$$F = \sum_{j}^{N_j} \left[(y_{1j,cal} - y_{1j,exp})^2 + \left(\frac{p_{j,cal} - p_{j,exp}}{p_{j,exp}} \right)^2 \right] +$$

$$+ \sum_{h}^{N_h} \left(\frac{h^E_{h,cal} - h^E_{h,exp}}{100 \; J/mol} \right)^2$$

$$+ \sum_{k}^{N_k} \left[\left(\frac{\gamma_{1k,cal} - \gamma_{1k,exp}}{\gamma_{1k,exp}} \right)^2 + \left(\frac{\gamma_{2k,cal} - \gamma_{2k,exp}}{\gamma_{2k,exp}} \right)^2 \right] \qquad (2)$$

where N_j, N_h and N_k are the number of VLE excess enthalpy and activity coefficient data points, respectively.

Totally this function depends on 330 Mod. UNIFAC interaction parameters. The linear term $\beta_{mn} * T$ in eq. (1) was only used if the temperature differences between the various data points affected by this parameter exceeded 100 K, the quadratic term $\delta_{mn} * T^2$ was introduced if the differences were greater than 200 K. If a parameter pair had to describe excess enthalpies as well, the largest temperature difference was artificially increased by 100 K. Thus, it can be stated that temperature-dependent parameters have only been fitted when it was justified.

Together with the 28 R- and 28 Q-values the number of adjustable variables becomes 386. These parameters intercorrelate complicatedly leeding to a complex optimization problem hardly to be divided into smaller independent subproblems.

3   Optimization with relaxation method

First optimizations were done with a relaxation method. Successively, in a cyclic sequence, every pair of interaction parameters α_{ij}, α_{ji} (eq. 1) is taken as the only variables and the objective function is minimized with respect to them. As the last part of a cycle, the R- and Q-values are optimized. When the algorithm does not proceed any more, the parameters β_{ij}, β_{ji} and δ_{ij}, δ_{ji} describing the temperature-dependence of the interaction parameters are additionally taken into account. For the refrigerant mixture database, normally five or six cycles are necessary to get close to a minimum.

Thus, only functions with at most 6 variables have to be minimized within a cycle step. Such a problem is easy to solve with common minimization routines. During each step only those data points that are involved with the actual parameters are considered, which saves a lot of computing time.

This approach -like all gradient methods- shows a serious disadvantage: it systematically searches for the next local minimum that can be reached. However, the function (eq. 9) has proved to offer several local minima of similar quality. Thus, several trials using different starting points should be carried out to increase the probability of reaching the global minimum. Additionally, the convergence in the near of the minimum is very slow.

The FORTRAN program was quite easy to develop and ran without problems on a mainframe computer, on a VAX workstation and even on a personal computer with a xx486 processor, where it took several days to converge.

The best quality that was reached after several optimization runs using the relaxation method with different starting values was[1]

$$F = 6.848,$$
$$\overline{\Delta p/p} = 2.77\%, \quad \overline{\Delta y} = 1.14\%,$$
$$\overline{\Delta \gamma/\gamma} = 4.98\%, \quad \overline{\Delta h^E} = 62.3 \text{ J/mol.}$$

4   Parallel Evolutionary Algorithms

By applying one method of biological evolution - the mutation-selection principle - to the field of mathematics, Evolutionary Algorithms have proved to be powerful and robust optimization methods. The foundations have been discussed in [2].

4.1   The EVOBOX code

The EVOBOX code was conceived for discrete grouping and continuous parameter optimizations. The task of determining the Modified UNIFAC parameter set happens to be a continuous parameter optimization problem. The 330

---

[1] Definitions:

$$\overline{\Delta p/p} = \sqrt{\frac{1}{N_j} \sum_j^{N_j} \left(\frac{p_{j,cal} - p_{j,exp}}{p_{j,exp}} \right)^2} \qquad (3)$$

$$\overline{\Delta y} = \sqrt{\frac{1}{N_j} \sum_j^{N_j} (y_{1j,cal} - y_{1j,exp})^2} \qquad (4)$$

$$\overline{\Delta \gamma/\gamma} = \sqrt{\frac{1}{2 N_k} \sum_k^{N_k} \left[\left(\frac{\gamma_{1k,cal} - \gamma_{1k,exp}}{\gamma_{1k,exp}} \right)^2 + \left(\frac{\gamma_{2k,cal} - \gamma_{2k,exp}}{\gamma_{2k,exp}} \right)^2 \right]} \qquad (5)$$

UNIFAC interaction parameters and the 28 R- and 28 Q-values are coded as negative or positive REAL values without any limitations. Every parameter of the matrix can be varied continuously and independently.

4.2   Parallel computing

By copying the parallel structure of nature in generational parent-to-child succession, parallelity was applied to the optimization program system, too. The determination of the objective function F represents the most time-consuming phase of the parameter optimization resulting from the repeatedly calculated vapor-liquid equilibrium conditions. These computations can be performed in parallel for all sets of parameters as the optimization algorithm only requires the quality values calculated for the selections and new mutations. Consequently, the use of parallel processors is possible without high programming expenditure. This kind of coarse grain parallelism causes a low level of data communications, so workstation clusters can be used as a 'virtual' parallel computer.

The EVOBOX code works on the processor as a so-called 'master' and is responsible for mutations and selections, while other processors configured as 'slaves' have to compute the quality functions of the different individuals. As a communications routine 'Parallel Virtual Machine (PVM)' [9] was implemented. For the optimization of the UNIFAC matrix, up to thirty workstations were used. The optimizations were allowed to run in the background of the cluster as low-priority batch jobs during normal computer operation.

4.3   Load management

Workstation pools in industry often consist of different architectures and types offering different computing power from the processors for a parallel application. As a consequence a heterogeneous workstation cluster temporarily installed with the help of a message passing software like PVM can only be used efficiently under a resource management system. In the case of the EVOBOX program the integration of a management system into the optimization code without any dependence on operating systems was chosen. This offers a high migration ability [3].

In the code system the resource manager supports three different applications which are performed by three corresponding subroutines.

The load management, an optimized partitioning of the next generation of parallel tasks, is done on basis of measured runtimes of the individual processes on the respective processors. Additionally a second subroutine administrates the inclusion and the release of additional workstations in dependence of the time of the day. With the help of this management tool also additional workstations can be included in the case of hardware failors or shutdowns caused by users. In an analog manner a third subroutine manages the restart of lost or stopped parallel processes in an optimization run.

5   Results of EVOBOX

The best quality that was reached using the EVOBOX code in a run of several weeks

$$\overline{F} = 5.135,$$
$$\overline{\Delta p/p} = 2.41\%, \quad \overline{\Delta y} = 1.02\%,$$
$$\overline{\Delta\gamma/\gamma} = 4.47\%, \quad \overline{\Delta h^E} = 52.5 \text{ J/mol}$$

In comparison to the results of the relaxation method, the reduction of the value of the objective function is about 25%, which is considered to be significant.

6   Prediction capability of the parameters

Meanwhile, several new VLE data sets have been published that were not integrated in the database when EVOBOX was started. Thus, there is now a chance to carry out genuine predictions by examining systems that did not have any influence on the adjusted parameters. The results are quite satisfactory. Two examples are discussed below.
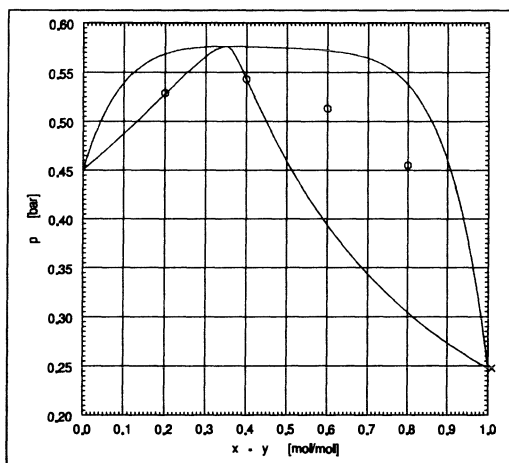
Fig. 1. VLE-estimation for the system R134a-R218 at T=220 K. Data from [1]

For R134a-R218, the isothermal data set at 220 K has large numerical deviations. The activity coefficients are strongly overestimated (Fig. 1). However, the qualitative description is correct, and even the predicted azeotropic concentration does not seem to be far away from the correct value. With increasing temperatures the phase behaviour is predicted more accurately.
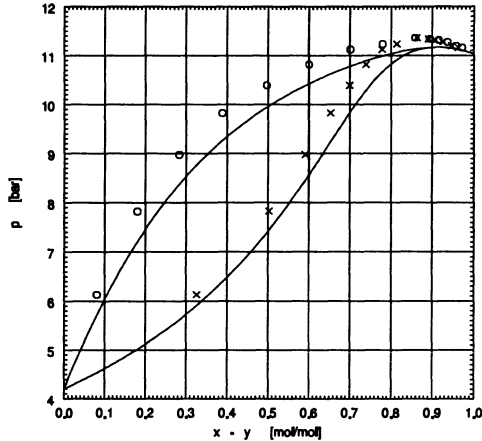
Fig. 2. VLE-estimation for the system R32-R12 at T=283.15 K. Data from [6]

R32-R12 has an azeotropic point near $x_{R32} = 0.9$ (Fig. 2). Beyond this point boiling- and dew-point line are very close together, which is predicted by Mod. UNIFAC with a remarkable accuracy.

In general, a lack of prediction capability occured for narrow boiling system with small deviations from Raoult's law, i.e. when the qualitative behaviour of the system performs highly sensitively to small errors in the activity coefficients.

7   Summary and Outlook

Adaptive evolutionary algorithms have proved to be a robust and effective optimization method for time-consuming simulations and adjustment calculations. The simple parallel algorithmic structures require only minor communications and allow workstation clusters to be used efficiently with a message passing communications software.

Regarding to the problem of determining optimized Modified UNIFAC parameters for refrigerants significantly inproved results compared to conventional minimization methods could be found in acceptable turn-around-times. By now, these parameters represent the only way to predict the behaviour of refrigerant mixtures. The group assignment seems to be reasonable, as it has proved to be capable to predict unknown phase equilibria, despite the fact that the database is relatively small.

Furthermore, it has been demonstrated that the quality of local minima that occur during the optimization of the UNIFAC matrix can differ significantly, which is caused by strong interdependencies of the parameters. This should be taken into account in further developments of the method.

8   List of Symbols

a_{ij}	UNIFAC interaction parameters	T	temperature (K)
F	objective function	x	liquid mole fraction
h^E	excess enthalpy	y	vapor mole fraction
i	number of component	α_{ij}	UNIFAC interaction parameters
j	number of an experimental point	β_{ij}	UNIFAC interaction parameters
N	number of experimental points	γ	activity coefficient
p	pressure (Pa)	δ_{ij}	UNIFAC interaction parameters
Q_k	group surface area parameter	R_k	group volume parameter

Subscripts

cal	calculated
exp	experimental

References

1. Anisimov, V. N., Zelesnyi, V. P, Semenjuk, J. V., Cerniak, J. A. (1996) Thermo-dynamische Eigenschaften des Gemisches FC218 - HFC134a (russ.), Inzenernyi fiziceskij zyrnal **69**, 5, 756-760
2. Axmann, J. K., Kleiber, M., Kothrade, A. (1996) Parallel Evolutionary Algorithms for Optimizing the Unifac Matrix on Workstation Clusters in: Keil, F., Mackens, W., Voß, H. Werther, J. (Eds.) Scientific Computing in Chemical Engineering, pages 11-21, Springer-Verlag, Berlin Heidelberg
3. Axmann, J. K., Krüger, S. (1996) Lastadaptiver Einsatz eines parallelen Optimierungscodes auf Basis Evolutionärer Algorithmen auf heterogenen Workstation-Clustern, in: Cap, C. (Ed.) Workstations und ihre Anwendungen, S. 171-184, SIWORK '96. vdf-Hochschulverlag, Zürich
4. Gmehling, J., Li, J., Schiller, M. (1993) A Modified UNIFAC Model, 2. Present Parameter Matrix and Results for Different Thermodynamic Properties, Ind. Eng. Chem. Res. **32** 178-193
5. Gmehling, J., Kolbe, B. (1988) Thermodynamik, Georg Thieme Verlag, Stuttgart - New York
6. Kang, Y. W., Chung, K. Y. (1996) Vapor-Liquid Equilibria for the systems Difluoromethane + Chlorodifluoromethane, Difluoromethane + Dichlorodifluoromethane, and Difluoromethane + Chloromethane at 10 °C, J. Chem. Eng. Data **41** 443-445
7. Kleiber, M. (1995) An extension to the UNIFAC group assignment for prediction of vapor-liquid equilibria of mixtures containing refrigerants, Fluid Phase Equilibria **107** 161-188
8. Stryjek, R., Vera, J. H. (1986) PRSV2 : A Cubic Equation of State for Accurate Vapor-Liquid Equilibria Calculations, Can. J. Chem. Eng. **64** 820-826
9. Sunderam, V. (1990) PVM: a framework of distributed computing, Concurrency: Practice and Experience **2** 4, 315-339

Simulation of Transport and Diffusion on the Voronoi Network

V.A. Luchnikov[1], N.N. Medvedev[1], V.P. Voloshin[1], and A. Geiger[2]

[1] Institute of Chemical Kinetics and Combustion, Novosibirsk, Russia
[2] Physical Chemistry, University of Dortmund, Germany

Abstract. The idea that the Voronoi network of a granular system lies "in the depth" of the empty space is used intuitively in different fields of science to study the transport of fluids, diffusion and other percolation and path problems. We discuss the concept of a "navigation map" for the interparticle empty space. It helps to study the spatial distribution and hierarchy of pores in noncrystalline packings generated in computer simulations. The approach is applied for a porosimetry analysis of packings of monodisperse spheres of different density. A generalization of the technique to systems of polydisperse spheres and nonspherical particles is also taken up.

1   Introduction.

The structure and distribution of pores is a factor, which governs many important physical phenomena in physical chemistry, catalysis and materials science. It determines the permeability of porous media, stability of powder materials, diffusion and thermodynamic properties of simple and complex liquids and glasses.

A promising way to study the structure of pores is the application of computer simulations. A model obtained by molecular dynamics or Monte Carlo methods comprises the coordinates of all atoms (particles). However the voids are not simply related to these coordinates. It needs additional efforts and algorithms to extract "physical" informations about the unoccupied volume and to make a quantitative analysis. This question had been understood and was raised long ago [1]. However, advances have been obtained in the last decade only. A reason for this is the use of a rigorous mathematical basis, which gives a geometrical technique to partition the space between the atoms [2,3]. This Voronoi-Delaunay approach is well-known in the study of atomic arrangements in liquids and amorphous structures [4]. Next, it had been applied to study interatomic voids [5,6]. The permeability and flow through packings of monodisperse spheres was simulated in [7,8]; paths for the diffusion of particles with different size in liquid and glassy polymers was studied in [9]; the thermodynamic aspects of voids in simple liquids was discussed in [10,11]; a porosimetry analysis for sphere packings was made in [12].

The main idea for a quantitative analysis of the voids inside an arbitrary ensemble of atoms (particles) is based on the analysis of "the navigation

map" of this ensemble. This map keeps track of the location of the "deepest" points (most distant from the surfaces of the particles) inside an ensemble and defines channels (fairways) connecting these points [13]. There are no principal problems to get this map because its mathematical construction is well-known. It is the Voronoi network [2,3] which exists for any system [14]. A practical question, however, is to have an efficient algorithm to calculate it for a given system. Of course, before the calculation of the Voronoi network, one has to construct the system to be studied. The next stage is then the analysis: the computation of the Voronoi network, of the holes of a given size, their spatial distribution, channels acceptable to a given probe, percolation characteristics of the porous space. This needs also mathematical and programming work.

Note, the conception of the navigation map is close to the idea of "the medial axes", which is used to describe the structure of a cavity inside a continuous medium, or, in the opposite, the structure of an individual domain with a given shape [15,16]. As it was remarked in [16], the medial axis is a "continuous version" of the Voronoi network.

2   Geometrical analysis

. The Voronoi-Delaunay approach is originally known for systems of discrete points. The mosaic of the Voronoi polyhedra (the Voronoi tessellation) covers the entire space without overlaps and gaps. The set of all edges and vertices of the Voronoi polyhedra defines the Voronoi network. Therefore it is a simply-connected and four-bonded network for any nondegenerate ensemble of points. The bonds of this network are segments of straight lines.

However for physical-chemical applications we deal with systems of *finite size* particles, the most simple one being a system of equal spheres. Fortunately, the properties of the Voronoi network for point systems are also true for this case.

The idea to use the Voronoi-Delaunay approach for a broader class of particles is very tempting. However, as it was remarked many times, the classical Voronoi-Delaunay construction cannot be used in general, see for example [17]. The original Voronoi-Delaunay tessellation does not take into account the size and the shape of particles.

The problem had been solved for systems of spheres of different radii [13,11,14]. Such systems are used as models of polydisperse powders, polyatomic materials and alloys. To take into account the surface of the particles, one should introduce a new geometrical construction: instead of the classical Voronoi polyhedron defined by the centers of spheres, one should define another volume, all points of which are closer to the *surface* of a given sphere than to the *surfaces* of the other spheres of the systems. This region was called a Voronoi S-region [13]. It is analogous to the usual Voronoi polyhedron, but its faces and edges are curved. The Voronoi S-regions generate a Voronoi

S-tessellation. The set of vertices and edges defines the Voronoi S-network of the system of polydisperse spheres. A special algorithm was created to calculate the S-constructions. An application of this technique to study 3D Apollonian packings was made in [18].

Studying the porous space, we are working with the Voronoi S-construction only. Here we will omit the letter S in the names, for simplicity.

In fact, the Voronoi-Delaunay ideas can be extended to systems of particles with arbitrary convex shapes. It opens a way to use a rigorous geometrical technique to study the structure of pores for a much broader class of particles then systems of spheres. Recently, the corresponding algorithm was developed and a system of straight lines and spherocylinders was analyzed [19]. Convex particles possess an important property: the closest distance from any point of space to the surface of a convex particle is single-valued. This condition is sufficient to be sure that the Voronoi tessellation exists for any system of convex particles.

In the general case the Voronoi network is the set of edges (bonds) and vertices (sites) of the Voronoi regions in the Voronoi tessellation of a given system of particles. The fact that the Voronoi network lies "in the depth" of the unoccupied space is valid in general. It follows directly from the definition of the Voronoi region. If we leave a bond of the Voronoi network (which is a common edge of the adjacent Voronoi regions), we will be inside of a Voronoi region and therefore closer to the surface of one of the particles. In this respect a bond is a fairway: if a probe leaves this line it can "run aground" on a surface of a particle. The Voronoi network is four-valenced: every site of the Voronoi network is the origin of four bonds. (It is assumed that the system is nondegenerate). This is easy to understand: any site of the Voronoi network is defined by four particles, but four particles open four and only four channels (bonds) from this site. This is true for any particle which has one and only one point of contact with a sphere [19].

There are also differences between the general and classical Voronoi network. A major one being the problem of simple connectedness of the network in 3D. Indeed, even for a system of polydisperse spheres an example can be constructed for a totally disconnected Voronoi network. Fortunately, we can ignore this theoretical possibility of the disconnectedness of the Voronoi network for relevant physical systems [14,19].

3   Algorithms for the navigation map

. To describe the Voronoi network, we should have the following sets of data: the list $\{D\}$ of the coordinates of the Voronoi sites and the table $\{DD\}$ for the connectivity of the sites. For thr metric analysis of the voids we should additionally keep the value of the radius of the inscribed sphere at every site (list $\{R_i\}$) and the minimum radius of the Delaunay spheres along every bond, the so called bottleneck radii (list $\{R_b\}$). These data give us the full

information to use the Voronoi network as a navigation map: the location of all "deepest" points, their connectivity, and the corresponding values of the bottleneck radii.

To create the Voronoi network of a monodisperse system one can use any algorithm for a classical Voronoi polyhedra calculation. The main task of these algorithms is usually the calculation of the circumsphere for a given set of four centers (a site of the Voronoi network) by solving the system of equations

$$(x_i - x)^2 + (y_i - y)^2 + (z_i - z)^2 = R^2, \quad i = 1, 2, 3, 4. \tag{1}$$

x_i, y_i, z_i are the coordinates of the centre of the i-th particle of a given quartet. The four unknown variables x, y, z and R are the coordinates and the radius of the circumsphere. The main step of the algorithm is the determination of the vertex which is adjacent to a given one (to find the second endpoint on the Voronoi bond). This can easily be done, because the second site on a bond is the center of the inscribed sphere, which is closest to the known vertex on the given Voronoi channel, see e.g. [20].

To create an algorithm for the Voronoi network of polydisperse spheres one can use the same ideas, however to find a site of the Voronoi network we should be able to obtain an inscribed sphere between four spherical particles of arbitrary radii. The solution of the following system of equations gives an answer to the question:

$$(x_i - x)^2 + (y_i - y)^2 + (z_i - z)^2 = (R_i + R)^2, \quad i = 1, 2, 3, 4. \tag{2}$$

Where R_i is the radius of the i-th particle. Fortunately, this system can be solved and analytical formulas for x_i, y_i, z_i and R can be obtained. As a result, the algorithm for a polydisperse system has the same efficiency as for monodisperse one. For details see [14].

In the general case of convex particles we cannot calculate Voronoi sites analytically. However we can use the same idea to find the next site of the Voronoi network: the adjacent site is the closest one to the known site on a given Voronoi bond. In this case we have to go step by step along the Voronoi bond from a known site to define a new site numerically. A general algorithm for the Voronoi network of such systems is proposed in [19]. It can be used for particles of any shape. The peculiarities of the particles are hidden in the distance function $d_i(\mathbf{r})$, which defines the minimal distance from a given point $\mathbf{r}$ to the surface of the i-th particle.

4   Permeability and diffusion.

The navigation map is a rigorous geometric construction and represents a real channel system in a sample. Physical assumptions will be made at the step of application to a given physical problem. For example one should define
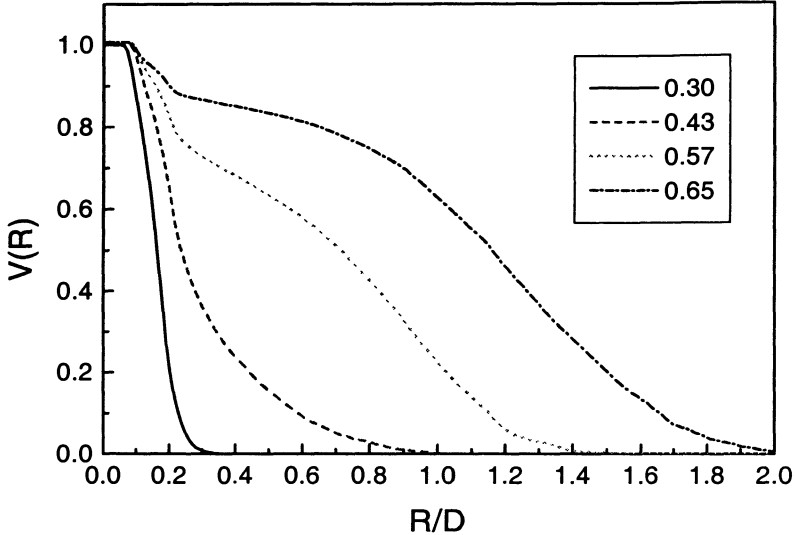
Fig. 1. Fraction of pore volume accessible to a probe of radius R_{probe} ("intrusion" curve) for packings of monodisperse spheres at different values of porosity ϵ (given in the insert). Diameter of spheres D is unity.

a "resistance" for fluids moving through a bottleneck, as it was made in [7,8] to study the permeability in a granular porous media. The results were successfully compared with experimental data measured on sand packs, bead packs, and a simple sandstone.

The problem of diffusion of hard particles in a porous media, can be simulated as a random walk on the navigation map. The probability to go along a given edge can be assumed to be proportional to the value of the Voronoi bond bottleneck for a given direction. Knowing the location of all vertices, their connectivity, and probabilities to go from one vertex to another, a Monte Carlo process for particle transport can easily be realized. In particular, forbidding the possibility to go up, we can simulate a rolling process of a ball inside a packing of spheres [21].

As an application of the Voronoi network analysis, we present the results of a study to characterize the hierarchy of pores in monodisperse packings of spherical particles at different densities. Recently such an analysis was proposed for the interpretation of mercury porosimetry experiments [12]. We have created a set of noncrystalline packings of 8000 Lennard Jones particles relaxed at zero temperature. The porosity of the different packings is in an interval from $\epsilon = 0.30$ to $\epsilon = 0.70$. The denser models represent the well-known Bernal-like noncrystalline packings of spheres. As the density decreases, we get more and more cavities inside the packing. The low density packings contain a percolative cluster of relatively large pores and, at the same time, a percolative cluster of closed packed particles.
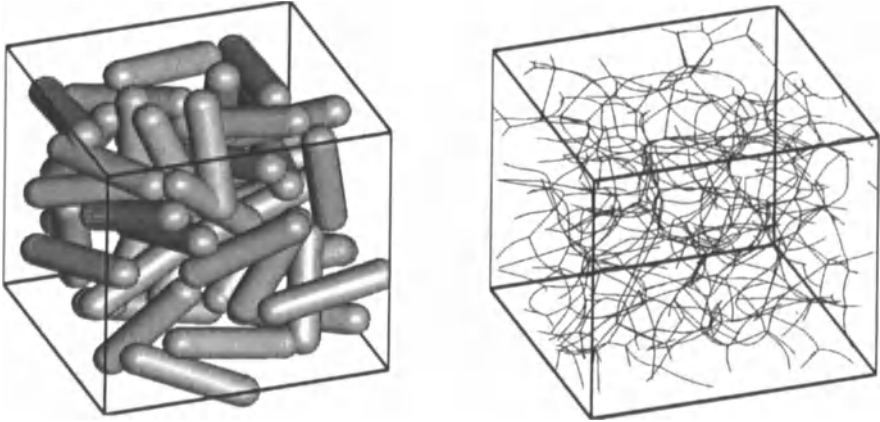
Fig. 2. Voronoi network of a system of nonspherical particles. a.) Representation of a molecular dynamic model of the isotropic phase of a liquid crystal by 50 spherocylinders. b.) The Voronoi network of this model (401 sites and 802 bonds). Periodic boundary conditions are used.

The "intrusion" curves for a set of our structural models are shown in Fig.1. They show the volume fraction of pores, where a probe of a given radius R_{probe} (radius of meniscus) can be placed, as a function of the value of R_{probe}. With decreasing probe size, the fraction of the volume increases to the total empty volume inside the model and becomes equal to unity with $R_{probe} = 0$. The curves characterize the nature of pores at different densities of packing.

In the terminology of percolation theory the study of pores is a bond percolation problem on the navigation map. Indeed, all bonds with a value of the bottleneck radius greater than the radius of a given probe, can be distinguished (coloured) on the network. Any cluster of coloured bonds defines a pore for a given probe: the probe can be moved inside the pore along the coloured bonds. Depending on the size of the probe particle, this can be a finite pore or a percolative one. It is not difficult to define all clusters of coloured bonds on the network and then to make their analysis, e.g., to calculate the volume of every pore.

The Voronoi network of a system of nonspherical particles is illustrated in Fig.2. As an example of a physical sample we use a simplified model of a liquid crystal. At first an atomically resolved molecular dynamic model of 50 molecules of 4-(trans- 4' -pentyl–cyclohexyl)–benzonitrile (PCH5) in the isotropic phase at $T = 330\ K$ had been created [22]. Then we have represented every molecule of the liquid crystal by a spherocylinder (cylinder with hemispheres at the ends). The model box of this system is shown on Fig. 2a. The length of every spherocylinder is $L = 1.3\ nm$ and the radius $r = 0.2\ nm$. The Voronoi network of this model is demonstrated in Fig.2b.

Actually, this Voronoi network with the bottleneck radii can be used for a pore analysis similar to that of the packings of spheres.

5   Conclusions.

We discussed a method to study the structure of the pore space in granular and atomic systems. It is based on the analysis of the Voronoi network. This network lies in the depth of the unoccupied space between particles and plays the pole of a "navigation map" of the system. It gives quantitative informations about the spatial distribution of pores in a model, which help to study flow and diffusion phenomena. The main idea of an algorithm to calculate the navigation map in 3D for systems of spheres and nonspherical particles is discussed. The approach is applied for a porosimetry analysis of packings of monodisperse spheres of different density. An application of the method to a system of spherocylinders (as a model of liquid crystals) is demonstrated.

References

1. F.A.L. Dullien, *Porous media: Fluid transport and pore structure*, Academic Press, 1979.
2. G.F. Voronoi, Z. Reine Angew. Math. **136**, 67–181 (1909).
3. A. Okabe, B. Boots, K. Sugihara, *Spatial Tessellations – Concepts and Applications of Voronoi Diagrams*, John Wiley and Sons, 1992.
4. J.L. Finney, Proc. Roy. Soc. London **319**, 479–494 and 495–507 (1970).
5. N.N. Medvedev, Yu.I. Naberukhin, V.P. Voloshin, "Geometry of empty space inside of granular system", Proceeding of VI-th IFP conference: Physical chemistry of colloids and interfaces in oil production, ed. H. Toulhoat and J. Lecourtier, Paris, 1992.
6. Yu.I. Naberukhin, V.P. Voloshin, N.N. Medvedev, Zh. Fiz. Khimii. **66**, 155–162 (1992).
7. S. Bryant, M. Blunt, Phys. Rev. A **46**, 2004–2011, (1992).
8. K.E. Thompson, H.S. Fogler, AIChE Journal **43**, 1377–1389 (1997).
9. M.L. Greenfield, D.N. Theodorou, Macromolecules **26**, 5461–5472 (1993).
10. R. Bieshaar, A. Geiger, N.N. Medvedev, Mol. Simulation **15**, 189–196 (1995).
11. S. Sastry, D.S. Corti, P.G. Debenedetti, F.H. Stillinger, Phys. Rev. E **56** 5524–5532 (1997).
12. V.P. Voloshin, N.N. Medvedev, V.B. Fenelonov, V.N. Parmon, "Simulation of the mercury porosimetry on the Voronoi network", Abstracts of the XXth International IUPAP conference in Stat. Phys., Paris, July 20–24, 1998, P009/62.
13. N.N. Medvedev, Dokl. Akad. Nauk. **337**, 767–773 (1994) (in Russian); Engl. transl.: Doklady. Phys. Chem. **337**, 157–163 (1994).
14. N.N. Medvedev, Computational porosimetry. In *Voronoi's impact on modern science*, Edited by P. Engel and H. Syta, Institute of Math., Kiev. 1998, Vol. 2, p. 164–175.

15. W.B. Lindquist, S.-M. Lee, D.A. Coker, K.W. Jones, P. Spanne, J. Geophys. Research **101**, 8297–8310 (1996).
16. H.I. Choi, S.W. Choi, H.P. Moon, Pacific J. Math. **181**, 57–88 (1997).
17. A.R. Kerstein, J. Phys. A: Math. Gen. **16**, 3071 (1983).
18. S.V. Anishchik, N.N. Medvedev, Phys. Rev. Lett. **75**, 4314–4317 (1995).
19. V.A. Luchnikov, N.N. Medvedev, L. Oger, J.-P. Troadec, "The Voronoi–Delaunay analysis of voids in systems of nonspherical particles", Phys. Rev. E, in press.
20. M. Tanemura, T. Ogawa, N. Ogita, J. Comp. Phys. **51**, 191–207 (1983).
21. P. Richard, L. Oger, J. Lemaitre, L. Samson, N.N. Medvedev, Phys. Rev. E, to be published.
22. S.Ye. Yakovenko, A.A. Minko, G. Krömer, A. Geiger, Liquid Crystals **17**, 127–145 (1994).

Monte Carlo modeling of surface diffusion in interacting systems with phase transitions

F. Nieto[1,3], A.A. Tarasenko[2,3] and C. Uebing[3,4]

[1] Departamento de Física and Centro Latinoamericano de Estudios Ilya Prigogine,
   Universidad Nacional de San Luis, CONICET
   Chacabuco 917, 5700 San Luis, Argentina
[2] Ukrainian Academy of Sciences, Institute of Physics, Kiev
[3] Max-Planck-Institut für Eisenforschung,
   Max-Planck-Str. 1, D-40237 Düsseldorf, Germany
[4] Lehrstuhl für Physikalische Chemie II, Universität Dortmund
   Otto-Hahn-Str. 6, D-44227 Dortmund, Germany

Abstract. Nowadays many experimental techniques for the measurement of surface diffusion coefficients exist. However, a lot more work remains to be done to establish the complete or at least a partial understanding of surface diffusion phenomena. In many cases, the interpretation of experimental surface diffusion data has been extremely complicated. Therefore, Monte Carlo studies of static and dynamic properties of adsorbed monolayers on metal surfaces by means of lattice gas modeling has attracted considerable attention during the last two decades. In this presentation recent progresses in the Monte Carlo modeling of surface diffusion processes in interacting systems with phase transitions will be discussed.

1   Introduction

Surface diffusion of adsorbates on metal and alloy surfaces has become an important subject of surface science. The detailed comprehension of surface diffusion is one of the key steps in understanding (and controlling) many interesting surface phenomena such as adsorption, desorption, catalytic reactions, melting, roughening, and crystal and film growth.

In recent years, the effects of lateral interactions on the chemical surface diffusion coefficient of adsorbed particles have been intensively investigated using many different theoretical and numerical methods. For instance, mean-field [1], Bethe-Peierls [2], real-space renormalization group (RSRG) [3, 4], transfer matrix [5] and Monte Carlo (MC) [6] methods have been used in order to describe the surface diffusion phenomenon. It was found that adparticle interaction can strongly influence surface diffusion, especially at low temperatures and in the close vicinity of surface phase transitions [7].

The MC simulation of surface diffusion is probably the most reliable numerical method which can be used to study adparticle diffusion on different lattices and for various sets of the interaction parameters. However, compared to the theoretical methods mentioned above the MC method is very

time consuming and requires powerful computers. Most of the results to be discussed below are obtained by a fully parallelized algorithm in conjunction with Cray T3E (LC768-128) supermassive parallel computer operated by the Max-Planck community in Garching/Germany.

The outline of this contribution is as follows. In Sec. 2 we will describe the basics of surface diffusion. The Monte Carlo simulation of surface diffusion is discussed in Sec. 3. Finally, selected results of recent studies are presented in Sec. 4.

2   Basics of Surface Diffusion

Phenomenologically, diffusion is described by Fick's laws. In particular, according to Fick's first law, the diffusion flux of particles driven by a gradient of the particle density, ρ, is given by

$$\boldsymbol{J} = -D_c\nabla\rho. \tag{1}$$

Here D_c is the chemical diffusion coefficient. It is probably important to note that the term "diffusion *coefficient*" is certainly misleading. Only for an isotropic medium, such as a gas, a liquid or a solid with cubic symmetry, D can be considered as a scalar coefficient. For an anisotropic solid Eq. 1 should be written as

$$\boldsymbol{J} = -\mathcal{D}_c\nabla\rho. \tag{2}$$

$\mathcal{D}_c$ denote the diffusion tensor, which can be represented by a 3×3 matrix. In general, it is possible to find principle axes which diagonalize $\mathcal{D}_c$. For the specific situation of surface diffusion, Eq. 1 can then be rewritten as

$$\boldsymbol{J} = -\begin{pmatrix} D_{xx}\frac{\partial\rho}{\partial x} \\ D_{yy}\frac{\partial\rho}{\partial y} \end{pmatrix}. \tag{3}$$

Here we implicitly assume that the x and y directions are located within the two-dimensional surface plane, and that the surface normal is directed along the z axis.

In the following we will restrict the considerations to solid surfaces of square symmetry (for which $D_{xx} = D_{yy}$) and, therefore, we can apply Eq. 1 with D_c as chemical diffusion "coefficient". Eq. 1 suffices to define D_c, but for practical considerations it is useful to combine it with the continuity equation $\nabla\boldsymbol{J} = -\partial\rho/\partial t$, which gives

$$\frac{\partial\rho}{\partial t} = \nabla\left(D_c\nabla\rho\right). \tag{4}$$

If D_c is independent of particle density ρ, i.e. $D \neq D_c(\rho)$, then Eq. 4 simplifies to

$$\frac{\partial\rho}{\partial t} = D_c\nabla^2\rho. \tag{5}$$

Eq. 5 is known as Fick's second law. From Eqs. 1 and 5 it is clear that the chemical diffusion coefficient D_c describes the response of a system in the presence of a concentration or particle density gradient. From that point of view, it is justified to conclude that the chemical diffusion coefficient emphasizes the macroscopic phenomenological point of view. However, the occurrence of chemical diffusion does not necessarily require the existence of macroscopic concentration gradients. This point has been discussed in more detail in Ref. [8].

In contrast to the chemical diffusion coefficient, which is a many particle diffusion coefficient, the tracer diffusion coefficient, D_t, describes the random walk of a tagged single particle. D_t is defined through the generalized definition

$$D_t = \lim_{t \to \infty} \left[\frac{1}{2dt} \left\langle |r_i(t) - r_i(0)|^2 \right\rangle \right] \tag{6}$$

where d is the Euclidean dimension, (in the case of surface diffusion $d = 2$); the vector $r(t)$ determines the position of a tagged particle at time t, and $\left\langle (r(t) - r(0))^2 \right\rangle$ is its mean square displacement.

For the sake of completeness, we introduce also the so-called jump diffusion coefficient D_j, defined by Reed and Ehrlich [9] as

$$D_j = \lim_{t \to \infty} \frac{1}{4t} \int dt \left\langle \sum_{i=1}^{N} v_i(0) \sum_{j=1}^{N} v_j(t) \right\rangle. \tag{7}$$

It can be shown that D_j can also be written as

$$D_j = \lim_{t \to \infty} \frac{1}{4t} \frac{1}{N} \left\langle \left(\sum_{i=1}^{N} \Delta r_i \right)^2 \right\rangle. \tag{8}$$

D_j is a many particle diffusion coefficient, which describes the motion of the center of mass.

3   The Monte Carlo Simulation of Surface Diffusion

For the computer simulation of surface diffusion two powerful methods are frequently used, the molecular dynamics (MD) scheme and the Monte Carlo (MC) scheme. Since most of the studies to be discussed in Sec. 4 are based on lattice gas models investigated via MC simulations, we will discuss this method in some detail here.

Within the lattice gas scheme the basic steps of surface diffusion are jumps of adatoms from filled initial sites i to adjacent vacant sites f. The activation energy for such jumps can be calculated as the energy difference between saddle point $\epsilon^*_{i \to f}$ and single site energy of the initial site ϵ_i, [6]

$$\Delta E = \epsilon^*_{i \to f} - \epsilon_i. \tag{9}$$

The associated jump probability P_J is given by

$$P_J = \frac{1}{\kappa} \exp\left(-\frac{\Delta E}{k_B T}\right), \tag{10}$$

with κ as a normalization factor. This choice ensures full microscopic reversibility and fulfills the condition of detailed balance [10]. However, the activation energies ΔE and the jump probabilities P_J are partly arbitrary since the detailed balance condition does not specify these quantities uniquely [11]. In order to optimize the computational time of a Monte Carlo algorithm, a suitable normalization of jump probabilities is indispensable. A natural choice for κ would be

$$\kappa = \kappa_{\max} = \exp\left(-\frac{\Delta E_{\min}}{k_B T}\right). \tag{11}$$

Here $\Delta E_{\min}$ represents the jump probability for the most favorable physically realizable jump [6]. This choice of κ generates the highest possible jump probabilities, i.e., minimizes the number of unsuccessful attempts, while avoiding jump events with $P_j > 1$. In some cases this choice of κ leads to an impractically large number of Monte Carlo steps required for the equilibration of the lattice gas and for the determination of the desired surface diffusion coefficients. Especially at very low temperatures and in ordered regions of the relevant phase diagram, hop events occur very infrequently. Therefore, smaller normalization factors $\kappa < \kappa_{\max}$ can be chosen. However, it should be verified very carefully that in such cases the fraction of jumps with jump probabilities $P_j > 1$ is still negligibly small ($< 0.1\%$).

The procedure for simulating jumps in the canonical ensemble has been described in some detail in Refs. [6, 12] and, therefore, we will present only the general schema of the computations. First, for a given lattice gas configuration an initial site i is randomly picked. If filled, an adjacent final site j is randomly selected. If the destination is vacant, a jump may occur with probability P_J (Eq. 10), otherwise, no jump occurs. Thermodynamic equilibrium is established before starting a diffusion run at the desired fixed coverage θ. Approach to equilibrium is monitored by following the configurational energy and in case of ordering by measuring corresponding order parameters of the system. Equilibrium is assumed to be established when these quantities fluctuate about their average values. In a recent publication, we have shown that in some systems even minute deviations from thermodynamic equilibrium may substantially influence the surface diffusion coefficients [13].

In the MC method the tracer diffusion coefficient D_t can be easily determined from measurements of the mean square displacements of N tagged adatoms according to Eq. 6. The displacements $\Delta r_i(t)$ are expressed in units of the lattice constant a_o.

The chemical diffusion coefficient D_c can be determined via two different approaches, the fluctuation method as well as the Kubo-Green method. In essence, the fluctuation method measures the particle number autocorrelation

function $f_n(t)/f_n(0)$ for a small probed region embedded in the whole two-dimensional lattice. It has been shown in detail how the decay of $f_n(t)/f_n(0)$ can be used to obtain the chemical surface diffusion coefficient, which is called D_F [14, 15]. Thus, this method is a computer simulation of the field emission fluctuation method [14] used experimentally for determining adsorbate diffusion coefficients. For the autocorrelation function one can write

$$\frac{f_n(t)}{f_n(0)} = \frac{\langle \delta N(t)\delta N(0)\rangle}{\left\langle (\delta N)^2 \right\rangle},\tag{12}$$

where N is the number of adatoms in the probed area. In Ref. [15] an analytical expression for the autocorrelation function of the particle density for a square probehole was given:

$$\frac{f_n(t)}{f_n(0)} = \left[\mathrm{erf}\left(\frac{\tau_\mathrm{o}}{t}\right)^{1/2} + \left(\frac{t}{\pi\tau_\mathrm{o}}\right)^{1/2}\left(\exp\left(-\frac{\tau_\mathrm{o}}{t}\right)-1\right)\right]^2.\tag{13}$$

In the very long time limit, i.e., when the mean square displacement of the diffusion particles $\Delta r_i(t)$ is long with respect to the lattice spacing, $\Delta r_i(t) \gg a_\mathrm{o}$, the correlation function is approximately given by [15]

$$f_n(t) \approx \frac{k_\mathrm{B}TK_T\theta^2 a_\mathrm{o}^2}{4\pi Dt}.\tag{14}$$

Here K_T denotes the isothermal compressibility of the adlayer. $\theta = \langle N\rangle/A$ is the mean density of adatoms, i.e., the mean number of adatoms per area A [15]. Equation 14 implies that the correlation function decays as t^{-1} at long times. However, Eq. 14 is valid only in the hydrodynamic regime, i.e., on a time and distance scale being large compared to a mean-free time and mean-free path ($\approx$ lattice spacing) of the lattice gas model [15].

The second method of determining the chemical diffusion coefficient D_c is based on the Kubo-Green equation, [9] here written as

$$D_{KG} = \underbrace{\left(\frac{\partial\mu/k_\mathrm{B}T}{\partial\ln\theta}\right)_T}_{\text{Thermodynamic factor}} \cdot D_j = \left[\frac{\left\langle(\delta N)^2\right\rangle}{\langle N\rangle}\right]^{-1}\cdot D_j,\tag{15}$$

where μ is the chemical potential, θ the coverage and D_j the jump diffusion coefficient given by Eq. 7. $\left\langle(\delta N)^2\right\rangle$ is the mean square number fluctuation in an area A containing $\langle N\rangle$ particles on the average. $[\partial\left(\mu/k_\mathrm{B}T\right)/\partial\ln\theta]_T$ is the well-known thermodynamic factor.

4   Influence of Phase Transitions on Surface Diffusion

In this section we focus on recent investigations of surface diffusion processes in the vicinity of phase transitions and critical points. This topic is of general

interest since at a phase transition the properties of a two-dimensional system changes from one phase to another abruptly. In case of a first-order phase transition the density (or the magnetization) changes abruptly, while in case of a continuous or second-order phase transition the symmetry of the phases changes. Most of the studies to be discussed below deal with surface diffusion in the vicinity of second-order phase transitions and critical points (Sec. 4.1). Unfortunately, only a few studies have addressed the interesting issue how a first-order phase transition influences surface diffusion. Some of those studies will be discussed in Sec. 4.2.

4.1   Influence of Second-order Phase Transitions
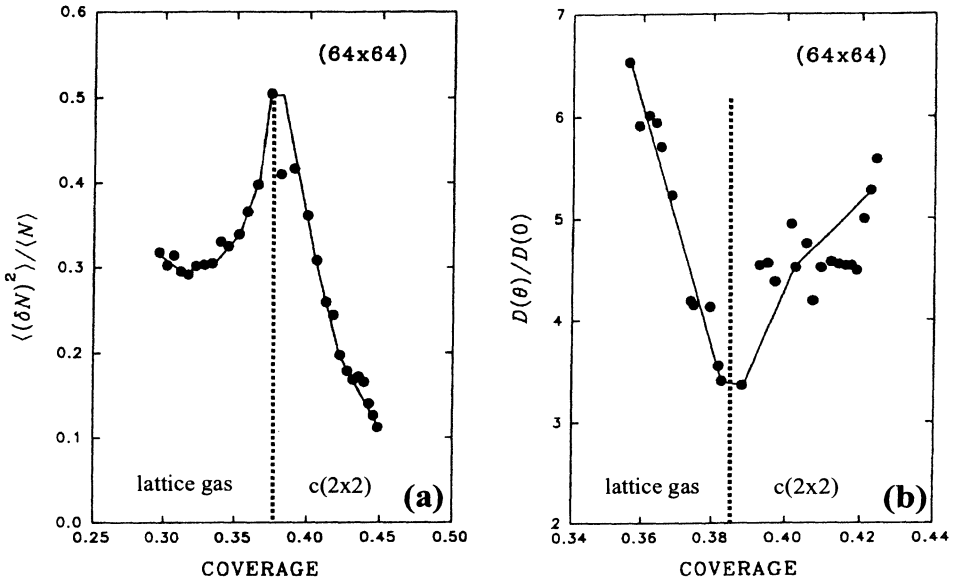
Fig. 1. (a) Mean square number fluctuation as a function of coverage for square lattices of 64×64 sites. Filled circles denote MC results.
(b) Normalized chemical diffusion coefficient as a function of coverage for $\varphi_{NN}/k_{\mathrm{B}}T = 5.28$, after [16].

At equilibrium (i.e. in the absence of macroscopic particle density gradients), D_t and D_c often strongly depend both on temperature and coverage due to the potential barrier for diffusion and lateral adsorbate-adsorbate interactions [6, 17, 18]. A few years ago, several studies were aimed to enhance our understanding of collective adsorbate diffusion in the vicinity of second order or continuous phase transitions on square lattices. The emphasis

of these studies was on the peculiarities in the coverage dependence of D_c near the critical points [16,19]. Results of Monte Carlo (MC) simulations for a square lattice with repulsive interactions between nearest neighbor particles indicate that the phase transition induced effects on D_c are localized in rather narrow regions near critical points [16]. The coverage dependence of the normalized mean square fluctuations (Fig. 1a), obtained at a temperature $\varphi_{NN}/kT = 5.28$ well below the critical temperature $\varphi_{NN}/kT_c = 1.76$, exhibits a narrow maximum centered around $\theta_c = 0.385$. In Ref. [16] it was found that this maximum increases with increasing lattice size L. This finding qualitatively agrees with results obtained via transfer-matrix techniques [16]. The coverage dependence of the chemical diffusion coefficient, obtained via the Kubo-Green method, clearly exhibits a minimum at the second-order phase transition (Fig. 1b) [16].
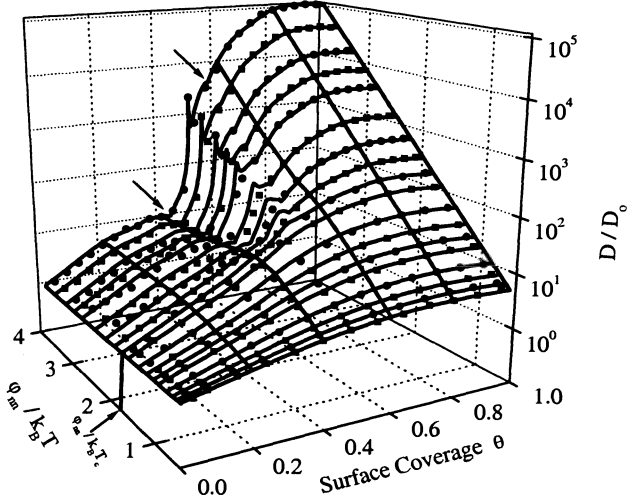
Fig. 2. 3D plot of the normalized chemical diffusion coefficient $\ln D/D_0$ vs. θ and $|\varphi_{nn}|/k_B T$, after [20]. Note the logarithmic axis. Solid lines represent RSRG results, symbols denote MC results. Arrows indicate the minima of D_c at the second-order phase transitions below T_c.

A comparison between normalized chemical diffusion coefficients of repulsively interacting adatoms on a square lattice obtained via RSRG treatment and MC simulations is shown in Fig. 2. The fit between RSRG and MC data is surprisingly good for the whole range of temperatures and coverages. Even for low temperatures, $T < T_c$, the deviations between data obtained by these quite different methods, are very small. Only in the vicinity of the critical point at half coverage there are visible discrepancies.

Employing the scaling arguments, it has been shown that in the vicinity of continuous surface phase transitions, the temperature dependence of D_c has power-law or inverse logarithmic singularities, $D_c \propto |\Delta T|^{\alpha/(1-\alpha)}$ or $\propto 1/|\ln|\Delta T||$ ($\alpha > 0$ is the specific heat exponent). Very recently such anomalies have also been seen in the temperature dependence of D_c (but not for D_t) for oxygen adsorbed on W(110) [21]. Monte Carlo simulations indicate that these singularities (i) occur in a very narrow temperature interval near the continuous phase transition between disordered lattice gas and ordered structures, (ii) can be reproduced only if the lattice size is large ($L > 500$) and (iii) are unequivocally attributable to the well known anomalies of the thermodynamic factor in the vicinity of continuous phase transitions [21]. Outside the critical region, the temperature dependence of D_c is regular and the deviations from the ideal Arrhenius behavior are relatively weak.

4.2   Influence of First-order Phase Transitions

Only a few attempts have been undertaken to investigate the influence of phase transitions of first-order on surface diffusion. In Ref. [22] a lattice gas on a square lattice with nearest neighbor attractive ($\varphi_{NN} > 0$) and next nearest neighbor repulsive interactions ($\varphi_{NNN} < 0$) has been investigated in detail. This model shows first and second-order phase transitions at low temperatures, depending on the ratio $R \equiv \varphi_{NNN}/\varphi_{NN} \leq 0$.

Fig. 3 shows typical adsorption isotherms $\theta = f(\mu)$ for equilibrated lattices gases with nearest neighbor attraction and next nearest neighbor repulsion. For $R = -2$ the isotherms show a wide plateau around $\theta = 0.5$ which corresponds to the p(2×1) lattice gas phase [13], which is separated from disordered lattice gas by second-order phase transitions. On increasing the temperature the plateau disappears above the critical temperature T_c. It is $\varphi_{NN}/k_B T_c = 0.90$ [13]. With decreasing next nearest neighbor repulsions φ_{NNN} the width of the plateau shrinks and finally disappears for the case $R = -0.5$. Second-order phase transitions are still present for $R = -1$ but disappear for $R = -0.5$. Obviously the p(2×1) ordered lattice gas phase is stabilized by the next nearest neighbor repulsive interactions. For $R = 0$ and $\varphi_{NN}/k_B T = 2.40$ and also for $R = -0.5$ and $\varphi_{NN}/k_B T = 4.01$ almost vertical jumps of the surface coverage θ are observed, which are attributed to first-order phase transitions between low density lattice gas (LG) and high density lattice fluid (LF).

Fig. 4 shows the normalized chemical diffusion coefficient obtained via Kubo-Green (D_{KG}) and fluctuation method (D_F) vs $\varphi_{NN}/k_B T$ at $\theta = 0.5$. The T range goes from that corresponding to disordered lattice gas deep into the p(2×1) ordered region for $R = -2$, $R = -1$. For $R = 0$ the lowest temperature studied lies within the miscibility gap of the phase diagram. The data were obtained in the canonical ensemble after full equilibration. Here we do not intent to discuss the general temperature dependence of the diffusion coefficient, which behaves as intuitively expected (see for instance Ref. [22]).
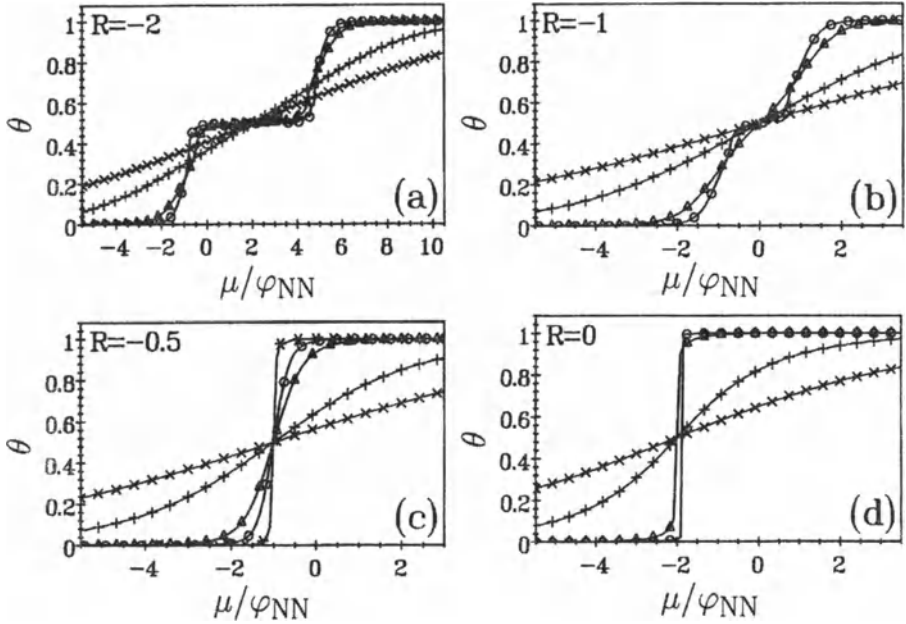
Fig. 3. Adsorption isotherm $\theta(\mu/\varphi_{NN})$ for the lattice gas model with various values of $R \equiv \varphi_{NNN}/\varphi_{NN}$ as indicated: (*): $\varphi_{NN}/k_BT = 4.01$; (o): $\varphi_{NN}/k_BT = 2.40$; ($\triangle$): $\varphi_{NN}/k_BT = 1.60$; (+): $\varphi_{NN}/k_BT = 0.48$; ($\times$): $\varphi_{NN}/k_BT = 0.24$. For the calculations a 64×64 lattice was used. Equilibration was carried out in the grand canonical ensemble, after [22].

More interesting than that is the comparison of Kubo-Green and fluctuation results. For $R = -2$ and $R = -1$ D_{KG} and D_F agree quantitatively over the entire T range. This is true for $R = -0.5$ and $R = 0$ only at relatively high temperatures. At lower temperatures there are significant deviations between both quantities, $D_F \ll D_{KG}$. This striking finding is completely unexpected since it has been shown in [13] that both methods give identical results for lattice gases with various sets of interaction energies. The reasons for these discrepancies are not fully understood. However, it is very likely that these discrepancies are related to the first-order phase transition at low temperatures at $R = -0.5$ and $R = 0$ well above T_c. Simulations for 256×256 lattices indicate that the observed deviations are not due to finite size effects.

The deviations between D_F and D_{KG} persist at temperatures well above the first-order phase transitions between LG and LF at $R = -0.5$ and $R = 0$. Characteristic snapshots such as shown in Ref. [22] indicate that even at such high temperatures the lattice gas starts to decompose into tiny domains of low and high density, respectively. It is intuitively obvious that even in a (thermodynamically) disordered region of the phase diagram, i.e. correspond-
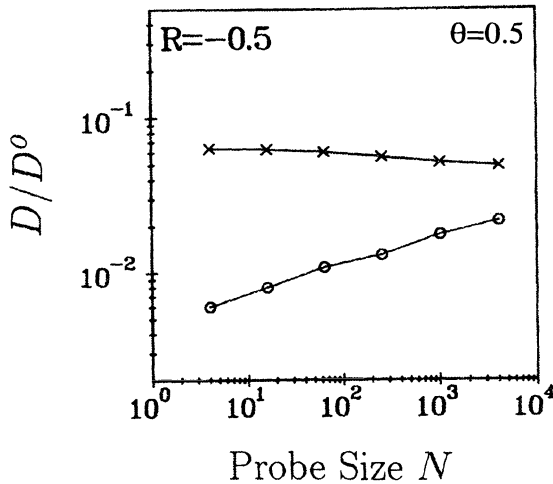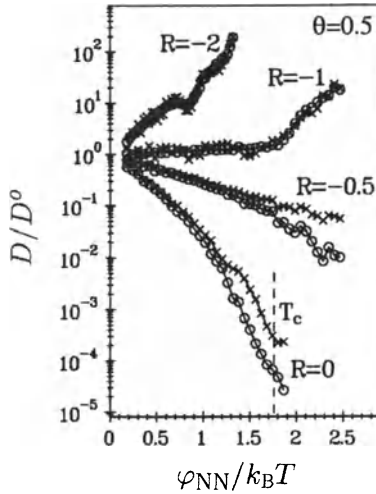
Fig. 4. Temperature dependence of D_F (○) and D_{KG} (×) at $\theta = 0.5$ for various values of R as indicated, after [22]. For the calculations 64 × 64 lattices were used. For $R = 0$ the critical temperature is given by $\varphi_{NN}/k_B T_c = 1.76$ (dashed line).

Fig. 5. D_F (○) and D_{KG} (×) vs size of the probed region at $\theta = 0.5$ and $\varphi_{NN}/k_B T = 2.40$ for the lattice gas model with $R = -0.5$, after [22]. For the calculations 256 × 256 lattices were used.

ing to disordered lattice gas, homogeneity at a given instant exists only on a length scale sufficiently larger than remanent correlation lengths. Therefore, some of the diffusion runs were repeated for lattices with 256 × 256 sites and probe sizes of up to 64 × 64 sites [22]. The results of this calculations are shown in Fig. 5. It is obvious that both D_F and D_{KG} depends slightly on the

probe size in such a way that the deviations between both quantities decrease with increasing probe size. However even for probes of 64×64 sites the deviations are still measurable. Therefore it can be concluded that the results of diffusion measurements may depend on the length scale of the measuring technique. The effect of the length scale is well pronounced in systems with substantial remanent "graininess", i.e. in the vicinity of a first-order phase transition [22].

5   Conclusion

This contribution has clearly shown that the Monte Carlo simulation of surface diffusion is a rapidly progressing field of research. It is evident that the Monte Carlo method has significantly contributed to the understanding of surface diffusion. Additional studies are highly desirable, for instance, to improve our understanding of surface diffusion in systems with first-order phase transitions.

Acknowledgment

References

1. A.A.Tarasenko and A.A.Chumak, Fiz. Tverd. Tela (Leningrad) 24 (1982) 2972, [Sov. Phys. Solid State **24**, 1683 (1982)].
2. A.A.Tarasenko and A.A.Chumak, Fiz. Tverd. Tela (Leningrad) 22 (1980) 2939, [Sov. Phys. Solid State **22**, 1716 (1980)].
3. A.A. Tarasenko and A.A. Chumak, Poverkhnost' Fiyika, Khimija, Mekhanika 11 (1989) 98, (in Russian).
4. A. A. Tarasenko, L. Jastrabik and C. Uebing, Phys. Rev. B 57 (1998).
5. A. V. Myshlyavtsev, A. A. Stepanov, C. Uebing and V. P. Zhdanov, Phys. Rev. B 52 (1995) 5977.
6. C. Uebing and R. Gomer, J. Chem. Phys. 95 (1991) 7626, 7636, 7641, 7648.
7. A.A. Chumak and A.A. Tarasenko, Surf. Sci. 364 (1996) 424.
8. A. A. Tarasenko, F. Nieto, and C. Uebing, 162-163 (1998) 59.
9. D.A. Reed and G. Ehrlich, Surf. Sci. 105 (1981) 603.
10. M. Tringides and R. Gomer, Surf. Sci. 166 (1986) 419.
11. K. Kehr and K. Binder, Simulation of Diffusion in Lattice Gases and Related Kinetic Phenomena, in *Applications of the Monte Carlo Method in Statistical Physics*, edited by K. Binder, volume 36 of *Topics in Current Physics*, page 181, Berlin, 1987, Springer-Verlag.

12. M. Tringides and R. Gomer, Surf. Sci. 145 (1984) 121.
13. C. Uebing and R. Gomer, J. Chem. Phys. 100 (1994) 7759.
14. R. Gomer, Surf. Sci. 38 (1973) 373.
15. G. Mazenko, J.R. Banavar, and R. Gomer, Surf. Sci. 107 (1981) 459.
16. A.V. Myshlyavtsev, A.P. Stepanov, C. Uebing, and V.P. Zhdanov, Phys. Rev. B 52 (1995) 5977.
17. R. Gomer, Rep. Prog. Phys. 53 (1990) 917.
18. V.P. Zhdanov, *Elementary Physicochemical Processes on Solid Surfaces*, Plenum, New York, 1991.
19. V.P. Zhdanov, Phys. Lett. A 161 (1992) 556.
20. A. Tarasenko, L. Jastrabík, F. Nieto, and C. Uebing, Phys. Rev. B , submitted.
21. V.P. Zhdanov and C. Uebing, J. Chem. Phys. 109 (1998) 3197.
22. C. Uebing and R. Gomer, Surf. Sci. 331-333 (1995) 930.

Hydrophobic Aggregation of Nonionic Surfactants in Aqueous Solution: An MD Simulation Study

Dietmar Paschek[1], Thomas Engels[2], Wolfgang v. Rybinski[2], and Alfons Geiger[1]

[1] Universität Dortmund, Physikalische Chemie, D–44221 Dortmund, Germany
[2] Henkel KGaA, 40191 Düsseldorf, Germany

Abstract. We have studied dilute aqueous solutions of nonionic surfactants of general structure $H(CH_2)_m(OCH_2CH_2)_nOH$ (abbreviated as C_mE_n) by an extensive series of classical molecular dynamics simulations. The temperature dependent association of surfactant molecules and hydrophobic test–particles has been determined by Widom's particle insertion method. The simulations were performed at constant ambient pressure conditions and temperatures between 275 K and 450 K. Our simulations suggest an entropy driven association process, which can be described well by temperature independent enthalpy and entropy contributions. These properties can be further reduced to group contributions. The resulting Gibbs free energy of transfer was used as a measure of the hydrophobicity and could be correlated with the experimental cloud point temperatures of binary aqueous mixtures of these surfactants. An empirical entropy correction leads to a quantitative description of the experimental data.

1 Introduction

Nonionic surfactants of the alkylpolyglycol ether type are key ingredients of detergent formulations because of their good detergency performance [1]. The interfacial and colloidal properties of alkylpolyglycol ethers have been the subject of numerous publications. In particular, the phase behavior of binary mixtures of water and nonionic surfactants has been studied intensively [2]. In such systems at low surfactant concentrations an increase in temperature induces the transition from the isotropic L_1 single-phase into a two-phase system with two coexisting liquid phases $(W + L_1)$. Since the transition is accompanied by a change from a transparent isotropic monomer or micellar solution into a turbid two-phase system it is usually called a "cloud–point". This phase transition is a consequence of a solubility decrease of the nonionic surfactant molecule with increasing temperature. The lower boundary curve of the two-phase region is shifted to lower temperatures with decreasing number of ethylene oxide units in the nonionic surfactant molecule.

It was the purpose of this investigation to study the temperature dependent interaction of a single nonionic surfactant molecule with water and

with hydrophobic test particles, using molecular dynamics computer simulations. The hydrophobic interaction with the test particle is quantified by the average chemical potential of this particle in the hydration shell of the surfactant molecule. This value is then used as a quantitative measure of the hydrophobicity of the solute. The hydrophobicity of the nonionic monomer is expected to change with temperature and its chemical composition. This should have an influence on the phase behavior of the system and therefore on the performance properties of the surfactant solution.

Here we consider three different nonionic surfactant molecules ($C_{12}E_3$, $C_{12}E_6$, C_8E_6) in aqueous solution to study the effect of varying chain length of both ether– and alkyl–group. From this limited number of simulations, which are based on the same set of interaction parameters, we are able to predict quantitatively the cloud point temperatures of a wide range of nonionic surfactants C_mE_n, introducing in a final step a single adjustable parameter (called stabilisation entropy).

2   MD–Simulations

All MD simulations were performed with the MOSCITO simulation package [3]. The simulated systems consisted of one surfactant molecule surrounded by water [4,5]. We employed SPC/E [6] as solvent model, since it reproduces the structural and thermodynamical properties of real water in the temperature regime above 270 K rather well [7] and gives an almost quantitative description of rare gas solubilities in water over the wide temperature range from 270 K to 650 K. For the solute molecules we use elements of different force–fields. The parameters can be found in the references cited in [8], with the exception of some torsion potentials. which we refined by the use of ab initio data. A detailed description of the analytic form of the interaction potentials and a compilation of all employed parameters are also given in [9]. All bond–lengths were kept fixed during the simulation runs.

3   Test Particle Method and QHI Model

The present study is aimed to determine the temperature dependence of the *hydrophobic interaction* of nonionic surfactants. For this purpose we study the solvent induced interaction of a hydrophobic test particle with nonionic surfactant molecules as a whole and with particular parts (groups) of the molecule. Since this type of interaction has to be determined as a free energy difference, we apply the Widom test particle method [10] as an efficient way to evaluate free energies from the simulation trajectories:

In the canonic ensemble the excess chemical potential μ_{ex} (the solvation free energy of a solute particle $(N + 1)$ in a N particle solvent) is given by [11]

$$\mu_{ex} = -\beta^{-1} \int \left\langle \exp\left(-\beta\, \phi(s_{N+1}, L)\right)\right\rangle_N ds_{N+1} , \tag{1}$$

where $\beta = 1/k_BT$ is the inverse temperature, s_N are scaled coordinates of the particles with $s_N = r_N/L$ and L being the box–length of the cubic system. Particle $N + 1$ is the inserted test particle. Eq 1 makes it possible to determine the excess chemical potential as a conventional thermodynamic average of a quantity $\exp{(-\beta\phi)}$. Here $\langle\ldots\rangle_N$ denotes ensemble averaging over the configurational space of the N–particle system and ϕ is the potential energy of particle $(N+1)$ inserted into the system of N solvent molecules at position s_{N+1}. Although not rigorously correct for the NPT ensemble, application of eq 1 serves as a reasonable estimate for the excess chemical potential in the present study, since the volume fluctuations [10] were not found to affect the data significantly. To speed up numerically the volume integration of eq 1, values for the potential energy were evaluated only for insertions in the *free volume* of a configuration. This has been determined by an *excluded volume map*, where the excluded volume is mapped on a grid with approximatly 0.2 Å mesh spacing. The excluded volume is defined by a distance less than 0.8 σ between the grid point and any molecular site (σ is the Lennard-Jones parameter of the interaction between test particle and molecular site). Figure 1 illustrates this particle insertion method. In preliminary trial runs this procedure has been found to affect the obtained chemical potential by less than 0.02 kJ mol^{-1}. To ensure a comparable statistics of the test particle chemical potential in the vicinity of the surfactant molecules, for any system about 120 *successful* insertions ($\equiv$ insertions into the *free volume*) per nm^3 and configuration were performed.

We consider the average chemical potential in the vicinity of a surfactant as a quantitative measure of "hydrophobicity". The construction of the *solute*
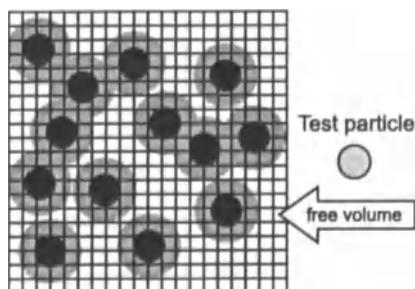
Fig. 1. Schematic illustration of the grid based excluded volume map. The grey regions represent the excluded volume of the black particles in the N–particle system. The radius of the excluded spheres is determined by the Lennard–Jones σ of the interaction with the test particle.
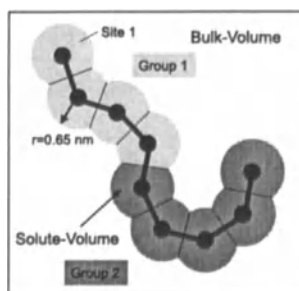
Fig. 2. Illustration of the QHI solute volume partitioning. Around each non-hydrogen center of the solute molecule a sphere of 0.65 nm radius is drawn. The solute volume of a particular site is defined by all points which have a larger distance to any other site. Sites belonging to particular parts of the molecule (e.g. alkyl-chain) can be combined to form a group solute volume.

volume (the integration volume) is indicated in Figure 2. Around each non hydrogen center of the solute molecule a sphere of 0.65 nm radius is drawn. The solute volume belonging to a particular site is defined by its larger distance with respect to any other site. As also indicated in Figure 2, the solute volume of different sites of the molecule can be added up to form a group. The described procedure ensures a strict additive partitioning of the entire solute volume. As *standard* test particle we use a Ne atom ($\sigma_{Ne-Ne} = 3.2$ Å, $\epsilon_{Ne-Ne}/k_B = 38.12$ K). The use of the rather small Ne–particle is advantagous since it guarantees a sufficiently large "free volume" fraction in order to ensure appropriate statistics for the obtained excess chemical potential values. Moreover, a variation of the test particle type should not affect the temperature dependence of the hydrophobic interaction dramatically since the excess chemical potential of particles of different size is more or less shifted by a constant value [13]. We will refer to values of the excess chemical potential for the *standard* Ne obtained from the outlined solute volume as quantified hydrophic interaction (QHI) model data.

4   Discussion

In Figure 3a the average chemical potential of the Ne particle in the bulk phase as well as in the shell volume of the surfactant $C_{12}E_6$ is shown as a function of temperature. There are two interesting features: First, we observe an *intersection* of the temperature dependences in bulk and shell. Moreover, for different parts of the shell (head–group and alkyl–chain) the intersection temperature is shifted significantly We find a typical intersection temperature of about 320 K for the alkyl chain and 380 K for the head group, independent of the specific surfactant solute molecule.

In Figure 3b the differences between the chemical potentials of Ne in shell and bulk, denoted as free energy of transfer from bulk to shell

$$\Delta_t G = \mu_{ex}(\text{Shell}) - \mu_{ex}(\text{Bulk}) , \tag{2}$$

are shown. To obtain these values, the group contributions are averaged over all solute molecules from our simulations. The error bars result from this averaging procedure. Figure 3b is indicating that the free energy of transferring a hydrophobic particle from the bulk to the solvation shell is a linear function of temperature. Therefore, a division into temperature independent enthalpic and entropic terms according to

$$\Delta_t G = \Delta_t H - T \Delta_t S \tag{3}$$

is reasonable. It becomes evident from Figure 3b that the polarity of a group controls the temperature dependence of the association with a hydrophobic particle. In other words, the transfer–entropy of an apolar test particle from bulk to shell depends strongly on the polarity of the group considered.
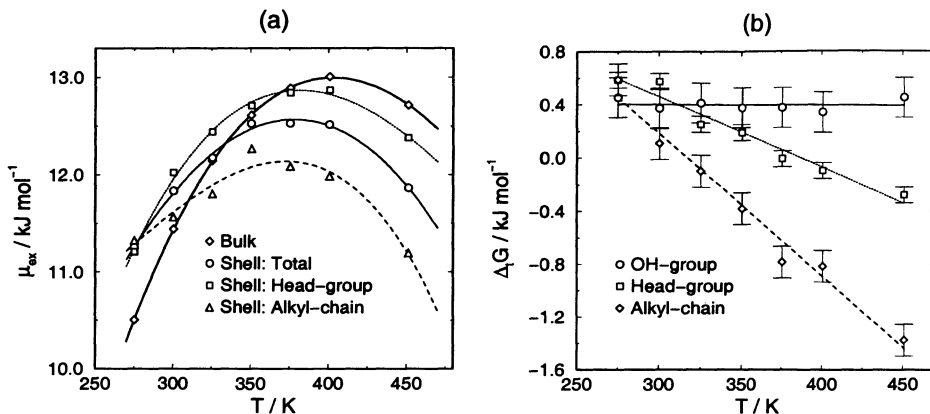
Fig. 3. (a) Comparison of the excess chemical potential of a Ne particle in the bulk phase with values obtained for the shell of the surfactant $C_{12}E_6$. Note the different temperature behavior of head–group (ether–chain plus OH–Group) and alkyl–chain. The lines represent fits of the data to polynomials of cubic order. (b) Average free energy of transferring a Ne particle from bulk to shell for several groups of the studied surfactants.

From the point of view of the hydrophobic test particle this can be understood by different temperature dependences of the water structure in the shell volume with respect to the bulk phase. In the vicinity of an OH–group the water structure is very similar to the bulk phase since the OH–group is involved into the hydrogen bond network. Therefore no significant temperature dependence is observed. The opposite situation is found for the hydration shell of an apolar alkane–chain.

In addition to the previous observations we find that the average excess chemical potential for the total surfactant solvation shell can be expressed as weighted sum of the group contributions. Moreover, the shell volumes attributed to the groups are rather well linearly related to the stoichiometric coefficients m and n. Assuming temperature independent enthalpies and entropies as indicated by the QHI–data, the observed group additivity suggests to predict the intersection temperature (where $\Delta_t G = 0$) for the entire molecule from the transfer properties of the different groups depending on the chemical composition according to

$$T_s = \Delta_t H / \Delta_t S \,, \tag{4}$$

with $\Delta_t H = (1 - \lambda) \, \Delta_t H^E + \lambda \, \Delta_t H^C$ and $\Delta_t S = (1 - \lambda) \, \Delta_t S^E + \lambda \, \Delta_t S^C$, where λ is the fraction of the hydration shell volumes of head-group and alkane-chain (superscripts E and C). We find, that λ can be expressed by the stoichiometric coefficients m and n
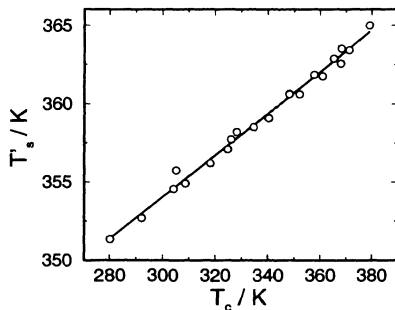
$$\lambda = m/(m + fn) \,, \tag{5}$$

Fig. 4. Correlation of the empirically corrected intersection temperatures T'_s with experimentally obtained cloud point temperatures T_c.

where f takes account of the actual size of the constituent groups. f was found to be 2.9 (The ether group units are about 3 times as big as the methylen groups). The values which we obtained by fitting eqs 3 and 5 to the data of Figure 3b, are $\Delta_t H^E = 2100$ J mol^{-1}, $\Delta_t H^C = 3400$ J mol^{-1}, $\Delta_t S^E = 5.3$ J K^{-1} mol^{-1} and $\Delta_t S^C = 10.7$ J K^{-1} mol^{-1}. With these parameters, obtained from the simulations of three specific surfactant molecules, we can now predict the intersection temperature T_s for any given surfactant molecule $C_m E_n$.

In the last part of this contribution we try to relate the predicted intersection temperature T_s, which is a purely molecular property, with macroscopic properties like the position of the lower critical solution temperature of aqueous surfactant mixtures or experimental cloud point temperatures. This approach is motivated by the fact that the location of the critical point of a van der Waals gas is determined by its mean field interaction parameters. However, in the present case we do not know much about such interaction parameters, nor about the structure of an appropriate equation of state. Nevertheless, neglecting any further structural aspects of the complex aqueous surfactant mixtures and starting from the MD–simulation results, we conjecture that the location of the intersection temperature T_s might be related to the lower critical solution temperature. A rather heuristic argument for such an expectation is the fact, that the transfer free energy of the hydrophobic test particle changes its sign at T_s, indicating an increasing tendency for aggregation with increasing temperature.

A comparison of the determined intersection temperatures with a large set of experimental cloud point temperatures [14] shows that the values are well correlated. However, the data do not coincide perfectly since the hydrophobic test particle employed is only a very rough estimate for the chemical potential of a complete surfactant molecule in a micellar solution. There is a far better correlation with the cloud point data when considering constant ether or alkane chain lengths. To take the apparently important chain length effect into account, we introduce now an empirical term, the so called *stabilisation entropy* $\Delta_{stab} S$ and replace in eq 4 $\Delta_t S$ by $\Delta_t S'$

$$\Delta_t S' = \Delta_t S + \Delta_{stab} S . \tag{6}$$

$\Delta_{stab}S$ is estimated to be linearly dependent on the size of the surfactant groups with $\Delta_{stab}S = m\ \Delta_{stab}S^C + n\ \Delta_{stab}S^E$. The values were determined empirically for optimum correlation to $\Delta_{stab}S^C = -0.024\ \mathrm{J\,K^{-1}\,mol^{-1}}$ and $\Delta_{stab}S^E = 0.025\ \mathrm{J\,K^{-1}\,mol^{-1}}$. The corresponding values for T'_s, shown in Figure 4, allow a quantitative prediction of the cloud point temperatures based on the given values, when using the scaling relation $T_c = (T'_s - T'^0_s)\,k_s$, with the parameters $k_s = 0.1324$ and $T'^0_s = 314.3$ K.

5   Conclusions

The hydrophobic hydration of nonionic akylpolyglycol ether type surfactant in dilute aqueous solutions have been studied by a series of classical molecular dynamics computer simulations covering the temperature range between 275 K and 450 K by applying Widom's particle insertion method. The temperature dependent association of surfactant molecules and hydrophobic neon test particles can be described well by temperature independent enthalpies and entropies of transfer of the test particle from the bulk to the hydration shell of the surfactant. These transfer properties can be reduced to group contributions. The resulting Gibbs free energy has been taken as a measure of the hydrophobicity and can be correlated with experimental cloud point temperatures of binary aqueous mixtures of these nonionic surfactants. A term called *stabilisation entropy* is introduced in order to take into account that interacting groups are not independent, but attached to neighbors within the chains. This empirical correction finally enables a quantitative prediction of the experimental cloud point temperatures for any kind of alkylpolyglycol ether surfactant in water.

References

1. H. Andree and P. Krings, *Waschmittelchemie* (Hüthig, Heidelberg, 1976), p. 84.
2. J. C. Lang and R. D. Morgan, J. Chem. Phys. **73**, 5849 (1980); D. J. Mitchell, G. J. T. Tiddy, L. Warring, T. Bostock, and M. P. McDonald, J. Chem. Soc. Faraday Trans. I **79**, 975 (1983).
3. D. Paschek, *MOSCITO - A free MD simulation package*, Universität Dortmund, 1998. http://ganter.chemie.uni-dortmund.de/.
4. Initially, a single solute molecule is placed in the center of a cubic water system with a density of 1.0 $\mathrm{g\,cm^{-3}}$ removing all overlapping water molecules. The system sizes were chosen sufficiently large to guarantee the absence of an interaction of the solute molecule with the hydration shell of its own image (System sizes: $C_{12}E_6$:1309 molecules, C_8E_6: 1316 molecules, $C_{12}E_3$: 689 molecules). The systems were simulated at seven different temperatures (275 K, 300 K, 325 K, 350 K, 375 K, 400 K and 450 K) and atmospheric pressure for an equilibration period of 0.1 to 0.5 ns. The production runs at similar conditions extended to time intervals between 1.0 and 1.3 ns. Approximately 5000 configurations,

equally spaced over the whole simulation run, were examined at each state-point. The bulk–water density at the studied state-points compares rather well with previously published data [7].

5. We employ a standard Verlet leap–frog integration scheme [15] in combination with SHAKE [16] to constrain bond lengths. Cubic periodic boundary conditions and time-steps of 2 fs were used. The simulations were performed in the Berendsen–NPT–Ensemble [17] with temperature and pressure relaxation times of $\tau_T = 0.5$ ps and $\tau_p = 1.7$ ps (assuming a κ_T of 4.59 bar^{-1}). To handle electrostatic interactions we employ the smooth particle mesh Ewald (SPME) method [18] with mesh spacings of about 1 Å, interpolation of 4'th order and a screening parameter of $\alpha = 2.98$ nm^{-1}. The interactions were truncated at a cutoff of 9 Å. Lennard-Jones cutoff–corrections for potential energy and virial were adequately considered. The pressure evaluation has been performed analogously to [19].

6. H. J. C. Berendsen, J. R. Grigera, and T. P. Straatsma, J. Phys. Chem. **91**, 6269 (1987).

7. B. Guillot and Y. Guissani, J. Chem. Phys. **99**, 8075 (1993); Y. Guissani and B. Guillot, J. Chem. Phys. **98**, 8221 (1993); L. A. Baez and P. Clancy, J. Phys. Chem. **101**, 9837 (1994); S. Harrington, P. H. Poole, F. Sciortino, and H. E. Stanley, J. Chem. Phys. **107**, 7443 (1997).

8. For the ether component we use a model originally derived for poly–oxy–ethylene (POE) by F. Müller–Plathe [20], where we refined the torsion potentials according to the ab initio data of Gejji et al. [21]. For the OH–Group the original OPLS–Parameters of ref [22] were employed, combined with a refined ab initio torsion potential explicitly derived for β–oxy–hydroxyl groups. For the united atom representation we used the modified OPLS–model parametrisation of Smit et al. [23] with zero charges on all alkane–sites.

9. D. Paschek, Dissertation, Universität Dortmund, 1998.

10. D. Frenkel and B. Smit, *Understanding Molecular Simulation — From Algorithms to Applications* (Academic Press, San Diego, USA, 1996).

11. B. Widom, J. Chem. Phys. **39**, 2808 (1963).

12. D. A. McQuarrie, *Statistical Mechanics* (Harper and Row, New York, 1973).

13. S. Garde, G. Hummer, A. E. García, M. E. Paulaitis, and L. R. Pratt, Phys. Rev. Lett. **77**, 4966 (1996).

14. H. Lange and M. J. Schwuger, in *Fatty Alcohols — Raw Materials, Methods, Uses*, 1. ed., edited by K. Henkel (Henkel KGaA, Düsseldorf, 1982), pp. 87–119; T. Engels (unpublished).

15. M. P. Allen and D. J. Tildesley, *Computer Simulation of Liquids* (Oxford Science Publications, Oxford, 1989).

16. J. P. Ryckaert, G. Ciccotti, and H. J. C. Berendsen, J. Comp. Phys. **23**, 327 (1977).

17. H. J. C. Berendsen, J. P. M. Postma, W. F. van Gunsteren, A. DiNola, and J. R. Haak, J. Chem. Phys. **81**, 3684 (1984).

18. U. Essmann, L. Perera, M. L. Berkowitz, T. A. Darden, H. Lee, and L. G. Pedersen, J. Chem. Phys. **103**, 8577 (1995).

19. S. Nosé and M. L. Klein, Mol. Phys. **50**, 1055 (1983); J. Alejandre, D. J. Tildesley, and G. Chapela, J. Chem. Phys. **102**, 4574 (1995).

20. F. Müller-Plathe, Acta Polymer. **45**, 259 (1994).

21. S. P. Gejji, J. Tegenfeldt, and J. Lindgren, Chem. Phys. Lett. **226**, 427 (1994).

22. W. L. Jorgensen, J. Phys. Chem. **90**, 1276 (1986).

23. B. Smit, S. Karaborni, and J. I. Siepmann, J. Chem. Phys. **102**, 2126 (1995).

Part III

Reaction Diffusion Problems

Molecular Dynamics Simulations of Polymer-Membrane/Solvent Interfaces

Claudia Schepers, Dieter Hofmann, and Dieter Paul

GKSS Research Center, Institute of Chemistry,
Kantstrasse 55, D - 14513 Teltow, Germany
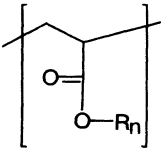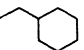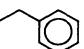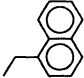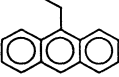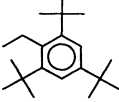Email: schepers@gkss.de

Abstract. Latest results from molecular dynamics (MD) simulations on pervaporation in the interfacial region between polymer and feed are reported. A binary organic mixture containing 80wt% n-heptane and 20wtpoly(methyl phenyl siloxane) (PMPhS) and selected poly(methacrylates) containing 6-membered rings like benzyl- (PBMA), cyclohexyl methyl- (PcHMA), a-naphthyl methyl- (PNMA), 9-anthryl methyl- (PAMA) and 2,4,6-tri-tert-butyl benzyl (PtBBMA) esters of methacrylic acid were studied. While a solubility related enrichment factor of 2 for the benzene component was observed for PMPhS all studied methacrylates sorbed preferentially the major component n-heptane. Although there was a fast diffusion observed in the case of PMPhS the selectivity is low in comparison to the PcHMA containing polymer membrane.

1 Introduction

Pervaporation is a concentration gradient driven technique to separate two liquids by the transport through suitable dense polymeric membranes. The membrane separates a liquid mixture (upstream side) from a vapor phase (downstream side), where the transport goes into the direction of the vapor [1]. The low energy costs in comparison to destillation procedures are industrially significant, e.g. the removal of water from ethanol with the help of poly(vinyl alcohol) (PVA) membranes is already technically utilized. There, the ethanol is enriched in the retentate at the upstream side. As reported elsewhere [2,3] the separation behavior of poly(dimethyl siloxane) (PDMS) is opposite to PVA. PDMS membranes enrich ethanol in the permeate stream (downstream side). Up to the present time it is not possible to theoretically predict the separation behavior of a membrane material efficiently. It is known that the mechanism has to be regarded in close connection with the static structure and the dynamic behavior of the separation system (membrane plus penetrants) on an atomistic scale. In this connection, detailed molecular dynamics (MD) simulations have proven to b useful for studying membrane separation problems, e.g. the separation of 90:10 wtethanol/water utilizing a PVA membrane has already been successfully simulated [3]. The investigation of amorphous polymer/solvent models enables to follow the movements of solvent molecules in the feed and in the polymer membrane over several

nanoseconds and to analyze their intermolecular interactions. Modeling can, thus, give a realistic description of important aspects of the pervaporation mechanism. Also trends concerning the suitability of a membrane material for a given solvent mixture could already be observed under favorable conditions [2,4,5]. Our main objectives are to arrive at a better theoretical understanding of pervaporation processes and to help experimentalists to find new and more efficient membrane materials particularly for the separation of organic liquid mixtures. Industrial interest is focused among others on the n-heptane/benzene (80:20 wt%) separation. As membrane polymers mainly poly(methacrylic acid esters) and for comparison also poly(methyl phenyl siloxane) (PMPhS)[3] have been investigated. Our main objectives are to arrive at a better theoretical understanding of pervaporation processes and to help experimentalists to find new and more efficient membrane materials particularly for the separation of organic liquid mixtures. Industrial interest is focused among others on the n-heptane/benzene (80:20 wt%) separation. As membrane polymers mainly poly(methacrylic acid esters) and for comparison also poly(methyl phenyl siloxane) (PMPhS)[3] have been investigated. One question was if there are any methacrylate based membranes in order to economically separate this binary organica mixture mentioned? To answer this question a study of selected poly(methacrylates) containing cyclic structures was started because experimentalists observed that methacrylates with 6-membered rings may have positive separation effects on the particular organic mixture. Latest, partly still preliminary, results of simulation are available for benzyl- (PBMA), cyclohexyl methyl- (PcHMA), a-naphthyl methyl- (PNMA), 9-anthryl methyl- (PAMA) and 2,4,6-tri-tert-butyl benzyl (PtBBMA) esters of methacrylic acid (table 1).

Table 1. Methacrylate based polymers

Repeat unit	Ester groups		Abbreviation
	$R_1=$	Cyclohexyl methyl-	PcHMA
	$R_2=$	Benzyl-	PBMA
	$R_3=$	α-Naphthyl methyl-	PNMA
	$R_4=$	9-Anthryl methyl-	PAMA
	$R_5=$	2,4,6-Tri-tert-butyl benzyl-	PtBBMA

The transport of a small molecules through dense amorphous polymers can be described by a solution-diffusion model, i.e. first the penetrant molecules have to be solved first in the membrane at the upstream side. Considering the fact that in pervaporation processes, besides the permeate pressure, the sorptive stage at the upstream side of the polymer membrane is often very decisive for the separation behavior, energetical interactions between the solvent molecules and the polymer segments are important for the intended separation effect. After the solution stage, the penetrants have to move through the membrane by diffusion. This process can only occur in the free volume of the polymer. Thus, usually polymers with a high amount of free volume (low density polymers) allow a faster diffusion then more dense materials. The transport of given components through a membrane can be described as a mass flux J (in kg/m^2). Another important membrane parameter is the enrichment factor β which can be defined as

$$\beta_B = \frac{(w_B)_{permeate}}{(w_B)_{feed}} \tag{1}$$

with w_B being the concentration of one component (B: benzene) to be removed from the feed stream (1). The parameter β_B is very sensitive to the feed composition, because in pervaporation the flux of one component can change quite rapidly due to interactions with the other component (coupling of fluxes). Therefore, the prediction of enrichment or selectivity is often very difficult. The situation is often further complicated by considerable swelling of the polymer matrix under the influence of the respective feed mixture.

2   Simulation Details

In the present investigation MD simulations of pervaporation processes were usually carried out over a period of one to four nanoseconds with system sizes of about 5000 Atoms. The size of any simulated system is generally limited by the power of the available computers. Until now all simulations were performed on IBM RS6000 and SGI Octane workstations and also on the CRAY C916 of the Deutsches Klimarechenzentrum (DKRZ) in Hamburg. This paper describes investigations of the interfacial region between several polymers and the mentioned solvent mixture. The poly(methacrylates) studied include homo- and copolymers as well as crosslinked polymers. Extensive packing and equilibration procedures are necessary to create the suitable models. To perform MD simulations at first the basic monomer units of interest are built. The construction of the respective polymer chain containing 100 repeat units is done by the Polymerizer module of the MSI software [6]. These chains undergo a static structure optimization via the steepest descents energy minimization. An initial amorphous packing of the respective polymer chain into a characteristic volume element (box) is done by the Amorphous Cell module. This module uses a modified Theodorou-Suter approach [6,7]

as packing algorithm. The packing cells to be filled with chain segments had a side length of 2.45nm in two dimensions while the third dimension after packing and equilibration is determined by the experimental density of the polymer. In cases where no experimental densities were available, the SYN-THIA module of the MSI software [6] was utilized to predict the density at 303K. Despite SYNTHIA cannot explicitly consider effects like structural isomerism, bifunctionality and crosslinking a good consistence between measured densities (density gradient column method) and SYNTHIA calculation results (table 2) was observed in cases with available experimental data.

Table 2. Densities of the examined poly (methacrylates) in gcm^{-3}

Polymer	SYNTHIA Prediction	Measured
PAMA	1.222	
PNMA	1.198	
PBMA-co-PGMA	1.178	1.19± 0.01
PcHMA-co-PGMA	1.110	1.11 ± 0.01
PtBBMA	0.967	

If a polymer, like the investigated methacrylates, contains a certain amount of 6-membered rings it is usually not possible to perform the initial packing routine at the real experimental density. This is mainly related with the introduction of a number of overlaps between adjacent rings and backbone bonds (catenations and spearings) by the packing algorithm. Therefore, the initial packing has to be performed at very low initial densities (e.g. 0.05 g cm-3). Nevertheless, there may be still some remaining ring catenations which have to be removed by a laborious manual procedure. Afterwards the box length has to be decreased via a stepwise procedure, where after each compression stage a careful equilibration (with an integration time of 0.1 fs only), has to be carried out. Any manipulation of the system causes unrealistic tensions that have to be removed during the following equilibration procedures. The single polymer box and the single solvent box were packed and equilibrated separately. There, 2D-PBC had to be used in the a and b directions, while penalty surface potentials force the non-periodic coordinates of the constituent atoms into a layer of a thickness of about 5nm along the c-direction. The layered interface simulation models are then composed of two sub-packing models in each case, one for the polymer and one for the organic feed mixture. Both cells are layered along the third dimension axis followed by a cautious approach of the cells' molecules (figure 1). Subsequently, the MD data production can be started up to a duration of several nanoseconds under 3D-PBC conditions. For the potential energy calculation the PCFF
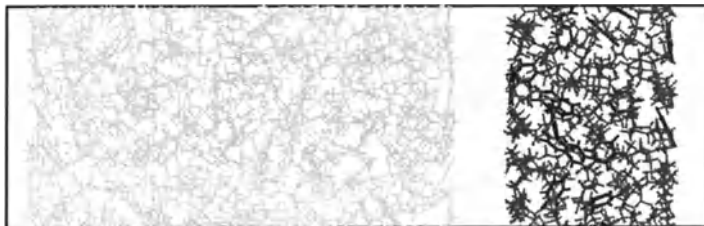
Fig. 1. Packed cell with PNMA-polymer and n-heptane/benzene mixture (80:20) before equilibration (light gray: polymer, medium gray: n-heptane, black: benzene).

forcefield [6] was applied. The following simulation parameters are utilized in all dynamic runs: constant number (N) of atoms, constant volume (V) and 303K (NVT). The cell dimensions are in all examples a,b= 2.45nm and c as given in table 3. Two advanced MD simulation stages of the initial adsorp-

Table 3. Cell length (c) and numbers of atoms (N) for the investigated models.

Polymer	c (nm)	N
PMBPhS	7.15	3709
PBMA-co-PGMA	6.94	4040
PcHMA-co-PGMA	7.37	4539
PNMA	7.90	4548
PAMA	8.89	5148
PtBBMA	9.73	6102

tion at the interfaces are shown for PNMA at 1.0 and 2.0 ns in the following figure 2.

So far, the interface simulations reflect a preferential initial n-heptane sorption. After a simulation time of 1 ns one single n-heptane molecule out of 54 left the solvent cage and got completely solved into the PNMA-matrix while this number increased to three after 2 ns. Figure 3 represents PMPhS

Fig. 2. Dynamic states of the PNMA-polymer and solvent at 1.0 ns (top) and 2.0 ns (bottom) of simulation time (light gray: polymer, medium gray: n-heptane, black: benzene).

after 3.5 ns of MD. There the sorption processes were faster then in all methacrylate systems investigated so far. The main difference between the investigated methacrylates and PMPhS is that the latter shows a preferential solubility-based selectivity for benzene with an enrichment factor $\beta_B = 2$ [3]. PMPhS would, therefore, preferentially remove benzene from the feed.
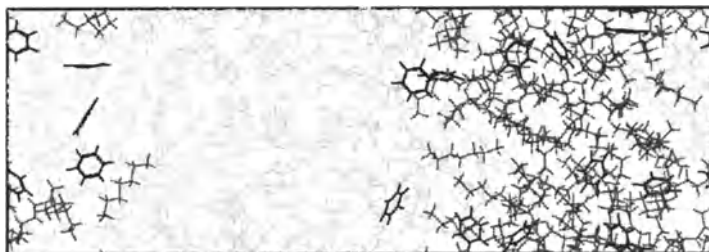

Fig. 3. Dynamic state of the PMPhS-polymer and solvent at a simulation time of 3.5 ns (light gray: polymer, medium gray: n-heptane, black: benzene).

In order to reduce extreme swelling crosslinking elements are often introduced in the starting material of a polymer synthesis. We have, therefore, also investigated the poly(cyclohexyl methyl methacrylate)-co-poly(glycidyl methacrylate) (PcHMA-co-PGMA) as a crosslinked model. Hitherto, there are no suitable modeling modules available for the construction of crosslinked polymers. Extensive construction strategies were employed to obtain these two component polymers. Nevertheless, as shown in figure 4 swelling effects can be observed as expected also in reality.

In comparison to the PNMA-homopolymer (figure 2), there is even more swelling of the PcHMA-copolymer visible after 2.0 ns at the polymer/solvent interface. While the preferential n-heptane selectivity is qualitatively as in the case of PNMA, the initial sorption process occurs considerably faster in PcHMA-co-PGMA (figure 4). Six n-heptane molecules are already sorbed completely after 2.0 ns, that means 11% of the major component of the feed.

Fig. 4. Dynamic state of the PcHMA-co-PGMA-polymer and solvent at a simulation time of 2.0 ns (light gray: polymer, medium gray: n-heptane, black: benzene).

Yet, no sorbed benzene-molecules are observed, that confirms the prediction of a high n-heptane selectivity of the PcHMA-co-PGMA material.

3   Temperature Distribution

A typical problem for simulations of interfaces with very different mobilities, e.g. solid phase and liquid phase, is the effect that, while the overall average system temperature as intended is at 303K, the individual phases may show different temperature averages. For the already mentioned PMPhS system [3] the overall temperature was 303K, while the polymer phase was at 310K and the feed at 290K. These temperature differences were even smaller ($<$4K) for the investigated methacrylates. Therefore, no specific action was necessary to reduce these effects.

4   Conclusions

MD simulations were used to obtain some qualitative information about the separation of the given binary organic mixture by pervaporation membranes. It was possible to create well equilibrated highly complex interface models mainly of different methacrylates and a feed mixture of n-heptane/benzene (80:20 wt%). From the investigated methacrylates by now, after 2ns of MD, only the PcHMA-co-PGMA showed already a significant tendency of a strongly preferred n-heptane removal from the feed. Also the other methacrylates seem to deplete the feed from the majority component n-heptane. For the system PMPhS-benzene/n-heptane, on the other hand, an enrichment factor of 2 of benzene was observed from the MD simulation. The initial sorption and diffusion processes of the other methacrylates are, however, considerably slower than in the cases of the PcHMA copolymer and PMPhS. Therefore, to obtain more representative data additional MD simulations are needed in these cases. Furthermore, it is intended to include studies of methacrylates with a very low density (predicted by the SYNTHIA module) in the simulations. Those polymer membranes are supposed to result in even faster sorption and diffusion processes.

Acknowledgments

References

1. Mulder M (1991) Basic Principles of Membrane Technology. Kluwer Academic Publ., Dordrecht Paul DR, Yampol'skii YP (1994) Polymeric Gas Separation Membranes. CRC Press, Boca Raton
2. Fritz L, Hofmann D (1998) Behaviour of water/ethanol mixtures in the interfacial region of different polysiloxane membrane—a molecular dynamics simulation study. Polymer 39:2531–2536
3. Hofmann D, Fritz L, Paul D (1998) Molecular modelling of pervaporation separation of binary mixtures with polymeric membranes. J Membr Sci 144:145–159
4. Fritz L, Hofmann D (1997) Molecular dynamics simulations of the transport of water-ethanol mixtures through polydimethylsiloxane membranes. Polymer 38:1035–1045
5. Marrink SJ, Berendsen HJC (1996) Permeation process of small molecules across lipid membranes studied by molecular dynamics simulations. J Phys Chem 100:16729-16738
6. MSI (1996) Polymer Modeling Software, Release 4.0.0, User Guide. 9685 Scranton Road, San Diego, CA 92121-3752 MSI (1996) Discover Simulation Tools, Release 96.0 and 4.0.0, User Guide. 9685 Scranton Road, San Diego, CA 92121-3752 and www.msi.com/doc/
7. Theodorou DN, Suter UW (1986) Atomistic modeling of mechanical properties of polymeric glass. Macromolecules 10:139-146

A continuation framework for invariant subspaces and its application to traveling waves

Wolf-Jürgen Beyn, Winfried Kleß, and Vera Thümmler

Fakultät für Mathematik, Universität Bielefeld
Postfach 100131, 33501 Bielefeld

Abstract. We present a continuation method for low-dimensional invariant subspaces of a parameterized family of large and sparse matrices. Such matrices typically occur when linearizing about branches of steady states in reaction-diffusion equations . Our continuation method provides bases of the invariant subspaces depending smoothly on the parameter. From these we can compute the corresponding eigenvalues efficiently. The predictor and the corrector step are reduced to solving bordered matrix equations of Sylvester type. For these equations we develop a bordered version of the Bartels-Stewart algorithm. The numerical techniques are used to study the stability problem for traveling waves in two examples: the Ginzburg-Landau and the FitzHugh-Nagumo system. In these cases there always exists a simple or multiple eigenvalue zero while the remaining eigenvalues determine the stability. We demonstrate the difficulties of separating these critical eigenvalues from clusters of eigenvalues that are generated by the essential spectrum of the continuous problem.

1   Introduction

Spatial discretizations of reaction-diffusion systems lead to parameterized dynamical systems $\dot{u} = F(u, \lambda)$ of large dimension. A considerable amount of software has been developed for pathfollowing branches of steady states, periodic and homoclinic orbits and their bifurcations (see e.g. [6], [14]). However, transferring these techniques to large and sparse systems is still a partially developed subject. One topic in this area is the calculation of low-dimensional invariant subspaces of matrices that occur as Jacobians $A(s) = D_u F(u(s), \lambda(s))$ at branches $(u(s), \lambda(s))$ of steady states. While it is possible to use the (easier accessible) singular subspaces for the branches themselves [12], invariant subspaces seem to be indispensable for questions of stability and local approximation of invariant manifolds [1].

In this paper we set up the basics of a continuation method for low-dimensional invariant subspaces of parameter-dependent large matrices. Essentially, we combine well-known predictor-corrector methods with a generalization of the Bartels-Stewart algorithm ([9]) that allows us to reduce to

linear systems with bordered matrices of the type

$$\begin{pmatrix} D_u F - \tau I & \phi \\ \hat{\phi}^T & 0 \end{pmatrix}, \ \tau \in \mathbb{C}, \phi, \hat{\phi} \in \mathbb{R}^{m,k}, k \ll m.$$

To these systems we apply the method of [10] which works with a black box solver for the large principle submatrix $D_u F - \tau I$ and which is robust even if this matrix is almost singular. As an application we consider the stability problem for traveling waves in reaction diffusion systems of spatial dimension one. The particular difficulties in this case arise from the essential spectrum (present in the infinite problem) that has to be separated from a few isolated eigenvalues which determine the stability.

This paper is largely based on the theses of the second [13] and the third author [19]. Full details will be provided in a forthcoming paper [2].

2   Continuation of invariant subspaces

We consider a family of matrices $A(s) \in \mathbb{R}^{m,m}$ depending smoothly on a parameter $s \in \mathbb{R}$. Our aim is to compute smooth matrices $\phi(s) \in \mathbb{R}^{m,k}$ the columns of which form a basis of a k-dimensional subspace $R(\phi(s))$ invariant under $A(s)$, i.e.

$$A(s)\phi(s) = \phi(s)\Lambda(s) \tag{1}$$

for some $\Lambda(s) \in \mathbb{R}^{k,k}$. With suitable choices of $\hat{\phi}, \phi_0 \in \mathbb{R}^{m,k}$ we will normalize $\phi(s)$ according to

$$\hat{\phi}^T \phi(s) = \hat{\phi}^T \phi_0. \tag{2}$$

2.1   Existence and smooth dependence

Assume that for some $s_0 \in \mathbb{R}$ we have a simple invariant subspace $R(\phi_0)$, $\phi_0 \in \mathbb{R}^{m,k}$ of $A(s_0)$ (see [18] for this notion) i.e. rank $\phi_0 = k$, $A(s_0)\phi_0 = \phi_0\Lambda_0$ for some $\Lambda_0 \in \mathbb{R}^{k,k}$ and $R(\phi_0)$ is the unique maximal subspace $E \subset \mathbb{R}^m$ satisfying $A(s_0)(E) \subset E, \sigma(A(s_0)_{|E}) \subset \sigma(\Lambda_0)$. Our continuation strategy is based on the following result (see [13]).

Theorem 1. *Under the above assumptions choose $\hat{\phi} \in \mathbb{R}^{m,k}$ such that $\hat{\phi}^T \phi_0$ is nonsingular. Then the implicit function theorem applies to the operator equation*

$$T(\phi, \Lambda, s) = \begin{pmatrix} A(s)\phi - \phi\Lambda \\ \hat{\phi}^T \phi - \hat{\phi}^T \phi_0 \end{pmatrix} = 0 \tag{3}$$

at $\phi = \phi_0, \Lambda = \Lambda_0, s = s_0$. *In particular, the partial derivative*

$$D_{\phi,\Lambda}T(\phi_0,\Lambda_0,s_o)(H,\Delta) = \begin{pmatrix} A(s_0)H - H\Lambda_0 - \phi_0\Delta \\ \hat{\phi}^T H \end{pmatrix}, \; H \in \mathbb{R}^{m,k}, \Delta \in \mathbb{R}^{k,k}$$

is nonsingular and for s close to s_0 there is a unique branch of solutions $\phi(s), \Lambda(s)$ of (1), (2). Moreover, $R(\phi(s))$ is a simple invariant subspace of $A(s)$.

2.2   The predictor and the corrector step

Assuming the conditions of Theorem 1 we can compute the tangent $(H_0, \Delta_0) = (\phi'(s_0), \Lambda'(s_0))$ to the branch $(\phi(s), \Lambda(s))$ at $s = s_0$ from a linear system of dimension $(m+k)k$

$$\begin{pmatrix} A(s_0)H_0 - H_0\Lambda_0 - \phi_0\Delta_0 \\ \hat{\phi}^T H_0 \end{pmatrix} = \begin{pmatrix} -A'(s_0)\phi_0 \\ 0 \end{pmatrix} \tag{4}$$

This system is a Sylvester type matrix equation for H_0 (cf. [9]) bordered by k^2 extra equations and unknowns. Since $\sigma(\Lambda_0) \subset \sigma(A(s_0))$ the Sylvester equation is singular and it is essential to use the bordering for a stable solution algorithm (see 2.3). Given a step size δ the predictor is given by $(\phi_1, \Lambda_1, s_1) = (\phi_0, \Lambda_0, s_0) + \delta(H_0, \Delta_0, 1)$.

In the corrector step we solve the system (3) with $(s, \hat{\phi}, \phi_0)$ replaced by (s_1, ϕ_0, ϕ_1). Starting at the predictor (ϕ_1, Λ_1), Newton's method generates the sequence $(\phi_\nu, \Lambda_\nu), \nu \geq 1$ defined by

$$\begin{pmatrix} A(s_1)\phi_{\nu+1} - \phi_{\nu+1}\Lambda_\nu - \phi_\nu\Lambda_{\nu+1} \\ \phi_0^T \phi_{\nu+1} \end{pmatrix} = \begin{pmatrix} -\phi_\nu\Lambda_\nu \\ \phi_0^T \phi_1 \end{pmatrix} \tag{5}$$

This system is of the same type as (4) and it is solved by the algorithm in 2.3. We notice that this approach differs from the conventional realization of Newton's method ([5], [4]) where $\Lambda_{\nu+1}$ is eliminated from the first equation of (5) with the help of the second equation.

2.3   A bordered Bartels-Stewart algorithm

The linear systems to be solved in (4) and (5) are of the form

$$\begin{pmatrix} AH - H\Lambda - \phi\Delta \\ \hat{\phi}^T H \end{pmatrix} = \begin{pmatrix} B \\ C \end{pmatrix} \tag{6}$$

where $H, B, \hat{\phi} \in \mathbb{R}^{m,k}$, $C, \Lambda, \Delta \in \mathbb{R}^{k,k}$ and $\sigma(\Lambda) \subset \sigma(A)$. We compute the complex Schur decomposition of the matrix Λ (see [9]).

$$Q^H \Lambda Q = \tilde{\Lambda}, \quad Q^H Q = I, \quad \tilde{\Lambda} \text{ upper triangular.} \tag{7}$$

This involves solving an eigenvalue problem of low dimension $k \ll m$. The system (6) may then be transformed by replacing the matrices H, Δ, B, C, Λ by $\tilde{H} = HQ, \tilde{\Delta} = \Delta Q, \tilde{B} = BQ, \tilde{C} = CQ, \tilde{\Lambda}$. Since $\tilde{\Lambda}$ is upper triangular, we can compute the columns $\tilde{H}_j, \tilde{\Delta}_j$ of $\tilde{H}, \tilde{\Delta}$ similar to the Bartels-Stewart algorithm ([9], 7.6.3) by a sequence of bordered linear systems

$$\begin{pmatrix} \tilde{A} - \tilde{\Lambda}_{j,j}I & -\phi \\ \hat{\phi}^T & 0 \end{pmatrix} \begin{pmatrix} \tilde{H}_j \\ \tilde{\Delta}_j \end{pmatrix} = \begin{pmatrix} \tilde{B}_j + \sum_{\nu=1}^{j-1} \tilde{\Lambda}_{\nu,j}\tilde{H}_\nu \\ \tilde{C}_j \end{pmatrix}, \quad j = 1, \dots, k.$$

Notice that the upper left block $\tilde{A} - \tilde{\Lambda}_{j,j}I$ is a large sparse and (almost) singular matrix, but that the bordered matrix is generally well conditioned. Linear systems of this type occur quite frequently in bifurcation problems and numerous approaches have been developed for their stable and efficient solution. We propose to use the mixed block elimination method of Govaerts, Pryce [10]. It requires for $\tilde{A} - \tilde{\Lambda}_{j,j}I$ and its transpose a black box solver which is normwise backward stable. It is obvious how to compute the matrices H and Δ from $\tilde{H}$ and $\tilde{\Delta}$. Moreover, we can avoid complex arithmetic by transforming to quasi upper triangular form in (7) (see [13] for the details).

2.4 Some details on the implementation

The previous sections just describe the core linear algebra used in our continuation method. The whole framework has several additional numerical features which will be briefly mentioned here (see [13], [2] for the details).

- An initial guess for an invariant subspace of prescribed dimension k is obtained by well known methods such as Cayley transforms combined with orthogonal subspace iteration. ([9], [8])
- A standard step-size selection strategy is used. If the matrices $A(s)$ arise from linearizing about a steady state branch of a dynamical system $\dot{u} = F(u, \lambda)$ then both continuation methods must be well suited to each other.
- The corresponding k-dimensional invariant subspace $R(\Psi(s))$ of $A^T(s)$ can be computed from one additional linear system.
- The normalizing matrices $\hat{\phi}$ are constantly re-orthogonalized along the branch in order to avoid ill-conditioning.
- Along the branch one tries to keep the dimension of the invariant subspace minimal but above k. Typically, changes in dimension occur when two real eigenvalues collide and become complex or vice versa. The bases of the left and right invariant subspaces are used to detect changes in dimension and provide initial guesses for the updated subspaces. Currently no device is implemented to guarantee that the continued part of the spectrum contains the rightmost eigenvalues in the complex plane. For some interesting algorithms in this direction we refer to [17], [8].

3   Stability of traveling waves

Consider a parabolic system

$$u_t = Au_{xx} + f(u, u_x), \qquad x \in \mathbb{R}, \quad t \geq 0, \tag{8}$$

where $u(x,t) \in \mathbb{R}^n, A \in \mathbb{R}^{n,n}$. Traveling wave solutions of this system are special types of bounded solutions $u(x,t) = \bar{v}(x - ct)$ where

$$\lim_{\xi \to \pm\infty} \bar{v}(\xi) = u_\pm, \qquad \lim_{\xi \to \pm\infty} \bar{v}'(\xi) = 0$$

A necessary condition for the asymptotic states $u_\pm$ is $f(u_\pm, 0) = 0$. In case $u_- = u_+$ we have a pulse and a front solution otherwise. In a moving coordinate frame $v(\xi, t) = u(\xi + ct, t)$ equation (8) transforms into

$$v_t = Av_{\xi\xi} + cv_\xi + f(v, v_\xi), \quad \xi \in \mathbb{R}, \quad t \geq 0, \tag{9}$$

with stationary solution $v(\xi, t) := \bar{v}(\xi)$. The stability is determined by the spectrum of the linearization of (9) at $\bar{v}$ given by

$$u_t = Au_{xx} + B(\cdot)u_x + C(\cdot)u =: Pu$$
$$\text{where} \quad B(x) = cI + D_2 f(\bar{v}(x), \bar{v}'(x)), \quad C(x) = D_1 f(\bar{v}(x), \bar{v}'(x)).$$

Since (8) is autonomous, the operator P has the eigenvalue zero. If the remaining spectrum is in the half plane $Re \leq -\gamma < 0$ then the wave turns out to be stable with asymptotic phase. We assume that the traveling wave has been computed on a finite interval $[x_-, x_+]$ to sufficient accuracy by standard methods for homoclinic or heteroclinic orbits in the steady state equation of (9) ([6]). Then we consider the eigenvalue problem $Pu = \lambda u$ on $[x_-, x_+]$ with either periodic or Dirichlet boundary conditions. An analysis of the perturbation of the spectra under this process is carried out in [3]. The finite problem is further discretized with constant stepsize $h = (x_+ - x_-)/M$ using centered second-order differences. One obtains a large block tridiagonal matrix (with some bordering due to the boundary conditions) for which we compute small invariant subspaces by the methods of section 2.

4   The complex Ginzburg-Landau equation

The complex Ginzburg-Landau equation is a well known modulation equation, used in physics, and chemistry [15] which depends on two parameters $\alpha, \beta \in \mathbb{R}$. We consider a two-parametric version ([16])

$$u_t = (1 + i\alpha)(u_{xx} - (1 + i\beta)^2 u + (1 + i\beta)(2 + i\beta)|u|^2 u). \tag{10}$$

We investigate the stability of the stationary solution $\bar{v}(x) = \cosh(x)^{-(1+i\beta)}$ of (10) (see [11]) where $u_\pm = \lim_{x \to \pm\infty} \bar{v}(x) = 0$. The linearization $L_{\alpha,\beta}$ of

(10) at $\bar{v}$ is given in real and imaginary parts by the following two-dimensional system

$$L_{\alpha,\beta} \begin{pmatrix} v \\ w \end{pmatrix} = \begin{pmatrix} 1 & -\alpha \\ \alpha & 1 \end{pmatrix} \left[\begin{pmatrix} v_{xx} \\ w_{xx} \end{pmatrix} - (M_1 + M_2\, M_3) \begin{pmatrix} v \\ w \end{pmatrix} \right]$$

where

$$M_1 = \begin{pmatrix} 1 - \beta^2 & -2\beta \\ 2\beta & 1 - \beta^2 \end{pmatrix}, M_2 = \begin{pmatrix} 2 - \beta^2 & -3\beta \\ 3\beta & 2 - \beta^2 \end{pmatrix}, M_3 = \begin{pmatrix} 3\bar{v}^2 + \bar{w}^2 & 2\bar{v}\bar{w} \\ 2\bar{v}\bar{w} & \bar{v}^2 + 3\bar{w}^2 \end{pmatrix}.$$

The operator $L_{\alpha,\beta}$ has a zero eigenvalue with geometric multiplicity at least two and corresponding eigenfunctions $\bar{v}'$ and $i\bar{v}$. The full spectrum for the values $x_\pm = \pm 20, h = 0.04, \alpha = -2, \beta = 3$ and the essential spectrum are shown in Fig. 1(a). The essential spectrum consists of two half-lines which cross the imaginary axis on the critical curve (cf. [3]).

$$\beta(\beta + 2\alpha) - 1 = 0. \tag{11}$$

We continue a four-dimensional subspace that belongs to the zero eigenvalues and the two real eigenvalues encircled in Fig. 1(a). With increasing β the stable eigenvalue passes zero (as shown by Mielke this happens precisely on the curve (11) where a generalized eigenvector corresponding to $i\bar{v}$ appears), then forms a complex pair with the unstable eigenvalue which finally moves to the left half plane. For the numerical eigenvalues $(x_\pm = \pm 10, h = 0.004)$ a perturbation of this motion appears in 1(b) (see [3] for details). This sensitive behaviour could only be revealed since the 4D-subspace stays separated and the remaining 4×4 eigenvalue problem can be solved very accurately.

5   The FitzHugh-Nagumo system

The FitzHugh-Nagumo equation is a model equation for the propagation of nerve impulses [7]. We consider a two-dimensional system with a small additional diffusive term

$$v_t = v_{xx} + F(v, w), \quad w_t = \epsilon w_{xx} + G(v, w),$$

$$F(v, w) = v - \frac{1}{3}v^3 - w, \quad G(v, w) = \Phi(v + a - bw), \quad a, b, \Phi \in \mathbb{R}.$$

For the parameters $a = 0.7, b = 0.8$ there is a branch containing stable and unstable waves (for details see [2]). We consider a specific part of the stable branch and follow again a four dimensional subspace with decreasing parameter Φ. Fig. 2(a) shows real and imaginary parts of the eigenvalues on this branch. While the two largest real eigenvalues remain separated from the essential spectrum the other two move towards it. The situation at $\Phi_{crit} = 0.062$
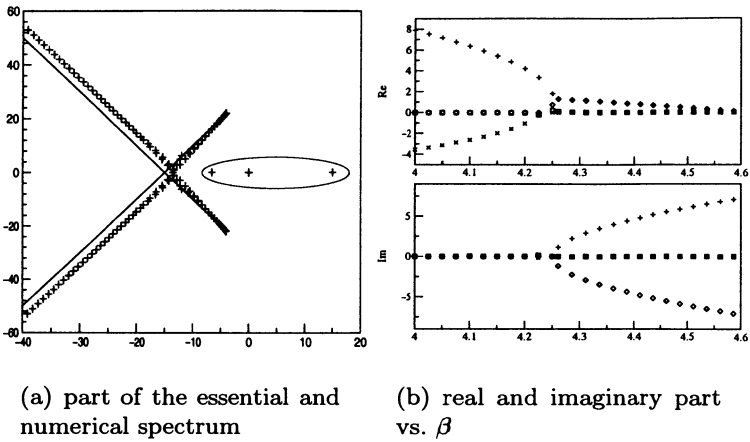
(a) part of the essential and numerical spectrum

(b) real and imaginary part vs. β

Fig. 1. Ginzburg-Landau equation, $\alpha = -2$

is shown in Fig. 2(b). At this point our algorithm breaks down (due to stagnation of the continuation steps) because these two eigenvalues can no longer be separated from the cluster that approximates the essential spectrum. Of course, concerning the stability problem there is no need to further include these eigenvalues in the continuation.
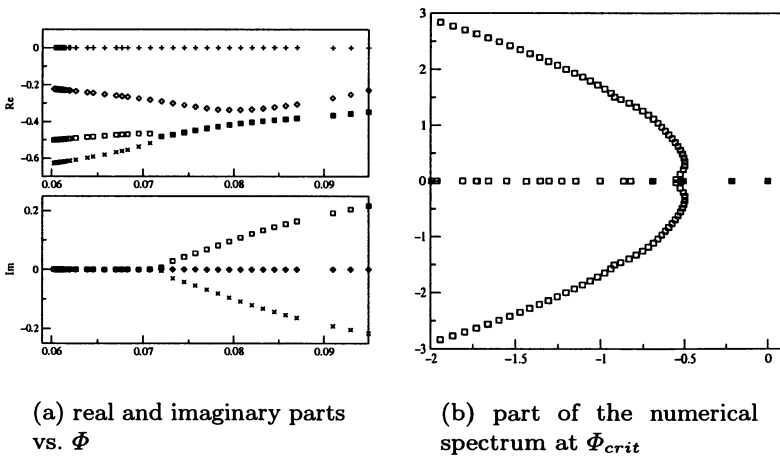

(a) real and imaginary parts vs. Φ

(b) part of the numerical spectrum at Φ_{crit}

Fig. 2. FitzHugh-Nagumo, stable wave, $x_- = 0, x_+ = 65, h = 0.1$

References

1. W.-J. Beyn and W. Kleß. Numerical Taylor expansions of invariant manifolds in large dynamical systems. *Numerische Mathematik*, 80:1–38, 1998.
2. W.-J. Beyn, W. Kleß, and V. Thümmler. Continuation methods for low-dimensional invariant subspaces with applications to dynamical systems of large dimension. in preparation, 1999.
3. W.-J. Beyn and J. Lorenz. Stability of traveling waves: Dichotomies and eigenvalue conditions on finite intervals. Preprint SFB 343 No. 094, University of Bielefeld, 1998.
4. F. Chatelin. *Eigenvalues of matrices*. John Wiley & Sons, 1993.
5. J. W. Demmel. Three methods for refining estimates of invariant subspaces. *Computing*, 38:43–57, 1987.
6. E. Doedel, T. Champneys, T. Fairgrieve, Y. Kuznetsov, B. Sandstede, and X.-J. Wang. *AUTO97 Continuation and bifurcation software for ordinary differential equations (with HomCont)*. Concordia Univ. Montreal, 1997.
7. R. FitzHugh. Impulses and physiological states in theoretical models of nerve membrane. *Biophysical Journal*, 1:445–466, 1961.
8. T. J. Garratt, G. Moore, and A. Spence. A generalised Cayley transform for the numerical detection of Hopf bifurcations in large systems. In *Contributions in numerical mathematics*, pages 177–195. World Sci. Publ., 1993.
9. G. H. Golub and C. F. van Loan. *Matrix Computations*. The John Hopkins University Press, 2 edition, 1989.
10. W. Govaerts and J. D. Pryce. Mixed block elimination for linear systems with wider borders. *IMA J. Numer. Anal.*, 13:161–180, 1993.
11. L. M. Hocking and K. Stewartson. On the nonlinear response of a marginally unstable plane parallel flow to a two-dimensional disturbance. *Proc. Roy. Soc. London Ser. A*, 326:289–313, 1972.
12. H. Jarausch. Analyzing stationary and periodic solutions of systems of parabolic partial differential equations by using singular subspaces as reduced basis. *Math. Comput. Modelling*, 20:69–87, 1994.
13. W. Kleß. *Numerische Approximation lokal invarianter Mannigfaltigkeiten in groen dynamischen Systemen*. PhD thesis, University of Bielefeld, 1997.
14. Y. Kuznetsov and V. Levitin. *CONTENT: A multiplatform environment for analyzing dynamical systems*. CWI Amsterdam, 1997.
15. C. D. Levermore and M. Oliver. The complex Ginzburg-Landau equation as a model problem. In *Dynamical systems and probabilistic methods in partial differential equations*, pages 141–190. Amer. Math. Soc., 1996.
16. A. Mielke. The complex Ginzburg-Landau equation on large and unbounded domains: sharper bounds and attractors. *Nonlinearity*, 10:199–222, 1997.
17. R. Neubert. Predictor-corrector techniques for detecting Hopf bifurcation points. *Internat. J. Bifur. Chaos Appl. Sci. Engrg.*, 3:1311–1318, 1993.
18. G. W. Stewart and J. Sun. *Matrix perturbation theory*. Academic press, 1990.
19. V. Thümmler. Numerische Stabilitätskriterien für wandernde Wellen. Diploma thesis, University of Bielefeld, 1998.

Sensitivity Analysis of Multicomponent Mass Transport in Porous Solids Descibed by Partial Differential Equations

Pavel Čapek[1] and Andreas Seidel–Morgenstern[1,2]

[1] Otto–von–Guericke Universität
[2] Max-Planck-Institut für Dynamik komplexer technischer Systeme
    D–39106 Magdeburg, Germany

Abstract. The sensitivity analysis of multicomponent mass transport in porous media is utilised for prediction of suitable experimental conditions and, consequently, for parameter estimation . Experimental data obtained using a suitable set-up were analysed for this purpose. The system of non–linear partial differential equations is first discretized in space and the resulting system of differential–algebraic equations (DAEs) is solved together with the derived system of DAEs for sensitivity functions.

Introduction

A proper description of mass transport of multicomponent mixtures inside porous materials is essential in the simulation and design of catalytic reactors, adsorption and membrane separation processes. Two convenient approaches to model the transport of gases in porous media are the Dusty Gas Model [1] or the Mean Transport–Pore Model (MTPM) [2]. Both models are based on the Maxwell–Stefan theory modified for mass transport of multicomponent gaseous mixtures in porous materials. They use two types of parameter sets: transport properties of gases and textural parameters of the porous solids. The transport properties of gases are usually known and do not depend on porous solids used. However, the textural parameters are usually not accessible on a theoretical basis and have to be determined experimentally. In order to estimate these textural parameters various techniques have been proposed and used. A particularly useful one utilises the fact that a temporary total pressure difference arises in a modified diffusion cell of the Wicke–Kallenbach type (Fig. 1) after perturbing the input composition [2]. The course of this spontaneous pressure difference allows the determination of all textural parameters. The cell contains porous pellets (length L) mounted in parallel in a stainless steel disk. The lower chamber of the cell is closed and equipped with a pressure gauge. Before the start of a run the cell was swept with gas B. At the start of the run a concentration step change at the inlet of the upper cell part was carried out by replacing gas B by another gas A (B → A). Common gases experimentally used are hydrogen (H_2), helium (He), nitrogen (N_2), argon (Ar) and their mixtures.
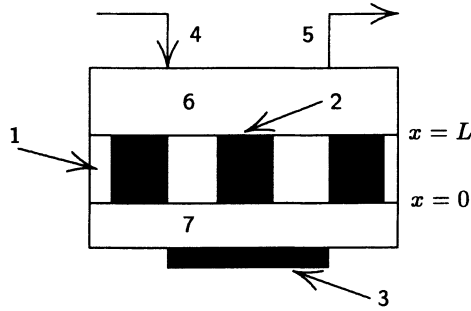
Fig. 1. Scheme of the modified WK cell. 1-Metallic disc with cylindrical holes for pellets, 2-pellets of total volume V_p and length L, 3-pressure transducer, 4-gas inlet, 5-gas outlet, 6-upper chamber of volume V_{cL}, 7-lower chamber of volume V_{c0}

The dynamics of the diffusion cell can be described by non-linear parabolic partial differential equations (PDEs) originating from mass balance considerations. The experimental method and, consequently, the PDE model should be applicable to estimate the textural parameters of very different porous solids. However, depending on the particular porous structure, optimum experimental conditions will be very different in each case. To quantify this aspect, a sensitivity analysis of the PDE system should be quite instructive [3]. It is the aim of this work to perform a numerical study of multicomponent mass transport in the Wicke–Kallenbach cell (WK cell) including sensitivity functions and to specify experimental conditions for reliable parameter estimation. The sensitivity analysis of MTPM was chosen to describe the intraparticle mass transport because this model best fitted experimental data.

Combined Isothermal Mass Transport

The MTPM is based on a few simplifying assumptions. Important for this work is the assumption of three averaged values of textural parameters, ψ, $\langle r \rangle$ and $\langle r^2 \rangle$, which are capable of modelling a real porous network. They are material constants which depend on neither a total pressure nor gases used. Their physical meaning is the following: ψ is the ratio of total porosity, ε, and tortuosity; $\langle r \rangle$ is the mean pore radius; $\langle r^2 \rangle$ is the mean of the square of transport pore radii. The two last parameters appear always in products with the first parameter, ψ, and, therefore, the vector of modified parameters, Θ, is introduced. Roughly speaking, each modified parameter is related to a different kind of mass transport:

- $\theta_1 \equiv \psi \quad \in \langle 0.01, \varepsilon \rangle \quad$ diffusion in the region of continuum
- $\theta_2 \equiv \psi \langle r \rangle \quad \in \langle 10^{-11}, 10^{-5} \rangle \quad$ mass transport in Knudsen region
- $\theta_3 \equiv \psi \langle r^2 \rangle \in \langle 10^{-20}, 10^{-10} \rangle$ viscous flux contribution.

All parameters are positive numbers lying usually in the intervals given above. In the model driving forces for combined mass transport of n components in a gaseous mixture are expressed by means of molar concentration gradients, $\partial c/\partial x$. The spatial coordinate in the porous material is denoted by $x \in \langle 0, L \rangle$ and c denotes the column vector with the component molar concentrations c_i as elements. The total molar concentration, c_T, is given by the sum of all molar concentrations, $c_T = \sum_{i=1}^{n} c_i$. The constitutive equations written in terms of molar flux densities, N, and molar concentration gradients have the general mathematical structure [4]

$$F(c, \Theta) \bullet N + G(c, \Theta) \bullet \frac{\partial c}{\partial x} = 0 \ . \tag{1}$$

The elements of square $n \times n$ matrices, H and G, are non–linearly dependent on molar concentrations, c, and textural parameters, Θ. A simplified version of MTPM [5] was used below for calculation of the matrix G. It is worthwhile to note that the model is linear and implicit in molar flux densities, N.

Balance of Diffusion Cell

The constitutive equations (1) are supplemented by n balances of components inside the porous pellet

$$A(c) \bullet \frac{\partial c}{\partial t} = -\frac{\partial N}{\partial x} \tag{2}$$

where t is time and $A(c)$ is generally a $n \times n$ square non–symmetric matrix with off–diagonal elements, $a_{ij} = \partial q_i/\partial c_j$, and diagonal elements, $a_{ii} = \partial q_i/\partial c_i + \varepsilon$. Herein q_i denotes the surface concentration of the i–th component. If no adsorption occurs in the porous solid, the matrix A is diagonal with identical elements, $a_{ii} = \varepsilon$. The mass balance of the upper chamber forms the boundary condition of (2) at $x = L$. The chamber balance is formulated assuming a well mixed volume and constant total molar concentration, c_T,

$$V_{cL}\frac{\partial c(t, L)}{\partial t} = F_L C_L - \left(F_L + \frac{V_p}{Lc_T} \sum_{k=1}^{n} N_k(t, L) \right) c(t, L) + \frac{V_p}{L} N(t, L) \ , \tag{3}$$

where F_L denotes input flow rate and C_L denotes the vector of input molar concentrations. In the small gas volume below the pellets (i.e. at $x = 0$) again ideal mixing is again assumed. Thus, the second boundary condition of (2) is

$$V_{c0}\frac{\partial c(t, 0)}{\partial t} = -\frac{V_p}{L} N(t, 0) \ , \tag{4}$$

Initial conditions for the system of equations are given by

$$c(0, x) = \{c_1^*, \ldots, c_n^*\}^T \tag{5}$$

with vector elements, $c_1^*, \ldots, c_n^*$, denoting the vector of constant component concentrations attained by sweeping the cell before the start of the step change.

The PDE system(1) - (5) was solved using the method of lines dividing the pellet body into m disjunctive cells [4]. After discretization the system of PDEs together with boundary conditions was transformed into a system of $n \times (m + 2)$ differential–algebraic equations (DAEs), where the vector $c(t, x)$ was approximated by the vector $u(t)$ and (2) by

$$E(u(t)) \bullet du(t)/dt = f(u(t), \Theta) \tag{6}$$

The specification of initial conditions of this transformed system is straightforward.

$$u(0) = \{c_1^*, \ldots, c_n^*, c_1^*, \ldots, c_n^*, \ldots\}^T . \tag{7}$$

Sensitivity Functions

The matrix $W(t)$ of sensitivity functions, w_{ij}, is defined as

$$W(t) \equiv \partial u(t)/\partial \ln \Theta . \tag{8}$$

The partial derivatives of state variables $u(t)$ were chosen with respect to the natural logarithm of Θ because of problem scaling where elements of Θ differ in orders of magnitude. Using (8) the following set of DAEs can be derived by partial differentiation of (6) with respect to the natural logarithm of the parameter vector Θ

$$\frac{\partial}{\partial u} \left(E(u) \bullet \frac{du}{dt} \right) \bullet W + E(u) \bullet \frac{dW}{dt} = \frac{\partial}{\partial u} f(u, \Theta) \bullet W + \frac{\partial}{\partial \ln \Theta} f(u, \Theta) \tag{9}$$

Here, u and W were used as shorthand for $u(t)$ and $W(t)$, respectively. The initial conditions of (9) follow from the fact that the system is in equilibrium and does not depend on transport parameters

$$W(0) = 0 . \tag{10}$$

The system (9) for sensitivity functions $W(t)$ has to be solved together with (6). The whole set of DAEs was solved in this work by implicit integrator DASSL [6]. As an appropriate number of disjunctive cells, $m = 128$ was determined by repeated integration and by comparison of results for various typical conditions. Partial derivation with respect to the vector of state variables u and the vector parameters Θ in (9) was carried out analytically. A natural requirement of Newton iteration built in the DASSL code is the evaluation of the Jacobian matrix for (6) and (9). The storage format chosen for this was the compressed sparse column [7]. After grouping of the column indices the Jacobian matrix was calculated numerically by finite differences. The solution of linear equations resulting in the Newton iteration was determined by the preconditioned biconjugate gradient method with incomplete LU preconditioner [7].

Results and Discussion

The solution of (6) and (9) together with (7) and (10) provide the approximations of state variables and sensitivity functions in the whole time and spatial domains. On the other hand, experiments carried out in the WK cell (Fig. 2) provide only the temporal total molar concentration differences recorded with certain frequency (e.g. 1 Hz) and, thus, for textural parameter estimation only the calculated total molar concentration difference is needed. It is defined for convenience in dimensionless form as relative total concentration difference

$$\Delta c_r(t) = \left(\sum_{i=1}^{n} c_i(t,0) - c_T(t,L) \right) \Big/ c^0 , \tag{11}$$

where the total molar concentration, c^0, used for normalization is proportional to the standard pressure (101325 Pa). Note, that the total molar concentration, c_T, in the above equation is constant as assumed in the boundary condition at $x = L$. According to (8) and (11) the vector of sensitivity functions of the relative total molar concentration difference, $\Omega(t) = \{\omega_1(t), \omega_2(t), \omega_3(t)\}$, is defined as $\Omega(t) \equiv \partial \Delta c_r(t) / \partial \ln \Theta$. The model formulated in the above paragraphs is non–linear in the three parameters Θ. The validity of the concrete results of sensitivity analysis reported below should be restricted to the concrete porous solid studied. However, this restriction is not very essential and results can be generalized for other solids with similar texture.

The transport of inert gases (H_2, He, N_2 and Ar) in an industrial catalyst for methanol synthesis was studied in this work. Its textural parameters were estimated by Marquardt's technique from selected experiments performed during this study. The estimated values of textural parameters, Θ, as well as parameters of the WK cell are given in Table 1. Despite of the fact that only inert gases were used for experiments additional simulations including equilibrium adsorption with typical adsorption coefficients were performed to judge its influence on parameter estimation. Preliminary calculations revealed that the total molar concentration, $c_T(t,L)$, and the type of applied gases had the major importance on the sensitivity functions. The cell construction (volume of pellets, V_p, volumes of chambers, V_{c0} and V_{cL}) and the adsorption effects were found to be of minor importance.

Table 1. Parameters of the WK cell, parameters of industrial catalyst for methanol synthesis and estimated values of textural parameters, Θ

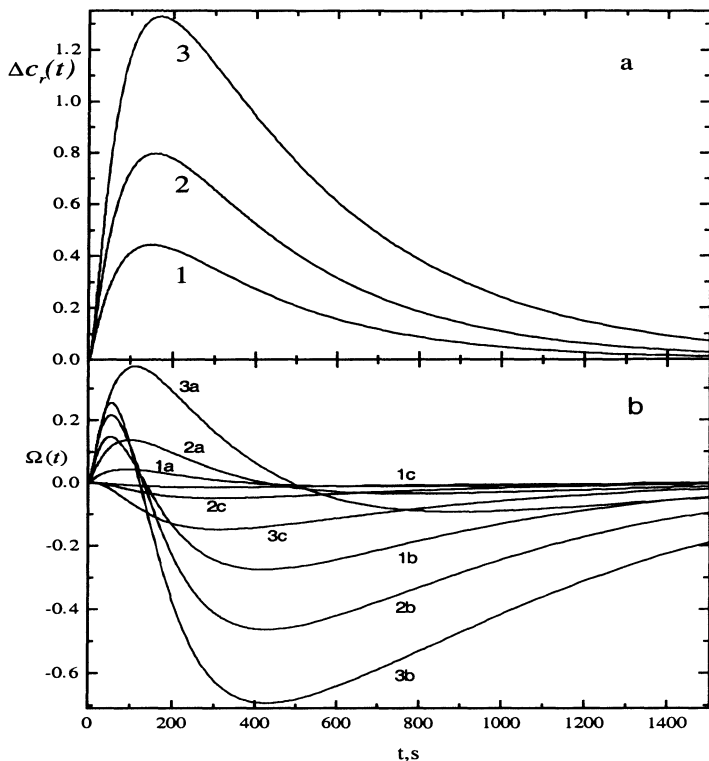| V_p	V_{c0}	V_{cL}	L	ε	θ_1	θ_2	θ_3
cm^3	cm^3	cm^3	mm	-	-	nm	nm^2
1.734	10.1	9.75	4.90	0.5736	0.0833	1.720	63.27

Fig. 2. Total molar concentration difference, $\Delta c_r(t)$, and sensitivity functions, $\Omega(t)$, for the step change Ar $\to$ H$_2$. The numbering of curves is related to total molar concentration (1–40.2 mol/m^3, 2–80.8 mol/m^3, 3–161.3 mol/m^3), letters a, b and c designate parameters (a–θ_1, b–θ_2, c–θ_3)

The influence of the total molar concentration on $\Delta c_r(t)$ and $\Omega(t)$ is illustrated for the step change Ar $\to$ H$_2$ and the sequence of three discrete levels (40.2 mol/m^3, 80.8 mol/m^3 and 161.3 mol/m^3, Fig. 2a,b).

After the step change the total molar concentration below the pellets rises. The higher the total molar concentration, the larger is the maximum of the total molar concentration difference. Because the studied catalyst had relatively narrow pores the mass transport in Knudsen region dominates in the case of the total molar concentration of 40.2 mol/m^3 (lines 1). Simply put, the sensitivity functions $\omega_1(t)$ and $\omega_3(t)$ are smaller than $\omega_2(t)$ in the whole time domain and, consequently, small changes of θ_1 and θ_3 do not result in significant change of the function $\Delta c_r(t)$. It can be concluded that experiments performed under conditions where the total molar concentration, $c_T(t, L)$, is less than 40.2 mol/m^3, are not suitable for the estimation of all three parameters and only the second parameter, θ_2, can be estimated reliably. This phenomenon was also observed for another catalyst with similar

Table 2. Maxima and minima of relative total molar concentration, $\Delta c_r(t)$, and sensitivity functions, $\Omega(t)$, for selected step changes and total molar concentrations

step change	$c_T(t,L)$ mol/m^3	$\Delta c_r(t)$ -	$10\omega_1(t)$ min	max	$10\omega_2(t)$ min	max	$10\omega_3(t)$ min	max
Ar→H$_2$	40.2	0.443	-0.106	0.431	-2.741	1.465	-0.141	0.002
Ar→H$_2$	80.8	0.798	-0.338	1.369	-4.627	2.150	-0.485	0.006
Ar→H$_2$	161.3	1.328	-0.912	3.689	-6.938	2.537	-1.473	0.017
Ar→He	160.9	1.110	-0.722	2.774	-6.389	2.427	-1.188	0.014
N$_2$→He	161.6	0.922	-0.658	2.459	-5.430	1.902	-1.065	0.011
(N$_2$,Ar)→(H$_2$,N$_2$)	41.3	0.220	-0.055	0.258	-1.389	0.670	-0.085	0.000
(N$_2$,Ar)→(H$_2$,N$_2$)	81.4	0.386	-0.167	0.769	-2.310	0.920	-0.284	0.003
(N$_2$,Ar)→(H$_2$,N$_2$)	163.3	0.630	-0.431	1.997	-3.441	0.993	-0.860	0.008

texture [5]. Higher total molar concentrations have a favourable influence on the range of sensitivity functions. Maxima of $\omega_1(t)$ and $\omega_3(t)$ increase more pronouncedly compared to the value for $\omega_2(t)$ as the mass transport in region of continuum becomes more significant. Values of determined maxima and minima of sensitivity functions are given in Table 2.

Concerning the relation of the total molar concentration, $c_T(t,L)$, the molar concentration difference, $\Delta c_r(t)$, and sensitivity functions, $\Omega(t)$, in principle the following rule holds: the higher the total molar concentration ⇒ the higher the total molar concentration difference ⇒ the better the conditions for estimation of all parameters (i.e. there is a higher sensitivity of $\Delta c_r(t)$ relative to small changes of θ_1 and θ_3). However, this rule is not valid for gaseous pairs He/Ar and He/N$_2$. Despite of the higher total molar concentration difference arising after a step change Ar → He the conditions for parameter estimation are better for the step change N$_2$ →He, see Table 2. A closer inspection of Table 2 reveals that the ratios of maxima/minima of $\omega_1(t)$ and $\omega_3(t)$ to maxima/minima of $\omega_2(t)$ are more favourable in the case N$_2$ → He.

The idea to use ternary mixtures with a certain composition for further improvement of parameter estimation was inspired by the work of Duncan and Toor [1]. They observed "uphill" diffusion in the ideal ternary mixture hydrogen–nitrogen–carbon dioxide. Despite of the very different experimental set–up, the performed simulations (and experiments) conducted in the spirit of Duncan and Toor's experiments resulted in greater differences among sensitivity functions, $\Omega(t)$, (Table 2) where the relevant step changes are denoted by (N$_2$,Ar) → (H$_2$,N$_2$). In the experiments the nitrogen mole fraction in both gas pairs was set equal to 0.5, i.e. ratios of components were (N$_2$/Ar) = (1/1) and (H$_2$,N$_2$) = (1/1). The observed behaviour of sensitivity functions can be

accounted for by the increased contribution of the bulk diffusion mechanism in ternary mixtures under elevated total molar concentration. The sensitivity functions, $\Omega(t)$, for simulated step changes of inlet composition between a single gas and a binary mixture (e.g. $(N_2,Ar) \rightarrow H_2$) exhibited roughly the same behaviour as for step changes between two single gases. Apparently, experiments carried out in this manner do not have the potential to improve parameter estimation.

Conclusions

A mathematical model of the WK cell was applied to quantify mass transport in porous media. To determine optimum experimental conditions for parameter estimation a sensitivity analysis was performed. The parameter which had the greatest influence on the sensitivity function behaviour was found to be the total molar concentration in the upper chamber of the WK cell. In order to estimate reliable textural parameters the total molar concentration has to be adjusted with respect to the actual porous medium. Conditions for a reliable estimation of all three parameters can be further improved by using response curves for the exchange of equimolar mixture of nitrogen and argon versus nitrogen and hydrogen.

References

1. Krishna R. and Wesselingh J.A. (1997) The Maxwell-Stefan approach to mass transfer. Chem. Engng. Sci. 52, 861-911.
2. Novák M., Ehrhardt K., Klusáček K. and Schneider P. (1988) Dynamics of non-isobaric diffusion in porous catalysts. Chem. Engng. Sci. 43, 185-193.
3. Caracotsios M. and Stewart W.E. (1985) Sensitivity analysis of initial value problems with mixed ODEs and algebraic equations. Comput. chem. Engng. 9, 359-365.
4. Ehrhardt K., Klusáček K. and Schneider P. (1988) Finite-difference scheme for solving dynamic multicomponent diffusion problems. Comput. Chem. Engng. 12, 1151-1155.
5. Čapek P., Hejtmánek V., Šolcová O. and Schneider P. (1997) Gas transport in porous media under dynamic conditions. Catal. Today 38, 31-38.
6. Petzold L.R. (1982) A description of DASSL: a differential/algebraic system solver. Sandia Tech. Rep. 82-8051.
7. Barrett R., Berry M., Chan T.F., Demmel J., Donato J., Dongarra J., Eijkhout V., Pozo R., Romine C. and Van der Vorst H. (1994) Templates for the solution of linear systems: Building blocks for iterative methods, 2nd edition, SIAM, Philadelphia, PA.

Simulation of the diffusant distribution in the diffuse furnace with wafers

Orest Korbetsky[1] and Victoria Kotchubey[1]

State University "Lviv Polytechnic", CAD/CAM Department,
Physical Chemistry Department, Bandera Str. 12, 2900646, Lviv, Ukraine,
korbeor@polynet.lviv.ua

Abstract. The authors propose a 2D-model for diffusant concentration distribution in a diffusion furnace with wafers inside for Integrated Circuits (IC) manufacturing. For obtaining the initial diffusion concentration at the inlet of the horizontal reactor a model for vaporization process in the saturator is proposed. Then treat the chemical reaction and PDE for concentration is solved using finite volume technique. These models are included in the CAD of IC process "ProMIC-T".

1   INTRODUCTION

Diffusion processes are widely used in the microelectronic industry for generating the concentration profiles in silicon semiconductors. So-called "open flow" systems with different sources of the diffusion (Fig. 1) is often employed in the semiconductor manufacturing. The diffusion process is conducted in the horizontal quartz tube furnace with hot walls. Liquid diffusant BBr_3 (source) is located in the saturator. Getting through the saturator, carrier gas (N_2) is saturated by vapour diffusant (BBr_3). Then it enters the diffusion furnace where it reacts with the oxygen (O_2), forms diffusant oxide B_2O_3 which is deposited on the silicon wafer forming a boron-silicate glass (BSG) layer. The silicon wafers are placed perpendicular to the moving flow. The initial stage of this process is called predeposition. A pure element, boron (B), precipitates as a result of interactions between the BSG and the silicon. Hereinafter this element diffuses in the depth of the silicon slice and creates a doping area. This stage is identified - drive-in. There is a simplified picture of running the diffusion process in the tube furnace (reactor) [1]. A problem is that concentration of the diffusant oxide near the wafers depends on many factors, such as temperature in the reactor, gas flow velocity, geometry of reactor, temperature in the saturator. We added a model of the stage of predeposition to the already existing program of modeling of the drive-in process - "ProMIC-T". Two mathematical models were developed, one for saturator and second for the process in the reactor.

2   A SATURATOR MODEL

Consider the widely used design of the saturator, as shown in Fig. 2. Into the saturator with known sizes and parameters (height, width, diameters of tubes
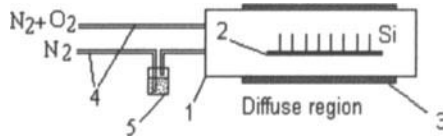
Fig. 1. Diffuse "open tube" furnace; 1. quarts tube, 2. wafers, 3. heater, 4. gas system, 5. saturator

and saturatorer) a carrier-gas is given (N_2). At the output the VGM-Vapour-Gas-Mixture consists of the feed gas and the saturated diffusing vapour. For the performance of the saturator it is decisive that the bubbles at the end of the saturator inlet are removed at constant flow. Thereafter, they accelerate for a small period and then rise vertically to the liquid surface through a liquid layer at constant velocity. Supposing that a bubble has the shape of a sphere, and there are no interactions among them, the diameter of a bubble can be obtained from force balances acting on a bubble at the moment of raising from the saturator inlet [2]:
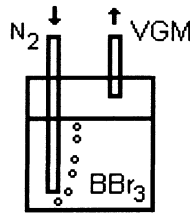
Fig. 2. A saturator scheme

$$R_{b.i} = \sqrt[3]{(3d_0\sigma)/4g(\rho_1 - \rho_g)} \tag{1}$$

where d_0 = diameter of the bubbler inlet (m), σ = surface tension (N/m), ρ_1 = liquid density (kg/m^3), g = carrier gas density (kg/m^3), ρ_g = the Earth acceleration (m/c^2) and $R_{b.i}$ = the initial bubble radius (m). When forming a continuous chain of spherical bubbles the velocity of their appearance equals their initial velocity which is

$$R_{b.i} = \sqrt[3]{3Q_g/4\pi w_0} \tag{2}$$

where Q_g = rate of carrier gas (m^3/c), w_0 = velocity of one bubble (m/c) and μ = liquid viscosity Pa · c.

$$w_0 = (\sigma^2 g/3\pi\mu\rho_1)^{1.5} \tag{3}$$

The difference between the pressure inside and outside of the bubble is the surface tension, which is created on the surface of the bubble:

$$P_2 - P_1 = 2\sigma/R_b \qquad (4)$$

where P_2 = a pressure in bubble (Pa), P_1 = outside hydrostatic pressure (Pa), R_b = radius of bubble with VGM inside (m).

The VGM in each bubble consists of two components: the feed gas, and the vapor of saturator liquid. Besides, certain amounts of gas diffuse through the wall of the bubble into the liquid and vice versa. Taking into account that diffusants are materials of significant volatility, as well as the fact that bubbles keep in the saturator for a very short time, this diffusion is neglected. Carrier-gas does not change its mass in mixtures [3]. Using Dalton's law the pressure inside the bubble is:

$$P_2 = P_{g.b} + P_{s.v} \qquad (5)$$

where $P_{s.v}$ = saturated vapour pressure inside bubble (Pa), $P_{g.b}$ = carrier gas pressure inside bubble (Pa), which is equal to:

$$P_{g.b} = (3/4)mRT/M\pi R_b^3 \qquad (6)$$

where m = carrier gas mass (kg), M = carrier gas molar mass (kg/mol), R = the gas constant 8.3143 Nm/(mol·K), T = saturator temperature (K).

Writing the dependence of $P_{s.v}$, as a function of temperature [4]

$$P_{s.v} = 133.322 \cdot 10^{7.709 - 1754.032/T} \qquad (7)$$

and inserting all dependencies into (4), a cubic equation results for the unknown R_b. Applying Redlich-Kwong's equation [5] leads to

$$P_{s.v} = RT/(V - b) - a/(V + b)VT^{0.5} \qquad (8)$$

where V = molar volume (mol/m^3), a and b are functions from critical temperature and pressure [5]. Solving the cubic equation for the determination of the mole volume, the saturated vapor mass is found in one bubble. Knowing the mass of carrier gas m and saturated vapor mass $m_{s.v}$ in the bubble their correlation coefficient

$$coeff = m/m_{s.v} \qquad (9)$$

3   A PROCESS MODEL IN THE REACTOR

The two-dimensional distribution of the diffusant in the reactor is described by the stationary diffusion equation in cartesian coordinates:
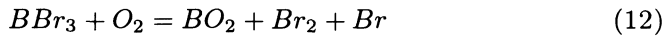
$$u\partial C/\partial x + v\partial C/\partial y = D(\partial^2 C/\partial x^2 + \partial^2 C/\partial y^2) - W \qquad (10)$$

where u, v are flow velocity components at x axis along the reactor (m/c) and y axis along diameter (m/c) correspondingly, D = diffusivity of B_2O_3 (m^2/c), W = rate of chemical reaction and C = concentration (m^3).

The process performs differently in the reactor, depending on the number of moles of the diffusant. In general, the rate of formation of B_2O_3 as a final product of reaction of boron tribromide oxidation is

$$4BBr_3 + 3O_2 = 2B_2O_3 + 6Br_2 \tag{11}$$
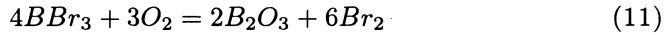
The chemical reaction runs at a condition of small BBr_3 and O_2 content in the VGM. The B_2O_3 deposition area is shifted from the diffusion furnace inlet of the reagents along the moving direction of the gas mixture. The distance of shift depends on the velocity of the gas flow and the rate of formation of intermediate products. In this case W $\neq$ 0, and after carrying out a thermodynamic analysis of system [6], a reaction mechanism as follows is expected:

$$BBr_3 + O_2 = BO_2 + Br_2 + Br \tag{12}$$

$$2BO_2 = B_2O_{3(gas)} + O \tag{13}$$

$$B_2O_{3(gas)} = B_2O_{3(solid)} \tag{14}$$

Using the method of stationary concentrations [7] the authors of paper [6] got a diffusant concentration distribution on condition that $[O_2] \gg [BBr_3]$ and the concentration $[O_2]$ along the reactor is constant. As a result, they found an equation:

$$[BBr_3] = [BBr_3]_0 \, exp(-x \cdot K_1 [O_2] / u) \tag{15}$$

where $[BBr_3]_0$ = initial concentration at the inlet x = 0 (m$^-$3), u = linear velocity (m/c), x = coordinate (m), K_1 = chemical reaction rate constant of (12).

Under high concentrations of oxygen and boron tribromide a deposition begins right in the area of the reagents blending, with the result that a depletion of VGM by reagents occurs [8]. In this case, chemical reaction occurs instantly and accordingly W = 0.

It is necessary to formulate the boundary and initial conditions for solving the equation (10):

At the reactor inlet, initial concentration C_0 which is obtained from the saturator correlation coef and reaction (11)

$$C = C_0 \tag{16}$$

At the reactor outlet and wall (absorption is neglected)

$$\partial C / \partial x = 0 \qquad (17)$$

At the wafers [9]

$$\partial C / \partial x = H \cdot C_g \qquad (18)$$

where H is the gas phase mass transfer coefficient of B_2O_3 and C_g is bulk concentration in the gas (m^{-3}), which is defined in [10]

$$H = 8.5 \cdot 10^9 \cdot exp(-3.53/kT) \qquad (19)$$

where k is Boltzmann constant $1.38 \cdot 10^{-23}$ (JK^{-1}).

The concentration is based on known, calculated beforehand field of flow and temperature [11]. The equation of diffusion (10) was discretised in space using a finite volume technique on a non-uniform cartesian grid. A view of the control volume is shown in Fig. 3. Discretisation of the grid was directed near hard surfaces (walls and wafers). A numerical hybrid scheme was used to raise accuracy without loss of stability. The motivation of the scheme is given in work [12]. Obtained as a result of approximation, the system of algebraic linear equations was solved by the SOR-method with the lower relaxation. The resulting analytical and numerical models are presented in the program "ProMIC-T" which describes the diffusion process (stage predeposition) in the diffusion furnace.
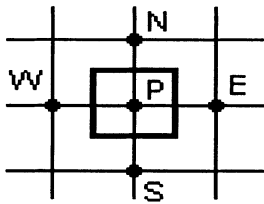
Fig. 3. View of typical control volumne

4   RESULTS

Note the following results of the simulations. A change of concentration occurred along radius and after decreasing the Reynolds and Schmidt numbers along tube axes. Concentration transfer between wafers basically occurred owing to diffusion. Its value rapidly decreases near the center of the wafer because of the deposition on the wafer surface (Fig. 4).

Fig. 5 shows the dependency of surface resistance of the wafer as a function of the diffusant consumption. As can be seen from this figure, simulation data mostly agree with experimental data. The models presented simulate
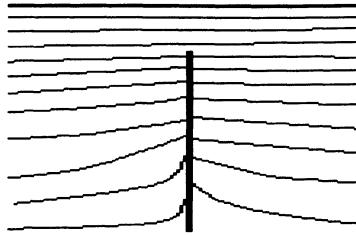
Fig. 4. Concentration field near wafer

the process quite good under high and low concentration of the diffusant, but do not give desired accuracy under medium concentrations.
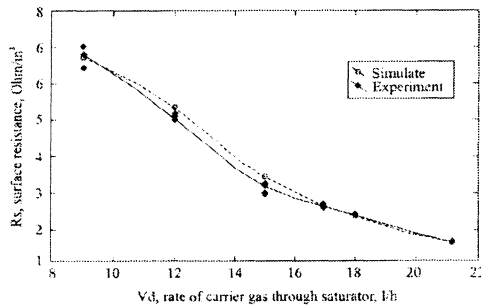

Fig. 5. Experimental data vs. simulated data by "proMIC-T"

5   CONCLUSIONS

The presented mathematical models of the saturator and the process in the diffusion furnace allow to simulate the diffusant distribution in the diffusion furnace. The model of the saturator estimates the influence of flow rate, saturator temperature and geometry of saturator for different types of sources. The model of diffusant distribution has two parts: first, in the case of a small amount of dopant in the gas mixture and second a large amount of dopant. In the first case an exponential dependence describes the diffusant distribution. In the second case numerical simulation is needed for solving diffusion equation with boundary and initial conditions. From the results of simulation the following conclusions can be drawn: the change of concentration occurs along the radius and after decreasing of Re and Sc numbers along tube axes. Concentration transfer between wafers basically occurs by diffusion. The program "ProMIC-T" comprises these models that allow to simulate two stages of the diffusion process.

6 REFERENCES

1. R.M. Burger, R.P. Donovan. Fundamentals of silicon integrated device technology. Vol.1. Oxidation, Diffusion and Epitaxy. Prentice-Hall, New Jersey, 1967
2. V.V. Kafarov. The basic of mass transfer. Visshay Shkola, Moscow, 1979
3. A.D. Fedorovsky, E.I. Nikiforovich, N.A. Prihod'ko. Transfer processes in gas-liquid system. Naukova Dumka, Kiev, 1988
4. I.M. Skvorcov, I.I. Lapidus, et al. Technology and apparatus of silicon and germanium gas epitaxy, Energiay, Moscow. 1978
5. R.C. Reid, J.M. Prausnitz, T.K. Sherwood. The properties of gases and liquids. McGraw-Hill, U.S.A, 1977
6. V.N. Dyagilev, L.A. Koledov, T.P. Gapeeva. About oxidation kinetics of tribromid boron in the "open flow system" reactor. MIET Collected articles of microelectronics problems (Chemical series) No. 19, Moscow, 1974
7. N.N. Emannuel', D.G. Knorre. Course of the chemical kinetics, Visshay Shkola, Moscow, 1969
8. V.N. Dyagilev, L.A. Koledov, T.P. Gapeeva. Obtaining conditions of uniform at thickens and diffusant concentration boron-silicate glass layer. MIET Collected articles of microelectronics problems (Chemical series) N. 19, Moscow, 1974
9. D.K. Pal, M.K. Kowar, A.N. Daw, P. Roy. Modelling of silicon epitaxy using silicon tetrachloride as the source. Microelectronics J. Vol. 26. No. 6, september 1995, P. 507-514.
10. A.N. Bubennikov, A.D. Sadovnikov. Physical-technological design of silicon VLSI bipolar elements. Radio and Sviaz, 1991.
11. O. Korbetsky, V. Tesluk. The gas movement simulation in the diffuse furnace with accounting of the thermal convection. J. Technical News, 1998/1(6), 2(7), Lviv, Ukraine
12. S.V. Patankar, D.B. Spalding. A calculation procedure for heat, mass and momentum transfer in three dimensional parabolic flows . Int. J. Heat Transfer.-1972.- Vol. 15, P.1787-1806

Modelling and Simulation of Transient Transport Processes Using Axial Dispersion Model

Xing Luo and Bernd Niemeyer

Trenn- und Umwelttechnik, GKSS-Forschungszentrum
Max-Planck-Straße, 21502 Geesthacht

1 Introduction

Transient analysis in heat and mass transfer processes is often demanded in chemical industries. In many apparatus the fluid flows are arranged parallel with each other (cocurrent flow or countercurrent flow). The general mathematical model describing the transient behaviour of the heat and mass transfer in such apparatus can be expressed with the following partial differential equation system

$$B_i \underbrace{\frac{\partial Y_i}{\partial \tau}}_{\substack{accumulation \\ term}} + \underbrace{U_i \frac{\partial Y_i}{\partial x}}_{\substack{convection \\ term}} = \underbrace{D_i \frac{\partial^2 Y_i}{\partial x^2}}_{\substack{dispersion \\ term}} + \underbrace{\sum_{j=1}^{n} Q_{ij}^* Y_j + Q_i}_{source\,terms} \qquad (i=1,2,\ldots,n) \quad (1)$$

One application of the present modelling and simulation is the analysis of the dynamic behaviour of heat exchangers. Roetzel developed an axial dispersion model which simplifies the mathematical model of real heat exchangers and reduced the problem into a dynamic system with one-dimensional spatial coordinate[1]. The general form of his model can be expressed as follows

$$B_i \frac{\partial t_i}{\partial \tau} + U_i \frac{\partial t_i}{\partial x} = D_i \frac{\partial^2 t_i}{\partial x^2} + \sum_{j=1}^{n_w} H_{ij}(t_{wj} - t_i) + Q_i \quad (i = 1, 2, \ldots, n_f) \quad (2)$$

$$b_{wi} \frac{\partial t_{wi}}{\partial \tau} = D_{wi} \frac{\partial^2 t_{wi}}{\partial x^2} + \sum_{j=1}^{n_f} H_{ij}(t_j - t_{wi}) + q_{wi} \qquad (i = 1, 2, \ldots, n_w) \quad (3)$$

In some processes the mathematical models might be strongly nonlinear. Applying the dispersion model to a simultaneous adsorption process of multicomponent system in liquid chromatography will yield [2]

$$\frac{\partial c_i}{\partial \tau} + F \sum_{j=1}^{n} \frac{\partial q_i}{\partial c_j} \frac{\partial c_j}{\partial \tau} + U_i \frac{\partial c_i}{\partial x} = D_i \frac{\partial^2 c_i}{\partial x^2} \qquad (i = 1, 2, \ldots, n) \quad (4)$$

where the Langmuir isotherm $q_i = a_i c_i / \left(1 + \sum_{j=1}^{n} b_j c_j\right)$ is used. In the present investigation such types of transport processes are described by a

general form of the partial differential equation system, which can be solved analytically by means of Laplace transform if the parameters involved are constant or by means of the finite-difference method with moving grid technique for general cases. Based on the analytical and numerical solutions, the software "TAIPE" is developed to simulate the transient transport processes.

2   Mathematical model of the transient transport processes with axial dispersion

In order to deal with the multicomponent diffusion problems, the governing equation system will be expressed in a more general form

$$B_i\frac{\partial Y_i}{\partial \tau} + U_i\frac{\partial Y_i}{\partial x} = \sum_{j=1}^{n} D_{ij}\frac{\partial^2 Y_j}{\partial x^2} + \sum_{j=1}^{n} Q_{ij}^*Y_j + Q_i \quad (i = 1, 2, \ldots, n)\,(5)$$

In fact, Eq. (5) describes a general one-dimensional transport process. The two terms of the left side of the equation are the mass/energy accumulation and the convective mass/energy transport, respectively. The first term of the right side represents the mass/energy transport driven by their field potentials, where D_{ij} is the axial dispersion coefficient defined by Fick's law or Fourier's law which represents not only the physical properties of materials (e.g. diffusivity, conductivity) but also the flow muldistributions and the microscopic details of the solid medium. Therefore the dispersion coefficient must either be measured or deduced from a similar system. The dispersion coefficient matrix used in Eq. (5) describes a multicomponent diffusion, in which the off diagonal coefficients $D_{ij,i\neq j}$ are called the "cross-term" diffusion coefficients and are often ten percent or less of the main diffusion coefficient D_{ii} [3]. In the present investigation the Danckwerts boundary condition [4]

$$x = 0: \quad \sum_{j=1}^{n} D_{ij}\frac{\partial Y_j}{\partial x} = \max(U_i, 0)(Y_i - Y_{in_i}) \qquad (i = 1, 2, \ldots, n)\,(6)$$

$$x = L: \quad \sum_{j=1}^{n} D_{ij}\frac{\partial Y_j}{\partial x} = \max(-U_i, 0)(Y_i - Y_{in_i}) \qquad (i = 1, 2, \ldots, n)\,(7)$$

is used. The boundary conditions (6) and (7) result from the conservation laws of mass and energy. They indicate that there is no axial dispersion before the inlet section and after the outlet section of the apparatus being investigated. Equations (5)-(7) together with the user-supplied initial distributions, inlet variations and source terms can then be solved analytically or numerically.

3 "TAIPE"-a powerful tool to simulate the transient transport processes

To obtain the dynamic response of the transport process defined by Eqs. (5)-(7), a software "Transient Analysis In Process Engineering" (TAIPE) is being developed, which offers the tools of the transient analysis for variable kinds of transport processes, their analytical and numerical solutions as well as frequently used mathematical subroutines. As examples two kinds of them will be described in details as follows.

3.1 The solution for linear processes with constant parameters

First we consider a simple case in which the parameters $B_i, U_i, D_{ij}, Q_{ij}^*$, are constant, the initial distributions are uniform and the source term Q_i and the inlet conditions are functions of time. Thus the Laplace transform can be applied to Eqs. (5)-(7), which yields an ordinary differential equation system

$$\sum_{j=1}^{n} D_{ij} \frac{d^2\tilde{Y}_j}{dx^2} - U_i \frac{d\tilde{Y}_i}{dx} - \sum_{j=1}^{n} (\delta_{ij}sB_i - Q_{ij}^*)\tilde{Y}_j = -(B_iY_{0_i} + \tilde{Q}_i)(i = 1, 2, \ldots, n) \quad (8)$$

$$x = 0: \quad \sum_{j=1}^{n} D_{ij} \frac{d\tilde{Y}_j}{dx} = \max(U_i, 0)(\tilde{Y}_i - \tilde{Y}_{in_i}) \qquad (i = 1, 2, \ldots, n) \quad (9)$$

$$x = 0: \quad \sum_{j=1}^{n} D_{ij} \frac{d\tilde{Y}_j}{dx} = -\max(-U_i, 0)(\tilde{Y}_i - \tilde{Y}_{in_i}) \quad (i = 1, 2, \ldots, n) \quad (10)$$

where $\delta_{ii} = 1, \delta_{ij,j\neq i} = 0$. In general, the solution of Eq. (8) in Laplace domain can be expressed in a matrix form

$$\boldsymbol{Y} = \boldsymbol{U}e^{\Lambda x}\boldsymbol{R} + \boldsymbol{S} \tag{11}$$

where $\boldsymbol{U} = \{\boldsymbol{u}_1, \boldsymbol{u}_2, \ldots, \boldsymbol{u}_m\}$, $\Lambda = diag\{\lambda_1, \lambda_2, \ldots, \lambda_m\}$. λ_i and $\boldsymbol{u}_i$ are the eigenvalues and the corresponding eigenvectors of Eq. (8), respectively. $\boldsymbol{S}$ depends on the initial values and source terms, whereas $\boldsymbol{R}$ is determined by the boundary conditions. The form of the complete expression of the solution is tedious but there is no mathematical difficulty to obtain it. Therefore it will not be listed here. The FFT algorithm is applied to Eq. (11) to get its inverse transformation numerically. However, this algorithm will introduce additional impulses near discontinuity points. The maximum magnitude of these additional impulses could reach 0.8949 times as much as the magnitude of the real step change [5]. This phenomena is called Gibbs phenomena and cannot be eliminated by increasing the number of the points. To avoid such additional impulses, a very small dispersion coefficient D_{ii} could be added into the governing equation system.

3.2   Numerical simulation for general cases

If the equation system is not linear, the Laplace transform cannot be applied to Eqs. (5)-(7). In such cases TAIPE uses the finite-difference method to solve the governing equation system numerically. The Crank-Nicholson scheme is used to discretize the partial differential equation system. The convection term is treated with the power-law scheme by Patankar [6], which is a good approximation of the exponential scheme. It should be mentioned that in chemical processes the axial dispersion coefficient might be very small. In such a case the numerical "diffusion" due to truncation error may be larger than the physical dispersion. The calculated profile would be flattened by the numerical diffusion as is shown in Fig. 1. Therefore a very small grid width is demanded for small values of dispersion coefficients,
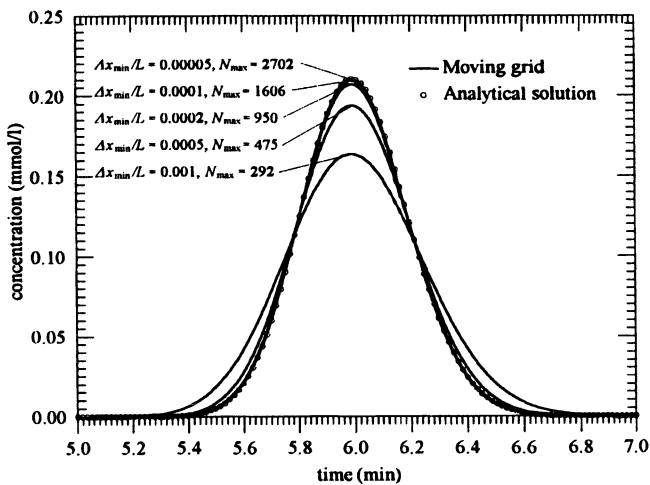
Fig. 1. The elution profile for a single system. Comparison of the numerical results with the analytical solution. $a = 5ml/ml$, $b = 0ml/mmol$, $F = 1$, $L = 20cm$, $V = 2ml$, $\dot{V} = 1ml/min$, $Pe = 2000$, $c_{inj} = 0.1mmol/ml (0 < \tau \leq 0.001min)$.

which means much more computing time. In TAIPE the moving grid technique is applied, which divides the spatial interval automatically according to the interpolation error [7]. Figure 1 shows the comparison of the numerical results with the analytical solution. With the decrease of the minimum allowed grid width the calculated response is closing to the exact solution. If $\Delta x_{min}/L = 0.00005$, the numerical profile coincides with the analytical one but the maximum number of cells N_{max} is only 2702.

4 Applications and Discussions

4.1 Single-blow problem

Single-blow testing techniques are widely used to determine the heat transfer coefficients of the compact heat exchangers. The earliest single-blow model was proposed and solved by Anzelius [8], Nusselt [9], Hausen [10] und Schumann [11], in which there is neither the axial heat conduction in the wall nor the axial heat dispersion in the fluid. Using finite-difference method, Cai et al. solved the single-blow problem with the axial heat conduction in the wall [12]. The model which takes the axial dispersion into account was solved by Luo analytically [13], in which the heat conduction in the wall is neglected. Now we will apply TAIPE to a more realistic model of the single-blow problem

$$B\frac{\partial t_f}{\partial \bar{\tau}} + \frac{\partial t_f}{\partial \bar{x}} - \frac{1}{Pe}\frac{\partial^2 t_f}{\partial \bar{x}^2} = NTU(t_w - t_f) \tag{12}$$

$$\frac{\partial t_w}{\partial \bar{\tau}} - \gamma_w\frac{\partial^2 t_w}{\partial \bar{x}^2} = NTU(t_f - t_w) \tag{13}$$

$$\bar{x} = 0: \quad t_f - \frac{1}{Pe}\frac{\partial t_f}{\partial \bar{x}} = t_{f_{in}}(\bar{\tau}), \frac{\partial t_w}{\partial \bar{x}} = 0 \tag{14}$$

$$\bar{x} = 1: \quad \frac{\partial t_f}{\partial \bar{x}} = \frac{\partial t_w}{\partial \bar{x}} = 0 \tag{15}$$

$$\bar{\tau} = 0: \quad t_f = t_w = t_0 \tag{16}$$

The influences of Pe and γ_w on the outlet fluid temperature responses of the exchanger to a step change in inlet fluid temperature are shown in Figures 2 and 3, respectively. Both of them agree well with the data given by Luo [13] and Cai et al. [12], respectively.

4.2 Nonlinear chromatography

The dispersion model of the liquid chromatography for a multicomponent system is given by Eq. (4). On the substitution of the Langmuir isotherm in Eq. (4), TAIPE is applied to simulate the process numerically. The concentration variations of a binary system and a ternary system are given in Figures 4 and 5, respectively. The parameters used in the figures are taken from the literature [2] for comparison. The figures show that the present results agree with the results of Seidel-Morgenstern using finite element method [2]. However, the peak values of Seidel-Morgenstern in Fig. 5 is a little lower than those in the present work, probably because the grid width he used is still not small enough.

5   Conclusions

Using axial dispersion model we can simplify a real transport process into a one-dimensional one. The influence of the flow maldistribution is taken into account by adding a dispersion term into the governing equations. If the parameters involved are constant, the resulting partial differential equation system can be solved analytically by means of Laplace transform. For general cases the finite-difference method with moving grid technique can be used. The software "TAIPE" is developed to simulate the general one-dimensional transient transport processes. The results given by TAIPE are compared with the available data and good agreements are found between them. Because TAIPE is designed for the general cases, it is expected that it would be very useful in the transient analysis in process engineering.
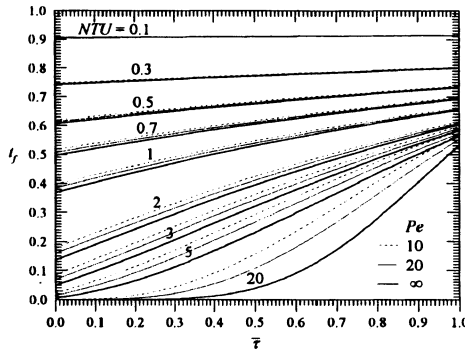
Fig.2. The outlet fluid temperature response to a step change in the inlet fluid temperature, $B = \gamma_w = 0$.
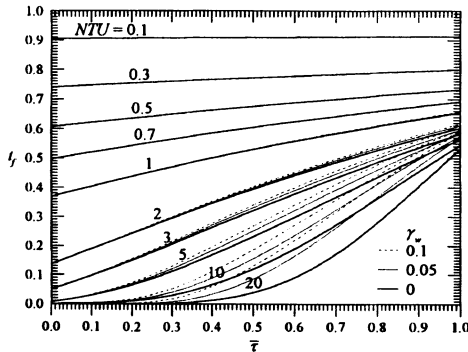
Fig.3. The outlet fluid temperature response to a step change in the inlet fluid temperature, $B = Pe = 0$.
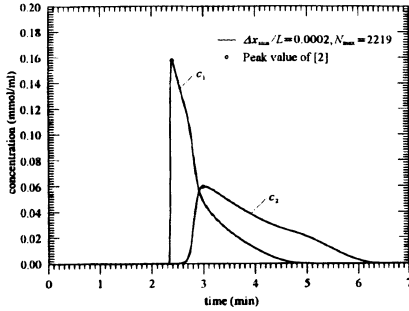
4131 **Fig. 4.** The elution profile for a binary system: $a_1 = 4ml/ml$, $b_1 = 4ml/mmol$, $a_2 = 5ml/ml$, $b_2 = 5ml/mmol$, $F = 1$, $L = 20cm$, $V = 2ml$, $\dot{V} = 1ml/min$, $Pe_1 = Pe_2 = 2000$, $c_{1inj} = c_{2inj} = 100mmol/ml (0 < \tau \leq 0.001min)$.

Fig. 5. The elution profile for a binary system: $a_1 = 4ml/ml$, $b_1 = 4ml/mmol$, $a_2 = 4.5ml/ml$, $b_2 = 4.5ml/mmol$, $a_3 = 5ml/ml$, $b_3 = 5ml/mmol$, $F = 1$, $L = 20cm$, $V = 2ml$, $\dot{V} = 1ml/min$, $Pe_1 = Pe_2 = 6000$, $c_{1inj} = 10mmol/ml$, $c_{2inj} = c_{3inj} = 100mmol/ml (0 < \tau \leq 0.001min)$.

Nomenclature

a,b   Langmuir constants

B   fluid/wall heat capacity ratio in the test core, dimensionless

c   concentration in the solution phase, mmol/ml

C   heat capacity, J/kgK

D   dispersion coefficient, cm^2/min

F   phase ratio, dimensionless

L   Length of the apparatus, cm

$\dot{M}$ mass flow rate, kg/s

NTU   number of transfer unit, dimensionless

Pe   dispersive Peclet number, , dimensionless

q   concentration in the absorbed phase, mmol/ml

s   Laplace parameter

t   temperature, K

U   flow velocity, $U = \dot{V}L/V$, cm/min

V   volume of the fluid in the apparatus, ml

$\dot{V}$ volumetric flow rate, ml/min

x   coordinate, cm

$\bar{x}$ dimensionless coordinate, $\bar{x} = x/L$, dimensionless

Greek symbols

γ_w dimensionless axial heat conductivity of the wall material,
        $\gamma_w = A_{qw}\lambda_w/\dot{M}_f C_f L$, dimensionless

τ time, min

$\bar{\tau}$ dimensionless time, $\bar{\tau} = \dot{M}_f C_f \tau / M_w C_w$, dimensionless

Subscript

f fluid

w solid wall

References

1. Roetzel, W., Transient Analysis in Heat Exchangers, proceedings of the ICHMT International Symposium on *New Development in Heat Exchangers*, Lisbon, 1993; published in New Developments in Heat Exchangers, pp. 547–575, N. Afgan et al (Editors), Gordon and Breach Publishers, OPA Amsterdam B. V., 1996.
2. Seidel-Morgenstern, A., *Mathematische Modellierung der präparativen Flüssigchromato-graphie*, Deutscher Universitäts-Verlag, Wiesbaden, 1995.
3. Cussler, E. L., *Diffusion-Mass Transfer in Fluid Systems*, 2nd edition, Cambridge University Press, Cambridge, 1997, pp. 185–187.
4. Danckwerts, P. V., Continuous Flow Systems - Distribution of Residence Times, *Chemical Engineering Science*, Vol. 2, No. 1, pp. 1–13, 1953.
5. *Handbook of Mathematics*, People's Education Publishing House, Beijing, 1979, pp. 537.
6. Patankar, S. V., *Numerical Heat Transfer and Fluid Flow*, McGraw-Hill, New York, 1980.
7. Nowak, U., Adaptive Linienmethoden für nichtlineare parabolische Systeme in einer Raumdimension, Technical Report of Konrad-Zuse-Zentrum für Informationstechnik Berlin, TR93 -14, 1993.
8. Anzelius, A., Über Erwärmung vermittels durchströmender Medien, *Zeitschrift für Angewandte Mathematik und Mechanik*, Vol. 6, No. 4, pp. 291 -294, 1926.
9. Nusselt, W., Die Theorie des Winderhitzers, *Zeitschrift des Vereines deutscher Ingenieure*, Vol. 71, No. 3, pp. 85–91, 1927.
10. Hausen, H., Über die Theorie des Wärmeaustausches in Regeneratoren, *Zeitschrift für Angewandte Mathematik und Mechanik*, Vol. 9, No. 3, pp. 173–200, 1929.
11. Schumann, T. E. W., Heat Transfer: A Liquid Flowing Through a Porous Prism, *Journal of the Franklin Institute*, Vol. 208, No. 3, pp. 405–416, 1929.
12. Cai, Z. H., Li, M. L., Wu, Y. W. and Ren, H. S., A Modified Selected Point Matching Technique for Testing Compact Heat Exchanger Surfaces, *International Journal of Heat and Mass Transfer*, Vol. 27, No. 7, pp. 971–978, 1984.
13. Luo, X., *Das axiale Dispersionsmodell für Kreuzstromwärmeübertrager*, Fortschritt-Berichte VDI, Reihe 19, Wärmetechnik/Kältetechnik, Nr. 109, VDI-Verlag GmbH, Düsseldorf, 1998.

A New Sparse Matrix Storage Method for Adaptive Solving of Large Systems of Reaction-Diffusion-Transport Equations

Nicolas Neuss

Ruprecht-Karls-Universität Heidelberg, 69120 Heidelberg, Germany

Abstract. We present a new method for storing sparse matrices as a block matrix-graph where the blocks are stored via a compact, row-ordered scheme. This combines the flexibility of the graph structure with the high efficiency of the compact storage technique. The inner compact pattern also allows identification of entries, which often leads to advantages with respect to memory and computing time. Using this technique in the PDE toolbox UG yields a flexible solver for large systems of reaction-diffusion-transport equations.

1   Introduction

Adaptivity is essential for the efficient numerical solution of partial differential equations. Together with the need to handle complicated domains, it is one of the main reasons why unstructured grids become almost mandatory for the discretization. These grids must be stored in an appropriate way, which is also influenced by the choice of programming language: FORTRAN implementations usually use index arrays, while C/C++ implementations often prefer pointers in order to represent the grid structure.

For the representation of the corresponding sparse linear systems, most applications use index arrays in the form of the "compact" or "Harwell-Boeing" storage technique[1]. Only rarely, the matrix is stored as a pointered graph (an example is given by the PDE package UG, see [Bas96],[BBJ+97]). Reasons are, first, that there are no well-known libraries for handling these graphs, and second, that due to the inefficient use of the memory cache this technique is less efficient on modern computers.

However, a pointer-based matrix graph has several advantages over the classical Harwell-Boeing format. First, it allows for the local insertion/deletion of matrix elements in $O(n)$ operations where n is the number of elements to be changed, which can be an advantage if moving reaction zones are adaptively resolved. Second, the unknowns can easily be reordered, which is useful for obtaining robust multigrid smoothers in regions of dominating convection or anisotropy. Finally, the parallelization on MIMD architectures can be done on an abstract graph level, see [BB94].

---

[1] See **http://math.nist.gov/MatrixMarket** for more information

For systems of PDEs, another point must be considered. Often, several unknowns are collocated, and it may be necessary to treat the linear system while respecting this block structure (e.g., for the definition of preconditioners for CG iterations or smoothers inside of a multigrid cycle). This may be achieved quite easily by replacing single matrix entries with blocks, which also increases the performance significantly: the ratio of index information versus value information decreases, additionally the enhanced data locality leads to faster execution.

Yet, there are many systems of PDEs where the use of a full block for each edge in the graph of the block matrix is not adequate. Often, equations are not coupled that much. For example, there are many discretizations of reaction-diffusion-transport systems where the reaction terms lead to interactions only (or almost only) inside of the diagonal block. Now, storing full blocks may introduce a tremendous overhead in memory and computing time.

Here we introduce a new approach: sparse blocks are stored at the edges of a graph which is closely connected to the underlying grid, see Fig. 1. The local sparsity pattern of these blocks is determined by selecting between a limited number of row-ordered patterns. Additionally, identification of equal matrix entries is permitted, which can cut down memory needs even further. In this way a fully implicit solution of this kind of systems is possible, thus avoiding the potential problems of splitting approaches (see [SM96]).

2   Model problem

Let Ω be a domain in $I\!\!R^2$ or $I\!\!R^3$. For $i = 1, \ldots, N$, let $u^{(i)}$ be given flow fields satisfying $\text{div}\,u^{(i)} = 0$ everywhere, and let $D^{(i)}$ be symmetric positive definite tensor functions (diffusion tensors). Then we search for a vector function $Y = (Y^{(i)})_{i=1,\ldots,N}$ (species concentrations) satisfying

$$\frac{\partial Y^{(i)}}{\partial t} - \text{div}(D^{(i)}(x)\nabla Y^{(i)}) + \text{div}(u^{(i)}Y^{(i)}) = F^{(i)}(Y)\,, \ \forall i = 1, \ldots, N \quad (1)$$

for all $x \in \Omega$ and $t > 0$. These equations are supplemented with suitable boundary conditions (Dirichlet, natural, inflow, outflow) as well as prescribed initial values at $t = 0$.

In most of the interesting cases, the flow fields $u^{(i)}$ are not known apriori, but determined by an additional equation coupled to the system (1). Examples are combustion processes or (multiphase) reactive flow in porous media.

3   Discretization and solving

For the space discretization, we use vertex-centered finite volumes on a triangulation T with vertices $v_\lambda, \lambda \in \Lambda$, Λ being some index set. This yields a

stiff system of ODEs which should be handled by an implicit time-stepping scheme. The simplest representative of such a scheme is the implicit Euler method. Here, the iteration step from time t_k to time $t_{k+1} = t_k + \Delta t$ is of the form

$$\left(\frac{M_\lambda \delta_{\lambda\mu}}{\Delta t} - A_{\lambda\mu}^{(i)}\right) y_\mu^{(i)}(t_{k+1}) = \frac{M_\lambda}{\Delta t} y_\lambda^{(i)}(t_k) + M_\lambda F^{(i)}(\boldsymbol{y}(t_{k+1})) \qquad (2)$$

with M_λ denoting the volume of the box centered at v_λ and $A_{\lambda\mu}^{(i)}$ arises from discretizing the diffusion and convection terms in 1. Equation (2) is a nonlinear system in the vector $\boldsymbol{y} = (y_\mu^{(i)})_{i=1,\dots,N;\mu\in\Lambda}$. By applying Newton's method, we have to solve a linear system $Ky = b$ where

$$K_{\lambda\mu} = \left(\frac{M_\lambda \delta_\mu^\lambda}{\Delta t} - A_{\lambda\mu} - \nabla F_{\lambda\mu}\right) \qquad (3)$$

is a block matrix (every entry $K_{\lambda\mu}$ is an $N \times N$-block). Only $K_{\lambda\lambda}$ may be full (depending on the sparsity of ∇F), whereas the off-diagonal blocks $K_{\lambda\mu}$ are diagonal matrices. The non-zero pattern (at least a superset) of the diagonal blocks is known apriori: it contains the diagonal $(K_{\lambda\lambda})_{ii}, i = 1, \dots, N$ plus entries $(K_{\lambda\lambda})_{ij}$ where $\frac{\partial F^{(i)}}{\partial y_j}$ does not vanish. In some important cases, we know even more:

1. If $D^{(i)} = D^{(j)}$ and $\boldsymbol{u}^{(i)} = \boldsymbol{u}^{(j)}$ in (1) for some indices $i \neq j$, the corresponding elements $(K_{ii})_{\lambda\mu}$ and $(K_{jj})_{\lambda\mu}$ are equal for $\lambda \neq \mu$.
2. If $D^{(i)} = 0, \boldsymbol{u}^{(i)} = 0$ in (1) for some index i, then the corresponding elements $(K_{\lambda\mu})_{ii}$ vanish for $\lambda \neq \mu$.

It is clear that a direct decomposition of such a matrix would not be the right choice for larger $|\Lambda|$. However, a multigrid algorithm with point-block Gauss-Seidel smoothing (also called collective Gauss-Seidel smoothing) is a good choice, since it is known to be robust for certain limiting cases: first, for dominating diffusion it is robust by the multigrid properties, for dominating convection it can be made robust by stream-wise ordering of unknowns, and for dominating reaction the method reduces to an ordinary implicit Euler scheme on decoupled systems of ODEs. Nevertheless, to be really efficient, the matrix-vector operations performed during the iteration have to take into account the sparse structure of the whole matrix as well as the special sparse structure of the block entries.

4   Sparse matrix storage methods

As mentioned in the introduction, the most frequently used storage method for sparse matrices is via index arrays, a possible implementation being the structure from Table 1.

Table 1. Array implementation of a sparse matrix

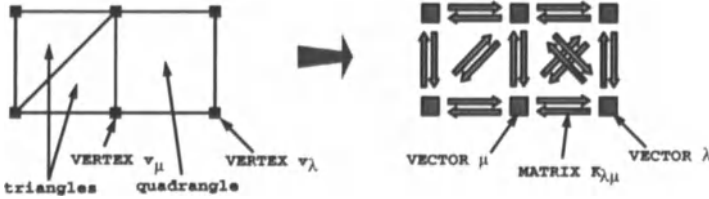| HARWELL_BOEING_TYPE_SPARSE_MATRIX		
int	nrows	number of rows
int	ncols	number of columns
int	N	number of nonzeros
int	row_off[nrows+1]	offsets for row starts/row ends in the col_ind and value arrays
int	col_ind[N]	N column indices
double	value[N]	N doublevalues

Fig. 1. Part of the grid and corresponding graph.

Table 2. The VECTOR and MATRIX data types.

VECTOR		
int	control	used bitwise
VECTOR	*pred, *succ	double linked list
MATRIX	*start	start of block row
double	value[nv]	block components

MATRIX		
int	control	used bitwise
MATRIX	*next	next in block row
VECTOR	*vect	column vector
double	value[nm]	block components

An alternative is storing a (block) matrix graph with the help of pointers. This format is used in the PDE toolbox UG, see [BBJ+97]. Here, a node of the matrix graph is called VECTOR, and an edge is called MATRIX. Bit information in the control field of VECTOR and MATRIX object allows for having different types of each. The pred and succ pointers connect all VECTOR objects in a doubly linked list which can be reordered without any effort. The start pointer in the VECTOR object gives access to the corresponding (block) matrix row which is a simple list connected by the next pointer of the MATRIX object. For our example in Section 6, we have one VECTOR for each vertex v_λ of T_h, and MATRIX structures exist only between vectors whose vertices are corners of a common element, see Fig. 1 and Table 2.

In the value array of the VECTOR object, the unknowns corresponding to that location are stored, e.g., the concentration of the chemical species at the

associated vertex of the triangulation. The value array of the MATRIX object contains the block $K_{\lambda\mu}$ for source VECTOR v_λ and destination VECTOR v_μ.

We now take advantage of the sparse structure of the blocks $K_{\lambda\mu}$ by storing only the nonzero entries in the value field, while the sparsity pattern is determined by one of several patterns of a form similar to Table 1. The type information in the control field of the MATRIX object determines which pattern is chosen. However, there is one important difference to Table 1: the double array value in Table 1 is replaced by an integer array offset. These integers are interpreted as offsets in the value-array of the MATRIX object in Table 2. Using the same offset several times then means using one double in the value array for several positions in the sparse block. This procedure, which we call *identification*, can lead to an enormous saving of memory for certain problems.

5   Efficiency tests

For testing the efficiency of the data structure described in Section 4, we concentrate on a basic building block of iterative solvers, namely the sparse matrix-vector-multiplication

$$x = Ky \tag{4}$$

where $K = (K_{\lambda\mu})_{ij}$, $\lambda, \mu \in \Lambda$, $i, j \in \{1, \ldots, N\}$, Λ indexes VECTORs, N is the number of species.

We choose the following easy testing configuration: the matrix graph is given by a nine-point stencil in 2D, the diagonal block has a full pattern (corresponding to a nonlinearity which couples each species with all others) while the pattern of the off-diagonal blocks is either full, or diagonal, or diagonal with all entries having the same value (in this case, only one value is stored). The ordering of the VECTORs is chosen to be lexicographic. The size of the matrix blocks (i.e. the number of species) is varied, and for each blocksize, the number of unknowns (given by the resolution of the underlying uniform square grid) is always chosen as large as possible, which may be considered as a worst case. Fig. 2 shows the results of this test. We can see that our matrix graph technique is much faster for problems with many species than for problems with only a few species.

To understand this phenomenon, one should know that on modern computers *random* access to main memory is much slower than register operations inside the CPU. This is overcome to a certain extent by the *caching* mechanism: between CPU and main memory lies a *cache* consisting of very fast memory chips. Whenever data from the main memory is asked for by the CPU, there is either a copy in the cache (which can be accessed without essential delay), or a whole block of data is transfered into the cache first
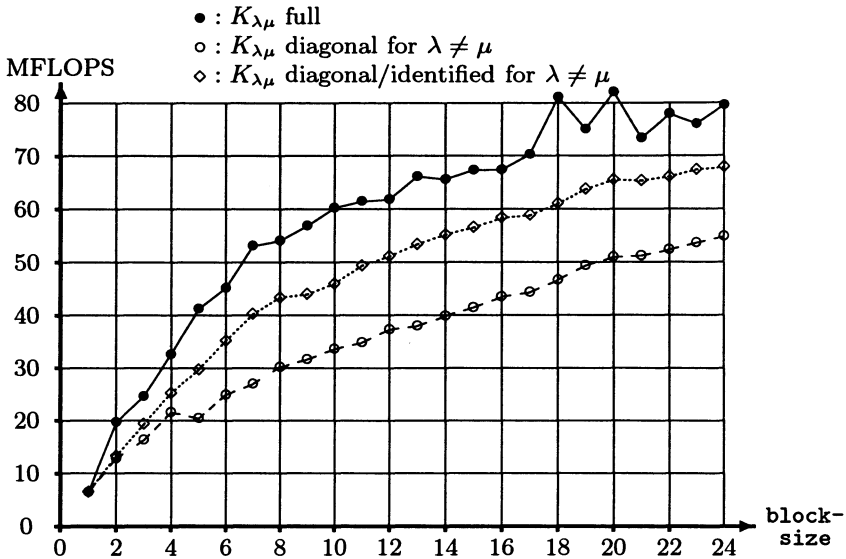
Fig. 2. Performance results (SGI Octane, 250 MHz).

(with some delay)[2]. Now the performance difference can be easily explained, since the grid-based graph structure represents a large memory overhead for few species, while the use of fixed sparsity patterns for the augmented blocks saves memory in the case of many species.

Doing the same test for the Harwell-Boeing scheme, one obtains performance values reaching from 40 MFLOPS (scalar case, and irregularly at larger blocksize) to slightly above 70 MFLOPS. Thus, for few species, the graph technique is much slower, while for the problems we are interested in, the performance is approximately the same or even better for the graph technique. It should be noted that the low efficiency for few species is much less dramatic if one considers the combination of assembling and solving. Since the matrix graph is coupled tightly to the underlying grid, the work for assembling will be of the same magnitude as the work for solving. In contrast, for many species the work for assembling can be much less than the work for solving by using identification of equal entries.

Finally, it is interesting to discuss how near these values are to the peak performance which can be obtained for this machine. If we measure the performance for a simple dot product between a short vector and chunks of a longer vector, which can be seen as the basic inner operation, we obtain a performance of about 100 MFLOPS. Thus, the limit performance of 80 MFLOPS

---

[2] Here are some numbers: on the SGI Octane the size of the (second level) cache is 1 MB, the blocks transferred to the cache have a length of 128 bytes and the delay time is something in the order of 100 CPU instructions.

is quite near to what one can reasonably expect. However, the main memory peak bandwidth of the SGI Octane lies at 1 GB/sec which would indicate a hardware limit of

$$(1 \text{ Multiplication} + 1 \text{ Addition}) \frac{1 \text{ GB/sec}}{8 \text{ Bytes}[=sizeof(double)]} = 250 \text{ MFLOPS} .$$

Yet, it seems as if this limit cannot be reached without very machine-specific optimizations.

Note that even higher MFLOPS rates can be obtained for algorithms which do more work locally (i.e. perform more floating point operations per cache miss). This is the case for direct solvers (see [Don98]) and for matrix–matrix–multiplications (both doing $O(N^3)$ operations on $O(N^2)$ data). For example, the LINPACK value of the SGI Octane is 409 MFLOPS.

6 Example

Consider the following setting, which arises for the modeling of a bio reme-diation problem[3]. First, a flow field is computed by solving Darcy's equation for a geostatistically generated permeability field. Apart from this stationary flow field, we have five substances in two states, mobile and immobile, plus an eleventh immobile species (bacteria). Following the procedure described in Section 2, we end up with a block sparse matrix with the block patterns

$$K_{\lambda\lambda} = \begin{pmatrix} * & 0 & 0 & 0 & 0 & * & 0 & 0 & 0 & 0 & 0 \\ 0 & * & 0 & 0 & 0 & 0 & * & 0 & 0 & 0 & 0 \\ 0 & 0 & * & 0 & 0 & 0 & 0 & * & 0 & 0 & 0 \\ 0 & 0 & 0 & * & 0 & 0 & 0 & 0 & * & 0 & 0 \\ 0 & 0 & 0 & 0 & * & 0 & 0 & 0 & 0 & * & 0 \\ * & 0 & 0 & 0 & 0 & * & * & * & * & * & * \\ 0 & * & 0 & 0 & 0 & * & * & * & * & * & * \\ 0 & 0 & * & 0 & 0 & * & * & * & * & * & * \\ 0 & 0 & 0 & * & 0 & * & * & * & * & * & * \\ 0 & 0 & 0 & 0 & * & * & * & * & * & * & * \\ 0 & 0 & 0 & 0 & 0 & * & * & * & * & * & * \end{pmatrix}, \quad K_{\lambda\mu} = \begin{pmatrix} a & 0 & 0 & 0 & 0 & 0 & 0 & 0 & 0 & 0 & 0 \\ 0 & a & 0 & 0 & 0 & 0 & 0 & 0 & 0 & 0 & 0 \\ 0 & 0 & a & 0 & 0 & 0 & 0 & 0 & 0 & 0 & 0 \\ 0 & 0 & 0 & a & 0 & 0 & 0 & 0 & 0 & 0 & 0 \\ 0 & 0 & 0 & 0 & a & 0 & 0 & 0 & 0 & 0 & 0 \\ 0 & 0 & 0 & 0 & 0 & 0 & 0 & 0 & 0 & 0 & 0 \\ 0 & 0 & 0 & 0 & 0 & 0 & 0 & 0 & 0 & 0 & 0 \\ 0 & 0 & 0 & 0 & 0 & 0 & 0 & 0 & 0 & 0 & 0 \\ 0 & 0 & 0 & 0 & 0 & 0 & 0 & 0 & 0 & 0 & 0 \\ 0 & 0 & 0 & 0 & 0 & 0 & 0 & 0 & 0 & 0 & 0 \\ 0 & 0 & 0 & 0 & 0 & 0 & 0 & 0 & 0 & 0 & 0 \end{pmatrix}, \quad \lambda \neq \mu .$$

Here, the letter a indicates that only one double value must be stored for $K_{\lambda\mu}$. Since we use hexahedra because of their better approximation proper-ties, we must store one diagonal block $K_{\lambda\lambda}$ and 26 off-diagonal blocks $K_{\lambda\mu}$ for every vertex of the grid. In total, this amounts to 1688 Bytes per ver-tex, while a performance measurement yields a value of 25 MFLOPS for a matrix–vector multiplication. The use of full blocks would be disastrous here, because it would need about 16 times more memory and the overall time for a matrix–vector multiplication would be more than eight times higher (a rough estimate of these numbers can be obtained from Fig. 2).

---

[3] This example is taken from a joint work with Christian Wagner (IWR, Universität Heidelberg) which will be covered in detail in a forthcoming paper.

In contrast, the Harwell-Boeing scheme is still an earnest competitor: with 2352 Bytes per grid node it needs about 40 % more memory to store the matrix while being about 75 % faster (45 MFLOPS). However, in any case it lacks the advantages of the graph structure concerning local modifiability, easy reordering and easy parallelization. For even larger number of species, also the advantage with respect to computing speed vanishes.

7 Conclusion

The augmentation of sparse blocks on a grid-based matrix graph allows for efficient storing and handling of general sparse matrices, if the size of the blocks (corresponding to the number of species for a convection–diffusion–reaction system of PDEs) is not very small. The use of this technique inside of the PDE toolbox UG gives the possibility to handle a broad class of convection-diffusion-reaction systems with parallel and adaptive multigrid.

Acknowledgment

References

[Bas96] P. Bastian. *Parallele adaptive Mehrgitterverfahren*. Teubner Skripten zur Numerik. Teubner, Stuttgart, 1996.

[BB94] P. Bastian and K. Birken. Dynamic Distributed Data (DDD) in a parallel programming environment — Specification and Functionality. Technical report, Rechenzentrum Universität Stuttgart, 1994.

[BBJ+97] P. Bastian, K. Birken, K. Johannsen, S. Lang, N. Neuß, H. Rentz-Reichert, and C. Wieners. UG – a flexible software toolbox for solving partial differential equations. *Comput. Visual. Sci.*, 1:27–40, 1997.

[Don98] J. J. Dongarra. Performance of various computers using standard linear equations software. Technical report, Computer Science Department, University of Tennessee, 1998.

[PEA+96] J. Philbin, J. Edler, O. J. Anshus, C. C. Douglas, and K. Li. Thread scheduling for cache locality. In *Proceedings of the Seventh ACM Conference on Architectural Support for Programming Languages and Operating Systems*, pages 60–73, Cambridge, MA, 1996. ACM.

[SM96] C. I. Steefel and K. T. B. MacQuarrie. Approaches to modeling of reactive transport in porous media. In P. C. Lichtner, C. I. Steefel, and E. H. Oelkers, editors, *Reactive Transport in Porous Media*, volume 34 of *Reviews in Mineralogy*, pages 83–129. Mineralogical Society of America, Washington, DC, 1996.

Part IV

Reaction Engineering

The Numerical Simulation of Annular Chromatography by Adaptive Finite Element Method

A. Thiele and L. Tobiska

Otto-von-Guericke-Universität Magdeburg, Institut für Analysis und Numerik

Abstract. The mathematical model of the annular chromatography consists of a coupled system of nonlinear convection diffusion equations. The model is discretized by the streamline diffusion method and the upwind finite element method, and the nonlinear system is solved by a simple iteration method. For linear adsorption isotherms both methods are compared on uniform and adaptive meshes, for various perturbation parameters and the influence of the coarse mesh and the flow direction on the quality of the numerical solution is considered. For the nonlinear convection diffusion equation we also examine the influence of the parameters of nonlinearity and the effect of a higher concentration at the inflow boundary.

1   Model of Annular Chromatography

A continuous rotating annular chromatograph was developed for preparative multicomponents separations [1]. Chromatography is increasingly applied for the separation and purification of different products in the biochemical and pharmaceutical industries. One way to perform a continuous separation is offered by the concept of annular chromatography (Figure 1).
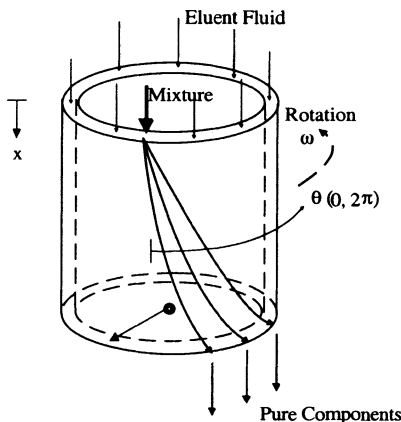
Fig. 1. Chromatograph

Here the stationary phase, a porous medium, is fixed between two concentric cylinders and this bed is rotating along a fixed feed port. The multicomponent mixture is dosed continuously on top of the apparatus at one rotating point and the mobile phase, an eluent fluid, is supplied everywhere else. The mixture is separated on its way downwards, because of their different affinity for the stationary phase [2]. Thus pure components can be collected continuously at the bottom of the apparatus at different angles relative to the stationary feed point.

Nonlinear adsorption isotherms according to the Multi-Langmuir equation are used to describe the equilibrium distribution between the mobile phase and the stationary phase. Based on the mass conservation combined with the nonlinear adsorption isotherms the mathematical model consists of a coupled system of nonlinear convection diffusion equations in two dimensions

$$\omega \frac{\partial c_i}{\partial \theta} + \omega F \frac{\partial q_i(c)}{\partial \theta} + u \frac{\partial c_i}{\partial x} = D_{ax} \frac{\partial^2 c_i}{\partial x^2} + D_{tan} \frac{\partial^2 c_i}{\partial \theta^2} \quad \text{in } \Omega, \quad i = 1, .., n$$

where q and c are related through the adsorption isotherms:

$$q_i(c) = \frac{a_i c_i}{1 + \sum_j b_j c_j} \quad i = 1, .., n.$$

There are n pure components in the mixture. The variables x and θ denote the axial coordinate and the angular coordinate respectively. Also, c_i is the concentration in the mobile phase and q_i the loading on the stationary phase, u is the axial velocity, ω the angular velocity and $D_{..}$ are the Dispersion coefficients. Finally F is given by $F = (1 - \epsilon)/\epsilon$ with the porosity ϵ.

2   Discretization

After introducing nondimensional variables, dispersion coefficients D_{ax} and D_{tan} and the width of the inflow are small parameters for practical problems. Because of the singular perturbation character of the problem stabilized discretisation methods and adaptive mesh refinements are used to guarantee a high accuracy of the numerical solution.

Let Ω be the unit square. For simulating the dosage of the mixture on top of the apparatus we take the following boundary condition:
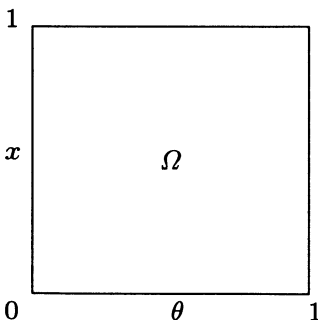
$$\Gamma_1 : c_i(\theta, 1) = \begin{cases} 1 & : \quad \theta \in [\gamma_1, \gamma_2] \\ 0 & : \quad \text{otherwise,} \end{cases}$$

$$c_i(0, x) = 0 \quad \forall x$$

$$c_i(1, x) = 0 \quad \forall x$$

$$\Gamma_2 : \frac{\partial c_i(\theta, 0)}{\partial n} = 0$$

where: $\gamma_1, \gamma_2 \in (0, 1)$ and $\gamma_2 > \gamma_1.$

Let $\gamma = \gamma_2 - \gamma_1$ be the width of the inflow.

We consider two types of stabilized discretizations for the problem above, an upwind finite element method and a streamline diffusion method. In both cases conforming finite elements with piecewise linear trial functions are used to approximate the solution.

The upwind finite element method is based on a special discretization of the convective term using a secondary grid of barycentric type [3]. In order to control the amount of upwinding and numerical viscosity in the scheme the corresponding weighting function is chosen as Samarskij upwinding.

In case of the streamline diffusion method we set the local streamline diffusion parameter δ_T equal to the diameter of the element T.

3 Solution of the Discrete Problem

In the case of low concentration of the mixture there is a linear relation between concentrations q_i and c_i:

$$q_i(c) = a_i \cdot c_i.$$

Then the above equations are linear and uncoupled:

$$-D_{tan}\frac{\partial^2 c_i}{\partial \theta^2} - D_{ax}\frac{\partial^2 c_i}{\partial x^2} + \omega(1 + Fa_i)\frac{\partial c_i}{\partial \theta} + u\frac{\partial c_i}{\partial x} = 0 \qquad \text{in } \Omega.$$

For the practical relevant case of higher concentration, the nonlinearity play an important rule. Thats why we examine the nonlinear case for one component. Solving the nonlinear case for one component we use a simple iteration method.

We note the equality

$$\frac{\partial q_i}{\partial \theta} = \Psi(c_i)\frac{\partial c_i}{\partial \theta} \qquad \text{with} \qquad \Psi(c_i) = \frac{a_i}{(1 + b_i c_i)^2}.$$

We set

$$\frac{\partial q_i^{k+1}}{\partial \theta} = \Psi(c_i^k)\frac{\partial c_i^{k+1}}{\partial \theta}$$

and obtain the following iteration rule:

$$D_{tan}\frac{\partial^2 c_i^{k+1}}{\partial \theta^2} + D_{ax}\frac{\partial^2 c_i^{k+1}}{\partial x^2} - \omega(1 + F\Psi(c_i^k))\frac{\partial c_i^{k+1}}{\partial \theta} - u\frac{\partial c_i^{k+1}}{\partial x} = 0.$$

As initial solution c_i^0 of the iteration we use the solution of the corresponding linear problem.

4   Numerical Tests

4.1   Influence of the perturbation parameter D

We investigate a simple linear case, for which we know the exact solution.
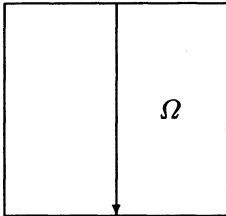
$$\omega = 0$$
$$u = -1$$
$$D = D_{tan} = D_{ax}$$
$$\gamma_1 = 0.495$$
$$\gamma_2 = 0.505$$
$$\gamma = 0.01$$

Ω

We compare the upwind finite element method and the streamline diffusion method using the exact solution for various small parameters D.
We use a coarse mesh and uniform refinement strategy as follows.

$\Longrightarrow$ 7 times
$\Longrightarrow$ 131841 Unknowns
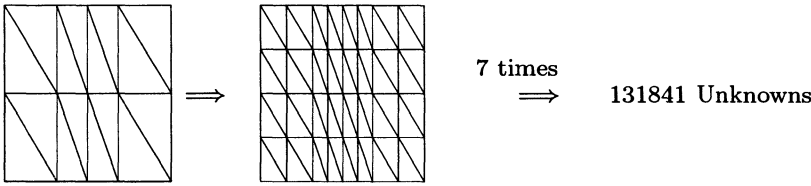
The Figures 2, 3 and 4 show $c_i(\theta, x = 0)$, the profiles at the outflow part.
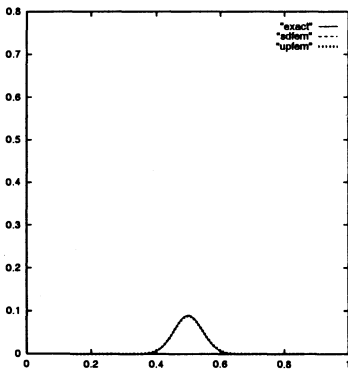
Fig. 2. $D_{ax} = D_{tan} = 10^{-3}$

The solutions of the streamline diffusion method and the upwind finite element method are compared with the exact solutions for various parameter D. The error of the solution using the upwind finite element method is always greater than the error of the solution using the streamline diffusion method (Table 1). The solution of the upwind finite element method is still acceptable for $D_{ax} = D_{tan} = 10^{-3}$ but is insufficient if the parameters D_{ax} and D_{tan} are very small.

Better solutions can be obtained by adaptive mesh refinements using the same number of unknowns. However, we still can observe the same effect with respect to the quality of the solution for decreasing values of D when comparing the upwind finite element solution with the solution of the streamline diffusion method calculated on a-priori or a-posteriori adaptive meshes.
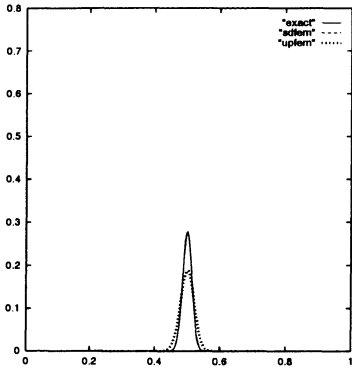
Fig. 3. $D_{ax} = D_{tan} = 10^{-4}$
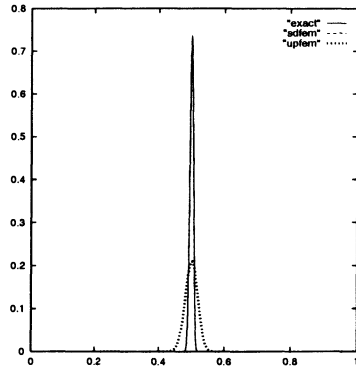
Fig. 4. $D_{ax} = D_{tan} = 10^{-5}$

Table 1. Relative error of $c_{i_{max}}(\theta, 0)$ using uniform meshes (%)

D	10^{-3}	10^{-4}	10^{-5}
UPFEM	1.57	32.1	71.5
SDFEM	0.51	0.41	0.005

4.2   Influence of the Mesh

Now we consider several coarse meshes (Figure 5 - 10), locally adapted to the behaviour of the solution, solving the same problem as before.
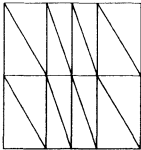
Fig. 5. Mesh m1
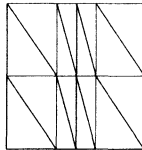
Fig. 6. Mesh m2
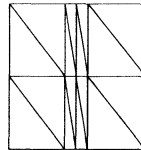
Fig. 7. Mesh m3
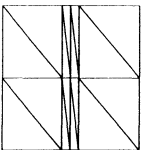
Fig. 8. Mesh m4
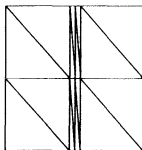
Fig. 9. Mesh m5
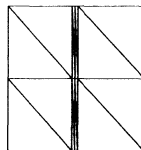
Fig. 10. Mesh m6

Let $D = D_{tan} = D_{ax} = 10^{-5}$.
We use the same mesh refinement as before and compute the solutions for the mehses m_i for both discretizations.
The solution of the streamline diffusion method is nearly independent of the used coarse mesh, but the solution of the upwind finite element method

strongly depends on the coarse mesh (Figure 11 and 12). The solution of the streamline diffusion method is acceptable in any case whereas the upwind finite element method requires locally adapted meshes (Table 2).
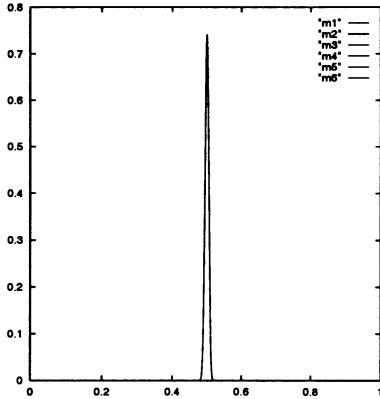
Fig. 11. SDFEM
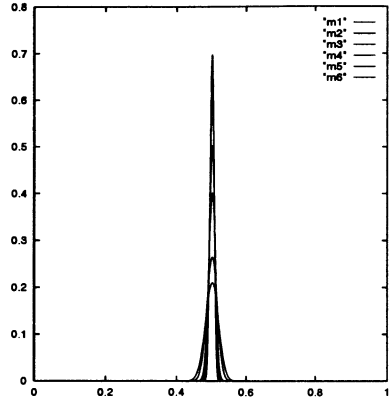
Fig. 12. UPFEM

Table 2. Relative error of $c_{i_{max}}(\theta, 0)$ (%)

Mesh	m1	m2	m3	m4	m5	m6
UPFEM	71.5	64.1	45.5	31.9	16.5	5.4
SDFEM	0.005	0.08	0.27	0.29	0.31	0.31

4.3   Influence of the flow direction

Now we consider the linear case with $\omega \neq 0$. Let $\omega(1 + F \cdot a) = 1$, $D = 10^{-4}$, $\gamma_1 = 0.0$ and $\gamma_2 = 0.01$, hence $\gamma = 0.01$.

$u : -5, -2, -1.1$

Ω
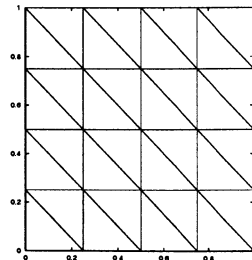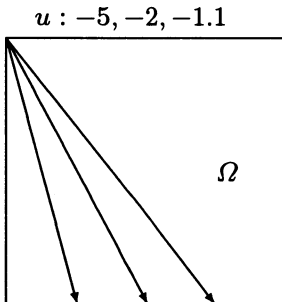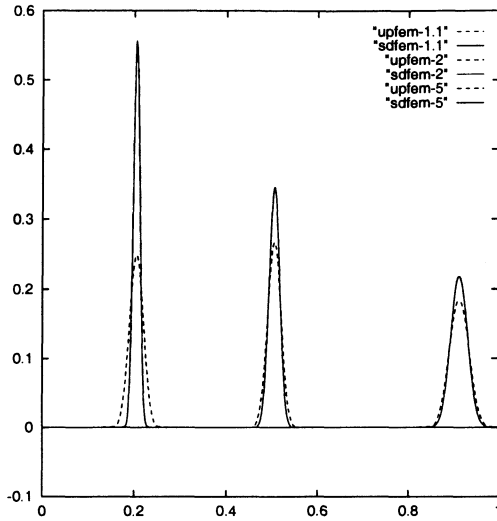
Fig. 13. SDFEM - UPFEM

We solve the problem for various u using an adaptive refinement strategy based on an error indicator like the gradient error indicator. The solution of the upwind finite element method is not acceptable if there is no alignment between the flow direction and the mesh, whereas the solution of the streamline diffusion method is better in all examples (Figure 13).

For the following numerical tests we only use the streamline diffusion method, because an optimal mesh alignment is not possible in the multicomponent case.

4.4   Influence of the Parameter of nonlinearity

Now we consider a nonlinear equation for one component, more precisely:

$$\Psi(c_i) = \frac{a_i}{(1 + b_i c_i)^2} \qquad \text{with} \qquad b_i \neq 0.$$

We are especially interested in the effect of the parameter of nonlinearity b_i on the profile of the solution at the outlet of the chromatograph.
Let $u = -2$, $\omega = 0.5$, $a_i = 1$, $F = 1$, $D_{ax} = 0.00114$ and $D_{tan} = 0.0$.
An increasing b_i leads to an elongation to the left side and to an asymmetric graph of the solution (Figure 14).

4.5   Concentration at the inflow

Last we change for fixed parameters $u = -2$, $\omega = 0.5$, $a_i = 1$, $F = 1$, $b_i = 1$, $D_{ax} = 0.00114$ and $D_{tan} = 0.0$, the height of concentration at the inflow boundary (Figure 15).
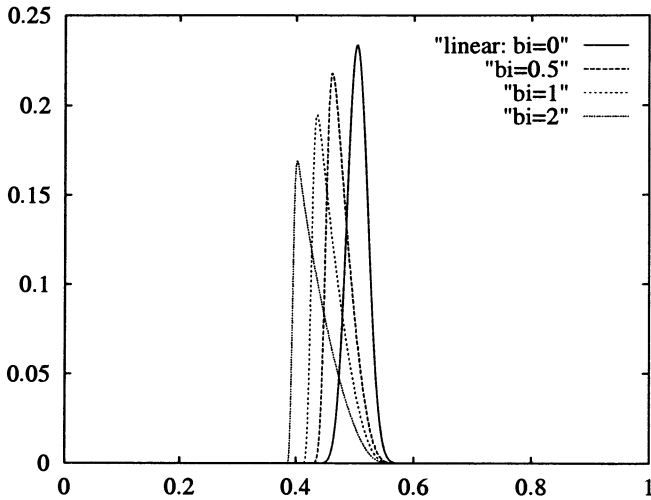
Fig. 14. Nonlinearity
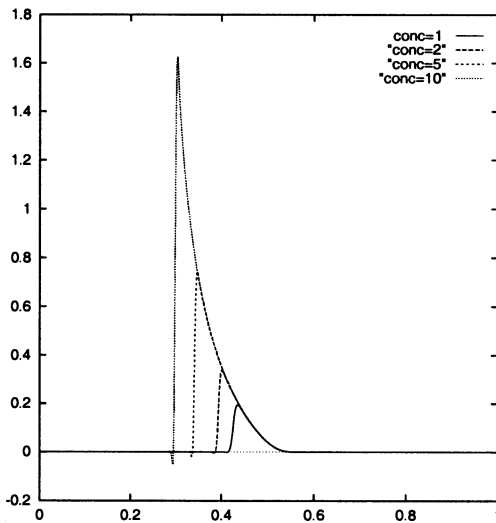
Fig. 15. Concentration at the inflow

References

1. A.V.P. Martin (1949) Dicuss. Faraday Soc. **7**, 332
2. C.H. Byers, W.G. Sisson, J.P. Carli, G. Carta (1989) Appl. Bioch. and Biotechn. **20/21**, 635
3. H.-G. Roos, M. Stynes, L. Tobiska (1996) Numerical Methods for Singularly Perturbed Differential Equations: Convection Diffusion and Flow Problems. Springer-Verlag Berlin Heidelberg New York

Modeling of Thermal Degradation of Polymers

Henning Bockhorn[1], Andreas Hornung[1], Ursel Hornung[1],
Petra Jakobströer[1], and Michael Wulkow[2]

[1] Institut für Chemische Technik, Universität Karlsruhe, Kaiserstr. 12, D-76128
    Karlsruhe, Germany
[2] CiT - Computing in Technology GmbH, Oldenburger Str. 200, D-26180
    Rastede, Germany

Abstract. A thorough understanding of the degradation mechanisms of polymers
is needed in order to predict the formation of gaseous products from thermal treat-
ment of plastic waste. To simulate the reactions of polydispers macromolecules a
high dimensional system of rate equations has to be solved. An efficient and flexible
algorithm based on a discrete Galerkin h-p-method which has been developed by
Wulkow was adapted in this study to the numerical simulation of polymer decom-
position.

Subject of investigation is the thermal degradation of polystyrene and polyethy-
lene. Random scission, "weak link"- scission, depropagation, inter- and intramolec-
ular H-transfer, β-scission, termination via recombination and the evaporation of
volatile oligomers is included in the kinetic schemes.

1   Introduction

Since several decades polymers are subject to investigation concerning their
reaction to thermal stress. In recent times the interest in thermal degradation
processes is intensified by the growing demand for recycling methods for
the increasing amount of plastic waste. A thorough understanding of the
degradation kinetics and advanced simulation methods are required to predict
the formation of gaseous products during the thermal treatment of plastic
waste [1].

The modeling of polymer reactions involves the solution of a high dimen-
sional system of rate equations. A number of methods has been developed
for this task, often employing simplifying assumptions. Recently, Wulkow de-
veloped an algorithm based on a discrete Galerkin h-p-method for modeling
of polymer reactions. The algorithm provides a method for the efficient and
flexible solution of polyreaction kinetics with no necessity of model reductions
and no restriction to the form of the molecular weight distribution [2].

The aim of this work is the modeling of complex polymer degradation
reactions. Two comprehensive models describing the thermal degradation of
polyethylene and polystyrene, respectively, are composed which establish a
basis for further work. Both polymers have been subject to numerous experi-
mental [3–11] and numerical [12–15] investigation. Several models include the
simultaneous independent scission of chains randomly and at the end [12,13].

However, these models do not take into account the nature of the radical chain mechanism where depropagation is a consecutive reaction of the slower bond scission.

Other studies use a radical chain mechanism usually accompanied by the assumption of quasistationarity for the radical concentration [14,5]. It is not considered that the polymer radical may undergo further bond scission. However, in case of high decomposition temperatures or stabilized radicals the secondary scission of radicals may have considerable influence. In this work the degradation process is simulated without the assumption of quasistationarity. Secondary scission of radicals is included in the thermal degradation mechanism of polystyrene because high radical concentrations are observed during the degradation [9].

2   Kinetic Scheme and Rate Constants

The degradation mechanisms of polyethylene and polystyrene both consist of a radical chain mechanism but they are different in several ways. Polystyrene pyrolysis yields monomer (>65%) and small oligomers [1] whereas polyethylene decomposes into a variety of saturated and unsaturated oligomers [16]. Additionally, the thermal degradation of polystyrene takes place at lower temperatures than the thermal degradation of polyethylene.

According to the degradation process of each polymer the kinetic schemes as discussed in the following are employed in the simulations.

Thermal Degradation of Polyethylene The initiation reaction of the thermal degradation of polyethylene is assumed to proceed via random chain scission of C-C bonds producing primary radicals. In literature the scission of "weak links" like branching points or the β-position of unsaturated links is also discussed [17,3,4]. The scission of "weak links" has an influence on the energy of activation but the product formation is not effected considerably. Because the "weak links" should be randomly distributed the random chain scission is supposed to be a suitable initiation step. One has to keep in mind that the energy of activation may be lower than the bond dissociation used in this simulation of 364 kJ/mol derived from the bond dissociation energy of butane [18]. As preexponential factor 10^{13} s^{-1} is proposed for the dissociation of molecules into radicals [18].

The macromolecular reactands include primary radicals, secondary radicals and unsaturated polymer and radical species. An overview is given in figure 1. A summary of the mechanistic scheme and the rate coefficients are displayed in table 1 and table 2, respectively.

Propagation reactions include intermolecular H-transfer and subsequent β-scission of the resulting secondary radical Rs to give again primary radicals and unsaturated polymer ^{D}PE. The depropagation reaction is not considered, because at low temperatures ethene is only a by-product [10]. Several authors
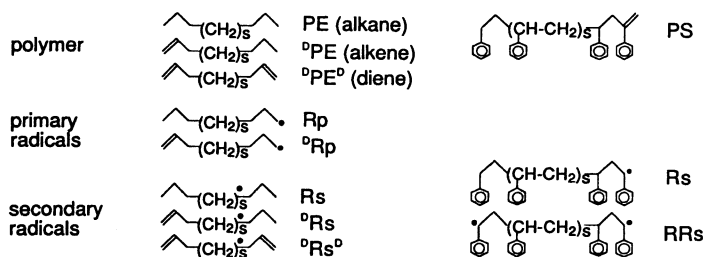
Fig. 1. Macromolecular reactands in PE and PS thermal degradation model

Table 1. Kinetic scheme of polyethylene thermal degradation

PE_s	$\longrightarrow$	$Rp_r + Rp_{s-r}$		
^DPE_s	$\longrightarrow$	$Rp_r + {}^DRp_{s-r}$	$s \times k_{ri}$	random chain scission
analog for $^DPE_s^D$				
$Rp_s + PE_r$	$\longrightarrow$	$PE_s + Rs_r$		
$Rp_s + {}^DPE_r$	$\longrightarrow$	$PE_s + {}^DRs_r$	$r \times k_{tr}$	intermol. H-transfer
$Rp_s + {}^DPE_r^D$	$\longrightarrow$	$PE_s + {}^DRs_r^D$		
analog for ^DRp_s				
Rs_s	$\longrightarrow$	$^DPE_r + Rp_{s-r}$	k_{bs}	$\beta - scission$
analog for ^DRs_s and $^DRs_s^D$				
$Rp_s + Rp_r$	$\longrightarrow$	PE_{s+r}	k_{tc}	recombination
analog for ^DRp_s and combinations				

additionally propose intramolecular H-transfer [4,3] which is not included in the mechanism of this work. This reaction increases the concentration of secondary radicals with the radical center near the end of the chain. Thus the amounts of small alkanes and alkenes would be increased, however, comparatively few products are affected. The energy of activation for intermolecular H-transfer is approximated by the activation energy for the hydrogen transfer from propane to ethyl radicals of 44 kJ/mol. The preexponential factor is proposed by Mita to be 10^7 to 10^8 (mol s)$^{-1}$ [17], therefore, a value of 5×10^7 (mol s)$^{-1}$ is used as preexponential factor in this calculation. The Arrhenius parameters for β-scission of secondary radicals are assumed to be 109 kJ/mol and 10^{13} s^{-1} [17].

Termination reactions are recombination and disproportionation of the radicals. The activation energies of such reactions are small, meaning that the radicals react when colliding. However, the influence of diffusion is not yet elucidated. A preexponential factor of 10^4 l (mol s)$^{-1}$ is proposed by

Mita [17]. The ratio of recombination to disproportionation for reactions of n-propane radicals is about 7/1 [17]. Therefore, as a first approximation only recombination is employed.

An essential feature of the polyethylene thermal degradation is the evaporation of gaseous compounds. The vapor pressure p_s of the oligomers in dependence on the number of carbon atoms n_C and temperature T / K can be estimated by the rule of Pictet-Trouton and the Clausius-Clapeyron equation. A similar estimation was performed by Ranzi et. al [14]. From the boiling temperatures of C_4 to C_{20} n-alkanes the boiling temperatures of the oligomers are approximated by $140 \times \sqrt{n_C}$. Then oligomers with their number of C-atoms larger than $n_C^* = (T/140)^2$ remain in the liquid phase at 1 atm pressure. Oligomers with their number of C-atoms smaller than n_C^* are supposed to be present in the gas phase.

Thermal Degradation of Polystyrene The initiation reaction of the thermal degradation of polystyrene is controversely discussed. The scission of "weak links" like head-to-head linkages or peroxides is assumed to be responsible for a rapid initial drop of the average molecular weight observed for radically polymerized polystyrene [17,6]. Recent studies evaluated the ratio of "weak links" to "strong links" to be 1/47 [13]. The ratio of "weak links" at the chain–end to "strong links" can maximally amount to $2/P_n$. Since P_n – the number average chainlength – for commercial polystyrene is typically in the range of 1000 only the scission of randomly distributed head-to-head bonds is considered in this work. However, further work is planned to investigate chain-end initiation and random scission of strong links. The preexponential factor k_{ri} used in the simulation represents the product of the pure rate of bond scission and the ratio of "weak links" to "strong links". Because the Arrhenius parameters of the initiation step have fundamental influence upon the overall reaction a parameter estimation is performed.

Table 2. Reaction rate parameters for PE and PS thermal degradation

	PE				PS			
	k_{ri}	k_{tr}	k_{bs}	k_{tc}	k_{ri}	k_d	k_{bb}	k_{ra}
$E_a/kJ/mol$	364	44	109	0	$-^*$	96	96	96
$lg(k_0 \times s)$	13.0	7.7	13.0	4.0	$-^*$	13.0	12.4	10.9

*parameter estimation see section 4

Depropagation and a back-biting mechanism – intramolecular H-transfer followed by β-scission – are responsible for the production of styrene monomer, dimer and trimer [8]. The energy of activation for depropagation is proposed by Richards and Salter to be 86-100 kJ/mol [7] in correspondence to values

of 103 kJ/mol calculated by Mita [17]. The mean value of 96 kJ/mol is used in the model. Because depropagation and β-scission of tertiary radicals are similar, the same activation energy is assumed. The termination reaction of polystyrene is found to be of first order [5]. Therefore, the first order termination via abstraction of small radicals – namely benzyl and diphenylpropane (DP) radical – from the tertiary radicals is introduced into the mechanism. The backbiting reaction may be simulated in one single step if a quasi equilibrium of secondary and tertiary radicals is assumed. The preexponential factor of the β-scission reactions can then be estimated according to the product ratio of monomer, dimer, trimer, benzyl and diphenylpropane radicals, respectively. Isothermal experiments yielded 65 % monomer, 1 % by-products including diphenylpropane and equal amounts of dimer and trimer [1]. The preexponential factors calculated according to these values are given in table 2. The kinetic scheme is shown in table 3.

Table 3. Kinetic scheme of polystyrene thermal degradation

$PS_s \longrightarrow Rs_r + Rs_{s-r}$		$s \times k_{ri}$	random chain scission
analog for Rs_s and RRs_s			
$Rs_s \longrightarrow Rs_{s-1} + styrene$		k_d	depolymerization
$RRs_s \longrightarrow RRs_{s-1} + styrene$		$2 \times k_d$	depolym. (dirad.)
$Rs_s \longrightarrow Rs_{s-2} + styrene\text{-}dimer$		k_{bb}	back-biting*
$Rs_s \longrightarrow Rs_{s-3} + styrene\text{-}trimer$			
analog for RRs_s			
$Rs_s \longrightarrow PS_{s-1} + benzyl\text{-}radical$		k_{ra}	radical abstr.*
$Rs_s \longrightarrow PS_{s-2} + DP\text{-}radical$			
analog for RRs_s			

* represents intramolecular H-transfer and subsequent β-scission

3   Simulation Procedure

The complete kinetic schemes are implemented into the simulation program PREDICI. The algorithm is based on a discrete Galerkin h-p-method which is described in detail by Wulkow [2]. The software includes a function for parameter estimation based on a modified Gauß-Newton method. The present models consist of up to seven distributions and 18 reaction steps ranging up to a chainlength of about 5000. Moreover, a correct point–wise resolution of the distributions is crucial for the evaporation process. Thus the complexity of the model can be considered as extremely high.

The initial distributions of the macromolecular reactands PE and PS are given by the generalized Schulz distribution [19]. Two initial distributions are employed in the simulation corresponding to an initial number average degree of polymerization $P_{n,0}$ of 500 and 2000 and a non-uniformity coefficient U_0 of 1 and 1/3, respectively.

4   Results and Discussion

Thermal Degradation of Polyethylene The thermal degradation of polyethylene is simulated at a decomposition temperature of 440 °C employing an initial distribution of $P_{n,0}=500$, $U_0=1$. Besides the evaporation of volatile alkanes contained in the initial distribution no significant product formation takes place within 400 min in contradiction to experimental results [10]. This indicates that the initiation rate is far too low. It can, therefore, be concluded, that either the scission of "weak links" like allyl-bonds is an important step in polyethylene decomposition, corresponding to a 50 - 60 kJ/mol lower activation energy[17], or that the preexponential factor is higher than the estimated value of 10^{13} s^{-1}.
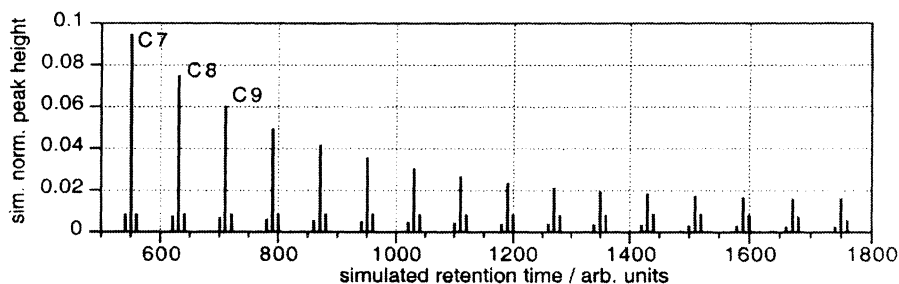
Fig. 2. Simulated gas-chromatogram of PE pyrolysis products

A part of the product distribution is shown in figure 2 in the form of a simulated gas-chromatogram. Alkanes are presented by the right peak of each group, alkenes and alkadienes by the middle and left peak, respectively. The alkenes clearly present the main products. This result is not in agreement with experiments, where alkanes are formed in even higher amounts than alkenes [11]. Further work should clarify wether the introduction of intramolecular H-transfer improves the agreement with experimental data.

Thermal Degradation of Polystyrene A parameter estimation is performed to evaluate the rate constant for random initiation k_{ri}. Experimental data from pyrolysis experiments in a gradient free isothermal reactor, developed for the determination of the decomposition kinetics of plastics [8],

are adapted. The parameter estimation for two degradation temperatures, 360 °C and 410 °C respectively, (initial distribution $P_{n,0}=500$, $U_0=1$) yields a preexponential factor $\log(k_0 \times s)$ of 8.8 - corresponding to $\log(k_0 \times s)=10.5$ per "weak link" if the share of "weak links" is 1/47 [13] - and an activation energy of 178 kJ/mol. Figure 3a) shows the comparison of the experimental conversion curve and simulations for two initial distributions.
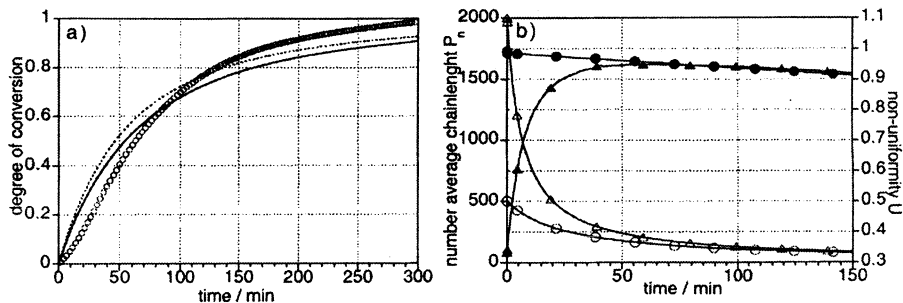
Fig. 3. (a) Degree of conversion for polystyrene thermal degradation, experiment *(circles)*; simulation $P_{n,0}=500$, $U_0=1$ *(solid line)*; $P_{n0}=2000$, $U_0=1/3$ *(dashed line)* (b) Simulated number average chainlength *(open marker)* and non-uniformity *(filled marker)*; $P_{n,0}=500$, $U_0=1$ *(circles)*; $P_{n,0}=2000$, $U_0=1/3$ *(triangles)*

The initial molecular weight distribution has only insignificant influence on the product formation. Of considerable interest is the developement of the molecular weight distribution shown in figure 3b). The number average chainlength P_n and the non-uniformity U for two different initial distributions ($P_{n,0}=500$, $U_0=1$ and $P_{n,0}=2000$, $U_0=1/3$) are displayed. Within the first 50 minutes of the degradation reaction the more uniform distribution is transformed via repeated scission and termination to the "most probable" distribution corresponding to $U=1$.

The evaluated activation energy for initial bond scission in polystyrene corresponds well to values obtained by Kuroki, 173 kJ/mol [6], and Carniti et al., 185 kJ/mol [9]. The preexponential factor proposed by Kuroki is three orders of magnitude higher, $\log(k_0 \times s)=12.0$ and similar to the preexponential factor $\log(k_0 \times s)=13.4$ evaluated by Carniti et al. [9]. The comparatively low value of $\log(k_0 \times s)=8.8$ per monomer unit derived in this work suggests that a further termination reaction of an approximate rate of 10^4 s^{-1} should be supplemented to the mechanism. Further work also will adress evaluation of models from overall kinetics as derived from isothermal measurements [8].

5 Conclusions

Complex reaction models are presented for the thermal decomposition of polystyrene and polyethylene establishing a basis for further work. The application of discrete h-p-Galerkin methods enables the simulation of complex thermal degradation processes of polymers within limited computation time. Further refinement of the kinetic scheme will allow the reliable prediction of the thermal degradation reactions of polymers and eventually polymer mixtures.

References

1. Bockhorn, H., Hornung, A., Hornung U. Macromolecular Symposia, in press
2. Wulkow, M. (1996) Macromol. Theory Simul. **5**, 393–416
3. Kuroki, R., Sawaguchi, T., Niikuni, S., Ikemura, T. (1982) Macromolecules **15**, 1460–1464
4. Holmström, A., Sörvik, E. M. (1974) J. Appl. Poly. Sci. **18**, 761–778
5. Lehrle, R. S., Peakman, R. E., Robb, J. C. (1982) Eur. Polym. J. **18**, 517–529
6. Kuroki, T., Ikemura, T., Ogawa, T., Sekiguchi, Y. (1982) Polymer **23**, 1091–1094
7. Richards, D. H., Salter, D. A. (1967) Polymer **8**, 139–152
8. Bockhorn, H., Hornung, A., Hornung, U. Twenty-Seventh Symposium (International) on Combustion, The Combustion Institute, Pittsburgh, PA, in press
9. Carniti, P., Gervasini, A., Beltrame, P. L. (1989) Journal of Polymer Science: Part A: Polymer Chemistry **27**, 3865–3873
10. Bockhorn, H., Hornung, A., Hornung, U. J. Anal. Appl. Pyrolysis, in press
11. Bockhorn, H., Hornung, A., Hornung, U., Schawaller, D. J. Anal. Appl. Pyrolysis, in press
12. Ebert, K. H., Ederer, H. J., Schröder, U. K. O., Hamielec, A. W. (1982) Makromol. Chem. **183**, 1207–1218
13. Madras, G., Smith, J. M., McCoy, B. J. (1996) Polymer Degradation and Stability **58**, 131–138
14. Ranzi, E., Dente, M., Faravelli, T., Bozzano, G., Fabini, S., Nava, R., Cozzani, V., Tognotti, L. (1997) J. Anal. Appl. Pyrolysis **40–41**, 305–319
15. Nyden, M. R., Coley, T. R., Mumby, S. (1997) Polymer Engineering and Science **37**, 1496–1500
16. Bockhorn, H., Hentschel, J., Hornung, A., Hornung, U. Chem. Eng. Sci., in press
17. Mita, I. (1978) in: Aspects of Degradation and Stabilization of Polymers. Degradation and Depolymerization Kinetics. Jellinek, H. H. G. (ed.), Elsevier, Amsterdam
18. Kerr, J. A. (1966) Chem. Rev. **66**, 465–500
19. Glöckner, G. (1987) Polymer Characterization by Liquid Chromatography. Elsevier, Amsterdam

Influence of Occupancy and Pore Network Topology on Tracer and Transport Diffusion in Zeolites

Marc-Olivier Coppens[1], Alexis T. Bell[2], and Arup K. Chakraborty[3]

[1] Department of Chemical Engineering
   Delft University of Technology, 2628 BL Delft, The Netherlands
[2] Department of Chemical Engineering
   University of California, Berkeley, CA 94720-1462, U.S.A.
[3] Department of Chemical Engineering and Department of Chemistry
   University of California, Berkeley, CA 94720-1462, U.S.A.

Abstract. We performed dynamic Monte-Carlo simulations of self-diffusion and transport diffusion on lattice models of zeolites, to study the influence of the strong adsorption sites and of various geometrical parameters. Despite the simplicity of the model, our results for self-diffusion confirm and explain the trends observed in pulsed-field gradient NMR experiments. Also for transport diffusion, agreement with recent chromatographic experiments is found. The Darken relationship could directly be verified at any occupancy. A mean-field theory predicts the results well, except for poorly connected lattices at high occupancy.

1 Introduction

With the advent of ever faster computers, dynamic Monte-Carlo simulations are an increasingly useful tool to investigate how diffusion in zeolites depends on various physico-chemical and geometrical parameters, such as the molecular occupancy θ, the pore network topology, and the types and numbers of adsorption sites. Knowing the sensitivity of the diffusivities to these parameters is essential to simulate and design separation and catalytic processes, which are often diffusion limited.

Parameters are easier to change in a computer than in an actual experiment, so that their influence can be more quickly revealed. Although computer simulations cannot replace experiments altogether yet, experimentally observed trends can be verified and explained. Moreover, carefully controlled diffusion experiments are hard to perform, and results based on different methods are regularly at odds, even for important zeolites like ZSM-5 [9,14,10]. Again, computer simulations can help to resolve these differences.

In this paper, we report on results from Monte-Carlo simulations of both self-diffusion, $\mathcal{D}$, and transport diffusion, $\mathcal{D}_T$, on lattice models of zeolites. More details about the method are provided in Sect. 2. Due to space limitations, we can only give an overview of the main findings; more information

can be found in [3–5]. Simulating hopping diffusion on a lattice is particularly useful to investigate the long-time diffusion properties that cannot be reached by performing more detailed, but far too slow Molecular Dynamics simulations. The coarse-grained, mesoscopic dynamic Monte-Carlo method is highly flexible and allows us to test a wide variety of problems. An analytical mean-field theory gives approximate solutions for the diffusivity, which can be compared with the Monte-Carlo results.

Self-diffusion, which is diffusion in the absence of a concentration gradient, is generally measured using a microscopic method, such as Pulsed-Field Gradient NMR. Our starting point in the study of the tracer or self-diffusivity, $\mathcal{D}$, is the wide variety of experimentally determined curves of $\mathcal{D}$ versus occupancy or loading θ, as reported in [8,10]. The Monte-Carlo simulations should give a better idea on the origin of this diversity.

Transport diffusion, on the other hand, occurs when a concentration gradient is present. The (Fickian) transport diffusivity is defined by the ratio of the flux to this concentration gradient. While the transport and self-diffusivities are equal at zero coverage, this is not the case at higher occupancies θ. A phenomenologic expression, known as the Darken relation, relates both diffusivities for pure components:

$$\mathcal{D}_T = \mathcal{D}_c \frac{d \ln p}{d \ln \theta}, \tag{1}$$

where θ is the sorbate occupancy or concentration in equilibrium with sorbate at pressure p. For a pure component, a simplified form of the Stefan–Maxwell approach shows that the ratio of both diffusivities can be related to the adsorption isotherm, and is a result of using a concentration gradient, instead of the more fundamental chemical potential gradient [11,12]. Macroscopic uptake or sorption measurements, if carried out carefully, can measure the transport diffusivity, $\mathcal{D}_T$, yet application of the Darken relationship leads to values for the so-called (thermodynamically) corrected diffusivity, $\mathcal{D}_c$, which are supposed to be, but are often not equal to independently measured self-diffusivities, $\mathcal{D}$. Differences can be as high as a few orders of magnitude and predicted trends as a function of loading can differ even qualitatively [10,2]. Monte-Carlo simulations of transport diffusion and comparison with self-diffusivities can directly test the relationship.

2   Method

A simple lattice model describes the zeolite pore network structure. During the Monte-Carlo simulations, molecules attempt to hop from one site on the lattice to another [17,6,16,3]. Time intervals are exponentially distributed. If a molecule attempts to hop to a free site, the hop is successful; if not, the molecule remains at the original site. A fraction f of the sites is strong, the remainder $1 - f$ is weak. The unit cell of the pore network can easily be

changed, so that any crystalline porous material can be simulated; we report results for a cubic lattice and for ZSM-5. Up to q molecules can occupy q sites inside the zeolite cages; intracage hopping is assumed to be a factor γ times more facile than hopping out and into another cage or, in the case of ZSM-5, to a channel site.

Self-diffusion is simulated in a sufficiently large collection of unit cells, applying periodic boundary conditions, i.e., molecules leaving the simulation space at one end enter the opposite end. A fraction θ of the sites is occupied. The self-diffusivity is evaluated using Einstein's relation:

$$\mathcal{D} = \lim_{t \to \infty} \frac{1}{6t} \langle |\boldsymbol{r}(t) - \boldsymbol{r}(0)|^2 \rangle, \tag{2}$$

in which $\boldsymbol{r}(t)$ is the position of a molecule at time t. For each set of parameters (f, q, θ, γ), ensemble averages $\langle \cdots \rangle$ are performed over a large number of simulations on different realizations of the network, resetting time to zero $(t = 0)$ after a long enough time for the system to equilibrate. More details can be found in [16,3,4].

Transport diffusion $\mathcal{D}_T(\theta)$ is simulated by imposing a concentration gradient $(\theta_2 - \theta_1)/L$ over the slab, where L is the length or the number of unit cells along the direction of the gradient. The average occupancy $\theta = (\theta_1 + \theta_2)/2$. The simulation program is similar to that for self-diffusion, although several runs with different L and (θ_1, θ_2) are performed, in order to verify linearity. The transport diffusivity is then estimated from:

$$\mathcal{D}_T = \lim_{t \to \infty} \frac{\mathcal{N}(t)}{S(\theta_2 - \theta_1)} \frac{L V_{u.c.}}{t}, \tag{3}$$

where $\mathcal{N}(t)$ is the net number of molecules flowing through the boundary planes on which the concentrations are imposed, S is the area of an edge, and $V_{u.c.}$ is the volume of the unit cell. Periodic boundary conditions are used along directions perpendicular to the gradient. Molecules leaving in the direction of the gradient are randomly readsorbed in order to conserve the occupancy. Molecules entering the bulk of the slab from the outside surface induce adsorption, while molecules hopping from within the slab to the outside surface lead to desorption, again to preserve equilibrium. Note that this is an approximation: statistical fluctuations of the occupancies on the outside layers are possible and could be simulated by imposing outside gas pressures and assuming a certain adsorption law, instead of imposing fixed boundary concentrations.

We could easily add interactions between neighboring molecules, but preferred to keep the model as simple as possible: it will indeed be seen from the simulations discussed in the next section that there is very good agreement with experimentally observed trends. Note, however, that interactions can be present and that, because of the modular structure of the model, additional features such as interactions can easily be added. Hopping rates could

be determined using, e.g., Transition State Theory or Molecular Dynamics (for a review, see [1,15]). Our model is indeed mesoscopic in nature, i.e., we desire to simulate the average- to long-time behavior of diffusion, based on parameters that can be obtained from short-time, microscopic methods.
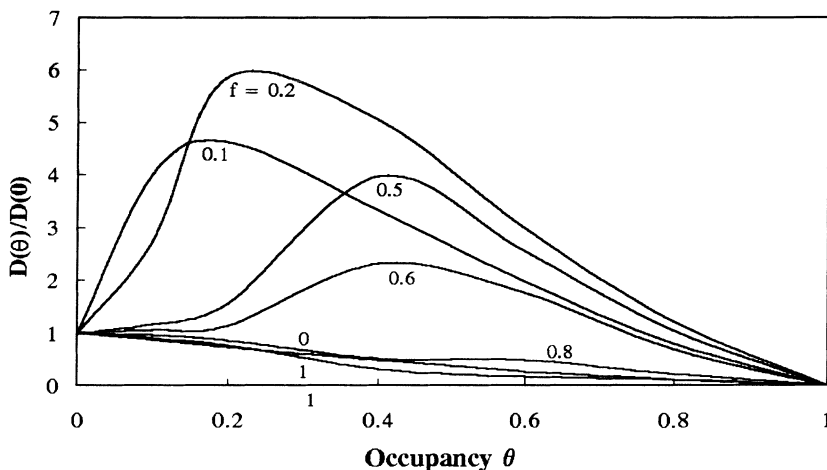
3   Results

3.1   Self-diffusion

Fig. 1. Self-diffusion in ZSM-5 with 2 sites per cage, $\tau_s/\tau_w = 100$ and $\gamma = 10$. Results are normalized with respect to diffusivity at zero occupancy

The topology of the pore network has an important effect on the self-diffusivity [3]. Let us first observe the situation with only one type of site and one site per cage, as is, e.g., the case for ZSM-5/silicalite. A molecule cannot move to a neighboring site when this site is occupied, thus increasing the probability to return to a recently occupied site, which is more likely to be vacant. These negative correlations in the molecular motion are more important at high occupancy θ on a poorly connected lattice, such as for ZSM-5, which has an average connectivity of 2.67 compared to 6 for a cubic lattice. If correlations were absent, the self-diffusivity would show a linear decrease with occupancy. The presence of correlations leads to negative deviations from this mean-field result.

A small fraction f of strong adsorption sites has a large impact on how the self-diffusivity $\mathcal{D}$ changes with occupancy θ. We simulated many cases [4], but one example, shown in Fig. 1, illustrates our main findings. The example in Fig. 1 is for ZSM-5 with 2 sites per cage, a ratio of average

adsorption times on strong and weak sites $\tau_s/\tau_w = 100$, and an intra- to extracage hopping probability ratio $\gamma = 10$, i.e., it is 10 times more likely for a molecule to attempt a hop to another site within the cage than it is to move out of the cage. For f near 0 or 1, the self-diffusivity decreases monotonically with θ. At low to average f, strong adsorption sites tend to be occupied first, enabling most molecules to move along paths that consist of mostly weak adsorption sites, when the occupancy is low. This leads to an increase of $\mathcal{D}$ with θ. At higher occupancies, the diffusivity reaches a maximum, then decreases, because the strong adsorption sites are saturated and molecules occupying both strong and weak adsorption sites increasingly hinder each others movement. This confirms the trends observed in PFG NMR experiments [8,10]. An initial plateau and inclination points, due to the filling of different types of sites (strong and weak sites in cages, less connected weak sites in the pore channels of ZSM-5), are also among the possibilities.
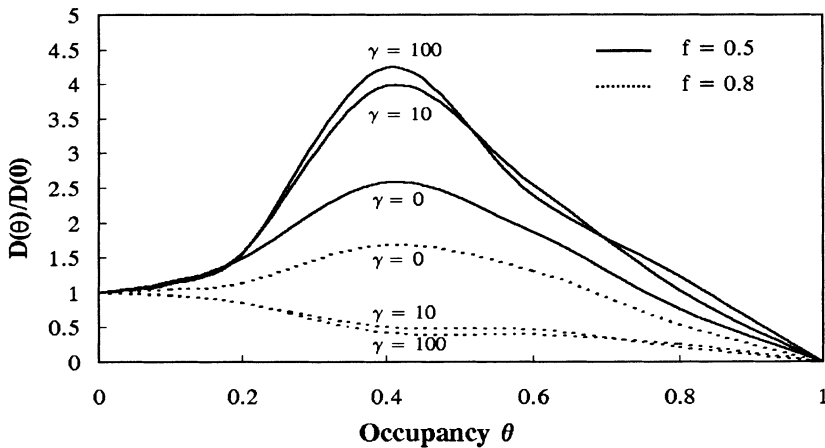
Fig. 2. Influence of the ratio of intra- to extracage hopping probabilities, γ, on the self-diffusivity in ZSM-5, with 2 sites per cage and $\tau_s/\tau_w = 100$

The effect of an increase in the number of sites per cage, $q > 1$, is to facilitate the passage of molecules through the cages, thus leading to higher peaks in the curves. Based on occupancy and flow balances between the different types of sites, algebraic equations for the self-diffusivity can be derived under the mean-field approximation that the concentration at each point is equal to the average concentration for that particular type of site (weak or strong cage or channel site). The formulae can be found in [4]. The higher q, the better the agreement between such mean-field calculations and the Monte-Carlo simulations, but qualitative agreement of the trends is remarkable, even for

one site per cage, except for average to high f and at high occupancy, because of the significance of correlation effects.

Also the intra- to extracage hopping probability ratio γ has an important influence for more complex lattices, such as ZSM-5 with 2 sites per cage. Figure 2 shows how an increase in γ leads to a significant increase in the self-diffusivity for $f = 0.5$, and how this trend is inverted for $f = 0.8$. When γ is high, a molecule adsorbed on a strong cage site is likely to attempt a move to the other cage site; if that site is weak, it will readily be vacated and diffusion is enhanced, but at higher f, it is likely to be strong as well, so that the cage is effectively blocked.

3.2 Transport diffusion
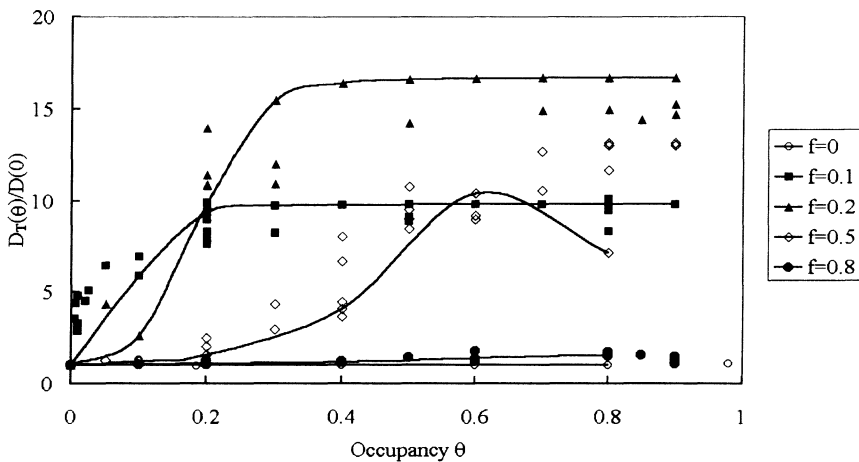
Fig. 3. Transport diffusion on a cubic lattice for $\tau_s/\tau_w = 100$ and different fractions f of strong adsorption sites. Symbols are Monte-Carlo simulation results, lines with symbols are corresponding mean-field results, using the Darken relationship

Figure 3 shows the transport diffusivity $\mathcal{D}_T$ on a cubic lattice as a function of occupancy, normalized with respect to the diffusivity in the limit of zero occupancy. The lines are mean-field approximations, the symbols are Monte-Carlo results. In the mean-field approximation, the transport diffusivity was calculated based on the Monte-Carlo or mean-field calculation of the self-diffusivity, $\mathcal{D}$, and applying the Darken relationship (1) with $\mathcal{D}_c = \mathcal{D}(\theta)$. A rather bold step was to use a Langmuir isotherm with mean-field approximations for the occupancies of strong and weak sites, to derive $d\ln p/d\ln\theta$.

In view of this approximation, the agreement is remarkably good, even up to high occupancies, except for intermediate fractions of strong sites $f \sim 0.5$.

Our results are in agreement with most experimental observations that, at very low occupancy ($\theta \to 0$), self- and transport diffusivities are equal to each other [10,13]. In this limit, the Darken relationship (1) holds with Henry's law, $p \sim \theta$. For $f = 0$ or $f = 1$ (only weak or strong sites), we also confirm that the transport diffusivity is independent of occupancy, as found in experiments and simulations of hopping diffusion of molecules that cannot pass each other [17].

Recent chromatographic experiments of diffusion of iso-butane and iso-butene in silicalite [7] show that the diffusivity of iso-butane hardly changes with occupancy, while the diffusivity of iso-butene sharply increases up to a constant plateau value at low occupancies, when a small fraction of defects in the silicalite are present. The defects act as strong adsorption sites for the unsaturated iso-butene (small $f > 0$), but not for the saturated iso-butane ($f = 0$). Therefore, this observation agrees well with our simulations. More details will be published shortly [5].

4   Conclusion

Diffusion in zeolites strongly depends on the pore network topology and on the types and fractions of the different adsorption sites. Simple Monte-Carlo simulations on a lattice model of the zeolite pore network enable us to efficiently study a particular system. The calculated trends are in agreement with experimental observations. This "meso-scale" method has the advantage that it can predict long time values using a few microscopic parameters, whereas more detailed methods cannot reach this long time regime for other than the simplest systems. Mean-field calculations can quickly estimate the diffusivity, although large deviations from the Monte-Carlo values occur when long-time correlations are present, i.e., at higher occupancies, when the site distribution is strongly heterogeneous and the connectivity of the network is low.

Acknowledgement

References

1. Bell A.T., Maginn E.J., Theodorou D.N. (1997) Molecular Simulation of Adsorption and Diffusion in Zeolites. In: Ertl G., Knozinger H., Weitkamp J. (Eds.) Handbook of Heterogeneous Catalysis. VCH, Germany.
2. Brandani S., Hufton J., Ruthven D. (1995) Self-Diffusion of Propane and Propylene in 5A and 13X Zeolite Crystals Studied by the Tracer ZLC Method. Zeolites 15:624–631
3. Coppens M.-O., Bell A.T., Chakraborty A.K. (1998) Effect of Topology and Molecular Occupancy on Self-Diffusion in Lattice Models of Zeolites – Monte-Carlo Simulations. Chem. Engng Sci. 53:2053–2061
4. Coppens M.-O., Bell A.T., Chakraborty A.K. (1998) Dynamic Monte-Carlo and Mean-Field Study of the Effect of Strong Adsorption Sites on Self-Diffusion in Zeolites. In press for Chem. Engng Sci.
5. Coppens M.-O., Bell A.T., Chakraborty A.K. (1999) In preparation.
6. Hinderer J., Keil F.J. (1996) Three-Dimensional Monte-Carlo Simulations of Diffusion and Reaction Phenomena in Zeolites. Chem. Engng Sci. 51:2667–2672.
7. Hufton J.R., Ruthven D.M., Danner R.P. (1995) Adsorption and Diffusion of Hydrocarbons in Silicalite at Very Low Concentration: Effect of Defect Sites. Microporous Materials 5:39–52
8. Kärger J., Pfeifer H. (1987) N.M.R. Self-Diffusion Studies in Zeolite Science and Technology. Zeolites 7:90–107
9. Kärger J., Ruthven D.M. (1989) On the Comparison Between Macroscopic and N.M.R. Measurements of Intracrystalline Diffusion in Zeolites. Zeolites 9:267–281
10. Kärger J., Ruthven, D.M. (1992) Diffusion in Zeolites and Other Microporous Solids. Wiley, New York
11. Krishna R. (1990) Multicomponent Surface Diffusion of Adsorbed Species: A Description Based on the Generalized Maxwell–Stefan Equations. Chem. Engng Sci. 45:1779–1791
12. Krishna R. (1993) A Unified Approach to the Modelling of Intraparticle Diffusion in Adsorption Processes. Gas Separation & Purification 7:91–104
13. Nijhuis T.A., Van den Broeke L.J.P., Van de Graaf J.M., Kapteijn F., Makkee M., Moulijn J.A. (1997) Bridging the Gap Between Macroscopic and NMR Diffusivities. Chem. Engng Sci. 52:3401–3404
14. Pfeifer H., Freude D., Kärger J. (1991) Basic Principles and Recent Results of ^{1}H Magic-Angle-Spinning and Pulsed Field Gradient Nuclear Magnetic Resonance Studies on Zeolites. In: Öhlmann et al. (Eds.) Catalysis and Adsorption by Zeolites. Elsevier, Amsterdam, 89–115
15. Theodorou D.N., Snurr R.Q., Bell A.T. (1996) Molecular Dynamics and Diffusion in Microporous Materials. In: Atwood J.L et al. (Eds.) Comprehensive Supramolecular Chemistry. Pergamon, Oxford, 507–548
16. Trout B.L., Chakraborty A.K., Bell A.T. (1997) Diffusion and Reaction in ZSM-5 Studied by Dynamic Monte-Carlo. Chem. Engng Sci. 52:2265–2276
17. Tsikoyiannis J.G., Wei J. (1991) Diffusion and Reaction in High-Occupancy Zeolite Catalysts – I. A Stochastic Theory Chem. Engng Sci. 46:233–253

Modeling of pressure fields in various environments including damping effects and change of wave velocity due to the emergence of cavitation bubbles

Sascha Dähnke[1] and Frerich J. Keil[1]

Technical University of Hamburg-Harburg, Eissendorfer Strasse 38, D-21071 Hamburg, Germany email: keil@tu-harburg.de

Abstract. In sonochemical reactors the effect of emerging cavitation bubbles has significant influence on the amplitude and structure of the sound field. Calculations show that the damping parameter and the phase velocity may, depending on the pressure amplitude, change in several orders of magnitude. In this work a new method will be presented, which enables one to calculate the time- dependent three-dimensional pressure field in sonochemical reactors of various shapes taking inhomogeneous distributed wave parameters into account, which are a function of the spatial depending pressure amplitude. Also some results for different reaction vessels are shown.

1 Introduction

The radiation of the liquid by ultrasound causes a series of compression and rarefaction cycles which create areas of high and low local pressures. During the rarefaction phase of the pressure wave a cavitation bubble will emerge if the local under-pressure reaches the cavitation threshold pressure (Apfel (1984); Trevena (1984)).

An important task for sonochemistry in industry is to develop ultrasonic reactors for different reactions with optimized characteristics, like a maximum volume fraction of cavitation zone which is essential to get a high reaction yield. To do so the sound field inside the sonoreactors has to be calculated. As a first step in this direction pressure fields in homogeneous media in reactors of different geometric shapes with various dimensions were calculated (Keil and Dähnke (1996) and Keil and Dähnke (1997) 11, 12). In three subsequent papers (Dähnke and Keil (1998) 5-7) a new model has been proposed to calculate the three-dimensional pressure field in a liquid with an inhomogeneous distribution of cavitation bubbles. In two following papers (Dähnke and Keil (1998) 8, Dähnke et al.(1998) 9), a new approach has been presented where the pressure field in any sonochemical reactor was calculated including an inhomogeneous density distribution of cavitation bubbles dependend on the spatial varying sound amplitude of the pressure waves. The bubble volume fraction β of the developing cavitation bubbles will be related to the pressure values, and the damping parameters α and phase velocities c resulting

from the bubbles present are calculated by the theories of Commander and Prosperetti (1989).

In this work a model is presented that predicts at least approximately the number and kind of cavitation bubbles in sonochemical reactors of different geometric shapes and applications.

2   Theory

The present work is based on the numerical solution of a modified time-dependent three-dimensional wave equation. It is a modification of the homogeneous wave equations in three-dimensions taking the results of Commander and Prosperetti (1989) and damping phenomena into account.

Our starting point is the three-dimensional homogeneous wave equation (Junger and Feit (1986)):

$$\Delta(\mathbf{r}, t) = \frac{1}{c_{liq}^2} \frac{\partial^2 p(\mathbf{r}, t)}{\partial t^2} \tag{1}$$

c_{liq} describes the sound velocity in the liquid onephase medium. The presence of cavitation bubbles in an ultrasonic irradiated fluid causes, amongst other effects, a local change of the density and the compressibility. Taking this into account, an additional term arises:

$$\Delta p(\mathbf{r}, t) + \rho_{mix}(\mathbf{r}) \left[\vec{\nabla} \frac{1}{\rho_{mix}(\mathbf{r})} \right] \left[\vec{\nabla} p(\mathbf{r}, t) \right] = \frac{1}{c_{mix}^2 (\mathbf{r})} \frac{\partial^2 p(\mathbf{r}, t)}{\partial t^2} \tag{2}$$

Damping of waves in a lossy fluid means an exponential decrease of wave energy with distance. It can be described in the one-dimensional case by the equation

$$p(x, t) = e^{i(kx - \omega t)} e^{-\alpha x}, \tag{3}$$

which expresses a propagating pressure wave, which amplitude decreases with $e^{\alpha x}$. Introducing the relation $x = c^* t$, applying an equation similar to (3) in three dimensions and calculating the second derivatives in space and time, a differential equation with a damping term results:

$$\frac{\partial^2 p(\mathbf{r}, t)}{\partial t^2} + 2\alpha' \frac{\partial p(\mathbf{r}, t)}{\partial t} = \frac{\alpha'^2 + \omega^2}{k^2} \Delta p(\mathbf{r}, t). \tag{4}$$

Considering the time-dependent wave equation, the description of the damping as a function of time leads to equivalent results.

Over the last decade, much work has been done to describe the influence of a bubbly liquid on the propagational characteristics of wave motion (Nakoryakov et al. (1993); Prosperetti et al. (1988); Prosperetti and Commander (1989); Gumerov (1994); Sangani (1991); Blake (1994) and Ye and Ding (1995)). The main wave parameters, namely damping coefficient α and phase velocity c_{mix}, may change in several orders of magnitude due to the

bubble presence. For example, the speed of sound in the bubbly medium (down to 20 ms^{-1}) is quite different from that of a pure liquid (in pure water approximately 1500 ms^{-1}) or the pure gas (340 ms^{-1} for air), which is in the bubble. One main result of the work of Commander and Prosperetti (1989), consists of the homogeneous wave equation (1) with an additional source term.

$$\Delta p(\mathbf{r}, t) = \left[\frac{1}{c_{liq}{}^2} + 4\pi \int\limits_0^\infty \frac{R_0 f(\mathbf{r}, R_0)}{\omega_0(R_0)^2 - \omega^2 + 2ib\omega} dR_0 \right] \frac{\partial^2 p(\mathbf{r}, t)}{\partial t^2} \qquad (5)$$

$R(\mathbf{r}, R_0, t)$ defines the instantaneous bubble radius at position r and time t having an equilibrium radius R_0 and $f(\mathbf{r}, R_0)dR_0$ the number of bubbles per unit volume with equilibrium radius R_0 between R_0 and $R_0 + dR_0$. ω is the angular frequency of the pressure field, ω_0 the resonance frequency of a single cavitation bubble and b a damping constant refering to one single vibrating bubble that arises from viscous, thermal and acoustic effects. A second final result of the work of Commander and Prosperetti is the complex wavenumber, k_{mix}, which is given by the dispersion relation

$$k_{mix}(\mathbf{r}) = \frac{\omega^2}{c_{liq}{}^2} + 4\pi\omega^2 \int\limits_0^\infty \frac{R_0 f(\mathbf{r}, R_0)}{\omega_0{}^2 - \omega^2 + 2ib\omega} dR_0 \ , \qquad (6)$$

which implies the damping coefficient $\alpha(\mathbf{r})$ and phase velocity $c_{mix}(\mathbf{r})$ of the acoustic waves. To calculate the wave number k_{mix}, a certain radial distribution has to be considered. We followed the suggestions of Commander and Prosperetti (1989), who proposed a gaussian radii distribution with a range of bubble radii from $R_1 = 5 \times 10^{-6}$m to $R_2 = 3 \times 10^{-3}$m and a standard deviation σ of about 2×10^{-3} m.

As yet, we are not aware of any experimental or theoretical results concerning the dependency of the bubble density distribution on the amplitude or frequency of the surrounding sound field. Therefore, as a first approximation, we start with a simple relationship between the bubble volume fraction and the pressure amplitude: The bubble volume fraction β should be linear dependent on the amplitude and restricted in a range from 10^{-4} up to 10^{-1}. Furthermore, no cavitation bubbles emerge below a pressure threshold of 10^6 Pa = 10 bar, which is the only parameter that is experimentally confirmed (Prosperetti and Commander (1989), Ye and Ding (1995),Yount et al. (1984)). The limit of the pressure amplitude, at which the bubble volume fraction reaches its upper limit, has been varied from $5*10^7$ Pa to 10^8 Pa to take more than one possible damping characteristic into consideration. Above these upper pressure limits, the bubble volume fraction remains constant.

Unfortunately, the complex character of the factor on the right-hand side of eq. (5) may cause a negative real part at certain pressure values. This leads to an unstable condition for a numerical solution of this equation. To calculate

the developing three-dimensional pressure field, the differential equation (4) will be solved by applying the approach of finite differences. The resulting finite difference equation which is based on eq. (4) is solved explicitly for $p(\boldsymbol{r}_i, t_{j+1})$, the pressure value at position $\boldsymbol{r}_i$, for a subsequent time-step. With this final equation one is able to calculate the pressure at a subsequent time step for the entire interior of the reactor if the pressure values at two previous points in time are known. The initial conditions can be described with a zero pressure amplitude at the time zero and a harmonic change of a certain pressure distribution at the surfaces of the transducers. At the transducer complex harmonic boundary conditions were used. The boundary conditions in the region of the transducer read

$$\bar{p}\,(\boldsymbol{r}, t) = p_0(\boldsymbol{r})cos(\omega t) + i \cdot p_0(\boldsymbol{r})sin(\omega t). \tag{7}$$

i represents the imaginary unit.This procedure enables one to determine immediately the sound field amplitude at each point in time and space by taking the absolute value of the complex pressure value. In order to determine an amplitude dependent bubble density for every point in time and space this is a very helpful procedure. At the water surface an ideal pressure-release boundary was assumed, signified by a vanishing pressure:

$$\bar{p}\,(\boldsymbol{r}, t) = 0. \tag{8}$$

The remaining boundaries are assumed to act like ideal-rigid walls, which can be described by a vanishing normal pressure derivative to the respective surface where n is the normal unit vector.

$$\frac{\partial\,\bar{p}\,(\boldsymbol{r}, t)}{\partial \boldsymbol{n}} = \boldsymbol{n}\,\overrightarrow{\nabla}\bar{p}\,(\boldsymbol{r}, t) = 0, \tag{9}$$

3   Modeled sonochemical reactors and boundary conditions

Two different types of ultrasonic reactors (Fig. 1) were analyzed and their pressure fields calculated as a function of the transducer's frequency and two different damping characteristics. The first reactor (Fig. 1a) has a simple geometry: the ultrasonic transducer is a circular plate with a diameter of 0.06 m which performs a harmonic movement in the z-direction. Acoustic waves are generated and emerge from the bottom of the reaction vessel. The outer shape of the reactor is a circular tube with a height of 0.15 m. The second reactor (Fig. 1b) that was modeled is a cylindrical tube with the same dimensions as reactor 1. An ultrasonic horn emits the acoustic waves from a height of 0.075 m downwards to the bottom. All the calculations were carried out for transducer frequencies of 20 and 50 kHz and an uniform transducer surface amplitude of 10^{-5} m.

(a)   (b)
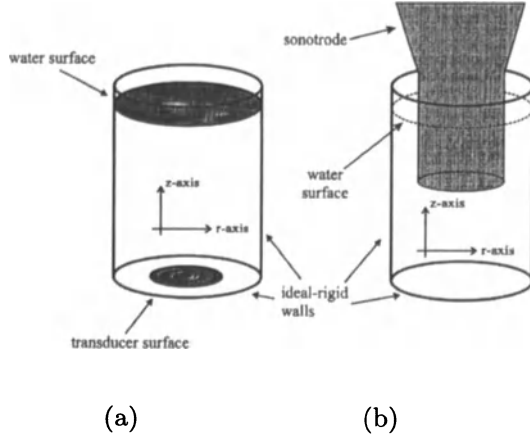
Fig. 1. Two types of modeled sonochemical reactors

4   Results

The influence of the emerging cavitation bubbles on the amplitudes and geometric structure of the sound field for two transducer frequencies of 20 and 50 kHz are analyzed. To show the difference of the sound field properties with and without the presence of bubbles is the main task in this section. In Fig. 2 the undamped pressure field amplitudes for the reactor of type (Fig. 1a) one for the two frequencies are shown.

a)   b)
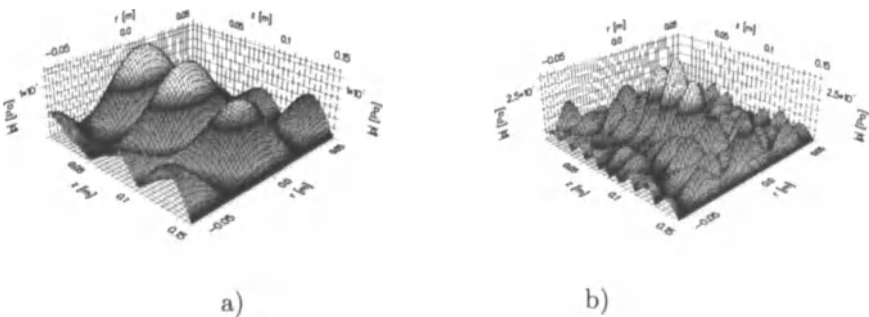
Fig. 2. Undamped pressure field for reactor type one for transducer frequencies of a) 20 kHz and b) 50 kHz.

On the left side of the coordinate system the transducer is located and the right side represents the water surface. One can see that the number of maxima and the absolute maximum of the pressure amplitudes is increased in Fig. 2 b). This is due to the higher frequency and the assumed constant

amplitude of the transducer. In Fig. 3, the results in the case of the cavitation bubble's presence are shown.

a)   b)
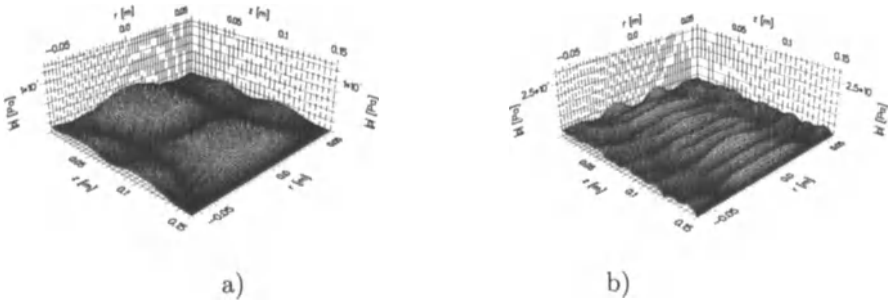
Fig. 3. Pressure field for reactor type one in the case of bubble presence for transducer frequencies of a) 20 kHz and b) 50 kHz.

The amplitudes in the case of bubble presence for both frequencies shows a remarkable decrease of approximately halb a magnitude. Furthermore, the structure of the sound field has significantly changed. The most remarkable structure change is visible in the case of a 20 kHz stimulation. The number of the main maxima is reduced from three to two. This effect is a result of the additional change of phase velocity which alters the wavelength of the sound waves. In Fig. 4 the pressure fields for reactor type two in the undamped case for both transducer frequencies are shown. The area of zero pressure amplitudes is dedicated to the body of the sonotrode.

a)   b)
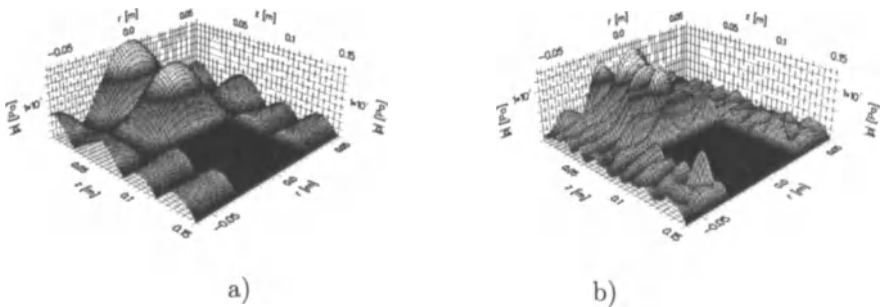
Fig. 4. Undamped pressure field for reactor type two for transducer frequencies of a) 20 kHz and b) 50 kHz.

For this reactor type the nearly identical total maximum of the pressure amplitudes for both frequencies is remarkable. This can be explained by the "disadvantageous" distance of the sonotrode to the opposite boundary regarding the frequency of 50 kHz. In this case, the distance may not be a multiple of the wavelength ($\lambda = 0.0288$ m, $dist = 0.075$ m $\rightarrow \lambda/dist = 2.604$; both boundary surfaces are determined to be ideal rigid) which causes a decrease of the acoustic energy density. The effect of emerging cavitation bubble

is presented in Fig. 5. Again the amplitudes and the structure of the sound field change significantly.
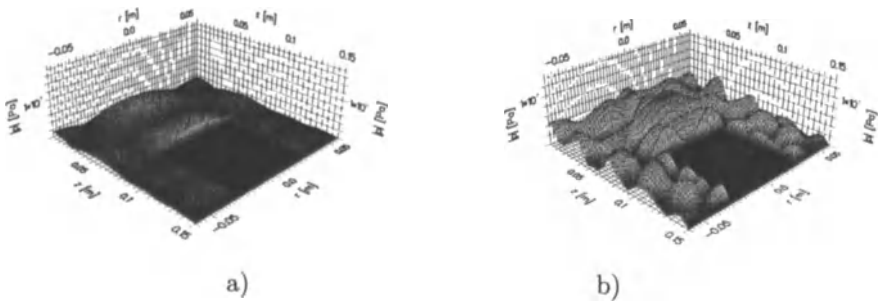
Fig. 5. Pressure field for reactor type two in the case of bubble presence for transducer frequencies of a) 20 kHz and b) 50 kHz.

Compared to the results of reactor type one for a frequency of 50 kHz the relative decrease of amplitudes is lower for reactor type two. It can be justified by the lower total maximum of the undamped field which causes smaller damping coefficients and changes of wave velocity.

5   Summary

A numerical method has been presented which predicts the pressure field distribution in ultrasonic reactors by solving the inhomogeneous three-dimensional time-dependent wave equation, using the approach of finite differences. The change of wave parameters due to the inhomogeneous distributed cavitation bubbles has been calculated using the work of Commander and Prosperetti (1989). To relate the bubble density to the sound field amplitude, a linear approach was initially employed. The influence of emerging cavitation bubbles on the amplitude and structure of the sound field could be shown.

6   Notation

b	damping constant refering to one single vibrating bubble arising from viscous, thermal and acoustic effects
c_{liq}	sound velocity in an homogeneous one-phase liquid
$c_{mix}(\mathbf{r})$	spatial dependent sound velocity in the mixture of liquid and gas bubbles
c	constant of the Gaussian distribution of the relative number of the bubbles as a function of their radius
$f(\mathbf{r}, R_0)$	relative bubble density at $\mathbf{r}$ for bubbles having a equilibrium radius R_0
i	imaginary unit
k	wave vector in an undamped fluid (without imaginary part)

k_{liq}	wave vector in an homogeneous one-phase liquid ($= 2\pi/\lambda$)
$k_{mix}(\mathbf{r})$	spatial dependent wave vector in the mixture of liquid and gas bubbles
$\mathbf{n}$	unit normal vector belonging to a certain boundary
$p(\mathbf{r}, t)$	pressure value depending on the vector $\mathbf{r}$ at a time t
$p(\mathbf{r}_i, t_j)$	pressure values at distinct points in the finite difference scheme
$p_0(\mathbf{r})$	pressure amplitude distribution at the surface of the transducer
$\mathbf{r}$	coordinate vector
t	time coordinate
Δt	finite difference time step
$\mathbf{u}$	velocity of the fluid medium
x	spatial coordinate in an one-dimensional system
$R(\mathbf{r}, R_0, t)$	instantaneous bubble radius at time t at position $\mathbf{r}$ having an equilibrium radius R_0
R_0	equilibrium radius of a cavitating bubble

7 Greek Letters

$\alpha(\mathbf{r})$	spatial-dependent attenuation coefficient due to the presence of cavitation bubbles in the liquid
$\alpha'(\mathbf{r})$	modified attenuation coefficient for the case of time-dependent damping
$\beta(\mathbf{r}, t)$	spatial- and time-dependent bubble volume fraction
κ_{liq}	compressibility of the homogeneous one-phase medium
ρ_{liq}	density of the homogeneous one-phase medium
$\rho_{mix}(\mathbf{r})$	spatial dependent density in the mixture of liquid and gas bubbles
ω	circle frequency
ω_0	resonance frequency of a cavitation bubble

8 Differential operators

$\vec{\nabla}$	nabla operator
Δ	laplace operator

9 References

1. Apfel, R.E., 1984, Acoustic cavitation inception. Ultrasonics 22, 167-173.
2. Blake, J.R.; Boulton-Stone, J.M. and Thomas, N.H. (editors), 1994, Bubble dynamics and Interface Phenomena. Kluwer Academic Publishers, London.

3. Commander K.W. and Prosperetti, A., 1989, Linear pressure waves in bubbly liquids: Comparison between theory and experiment. J. Acoust. Soc. Am. 85, 732-746.

4. Junger, M.C. and Feit, D., 1986, Sound, Structures, and Their Interaction. MIT Press, London.

5. Dähnke, S. and Keil, F. J. Modeling of three-dimensional pressure fields in sonochemical reactors with a homogeneous and inhomogeneous density distribution of cavitation bubbles Ind.Eng.Chem.Res. (1998) 37 848-864

6. Dähnke, S. and Keil, F. J. Modeling of sound fields in liquids with an inhomogeneous distribution of cavitation bubbles as a basis for the design of sonochemical reactors. Chem. Ing. Tech. (1998) (in german) (submitted)

7. Dähnke, S. and Keil, F. J. Modeling of linear pressure fields in sonochemical reactors of various shapes considering an inhomogeneous density distribution of cavitation bubbles. Chem. Eng. Sci. (1998) (in press)

8. Dähnke, S. and Keil, F. J. Modeling of sound fields in liquids with an inhomogeneous distribution of cavitation bubbles as a basis for the design of sonochemical reactors. Chem.-Eng.-Tech. (1998) (in german) (submitted)

9. Dähnke, S. and Keil, F. J. A comparative study on the modeling of sound pressure field distributions in a sonoreactor with experimental investigation. Ultrasonics Sonochemistry (1998) (submitted)

10. Gumerov, N.A., 1994, Equations describing the propagation of nonlinear modulation waves in bubbly liquids. in: Blake, J.R.; Boulton-Stone, J.M. and Thomas, N.H. (editors) Bubble dynamics and Interface Phenomena. Kluwer Academic Publishers, London.

11. Keil, F. J. and Dähnke, S. Numerical calculation of pressure fields in sonochemical reactors. Chem. Ing. Tech. (1996) 68 419-422 (in german)

12. Keil, F. J. and Dähnke, S. Numerical calculation of pressure fields in sonochemical reactors - Linear effects in homogeneous phase. Periodica Polytechnica Ser. Chem. Eng. (1997) 41 41-55

13. Keil, F. J. and Dähnke, S. Numerical calculation of scale-up effects of pressure fields in sonochemical reactors - homogeneous phase. Hung. J. Ind. Chem. (1997) 25 71-80

14. Nakoryakov, V.E.; Pokusaev, B.G. and Shreiber, I.R., 1993, Wave Propagation in Gas-Liquid Media. CRC Press, London.

15. Prosperetti, A.; Crum, L.A. and Commander, K.W., 1988, Nonlinear bubble dynamics. J. Acoust. Soc. Am. 83, 502-514.

16. Sangani, A.S., 1991, A pairwise interaction theory for determining the linear acoustic properties of dilute bubbly liquids. J. Fluid Mech. 232, 221-284.

17. Trevena, D.H., 1984, Cavitation and the generation of tension in liquids. J. Phys. D 17, 2139-2164.

18. Ye, Z. and Ding L., 1995, Acoustic dispersion and attenuation relations in bubbly mixture. J. Acoust. Soc. Am. 98, 1629-1636.

19. Yount, D.E.; Gillary, E.W. and Hoffman, D.C., 1984, A microscopic investigation of bubble formation nuclei. J. Acoust. Soc. Am. 76, 1511-1521.

On the Solution of Nonlinear Fractional-Order Differential Equations Used in the Modeling of Viscoplasticity

Kai Diethelm[1] and Alan D. Freed[2]

[1] Institut für Angewandte Mathematik, Technische Universität Braunschweig, Pockelsstr. 14, 38106 Braunschweig, Germany
[2] Polymers Branch, MS 49-3, NASA Lewis Research Center, 21000 Brookpark Road, Cleveland, OH 44135-3191, USA

Abstract. The authors have recently developed a mathematical model for the description of the behavior of viscoplastic materials. The model is based on a nonlinear differential equation of order β, where β is a material constant typically in the range $0 < \beta < 1$. This equation is coupled with a first-order differential equation. In the present paper, we introduce and discuss a numerical scheme for the numerical solution of these equations. The algorithm is based on a PECE-type approach.

1 Introduction

In recent work [7], the authors have constructed a mathematical model for the description of the behavior of viscoplastic materials under certain conditions. In particular, we are interested in describing the strain and entropy reacting in response to changes in stress and temperature. In the theory of viscoelasticity, it is well known [4] that the constitutive equations governing these phenomena involve differential equations of fractional order. Since the theory of viscoelasticity is essentially a linear theory, these differential equations are also linear, and therefore they may be solved using rather simple methods. For our situation, we have found that we have to replace these linear equations by nonlinear ones. The standard solution methods for the linear equations usually fail in the nonlinear case. In order to resolve the situation, we now present a numerical scheme that allows us to handle these equations. In the derivation of the algorithm, we have taken particular care of the fact that the model does not consist of fractional differential equations only, but that first-order differential equations are contained too. This has imposed the requirement to find coherent schemes for both types of differential equations.

In the following section, we briefly review our mathematical model. Having done this, we will introduce and discuss our new numerical method in §3.

2   The Mathematical Model

In order to motivate the algorithm that we developed, we give a short description of our mathematical model, thus explaining the equations we want to solve. For this description of our model of viscoplastic materials, it is useful to first briefly recall some key facts from fractional calculus.

The Riemann-Liouville derivative of order $\beta > 0$ of a function f with respect to the point t_0 is denoted and defined by [18, p. 59]

$$D_{t_0}^{\beta} f(t) = \frac{1}{\Gamma(m-\beta)} \frac{d^m}{dt^m} \int_{t_0}^{t} f(u)(t-u)^{m-\beta-1} du \tag{1}$$

where m is the integer defined by the relation $m-1 < \beta \leq m$. If β is a natural number, then we recover the classical definition of the derivative. This form of a derivative has got very nice and useful mathematical properties [18,19], but a direct application to physical problems often leads to difficulties when trying to handle initial conditions in a meaningful way. The reason is that the fractional derivative of a constant is not identically zero. Therefore, it is common to use Caputo's [3] variant of the Riemann-Liouville derivative, i.e.

$$d_{t_0}^{\beta} f(t) = D_{t_0}^{\beta} \left(f - \sum_{k=0}^{m} \frac{(\cdot - t_0)^k}{k!} y^{(k)}(t_0+) \right)(t), \tag{2}$$

where m is as above; cf. also the survey article [16] and the references cited therein. There is one particularly important property that both these (and indeed all other) fractional derivatives share, namely the fact that these operators are not local. This means that the value of $d_{t_0}^{\beta} f(t)$ depends on all the values of f in the interval $[t_0, t]$ (i.e. on the entire history of the function f). In sharp contrast to this, differential operators of integer order are always local, i.e. they can be evaluated from functions values of f in an arbitrarily small neighborhood of t. This hereditary behavior makes fractional differential operators a natural choice when it comes to modeling path-dependent phenomena. On the other hand, the property has got an influence on the numerical scheme: The fact that we cannot neglect the past history of f implies an increased arithemtic complexity of the algorithm compared to similar methods for integer-order equations.

In our model presented in [7], a simplified form of which we shall now briefly review, we have essentially set up three sets of equations. The first set describes the hydrostatic response (i.e. the dilatational kinetics), the second set deals with deviatoric response (i.e. the distortional kinetics), and the last set covers the evolution of an internal stress.

Our description starts with the first group of relations. We have decomposed the dilatational strain response e additively into an elastic (reversible) part e^e and a plastic (irreversible) part e^p, i.e.,

$$e = e^e + e^p, \tag{3}$$

where the individual parts fulfil the relations

$$e^{\mathrm{e}} = 3\alpha(T - T_0) - \frac{p}{\kappa^{\mathrm{e}}}, \tag{4}$$

$$\dot{e}^{\mathrm{p}} = -\frac{1}{\tau_0} \exp\left(-\frac{Q}{RT}\right) \frac{\xi p - x}{\kappa^{\mathrm{p}}}. \tag{5}$$

Here α is the mean coefficient of thermal expansion (and thus a material constant), T is the current temperature, T_0 is the temperature at the beginning of the experiment, p is the pressure, κ^{e} and κ^{p} are the elastic and plastic bulk moduli, τ_0 is a characteristic time, Q is the activation energy, $R = 8.3145$ J/mol K is the universal gas constant, and x is the hydrostatic component of the internal stress. These relations describe the dilatational kinetics of the model. Formulae (3–5) constitute the standard linear solid of viscolelasticity in disguise, at least when $x = -\kappa^{\mathrm{p}}[e - 3\alpha(T - T_0)]$. This choice for a constitutive relation was made because, based on our present knowledge of hydrostatic data, this seems to be the best model currently available for the problem at hand.

For the distortional response $\mathbf{E} = \mathbf{E}^{\mathrm{e}} + \mathbf{E}^{\mathrm{p}}$ (also decomposed into elastic and plastic components), we have found

$$\mathbf{E}^{\mathrm{e}} = \frac{1}{2\mu^{\mathrm{e}}}\mathbf{S} \tag{6}$$

and

$$\dot{\mathbf{E}}^{\mathrm{p}} = \frac{1}{\tau}\left(\frac{\|\mathbf{S} - \mathbf{X}\|}{\mu^{\mathrm{p}}(1 - \xi)}\right)^{\mathrm{n}} \frac{\mathbf{S} - \mathbf{X}}{2\|\mathbf{S} - \mathbf{X}\|}. \tag{7}$$

In these equations, μ^{e} and μ^{p} are the elastic and plastic shear moduli, $\mathbf{S}$ is the deviatoric stress, $\tau = \tau_0 \exp(Q/RT)$, ξ quantifies the ratio $\|\mathbf{S}\|/\|\mathbf{X}\|$ at saturation satisfying the restriction $0 < \xi < 1$, and n establishes the stress dependence. These relations are motivated by corresponding models from nonlinear viscoelasticity [12].

Whereas fractional derivatives are a very natural and common tool in the classical models of viscoelasticity [4], it seems that in the rather young area of viscoplasticity, the only such model to have been proposed is by Lion [14]. Our approach distinguishes itself from his in that we consider a nonlinear material model that is, we believe, more keeping in line with dislocation physics.

There is abundant metallographic and experimental evidence implying that microstructure evolves in a path-dependent manner and, consequently, the state of stress that a microstructure generates will be hereditary in nature. Therefore, as mentioned above, the internal stress can be considered as a viable candidate for postulating fractional-order equations for its evolution.

Thus, for the evolution of the internal stress $\chi = \mathbf{X} - x\mathbf{I}$ ($\mathbf{I}$ being the identity tensor), we demand in the model that

$$x = -\kappa^{\mathrm{p}}\left(e - 3\alpha(T - T_0)\right) \tag{8}$$

$$d_{t_0}^{\beta} \mathbf{X} = \frac{2\mu^{e}}{\tau_0^{\beta-1}} \left(\dot{\mathbf{E}}^{p} - \frac{1}{\tau} \left(\frac{\|\mathbf{S} - \mathbf{X}\|}{\mu^{p}(1-\xi)} \right)^{n} \frac{\mathbf{X}}{2L} \right), \tag{9}$$

$$d_{t_0}^{\beta} L = \frac{\mu^{p}}{\tau\tau_0^{\beta-1}} \left(\left(\frac{\|\mathbf{S} - \mathbf{X}\|}{\mu^{p}(1-\xi)} \right)^{n} - \left(\frac{L}{\xi\mu^{p}} \right)^{n} \right), \tag{10}$$

where β is a material constant.

These equations fully describe our model for the viscoplastic material, expressing the unknown quantities χ (internal pressure) and L (limit strength of χ) in terms of the control variables T (temperature), $\mathbf{S}$ (deviatoric stress), and p (pressure). Of course, we have to assume that initial values for the unknown functions at time $t = t_0$ are given.

The reader is referred to [7] for further details.

3   The Numerical Algorithm

3.1   Preliminary Remarks

The viscoplastic material model just presented, which we believe has the potential to apply to plastics and metallics alike for a broad class of applications, requires the simultaneous solution of a linear first-order differential equation for the plastic dilatation e^{p}, a nonlinear first-order differential equation for the plastic distortion $\mathbf{E}^{p}$, and two nonlinear fractional-order differential equations for the internal stress $\mathbf{X}$ and its limit strength L. It is imperative that one has a coherent numerical scheme for handling these various types of differential equations simultaneously, which is what we now turn our attention to. For the sake of simplicity, we restrict ourselves to the case important for the application we have in mind, viz. $0 < \beta < 1$, and we only state here that the considerations below can be generalized to arbitrary positive β.

The definition of the fractional derivative and some well known results of fractional calculus (cf., e.g., [6]) tell us that we can interpret a fractional differential equation

$$D_{t_0}^{\beta}(y - y_0)(t) = f(t, y(t)), \qquad y(t_0) = y_0 \tag{11}$$

as a strongly singular Volterra integral equation of the second kind,

$$\frac{1}{\Gamma(-\beta)} \int_{t_0}^{t} \frac{y(u) - y_0}{(t - u)^{\beta+1}} du = f(t, y(t)), \qquad y(t_0) = y_0 \tag{12}$$

thus forcing us to regularize the integral in Hadamard's finite-part sense. The numerical methods developed for this purpose, however, are currently able to cope with linear equations only [6,8,9]. Alternatively, we can apply a fractional integral operator to the differential equation and incorporate the

initial conditions, thus converting the equation into a weakly singular Volterra equation of the second kind

$$y(t) = y(t_0) + \frac{1}{\Gamma(\beta)} \int_{t_0}^{t} (t - u)^{\beta-1} f(u, y(u)) du \tag{13}$$

where a regularization is not necessary any more. It seems [17] that there exists only a very small number of software packages for nonlinear Volterra equations [1,2]. Moreover, these routines are tailored specifically for equations with smooth kernels, and it is known (cf., e.g., [2, p. 63]) that they fail to produce reliable results (and return error flags instead) even if the kernels are continuous but not differentiable. In our situation the kernel is not continuous (actually it even is unbounded), and therefore these classical numerical algorithms are unable to handle our equation.

3.2   Description of the Algorithm

In the following, we shall now present our scheme for the numerical solution of the general fractional differential equation (11) that may of course be used for the special case discussed in the previous section, viz., eqs. (9) and (10). In the development we have in mind that these fractional differential equations are coupled with the first-order differential equations (4)–(7), and thus we need to combine the fractional-order algorithm with a classical method. The results of [15] give us the general advice to choose these two algorithms such that both methods are based on analoguous construction principles. We thus chose an Adams-Bashforth-Moulton approach for both integrators. Whereas this approach is very well known for first-order equations [10,11], we shall give some more details for the fractional variant.

The key to the derivation of the method is to replace the original fractional differential equation (11) by the equivalent weakly singular Volterra equation (13) and to implement a product integration method for the latter. What we do is simply use the product trapezoidal quadrature formula with nodes t_j $(j = 0, 1, \ldots, n+1)$, taken with respect to the weight function $(t_{n+1} - \cdot)^{\beta-1}$, to replace the integral. In other words, we apply the approximation

$$\int_{t_0}^{t_{n+1}} (t_{n+1} - u)^{\beta-1} g(u) du \approx \int_{t_0}^{t_{n+1}} (t_{n+1} - u)^{\beta-1} g_{n+1}(u) du \tag{14}$$

where g_{n+1} is the piecewise linear interpolant for g with nodes and knots chosen at the t_j, $j = 0, 1, 2, \ldots, n+1$. An explicit calculation yields that we can write the integral on the right-hand side of eq. (14) as

$$\int_{t_0}^{t_{n+1}} (t_{n+1} - u)^{\beta-1} g_{n+1}(u) du = \sum_{j=0}^{n+1} a_{j,n+1} g(t_j), \tag{15}$$

where

$$a_{j,n+1} = \int_{t_0}^{t_{n+1}} (t_{n+1} - u)^{\beta-1} \phi_{j,n+1}(u) du, \tag{16}$$

and

$$\phi_{j,n+1}(u) = \begin{cases} (u - t_{j-1})/(t_j - t_{j-1}) & \text{if } t_{j-1} < u < t_j, \\ (t_{j+1} - u)/(t_{j+1} - t_j) & \text{if } t_j < u < t_{j+1}, \\ 0 & \text{otherwise.} \end{cases} \tag{17}$$

In the case of equispaced nodes $t_j = t_0 + jh$ with some fixed h, the relations of eq. (16) reduce to

$$a_{j,n+1} = \begin{cases} \dfrac{h^\beta}{\beta(\beta+1)} \left(n^{\beta+1} - (n-\beta)(n+1)^\beta\right) & \text{if } j = 0, \\[3mm] \dfrac{h^\beta}{\beta(\beta+1)} & \text{if } j = n+1, \end{cases} \tag{18}$$

whereas for $1 \le j \le n$, we have

$$a_{j,n+1} = \frac{h^\beta}{\beta(\beta+1)} \left((n-j+2)^{\beta+1} - 2(n-j+1)^{\beta+1} + (n-j)^{\beta+1}\right). \tag{19}$$

This then gives us our corrector formula, i.e. the fractional variant of the one-step Adams-Moulton method, which is

$$y_{n+1} = y_0 + \frac{1}{\Gamma(\beta)} \left(\sum_{j=0}^{n} a_{j,n+1} f(t_j, y_j) + a_{n+1,n+1} f(t_{n+1}, y_{n+1}^P)\right). \tag{20}$$

The remaining problem is the determination of the predictor formula that we require to calculate the value y_{n+1}^P. The idea we use to generalize the one-step Adams-Bashforth method is the same as the one described above for the Adams-Moulton technique: We replace the integral on the right-hand side of eq. (13) by the product rectangle rule, i.e.

$$\int_{t_0}^{t_{n+1}} (t_{n+1} - u)^{\beta-1} g(u) du \approx \sum_{j=0}^{n} b_{j,n+1} g(t_j), \tag{21}$$

where now

$$b_{j,n+1} = \int_{t_j}^{t_{j+1}} (t_{n+1} - u)^{\beta-1} du = \frac{1}{\beta} \left((t_{n+1} - t_j)^\beta - (t_{n+1} - t_{j+1})^\beta\right). \tag{22}$$

Again, in the equispaced case, we have the simpler expression

$$b_{j,n+1} = \frac{h^\beta}{\beta} \left((n+1-j)^\beta - (n-j)^\beta\right). \tag{23}$$

Thus, the predictor y_{n+1}^P is determined by

$$y_{n+1}^P = y_0 + \frac{1}{\Gamma(\beta)} \sum_{j=0}^{n} b_{j,n+1} f(t_j, y_j).\qquad(24)$$

This completes the description of our basic algorithm, the fractional version of the one-step Adams-Bashforth-Moulton method. Recapitulating, we see that we first calculate the predictor y_{n+1}^P according to eq. (24), then we evaluate $f(t_{n+1}, y_{n+1}^P)$, use this to determine the corrector y_{n+1} by means of eq. (20), and finally evaluate $f(t_{n+1}, y_{n+1})$ which is then used in the next integration step. Therefore, methods of this type are usually called predictor-corrector or, more precisely, PECE (Predict, Evaluate, Correct, Evaluate) methods.

3.3   Main Properties of the Algorithm

We shall now describe the main properties of the algorithm. In particular, we find that, with respect to the most important questions, the behaviour of the method is independent of the parameter β and that it behaves very much like the classical one-step Adams-Bashforth-Moulton method (i.e. the case $\beta = 1$). Therefore, a combination of the fractional Adams-Bashforth-Moulton scheme outlined above with its classical version is very natural when the set of equations to be solved consists, as in our case, of first-order differential equations combined with fractional-order differential equations. Moreover, it can even be generalized to include more fractional order equations, even if the order of the differential operators involved varies from equation to equation.

Stability. The issue of stability is very important when implementing the method on a computer in finite-precision arithmetic because we must take into account effects due to rounding errors. It is known [11, Ch. IV] that the classical Adams-Bashforth-Moulton method (for first-order equations) is a reasonable and practically useful compromise in the sense that its stability properties allow for a safe application to mildly stiff equations without undue propagation of rounding errors, whereas the implementation does not require extremely time consuming elements. From the results of [15] we can see that these properties remain unchanged when we look at the fractional version of the algorithm instead of the classical one, and thus it is also clear that the behaviour does not depend on the order of the differential operators involved.

Convergence. Of course, stability alone is not sufficient in practice to make sure that the numerical solution is a good approximation to the exact solution. We must also address the problem of error estimates, i.e. the question of convergence. In this context, we can use some of the standard analysis techniques [13, §§8.2 & 8.3] to derive that (assuming sufficient smoothness of

the functions involved) the convergence order of the scheme is 2, i.e. we have an error bound of the form

$$\max_j |y(t_j) - y_j| = O(h^2) \tag{25}$$

where $h = \max_j(t_{j+1} - t_j)$ for all $t_j \in [t_0, t_0 + t^*]$ with some fixed $t^* > 0$.

References

1. Blom J. G., Brunner H. (1991) Algorithm 689: Discretized collocation and iterated collocation for nonlinear Volterra integral equations of the second kind.. ACM Trans. Math. Software **17**, 167–177
2. Bownds J. M., Appelbaum L. (1985) Algorithm 627: A FORTRAN subroutine for solving Volterra integral equations. ACM Trans. Math. Software **11**, 58–65
3. Caputo M. (1967) Linear models of dissipation whose Q is almost frequency independent, II. Geophys. J. Royal Astronom. Soc. **13**, 529–539
4. Caputo M., Mainardi F. (1971) A new dissipation model based on memory mechanism. Pure and Applied Geophysics **91**, 134–147
5. Carpinteri A., Mainardi F. (Eds.) (1997) Fractals and Fractional Calculus in Continuum Mechanics. Springer, Wien
6. Diethelm K. (1997) An algorithm for the numerical solution of differential equations of fractional order. Elec. Transact. Numer. Anal. **5**, 1–6.
7. Diethelm K., Freed A. D. (1998) Viscoelastic/viscoplastic material modeling using the fractional calculus. Submitted for publication
8. Diethelm K., Walz G. (1997) Numerical solution of fractional order differential equations by extrapolation. Numer. Algorithms **16**, 231–253
9. Gorenflo R. (1997) Fractional calculus: Some numerical methods. In [5], 277–290
10. Hairer E., Nørsett S. P., Wanner G. (1993) Solving Ordinary Differential Equations I: Nonstiff Problems, 2nd edn. Springer, Berlin
11. Hairer E., Wanner G. (1991) Solving Ordinary Differential Equations II: Stiff and Differential-Algebraic Problems. Springer, Berlin
12. Krempl E., Bordonaro C. M. (1995) A state variable model for high strength polymers. Polymer Engineering and Science **35**, 310–316
13. Linz P. (1985) Analytical and Numerical Methods for Volterra Equations. SIAM, Philadelphia, PA
14. Lion A. (1997) Constitutive modelling of viscoplastic material behaviour based on evolution equations of fractional order. In: Khan A. S. (Ed.) Physics and Mechanics of Finite Plastic and Viscoplastic Deformation. Neat Press, Fulton, MD, 61–62
15. Lubich C. (1986) Discretized fractional calculus. SIAM J. Math. Anal. **17**, 704–719
16. Mainardi F. (1997) Fractional calculus: Some basic problems in continuum and statistical mechanics. In [5], 291–348
17. National Institute of Standards and Technology: Guide to Available Mathematical Software. http://gams.nist.gov
18. Oldham K. B., Spanier J. (1974) The Fractional Calculus. Academic Press, New York, NY
19. Samko S. G., Kilbas A. A., Marichev O. I. (1993) Fractional Integrals and Derivatives: Theory and Applications. Gordon and Breach, Yverdon

Stability analysis of chemical reactors

M. A. Efendiev[1] and A. Schuppert[2]

[1] Free University of Berlin
    Dept. of Math. I, Arnimallee 2 - 6, 14195 Berlin
[2] Bayer AB Leverkusen
    ZT- TE 2, E 41, 51368 Leverkusen

Abstract. In this paper we present stability of a class of exothermic chain reactions both from coolant and dilution rates. Moreover the influence of diffusion is also considered. Our analysis is based on upscaling balance conditions for equilibria concentrations.

1 Upscaling balance conditions for equilibria concentrations

Following Feinberg [3] we write chemical reactions of species $x_0, \ldots, x_n$ as

$$y_0^{(j)} x_0 + \ldots + y_n^{(j)} x_n \xrightarrow{k_j} \bar{y}_0^{(j)} x_0 + \ldots + \bar{y}_n^{(j)} x_n \tag{1}$$
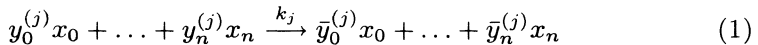
with integer stoichiometric coefficients $y^{(j)}, \bar{y}^{(j)} \geq 0$ and positive real reaction rate coefficient k_j. Then the associated dynamics is given by

$$\dot{x} = \sum_{j=1}^{M} k_j x^y (\bar{y}^{(j)} - y^{(j)}). \tag{2}$$

Here $x = (x_0, \ldots, x_n) \in \mathrm{R}^{n+1}$ is the vector of concentrations and $x^y := x_0^{y_0} \cdots x_n^{y_n}$ represents the usual mass action kinetics.

Note that the external feed concentrations can be incorporated in this model by adding formal reactions

$$0 \xrightarrow{k_0^i} x_i. \tag{3}$$

For the radical starter reactions considered in the present paper, we can therefore introduce a crucial small parameter $\epsilon > 0$, in this sense, by the feed "reaction"

$$0 \xrightarrow{k_0 = \epsilon} S \tag{4}$$

with $\epsilon := S_0$ denoting the feed concentration of the radical starter. Let $\alpha = (\alpha_0, \ldots, \alpha_n) \in R^{n+1}$ denote the scaling that is

$$\begin{pmatrix} x_0 \\ \vdots \\ x_n \end{pmatrix} = \begin{pmatrix} \epsilon^{\alpha_0} & & 0 \\ & \ddots & \\ 0 & & \epsilon^{\alpha_n} \end{pmatrix} \begin{pmatrix} \xi_0 \\ \vdots \\ \xi_n \end{pmatrix} \tag{5}$$

Substituting (5) into (2) we obtain

$$\epsilon^{\alpha j}\dot{\xi}_j = \sum_{j=1}^{M} k_j \epsilon^{\alpha_0 \cdot y_0^{(j)} + \cdots + \alpha_n \cdot y_n^{(j)}} \xi_0^{y_0^{(j)}} \cdots \xi_n^{y_n^{(j)}} (\bar{y}^{(j)} - y^{(j)}). \tag{6}$$

With the abbreviation $\alpha \cdot y^{(j)} = \alpha_0 y_0^{(j)} + \cdots + \alpha_n y_n^{(j)}$ for the scalar product, the equilibrium equation (6) is

$$\sum_{j=1}^{M} k_j \epsilon^{\alpha \cdot y^{(j)}} \xi^{y^{(j)}} (\bar{y}^{(j)} - y^{(j)}) = 0 \tag{7}$$

for the scaled steady state $\xi = \xi(\epsilon)$.

Definition

We call $\alpha = (\alpha_0, \cdots, \alpha_n) \in R^{n+1}$ a scaling exponent *for the steady state concentrations* $x = (x_0, \cdots, x_n)$ *of (2) , if there exists a sequence of scaled equilibria* $\xi(\epsilon_\ell) = (\xi_0(\epsilon_\ell), \cdots, \xi_n(\epsilon_\ell)), \epsilon_\ell \to 0, \ell \to \infty$ *of (7), such that for all* $m = 0, \ldots, n$ *the following nondegeneracy conditions holds:*

$$0 < \liminf_{\ell \to \infty} \xi_m(\epsilon_\ell) \le \limsup_{\ell \to \infty} \xi_m(\epsilon_\ell) < \infty. \tag{8}$$

Theorem 1.1 (see also [1], [2]) Any scaling exponent $\alpha = (\alpha_0, \ldots, \alpha_n) \in R^{n+1}$ satisfies

$$\min_{j: y_m^{(j)} \neq 0} \{(\alpha \cdot y^{(j)})\} = \min_{i: \bar{y}_m^{(i)} \neq 0} \{(\alpha \cdot y^{(i)})\}, \tag{9}$$

for all fixed $m = 0, \ldots, n$.

Proof:

Let $\alpha = (\alpha_0, \ldots, \alpha_n)$ be any scaling exponent. We rewrite equation (7) for the scaled steady state $\xi = \xi(\epsilon)$ in components $m = 0, \cdots, n$ as

$$\sum_{j=1}^{M} k_j \epsilon^{\alpha \cdot y^{(j)}} \xi^{y^{(j)}} y_m^{(j)} = \sum_{i=1}^{M} k_i \epsilon^{\alpha \cdot y^{(i)}} \xi^{y^{(i)}} \bar{y}_m^{(i)} \tag{10}$$

or, equivalently,

$$\sum_{j: y_m^{(j)} \neq 0} k_j \epsilon^{\alpha \cdot y^{(j)}} \xi^{y^{(j)}} y_m^{(j)} = \sum_{i: \bar{y}_m^{(i)} \neq 0} k_i \epsilon^{\alpha \cdot y^{(i)}} \xi^{y^{(i)}} \bar{y}_m^{(i)} \tag{11}$$

Fix m. We sort the terms on either side of (11) by increasing powers $\alpha \cdot y^{(j)}, \alpha \cdot y^{(i)}$ of ϵ respectively. Note that all terms are strictly positive, by the nondegeneracy assumption (8). Let

$$\min_{j: y_m^{(j)} \neq 0} \{\alpha \cdot y^{(j)}\} = \alpha \cdot y^{(j_0)} \text{ and } \min_{i: \bar{y}_m^{(i)} \neq 0} \{\alpha \cdot y^{(i)})\} = \alpha \cdot y^{(i_0)},$$

in (11). The the leading (alias: lowest) power of ϵ in the m-th component of (11) is given by $\alpha \cdot y^{(j_0)}$ on the left, as compared to $\alpha \cdot y^{(i_0)}$ on the right.

These leading powers may in fact be realized by several other scalar products $\alpha \cdot y^{(j)}, \alpha \cdot y^{(i)}$ in addition. Comparing coefficients, we divide (11) by ϵ to the power $\min(\alpha \cdot y^{(j_0)}, \alpha \cdot y^{(i_0)})$, and let $\epsilon \to 0$. This immediately yields

$$\alpha \cdot y^{(j_0)} = \alpha \cdot y^{(i_0)}$$

by positivity of all terms in the sums. This proves the theorem .

2   Model reactor

As a paradigm to the problem of stability analysis of a chemical reactor we consider the following radical reaction

$$S \to 2S^\bullet$$
$$S^\bullet + E \to E^\bullet + D_1 \tag{12}$$

$$E + E^\bullet \to P^\bullet$$
$$P^\bullet + E \to P + E^\bullet \tag{13}$$

$$2E^\bullet \to D_2$$
$$E^\bullet + S^\bullet \to D_3 \tag{14}$$
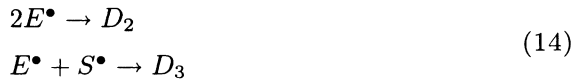
Here S is a radical starter, such as hydrogen peroxide or UV-light, and the chain (13) converts the educt E into the product P. This reaction scheme is not only the basis for radicalic dimerisations, but with small changes it can also be found in hydrocarbon-cracking and radicalic polymerisations (see [4]). The corresponding radicals are $S^\bullet, E^\bullet, P^\bullet$. Inconsequential side products are denoted by D_1, D_2, D_3. The starter reactions (12) get the chain (13) going, by the restroing the educt radical $E^\bullet$. Chain termination reactions are considered in (14). Assuming that, aside from some small regions of laminarity, the reactor volume is essentially mixed, then for the concentrations S, E and for the radicals, s, e, p we have

$$\dot{S} = S_0 - k_1 S - DS$$
$$\dot{E} = E_0 - k_2 s E - k_3 e E - k_4 p E - DE$$
$$\dot{s} = 2k_1 S - k_2 s E - k_6 e s - Ds$$
$$\dot{e} = k_2 s E - k_3 e E + k_4 p E - 2k_5 e^2 - k_6 e s - DE \tag{15}$$
$$\dot{p} = k_3 e E - k_4 p E - Dp$$
$$\dot{T} = h_1 k_1 S + h_2 k_2 s E + h_3 k_3 e E + h_4 k_4 p E + h_5 k_5 e^2 + h_6 k_6 e s - \kappa(T - T_0)$$

Here T denotes temperature, h_i are the reaction enthalpies, and the reaction rates

$$k_i = k_i(T) = k_i^* \exp(-\gamma_{i/T}) \tag{16}$$

are of Arrhenius type with activation energies γ_i and rate constants $k_i^*, i = 1, \dots, 6$. Externally sustained, space dependent feed concentrations are denoted by E_0, S_0. D and κ indicates dilution and external cooling rates with coolant temperature T_0 respectively. Our next step is based on the application of upscaling balance condition (9) to the reaction mechanism (12)–(14). To this end, following (3) we add to (12)–(14) formal reactions

$$0 \xrightarrow{k_0 = S_0} S$$

$$0 \xrightarrow{k_0^1 = E_0} E \tag{17}$$

Following mathematical convention, we introduce

$$\epsilon := S_0 \tag{18}$$

and consider the limit $\epsilon \uparrow 0$ henceforth. For the reaction mechanism (12)–(14), (17) with $x = (x_0, \dots, x_n) = (S, E, s, e, p)$ and $D = 0$ upscaling balance condition (9) for the scaling exponent

$$\alpha = (\alpha_0, \dots, \alpha_4) := (\alpha_S, \alpha_E, \alpha_s, \alpha_e, \alpha_p)$$

takes the form

$$
\begin{aligned}
S) &= \min\{\alpha_S\} = \min\{1\} \\
E) &= \min\{\alpha_E + \alpha_s, \alpha_E + \alpha_e, \alpha_E + \alpha_p\} = 0 \\
s) &= \min\{\alpha_E + \alpha_s, \alpha_s + \alpha_e\} = \alpha_S \\
e) &= \min\{\alpha_E + \alpha_e, 2\alpha_e, \alpha_s + \alpha_e\} = \min\{\alpha_E + \alpha_s, \alpha_E + \alpha_p\} \\
p) &= \min\{\alpha_E + \alpha_p\} = \min\{\alpha_E + \alpha_e\}
\end{aligned}
\tag{19}
$$

It is not difficult to prove, that (19) yields

$$\alpha = \left(1, -\frac{1}{2}, \frac{3}{2}, \frac{1}{2}, \frac{1}{2}\right) \text{ in the case } D = 0 \tag{20}$$

Analogously we have

$$\alpha = (1, 0, 1, 1, 1) \text{ in the case } D \neq 0 \tag{21}$$

We will use the expressions (20) and (21) for the scaling exponent in our stability analysis.

3   Stability analysis

As we mentioned above, for stability analysis we make use of asymptotic expansions of equilibria concentrations

$$x(\epsilon) = (S(\epsilon), E(\epsilon), s(\epsilon), e(\epsilon), p(\epsilon)) \tag{22}$$

in $\epsilon := S_0$. First we restrict ourselves to the case $D = 0$. To this end we consider the following 6×6 matrix (linearization at $x(\epsilon)$) $A(\epsilon)$.

$$A(\epsilon) = \begin{bmatrix} -k_1 & 0 & 0 & 0 & 0 & k_1'S \\ 0 & -k_3e - k_4p - k_2s & -k_2E & -k_3E & -k_4E & \Theta_1 \\ 2k_1 & -k_2s & -k_2E - k_6e & -k_6s & 0 & \Theta_2 \\ 0 & k_2s - k_3e - k_4p & k_2E - k_6e & -k_3E - 4k_se - k_6s & k_4E & \Theta_3 \\ 0 & k_3e - k_4p & 0 & k_3E & -k_4E & \Theta_4 \\ \eta_1 & \eta_2 & \eta_3 & \eta_4 & \eta_5 & \Theta_5 \end{bmatrix}$$

where by $\Theta_j, \eta_j, j = 1, \ldots, 5$ we denote the derivatives with respect to T and educts, respectively. Note, that $k_1' = \frac{d}{dT}k_1$.

We consider the following eigenvalue problem

$$A(\epsilon)x(\epsilon) = \lambda(\epsilon)x(\epsilon) \tag{23}$$

and are interested in the stability of chemical reaction under consideration. We begin our stability analysis by grouping the matrix $A(\epsilon)$ according to its leading order in ϵ. As was mentioned above, for this purposes we use scaling exponents (20). Thus $A(\epsilon)$ can be decomposed as

$$A(\epsilon) = A_0(\epsilon) + o(\epsilon^{1/2}) \tag{24}$$

It remains to compute $\lambda_j(A_0(\epsilon)), j = 1, \ldots, 6$. Note that the (5×5) matrix which consists of first five columns and rows of $A(\epsilon)$ has the first five negative eigenvalues. We denote this matrix by $\tilde{A}_{0,5}(\epsilon)$. It is not difficult to see that, some of eigenvalues of $\tilde{A}_{0,5}(\epsilon)$ have zero limit as $\epsilon \to 0$, (remaining negative for $\epsilon > 0$).

Remark 3.1. In the case $D = 1$ the corresponding matrix (dominant) $\tilde{A}_{0,5}(\epsilon)$ has negative eigenvalues $\tilde{\lambda}_1(\epsilon), \ldots, \tilde{\lambda}_5(\epsilon)$ with $\lim_{\epsilon \to 0} \tilde{\lambda}_j(\epsilon) = \lambda_{j,0}^* < 0$ (so-called stabilization effect of dilution rate).

Thus for stability analysis it remains to check of the influence of the coolant rate κ. For simplicity of computations we assume that $k_3 = k_4$. It is not difficult to see that (using some transformation) the stability analysis of the (6×6) matrix $A(\epsilon)$ reduced to that of the (4×4) matrix of the form

$$
\begin{bmatrix}
-\frac{E_0}{E} & -c & -k_3 E & -k_4 E \\
-\frac{h_3+h_4}{2}\frac{E_0}{E} & c-\kappa & h_3 k_3 E + 2h_5 k_5 e & h_4 k_4 E \\
0 & 0 & -k_3 E - 2k_5 e & k_4 E \\
0 & 0 & k_3 E & -k_4 E
\end{bmatrix}.
\tag{25}
$$

Here $c = \frac{\gamma_3}{T^2}$ is a constant depending on the activitation energy and the given temperature T. Hence it follows from (25) we have stability (for given temperature T) when κ is sufficiently large, that is there exists $\kappa_c > 0$ such that $\kappa \geq \kappa_c$ we have stability and $0 < \kappa < \kappa_c$ is the instability region (T is fixed).

Remark 3.2. In the same manner one can analyze the influence of the presence of diffusion, the so-called diffusion effect. Indeed in this case stability analysis will be governed by the equation

$$
\det(A(\epsilon) - \mu \tilde{D} - \lambda Id) = 0
$$

where $A(\epsilon)$ is the same (6×6) matrix as above, $\tilde{D} = \mathrm{diag}\,(d_1, \ldots, d_6), \mu \in R_+, Id$ is the identity matrix. Here we also have for the (5×5) matrix $\tilde{A}_{0,5}(\epsilon)$ strong stable directions due to the presence of diffusion.

Conclusions: We presented stability analysis for a class of exothermic radical chemical reactions, which run with low starter concentrations, providing nevertheless sufficiently many radicals. Our mathematical analysis is based on upscaling balance condition, which in turn allow us to predict stable (strong stable) directions of educts under considerations. Moreover our analysis describes (mathematically) phenomena, when CFSTR reactor remaining stable for a while, suddenly become unstable (effect of temperature).

References

1. M. A. Efendiev, A. Schuppert, M. Wolfrum: Isothermal upscaling of exothermic reactors: An example. *Journal Nonlinerar Analysis*, TMA; vol 30, No 6, pp 3455-3461. 1997
2. M. A. Efendiev, B. Fiedler. *Stable upscaling to exothermic reactor with several educts.* Proceedings of Int. Symposium "Untersuchung Nichtlinear-Dynamischer Effekte in produktionstechnischen Systemen". Bremen, Etelsen, 1997.
3. M. Feinberg. *Chemical reaction network structure and the stability of complex isothermal reactors*, Part I, Part II, in "Chem. Eng. Sci.", 42 (1987), pp 2229-2268, 43 (1988), pp 1-25.
4. K. T. Laidler. *Chemical Kinetics.* Harper Collins Publishers, 1987.

Simulation of the Non-Stationary Behaviour of Fixed-Bed Reactors for the Determination of Kinetic Expressions in Consideration of Inhomegeneous Concentration Profiles Inside the Catalyst Pellets

Abdul Garayhi and Frerich Keil

Technical University of Hamburg-Harburg, Dept. of Chemical Engineering,
D-21071 Hamburg, Germany

Abstract. A model for the simulation of fixed-bed reactors is presented. Special care is taken of single catalyst pellets, that are assumed to be heterogeneous in spatial direction. All the reaction steps and equilibrium conditions may be included. The resulting ODE-PDE system is solved by the package *pdex1m*. A complete example set of parameters is presented as well as calculation results.

1 Problem formulation

Industrial reactors are more and more optimized with respect to their dynamical behaviour. The predominant applications are simulations of start-up or shut-down procedures and the calculation of non-stationary reactor operation.

It is well known that kinetic expressions that are based on measurements under stationary conditions may not give satisfactory results under non-stationary conditions. Therefore it is often necessary to conduct experiments under non-stationary conditions [1]. These require a more sophisticated analysis, which in return often requires the simulation of the reactor behaviourunder non-stationary conditions. Such simulations will be presented in this paper. As many common simplifications do not apply to the non-stationary operation, the appropriate modeling of the mass-transfer processes is indispensable [2]. The kinetics of adsorption/desorption processes may be included as well as changes of the catalyst behaviour over time.

2 Model Description and Equations

The model presented here combines a model of the reactor with a detailed description of the catalyst. Due to numerical difficulties the latter is usually neglected or included just by simple constants, e.g. effectiveness factors. There are many cases in which these simplification do not hold, e.g. rapid catalyst deactivation.

2.1   Assumptions

The model can be separated into two parts, some equations describe the behaviour within the catalysts, others the reactor. The following assumptions are made:

- The catalyst pellets are heterogeneous in spatial direction. There are two separate phases representing the gaseous and adsorbed components. The structure parameters, the catalytic activity, and the physical gas properties are not necessarily homogeneous and may change with the particle radius.
- The ideal gas law holds for the gas phase. The model equations can be easily adopted to different equations-of-state by a compressibility factor.
- Due to symmetry, only one spatial direction must be considered within the catalyst pellets. If only one spatial co-ordinate must be taken into account, the equations given here apply to a planar, a cylindrical, or a spherical geometry, if Cartesian, cylindrical, or spherical co-ordinates are employed. More complicated geometries require only little modifications in the model equations.
- All transport processes within the catalyst pores are described by the Dusty-Gas-Model [3].
- Adsorption and desorption processes are treated as chemical reactions. Gaseous and adsorbed parts of a component are treated as two different species.
- In the example calculations treated here, chemical reactions are resolved to their elementary steps. The formal model equations need not to be changed, if elementary steps are treated as equilibrium conditions or if some are lumped to total reactions.
- The equations presented apply to the isothermal case. They can easily be adopted to non-isothermal conditions.

2.2   Equations for the Catalyst Pellets

At first, the model for the catalytic reaction will be outlined. The material balance over a differential volume element gives a system of parabolic partial differential equations (PDE)

$$\frac{\partial \boldsymbol{n}}{\partial t} = dV \cdot \frac{\partial}{\partial \tilde{z}} \left(cRT \frac{r_P^2}{8\eta} \frac{\epsilon}{\tau} \frac{\partial c_t}{\partial \tilde{z}} + \boldsymbol{D} \frac{\partial \boldsymbol{c}}{\partial \tilde{z}} \frac{\epsilon}{\tau} + \frac{(1-\epsilon)}{\tau} \boldsymbol{D}^S \frac{\partial \boldsymbol{c}}{\partial \tilde{z}} \frac{\epsilon}{\tau} \right) + dV \cdot \sum_j \boldsymbol{\nu}_j r_j \, . \tag{1}$$

Under the assumptions given above these equations have a special structure, so the system can be transformed into the dimensionless system

$$\frac{\partial(\psi \boldsymbol{x})}{\partial \theta} = \frac{\partial}{\partial z} \left[\left(\beta^0 \frac{1}{\tau} (\psi \boldsymbol{x}) e^T + \boldsymbol{\delta} \frac{1}{\tau} \right) \frac{\partial(\psi \boldsymbol{x})}{\partial z} \right] + \frac{1}{\epsilon} \sum_j \boldsymbol{\nu}_j \omega_j \tag{2}$$

in the gas phase, and

$$\frac{\partial(\psi\boldsymbol{x})}{\partial\theta} = \frac{\partial}{\partial z}\left(\boldsymbol{\delta}^S\frac{1}{\tau}\right)\frac{\partial(\psi\boldsymbol{x})}{\partial z} + \frac{1}{1-\epsilon}\sum_j\boldsymbol{\nu}_j\omega_j \tag{3}$$

in the solid phase.

The dimensionless numbers are calculated according to

$$z = \frac{\tilde{z}}{L}; \ \theta = \frac{\Delta t}{L^2}; \ \psi = \frac{p}{p|_{z=0.5}}; \ \omega = \frac{rL^2RT}{\Delta\,p|_{z=0.5}}; \ \beta^0 = \frac{r_P^2\,p|_{z=0.5}}{8\eta\Delta} \tag{4}$$

$$\boldsymbol{\delta}^S = \begin{cases} \frac{D_i^S}{\Delta} \ | \ i = j \\ 0 \quad | \ i \neq j \end{cases} \tag{5}$$

$$-\boldsymbol{\delta}^{-1} = \begin{cases} \frac{x_i\Delta}{D_{ij}} + \sum_{\substack{l=1 \\ l\neq i}}^{N}\frac{x_l\Delta}{D_{il}} + \frac{\Delta}{D_i^K} \ | \ i \neq j \\ 0 \qquad\qquad\qquad\qquad | \ i = j \end{cases}. \tag{6}$$

2.3   Equations for the Reactor

Secondly, a model for the reactor is necessary. For this purpose the common reactor models are employable. Spatially continuous models like one-, two-, or three-dimensional dispersion models are not applicable with the available numerical methods, if the radial profile within the pellets is resolved as above, because the computational demand is too high. Alternatively a cell model is employed in the present work. In such models the fixed-bed reactor is given as a one-, two-, or three-dimensional network of ideal continuous-fed stirred tank reactors (CSTR). Usually 1-6 cells are required to simulate the behaviour of a fixd-bed gas reactor. The cell model is equivalent to a relatively coarse spatial discretisation of the continuous profiles, while the transitions between the points are modeled to fulfil physico-chemical laws. In that way the errors due to the coarse discretisation are mainly compensated. Compared to dispersion models far less floating point operations are required, which significantly decreases the round-off errors as well as the computation time.

The balance over a cell leads to a system of ordinary differential equations (ODE) for every single cell

$$\frac{d\boldsymbol{n}_R}{dt} = (\boldsymbol{x}_{in} - \boldsymbol{x}_R)\cdot\dot{n}_{total,in}$$

$$-\frac{Bi\Delta}{L}\frac{p|_{z=0.5}}{RT}b\left[(\boldsymbol{x}_R - \boldsymbol{x}|_{z=0.5}) - \boldsymbol{x}_R\cdot\sum_i(x_{R,i} - x_i|_{z=0.5})\right] \tag{7}$$

with

$$Bi = \frac{kL}{\Delta}. \tag{8}$$

They result in the dimensionless form

$$\frac{d\boldsymbol{x}}{d\theta} = \frac{1}{\theta_R}(\boldsymbol{x}_{in} - \boldsymbol{x}) - Bi \cdot \kappa \left[(\boldsymbol{x}_R - \boldsymbol{x}|_{z=0.5}) - \boldsymbol{x}_R \cdot \sum_i (x_{R,i} - x_i|_{z=0.5}) \right],$$
(9)

if the outer diffusion resistance is neglected

$$\frac{d\boldsymbol{x}_R}{d\theta} = \frac{1}{\theta_R}(\boldsymbol{x}_{in} - \boldsymbol{x}) - \kappa \cdot \epsilon \cdot (1 - x_R e^T) \left(\frac{1}{\tau} \boldsymbol{x}|_{\tilde{z}=L/2} e^T + \delta \right) \frac{\partial \boldsymbol{x}}{\partial z} \Big| \tilde{z} = L/2$$
(10)

will result similarily.

2.4   Initial and Boundary Conditions

The initial material distribution can be set arbitrarily. In the present example

$$\boldsymbol{x}_{gas}(t=0) = \boldsymbol{x}_{gas,0}, \ \boldsymbol{x}_R(t=0) = \boldsymbol{x}_{R,0}, \ \boldsymbol{x}_{solid} = 0$$
(11)

was assumed.

The boundary conditions for the gaseous phase are

$$Bi \cdot (\mathbf{x}_R - \boldsymbol{x}) = \frac{1}{\tau}(\boldsymbol{x}e^T + \delta)\frac{\partial \boldsymbol{x}}{\partial z}$$
(12)

if the film mass transfer resistance is taken into account, or

$$\boldsymbol{x}\left(r = \frac{L}{2}\right) = \boldsymbol{x}_R$$
(13)

if it is neglected.

Similar conditions can be found for the solid phase. If the surface diffusion is neglected ($\delta^S = 0$), the eq. (3) will become ODEs at the discretisation points. So

$$\frac{\partial(\psi \boldsymbol{x})}{\partial \theta} = \frac{1}{1-\epsilon} \sum_j \boldsymbol{\nu}_j \omega_j$$
(14)

is used at the boundary.

In the present example a one-dimensional model was used. The cell inlet concentrations are given by

$$\boldsymbol{x}_{in,0} = \boldsymbol{x}_{in,reactor}, \ \boldsymbol{x}_{in,i} = \boldsymbol{x}_{i-1}.$$
(15)

Care must be taken of the reactor residence time, θ_R. The usual residence time is the first moment of the residence time distribution. The integral may not exist (e.g. in the case of irreversible adsorption). Therefore a characteristic hydrodynamic residence time

$$t_r = \frac{n(t)}{\dot{n}_{in,0}}$$
(16)

is employed. The real hydrodynamic residence time of cell i is given by the correction

$$\theta_{R,i} = \theta_{R,i,0} \cdot \prod_{l=1}^{i-1} \left(1 + \sum_{j=1}^{n_R} \sum_{k=1}^{n_c} \nu_{jk} \omega_j \theta_{R,l} \right) . \tag{17}$$

3 Programming

For the numerical solution of the relatively large system of parabolic PDEs the package *pdex1m* [4], version 0.95, is employed. It implements a semi-implicit extrapolation method. The moving-grid option was not used. The code was modified in order to increase the number of solvable equations to 200. Since the program cannot process combined ODE-PDE systems, the equations (9-10) are solved at all inner points with a local x_R.

Table 1 lists a typical parameter set for a calculation with one cell where adsorption becomes rate determining.

4 Example Calculations

As an example the transient response of a system with a Langmuir-Hinshelwood type kinetics to different input signals is calculated. The reaction scheme is

$$A + (\ )^* \rightarrow (A)^* \tag{18}$$
$$B + (\ )^* \rightarrow (B)^* \tag{19}$$
$$(A)^* + (B)^* \rightarrow (C)^* + (D)^* \tag{20}$$
$$(C)^* \rightarrow C + (\ )^* \tag{21}$$
$$(D)^* \rightarrow D + (\ )^* \tag{22}$$
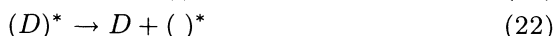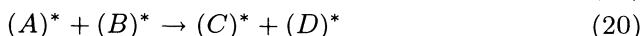
In the Fig. 1, 2 the mole fraction of reactant A is given as it would be recorded in an experiment. Figure 1 shows the response function to a concentration change in the gas phase. The catalyst surface is clean at the beginning. The minimum in Fig. 1 at time 25 is explainable by the adsorption processes involved [5]. Such processes may have the effect that measurements will not give the desired information about the catalytic mechanism. For the details of the theoretical fundamentals the reader is referred to the literature. Alternatively periodic signals can be used for the investigation of the catalyst [6]. The system is the same as in the first example, but the feed composition changes sinusodially. It is evident, that the signal is a combination of the influences from the system and initial effects. After the initial period the non-stationary behaviour of the catalytic system still can be measured. The results are presented in Fig. 2.
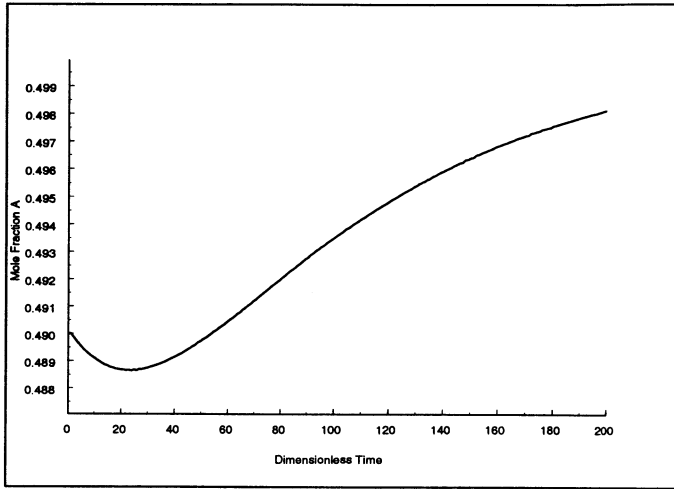
Fig. 1. Response of a Reactant to a Step Change
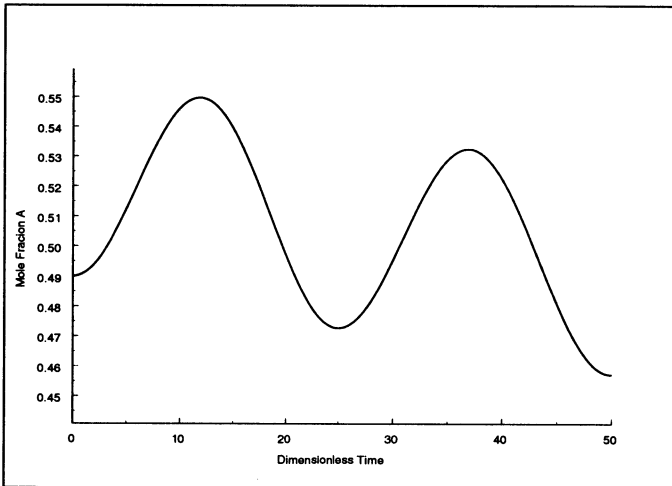
Fig. 2. Response of a Reactant to a Sinusodial Feed

5   Notation

Bi	$[-]$	Biot-Number
b	$[\frac{1}{m}]$	Volume specific surface
$\boldsymbol{c}$	$[\frac{mol}{m^3}]$	Concentration
c_t	$[\frac{mol}{m^3}]$	Total Concentration
$\boldsymbol{D}$	$[\frac{s}{m^2}]$	Dusty-Gas diffusion matrix
$\boldsymbol{D}^S$	$[\frac{m^2}{s}]$	Surface Diffusion matrix
D_{ij}	$[\frac{m^2}{s}]$	Binary diffusivity
D^S	$[\frac{m^2}{s}]$	Surface diffusivity
D^K	$[\frac{m^2}{s}]$	Knudsen diffusivity
$\boldsymbol{e}$	$[-]$	Vector with all elements equal to 1
i, j	$[-]$	Index
k	$[\frac{m}{s}]$	Mass transfer coefficient
L	$[m]$	Characteristic length, here particle diameter
$\boldsymbol{n}$	$[mol]$	Mole vector
$\dot{n}_{total,in}$	$[\frac{mol}{s}]$	Feed
p	$[Pa]$	Pressure
R	$[\frac{J}{molK}]$	Universal gas constant
r	$[\frac{mol}{m^3 s}]$	Reaction rate
r_P	$[m]$	Mean pore radius
T	$[K]$	Temperature
t	$[s]$	Time
V	$[m^3]$	Volume
$\boldsymbol{x}$	$[-]$	Mole fractions of the components
$\boldsymbol{x}_R$	$[-]$	Mole fractions of the components in the reactor
$\boldsymbol{x}_{in}$	$[-]$	Mole fractions of the components in the feed
z	$[-]$	Dimensionless spatial co-ordinate
$\tilde{z}$	$[m]$	Spatial co-ordinate

Greek Symbols

β_0	$[-]$	Convective factor
Δ	$[\frac{m^2}{s}]$	Characteristic diffusivity
δ	$[-]$	Dimensionless Dusty-Gas diffusion matrix
$\boldsymbol{\delta}^S$	$[-]$	Dimensionless surface diffusivity matrix
ϵ	$[-]$	Porosity
η	$[Pas]$	Viscosity
θ	$[-]$	Dimensionless time
θ_R	$[-]$	Dimensionless residence time
κ	$[-]$	Dimensionless volume specific surface
$\boldsymbol{\nu}$	$[-]$	Vector of stoichiometric coefficients
τ	$[-]$	Tortuosity
ψ	$[-]$	Pressure ratio
ω	$[-]$	Dimensionless rate of reaction

Table 1. Typical values for the dimensionless variables

Bi	11
$n_{gaseous,solid}$	4,4
x_{in}^T	$(0.4, 0.6, 0, 0)$
β_0	$6.3 \cdot 10^{-4}$
$-\delta^{-1}$	$\begin{cases} \frac{1}{0.2} \mid i \neq j \\ 0 \quad \mid i = j \end{cases}$
δ^S	0 (all entries)
ϵ	0.6
θ_R	50
κ	1.8
ν_1^T	$(-1, 0, 0, 0, 1, 0, 0, 0,)$
ν_2^T	$(0, -1, 0, 0, 0, 1, 0, 0)$
ν_3^T	$(0, 0, 0, 0, -1, -1, 1, 1)$
ν_4^T	$(0, 0, 1, 0, 0, 0, -1, 0)$
ν_5^T	$(0, 0, 0, 1, 0, 0, 0, -1)$
τ	3
ω_1	$0.045 \cdot x_{gas,1} \cdot \left(3 - \sum_{j=1}^4 x_{solid,j} \right)$
ω_2	$0.045 \cdot x_{gas,2} \cdot \left(3 - \sum_{j=1}^4 x_{solid,j} \right)$
ω_3	$150 \cdot x_{solid,1} \cdot x_{solid,2}$
ω_4	$0.15 \cdot x_{solid,3}$
ω_5	$0.15 \cdot x_{solid,4}$

References

1. Bennett, C., The Tansient Method and Elementary Steps in Heterogeneous Catalysis, Catal. Rev. - Sci. Eng. 13 (1976) 121-148
2. Dekker, F. H. M., Bliek, A., Kapteijn, F., Moulijn, J. A., Analysis of Mass and Heat Transfer in Transient Experiments Over Heterogeneous Catalysts, Chem. Eng. Sci. 50 (1995) 3573-3580
3. Mason, E. A., Malinauskas, A. P., Gas Transport in Porous Media: The Dusty-Gas Model, Elsevier Scientific Publishing Company, Amsterdam, Oxford, 1983
4. Nowak, U., A Fully Adaptive MOL-Treatment of Parabolic 1-D Problems with Extrapolation Techniques, Appl. Num. Math. 20 (1996) 129-145
5. Do, D. Rice, R., Determination of the Condition for the Existence of Composition Minima in a CSTR via Spectral Analysis, Chem. Eng. Sci., 40 (1985), 291-298
6. Leder, F., Butt, J. B., The Dynamic Behaviour of a Fixed-Bed Catalytic Reactor, AIChE J, 12 (1966) 1057-1063

A dynamic model for the Venturi Loop Reactor Venturi loop reactor

Robbert de Graaf[1], Remco Reinstra[1], Maurits Wieberdink[1] and Michiel Kreutzer[2]

[1] Groningen University, R.A.de.Graaf@chem.rug.nl,The Netherlands
[2] University of Delft, M.T.Kreutzer@ts.chem.rug.nl, The Netherlands

Abstract. A dynamic model of a venturi loop reactor was set-up. First steady state calculations describing the hydrodynamics and mass transfers coefficients were performed. The second group of simulations concentrated on the performance of the system for different kinetics and operating conditions. Finally the scale up of the reactor was modelled resulting in the conclusion that using proper chosen scaling rules, the reaction time and time dependency of the key variables can be kept uniform.

1 Introduction

In a venturi loop reactor mass transfer [1] between gas and liquid plays an important role. In literature already a lot of attention is paid to the measurement of this mass-transfer but also data about the interfacial areas, the hydrodynamics and the gas etrainment rate [2] exist. With the help of all these experimental data and the increasing computational power of the computer, it should be possible to build a suitable simulation model predicting the operation and scale-up [3]. This should lead to the possibility to bypass steps in the development from lab process to the final plant. Such a model should incorporate hydrodynamic behaviour, mass and heat transfer models [4] in combination with heterogeneous catalyst, physical properties and start-up and shut-down processes. The objective of the research performed was to model a venturi loop reactor, applicable to arbitrarily chosen kinetics, reactants and processing conditions. With the model; interpretation of experimental data, optimisation and scale-up should be made easier and much faster.

2 Theory

The principle design of the venturi loop reactor is shown in figure 1. In order to model such a system it was subdivided into six parts. For both the main reaction vessel and the venturi injector the same mass balances, reaction
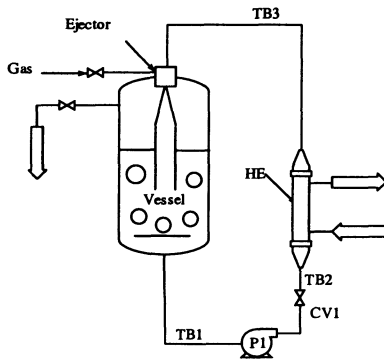
Fig. 1. Operating principle of a venturi loop reactor; pump (P1), Control valve (CV1), Main reaction vessel (VES), Venturi ejector (VEJ), Tubes (TB 1-3), and the heat exchanger (HE)
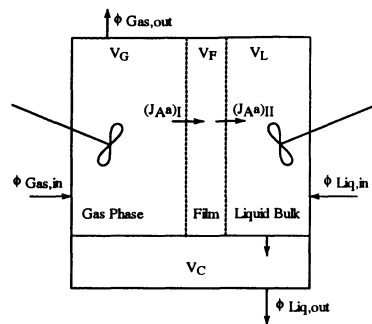
Fig. 2. Reaction model (both for the vessel and the venturi)

kinetics and enthalpy balances were set up. For the pump, control valve, tubes and heat exchanger different models were set up. The venturi ejector is a very efficient gas-liquid contactor. The liquid feed is led through a small nozzle, resulting in a high liquid velocity. This high velocity jet passes through a small tube, which is slightly larger in diameter. Gas is fed near the nozzle. Instabilities at the jet surface entrain the gas. A continuous enlargement of the jet causes finally a mixing shock. The two-phase stream of gas and liquid, flow downward through a wider section of the venturi. In the mixing shock liquid and gas is finely dispersed and most of the kinetic energy of the liquid is dissipated. This results in the formation of very small gas bubbles. These fine gas bubbles in turn lead to high mass transfer rates. Because of the high energy dissipation in the mixing shock the mass transfer in the venturi tube is a few orders of magnitude larger than the mass transfer in the main vessel. For a system where the absorption of gas is the limiting step (Ha > 2, Fast reaction), the venturi ejector almost solely determines the reaction time of the system, although the residence time in the ejector is small compared to the vessel. The energy dissipated by the liquid flow in the mixing shock is estimated as the kinetic energy of the jet leaving the nozzle:

$$W_L = \frac{1}{2}\rho u_N^2 \phi_L \tag{1}$$

where $\rho [kg\, m^{-3}]$, $u_N [m\, s^{-1}]$ and $\phi_L [m^3 s^{-1}]$ are the density of the liquid, the velocity of the liquid leaving the nozzle and the throughput of the liquid. The energy consumed by the gas flow is estimated by:

$$W_G = (P_{out} - P_{GC})\phi_G \tag{2}$$

where $P_{out}[N\ m^{-2}], P_{GC}$ and $\phi_G[m^3 s^{-1}]$ are the pressure of the stream leaving the ejector, the gas pressure near the nozzle and the gas throughput. Combining both equations lead to the dissipation of energy in the mixing shock per unit volume or:

$$\epsilon = \frac{W_L - W_G}{\epsilon_L \rho_L V_{EJ}} \tag{3}$$

where $\epsilon_L[-]$ and $V_{EJ}[m^3]$ are the liquid hold–up in the ejector and the volume of the ejector. This dissipation is used to calculate the bubble diameter[1]:

$$d_b = 0.62 \left(\frac{We_C}{2}\right)^{0.6} \left(\frac{\sigma}{\rho_L^2 \rho_G}\right)^{0.6} \epsilon^{-0.4} \left(\frac{1 + \epsilon_G}{1 + 0.2\epsilon_G}\right)^{1.2} \tag{4}$$

where $We_C[-]$, $\sigma[Nm^{-1}]$, $\epsilon[W\ kg^{-1}]$ and $\epsilon_G[-]$ are the Weber number, the surface tension, the local energy dissipation and the gas hold–up in the venturi. Now the $k_L[ms^{-1}]$ in the venturi can be calculated according to the following relation [5]:

$$k_L = 0.302 \left(\frac{\epsilon}{\eta_L}\right)^{1/4} \sqrt{D_A} \tag{5}$$

where $\epsilon[Wkg^{-1}]$, $\eta[m^2 s^{-1}]$ and $D_A[m^2 s^{-1}]$ are the energy dissipation rate, the liquid viscosity and the diffusion coefficient.

The main reaction vessel behaves like a bubble column. The jet of the ejector enters the main vessel where it hits a collision plate. The jet velocity is transferred into a circulation flow in the reaction vessel. The formed bubbles, rise upward and grow in size through coalescense. As a first assumption, the mixing in the vessel is not included in the model. Both the liquid- and the gas volume are well mixed in relation to the reaction rate. The headspace of the reactor is assumed to be small and therefore not modelled. Three different sections can be distinguished in the main vessel [see figure 2].

- The liquid volume above the collision plate (V_L). This volume is in contact with the gas volume through a film volume (V_F).
- A clear liquid volume that is below the collision plate (V_C).
- The gas volume (V_G) in the top of the main vessel

The liquid volume is treated as two separate volumes. The volume under the collision plate which is regarded as a single phase reactor and the volume above the collision plate which behaves like a two phase bubble column to which the specific area is related. Since the venturi and the main vessel both are gas-liquid contactors, the description of mass transfer and reaction is almost identical. A difference between the main vessel and the ejector is that

all the liquid in the ejector behaves as a plug flow, while the main vessel is divided in a mixed volume and a plug flow part below the collision plate.

Beside models for the reaction section also models for the pump zone, the tubes, the control valve and the heat-exchanger were set-up. For all the tubes (also the tubes in the heat exchanger) the axial dispersion model was used. In case of the heat exchanger also a shell side was incorporated using the same model as was used for the tubes. The numerical solution of the partial differential equations for a heat exchanger is sensitive to the algorithm applied. Stable results were obtained using a backward finite elements method for the tube sides (no strong diffusive terms) and a forward finite element method for the shell side.

3   Testing

The models as described in the theory contain dynamic and non-dynamic equations. Both parts have to be tested and solved. As solver software gPR-OMS was choosen. This software package is developed at the Imperial College and on this moment commercially available at PSE ltd.. This software package is capable of solving large sets of equations (linear and partially differential equations). Beside that it has as advantage that it is able to model discrete events. Each model was tested separately. MathCAD calculations were used to calculate steady state values. These results were validated with the individual gPROMS models by letting the gPROMS simulations run to steady state. No deviations were found in the models indicating that the gPROMS models were stable. The dynamic part of the system was tested by checking the mass and energy balances. The tests showed errors of less than 0.5 %. These errors were decreased by increasing the amount of gridpoints. It should be noted at this point that in the model neither the throughput nor the pressure drop is explicitly given. The model calculates the recycle flowrate from the combined pressure-throughput relations in the separate models.

4   Results and Discussion

4.1   Hydrodynamics, kinetics and mass transfer

An important design value in venturi loop reactors is the gas entrainment rate. Comparing simulated gas entrainment rates with measured rates, no differences were found. In our case a Henzler type relation [6] was used:

$$\frac{Q_G}{Q_L} = B \left(1 - C_1 \left(\frac{\rho_G}{\rho_L} \right)^{C_2} \frac{d_M}{d_N} \left(\frac{P_{Out} - P_{GC}}{1/2 \rho_L u_N^2} \right)^{1/2} \right) \tag{6}$$

where $Q_G[m^3 s^{-1}]$, Q_L, P_{out}, P_{GC}, ρ_L, ρ_G, $d_m[m]$, d_n, $u_N[ms^{-1}]$, B, C1 and C2 are the gas and liquid flow rates discharging through the gas suction

chamber of the ejector, the pressure of the stream leaving the ejector, the gas pressure near the nozzle, the density of the liquid and the gas, the nozzle velocity by the nozzle cross section, the nozzle diameter, the mixing tube diameter and three nozzle dependant constants.

Calculations of the mass transfer capability of the ejector showed that the $k_L a$ is about 18 to 20 times higher compared to the $k_L a$ in the main reaction vessel. These values are also comparable to measured values [1]. Beside calculating the mass transfer characteristics, also the influence of an arbitrary reaction on the mass transfer was examined. The present model describes reactions of type:

$$A + \nu_B B \xrightarrow{k_r} \nu_P P + \nu_Q Q + \dots \quad with \quad k_r = k_\infty \, e^{\frac{-E_A}{RT}} \qquad (7)$$
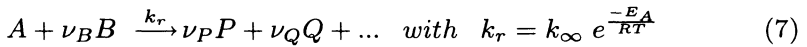
Different reaction times were simulated by varying the activation energy, see table [1]. The reaction time was defined as the time needed to obtain 99,9% conversion.

Table 1. Activation energy, rate constants and reaction times (T= 298 K)

$E_a [Jmol^{-1}]$	$k_r [m^3(mols)^{-1}]$	Reaction time[min]
2000	17.4	21
4000	7.75	26
8000	1.54	43
16000	0.0609	113
32000	9.5310^{-5}	750

Because of the large differences in reaction time, all test results were plotted against the conversion, rather than time. In the design of a venturi reactor for a single reaction, it is important that the gas dissolved in both the ejector and the vessel is converted before it enters the loop. If the gas concentration in the loop is high, the capacity is limited by the kinetics, as opposed to the mass transfer. In order to verify that both the regime of chemically enhanced absorption and physical absorption are treated, the Hatta number for the fastest and the slowest reaction in the vessel and the ejector were calculated [figure 3]. The results showed that both regimes were covered. In figure 6 the bulk concentration of the dissolved gas is plotted (slowest reaction). The solubility of the used gas was 1.2 $mol \; m^{-3}$. For the very slow reaction, the concentration of the dissolved gas is of this order of magnitude. For faster reactions, the concentration drops to near zero values, as can be expected for higher Ha-numbers. The amount of mass transfer in the vessel, relative to the mass transfer in the total system, was also computed. From these results it

could be concluded that the vessel volume is only important for the capacity of the reactor if the reaction rate is moderate (Ha $\ll$ 0.5).

4.2   Operating condition

For the slowest and the fastest reaction rates the reaction time has been investigated as a function of the operating conditions [Figure 4].
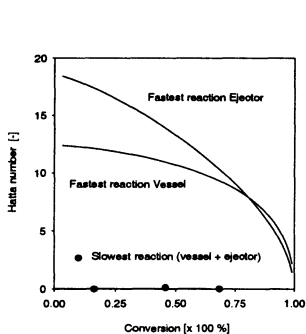
Fig. 3. Hatta numbers in the ejector and the main reaction vessel.
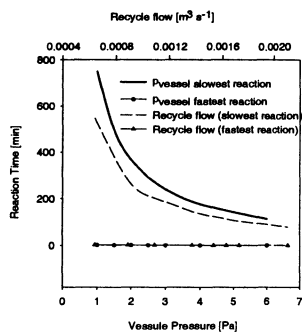
Fig. 4. Reaction time versus the recycle flow and vessel pressure

Increasing the gas pressure in the system increases the concentration of the gas, which yield higher mass transfer capacities in the system. So using elevated pressures, the time required to complete the reaction, can be reduced independent of the used kinetics. Simulations were performed where the vessel top pressure was varied from 1 to 6 bar. In these runs, the ejector outlet pressure was equal to the top pressure, and the gas suction pressure was 0.2 bar lower than the outlet pressure (constant pressure drop in the ejector) [Figure 4]. The liquid recycle flowrate has also a profound effect on the reaction time in case of fast reactions[Figure 4]. Increasing this the recycle flow increases the gas entrainment and thus a higher mass transfer is obtained.

4.3   Scale-up

The scale-up rules for any chemical reactor are deduced by identifying the rate-controlling step. In the venturi loop reactor, this may be the absorption of gas in the liquid. The subsequent reaction in the liquid is faster, and need not be considered in a scale-up or mixing behaviour study. The rate of absorption is dependent on the interfacial concentrations, mass transfer

coefficient, specific area and kinetic and physical properties of the system. Careful examination of the model equations learns that for an identical reaction system on a large and small scale, k_L and a can be kept constant if the dissipation of energy (ejector and main reaction vessel) per unit volume is the same on the large and small scale. Dissipation of energy (ϵ)is calculated by:

$$u_n = \frac{\phi_L}{\frac{1}{4}\pi d_N^2} \tag{8}$$

$$\epsilon = \frac{\frac{1}{2}\rho_L u_N^2 \phi_L - \Delta P_{EJ}\phi_G}{\rho_L \epsilon_L V_{EJ}} \tag{9}$$

where ϕ_L is the Liquid throughput $[m^3\ s^{-1}]$, d_n the nozzle diameter [m], ρ the density $[kg\ m^{-3}]$, ϵ is the energy dissipation $[W\ m^{-3}]$ and u_n the nozzle velocity $[m\ s^{-1}]$. The pilot scale system was geometrically scaled-up by a factor 3. In the case of the unscaled situation our energy dissipation was $\epsilon = 400[W\ m^{-3}]$. By solving the above system of equations for $\epsilon = 400[W\ m^{-3}]$ in the scaled system, the flowrate in this system will be $\phi_{Large} = 0.02105\ [m^3\ s^{-1}]$ A simulation of the scaled system, where all dimensions are multiplied by a factor of 3, was performed using this liquid flowrate. The resulting reaction time for the large system was approximately 86.5% of the reaction time for the small system. Figure 5 illustrates that in the ejector the scale rule works satisfactory: the dissipation of energy is almost the same in both systems, and so are the mass transfer coefficients. Figure 6 shows that the situation in the main reaction vessel is completely different. The scaled vessel also contributes in an appreciable amount to the absorption of gas. A scaling rule for the vessel must be included. This is to be expected because the slowest reaction rate was used. In the vessel, the product $k_L a$ is a function of the superficial gas velocity and the physical properties. The superficial gas velocity on its turn is dependent on the vessel diameter. A new simulation was done, where the diameter (not the volume) of the vessel was altered to obtain the same superficial gas velocity in the vessel as in the small system (a scaling rule common to bubble columns). This resulted in the right behaviour as can be seen in figure 6.

$$(D_{ves})_{Large} = \sqrt{D_{ves}^2 \frac{(\phi_L)_{large}}{(\phi_L)_{small}}} = 1.074[m] \tag{10}$$

where D_{ves} is the vessel diameter [m]. The results of the second simulation show a much better agreement [Figure 6].

5   Conclusions

The influence of the reaction rate can be well explained by the present knowledge of two-phase reactors in general and venturi loop reactors in specific.
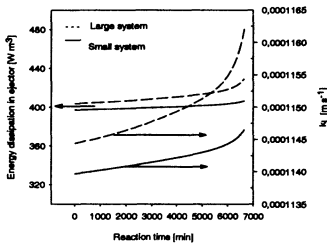
Fig. 5. Energy dissiation and k_l versus the reaction time for the scaled up and the original system.
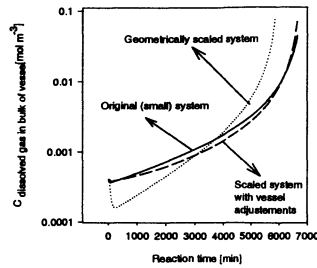
Fig. 6. Concentration of gas dissolving in the vessel in case of a slow reaction. Three situations are plotted in this graph: 1) The original small scale situation 2) The geometrically scaled up situation 3) The scaled up situation with adjustments made to the vessel

The results of the steady state calculations for hydrodynamic variables agree well with data found in the literature; all the variables are at least of the same order of magnitude. Since the system is sensitive to the empirical parameters in the equations for gas entrainment and $k_L a$ values, closer comparison with data in the literature is impossible. With the model operating conditions could be predicted. Also the use of the model for the study of scale-up was successful. Using proper chosen scaling rules, the reaction time and time dependency of the key variables were uniform in the small and large system. In general the conclusion is drawn that the model is well in agreement with venturi loop know how.

References

1. Cramers P.H.M.R., Beenackers A.A.C.M. and Dierendonck van L.L. (1992), Chemical Engineering and Science, Vol 47, No 13/14 pp. 3557-3564.
2. Hinze, J.O., (1955), AIChE Journal, 1 3,289-295.
3. Dierendonck van, L.L., Meindersma, G.W., and Leuteritz, G.M., (1988), Scale-up of G-L-reactions made simple with loop reactors, Sixth European conference on mixing, Pavia (italy).
4. Beenackers A.A.C.M. and van Swaay W.P.M., (1993), Chemical Engineering Practice, Vol. 48, No. 18, pp.3109-3139.
5. Kawase, Y., and Moo-Young, M., (1990), Chem.Eng.J., 43, B19-B41.
6. Henzler, H.J., (1981), Verfahrenstechnik, 15, 738-749.

Numerical Modelling of Multiphase–Multicomponent Systems in Porous Media

R. Huber and R. Helmig

University of Technology Braunschweig, Institute of Computer Applications in Civil Engineering
Pockelsstrasse 3, D - 38106 Braunschweig; r.huber@tu-bs.de

Abstract. Flow and transport processes in the subsurface are of major interest for the study of NAPL (non-aqueous phase liquids) contaminations and for the development of efficient remediation techniques and strategies.

For the simulation of NAPL infiltrations the gaseous diffusion in the soil air is an important transport mechanism in the unsaturated zone. Due to the thermodynamic equilibrium organic chemicals migrate from the soil air into the groundwater travelling considerable distances from the infiltration source. Numerical simulations can be used as a prognosis tool to predict the movement of contaminant plumes in the subsurface.

New clean-up methods such as alcohol flooding, SEAR (surfactant-enhanced aquifer remediation), SVE (soil vapor extraction), and steam injection are developed and investigated using numerical simulators. E.g., miscible displacement and enhanced dissolution are the key processes for alcohol flooding to remove residual organic contaminants from the subsurface. This involves the phase partitioning of the different compounds over the ambient phases.

The modelling of multiphase-multicomponent systems in porous media is presented. Furthermore, a contamination and a remediation scenario are studied by the use of a numerical simulator.

1 Introduction

Subsurface multiphase flow is of interest for the simulation of contamination scenarios involving nonaqueous/organic liquid phases, e.g., halogenated or aromatic hydrocarbons, to develop effective remediation strategies. Furthermore, the design of new in–situ clean–up technologies require the development of numerical simulators which describe the flow and reactive processes in the soil accurately.

Multiphase models can be subdivided into those which assume immiscible fluid phases and the class of compositional models. The latter ones take into account interphase mass transfer processes. Under natural conditions only a small portion of a component partitions into the other phases (see e.g., Helmig[1]). The mass transfer can be described either using the local equilibrium assumption (LEA) or a nonlinear kinetic model. However, for

remediation techniques such as alcohol or surfactant flooding one component (alcohol or surfactant) may be fully miscible into the ambient phases (Delshad et al.[2]). In this case, a different approach is used.

In the following two formulations are presented: The first formulation considers three components which partition in relative small amounts into the up to three phases. The second formulation is for a two–phase three–component system where one component is fully miscible.

2   Governing Equations

Three–phase systems in the subsurface typically consist of two liquid phases (aqueous/water (w) and a non–aqueous phase liquid (n), in short NAPL) and one gaseous phase (g). For immiscible flow the conservation of each phase $\alpha \in \{w, n, g\}$ is utilized (e.g., Aziz & Settari[3]). However, for compositional flow and transport, conservation of the components (chemical species: organic compound (^{c}), water (^{w}), air (^{a}), alcohol (^{al})) needs to be considered (Forsyth & Shao[4]):

$$\frac{\partial}{\partial t} \sum_\alpha (\phi \, \varrho_\alpha \, S_\alpha \, X_\alpha^\kappa) = - \sum_\alpha \nabla \cdot [\varrho_\alpha \, v_\alpha \, X_\alpha^\kappa]$$
$$+ \sum_\alpha \nabla \cdot [\phi \, \varrho_\alpha \, S_\alpha \mathbf{D}_\alpha^\kappa \, \nabla X_\alpha^\kappa] + q^\kappa \, , \, \kappa \in \{c, w, a\} \tag{1}$$

where ϕ is the porosity, ϱ_α, S_α, v_α are the density, saturation and the Darcy velocity of each phase α, respectively. X_α^κ is the (molar) fraction of component κ in phase α, $\mathbf{D}_\alpha^\kappa$ the hydrodynamic dispersion tensor, and q^κ is the source rate of κ.

The generalized Darcy's law for multiphase flow in porous media is described by:
$$v_\alpha = -\lambda_\alpha \, \mathbf{K} \, (\nabla p_\alpha - \varrho_\alpha \, g) \quad , \, \alpha \in \{w, n, g\} \tag{2}$$

where λ_α is the α–phase mobility which is the ratio of relative permeability $k_{r\alpha}$ to viscosity μ_α. $\mathbf{K}$ is the absolute permeability tensor, p_α the α–phase pressure and g the gravitational acceleration vector.

These two laws are supplemented by the constraint that the sum of all phases is always one, i.e., $S_w + S_n + S_g = 1$, and the following constitutive relationships: The relative permeabilities are assumed to be functions of the phase saturations and the interfacial tension. The differences of the phase pressures of the three–phase system are described by capillary pressure–saturation relations. The aqueous phase is assumed to be the most wetting phase forming a continuous film along the pore walls. NAPL as the intermediate wetting phase separates the water and gas phases.

3   Numerical Formulations

Formulations of immiscible two–phase and three–phase flow are studied extensively by Helmig[1] and Huber & Helmig[5]. Based on them, the here presented formulations are developed. The compositional formulations employ a balancing of the components on a molar basis. The substitution of Darcy's law (2) into the component conservation equations (1) and a finite volume (box) discretization (see Fig. 1) with backward Euler time discretization, mass lumping and rearrangement of the accumulation terms yields the following discrete formulation (Helmig[1], Forsyth & Shao[4], Forsyth[6], Panday et al.[7]):

$$\frac{V_i}{\Delta t} \left\{ \left[\phi \, Z^\kappa \sum_\alpha \varrho_\alpha \, S_\alpha \right]_i^{t+\Delta t} - \left[\phi \, Z^\kappa \sum_\alpha \varrho_\alpha \, S_\alpha \right]_i^t \right\}$$

$$= \sum_\alpha \sum_{j \in \eta_i} (\varrho_\alpha \, \lambda_\alpha \, X_\alpha^\kappa)_{ups(i,j)}^{t+\Delta t} \; \gamma_{\alpha ij} \; \left(\psi_{\alpha j}^{t+\Delta t} - \psi_{\alpha i}^{t+\Delta t} \right)$$

$$+ \sum_\alpha \sum_{j \in \eta_i} \varrho_{\alpha,ij}^{t+\Delta t} \, \gamma'_{\alpha ij} \left(X_{\alpha j}^{\kappa,t+\Delta t} - X_{\alpha i}^{\kappa,t+\Delta t} \right)$$

$$+ V_i \, q_{\alpha i} = 0 \,, \qquad \kappa \in \{c,w,a\} \qquad (3)$$

where Z^κ is the overall global mole fraction of component κ and $\psi_{\alpha i} = p_\alpha - \varrho_\alpha \, g$. η_i is the set of all neighbor boxes/nodes which share a box boundary with B_i, or in other words, all indices j with $|\gamma_{\alpha ij}| > 0$. $V_i = \int_{B_i} dx$ is the volume of box B_i. The transmissivity terms $\gamma_{\alpha ij}$ and $\gamma'_{\alpha ij}$ for the box scheme, which are factors of the discrete fluxes between neighboring boxes, are given by

$$\gamma_{\alpha ij} = \sum_{e:i,j \in e} \mathbf{K} \cdot \nabla N_j \cdot \mathbf{n}(l_{ij}^e) \, A(l_{ij}^e) \qquad (4)$$

$$\gamma'_{\alpha ij} = \sum_{e:i,j \in e} \phi \, S_\alpha \, \mathbf{D}_\alpha^\kappa \cdot \nabla N_j \cdot \mathbf{n}(l_{ij}^e) \, A(l_{ij}^e) \quad . \qquad (5)$$

$\mathbf{n}$ is the outward unit normal vector w.r.t. box B_i. In the case of quadrilateral elements each element is divided into four subcontrol–volumes each belonging to a box associated with an element node (see Fig. 1). $A(l_{ij}^e)$ is the area of box boundary segment l_{ij}^e between boxes i and j inside of element e. The mobilities, densities and phase mole fractions in the advective flux term in (3) are upstream weighted. The α–phase upstream direction at the interface between boxes associated with nodes i and j is determined by

$$ups(i,j) = \begin{cases} i & \text{if} \quad (\psi_{\alpha j} - \psi_{\alpha i}) \le 0 \\ j & \text{if} \quad (\psi_{\alpha j} - \psi_{\alpha i}) > 0 \end{cases} \quad . \qquad (6)$$
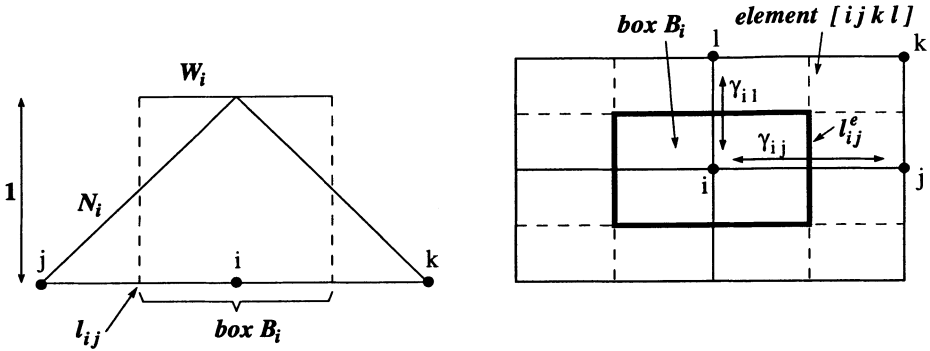
Fig. 1. Box scheme in 1D (left) and for a rectangular mesh (right).

This upstream weighting of saturation dependent terms is necessary to obtain a stable solution, especially in the case of convection–dominated processes where the equations are essentially hyperbolic (e.g., Forsyth[6]). The resulting scheme represents a five–point discretization in 2D. However, there is also the choice of a control–volume finite element discretization which gives a nine–point stencil (Forsyth[6], Helmig[1]).

The slightly miscible three–phase three–component formulation uses a variable substitution algorithm for the primary variables (see Tab. 1). The phase molar fractions for each component are derived using the concept of K–factors (Henry's and Raoult's laws).

The strongly miscible two–phase three–phase formulation uses as primary variables the fixed set (Z^c, p_w, Z^{al}). Phase states, phase molar compositions and interfacial tensions are obtained using a ternary diagram.

Both presented compositional multiphase simulators utilize the Newton–Raphson concept to solve the nonlinear discrete system equations. The Jacobian is constructed with a chord slope technique. The resulting systems of equations are solved using an ILU decomposition and a BICGSTAB solver.

Table 1. Phase states and primary variables of 3–phase 3–component formulation:

Resident Phases	Primary Variables V^c V^w	V^a
aqueous, NAPL, gas	S_n S_g	p_g
aqueous, NAPL	S_n Z^a	p_g
NAPL, gas	S_n Z^w	p_g
aqueous, gas	Z^c S_g	p_g
aqueous	Z^c Z^a	p_g
NAPL	Z^a Z^w	p_g
gas	Z^c Z^w	p_g

4   LNAPL Infiltration Simulation

The infiltration of an LNAPL (lighter–than–water nonaqueous phase liquid) into the subsurface due to a hypothetical accidental spill is simulated. The vertical two–dimensional model domain has dimensions of 50m x 4m. The infiltration source is located on the ground surface at x=15m. The water table varies linearly from z=2m at the left boundary to z=1m at the right boundary. On the ground surface atmospheric pressure is prescribed. The bottom is impermeable. Mass transfer from the NAPL into the aqueous and gaseous phases is described. For the dispersion, longitudinal and transversal dispersivities of 50m and 0.1m, resp., are used. Molecular diffusion is neglected. A mesh of 50 x 40 elements is used. We employ a full three–phase formulation with a local equilibrium assumption for the mass transfer.

Before the NAPL infiltraton starts, the system has been allowed to reach from a fully saturated state an equilibrium state. The vadose zone is then almost entirely at residual water saturation. Infiltrating NAPL is moving mainly downwards due to gravitational forces. At the water table LNAPL is pooling. When the infiltration has stopped, the NAPL saturations above the pool approach the NAPL residual saturation. The state after 6 days is shown in Fig. 2.
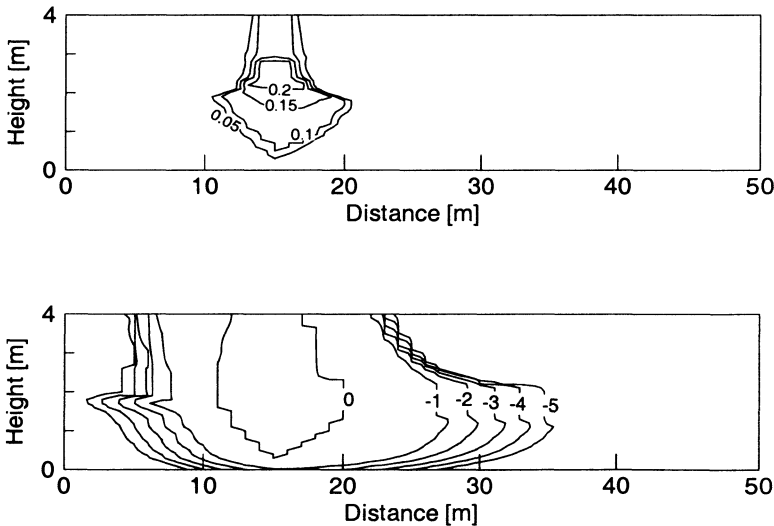
Fig. 2 top: NAPL saturation; below: $\log_{10}$ normalized contaminant mole fractions in the aqueous phase.

In the vadose zone, the contaminant transport occurs mainly in the non-aqueous phase. However, when the NAPL phase reaches the water table, organic compounds dissolve into the flowing groundwater in the saturated zone and migrate by advective transport down–gradient (to the right in Fig. 2).

5   Alcohol Flooding Simulation

Alcohol–water floods can be used to mobilize residual NAPL in the subsurface (after an accidental spill) and remove it by enhanced dissolution and/or immiscible and miscible displacement. In the following, an experimental study by Brandes [8] is simulated. He used a one–dimensional vertical upward flood of one pore volume (PV) of a 70% by volume t–butyl alcohol (TBA) solution followed by a water flood to remove tetrachloroethylene (PCE) which was initially at residual saturation from a column. The 60cm long column is filled with glass beads. Injection is done under a hydraulic gradient of 0.3. The column is discretized using 100 elements.

In Fig. 3 (left) the simulation results after injection of 0.5 PV are depicted. Alcohol is partitoning into the NAPL causing a swelling and mobilization. Thus, ahead of the alcohol solution front a NAPL bank forms which merges at its tail into a miscible front. The remaining PCE is removed by enhanced dissolution into the alcohol–water mixture. The simulated effluent concentrations (in Fig. 3 (right)) reproduce the experimental data only partly. This is probably due to kinetic mass transfer and side effects of the conducted experiment. However, Brame [9] who also based a simulation on this experiment obtained similar effluent rates. Simulations of complex processes like this one are impeded by a lack of data for relative permeabilities and capillary pressures which are in this case strongly dependent on the overall composition of the system. Unfortunately, they are difficult to measure under such complicated conditions. The simulation overpredicted the recovery of PCE with 100% compared to about 95% in the experiment.

6   Conclusions

Two compositional multiphase porous media flow formulations which are based on a finite volume discretization are presented. A (slightly miscible) three–phase three–component formulation is applied to a typical contamination scenario of a temporary LNAPL spill.
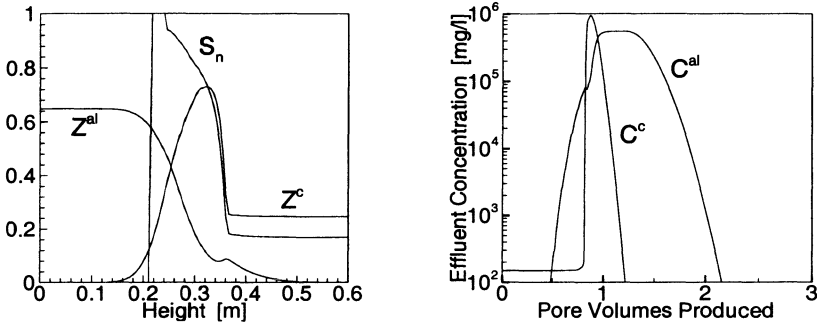
Fig. 3 left: NAPL saturation S_n and global mass fractions of PCE Z^c and TBA Z^{al}; right: effluent concentrations of PCE C^c and TBA C^{al}

Simulation results indicate that in general organic chemicals do not migrate far from their source in form of a nonaqueous phase. However, if NAPL is present in the subsurface, it acts as a long–term contamination source, especially to the groundwater. Dissolved organics may travel large distances and threaten the supply of drinking water. Also, a strongly miscible two–phase three–component simulator is introduced which can be employed to study and improve the clean–up performance of alcohol flooding operations. One major danger in improper use of this technique is the uncontrolled mobilization of dense NAPLs which would migrate downwards in the saturated zone where it would be much more difficult to assess and remediate them.

References

1. Helmig, R., Multiphase Flow and Transport Processes in the Subsurface – A Contribution to the Modeling of Hydrosystems –, Springer–Verlag, Berlin, 1997.
2. Delshad, M., Pope, G.A. & Sepehrnoori, K., A Compositional Simulator for Modeling Surfactant Enhanced Aquifer Remediation, J. Contam. Hydrol., 23, pp. 303–328, 1996.
3. Aziz, K. & Settari, A., Petroleum Reservoir Simulation, Applied Science Publ., London, 1979.
4. Forsyth, P.A. & Shao, B.Y., Numerical simulation of gas venting for NAPL site remediation, Adv. Wat. Res., 14, pp. 354–367, 1991.
5. Huber, R. & Helmig, R., Investigation and Simulation of Three–Phase Flow in Porous Media, Sci. Report No. 2, Chair of Numerical Methods and Information Processing, Univ. of Techn. Braunschweig, Germany, 1997.
6. Forsyth, P.A., A control volume finite element approach to NAPL groundwater contamination, SIAM J. Sci. Stat. Comp., 12, pp. 1029–1057, 1991.
7. Panday, S. Forsyth, P.A., Falta, R.W., Wu, Y.S. & Huyakorn, P.S., Considerations for robust compositional simulations of subsurface nonaqueous phase liquid contamination and remediation, Wat. Res. Res., 31, pp. 1273–1289, 1995.
8. Brandes, D., Effect of Phase Behavior on residual dense nonaqueous phase liquid displacement from porous media by alcohol flooding, PhD thesis, Clemson Univ., 1992.
9. Brame, S.E., Development of a Numerical Simulator for the in–situ remediation of dense nonaqueous phase liquids using alcohol flooding, MS thesis, Clemson Univ., 1993.

Efficient Computation of Singularities of Chemical Reactor Models

Johannes Khinast[1] and Dan Luss[2]

[1] Department of Chemical and Biochemical Engineering, Rutgers University, Piscataway, NJ 08854-8058, USA, khinast@sol.rutgers.edu

[2] Department of Chemical Engineering, University of Houston, Houston, TX 77204-4792, USA, dluss@uh.edu

Abstract. Computing the loci of singular points of PDEs requires repeated computation of the Jacobian or monodromy matrix and of the corresponding eigenvalues and eigenvectors of the discretized equations. This is a very tedious task for large sets of equations. We propose to simplify these computations by a combined use of *shooting, quasi-Newton* methods and *direct linearization* embedded in a *continuation* scheme [8]. In this paper we describe the large reduction in the numerical effort that may be accomplished by direct Fréchet differentiation of the PDEs, i.e., the direct linearization. This method is more general than earlier approaches and can be applied to general bifurcation problems, which is illustrated by two examples.

1 Introduction

Singular points are the boundaries between qualitatively different types of model behavior, e.g., the transition from steady to periodic solutions. A bifurcation analysis determines and tracks singular points in the parameter space. We present here a method for computing the bifurcations of chemical reactor models, described by a set of coupled nonlinear PDEs, e.g.,

$$C\frac{d\boldsymbol{u}}{dt} = \boldsymbol{f}(\boldsymbol{u}, \nabla\boldsymbol{u}, \nabla^2\boldsymbol{u}, \lambda), \tag{1}$$

where C is the capacitance matrix, $\boldsymbol{u}$ the state vector, $\boldsymbol{f}$ a vector of nonlinear functions, and λ a *distinguished* or *bifurcation parameter*. For convenience, we do not refer to the other parameters $\boldsymbol{p}$ in the equations. Spatial discretization leads to equations of the form

$$\hat{C}\frac{d\hat{\boldsymbol{u}}}{dt} = \boldsymbol{f}(\hat{\boldsymbol{u}}, \lambda), \quad \hat{\boldsymbol{u}} \in \Re^N. \tag{2}$$

To avoid spurious solutions one is often forced to use a large number of grid points. Typically, 2-D problems require $10^4 - 10^5$ grid points, 3-D problems $10^5 - 10^7$ grid points. Thus, N is usually a large number ($N > 10^4$).

A singular point is defined to be of codimension k, if k parameters (including the bifurcation variable) have to be varied to obtain all the possible qualitatively different features (unfolding) next to it. We list in Table 1 singular points of steady-state and periodic solutions of codimension 1 and 2.

(The list of codimension-2 singular points is not complete). The corresponding defining conditions may be found in[1] and are also given in [4, 5, 6]. These conditions require computing the eigenvalues of either the Jacobian matrix (steady-state analysis) or of the monodromy matrix (periodic states). Determination of singularities with $k > 1$ requires the computation of higher-order derivatives.

Table 1. Singular points of codimension 1 and 2 for steady-state and periodic solutions.

Steady-State		Periodic	
Codim 1	*Codim 2*	*Codim 1*	*Codim 2*
• Limit point	• Hysteresis	• Saddle-node	• Period $n, n > 2$
• Hopf point	• Isola (ell., hyp.)	• Period-doubling	• Twist
• Boundary point	• Double limit	• Quasi-periodic	• 1:1 resonance
	• Double Hopf	bifurcation	• Degenerate period
	• Hopf-Hopf		doubling
	• Boundary-Hopf		• Degenerate quasi-
	• Boundary-Limit		periodic bifurcation
	• Hopf-Limit		• etc.
	• etc.		

We propose to simplify the computation of the loci of singular points for high-dimensional models by a combined use of *shooting, quasi-Newton* methods and *direct linearization* embedded in a *continuation* scheme [8]. In this paper we describe the large reduction in the numerical effort accomplished by direct Fréchet differentiation (direct linearization) of the model.

2   Direct Differentiation Method

Computation of the discretized Jacobian or monodromy matrix and of the corresponding eigenvalues and eigenvectors is very time consuming and becomes unpractical for large systems. Additionally, for large matrices the influence of numerical inaccuracies becomes significant in the computation of eigenvalues and eigenvectors. In a normal bifurcation analysis the model equations are first discretized in space and then the Jacobian or monodromy matrix plus corresponding eigenvectors and eigenvalues are computed. We, however, propose to first linearize the PDEs by Fréchet differentiation, to subsequently define the conditions of the singular points and then use spatial discretization. We therefore circumvent the need to compute the Jacobian

or monodromy matrix and the corresponding eigenvectors by using Fréchet differentiation of the PDEs. Thus, we only compute a product of the matrix with its eigenvector, e.g. by using the identity $\boldsymbol{J} \cdot \boldsymbol{v} = \boldsymbol{L}\boldsymbol{v}$, where $\boldsymbol{L}\boldsymbol{v}$ is the linearized operator. While direct linearization of ODEs has been used in the past to determine simple bifurcation points of ODEs (e.g., [7]) the approach presented here can be extended to general and more complicated bifurcations of reactor models. This method is illustrated by two examples. The applicability of the procedure to more general bifurcation problems is yet to be tested.

Example 1. The single-phase model of a cooled countercurrent reactor [5] is given by Eq. (1) with

$$
\boldsymbol{f}(\boldsymbol{u}) = \begin{pmatrix} \frac{1}{\Phi_h^2} \frac{\partial^2 \Theta}{\partial \xi^2} + \beta \cdot B(\Theta) \cdot 0.5 \cdot [(1 - x_1) + (1 - x_2)] - \Delta \cdot (\Theta - \Theta_c) \\ \frac{1}{\Phi_m^2} \frac{\partial^2 x_1}{\partial \xi^2} - \frac{1}{Da} \frac{\partial x_1}{\partial \xi} + B(\Theta) \cdot (1 - x_1) \\ \frac{1}{\Phi_m^2} \frac{\partial^2 x_2}{\partial \xi^2} + \frac{1}{Da} \frac{\partial x_2}{\partial \xi} + B(\Theta) \cdot (1 - x_2) \end{pmatrix} = \boldsymbol{0}.
$$

$$(3)$$

where $\boldsymbol{u} = (\Theta, x_1, x_2)^T, x_1$, and x_2 are the conversions in the two countercurrent flow compartments, Θ the dimensionless temperature, $B(\Theta)$ a nonlinear rate expression. The corresponding boundary conditions are:

$$
\frac{Da}{\Phi_h^2} \frac{\partial \Theta}{\partial \xi} = \frac{1}{2}(\Theta - 1), \quad \frac{Da}{\Phi_m^2} \frac{\partial x_1}{\partial \xi} = x_1, \quad \frac{\partial x_2}{\partial \xi} = 0 \quad at \quad \xi = 0 \qquad (4)
$$

$$
\frac{Da}{\Phi_h^2} \frac{\partial \Theta}{\partial \xi} = \frac{1}{2}(\Theta - 1), \quad \frac{Da}{\Phi_m^2} \frac{\partial x_2}{\partial \xi} = -x_2, \quad \frac{\partial x_1}{\partial \xi} = 0 \quad at \quad \xi = 1. \qquad (5)
$$

To illustrate the concept, we determine the extinction (limit) point of the model as a function of the cooling capacity, Δ. At the limit point

$$
\boldsymbol{f}(\boldsymbol{u}, \lambda) = \boldsymbol{0} \qquad (6)
$$

$$
\boldsymbol{J}(\boldsymbol{u}, \lambda) \cdot \boldsymbol{v} = \boldsymbol{0} \qquad (7)
$$

$$
< \boldsymbol{v}, \boldsymbol{v} >= 1, \qquad (8)
$$

where $\langle \cdot, \cdot \rangle$ denotes the inner product, $\boldsymbol{J}$ is the Jacobian matrix of $\boldsymbol{f}$, and $\boldsymbol{v}$ is the zero-eigenvector of $\boldsymbol{J}$. As the eigenvector is defined up to a multiplicative constant, we assign a value to the norm of $\boldsymbol{v}$ (Eq. 8). These 3 equations define the state vector $\boldsymbol{u}$, the eigenvector $\boldsymbol{v}$ and λ at the limit point. To avoid computing the discretized Jacobian matrix of $\boldsymbol{f}$, we obtain by direct Fréchet differentiation the set of linear differential equations (+BC's)

$$J \cdot v = D_u f(u, \lambda) \cdot v = Lv = 0 \tag{9}$$

$$Lv = \begin{pmatrix} \frac{1}{\Phi_h^2} \frac{\partial^2 v_1}{\partial \xi^2} + 0.5 \cdot \beta \cdot \left(\frac{\partial B(\Theta)}{\partial \Theta} [(1-x_1) + (1-x_2)] v_1 - B(\Theta) \cdot [v_2 + v_3] \right) - \Delta \cdot v_1 \\ \frac{1}{\Phi_m^2} \frac{\partial^2 v_1}{\partial \xi^2} - \frac{1}{Da} \frac{\partial v_1}{\partial \xi} + \left(\frac{\partial B(\Theta)}{\partial \Theta} (1 - x_1) v_1 - B(\Theta) \cdot v_2 \right) \\ \frac{1}{\Phi_m^2} \frac{\partial^2 v_2}{\partial \xi^2} + \frac{1}{Da} \frac{\partial v_2}{\partial \xi} + \left(\frac{\partial B(\Theta)}{\partial \Theta} (1 - x_2) v_1 - B(\Theta) \cdot v_3 \right) \end{pmatrix}$$

$$\tag{10}$$

$$\frac{Da}{\Phi_h^2} \frac{\partial v_1}{\partial \xi} = \frac{1}{2} v_1, \quad \frac{Da}{\Phi_m^2} \frac{\partial v_2}{\partial \xi} = v_2, \quad \frac{\partial v_3}{\partial \xi} = 0 \quad at \quad \xi = 0 \tag{11}$$

$$\frac{Da}{\Phi_h^2} \frac{\partial v_1}{\partial \xi} = -v_1, \quad \frac{Da}{\Phi_m^2} \frac{\partial v_3}{\partial \xi} = -v_3 \quad \frac{\partial v_2}{\partial \xi} = 0 \quad at \quad \xi = 1, \tag{12}$$

where $v = [v_1, v_2, v_3]^T$. Eq. (6)-(8) are then discretized $(\hat{u}, \hat{v})$ and solved simultaneously by either a Newton or quasi-Newton method [8]. Instead of discretization shooting may be used. However, shooting in space direction is only recommended if no significant boundary layers exist. The locus of the extinction point is tracked with respect to a second parameter Δ - the cooling capacity - by a continuation method [2] as can be seen in Figure 1. In this case a finite difference approximation with 100 equidistant node points and Broyden's method have been used. Parameter values are reported in [5].

Example 2: A reverse-flow reactor (RFR) is a forced periodic system in which the flow direction is periodically reversed to trap a hot zone within a packed-bed reactor. The RFR operates under conditions for which multiple periodic, quasi-periodic and chaotic states exist. The dimensionless energy and species balances and boundary conditions for a single exothermic first-order reaction in a cooled RFR are [3]:

$$f(u) = \begin{pmatrix} \frac{1}{\zeta} \frac{\partial \Theta}{\partial \tau} - \frac{1}{Pe_h} \frac{\partial^2 \Theta}{\partial \xi^2} + f \frac{\partial \Theta}{\partial \xi} - Da \cdot \beta \cdot B(\Theta) \cdot (1 - x) + \Delta(\Theta - \Theta_c) \\ \frac{1}{Le} \frac{\partial x}{\partial \tau} - \frac{1}{Pe_m} \frac{\partial^2 x}{\partial \xi^2} + f \frac{\partial x}{\partial \xi} - Da \cdot B(\Theta) \cdot (1 - x) \end{pmatrix} = 0$$

$$\tag{13}$$

$$\frac{\partial u}{\partial \xi} = Pe \cdot u \quad at \quad \xi = 0; \quad \frac{\partial u}{\partial \xi} = 0 \quad at \quad \xi = 1 \tag{14}$$

$$u = \begin{pmatrix} \Theta - 1 \\ x \end{pmatrix}, \quad Pe = \begin{pmatrix} Pe_h & 0 \\ 0 & Pe_m \end{pmatrix}, \quad B(\Theta) = \frac{a_\nu k_c exp\left\{ \gamma \frac{\Theta - 1}{\Theta} \right\}}{a_\nu k_c + k_\infty exp\left\{ -\frac{\gamma}{\Theta} \right\}}$$
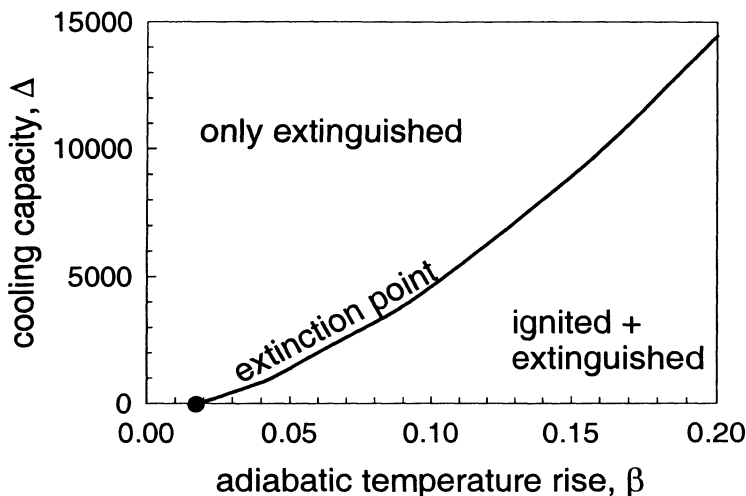
Fig. 1. Extinction point of the cooled counter-current reactor in the plane of the cooling capacity vs. adiabatic temperature rise β(feed concentration). Below the solid curve ignited and extinguished states coexist for the same set of parameters. Below $\beta = 0.017$ no ignited states exist even for adiabatic operation.

$$u(\tau = 0, \xi) = u(\tau = 1, 1 - \xi). \tag{16}$$

where τ and ξ are the time and spatial coordinate, and f is switched between $+1$ to -1 at every interval $\tau_f = 1$. Eqs. (14) are the boundary conditions for the flow in the right direction ($f = +1$). For the left flowing period ($f = -1$) symmetric boundary conditions apply. The temporal boundary condition (16) enforces the periodicity of the solutions. Typically, two limit points (saddle node bifurcation) of the periodic solutions coalesce upon crossing the *hysteresis point* [1]). It is defined by Eqs.(6), (7) and

$$J^*(u, \lambda) \cdot y = 0 \tag{17}$$

$$\langle y, D_{uu}^2 f(u, \lambda) \cdot (v, v) \rangle = 0 \tag{18}$$

$$< y, v >= 1 \tag{19}$$

where $*$ denotes the conjugate transpose. v and y are the eigenvector and adjoint eigenvector of J, and $D_{uu}^2 f(u, \lambda)$ the second Fréchet derivative. These 5 equations determine 3 variables (u, v, y), λ and an additional parameter p_1 at the hysteresis point. An isolated branch of solutions appears (or disappears) upon crossing the *isola variety* [1], which satisfies Eqs. (6), (17) and

$$\langle y, D_\lambda f(u, \lambda) \rangle = 0 \tag{20}$$

$$< y, y >= 1. \tag{21}$$

The linearized operator in this case is:

$$Lv = \begin{pmatrix} \frac{1}{\zeta}\frac{\partial v_1}{\partial \tau} - \frac{1}{Pe_h}\frac{\partial^2 v_1}{\partial \xi^2} + \frac{\partial v_1}{\partial \xi} - Da\beta\left[\frac{\partial B}{\partial \Theta}v_1(1-x) - Bv_2\right] + \Delta v_1 \\ \frac{1}{Le}\frac{\partial v_2}{\partial \tau} - \frac{1}{Pe_m}\frac{\partial^2 v_2}{\partial \xi^2} + \frac{\partial v_2}{\partial \xi} - Da\left[\frac{\partial B}{\partial \Theta}v_1(1-x) - Bv_2\right] \end{pmatrix} \tag{22}$$

$$\frac{\partial v}{\partial \xi} = Pe \cdot v \quad at \quad \xi = 0; \qquad \frac{\partial v}{\partial \xi} = 0 \quad at \quad \xi = 1. \qquad v = (v_1, v_2)^T \tag{23}$$

$$v(\tau = 0, \xi) = v(\tau = 1, 1 - \xi) \tag{24}$$

The adjoint problem L^*y may be determined by the relation

$$\langle Lv, y \rangle = \langle v, L^*y \rangle \tag{25}$$

by partial integration. Thus, the adjoint problem L^*y is:

$$L^*y = \begin{pmatrix} -\frac{1}{\zeta}\frac{\partial y_1}{\partial \tau} - \frac{1}{Pe_h}\frac{\partial^2 y_1}{\partial \xi^2} - \frac{\partial y_1}{\partial \xi} - Da\frac{\partial B}{\partial \Theta}(1-x)[\beta y_1 + Ley_2/\zeta] + \Delta y_1 \\ -\frac{1}{Le}\frac{\partial y_2}{\partial \tau} - \frac{1}{Pe_m}\frac{\partial^2 y_2}{\partial \xi^2} - \frac{\partial y_2}{\partial \xi} + DaB(\Theta)[\beta_1 y_1\zeta/Le + y_2] \end{pmatrix} \tag{26}$$

$$\frac{\partial y}{\partial \xi} = 0 \quad at \quad \xi = 0; \qquad -\frac{\partial y}{\partial \xi} = Pe \cdot y \quad at \quad \xi = 1, \quad y = (y_1, y_2)^T. \tag{27}$$

$$y(\tau = 0, \xi) = y(\tau = 1, 1 - \xi) \tag{28}$$

The Fréchet derivative with respect to $\lambda = u$, the superficial gas velocity, is

$$D_\lambda f = \begin{pmatrix} \frac{1}{Da\zeta}\frac{\partial \Theta}{\partial \tau} - \frac{1}{DaPe_h}\frac{\partial^2 \Theta}{\partial \xi^2} - \beta_1 \cdot B_1(\Theta) \cdot (1-x) \\ \frac{1}{DaLe}\frac{\partial x_1}{\partial \tau} - \frac{1}{DaPe_{m,1}}\frac{\partial^2 x_1}{\partial \xi^2} - B_1(\Theta) \cdot (1-x) \end{pmatrix}, \tag{29}$$

since the Peclet, Lewis, and Damkoehler numbers $(Pe_h, Pe_m, Le, \zeta, Da,)$ are functions of u (see [3]). The second Fréchet-derivative $D_{uu}^2 f \cdot (v, b)$ is computed from the equation:

$$D_{uu}^2 f \cdot (v, b) = -Da \begin{pmatrix} \beta\left[\frac{\partial^2 B}{\partial \Theta^2}v_1 b_1(1-x) - \frac{\partial B}{\partial \Theta}(v_1 b_2 + v_2 b_1)\right] \\ \left[\frac{\partial^2 B}{\partial \Theta^2}v_1 b_1(1-x) - \frac{\partial B}{\partial \Theta}(v_1 b_2 + v_2 b_1)\right] \end{pmatrix}. \tag{30}$$

In order to track a hysteresis point Eqs. (6), (7), (17)-(19) have to be satisfied and for the isola point Eqs. (6), (17), (20) and (21) have to be satisfied. Again these equations are discretized $(\hat{u}, \hat{v}, \hat{y})$ in space and time and solved simultaneously. This procedure leads to a significant reduction in the computational effort. Figure 2 describes the hysteresis and isola points in the parameter space. The corresponding parameters are reported in [3]. Orthogonal collocation on finite elements with 50-80 collocation points was used to spatially discretize the grid. Shooting in time was used to solve for the symmetric boundary conditions.

Acknowledgements
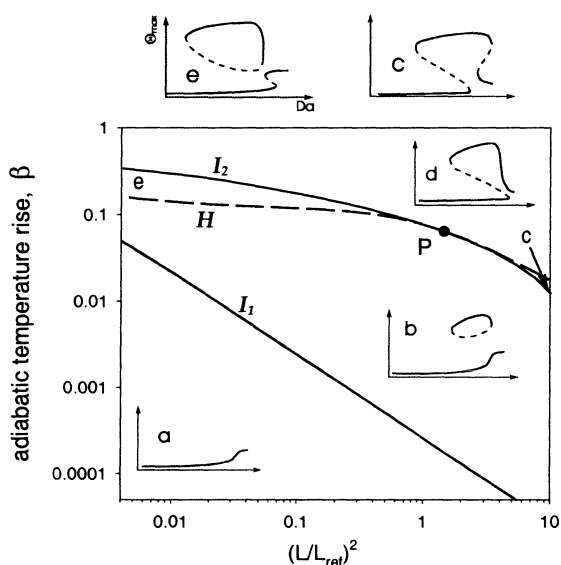
Fig. 2. Five different regions in the $\beta - (L/L_{ref})^2$ plane with qualitatively different bifurcation diagrams of Θ_{max} vs. Da (shown as insets). a) only extinguished, b) isola and extinguished, c) mushroom with four limit points, d) mushroom with two limit points, e) isola and two limit points. L/L_{ref} = dimensionless reactor length. Parameters are given in [3].

References

1. Golubitsky, M. and Schaeffer, D.G., "Singularities and Groups in Bifurcation Theory", Vol. 1. Springer, New York (1985)
2. Keller, H.B., "Numerical Solutions of Bifurcation and Nonlinear Eigenvalue Problems", Applications of Bifurcation Theory (ed. P.H. Rabinowitz), *Academic Press*, New York, 159–385 (1977)

3. Khinast, J., Luss, D., Mapping Regions with Different Bifurcation Diagrams of a Reverse Flow Reactor, *AIChEJ.*, 43, 8, p.2034, (1997)
4. Khinast, J., Luss, D., Harold, M.P, Ostermaier, J.J., McGill R., Continuously Stirred Decanting Reactor - Operation and Stability Considerations, *AIChEJ.*, 44, 2, p. 372, (1998a)
5. Khinast, J., Gurumoorthy, A., Luss, D., Complex Dynamic Features of a Cooled Reverse-Flow Reactor, *AIChEJ.*,44,5, p.1128, (1998b)
6. Khinast, J., Luss, D, Leib T.M., Harold, M.P., The adiabatic boiling slurry reactor: Feasible operation and stability, *AIChEJ.*, 44, 8, p.1868, (1998c)
7. Kubicek M., and M Holodniok, Evaluation of Hopf Bifurcation Points in Parabolic Equations Describing heat and Mass Transfer in Chemical Reactors", *Chem. Eng. Sci.*, 39(3), 593, (1984)
8. Luss, D. and Khinast, J., Efficient Bifurcation Analysis of Forced Periodic Processes, Scientific Computing in Chemical Engineering, Hamburg, Springer Verlag, (1999)

Computational numerical approaches in the simulation of SMB process

Celina P. Leão, Diana Azevêdo, and Alírio E. Rodrigues

LSRE - Laboratory of Separation and Reaction Engineering
Faculdade de Engenharia da Universidade do Porto, 4099 Porto Codex, Portugal
e-mail: leao@raff.fe.up.pt, dazevedo@raff.fe.up.pt, arodrig@fe.up.pt

Abstract. This work compares different strategies to solve a mathematical model in order to predict the transient and steady-state behavior of a SMB unit. The model assumes axial dispersion flow for the liquid phase and plug flow for the solid phase. Intraparticle mass transfer was described in terms of a simple linear driving (LDF) approximation. Equilibrium isotherms may be inserted into the PDE code system or written out as separate algebraic equations, especially if they are non-linear. Different public domain solvers were used to integrate numerically the systems of PDEs, ODEs and PDAEs obtained. For the transient model PDECOL was used to solve the PDEs and the DASSL code was used when the isotherm equation was written separately as an algebraic equation. For the steady-state model, the codes COLNEW and COLDAE were used, respectively. Simulations of the glucose/fructose separation were performed for a 12 column configuration considering linear isotherms. An extension was also proposed which considered the mass transfer not only in the macropores but also in the micropores.

1 Introduction

The Simulated Moving Bed (SMB) [1] processes are widely used for various kinds of multicomponent mixture separations. It was developed by UOP in the early 60's and since then its area of application has been increased from the separation of normal paraffins till the separation of enantiomers in the pharmaceutical and fine chemistry industries [2-4]. The counter-current movement between the solid and liquid phases is the basic principle of the SMB technology. The two products to be separated, included in the feed, have different adsorption affinities which permits that the more retained feed component moves towards the extract outlet, while the other moves towards the raffinate outlet (less retained feed component). Due to practical problems the solid phase movement is simulated by shifting the feed and withdrawal points along the adsorbent bed, in the same direction of the fluid flow. The system studied in this work was the separation of glucose and fructose [5]. The scheme of the SMB and the equivalent TMB used, are described in several works developed [4,6]. This work presents two models to predict the performance and concentration profiles in a SMB unit based on the equivalence with the TMB concept. Both models assume axial dispersion flow for the liquid phase and plug flow for the solid phase.

2   Mathematical Models

2.1   LDF approximation

For the first model, a simple linear driving force (LDF) approximation was used to describe the intraparticle mass transfer. It is a model similar to the one used by [4], however, in this work we took into account linear adsorption equilibrium for both components. The basic dimensionless mass balance equations in the fluid phase of a TMB section volume element and in the adsorbent particles, as well as the initial and boundary conditions, are written as:

- mass balance in the fluid phase of a TMB section volume element:

$$\frac{\partial c_{ij}}{\partial \theta} = \gamma_j \left[\frac{1}{Pe_j} \frac{\partial^2 c_{ij}}{\partial x^2} - \frac{\partial c_{ij}}{\partial x} \right] - \frac{(1-\varepsilon)}{\varepsilon} \alpha_j (q_{ij}^* - q_{ij}) \qquad (1)$$

- mass balance in the particle (solid phase)

$$\frac{\partial q_{ij}}{\partial \theta} = \frac{\partial q_{ij}}{\partial x} + \alpha_j (q_{ij}^* - q_{ij}) \qquad (2)$$

- linear adsorption equilibrium

$$q_{ij}^* = K_i c_{ij} \qquad (3)$$

- initial and boundary conditions

$$c_{ij}(x, t = 0) = q_{ij}(x, t = 0) = 0 \qquad (4)$$

$$[a]x = 0, \qquad c_{ij} - \frac{1}{Pe_j} \frac{dc_{ij}}{dx} = c_{ij,o} \qquad (5)$$

$$[b]x = 1, \qquad \frac{dc_{ij}}{dx} = 0 \qquad \text{and} \qquad q_{ij} = q_{ij+1,o} \qquad (6)$$

the spatial and time dimensionless variables were, $x = z/L_j$, and $\theta = t/\tau_s$ with $\tau_s = L_j/u_s$, where L_j is the section length. The subscripts $i = 1, 2$, refers to the components to be separated in the feed (glucose and fructose, respectively), and $j = 1, 2, 3, 4$ refers to the section number; c_{ij} and q_{ij} are the liquid and average adsorbed phase concentrations of component i in section j of the TMB, respectively; K_i are the equilibrium constant of component i. The model parameters presented are: $\alpha_j (= kL_j/u_s)$, the number of mass transfer units in a TMB section; $Pe_j (= \nu_j L_j/D_{Lj})$, the Peclet number; $\gamma_j (= \nu_j/u_s)$, the ratio between fluid and solid velocities in section j; and $(1-\varepsilon)/\varepsilon$, the ratio between solid and fluid volumes. To the left boundary conditions (5), four equations must be added regarding to the mass balance equations at each node,

$$c_{i1,0} = \frac{Q_4}{Q_1} c_{i4,L_4} \qquad j = 1 \text{(eluent node)} \tag{7}$$

$$c_{ij,0} = c_{i(j-1),L_{j-1}} \qquad j = 2, 4 \text{(extract and raffinate nodes)} \tag{8}$$

$$c_{i3,0} = \frac{Q_2}{Q_3} c_{i2,L_2} + \frac{Q_F}{Q_3} c_i^F \qquad j = 3 \text{(feed node)} \tag{9}$$

where Q_j is the liquid flow rate through section j and c_i^F is the feed concentration of component i. This model was the one used to compare the four strategies presented. The set of equations (1-9), defines a problem of second order PDAE's due the presence of the algebraic equation (3) for each component in each of the four sections. The second order derivative term, representing the axial dispersion term, renders the model a parabolic classification, while the second equation is hyperbolic. This set of equations can be transformed into a system of PDEs by incorporating the algebraic equations (equilibrium isotherms) into the of mass balance equations (1-2). If we consider the terms with respect to the time derivative equal to zero, i.e. $\frac{\partial c_{ij}}{\partial \theta} = \frac{\partial q_{ij}}{\partial \theta} = 0$, the system of PDE's becomes a system of ODE's of second order. This system can be transformed into a system of DAE's if the equilibrium isotherms are written out as separate algebraic equations.

2.2   bi-LDF approximation

The second model considers a bi-linear driving force (bi-LDF) approximation [7] to describe the diffusion in bidisperse solids, which have both macropores and micropores. The equation concerning the mass balance in the liquid phase in a TMB section volume element is changed to (10), and one more differential equation per component is added (11), defining the mass balance in the intraparticle fluid phase of a TMB section volume element:

- mass balance in outer fluid phase a TMB section volume element:

$$\frac{\partial c_{ij}}{\partial \theta} = \gamma_j \left[\frac{1}{Pe_j} \frac{\partial^2 c_{ij}}{\partial x^2} - \frac{\partial c_{ij}}{\partial x} \right] - \frac{(1-\varepsilon)}{\varepsilon} \alpha_{pj} (c_{ij} - \bar{c}_{pij}) \tag{10}$$

- mass balance in intraparticle fluid phase of a TMB section volume element:

$$\frac{\partial \bar{c}_{pij}}{\partial \theta} = \frac{\partial \bar{c}_{pij}}{\partial x} + \frac{1}{\varepsilon_p} \alpha_{pj} (c_{ij} - \bar{c}_{pij}) - \frac{1}{\varepsilon_p} \alpha_{\mu j} (\bar{q}_{ij}^* - \bar{q}_{ij}) \tag{11}$$

- mass balance in the microparticles present in a TMB section volume element:

$$\frac{\partial \bar{q}_{ij}}{\partial \theta} = \frac{\partial \bar{q}_{ij}}{\partial x} + \alpha_{\mu j} (\bar{q}_{ij}^* - \bar{q}_{ij}) \tag{12}$$

- linear adsorption equilibrium

$$\bar{q}_{ij}^{*} = K_i \bar{c}_{pij} \tag{13}$$

where $\bar{c}_{pij}$ and $\bar{q}_{ij}$ are the mean intraparticle fluid and solid phase concentrations, respectively, averaged over the particle volume. The new model parameters are, $\alpha_{p_i} = k_p L_j / U_s$, number of macropore mass transfer units in a TMB section; $\alpha_{\mu j} = k_\mu L_j / U_s$, number of microparticle mass transfer units in a TMB section. The boundary and initial conditions are the same as in the previous model (4-5) for the fluid phase concentration c_{ij} . For the intraparticle concentration $\bar{c}_{pij}$ and $\bar{q}_{ij}$ the right end boundary conditions are:

$$x = 1, \qquad \bar{c}_{pij} = \bar{c}_{pij+1,0} \qquad \text{and} \qquad \bar{q}_{ij} = \bar{q}_{ij+1,0} \tag{14}$$

3   Differential Equation Solvers

- PDECOL package [8] is a package for numerical solutions of a system of nonlinear partial differential equations in one space and one time dimension. It implements finite element collocation methods, with B-splines as basis functions, for the spatial discretization. The PDE system is then reduced to an initial-value ODE system, which is solved with a time integrator derived from [9] with dimension, for both models, as described in Table 1. The set of equations to be solved with the PDECOL package are (1-2) for the simple LDF model and (10-12) for the bi-LDF model. For both models, the equilibrium isotherm equations, (3) and (13), were directly inserted into the corresponding mass balance equations. The initial and boundary conditions are the same as previously defined.
- DDASSL subroutine [10] solves a system of ordinary differential-algebraic equations (ODAEs) in t by using the backward differentiation formulas of orders one through five. To use DDASSL we first need to transform the system of PDAEs (1-5) in t and x, into a system of ODAEs initial value problem in t. The spatial derivatives are approximated by finite element collocation method, as indicated in Table 1, to obtain an initial value DAE system. In this case, the algebraic relationship (3) is simple and linear and there is virtually no reason to work with it separately. However, when this relationship is non-linear, it is better to keep the algebraic form, not only because of the complexity of the problem but because it permits the study of the effect of modeling changes.
- COLNEW is a modification of the package COLSYS [12] and solves systems of boundary ordinary differential equations. It incorporates a new basis representation replacing b-splines, and improvements for the linear and nonlinear algebraic equation solvers. The system of ODEs to be solved was derived from (1-2) for the simple LDF model and (10-12) for the bi-LDF model, considering the time dependent terms equal to zero, and with the linear equilibrium isotherm inserted into the corresponding

mass balance equations. The final size of the two systems to be solved are illustrated in Table 1.

- COLDAE subroutine [13] is a modification of the package COLNEW. It works practically the same way as COLNEW and optionally, solves semi-explicit DAEs with index at most 2. It uses the collocation method at Gaussian points and a Runge-Kutta-monomial solution representation is utilized. It was applied to the model described previously (1-2) with the time dependent time terms set to zero plus the algebraic equations (3). The way to identify the difficulty of solving numerically a system of DAE's is the index [10]. Applying analytical differentiations repeatedly if necessary, will yield to an explicit ODE system for all the unknowns, with the exception for singular problems. The number of differentiations needed for this transformation is called the index of the DAE. Differentiating the equilibrium isotherm equation (3) yields,

$$\frac{\partial q_{ij}^*}{\partial x} = K_i \frac{\partial c_{ij}}{\partial x} \tag{15}$$

Doing this, we obtain a differential equation for all the unknowns. The index of this system is one. Note that if we carry out the substitution for q_{ij}^* then the resulting system is an ODE as previously solved. The final size of the system to be solved is illustrated in Table 1.

Table 1. Relevant parameters for the four packages used

Code Name	Spatial Discretization	Time Integrator	Tolerance	System Dimension
PDECOL	Collocation;	Gear's method	10^{-7} (LDF)	448 (LDF)
	B-splines basis		10^{-10} (bi-LDF)	672 (bi-LDF)
DDASSL	Collocation;	backward		
	Hermite cubic basis[1]	differentiation	10^{-7} (LDF)	672 (LDF)
COLNEW	modified B-splines		10^{-8} (LDF)	448 (LDF)
	bsis	−	10^{-9} (bi-LDF)	672 (bi-LDF)
COLDAE	collocation at Gaussian			
	points; Rung-Kutta-	−	10^{-8} (LDF)	672 (LDF)
	monomial solution			

---

[1] provided by the user, described in [11].

4   Simulation results and discussion

Computer simulations were carried out to permit the estimation of the transient and steady-state concentration profiles of the glucose/fructose separation system, and to verify the effect of the strategy chosen to solve the model, in the final results. The first model, as described by (1-7), was solved using the four packages previously mentioned, PDECOL, DDASSL, COLNEW and COLDAE. The second model was solved using the PDECOL and COLNEW packages. In all the simulations, the polynomials used were of order 3 and the tolerance on the time integrator set as described in Table 1. For the second model was necessary to decrease the tolerance parameter in order to reduce the global mass balance errors. For the spatial variable discretization fourteen finite elements were considered with two collocation points in each.

The operating conditions and model parameters used in the simulation of the TMB are listed in Table 2. The operating conditions were estimated by the method developed by [5], considering the equilibrium theory, linear isotherms, and a margin parameter $\beta = 1.2$.

Table 2. Operating conditions and models parameters used in the simulations of the TMB/SMB system, for the two models.

Model Parameters	Operating conditions	Columns
SMB:	SMB:	SMB:
Pe $= 2000$	$T = 20^0 C$	$D_c = 2.6cm$
$(1 - \varepsilon)/\varepsilon = 1.5$; $\varepsilon_p = 0.1^3$	Feed conc. $= 30g/l$ each	$L_c = 11.5cm$
$\alpha_j = 3.15$; $\alpha_{pj} = 10.0^3$	$t^* = 105s$	Configuration: 3-3-3-3
$\alpha_{\mu j} = 3.15^3$	$Q_{Rec} = 19.43^1$ ml/min	$L_j = 34.5cm$
$K_{GI} = 0.314^2 K_{Fr} = 0.625^2$	$Q_D = 10.22^1$ ml/min	
$\overline{TMB:}$	$Q_E = 7.81^1$ ml/min	
$\gamma_1 = 1.125\gamma_2 = 0.565$	$Q_F = 3.02^1$ ml/min	
$\gamma_3 = 0.781\gamma_4 = 0.392$	$Q_R = 5.43^1$ ml/min	

Regardless the numerical package used, the same profile is obtained when the system reaches the steady-state, as expected. Although PDECOL solves the SMB transient model, the steady-state solution, that obtained as $t \rightarrow \infty$, should be the same as that given by the ODE solver, under the same conditions.

---

[1] values estimated by the method developed by Ruthven and Ching
[2] data measured at our laboratory
[3] data considered for the bi-LDF model

Table 3 summarizes the final results for the performances parameters obtained by using the four different packages in the resolution of the two mathematical model, simple LDF and bi-LDF approximation, as the run time consumed. All simulations were run in a Pentium II 300 MHz. The only difference obtained in the purity parameters for the simple LDF and bi-LDF models considered, is due to the fact that the absorbent particle is taken to be more porous ($\varepsilon_p = 0.1$) in the second model. A more detailed physical description may be found elsewhere [14].

Table 3. Final results for the performance parameters obtained by using the four different packages in the resolution of the two mathematical model, simple LDF and bi-LDF approximation, as the run time needed.

	Simple LDF				bi - LDF	
	PDECOL	DDASSL	COLNEW	COLDAE	COLNEW	PDECOL
Pu F (%)	72.4	72.0	72.4	72.4	77.0	76.8
Pu G (%)	66.3	66.0	66.3	66.3	67.2	66.5
Rc F (%)	61.0	60.8	60.9	60.9	59.2	58.6
Rc G (%)	76.9	77.0	76.8	76.8	82.3	82.6
Sc F (l/g)	0.240	0.242	0.240	0.240	0.247	0.250
Sc G (l/g)	0.190	0.189	0.190	0.190	0.178	0.177
Pr F (g/hr IS)	7.539	7.541	7.530	7.529	7.310	7.300
Pr G (g/hr IS)	9.504	9.506	9.501	9.501	10.200	10.300
Run Time (min)	108	> 180	0.26	0.20	0.30	150

5   Conclusions

The models used to predict the transient and steady-state performance of the SMB were described based on the analogy with the TMB. A test system was considered for SMB operation: the glucose/fructose separation. Transient and steady-state systems for both models, depending of the user's interest and under properly selected conditions, simulate efficiently the separation system. Steady-state models can be used for a preliminary estimation of the concentration profiles and the performance parameters with less computational time. With the transient model, the user can have an exact representation of the evolution of internal concentration profiles through the time period and estimate how long the operation of an actual plant would take to reach the steady-state. The run time, for the system of DAEs, is slightly lower than that taken by the ODEs systems. However, the opposite situation occurs for the

partial differential equations. The system of PDAEs needs more run time to be solved than the PDE system. It may be possible to over come this problem by using the same subroutine for the spatial discretization as implemented by PDECOL in DASSL code with the corresponding modifications.

References

1. Broughton D. B., Gerhold C. G. (1961) Continuous Sorption Process Employing Fixed Bed of Sorbent and Moving Inlets and Outlets, U.S. Patent N°. 2985589.
2. Broughton D. B (1968), Molex: Case History of a Process, Chem. Eng. Progress 64, 60–65.
3. Nicoud R. M. (1997) Recent Advances in Industrial Chromatographic Processes, In Recent Advances in Industrial Chromatographic Processes, 15 May, Nancy, France.
4. Pais L. S., Loureiro J. M., Rodrigues A. E. (1997) Modeling, simulation and operation of a simulated moving bed eparation for continuous chromatographic separation of 1,1'-bi-naphthol enantiomers, Journal of Chromatography A 769, 25–35.
5. Ruthven D. M., Ching C. B. (1989) Counter-Current and Simulated Moving Bed Adsorption Separation Process, Chem. Eng. Sci. 44, 1011.
6. Leão C. P., Pais L. S., Santos M., Rodrigues A. E. (1997) Simulated Moving Bed Adsorptive Reactor, 2nd International Conference on Process Intensification in Practice, Edited by J. Semel, 143.
7. Azevedo D. C. S., Rodrigues A. E. (1998) Bi-Linear Driving Force Approach in the Simulation of Adsorptive Separation Processes: Application to Fixed and Simulated Moving Bed, Proc. Of CHEMPOR'98, Vol. II 849.
8. Madsen N. K., Sincovec R. F. (1979) PDECOL: General Collocation Software for Partial Differential Equations, ACM Trans. Math. Software, 5, 326.
9. Hindmarsh A. (1976) Preliminary Documentation of GEARIB - Solution of Implicit Systems of Ordinary Differential Equations with Banded Jacobian, Report UCID-30130, Lawrence Livermore Laboratory.
10. Brenan K., Campbell S., Petzold L. (1989) Numerical Solution of Initial-Value Problems in Differential-Algebraic Equations, Elsevier, New York.
11. Leão C. P. (1998) LSRE Internal Report, Porto.
12. Ascher U., Christiansen J., Russell R. D. (1981) Collocation Software for Boundary-Value ODEs, ACM Trans. Math Software, 7, 209.
13. Bader G. Ascher U. (1987) A New Basis Implementation for a mixed Order Boundary Value ODE Solver, SIAM J. Scient. Stat. Comput., 8, 483.
14. Azevedo, D. C. S., Rodrigues A. E. (1999) Bi-Linear Driving Force Approximation in the Modeling of Simulated moving Bed using Bidisperse Adsorbents, Ind. Eng. Chem. Res. (submitted).

A Two Dimensional Population Model for a Continuous Crystallizer

A. Mitrović[1], S. Motz[1], A. Gerstlauer[2], C. Gahn[2], and E.-D. Gilles[1]

[1] Institut für Systemdynamik und Regelungstechnik, University of Stuttgart,
   Pfaffenwaldring 9, D-70550 Stuttgart, Germany, mitro@isr.uni-stuttgart.de
[2] BASF AG, 67056 Ludwigshafen, Germany

Abstract. In this contribution a population model with two particle coordinates is developed for a continuous crystallizer . The considered particle coordinates are the crystal length and the internal lattice strain of individual crystals. The presented simulation results show a strong dependence of the steady state mass density function on the different assumptions for the relaxation of the internal lattice strain during crystal growth.

1   Introduction

Crystallization from solution or melt is one of the oldest and economically most important industrial separation and purification processes. For many crystallization applications the crystal size distribution (CSD) is of primary importance. Quality requirements such as the ability to flow or the dissolution rate of the produced particles can be directly related to the CSD.

   One of the major problems in crystallization modeling is that up to now, detailed microscopic theories and submodels are rarely included into macroscopic models for crystallizers. On a microscopic scale, phenomena such as primary nucleation, crystal growth and attrition of crystals due to crystal-stirrer collisions have to be investigated and modeled in a quantitative way.

   A commonly accepted concept for the modeling of dispersed phase systems is the population balance approach [5]. The main aspects of this contribution are the development of a detailed population model using two particle coordinates and the numerical solution of the resulting set of model equations.

2   Model Development

For modeling purposes the suspension within a continuous crystallizer can be decomposed into two phases: a continuous liquid phase (L) and a dispersed solid phase (S). The continuous liquid phase contains a binary mixture of dissolved crystals (solute component A) and solvent (component B). The composition of the mixture can be characterized by the mole fraction $x_{L,A} = n_{L,A}/n_L$ calculated by the total number of moles and the number of moles of dissolved crystals $n_{L,A}$.

The dispersed solid phase consists of individual crystals. To characterize an individual crystal particle coordinates have to be defined. These particle coordinates have to describe the present state of a specific crystal.

2.1   Definition of Particle Coordinates

Wang and Mersmann [6] observed, that attrition fragments of the same initial size have different growth rates. In population models for crystallization processes presented in literature (e.g. [2,9]), this distribution of growth rates is neglected and only a size and/or supersaturation dependent growth rate is used. To describe the observed growth rate distribution a more detailed approach is needed. It is essential to characterize the crystals not only by their length, but also by a second particle coordinate. This second particle coordinate should account for the internal lattice strain of individual crystals which is identified to be a main source of growth rate dispersion [10].

In Gahn [7] the driving force for crystal growth $\Delta c_{L,A}$ is defined as the difference between the molar density of the solute in the liquid phase and the real molar density of the solute at saturation $\Delta c_{L,A} = c_{L,A} - c_{L,A,sat,real}$. The real molar density $c_{L,A,sat,real}$ at saturation of an individual crystal depends on the molar plastic deformation energy w_P (internal lattice strain) of the crystal and on the ideal molar density $c_{L,A,sat,ideal}$ at saturation according to Gahn [7]

$$c_{L,A,sat,real} = c_{L,A,sat,ideal} \cdot exp \left[\frac{w_P}{RT} \right] . \tag{1}$$

In the above equation R and T denote the ideal gas constant and the actual temperature, respectively.

2.2   Population Balance of the Dispersed Phase

Using the identified particle coordinates L and w_P, the population balance for the number density function $F(L, w_P, t)$ is given by

$$\frac{\partial F(L, w_P, t)}{\partial t} = -\frac{\partial v_L F}{\partial L} - \frac{\partial v_w F}{\partial w_P} + \dot{F}_{in} - \dot{F}_{out} + \dot{F}^+_{nuc} + \dot{F}^\pm_{attr} - \dot{F}^-_{dis}. \tag{2}$$

The first two terms on the right hand side represent the convective transport in the direction of the particle coordinates L and w_P due to crystal growth and relaxation of the internal lattice strain. The terms $\dot{F}_{in}$ and $\dot{F}_{out}$ denote the particle number fluxes due to in- and outflow of the continuous crystallizer. The source and sink terms due to primary nucleation, particle attrition and dissolution of particles are denoted by $\dot{F}^+_{nuc}, \dot{F}^\pm_{attr}$, and $\dot{F}^-_{dis}$. Aggregation of crystals is not considered. In the following section the phenomena underlying these terms will be discussed together with the expressions required for their calculation. For the population balance (2) suitable initial and boundary conditions have to be defined.

2.3   Primary Nucleation

In the presented model it is assumed that primary nucleation occurs only at a specific critical nucleation length L_{crit} . This length can be calculated by the Gibbs-Thomson equation [11]. The particle number flux $\dot{F}_{nuc}^{+}$ of primary nucleation can be formulated using a Dirac δ distribution at the position L_{crit} and the nucleation rate B_{nuc} per unit volume of the continuous phase.

$$\dot{F}_{nuc}^{+} = \delta(L - L_{crit}) \cdot B_{nuc}(T, S_{rat}) \cdot V_L \tag{3}$$

Mersmann et al. [8] derived an equation for the volumetric rate of primary nucleation B_{nuc}. This nucleation rate depends mainly on the temperature T and the supersaturation $S_{rat} = c_{L,A}/c_{L,A,sat,real}$.

2.4   Crystal Growth

The convective transport $v_L F$ in the direction of the particle coordinate L is determined by the velocity v_L. This internal velocity is equivalent to the crystal growth rate G. In Mersmann et al. [8] a growth rate $G = G(\Delta c_{L,A}, L)$ is given for surface integrated (integration rate constant k_r) and diffusion limited (mass transfer coefficient k_d) crystal growth.

$$\frac{G(\Delta c_{L,A}, L)}{2k_d(L)} = \frac{\Delta c_{L,A}}{c_S} + \frac{k_d(L)}{2k_r c_S} - \sqrt{\left(\frac{k_d(L)}{2k_r c_S}\right)^2 + \frac{k_d(L)}{k_r c_S}\frac{\Delta c_{L,A}}{c_S}} \tag{4}$$

Where c_S denotes the molar concentration of the solid Phase. The influence of the deformation energy (internal lattice strain) on the growth rate results in dissolution of crystals for high values of the deformation energy w_P. The dissolution rate $G_{Diss}(\Delta c_{L,A}, L)$ used in the model is given by the mass transfer limited part of the growth rate (4).

2.5   Relaxation of Lattice Strain during Crystal Growth

One of the main issues of the two dimensional population model is to identify approaches for the relaxation of the internal molar lattice strain w_P during crystal growth, i.e. to define the velocity $v_w = dw_P/dt$ in direction of the particle coordinate w_P . Therefore assumptions about the behavior of the absolute internal lattice strain W_P during crystal growth have to be made. The absolute lattice strain W_P can be calculated from the molar lattice strain w_P by using the volume shape factor k_V according to

$$W_P = k_V c_S L^3 w_P . \tag{5}$$

The total differentiation of equation (5) with respect to time yields

$$\frac{dW_P}{dt} = k_V c_S \left[3L^2 w_P \frac{dL}{dt} + L^3 \frac{dw_P}{dt} \right] = k_V c_S \left[3L^2 w_P G + L^3 v_w \right] . \qquad (6)$$

In equation (6) the change of crystal length with time is given by the growth rate. The remaining two unknowns are the time derivatives of W_P and w_P. To calculate the time derivative of w_P different assumptions for the behavior of dW_P/dt have to be made. Four cases are presented in Table 1.

Table 1. Assumptions for the change of the absolute lattice strain W_P

Case	W_P	dW_P/dt	dw_P/dt
1	const.	0	$-\frac{3w_P}{L}G$
2	$\sim L$	$k_V c_S K_2 \cdot G$	$\left[\frac{K_2}{L^3} - \frac{3w_P}{L} \right] G$
3	$\sim L^2$	$2k_V c_S K_3 L \cdot G$	$\left[\frac{2K_3}{L^2} - \frac{3w_P}{L} \right] G$
4	$\sim L^3$	$3k_V c_S K_4 L^2 \cdot G$	$\left[\frac{3K_4}{L} - \frac{3w_P}{L} \right] G$

All assumptions for W_P except the first one $W_P = $ constant, lead to expressions for the relaxation of molar lattice strain which are determined by the crystal growth rate G and a free parameter K_2, K_3 and K_4, respectively. For the numerical simulation, dissolving crystals are assumed to maintain their individual lattice strain during dissolution.

2.6   Attrition

The particle number flux due to attrition $\dot{F}_{attr}^{\pm}$ can be separated according to

$$\dot{F}_{attr}^{\pm} = \dot{F}_{attr,1}^{+} + \dot{F}_{attr,2}^{+} - \dot{F}_{attr}^{-}. \qquad (7)$$

These particular source and sink terms can be interpreted as a particle number flux $\dot{F}_{attr}^{-}$ due to the removal of large crystals that collide with the stirrer, a particle number flux $\dot{F}_{attr,2}^{+}$ due to the generation of abraded large crystals with a length L^* somewhat smaller than the original crystal and finally a particle number flux $\dot{F}_{attr,1}^{+}$ due to generation of N_{frag} attrition fragments with a size distribution $f_{frag}(L)$ resulting from crystal-stirrer collisions. To add the second particle coordinate w_P into the attrition model it is assumed that remaining large crystals $\dot{F}_{attr,2}^{+}$ do not change their lattice strain due to collisions with the stirrer. An attrition fragment gets its initial lattice strain w_P' according to [7] only as a function of its initial fragment length L' by $w_P' = \Gamma_P/L'$, where Γ_P is a parameter depending on the used chemical system and has to be adapted to measurements.

The source and sink terms resulting from attrition due to crystal-stirrer collisions can be calculated for the two particle coordinates L and w_P by integration over the stirrer radius r, with $R = 0.5d_{st}$.

$$\dot{F}_{attr}^-(L, w_P) = \int_0^R \dot{F}_{attr,r}^-(L, w_P, r)dr$$

$$\dot{F}_{attr,2}^+(L, w_P) = \int_0^R \left(\int_0^{w_{p\infty}} \int_L^{L_\infty} \delta\left[L^* - L, w_P' - w_P\right] \cdot \dot{F}_{attr,r}^-(L', w_P', r)dL'dw_P' \right) dr$$

$$\dot{F}_{attr,1}^+(L, w_P) = \int_0^{w_{p\infty}} \delta(w_P - w_P') \int_0^R \left(\int_L^{L_\infty} [h(L - L_{min}) - h(L - L_{max}(L', r))] \right.$$
$$\left. N_{frag}(L', r) \cdot f_{frag}(L', L, r) \cdot \dot{F}_{attr,r}^-(L', w_P', r) \, dL' \right) drdw_P \tag{8}$$

In the above equations h is the heavyside function and the sink $\dot{F}_{attr,r}^-$ describes the particle number flux due to crystal-stirrer collision at a position r on the stirrer blade. This particle number flux is given by

$$\dot{F}_{attr,r}^-(L, w_P, r) = \frac{\dot{V}_{pump}}{V} \, \eta_{geo}(r) \, \eta_{tar}(L, r) \, F(L, w_P) \, , \tag{9}$$

where $\dot{V}_{pump}$ is the volumetric flow rate of the stirrer. The collision probabilities η_{geo} and η_{tar} and other parameters of the attrition model are based on theoretical considerations and are experimentally verified by Gahn [7]. Most of the parameters are specific to the used chemical system.

2.7   Material Balance of the Continuous Phase

The differential equation for the mole fraction $x_{L,A}$ of the solute can be derived by a total and a component material balance for the liquid phase.

$$n_L \frac{dx_{L,A}}{dt} = c_{L,in}\dot{V}_{L,in}(x_{L,A,in} - x_{L,A}) - (1 - x_{L,A})(\dot{n}_{nuc} - \dot{n}_{dis} + \dot{n}_{gr}) \tag{10}$$

The total molar fluxes between the continuous liquid phase and the dispersed solid phase $\dot{n}_{nuc}$, $\dot{n}_{dis}$ and $\dot{n}_{gr}$ due to primary nucleation, dissolution and growth in equation (10) are given by

$$\dot{n}_{nuc} = -k_V \, c_S \, L_{crit}^3 \, B_{nuc} \, V_L \, , \quad \dot{n}_{dis} = -k_V \, c_S \int_0^{w_{p\infty}} L_{crit}^3 D_{dis} \, dw_P$$
$$\dot{n}_{gr} = -k_V \, c_S \int_0^{L_\infty} \int_0^{w_{p\infty}} L^3 \cdot \left(\frac{\partial(G F)}{\partial L} + \frac{\partial(v_w F)}{\partial w_P} \right) dw_P dL \, . \tag{11}$$

The expression for the total molar flux $\dot{n}_{dis}$ due to dissolution shows that small dissolving crystals which reached the critical length L_{crit} are removed from the crystal population by a dissolution rate D_{dis} that can also be found

in the sink term $\dot{F}_{dis}^{-}$ of the population balance. With these total molar fluxes equation (10) represents an ordinary integro-differential equation. The total number of moles in the continuous liquid phase is given by the molar density c_L and the volume V_L of the continuous phase $n_L = c_L V_L$. Further equations to calculate the volumes V_S and V_L of the solid and the liquid phase are required. The volume V_S can be calculated by integrating the number density function $F(L, w_P)$ multiplied by the volume of one crystal over all crystal lengths.

$$V_S = k_V \int_0^{L_\infty} \int_0^{w_{p\infty}} L^3 F(L, w_P) dw_P dL \tag{12}$$

The volume $V_L = V - V_S$ of the liquid phase is then defined by the constant total volume V and the volume V_S. To calculate the particle number flux

$$\dot{F}_{out} = \frac{\dot{V}_{L,out}}{V_L} F(L, w_P) \tag{13}$$

due to product removal in the population balance, an expression for the outlet volumetric flow rate $\dot{V}_{L,out}$ of the dispersed solid phase is required. After longer algebraic manipulations an equation to calculate the volumetric flow rate $\dot{V}_{L,out}$ required in equation (13) can be derived.

$$\dot{V}_{L,out} = \frac{1-\varepsilon_S}{\varepsilon_S + (1-\varepsilon_S)(\bar{\nu}_{L,B}^* + x_{L,A,in}(\bar{\nu}_{L,A}^* - \bar{\nu}_{L,B}^*))} \cdot \left[(\bar{\nu}_{L,B}^* + x_{L,A,in} \cdot \right.$$
$$\left. (\bar{\nu}_{L,A}^* - \bar{\nu}_{L,B}^*)) c_{L,in} \dot{V}_{L,in} + \left(c_S^{-1} - \bar{\nu}_{L,A}^*\right) \right] \tag{14}$$

In the above equation the partial molar volumes of the components A and B are denoted by $\bar{\nu}_{L,A}^*$ and $\bar{\nu}_{L,B}^*$, the volumetric holdup of the solid phase is given by ε_S. This new equation can be interpreted as a balance of the in- and outflowing volumetric fluxes.

3   Numerical Methods

The numerical solution of the mathematical model by simulation tools (e.g. DIVA [1], MatLab [3]) requires a semi-discretization (method-of-lines approach) of the partial integro-differential equation (2). The discretization of the particle coordinates was done by a non-equidistant finite volume method [4]. For a detailed description of issues related to the numerical solution of population balance models see also [12].

The following equation demonstrates the discretization of the convective transport in the direction of L at a specific point, which can be derived by an integration over the finite volume surrounding the considered point.

$$\int_{L_k^-}^{L_k^+} \int_{w_{p,j}^-}^{w_{p,j}} \frac{\partial v_L F}{\partial L} dw_P dL = [v_L F]_{L_k^+, w_{p,j}} \Delta w_{p,j} - [v_L F]_{L_k^- w_{p,j}} \Delta w_{p,j} \tag{15}$$

The required values at the volume boundaries are determined by profile assumptions [4] and by the direction of transport. In this case constant profiles are assumed. The growth rate of crystals depends on the internal lattice strain w_P . Due to a high lattice strain the growth rate can become negative. In that case the discretization strategy has to be changed. This results in a switching of the profile assumptions depending on the velocities v_L and v_w and on the particle coordinates.

4   Simulation Results

The semi-discretized model equations were implemented into the MatLab [3] simulation environment. Dynamic and steady state simulations were performed for potassium nitrate. Due to space limitations only steady state simulation results will be shown. The following figure presents a comparison between the four different assumptions for the growth behavior of the absolute lattice strain from Table 1.
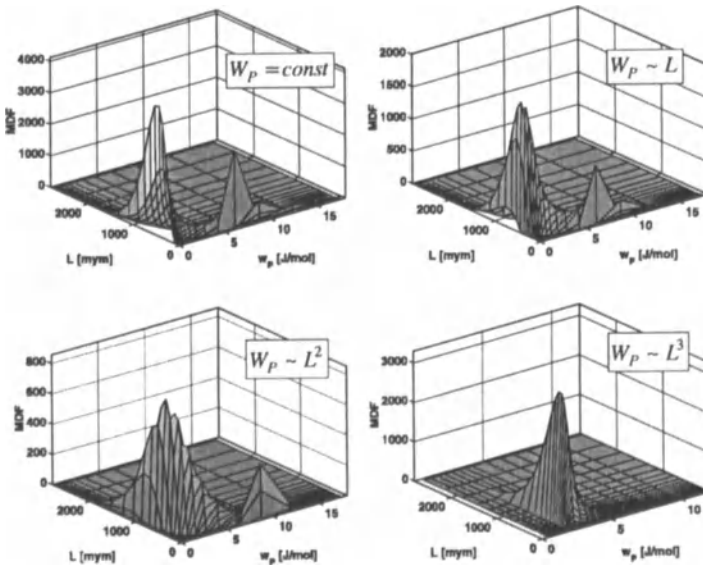
Fig. 1. Steady state simulation results for different growth assumptions

In Fig. 1 mass density functions (MDF) are presented versus the particle coordinates crystal length L and internal lattice strain w_P. The first mass density function shows the result for a constant absolute lattice strain during crystal growth. In that case the molar lattice strain of the crystals diminishes fast. Thus, most of the crystals in the depicted MDF have very low lattice strains. The second and third MDF in Fig. 1 are simulation results for cases in

which the absolute lattice strain changes proportional to the length $W_P \sim L$ and the surface area $W_P \sim L^2$. Comparing the first three MDFs it is observed, that higher orders in the dependency of W_P on L lead to higher molar lattice strains of crystals at steady state.

The fourth MDF is qualitatively different from the others presented in Fig. 1. Due to the formulation of the absolute lattice strain proportional to the volume $W_P \sim L^3$, the minimum molar lattice strain to be reached is set by the value of the constant K_4 shown in Table 1.

In summary the presented simulation results show a strong dependence of the MDF, and accordingly of the crystal population, on the different assumptions for the behavior of the absolute lattice strain during crystal growth.

5   Conclusions

In this contribution a population model with two particle coordinates was developed for a continuous crystallizer. The considered particle coordinates are the crystal length L and the internal lattice strain w_P of individual crystals. The numerical solution of the resulting system of model equations was done by a finite-volume semi-discretization following the method-of-lines approach.

The presented simulation results show a strong dependence of the steady state mass density function on the different assumptions for the relaxation of the internal lattice strain. This results in the implication that the molar lattice strain should not be neglected as a characteristic particle coordinate.

References

1. A. Kröner, P. Holl, W. Marquardt, E.D. Gilles, Comp. Chem. Eng. 14, 1990, 1289–1295
2. S. Miller, J. Rawlings, W. Witkowski, Ind. Eng. Chem. Res. 32(7), 1993, 1275–1296
3. MatLab 5.2, The MathWorks Inc., 24 Prime Park Way, Natick, MA 01760–1500, USA
4. J. H. Ferziger, M. Perić, Computational Methods for Fluid Dynamics, Springer Verlag, Berlin, 1996
5. D. Ramkrishna, Reviews in Chem. Eng., 3, 49–95, 1985
6. S. Wang, A. Mersmann, Chem. Eng. Sci., 47, 1365–1371, 1992
7. C. Gahn, PhD Thesis, TU München, 1997
8. A. Mersmann, M. Angerhöfer, T. Gutwald, R. Sangl, Sep.Tech., 2, 85–97, 1992
9. R. Eek, S. Dijkstra, G. M. van Rosmalen, AIChE Journal, 41(3), 1995, 571–584
10. A. van der Heijden, PhD Thesis, Katholieke Universiteit Nijmegen, 1992
11. J. Dirksen and T. Ring, Chem. Eng. Sci., 46(10), 2389–2427, 1991
12. S. Kumar, D. Ramkrishna, Chem. Eng. Sci., 51(8), 1311–1332, 1996

PE - a Scientific Computer Program for the Calculation of Fluid-Phase Equilibria

Oliver Pfohl[1], Stanimir Petkov[2], and Gerd Brunner[2]

[1] Bayer AG, Fluid Process Technology / Thermophysical Properties
   51368 Leverkusen, Germany
[2] Technische Universität Hamburg-Harburg, Arbeitsbereich Thermische
   Verfahrenstechnik, 21071 Hamburg, Germany

Abstract. The calculation of phase equilibria may serve as a cheap alternative compared to the measurement of phase equilibria. This is especially true for high pressure where the necessary equipment to measure phase equilibria is more expensive than at low pressure. The calculation may often serve as a fast alternative compared to measurements, also. The program PE (= Phase Equilibria) has been developed for modeling phase equilibria with equations of state (EOS) [1,2]. PE offers more than 40 different EOS, allowing the user to choose the one which best fits his needs. PE also offers powerful routines to determine adjustable EOS pure-component and mixture parameters by correlating experimental data and subroutines to use these parameters for predictions at conditions not investigated experimentally, yet.

1 Introduction

The knowledge of phase equilibria is essential for separation processes that are controlled by equilibrium like distillation, extraction and absorption. The distance to phase equilibrium is the driving force of these processes. At the department *Thermische Verfahrenstechnik* at the Technical University of Hamburg-Harburg high-pressure phase equilibria with supercritical compounds have been investigated experimentally since 1982. About ten apparatuses for measurements of phase equilibria have been constructed. The experimental results cover systems with carbon dioxide, hydrogen, water, ethanol, hexadecane, benzene derivatives and phenol derivatives as well as multicomponent mixtures from natural sources. The results cover a temperature range from 300 to 600 K and pressures up to 50 MPa [3,4]. In order to keep the number of necessary experiments low, the program package PE for the calculation of phase equilibria has been developed within the last decade. In the beginning, the program PE has been created on Hewlett-Packard UNIX workstations using FORTRAN and hp-Starbase-Graphics. Starting late 1997, an user friendly interface was developed for Windows NT/95/98 enabling its use on commercial PC. The Windows version of PE uses windows, menus, and dialog boxes and supports multitasking. Further, the graphical output files in PostScript and Enhanced Windows Metafile format are fully compatible with other Windows programs like Microsoft®Office, CorelDRAw$^T M$,

Micrografix®Picture Publisher. *PE* can be downloaded from
http://vt2pc8.vt2.tu-harburg.de.

2   Equations of State

PE offers about 40 different equations of state:

- Cubic EOS with different a - functions and volume translations (Soave-Redlich-Kwong [5], Peng-Robinson [6], ...)

- EOS based on statistical mechanics (BACK [7], SAFT [8, 9], SAFT-2 [10], ...)

- EOS explicitly accounting for association (SAFT [8, 9], SAFT-2 [10], Cubic Plus Association [11], Anderko [12], ...)

SAFT-2 has been developed by Pfohl and Brunner [10] in order to combine the benefits of original SAFT and the BACK EOS:

- BACK can describe small molecules as often used as supercritical solvents (carbon dioxide, ethane, nitrogen and propane) extremely well including the critical region [13]. This is of special interest for gas-extraction processes which are often carried out in this region in order to utilize the high compressibility of the solvent there [14].

- Original SAFT can describe large and associating molecules well - but fails to reproduce pure-component properties of many supercritical solvents with physical meaningful parameters, if the correct reproduction of critical temperature and pressure is enforced [13].

SAFT serves as an example for a physically sound EOS implemented in *PE*, here. Original SAFT [8, 9] describes molecules as chains of m_i covalently bonded spheres with the diameter d_i. Using *Physical Theory*, association between molecules can be accounted for. The molecules are equipped with so-called sites, therefore. The different effects lead to four different contributions of the residual Helmholtz energy a^r. The first term in Eq. (1) is the hard sphere term by Boublik [15] and Mansoori et al. [16], which reduces to the hard sphere term by Carnahan and Starling [17] for pure compounds. The second term accounts for covalently bonded spheres within a molecule. The third term is the term by Alder et al. [18] which is also used in the BACK EOS [7] for dispersive forces between molecules. The fourth term accounts for association / solvation: X^{Ai} is the fraction of sites of type A on the molecule

type i, which does not bond.

$$\tilde{a}^r = \frac{a^r}{RT} \quad = \frac{\zeta_2^3 + 3\zeta_1\zeta_2\zeta_3 - 3\zeta_1\zeta_2\zeta_3^2}{\zeta_0\zeta_3(1-\zeta_3)^2} - \left(1 - \frac{\zeta_2^3}{\zeta_0\zeta_3^2}\right)ln(1-\zeta_3)+$$

$$\sum_{i=1}^{N} z_i(1-m_i)ln(g_i(d_i))+$$

$$\left(\sum_{i=1}^{N} z_i m_i\right)\sum_{i=1}^{4}\sum_{j=1}^{9} D_{ij}\left(\frac{u}{kT}\right)^i\left(\frac{\zeta_3}{\sqrt{2\pi/6}}\right)^j +$$

$$\sum_{i=1}^{N}\sum_{A_i} z_i\left(lnX^{A_i} + \frac{1-X^{A_i}}{2}\right)$$

(1)

The average packing fraction ζ_3 in a mixture is determined similar to the average molecular surfaces and length according to Eq. (2). The temperature dependence of the sphere volumes is the same as in the BACK EOS: in Eq. (3), v^0 is the sphere volume at a given temperature which would be occupied by a single sphere in a packing of identical spheres; the sphere diameter di is obtained by Eq. (4), then.

$$\zeta_k = \frac{\pi\rho N_{A\nu}}{6}\sum_{i=1}^{N} z_i m_i d_i^k$$

(2)

$$\nu_i^0 = \nu_i^{00}\left(1 - 0,12exp\left(\frac{-3u_i^0}{kT}\right)\right)^3$$

(3)

$$\nu_i^0 = \frac{N_{A\nu}d_i^3}{\sqrt{2}}$$

(4)

The effective depth of the intermolecular potential is determined according to one-fluid mixing rules (section 3) based on the temperature-dependent pure-component potential depth given in Eq. (5).

$$u_i = u_i^0\left(1 + \frac{e_i}{kT}\right)$$

(5)

The fraction of non-associating sites X^{A_i} in Eq. (6) decreases with a rising concentration of free sites which can associate with the former, $N_{A\nu}\rho\sum\sum z_j X^{B_j}$, and the association strength, $\Delta^{A_iB_j}$, defined in Eq. (7).

$$X^{A_i} = \left(1 + N_{A\nu}\rho\sum_{j=1}^{N}\sum_{B_j} z_j X^{B_j}\Delta^{A_iB_j}\right)^{-1}$$

(6)

$$\Delta^{A_iB_j} = g_{ij}\left(exp(\frac{\varepsilon^{A_iB_j}}{kT}) - 1\right)\sigma_{ij}^3\kappa^{A_iB_j}$$

(7)

with $\sigma_{ij} = \frac{\sigma_i + \sigma_j}{2}$ and $\nu_i^{00} = \frac{N_{Av}\sigma_i^3}{\sqrt{2}}$.

The system of non-linear equations, multiple Eq. (6), is solved by iterative methods. Solvation, called cross-association, is accounted for by using the geometric means of the pure-component parameters ε and κ, which describe the pure compounds' association.

In SAFT-2, convex bodies from the BACK EOS are used to model supercritical compounds. Sphere chains from SAFT are used to model all other large and associating molecules. Both EOS are combined by the use of the average radial distribution of convex bodies at contact by Boublik [19]: Eq. (8).

$$g_{ij}^{CB,av} = \frac{1}{1-\nu} + \frac{3V_iS_j(r-t)+(3V_iT_j+R_i^2S_j)s}{(1-\nu)^2(eV_i+2S_iR_j+R_iS_j)} + \frac{6V_iS_jqs}{9(1-\nu)^3(3V_i+2S_iR_j+R_iS_j)} \tag{8}$$

The advantageous use of convex bodies instead of sphere chains for the supercritical solvent in SAFT-2 is demonstrated for pure carbon dioxide, below. The arrows point to the areas of interest with respect to the solvent's high compressibility in gas-extraction processes.
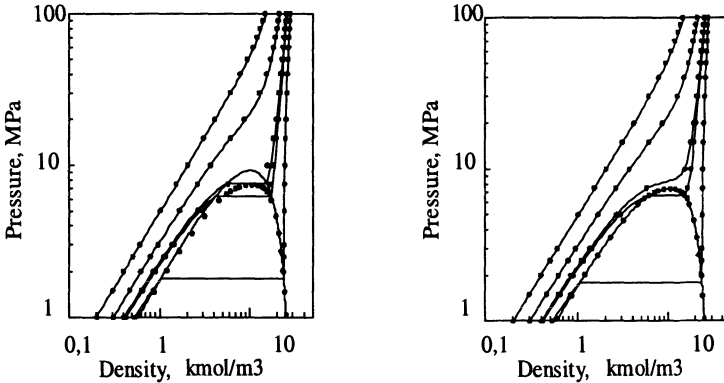
Fig. 1. Left diagram: Sphere chains from original SAFT with parameters from [9] overestimate critical temperature and critical pressure [13]. Right diagram: In SAFT-2, convex bodies from BACK with parameters from [10] yield excellent pure-component properties.

3   Mixing Rules

PE offers different mixing rules for each EOS for the calculation of mixture properties (here: potential depth u) from the pure-component properties (u_i) and mixture composition (z_i). The two mixing rules proposed by Pfohl and Brunner [10] for use in SAFT and SAFT-2 serve as an example for mixing

rules implemented in PE, here. The van der Waals and volume fraction mixing rule of SAFT [9] have been extended according to the ideas of Mathias, Klotz, and Prausnitz [20]. They have been applied to SAFT and SAFT-2. Both extensions are based on segments and thus promise higher predictive capabilities than the original two-parameter mixing rules of SAFT.

2-parameter van-der-Waals mixing rule

$$u = \frac{\sum_i \sum_j z_i z_j V_{ij} \sqrt{u_i u_j}(1-k_{ij}) + \sum_i z_i \left(\sum_j z_j (\sqrt{u_i u_j} V_{ij} \lambda_{ji})^{1/3}\right)^3}{\sum_i \sum_j z_i z_j V_{ij}} \tag{9}$$

2-parameter volume-fraction mixing rule

$$u = \sum_i \sum_j f_i f_j \sqrt{u_i u_j}(1 - k_{ij}) + \sum_i f_i \left(\sum_j f_j (\sqrt{u_i u_j} \lambda_{ji})^{1/3}\right)^3 \tag{10}$$

(here: f_i = volume fractions of component i, k_{ij} and λ_{ij} = adjustable binary parameters)

4   Determination of Pure-Component Parameters

PE offers routines to determine pure-component parameters for all EOS based on pure-component vapor pressures and densities. Further, a subroutine exists that enforces parameters that result in a correct reproduction of critical temperature and critical pressure. The correct reproduction of the critical temperature and pressure of the supercritical solvent is essential for modeling gas-extraction processes near the critical point of the solvent.

5   Determination of Mixture Parameters

PE offers routines to determine binary interaction parameters for the optimum reproduction of experimentally determined binary (or ternary) phase equilibria. Using PE, optimizations of interaction parameters can be performed according to one of two different ways. Using a Simplex-Nelder-Mead algorithm in order to obtain the optimum interaction parameters is the standard method. However, the Simplex-Nelder-Mead algorithm requires initial guesses for the interaction parameters and will not necessarily find the way from one local optimum to another optimum. Therefore a second method - the so-called grid - enables to find initial guesses and different minima on the expense of increased time consumption.

6   Prediction of Binary Equilibria

PE offers routines to predict phase equilibria where no experimental data might be available.
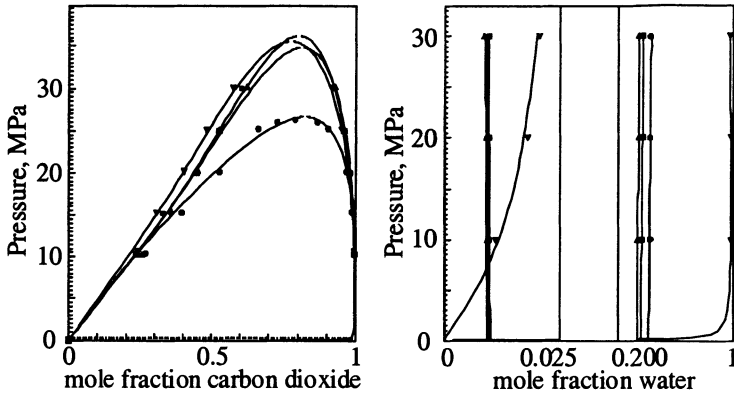
Fig. 2. Calculation of binary VLE and LLE at 373.15 K with the Peng-Robinson EOS in systems containing carbon dioxide and water. Experiments [3]: o-cresol = •, m-cresol = ■ , p-cresol = ▲, phenol / carbon dioxide = ▼. Two interaction parameters of the Mathias-Klotz-Prausnitz mixing rule [20] have been adjusted for each binary system.
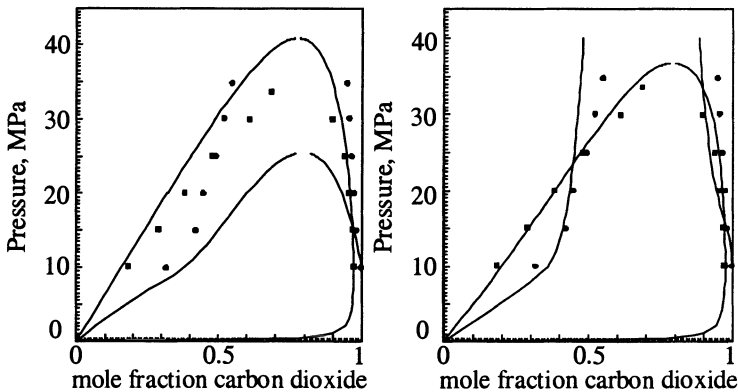
Fig. 3. The above predictions for the binary systems carbon dioxide + p-cresol at 323.15 K and 473.15 K are based on the parameters regressed from the binary systems at 373.15 K shown above. Experimental data: 323.15 K = •, 473,15 K = ■ [3,4].

SAFT-2 gives better predictions for the phase behavior at these temperatures than the Peng-Robinson EOS. In SAFT-2, p-cresol is modeled as a sphere chain with two association sites and carbon dioxide is modeled as a convex body [4, 10].

7 Prediction of Ternary Equilibria

PE includes routines to predict phase equilibria with more than two compounds based on binary interaction parameters regressed from binary systems.
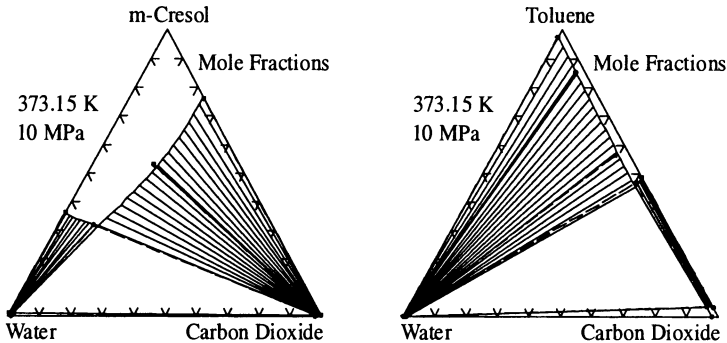
Fig. 4. Predictions of ternary systems calculated with the Peng-Robinson EOS [6] with the Mathias-Klotz-Prausnitz mixing rule [20] and binary parameters from the binary systems, above. Experimental results: [3].
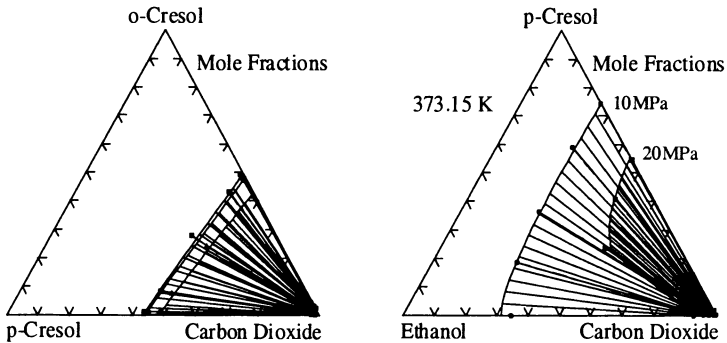
Fig. 5. Predictions of ternary systems calculated with SAFT-2 [10] with the van der Waals - Mathias - Klotz - Prausnitz mixing rule [20] and binary parameters from the binary systems. Experimental results: [4]. Left diagram: 356.15 K / 18.3 MPa = ● , 373.15 K / 19.0 MPa = ■, 373.15 K / 22.0 MPa = ▲.

8 Acknowledgement

meinschaft to the projects Br846/2, /4, /7, /8, /10, /11, and Do337/2 are gratefully acknowledged.

References

1. High-Pressure Fluid-Phase Equilibria Containing Supercritical Fluids, 8th International Conference on Properties and Phase Equilibria for Product and Process Design at Noordwijkerhout, **1998**
2. Pfohl, Petkov, Brunner, Usage of PE - A Program to Calculate Phase Equilibria, Herbert Utz Verlag, ISBN 3-89675-410-6, **1998**
3. Pfohl, Avramova, Brunner; *Fluid Phase Equilib.* **1997**, 141, 179.
4. Pfohl, Pagel, Brunner; *Fluid Phase Equilib.*, Sep. **1998**
5. Soave, Chemical Engineering Science 1972, 27, 1197.
6. Peng, Robinson; *Ind. Eng. Chem. Fundam.* **1976**, 15(1), 59.
7. Chen, Kreglewski; *Ber. Bunsenges.* **1977**, 81(10), 1048.
8. Chapman, Gubbins, Jackson, Radosz; *Fluid Phase Equilib.* **1989**, 52, 31.
9. Huang, Radosz; *Ind. Eng. Chem. Res.* **1990**, 29, 2284 & **1991**, 30, 1995.
10. Pfohl, Brunner; *Ind. Eng. Chem. Res.* In press **1998**.
11. Kontogeorgis, Voutsas, Yakoumis, Tassios; *I& EC Res.* **1996**, 35, 4310.
12. Anderko; *Fluid Phase Equilib.* **1989**, 45, 39.
13. Pfohl, Giese, Dohrn, Brunner; *Ind. Eng. Chem. Res.*, **1998**, 37, 2966
14. Brunner; *Gas Extraction, Springer.* New York, **1994**.
15. Boublik, T. Hard-Sphere Equation of State. *J. Chem. Phys.* **1970**, 53, 471.
16. Mansoori, G.A.; Carnahan, N.F.; Starling, K.E.; Leland, T.W. Equilibrium, Thermodynamic Properties of the Mixture of Hard Spheres. *J. Chem. Phys.* **1971**, 54 (4), 1523.
17. Carnahan, N.F.; Starling, K.E. Equation of State for Nonattracting Rigid Spheres. *J. Chem. Phys.* **1969**, 51(2), 635.
18. Alder, B.J.; Young, D.A.; Mark, M.A. Studies in Molecular Dynamics. X. Corrections to the Augmented van der Waals Theory for the Square Well Fluid. J. Chem. Phys. **1972**, 56(6), 3013.
19. Boublik; *J. Chem. Phys.* **1975**, 63(9), 4084.
20. Mathias, Klotz, Prausnitz; *Fluid Phase Equilib.* **1991**, 67, 31.

Solving Chemical Engineering Problems with Front Propagation Using an Adaptive Moving Grid Method

A. Salden, J. Frauhammer and G. Eigenberger

Institut für Chemische Verfahrenstechnik, Universität Stuttgart,
Böblinger Str. 72, D-70199 Stuttgart, Germany

Abstract. A simple and efficient moving grid method for the simulation of one dimensional chemical engineering problems with steep propagating fronts is presented. A combination with a fully adaptive static regridding technique as implemented in PDEXPACK was used. The moving grid method was tested for the simulation of an adiabatic fixed bed adsorption process. Compared to conventional adaptive methods on a static grid a significant reduction of the CPU time and a higher stability of the simulation could be achieved.

1 Introduction

Many chemical engineering processes are characterized by steep propagating fronts in the spatial profiles of the state variables. Examples are fixed bed reactors, adsorption columns, ion exchangers and regenerative heat exchangers. Usually the fronts are significant but continuous changes of the variables within a limited region of the spatial domain. However, also discontinuous fronts can be observed. For the description of these processes often one dimensional models are sufficient. Commonly, the model equations consist of partial differential as well as algebraic equations. A widely used numerical method for the solution of such sets of equations is the *method of lines* treatment. In this approach the partial differential equations are discretized in space. The resulting set of differential algebraic equations can then be solved by efficient and robust solvers such as LIMEX [3] or DASSL [2].

If the systems show steep moving fronts in the spatial profiles of the state variables either a very fine equidistant grid has to be used or the space grid has to be adapted locally during the time integration in order to reduce numerical dispersion. The use of a fine grid throughout the whole space domain results in impractically huge sets of equations. In contrast, adaptive methods guarantee high accuracies while the calculation effort is significantly reduced.

As an additional approach to increase the efficiency of the *method of lines*, moving grid methods have been proposed. In contrast to a static grid adaption a contiuous dynamic adaption of the spatial grid is performed. The major objective of these methods is to reduce the dynamics of the solution on the moving grid which makes a frequent grid adaption unnecessary. The smaller changes of the state variables result in larger time steps.

Another problem arises when moving discontinuities occur. For the simulation it is necessary to know the exact location of the discontinuities since, e.g., the model equations or the physical properties change. Using high accuracy adaptive methods with an automatic control of the time steps and the space grid, these model shifts evoke convergence problems. In this case moving grid methods also can help, being able to capture the location of the discontinuities [4].

In conventional moving grid methods the grid velocity is calculated for each time step based upon special mathematical criteria, e.g. the minimization of the time rate of change of the state variables [9] or the principle of equidistribution of the spatial error [12]. In order to avoid a crossing of the grid trajectories these methods require strict grid regularization procedures which are often difficult to handle.

In this paper a simple and efficient moving grid method is presented. The algorithm is a modification of the method developed by NOWAK [6]. The benefits of this method are demonstrated for the example of the modeling and simulation of an adiabatic fixed bed adsorber for waste air purification.

2   Adapive Moving Grid Methods

In this section the algorithm of the developed adaptive moving grid method is described. As an illustrative example the following one dimensional system of parabolic partial differential equations is treated:

$$\underline{\mathbf{B}}\frac{\partial \mathbf{y}}{\partial t} = -\underline{\mathbf{v}}\frac{\partial \mathbf{y}}{\partial z} + \frac{\partial}{\partial z}\left(\underline{\mathbf{D}}\frac{\partial \mathbf{y}}{\partial z}\right) + \mathbf{Q} \tag{1}$$

or

$$\underline{\mathbf{B}}\frac{\partial \mathbf{y}}{\partial t} = \mathbf{f}(\mathbf{y}, \mathbf{y}_z, \mathbf{y}_{zz}) \tag{2}$$

In this notation $\mathbf{y}$ is the vector of the state variables, i.e. the unkowns of the system with the dimension m. $\underline{\mathbf{B}}$, $\underline{\mathbf{v}}$ and $\underline{\mathbf{D}}$ are matrices with the dimension $(m \times m)$ and depend on $\mathbf{y}$, z and t. The vector $\mathbf{Q}$ representing sources and sinks has the same dimension as $\mathbf{y}$ and also depends on $\mathbf{y}$, z and t.

The system in eq. (1) can be solved numerically using the *method of lines*. A finite difference method has been used for the spatial discretization.

$$\underline{\mathbf{B}}_i\frac{\partial \mathbf{y}_i}{\partial t} = \mathbf{f}(\mathbf{y}_i, \mathbf{y}_z|_i, \mathbf{y}_{zz}|_i) \qquad i = 1, \ldots, n \tag{3}$$

In moving grid methods the location of the spatial grid points is no longer fixed during one integration step ($z_i = z_i(t)$, $i = 1, \ldots, n$). The transition to a moving grid requires a transformation of the model equations in a moving coordinate system. In eq. (3) the partial derivative $\partial \mathbf{y}_i/\partial t$ is the variation of $\mathbf{y}_i$ with time at a fixed position in the spatial domain. The change of $\mathbf{y}_i$ with

time while moving along the space coordinate with the velocity $w_i = dz_i/dt$ is described by the total derivative

$$\frac{d\mathbf{y}_i}{dt} = \frac{\partial \mathbf{y}_i}{\partial t} + \frac{\partial \mathbf{y}_i}{\partial z}\frac{dz_i}{dt} = \frac{\partial \mathbf{y}_i}{\partial t} + w_i \frac{\partial \mathbf{y}_i}{\partial z} \qquad (4)$$

Thus, eq. (3) is transformed by replacing the partial derivative with eq. (4):

$$\underline{\mathbf{B}}_i \left(\frac{d\mathbf{y}_i}{dt} - \mathbf{y}_z|_i \frac{dz_i}{dt} \right) = \mathbf{f}(\mathbf{y}_i, \mathbf{y}_z|_i, \mathbf{y}_{zz}|_i) \qquad i = 1, \ldots, n \qquad (5)$$

If the velocity $w_i = dz_i/dt$ is equal to zero the partial derivative $\partial \mathbf{y}_i/\partial t$ coincides with the total derivative and eqs. (5) and (3) are equal. Since the location of the grid points changes with time they can be considered as additional state variables requiring n additional equations.

In contrast to conventional moving grid methods, in the considered method the movement of the grid points is not calculated based upon universal criteria. Instead, the additional equations to describe the movement of the grid points can be obtained due to the following simple and very efficient considerations [4]. The basic idea behind the developed algorithm is to couple specific grid points (*moving points*) directly to the propagating fronts, moving them with the real physical front velocity. All other grid points are moved in such a way that a crossing of their trajectories is avoided.

For many chemical engineering problems simple and often algebraic equations for the calculation of the front velocity can be derived. Well known examples are the equations for propagating reaction fronts in catalytic fixed bed reactors [5] or the method of non-linear wave dynamics for the calculation of the movement of the mass transfer zones in adsorption and ion exchange columns [10]. This a priori information is used to link the *moving points* to the front, moving them with the front velocity (cf. section 3).

$$\frac{dz_{i_k}}{dt} = w_k = w_{phys,k} \qquad k = 1, \ldots, n_{MP} \qquad (6)$$

The first and the last grid point of the spatial domain, i.e. z_1 and z_n are fixed. This leads to the following conditions:

$$\frac{dz_1}{dt} = 0 \quad \text{and} \quad \frac{dz_n}{dt} = 0 \qquad (7)$$

For all other grid points the only requirement is that they do not cross each other. This is fullfilled if the ratio of two adjacent grid point distances ($z_i - z_{i-1}$) and ($z_{i+1} - z_i$) remains constant during the movement of the grid. For a grid with $z_{i-1} < z_i < z_{i+1}$ this can be expressed as:

$$\left.\frac{z_{i+1} - z_i}{z_i - z_{i-1}}\right|_t = \left.\frac{z_{i+1} - z_i}{z_i - z_{i-1}}\right|_{t+dt} \qquad (8)$$

Based on a taylor series the following equation can be derived [4]:

$$\frac{z_{i+1} - z_i}{z_{i+1} - z_{i-1}} \frac{dz_{i-1}}{dt} - \frac{dz_i}{dt} + \frac{z_i - z_{i-1}}{z_{i+1} - z_{i-1}} \frac{dz_{i+1}}{dt} = 0 \qquad (9)$$

This equation is valid for all grid points between the boundaries of the spatial domain and the various *moving points*. Equation (9) can be understood as a linear interpolation of the grid velocities.

A very efficient method is obtained if the moving grid method is combined with an adaptive static regridding algorithm. In this work a fully adaptive *method of lines* treatment was applied based on regridding techniques such that both the spatial discretization error and the error arising from the time integration can be controlled [6,7]. Based on this algorithm the program package PDEXPACK [8] has been developed to solve parabolic differential equations of the gerneral form given in eq. (1). For the calculation of the transformed model equations on a moving grid minor modifications of the error control had to be implemented [4].

3   Performance of the adaptive moving grid method

In this paper the adsorption of toluene at a commercial DAY zeolite is considered. This system is a typical example for a technical application for adsorptive waste air purification. Using a zeolite monolith a narrow mass transfer zone can be obtained.

A one dimensional two phase model with axial dispersion of the adiabatic adsorption fixed bed has been derived. This model descibes the adsorption process with a sufficient accuracy. The following assumptions have been made: The fluid phase and the quasihomogeneous adsorbent phase have been modeled seperately, except for a quasihomogeneous energy balance. Mass transfer in axial direction can be described by an convection dispersion model. Radial gradients of the state variables can be neglected. Mass exchange between the fluid and the adsorbate phase is calculated based on a linear driving force approximation. Due to low adsorptive concentrations the total mass flux in axial direction can be considered as constant. The following system of equations has been derived under these assumtions [11]:

$$\frac{\partial c}{\partial t} = -v \frac{\partial c}{\partial z} + \frac{D}{\varepsilon} \frac{\partial^2 c}{\partial z^2} - \frac{\varrho}{\varepsilon} K (q^* - q) \qquad (10)$$

$$\frac{\partial q}{\partial t} = K (q^* - q) \qquad (11)$$

$$(\varepsilon C_f + \varrho C_s) \frac{\partial T}{\partial t} = -\varepsilon v C_f \frac{\partial T}{\partial z} + \lambda \frac{\partial^2 T}{\partial z^2} - \varrho K (q^* - q) (-\Delta H_A) \qquad (12)$$

The equilibrium loading q^* of toluene on the DAY zeolite can be described with the LANGMUIR isotherm. The mass exchange coefficient K is calculated

due to GLUECKAUFs approach. DANCKWERTS boundary conditions of the material balance in the gas phase and the quasihomogeneous energy balance are used. In this example the adsorption of toluene on a completely regenerated adsorbent at ambient temperature is considered. Due to space limitations the numerical values of the process parameters as well as the thermodynamic properties will not be presented here.

In Fig. 1 the dynamic system behaviour for the adsorption process is depicted. The numerical solution of the model equations was performed with PDEXPACK on a static adaptive discretization grid. This simulation run serves as a reference for the later calculation of the model on an adaptive moving grid. Fig. 1 show the axial profiles of gas phase concentration and column temperature at different times. Due to the adsorption of toluene, the toluene concentration decreases over the bed length and a concentration front forms propagating slowly through the column. As a result of the exothermic adsorption process the temperature rises. Thus, a pure thermal wave is generated which propagates through the fixed bed traveling in front of the slower adsorption front. This temperature front heats up the adsorber. Due to the cool feed gas stream the adsorbent is cooled back to ambient temperature in regions behind the adsorption front where equilibrium is reached. This second temperature wave is coupled to the slow adsorption wave. When the adsorption wave reaches the end of the column the capacity of the adsorbent is exhausted and breakthrough occurs.

The dynamic system behaviour of complex non-linear adsorption processes can be described at least approximately by the phenomena of non-linear wave dynamics [10]. These theories are based on simple equilibrium models of the adsorption process without axial dispersion. Such a reduced model can easily be derived from the detailed model given in the eqs. (10-12). All mass exchange resistances are neglected so that local equilibrium can be assumed. Axial dispersion effects are neglected. This yields the following equations:

$$\frac{\partial c}{\partial t} + \frac{\varrho}{\varepsilon}\frac{\partial q}{\partial t} = -v\frac{\partial c}{\partial z} \tag{13}$$

$$(\varepsilon C_f + \varrho C_s)\frac{\partial T}{\partial t} + \varrho(-\Delta H_A)\frac{\partial q}{\partial t} = -\varepsilon v C_f\frac{\partial T}{\partial z} \tag{14}$$

The equilibrium model without axial dispersion represents a system of first order hyperbolic partial differential equations. For the solution of these sytems an extensive mathematical theory exists. In this work we used the method of characterisics proposed in [10] which is particularly suitable for systems of two hyperbolic equations.

In Fig. 1 the solutions of the detailed model and the reduced model are compared. Due to dispersive effects and finite mass exchange fluxes a characteristic spreading of the fronts in the detailed simulation can be observed. But the comparison shows that the reduced model correctly predicts both the wave velocity and the plateau. This suggests to use the simple analytical solutions of the reduced model to calculate the velocity of the *moving points*.
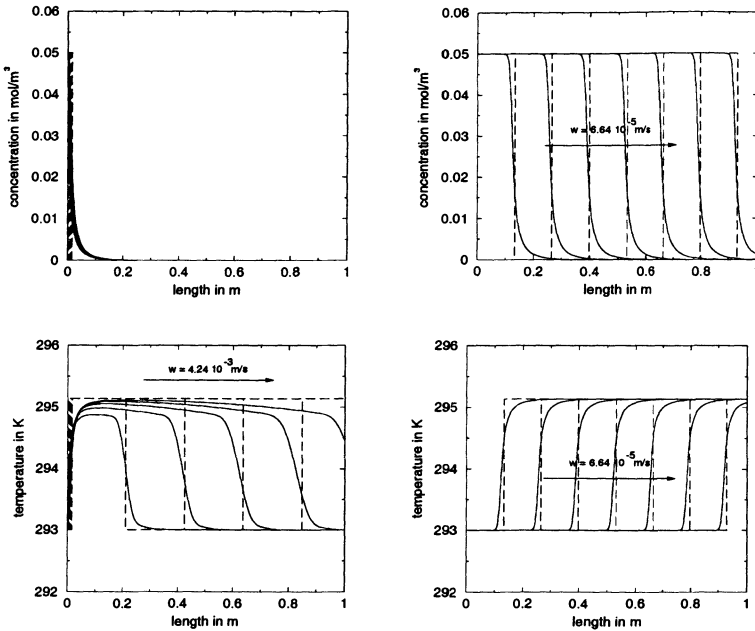
Fig. 1. Axial profiles of gas phase toluene concentration (top) and column temperature (bottom) at different times: 0 to 250 s (left) and 2000 to 14000 s (right). Detailed model (—), reduced model (– – –).

3.1   Comparison of the static grid and the moving grid solutions

In the following section the performance of the numerical solutions based on the adaptive static grid and the adaptive moving grid method is compared. To obtain a solution with the adaptive moving grid method the model equations (10-12) have to be transformed to the moving coordinates according to the algorithm described in section 2. The velocity of the *moving points* is calculated with the solution of the reduced model. All other grid points are moved as shown in section 2.

Fig. 2 illustrates the movement of the grid, represented by the velocity of the grid points, in comparison with the axial temperature profile at different times. Fig. 2 shows that the location of the front is correctly captured throughout the complete simulation. The labeled grid points are the two *moving points* MP1 and MP2. The velocity of the other grid points results from a linear interpolation between the *moving points* and the static boundaries. As a result of the additional regridding procedure, the grid density around the front is increased whereas it decreases in the other regions.

The results of a direct comparison between the static grid method and the moving grid method are resumed in Tab. 1. The results are judged by the number of required grid points $\bar{n}_z$ and the time steps n_t until $t = 24000$ s. At this time even the slow adsorption wave has broken through. Due to the
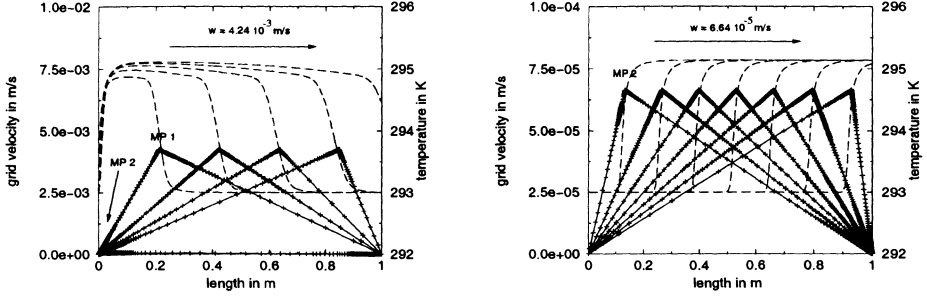
Fig. 2. Grid velocity in comparison to the momentary location of the temperature front. 0 to 250 s (left) and 2000 to 14000 2 (right). Temperature (– – –), grid velocity (—), grid points (+).

regridding the number of the grid points varies between n_z^{min} and n_z^{max}. $\bar{n}_z$ represents the time average. The CPU time of the simulation runs refers to a SUN ULTRA 1.

Table 1. Performance of the adaptive static grid method (tol=10^{-5}) and the adaptive moving grid method (tol=10^{-4}).

	Static grid	Moving Grid
n_t	1519	101
$\bar{n}_z$	1120	374
n_z^{min}	55	33
n_z^{max}	1597	1577
CPU time in s	3063	309

As a result of the convection dominant system ($Pe \approx 10^5$) the error tolerances for the simulation at a static grid have to be very small in order to guarantee a sufficient stability of the solution by small time steps and a very fine grid. The calculations with a moving grid can be performed with destinctively higher tolerances without a loss of stability.

As illustrated in Tab. 1 the calculations with a moving grid descrease the required time steps by factor 15. This is a result of the reduced dynamics of the system in the transformed coordinates. Due to the higher error tolerances the average number of grid points is also smaller. But the simultaneous calculation of the movement of the grid points results in a larger set of equations. Thus, only an overall decrease in CPU time by factor 10 is achieved.

4 Conclusions

We presented a simple and very efficient adaptive moving grid method for the simulation of one dimensional processes with steep propagating fronts. This method was used in combination with an adaptive regridding technique as implemented in PDEXPACK. We successfully tested this method for the simulation of various fixed bed processes . It was shown that using this method a significant reduction of the CPU time can be obtained. The accuracy and the stability of the solution are very good.

References

1. BLOM, J. G., J. M. SANZ-SERNA and J. G. VERWER: *On Simple Moving Grid Methods for One-dimensional Evolutionary Partial Differential Equations.* J. Comput. Phys., 74:191–213, 1988.
2. BRENAN, K. E., S. L. CAMPBELL and L. R. PETZOLD: *Numerical Solution of Initial-Value Problems in Differential-Algebraic Equations.* North-Holland, 1989.
3. DEUFLHARD, P., E. HAIRER and J. ZUGCK: *One Step and Extrapolation Methods for Differential Algebraic Systems.* Numer. Math., 51:501–516, 1987.
4. FRAUHAMMER, J., H. KLEIN, G. EIGENBERGER and U. NOWAK: *Solving moving boundary problems with an adaptive moving grid method: Rotary heat exchangers with condensation and evaporation.* Chem. Engng. Sci., 53(19):3393-3411, 1998.
5. GILLES, E. D.: *Quasi-stationäres Verhalten von wandernden Brennzonen.* Chem. Engng. Sci., 29:1211–1216, 1974.
6. NOWAK, U.: *Adaptive Linienmethoden für nichtlineare parabolische Systeme in einer Raumdimension.* TR 93-14, Konrad-Zuse-Zentrum für Informationstechnik, Berlin, 1993.
7. NOWAK, U.: *A fully adaptive MOL-treatment of parabolic 1-D problems with extrapolation techniques.* Appl.Numer. Math., 20:129–145, 1996.
8. NOWAK, U., J. FRAUHAMMER and U. NIEKEN: *A fully adaptive algorithm for parabolic partial differential equations in one space dimension.* Computers chem. Engng., 20(5):547–561, 1996.
9. PETZOLD, L. R.: *Observations on an adaptive Moving Grid Method for one-dimensional Systems of Partial Differential Equations.* Applied Numerical Mathematics, 3:347–360, 1987.
10. RHEE, H. K., R. ARIS and N. R. AMUNDSON: *First-Order Partial Differential Equations*, volume 2. Prentice Hall, 1989.
11. SALDEN, A., T. BOGER and G. EIGENBERGER: *Adsorptive Abtrennung und Rückgewinnung organischer Komponenten aus Abluft.* PEF-report, Forschungszentrum Karlsruhe, 1997.
12. ZEGELING, P. A., J. G. VERWER and J. C. H. VAN EIJKEREN: *Application of a Moving-Grid Method to a Class of 1D Brine Transport Problems in Porous Media.* TR NM-R9112, CWI, Center for Mathematics and Computer Science, 1991.

Dynamic Simulation of Reactive Absorption Processes for the Purification of Coke Oven Gases

R. Schneider, E.Y. Kenig, and A. Górak

Essen University, Chair of Thermal Process Eng., Mech. Eng. Dept.,
D -45141 Essen; e-mail: ralf.schneider@uni-essen.de

Abstract. Reactive absorption processes represent complex mass transfer of multicomponent systems combined with chemical reactions. Therefore, traditional equilibrium stage models and efficiency approaches are usually inadequate and a rigorous two-phase model, based on the two film theory had to be developed. This dynamic model takes into account diffusional interactions and the influence of chemical reactions on mass transfer as well as thermodynamic non-idealities and considers the impact of special column internals like structured packings on hydrodynamics. By making use of the Nernst-Planck equation for the description of mass transfer, the influence of additional driving forces in electrolyte systems like electrical potential gradients are expressed. This rigorous dynamic rate-based approach leads to a system of partial differential equations, which had to be discretized in axial direction. The resulting DAE system has been implemented into SpeedUp® and solved numerically. For the H_2S scrubber some simulation results are presented with the consideration of three liquid distributors and a structured packing section. For the validation of the model, pilot plant steady state experiments have been carried out at *Thyssen Still Otto* in Duisburg. The simulation results are in good agreement with the experimental data.

1 Introduction

The recent strong emphasis on environmental protection and more stringent requirements gave new impetus to improvements of coke oven gas purification processes. Coke oven gas mainly consists of a mixture of carbon monoxide, hydrogen, methane and carbon dioxide. It is contaminated with a variety of organic and inorganic compounds, which have to be separated in absorption columns before using it as synthesis gas in further process steps. The objective of these scrubber units is a selective removal of H_2S, NH_3 and HCN, whereas competing reactions of the major impurity CO_2 have to be suppressed. As an example of innovative purification processes the Ammonia Hydrogen Sulfide Circulation Scrubbing (ASCS) has been investigated, in which the ammonia available from the raw gas is used instead of an external solvent. Computer simulations based on detailed physical models will reduce the experimental expenditure and support optimal operation strategies as well as energetic and design optimizations. In addition, the changing feed compositions of coal and coke gas necessitate a process control based on dynamic model equations which will be presented in this work.

2   Modeling aspects

2.1   Model complexity

Traditional equilibrium models are based on the assumption that both phases leaving a stage are in thermodynamic equilibrium. In practice, equilibrium is rarely attained since mass and heat transfer are actually rate-based processes that are driven by gradients of chemical potential and temperature. Therefore, traditional models and efficiency approaches are usually inadequate. Mass transfer resistances can only be considered by rate-based models with separate balance equations for each phase (see e. g. [1–3]). The interfacial molar and heat fluxes are calculated explicitly, e. g. by the Maxwell-Stefan approach that considers molecular interactions and diffusional phenomena in multicomponent mixtures [2,3]. In rigorous and predictive models the influence of chemical reactions on mass transfer cannot be neglected, if both phenomena occur with similar velocities. In the case of a single irreversible reaction, this influence can be estimated by enhancement factors [4]. This approximation fails for complex reaction schemes with many parallel and reversible reactions like in the chemisorption process (Fig. 2) considered in this work. In this case, the direct impact on mass transfer can be expressed by differential mass balances for the liquid film region in terms of the two film model [5].

2.2   Rate-based approach for reactive absorption

A rigorous two-phase model for the coke oven gas purification based on the two-film theory has been developed. This advanced dynamic rate-based approach takes into account thermodynamic non-idealities and considers the impact of special column internals like structured packings on the hydrodynamics. It comprises the material and energy balances of a differential element of the two-phase volume in the packing. Each element consists of an ideally mixed vapor and liquid bulk phase and two film regions adjacent to the interface (Fig. 1).

2.3   Dynamic differential balances

In this dynamic non-equilibrium stage model molar holdup terms have to be considered in the mass balances which represent the basic differential equations. In the dynamic component material balances for the bulk phases both, changes of the specific molar component and the total molar holdup, are considered:

$$\frac{\partial}{\partial t}U_i^{lb} = -\frac{\partial}{\partial z}(Lx_i^{lb}) + (n_i^{lb}a^i + R_i^{lb}\Phi_{liq})A_c \quad ; i = 1, \ldots, m \qquad (1)$$

where m is the number of components in the liquid phase, and the component holdups are given as follows:
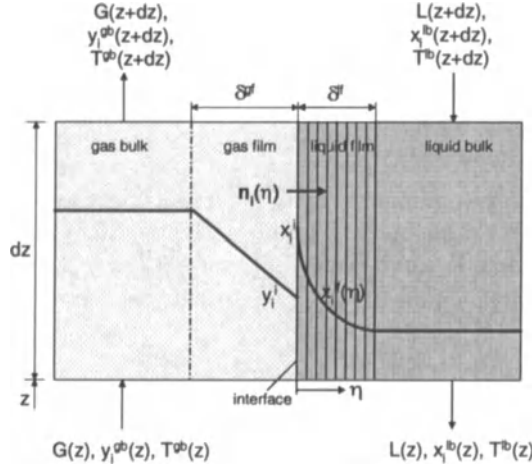
Fig. 1. Differential absorber cross-section and schematic concentration profile for the rate-based approach

$$U_i^{lb} = x_i^{lb} U_i^{lb} \quad ; i = 1, \ldots, m \tag{2}$$

and the summation equation for the liquid bulk mole fractions is

$$\sum_{i=1}^{m} x_i^{lb} = 1 \tag{3}$$

The volumetric liquid holdup Φ_{liq} depends on the vapor and liquid flows and is calculated from empiric correlations for the column packing [6]. The vapor holdup has been neglected due to the low operating pressure of the column ($p \leq 1, 2bar$):

$$0 = \frac{\partial}{\partial z}(Gy_i^{gb}) - n_i^{gb} a^i A_c \quad ; i = 1, \ldots, m \tag{4}$$

The bulk phase balances are completed by the summation equation for the gas bulk mole fractions:

$$\sum_{i=1}^{m} y_i^{gb} = 1 \tag{5}$$

In addition to the bulk balances, differential component mass balances for the liquid film region are introduced:

$$\nabla n_i^{lf} - R_i^{lf} = 0 \tag{6}$$

Due to the chemical conversion in the liquid film, the molar fluxes at the interface n_i^i and at the boundary between the film and the liquid bulk

phase n_i^{lb} will differ. The system of equations is completed by the conservation equations for the mass and energy fluxes at the phase interface and the necessary linking conditions between the sections.

2.4   Chemical reactions

The selective absorption of coke plant gas impurities results from a complex system of parallel liquid phase reactions (Fig. 2). They are considered not only in the liquid bulk phase mass balance (1) but also in the differential balances for the liquid film (6) in order to express their direct influence on mass transfer.

Instantaneous reversible reactions:

$$NH_3 + H_2O \rightleftharpoons NH_4^+ + OH^-$$
$$H_2S + H_2O \rightleftharpoons HS^- + H_3O^+$$
$$HCN + H_2O \rightleftharpoons CN^- + H_3O^+$$
$$HCO_3^- + H_2O \rightleftharpoons CO_3^{2-} + H_3O^+$$
$$H_3O^+ + OH^- \rightleftharpoons 2 H_2O$$
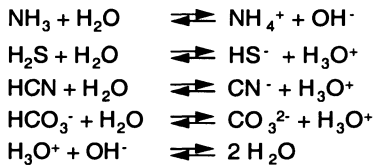
Kinetic controlled reversible reactions:

$$CO_2 + OH^- \rightleftharpoons HCO_3^-$$
$$CO_2 + 2 H_2O \rightleftharpoons HCO_3^- + H_3O^+$$
$$CO_2 + NH_3 + H_2O \rightleftharpoons H_2NCOO^- + H_3O^+$$
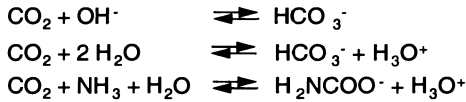
Fig. 2. System of parallel liquid phase reactions

The reactions including CO_2 obey first and second order kinetics, whereas the other reversible reactions are based on simple proton transfers and are therefore regarded as instantaneous by the corresponding mass action laws. The CO_2 absorption is hindered by a slow chemical reaction which is required to convert the dissolved carbon dioxide molecules into the more reactive ionic species. Therefore, when gases containing H_2S, NH_3 and CO_2 are contacted with water, the H_2S and ammonia are absorbed much more rapidly than CO_2 and this selectivity can be accentuated by optimizing the operating conditions [7]. Nevertheless, all chemical reactions are coupled by hydronium ions (Fig.2) and additional CO_2 absorption leads to the desorption of hydrogen sulfide and decreases the scrubber efficiency.

2.5   Mass transfer

The most important difference between the rate-based approach and the equilibrium stage model is the direct calculation of the interfacial molar fluxes. Our advanced model uses the *Nernst-Planck* equation (7) for the description of mass transfer to consider the influence of additional driving forces in electrolyte systems like electrical potential gradients:

$$n_i^{lf} = -c_i^{lf} D_{i,eff}^l \left(\nabla x_i^{lf} + x_i^{lf} z_i \frac{F}{RT} \nabla\varphi \right) + x_i^{lf} n_{H_2O}^{lf} \qquad (7)$$

The consideration of the electrical potential requires an additional condition, namely the electroneutrality (8), which has to be met in every section of the liquid phase,

$$\sum_{i=1}^{m} x_i z_i = 0 \qquad (8)$$

where z_i is the ionic charge of species i. For the determination of the mass transfer coefficients and film thicknesses empirical correlations have been used, which express the influence of column internals and hydraulics [8].

2.6   Thermodynamics

Thermodynamic non-idealities have been considered in the transport equations and the phase equilibrium. The liquid phase diffusion coefficients are determined by the *Nernst-Hartley* equation [9], which expresses the transport properties in weak electrolyte systems. At the gas-liquid interface, the thermodynamic equilibrium between the two phases is assumed:

$$y_i^i = K_i x_i^i \quad ; i = 1, \ldots, m \qquad (9)$$

The distribution coefficient K_i comprises fugacities in both phases and activity coefficients in the liquid phase. They are calculated from the three-parametric Electrolyte-NRTL method, included in the *Properties Plus* package of ASPEN *PLUS*^{TM}.

3   Experimental investigation

Pilot plant experiments have been carried out at real process conditions in an ASCS sidestream of the coke plant "August Thyssen" (Duisburg, Germany). The DN 100 pilot column was made of stainless steel and equipped with about 4m of structured packing (SULZER Mellapak$^{®}$ 350Y), three liquid distributors and a digital control system. Several steady state experiments have been compared with the simulation results and supported the design optimization of the coke gas purification process [10].

4   Simulation results

The above rigorous dynamic model constitutes a system of partial differential equations, which had to be discretized in axial and film direction. The

resulting DAE system has been implemented into SpeedUp® and solved numerically. For the H_2S scrubber some steady state and dynamic simulation results are presented.

4.1   Steady-state simulations

The first simulations for the H_2S scrubber were based on the equilibrium stage model extended by the chemical reaction kinetics. This approach was completely inconsistent with the experimental studies, because the selectivity towards H_2S and HCN absorption could not be expressed. Therefore, the advanced rate-based approach has been implemented into the numerical solver. The differential balance in the film (6) leads to non-linear concentration profiles along the film coordinate (Fig. 3) representing the direct influence of the chemical reactions on the mass transfer (see also [5]). The greatest concentration gradients appear for the ionic components near the interface, which corresponds to the very fast transfer of protons and causes a significant enhancement of the H_2S and NH_3 transport.
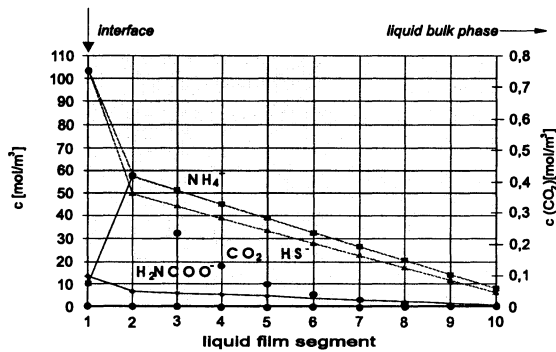
Fig. 3. Concentration profiles in the liquid film

This differential model for the stage has been extended step by step to the whole absorber. In addition, the three liquid distributors and the column bottom have been considered. Their liquid holdup exceeds the total molar holdup of the packing and therefore influences the chemical conversion. The axial steady state concentration and temperature profiles are now in good agreement with the experimental results (Fig. 4). The aqueous ammonia solution, leaving a previous column after the physical absorption of NH_3 from the raw gas, results in the required elimination of H_2S by chemisorption. Substantial amounts of HCN are also removed in this selective absorber.

4.2   Dynamic simulations

For the numerical solution of the DAE system presented above, a careful analysis of the whole system of equations was necessary in order to prevent high index problems.
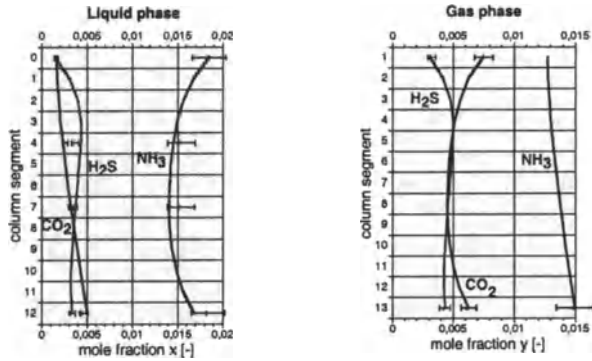
Fig. 4. Calculated axial concentration profiles and experimental results (points) for both phases

This differential index is defined as the number of time differentiations of the algebraic equations necessary to obtain a set of pure differential equations (ODE) and must not exceed 1 for a correct solution with SpeedUp.
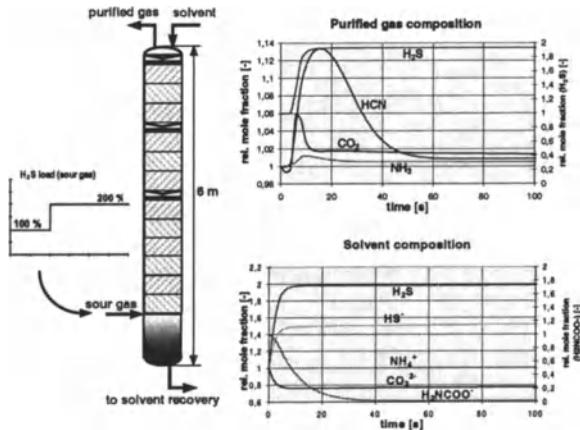
Fig. 5. Relative dynamic changes of top (gas) and bottom (liquid) compositions referring to the steady state conditions at $t = 0$

Therefore, an appropriate set of initial conditions is required. Fig. 5 shows dynamic concentration profiles for the purified gas at the top and the solvent

at the bottom of the column after introducing a disturbance of the coke oven gas feed composition, in this case doubling the amount of H_2S. Additional H_2S is absorbed, but the parallel reactions of CO_2 lead to an increasing amount of carbon dioxide in the purified gas. The corresponding solvent composition proves the CO_2 formation due to the decreasing mole fractions of the carbonate (CO_3^{2-}) and carbamate (H_2NCOO^-) ions.

5   Conclusions

Predictive simulation of complex reactive absorption processes like coke gas purification requires a rigorous and detailed rate-based approach due to mass transfer resistances and the significant influence of fast chemical reactions. On this framework, a model, based on the two-film theory and considering kinetic reaction rates, thermodynamic non-idealities, non-isothermal effects and additional influences of electrolytes has been developed. Instead of introducing correction terms like enhancement factors to express the influence of chemical conversions on mass transfer, the differential balances for the liquid film region including all parallel reactions have been formulated. The whole DAE system has been implemented into SpeedUp and solved numerically with relevant prevention of high-index problems. Several steady state and dynamic simulations have been performed, their results are in good agreement with the experimental data.

References

1. Taylor, R., Krishna, R., 1993, Multicomponent Mass Transfer, John Wiley, New York.
2. Górak, A., 1995, Simulation thermischer Trennverfahren von Mehrstoffgemischen. Prozeßsimulation, VCH-Verlagsgesellschaft, Weinheim.
3. Zarzycki, R., Chacuk, A., 1993, Absorption, Pergamon Press, New York.
4. Van Krevelen, D.W., Hoftijzer, P.J., 1948, Rec. Trav. Chim., 67, 563 ff.
5. Kenig, E.Y., Górak, A., 1995, A film model based approach for simulation of multicomponent reactive separation, Chem. Eng. Proc. 34, 97–103.
6. Mackowiak, J., 1991, Fluiddynamik von Kolonnen mit modernen Füllkörpern und Packungen für Gas-Flüssigkeitssysteme, Verlag Salle+Sauerländer, Frankfurt/ Aarau.
7. Kohl, A.L., Riesenfeld, F.C., 1985, Gas Purification, 4th ed., Gulf Publishing.
8. Rocha, J.A., Bravo, J.L., Fair, J.R., 1996, Distillation Columns Containing Structured Packings - 2. Mass Transfer Model, Ind. Eng. Chem. Res. 35, 1660-1667.
9. Horvath, A.L., 1985, Handbook of Aqueous Electrolyte Solutions, Ellis Horwood.
10. Thielert, H., 1997, Simulation und Optimierung der Kokereigaswäsche, Diss. Berlin.

Remarks on the Numerical Treatment of Polymerization Processes

Peter Seifert

Technische Universität Dresden, Institut für Numerische Mathematik,
Mommsenstr. 13, D-01062 Dresden, Germany

Abstract. The mathematical models resulting from many problems in chemical kinetics are often initial-value problems (IVP) for systems of ordinary differential equations with special properties: the equations are nonlinear and also stiff. We consider mathematical problems of this kind for special chemical processes of radical polymerization, where systems of very large dimension occur, and describe a solution procedure with well-known IVP-solvers. Furthermore, the influence of incomplete micromixing on these chemical processes is taken into account. This requires the solution of initial-boundary problems for parabolic differential equations, which will be done using the numerical method of lines.
Results of examples of the described kind and comments on performance are given.

1 Introduction

Considering chemical reactions, each of them is divided into a set of so-called elementary reactions. A distinguishing feature of these elementary processes is often the very large difference between their reaction rates, i.e. between the lengths of the reactions. These effects are of great influence on the mathematical task belonging to the chemical problem.

In most cases, the resulting mathematical model consists of the same number of ordinary differential equations (ODEs) like elementary reactions. These equations are nonlinear of polynomial form and stiff as well, which determines the numerical procedure for their solution.

The polymerization processes studied by us together with chemists are interesting applications for such chemical reactions. In the following, two special examples of polymerizations will be described, and the solutions of mathematical tasks belonging to them will be discussed.

2 Polymerization

The basic principle of our polymerization model can be characterized that m monomers X_i, $i = 1(1)m$ react together with an initiator I in a solvent S in a chemical reactor and form polymer-radicals Y_i, $i = 1(1)m$ ("living" polymers) and a macromolecule Z ("dead" polymer). These last substances are chains of the monomers, the Y_i can rise further while the growth of Z is finished.

The whole process is going off in form of the following elementary reactions: initiation, growth, transfers of the reagents and chain termination. In addition, it is assumed that the initial substances are ideally mixed in the reactor. For sake of simplicity, we use the same denotations for the reagents and their concentrations.

Our polymerization process now contains $M = 2m + 3$ reacting substances, the concentrations of which we arrange in form of a vector $u \in \mathbb{R}^M$ in the following manner

$$u = u(t) = (I, X_1, ..., X_m, Y_1, ..., Y_m, Z, S)^T. \tag{1}$$

The mathematical model consists of M ODEs

$$\frac{du}{dt} = f(u), \tag{2}$$

for $t > t_0$ and the initial conditions

$$u(t_0) = \varphi \tag{3}$$

with constant values of the components of $\varphi \in \mathbb{R}^M$. The vector $f \in \mathbb{R}^M$ puts together the reaction terms in our model, i.e. the mentioned polynomial terms, which we abbreviate with

$$f(u) =: r_u =: (r_I, r_{X_1}, ..., r_{Y_1}, ..., r_Z, r_S)^T. \tag{4}$$

This initial-value problem must be solved numerically. For this purpose, suitable well-known high quality IVP-solvers are at disposal taking into account the special structure of the Jacobian and the stiffness of the ODEs caused by the different reaction rates.

We consider some of such solvers and simultaneously we test and compare them to get some informations about their effectiveness. Particularly, we are successful with the solvers LSODE (by A.C.HINDMARSH) and VODE (by P.N.BROWN, G.D.BYRNE and A.C.HINDMARSH) using multistep methods, especially backward differentiation formulas of different order for our stiff equations, and with the solvers RODAS and RADAU5 resp. (by E.HAIRER and G.WANNER) which employ an embedded Rosenbrock method of order (3)4 and an implicit Runge-Kutta method of order 5 resp. .

3   Controlled Polymerization

Recently, chemists proposed and investigated some extended models of the polymerization process, in order to get a better regulation of the reactions, i.e. to achieve a more regular growth of the polymers (see [5] and [6]). An example of these so-called *controlled polymerization* processes includes, apart

from initiator I, monomer X, belonging polymer-radical Y $(m = 1)$ and arising macromolecule Z, also a terminator-radical U, a product substance V by decay of U, and a so-called "sleeping" polymer-radical W, controlled by U. Moreover, interim results for polymer-radicals of different chain lengths are introduced, which yields further ODEs for their concentrations Y_j and W_j, $j = 1(1)n$.

In order to give an impression of the principal mathematical structure of the differential equations (2), that means of the character of the nonlinearities on the right hand sides, the resulting system of ODEs for one of these extended models is presented in the following. Our special system can be written in form of two groups (5) and (6) of equations, where the first group is independent of the second, a fact, which is also of significance for the solution algorithm. We have

$$\frac{dI}{dt} = r_I := -k_I I,$$

$$\frac{dX}{dt} = r_X := -2k_I f I - (k_p - k_m)XY$$

$$\frac{dY}{dt} = r_Y := 2k_I f I + k_d W - k_c YU - k_{tN_O}YV - k_{tc}Y^2,$$

$$\frac{dZ}{dt} = r_Z := k_m XY + 0.5k_{tc}Y^2 + k_{tN_O}YV + k_{decomp}W, \qquad (5)$$

$$\frac{dU}{dt} = r_U := k_d W - k_c YU - k_{dN}U^2,$$

$$\frac{dV}{dt} = r_V := 0.5k_{dN}U^2 - k_{tN_O}YV,$$

$$\frac{dW}{dt} = r_W := k_c YU - k_d W - k_{decomp}W$$

with the abbreviations $r_I, r_X, \ldots$ for the right hand sides and

$$\frac{dY_1}{dt} = 2k_I f I - (k_m + k_p)Y_1 X + k_d W_1 - k_c Y_1 U$$
$$\quad -k_{tN_O}Y_1 V - k_{tc}Y_1 Y + k_m YX,$$

$$\frac{dY_j}{dt} = -(k_m + k_p)Y_j X + k_p Y_{j-1}X + k_d W_j - k_c Y_j U$$
$$\quad -k_{tN_O}Y_j V - k_{tc}Y_j Y, \qquad j = 2(1)n - 1, \qquad (6)$$

$$\frac{dY_n}{dt} = -k_m Y_n X + k_p Y_{n-1}X + k_d W_n - k_c Y_n U$$
$$\quad -k_{tN_O}Y_n V - k_{tc}Y_n Y,$$

$$\frac{dW_j}{dt} = k_c Y_j U - k_d W_j - k_{decomp}W_j, \qquad j = 1(1)n$$

where

$$Y = \sum_{j=1}^{n}Y_j, \qquad W = \sum_{j=1}^{n}W_j.$$

The values

$$f, k_I, k_p, k_m, k_c, k_d, k_{tN_O}, k_{tc}, k_{decomp}, k_{dN}$$

denote the reaction rates of our example. They are constant but usually very different in magnitude.

The initial values of the two systems (5) and (6) at $t = t_0$ consist of the nonzero values of I, X, W, W_1, while the other concentrations Y, Z, U, V, W_j for $j = 2(1)n$ and Y_j for $j = 1(1)n$ are zero at this point.

The requirement of the chemists was a large number of interim polymer-radicals, that means $n \gg 1$. Therefore splitting into the two systems is quite advantageous for the solution process, because system (5) can be solved independently of system (6), and on the other hand, the last system has a banded Jacobian with a bandwidth of only 4.

For a numerical example, we integrate over the time interval [0,200 min] and for $n = 10000$, the reaction rates lie between 10^{-5} and 10^8.

The numerical computations show the usual results for polymerization processes: the polymer-radicals arise and change very quickly at the beginning of the time interval, while the macromolecule is growing relatively slow. The other reagents also change as expected in very different manner.

4   Influence of Incomplete Micromixing

We find a more complicated situation, if the reagents being put together are not ideally mixed or the reactions have an effect only in parts of a chemical reactor. In this case, micromixing processes influence the polymer properties, the product quality and the reactor stability.

The chemical model used by us in this case is based on a description of the process within small deforming fluid elements, so-called slabs or striations, and we have different concentrations of the reacting substances in different striations. The thickness of the slabs depends on the viscosity of the reacting mixture and the energy dissipation. The exchange of substances between adjoining striations proceeds only by diffusion.

We assume analogously to Section 2 that m monomers react together with an initiator in a solvent in our process, i.e. we have to consider $M = 2m + 3$ substances. The concentrations and therefore $u \in I\!\!R^M$ are depending now on time t and a spatial variable x , and we get the mathematical model of an initial-boundary-value problem of M partial differential equations

$$\frac{\partial u}{\partial t} = D\frac{\partial^2 u}{\partial x^2} + f(u), \tag{7}$$

with $0 < x < l_1 + l_2$ and $t > t_0$, the initial conditions

$$u(t_0, x) = \varphi(x) \tag{8}$$

with piecewise constant components of $\varphi(x) \in I\!R^M$ and the Neumann boundary conditions

$$\frac{\partial u(t,0)}{\partial x} = \frac{\partial u(t, l_1 + l_2)}{\partial x} = 0. \tag{9}$$

The values $l_1, l_2 > 0$ characterize the thickness of the striations. The diffusion matrix D is of diagonal form

$$D = diag(d_i)$$

with the diffusivities

$$d_i = \begin{cases} c > 0 \\ 0 \end{cases}, \quad i = 1(1)M$$

as diagonal elements. The vector $f \in I\!R^M$ contains the reaction terms of our model analogously as described in (4) of a form similarly as in (5).

For the numerical treatment, we use the numerical method of lines with at first a semidiscretization in spatial direction x by standard difference formulas. A uniform grid is sufficient in most cases of the accuracy requirements with which we are confronted. The resulting IVP with the variables $u_j(t)$ as approximations for $u(t, x_j)$ along the lines $x = x_j$, $j = 1(1)N$ contains $M \cdot N$ ODEs

$$\frac{dy}{dt} = g(t, y) \tag{10}$$

and the initial conditions

$$u_j(t_0) = \varphi(x_j), \quad j = 1(1)N, \tag{11}$$

where

$$y = y(t) = (y_1, ..., y_{M \cdot N})^T = (u_1, ..., u_j, ..., u_N)^T,$$

$$u_j = (I_j, X_{1j}, ..., Y_{1j}, ..., Z_j, S_j)^T, \quad j = 1(1)N,$$

$$g = (g_1, ..., g_{M \cdot N})^T.$$

This task will be treated with the IVP-solvers mentioned in Section 2 taking into account the structure of the banded Jacobian matrix of (10).

Interesting examples of this kind are polyreactions in microgravity environment, which are based on tests with the "Drop Tower" of the Centre of Applied Space Technology and Microgravity (ZARM) at the University of Bremen. In this case, photoinitiated radical polymerization processes with Metacrylate, which are "very fast" reactions, occur simultaneously with microgravity effects.

In our example, one monomer (Metacrylate, $m = 1$) is taken, and the initiation is done by laser beams. Thus, we have a system of $M = 5$ partial differential equations for the diffusion-reaction process. Two different striations are introduced, one, where the laser beams are of influence, and one
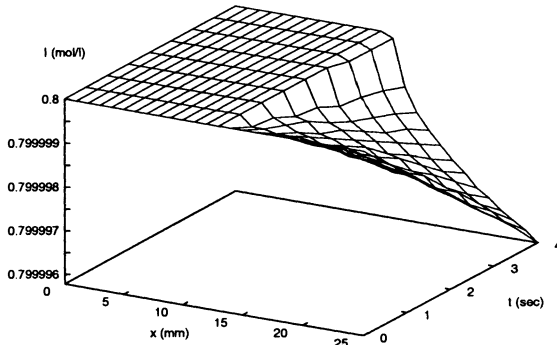
Fig. 1. Initiator
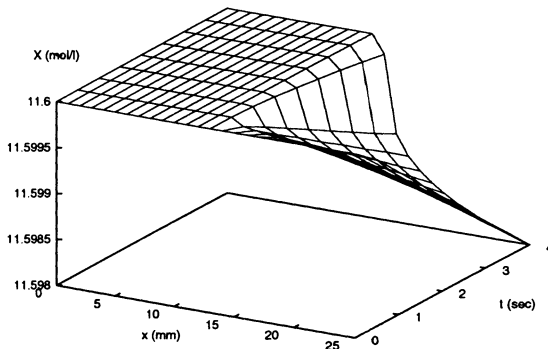
Fig. 2. Monomer

with no reactions. We choose equidistant gridpoints x_j in spatial direction and then have to solve an IVP with nearly 1000 ODEs after semidiscretization. The Jacobian matrix of the ODEs is banded with a bandwidth 11. The reaction rates move between 10^{-4} and 10^5, and it is assumed that they depend on the spatial variable, i.e.

$$k_I = k_I(x), ...$$

More details, e.g. special values of the reaction rates, can be found in [2]. The integration in time direction is done over the small interval [0,4 sec]. The diffusion coefficients $d = d_i$ are constant during a single process and are investigated for values from $6 \cdot 10^{-6}$, where it is also possible to assume

that the polymer radicals and the molecules do not diffuse, up to turbulent diffusivities 10^{-1}.
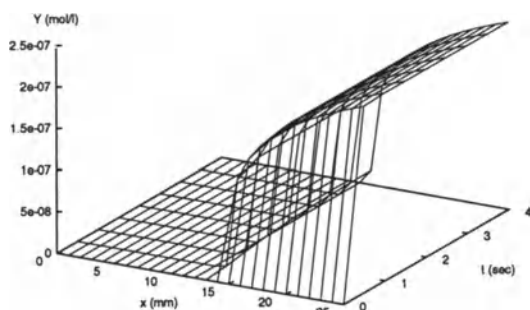
Fig. 3. Polymer-radical
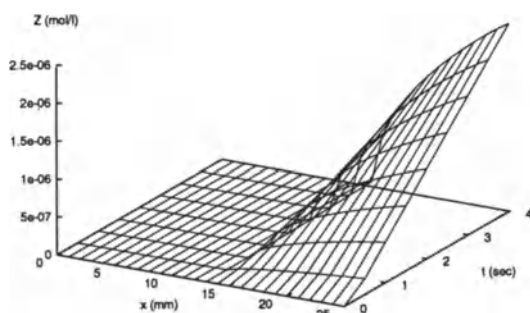
Fig. 4. Macromolecule

The results, shown in Figs. 1-4, are received for a diffusion coefficient in the range of normal liquids $(d_i = 6 \cdot 10^{-6})$, where all reagents diffuse. In the right part of the spatial interval, we see the influence of the laser beams, while the reactions are not active in the left part, the diffusion seems to be only in its starting phase. Comparing the polymer-radical and the macro-molecule, we remark the different velocities in decreasing and increasing of their concentrations. The very fast changes of the radical at the beginning of

the reaction process are also obvious. This fact and the comparison with the other concentrations confirm the stiffness of our problem.

Greater values of the diffusion coefficients cause an apparent balance of the concentrations, partly more rapidly, especially very soon for the initiator and the monomer, but relatively slowly for the polymer-radical, where the very fast reacting process dominates.

We obtain results of similar character for polymerization processes, where quantities of some reagents are added during the considered time.

The processes can be described as follows: Particularly at first, a prepolymerization in an ideally mixed reactor is carried out. Considering the case of radical homopolymerization with an initiator and one monomer in a solvent, we get a polymer-radical and the macromolecule as resulting substances. This requires only the solution of an IVP with 5 ODEs.

At a later point in time, we add quantities of the initiator, of the monomer or other monomers or of the solvent, and have now to take account of the incomplete micromixing and therefore to solve an initial-boundary-value problem with 5 or more partial differential equations. The solutions again show the very different decreasing and increasing of the reagents in time direction and also the influence of the diffusivity on the whole process parallel in time. Detailed results can be found in [3].

References

1. Guzhev,D.S., Kalitkin,N.N., Seifert,P., Shirkov,P.D. (1992) Numerical methods for problems of chemical kinetics with diffusion. Mathematical Modelling 4, 98-110 (Russian)
2. Engelmann, U., Schmidt-Naake, G., Maier, J., Seifert, P. (1994) Influence of micromixing on the free-radical polymerization in a discontinuous process. Macromol. Theory Simul. 3, 855-883
3. Seifert, P. (1996) Numerical treatment of diffusion-reaction equations with the method of lines, in Keil, F., Mackens, W., Voß, H., Werther, J. (eds.) Scientific Computing in Chemical Engineering. Springer Berlin Heidelberg, 212-218
4. Seifert, P. (1996) Chemical and other applications of the numerical method of lines. Z. Angew. Math. Mech. 76, S1, 533-534
5. Schmidt-Naake, G., Drache, M., Taube, C. (submitted 1998) Controlled free radical suspension polymerization. Angew. Makromol. Chem.
6. Schmidt-Naake, G., Han, Ch.H., Drache, M. Koch, A. (1998) Simulation of N-Oxyl-controlled radical polymerization of styrene. 6th International Workshop on Polymer Reaction Engineering 134, Wiley-VCH, 599

Direct Determination of Cyclic Steady States of Cyclically Operated Packed Bed Reactors

T.L. van Noorden[12], S.M. Verduyn Lunel[1], and A. Bliek[2]

[1] Vrije Universiteit Amsterdam, Department of Mathematics, De Boelelaan 1081A, 1081HV Amsterdam, The Netherlands,
[2] Universiteit van Amsterdam Department of Chemical Engineering, Nieuwe Achtergracht 166, 1018 WV Amsterdam, The Netherlands

Abstract. We study the convergence behaviour of cyclically operated reactors . Typically, the reactor will converge to a cyclic steady state . However, the determination of this cyclic steady state by dynamical simulation techniques may be so computationally inefficient that model equations need to be oversimplified. Several convergence acceleration techniques are studied and illustrated by two simple systems for pressure swing adsorption. We show that the largest eigenvalue of the Jacobian of the system can be used as a useful criterion in deciding which acceleration method to use.

1 Introduction

Cyclic processes, such as temperature swing and pressure swing separation, the simulated moving bed separator, the reverse flow reactor, and the newly developed pressure swing reactor are important in the present day chemical industry. When simulating these processes, the long time behaviour is the relevant behaviour. The typical long time behaviour of a cyclic process is a periodic state, a so called "cyclic steady state" (CSS).

A natural way to determine a CSS of a cyclic process is to simulate the total behaviour of the process. The large disadvantage of this method is that the convergence to a CSS may be very slow, in particular in case of large capacity terms and slow kinetic terms. For packed bed reactors as named above, typically the buffer terms are large. In such cases the dynamic simulation of the process may need tens of thousand of cycles to converge.

This slow convergence enforces the use of over-simplified models to be able to make any computations at all. The use of more realistic models therefore requires faster numerical techniques. In the literature a number of methods has been proposed. Most of these methods, however, have very much an 'ad hoc' character and only work for a limited class of periodic processes.

Smith and Westerberg [1] use Broyden's method to accelerate the convergence and Newton's method is studied by Croft and Levan [2]. Nilchan and Pantelides [7] use a simultaneous discretization of both the spatial and temporal domain to calculate a CSS of two different PSA systems.

In Kvamsdal [5] a number of different acceleration methods are compared for a specific model. In this paper we continue this approach and compare a

number of methods for a given proto-type model. We show that the largest eigenvalue of the Jacobian of the map defined by simulating one cycle determines the asymptotic convergence rate of the system to a CSS. The largest eigenvalue of the Jacobian is easily computed and can be used as an apriori-criterium to decide which method to use.

In general the modeling of chemical processes amounts to strongly nonlinear equations. Although the goal of our study is to understand better general cyclic chemical processes in order to find a more generic simulation strategy, in this paper we investigate two simple pressure swing adsorption systems with *linear* convergence behaviour. It should be understood that the results presented here are only the first step along the road to a more profound insight into general cyclic processes and that the emphasis of this work lies on the convergence acceleration methods; the two simple pressure swing adsorption systems are only used to illustrate these methods. Further investigations and the analysis of nonlinear models are in progress [6].

2   System Description

In this paper we study two pressure swing adsorption (PSA) systems. These are the process of pressure swing adsorption of H_2O from air onto alumina (System I) and the process of pressure swing adsorption of CO_2 from He gas onto silica gel (System II). These two systems have been investigated before in [4], [1] and [3]. For both systems we will use the same model (model I), which will be described below.

A PSA system is operated in four consecutive steps: the adsorption step, the blowdown step, the purge step and the pressurization step. A sequence of these steps is called a *cycle*. If the reactor is operated for a large number of cycles, the amount of adsorbens that is adsorbed in the adsorption step and the amount of adsorbens that is purged in the purge step will attain an equilibrium and the state of the reactor will converge to a periodic state. This periodic state is called a cyclic steady state (CSS). A more detailed description of a pressure swing adsorption process is found in [4].

2.1   The Model

The model we use for the H_2O-air-alumina and the CO_2-He-silica gel pressure swing adsorption processes is based on the following assumptions:

  I The system is isothermal with negligible axial pressure drop.
 II Radial and axial dispersion is negligible.
III The equilibrium concentration of the adsorbens in the solid phase depends linearly on the concentration of the adsorbens in the gas phase. The mass transfer rate is represented by a linear driving force expression.
 IV The feed consists of a single trace component in a carrier which is inert to the adsorbent.

V The pressure is constant during the adsorption and desorption steps.
VI We consider the gas phase to be ideal.
VII The flow pattern of the gas phase is assumed to be a plug flow pattern.

These assumptions result in the following set of dimensionless equations

$$c_t(x,t) = -K_1(u(x,t)c(x,t))_x + K_2 K_3(c(x,t) - q(x,t)/p(t)) , \qquad (1)$$

$$q_t(x,t) = K_3(c(x,t) - q(x,t)/p(t) \qquad (2)$$

for $0 \le x \le 1$ and $t \ge 0$. Here c denotes the dimensionless gas phase concentration, q the dimensionless solid phase concentration, u the dimelsionless gas phase velocity and p the dimensionless pressure. The relation between the three dimensionless parameters K_1, K_2 and K_3 and the physical parameters is given by

$$K_1 = UT/L ; \quad K_2 = \frac{1-\epsilon}{\epsilon} K ; \quad K_3 = T k_{\mathrm{ads}} , \qquad (3)$$

where U is a characteristic velocity, T the duration of one cycle, L the bed length, ϵ the bed porosity, K the adsorption equilibrium constant and k_{ads} the external film mass transfer coefficient during the adsorption step.

The parameters that change periodically are p, u and boundary concentrations of the adsorbate in the feed and purge streams (Table 1). The values of the physical parameters for system I and II are given in Table 2 [4].

Table 1. The periodic values of u, p and the boundary conditions

	u(x,t)	p(t)	c(0,t)	c(1,t)
pres. step	$\frac{p'(t)}{K_1 p(t)}(x-1)$	$\frac{P_L}{P_H} + \frac{t}{t_{\mathrm{pres}}}(1 - \frac{P_L}{P_H})$	1	-
ads. step	1	1	1	-
blow. step	$\frac{p'(t)}{K_1 p(t)}(x-1)$	$1 - (1 - \frac{P_L}{P_H})\frac{t}{t_{\mathrm{blo}}}$	-	-
purge step	-2	$\frac{P_L}{P_H}$	-	0

3   Determination of the CSS of a PSA System

In this section we discuss several methods to obtain the possible CSS's of a PSA system. These methods are: the dynamical simulation method, Newton's method and Broyden's method . For all three methods, we first discretize the space variable of the dimensionless equations with centred second order finite differences on 256 nodes for both the gas phase and the solid phase concentration. We then obtain a large system of time periodic ODE's

$$x'(t) = M(t)x(t) + r(t) , \quad M(t+T) = M(t) , \quad r(t+T) = r(t) . \qquad (4)$$

Table 2. The physical parameter values for system I and II

	I	II		I	II
k_{ads}	2.583e-4 s^{-1}	4.67e-2 s^{-1}	K	9084	52.7
ϵ	0.40	0.42	t_{pres}	30 s	20 s
t_{ads}	270 s	180 s	t_{blo}	30 s	20 s
t_{pur}	270 s	180 s	L	0.5 m	1.1 m
u_{ads}	0.25 m/s	0.1 m/s	u_{des}	-0.5 m/s	-0.2 m/s
P_H	5.0 atm	4 atm	P_L	1.0 atm	1.3 atm

This system is integrated in time with the classical four stage Runge-Kutta method with 60000 time steps per period. A CSS of the PSA system is now equivalent to a T-periodic solution x ($x(0) = x(T)$) of this system. The map g that assigns to $x(0)$ the solution at time $t = T$ with $x(0) = x_0$ is called the Poincaré or period map. Thus a T-periodic solution is a solution of the fixed-point equation $x_0 = g(x_0)$. Methods to solve this equation are called shooting methods. The three methods for obtaining a CSS of a PSA system differ in the way the fixed point equation is solved.

3.1   Dynamical Simulation

This method consists of directly integrating the model equations for a number of cycles starting from an initial condition. In this way the dynamics of the process are simulated. However, it may happen that the process converges very slowly to a CSS and a large number of "redundant" cycles of the process are to be computed before a CSS is obtained.

We can also look at this method as the iteration of the period map g. Following the dynamics of the system is equivalent to iterating this map g and the convergence rate of the dynamical simulation method to a fixed-point depends on the physical parameters of the cyclic process. Thus if the PSA process that is simulated converges slowly to a CSS then the dynamical simulation method will also converge slowly. On the other hand, if the process converges fast then the dynamical simulation method will also converge fast.

We say that the system has reached a CSS if the "error" ε_i satisfies

$$\varepsilon_i = |g^{i+1}(x_0) - g^i(x_0)| < 10^{-12} , \tag{5}$$

where x_0 is an initial value for the iteration of g.

We have studied the convergence rate of the dynamical simulation method for both described PSA systems. In Fig. 1 the error versus the CPU time in seconds is given for the two above described PSA systems. We see that System I converges very slowly (769 iterations of g) to a CSS, whereas System

II converges very fast (31 iterations of g). The model equations for these two processes are linear. This implies that the map g is affine, i.e., it can be written as

$$g(x) = Ax + b \, , \tag{6}$$

where A is a linear operator and b a constant vector. ¿From this we can see that the dynamical simulation method will converge to a fixed-point with rate equal to the large eigenvalue of A. For System I, the largest eigenvalue of the Jacobian equals 0.9692739 and for System II, the largest eigenvalue equals 0.4575510. If we compare these values with the convergence rate of the dynamical simulation of System I and II, we find a good agreement (see Table 3).

Table 3. The convergence rate of the dynamical simulation for system I and II

system I ε_i	$i = 603...608$ $\varepsilon_i/\varepsilon_{i-1}$	system II ε_i	$i = 19...24$ $\varepsilon_i/\varepsilon_{i-1}$
0.13104E-05	0.96875	0.27185E-04	0.46857
0.12694E-05	0.96872	0.12529E-04	0.46088
0.12296E-05	0.96867	0.56946E-05	0.45450
0.11910E-05	0.96863	0.25701E-05	0.45132
0.11537E-05	0.96860	0.11606E-05	0.45157
0.11174E-05	0.96856	0.52708E-06	0.45414
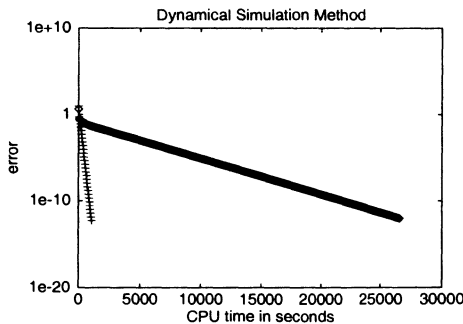
Fig. 1. The error versus the CPU time in seconds for the dynamical simulation method for System I (*thick black line*, 769 iterations) and System II (+ 's, 31 iterations)

3.2   Newton's Method

In section 3.1, we found fixed-points of the map g by iterating the map itself. If we define the map $f = g -$ Id, then fixed-points of g become zeros of f. So we can use Newton's method, or a quasi-Newton method, such as Broyden's method, to compute the zeros of f. In this section we will discuss Newton's method. The next section deals with Broyden's method.

Newton's method generates approximations of a zero of f using the iteration scheme

$$x_{i+1} = x_i - J_f^{-1}(x_i)f(x_i) , \tag{7}$$

where $J_f^{-1}(x_i)$ is the inverse of the Jacobian of f at x_i. Note that each iteration of Newton's method requires the computation of J_f. Our model equations are linear and therefore we only need to evaluate J_f once. If we could exactly compute J_f, Newton's method would converge in one iteration, but due to inaccuracies, there results an iteration of defect correction type that needs a few iterations to converge.

Let N denote the number of nodes in the spatial discretization of the model equations (in our case $N = 512$). The evaluation of J_f requires the computation of the dependencies of f on each of these N variables. If we use first order finite differences to compute these dependencies, this results in simulating $N + 1$ cycles with different initial conditions. Therefore if the dynamical simulation method already converges in less than N cycles, Newton's method will not accelerate the convergence.

In Fig. 2 the convergence times for both systems are shown and we see that Newton's method accelerates the convergence to a fixed-point for System I, but not for System II. We also see that the convergence times for Newton's method for both the test systems are approximately the same.
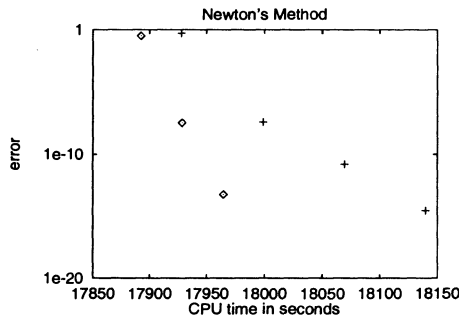
Fig. 2. The error versus the CPU time in seconds for Newton's method for System I ($\diamond$) and System II (+)

3.3   Broyden's Method

Rather that computing the Jacobian of f, Broyden's method [8] uses an approximation of J_f which is updated each iteration.

To be more precise, Broyden's method produces approximations to a zero of f using the following iteration scheme

$$x_{i+1} = x_i + H_i f(x_i) \,, \tag{8}$$

with H_i iterative approximations to $-J_f^{-1}(x_i)$ which are defined by

$$H_{i+1} = H_i - \frac{(p_i + H_i y_i) p_i^T H_i}{p_i^T H_i y_i} \,, \tag{9}$$

where $y_i = f(x_{i+1}) - f(x_i)$ and $p_i = x_{i+1} - x_i$. The advantage of this method is that, in contrast to Newton's method, for each iteration only one cycle needs to be simulated. This implies that the work of one iteration of Broyden's method is comparable to an iteration of the dynamical simulation method. As the initial approximation of the inverse of the J_f we use $H_0 = \mathrm{Id}$.

It can be shown that for linear problems, this method converges in at most $2N$ iterations which is approximately twice the time needed for Newton's method to converge [9]. Our computations show that this is a very conservative bound for the convergence rate of out test problems. For System I, Broyden's method converges in 99 iterations and for System II even in 14 iterations, thus for the two test systems Broyden's method converges much faster than the dynamical simulation method and also in far less than N steps (see Figure 3).
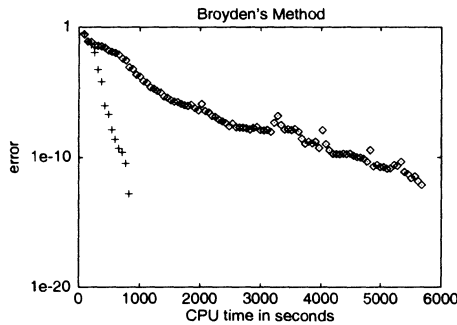
Fig. 3. The error versus the CPU time in seconds for Broyden's method for System I ($\diamond$, 99 iterations) and System II ($+$, 14 iterations)

4   Conclusions

We find that for linear systems the largest eigenvalue of the Jacobian of g indicates the convergence rate of the dynamical simulation method. Using this

information we can determine on beforehand how many cycles the dynamical simulation method needs to converge and thus whether Newton's method will have a shorter convergence time or not. For Broyden's method we know that it converges in at most twice the convergence time of Newton's method, but the two test systems show that it converges much faster. For System I Broyden's method reduces the convergence time with a factor five, whereas for System 2 it is only slightly faster than the dynamical simulation method.

Here we will also make a remark about the double discretization method. This method consists of discretizing the spatial as well as the temporal domain simultaneously and directly imposing the periodic boundary conditions. In this way we obtain a system of algebraic equations. The disadvantage of this method is that it can only handle coarse discretizations. We find that if the discretization is made too fine, the number of variables becomes too large, even if routines for sparse systems are used, to be handled by the computers we use. Therefore we do not give results for this method.

The next step in the search for a more generic simulation strategy for cyclic processes is to study the acceleration methods we present in this paper applied to nonlinear models. Nonlinear models are obtained if for example temperature dependencies, reaction kinetics or nonlinear isotherm are incorporated in the model. In contrast to linear models, for nonlinear models we also have to address questions about uniqueness of CSS's. Another issue for nonlinear systems is the dependence of the performance of acceleration methods upon the initial approximation of a CSS.

References

1. Smith IV O.J., Westerberg A.W. (1992) Acceleration of Cyclic Steady State Convergence for Pressure Swing Adsorption Models. Ind. Eng. Chem. Res. **31**, 1569–1573.
2. Croft D.T., Levan M.G. (1994a) Periodic States of Adsorption Cycles–I. Direct Determination and Stability. Chem. Eng. Sci. **49**, 1821–1829.
3. Raghavan N.S., Hassan M.M., Ruthven D.M. (1985) Numerical Simulation of a PSA System. AIChE J. **31**,385–395.
4. Kvamsdal H.M., Hertzberg T. (1995) Optimization of Pressure Swing Adsorption Systems – The Effect of Mass Transfer During the Blowdown Step. Chem. Eng. Sci. **50**, 1203–1212.
5. Kvamsdal H.M. (1995) Studies on Modeling, Simulation and Optimization of PSA Systems. PhD Thesis, University of Trondheim.
6. Van Noorden T.L., Verduyn Lunel S.M., Bliek A. Numerical Determination of Cyclic Steady States of Cyclically Operated Packed Bed Reactors, in progress.
7. Nilchan S., Pantelides C.C. (1998) On the Optimisation of Periodic Adsorption Processes. Adsorption **4**, 113–147.
8. Broyden C.G. (1965) A Class of Methods for Solving Nonlinear Simultaneous Equations. Math. Comput. **19**, 577–593.
9. Gay D.M. (1979) Some Convergence Properties of Broyden's Method. SIAM J. Numer. Anal. **16**, 623–630.

Part V

Simulation of Reactive Flows

On Error Control for Reactive Flow Problems

Roland Becker[1], Malte Braack[1] and Rolf Rannacher[2]

[1] Cermics, INRIA, Caiman, BP 93, F-06902 Sophia-Antipolis Cedex
[2] Institute of Applied Mathematics, University of Heidelberg, D-69120 Heidelberg

Abstract. In this note, we present the application of weighted-residual techniques for a posteriori error estimation to reactive flow problems. The main goal is to control arbitrary functionals of the solutions and to obtain economical locally refined meshes. The discretization error is controlled by considering an associated dual problem, where the dual solution represents the sensitivity of the error to the local mesh-size distribution. The Galerkin orthogonality of the finite element discretization leads to an error estimator in which local residuals of the computed solution are multiplied by weights involving second derivatives of the dual solution. This estimator is used as a stopping criterion for the simulation and for local mesh refinement. In an iterative process the mesh is adapted in order to produce the minimal overall error for a prescribed number of grid nodes.

1 Introduction

The Navier-Stokes equations including Arrhenius-type chemical production terms for the simulation of reactive flow problems lead to an extremely complex nonlinear system of PDEs. The use of adaptive meshes for this kind of problems is crucial in reducing the computational cost. The adaptive process should not only be efficient, but also reliable in order to allow for quantitative error control. Especially for comparisons between numerical and experimental results (e.g., laser measurements in flames) error control for relevant quantities is desirable. In this note, we show how the general approach of Becker and Rannacher [2] to error control for finite element schemes can be applied to stationary reactive flow problems.

The underlying equations describe the conservation of mass, momentum, energy and species mass fractions. We use the equations in the primitive variables, p for pressure, v for the velocity, T for the temperature and w_i for the species mass fractions,

$$\nabla \cdot (\rho v) = 0 \,, \tag{1a}$$

$$(\rho v \cdot \nabla)v - \nabla \cdot \mu \nabla v + \nabla p = \rho \cdot f_e \,, \tag{1b}$$

$$\rho v \cdot \nabla T - \frac{1}{c_p} \nabla \cdot (\lambda \nabla T) = \frac{1}{c_p} f_T(T, w) \,, \tag{1c}$$

$$\rho v \cdot \nabla w_i - \nabla \cdot (\rho D_i \nabla w_i) = f_i(T, w) \,, \quad i = 1, \ldots n \,, \tag{1d}$$

$$\rho = \frac{PM}{RT} \,, \tag{1e}$$

including several well known physical coefficients. We are mainly interested in low-speed flows. Therefore, there is no need to worry about the entropy condition because there are no shock waves.

Since our application is directed to low-Mach-number flow, the flow is hydro-dynamically incompressible while strong heat release leads to thermo-dynamical changes. We apply the approximation for low-Mach-number combustion [9], splitting the total pressure $p(x,t)$ in two parts, the thermodynamic part $P_{th}(t)$, which is uniform in space, and the hydrodynamic part $p_{hyd}(x,t)$, which is several magnitudes smaller than P_{th} and is neglected in the equation of state (1e). This approximation implies the elimination of acoustic waves. We denote by $u = (p, v, T, w)$ the set of unknowns. Because the density is given by the algebraic relation (1e), the gradient $\nabla\rho$ can be expressed by the derivatives of T and M while the minor influence of ∇p_{hyd} is neglected.

Due to the exponential dependence on temperature (Arrhenius law) and polynomial dependence on w, the source terms $f_i(T, w)$ are highly nonlinear. In general, these zero-order terms lead to a coupling between all chemical species mass fractions. For accurate modeling of the underlying chemical processes a large number of chemical species is necessary, (e.g., $n \sim 30 - 40$ for a methane flame). This leads to very high computational cost. The use of adaptive meshes is particularly important for resolving thin reaction zones.

2   Finite Element Discretization

Our discretization is based on conforming finite elements on quadrilateral meshes $\mathcal{T}_h = \{K\}$ for the computational domain Ω. The trial space consists of continuous and piecewise bilinear functions (Q_1-elements) for all variables. It is well known that the original Galerkin formulation is not stable for the Stokes system, because the Babuska-Brezzi stability condition is not fulfilled [5]. We stabilize the formulation by introducing additional least-square terms in the equation for the pressure [6]. For convection dominated flow, we use streamline diffusion for velocity, temperature and all chemical species. We refer to [10,4,1] for more details.

We introduce the semi-linear form $a(\cdot, \cdot)$ defined by

$$\begin{aligned}
a(u, \phi) = {} & (\rho\nabla \cdot v - T^{-1}v \cdot \nabla T + M^{-1}v \cdot \nabla M, \chi) \\
& + (\rho v\nabla \cdot v, \psi) + (\mu\nabla v, \nabla\psi) - (p, \nabla \cdot \psi) \\
& + (\rho c_p v\nabla \cdot T, \pi) + (\lambda\nabla T, \nabla\pi) + (f_T(T, w), \pi) \\
& + \sum_{i=1}^{n} [(\rho v\nabla \cdot w_i, \sigma_i) + (\rho D_i\nabla w_i, \nabla\sigma_i) + (f_i(T, w), \sigma_i)]
\end{aligned}$$

for test functions $\phi = (\chi, \psi, \pi, \sigma) \in V$. The variational space V consists in each component of subspaces of $H^1(\Omega)$ (for the velocity, the temperature and

the species). If Diriclet conditions are opposed at the whole boundary, the hydrodynamical pressure is only determine modulo a constant. Therefore, for p the space $L^2(\Omega)/I\!\!R$ is appropriate. Using this semi-linear form, the system (1a)-(1e) reads in variational formulation

$$u \in V : \quad a(u, \phi) = (f, \phi) \quad \forall \phi \in V. \tag{2}$$

Let $a'(u_h; \cdot, \cdot)$ denote the Frechét derivative of a at a discrete $u_h \in V_h$. The linear equations which have to be solved during one step of the nonlinear iteration, are of the form

$$a'(u_h; w_h, \phi) = (r_h, \phi), \tag{3}$$

for a correction $w_h \in V_h$ and the residual r_h. The discrete spaces V_h we use, consist of continuous and piecewise bilinear functions. For this choice of elements, the bilinear form $a'(u_h; \cdot, \cdot)$ is not stable, because the Inf-Sup condition is not fulfilled [6]. However, it can be stabilized by modifications of the test functions:

$$a'_h(u_h; w_h, \phi) := a'(u_h; w_h, \phi + S_h \phi)$$

with a certain operator $S_h : V_h \to V_h$. When L denotes the nonlinear operator associated to the system (1a)-(1e) and $L'(u_h)^*$ the adjoint of the linearization at u_h, we choose

$$S_h = -\delta_h L'(u_h)^*, \tag{4}$$

with symmetric δ_h depending on the local mesh size. This choice of S_h includes in our case the following features

- pressure-velocity stabilization (Hughes and Franca [6])
- streamline diffusion (Johnson [7])
- (div,div) stabilization (Franca and Frey [4])

Furthermore, this choice of S_h has a nice feature concerning the associated dual problem, which will be explained later.

Solving the linear equations (3) for successive updates $u_h^{i+1} := u_h^i + w_h^i$ until convergence corresponds to solving the discrete nonlinear equation

$$u_h \in V_h : \quad a(u_h, \phi + S_h \phi) = (f, \phi + S_h \phi) \quad \forall \phi \in V_h,$$

which is consistent with (2).

3   Solver

The solution procedure consists of several nested loops. On the initial mesh, the outermost loop is an implicit time-iteration. During each time step, the

arising nonlinear system is solved by a quasi-Newton iteration. Each Newton step requires the solution of a linear system which represents a discretization of a linear PDE. On the successive refined meshes no time-stepping is necessary.

Even in the case of a simple Laplace operator (which is always a part of our system), the inversion by a direct solver or a simple iterative scheme as in the Conjugated Gradient Method (CG) is prohibitive, since it requires N^2 operations due to the bad condition of the matrix. Therefore, we use the Generalized Minimal Residual (GMRES) algorithm which is preconditioned by a multigrid iteration (V-cycle). GMRES is appropriate for non-symmetric and indefinite matrices. The use of a multigrid preconditioner makes the condition number independent from the number of grid points, which is especially important on locally refined meshes. The smoothing is obtained by a block-ILU decomposition on each level of the hierarchical mesh.

4   Error Estimate

In reactive flow computations it is often necessary to apply error control only for functionals of the solution. This holds especially for optimization problems and for comparisons between simulations and experimental results. In this cases, error control in a global norm for all components of the solution seems not appropriate. We develop the general approach of a *posteriori* error control for a functional $J(u)$ of the solution [2] in the context of combustion problems. The functional can represent, e.g., the maximum temperature, local values of temperature, a species mass fraction or a line average of certain components of the system. The error functional can be chosen according to the aims of the simulation. The stopping criterion for the adaptive iteration is

$$|J(u) - J(u_h)| < TOL \,,$$

for a given tolerance TOL. We use a duality argument in order to control these local quantities. By solving a linearized dual problem we determine weights for the error contribution of the local residuals. This information is used for quantitive error control and as a criterion for local mesh refinement. We assume J to be linear, although the approach can be extended to nonlinear functionals, see [2]. We have an a *posteriori* error estimate of the form

$$|J(e)| \leq \sum_K \omega_K \rho_K \,,$$

where ρ_K are element-wise residuals and ω_K are weights bounded by

$$\omega_K \leq C_I h_K^2 \|D^2 z\|_K \,.$$

Here, z is the solution of the corresponding dual problem

$$a'(u; \phi, z) = J(\phi) \quad \forall \phi \in V \,.$$

The evaluation of the weights ω_K requires approximation since the dual problem is posed on the continuous level and its coefficients depend on the unknown solution u. We propose to use a numerical approximation of the form

$$\omega_K \simeq \widetilde{\omega}_K = C_I h_K^2 \|D_h^2 z_h\|_K \,,$$

where z_h is the solution of the perturbed discrete dual problem

$$z_h \in V_h : a_h'(u_h; \phi, z_h) = J(\phi) \quad \forall \phi \in V_h. \tag{5}$$

For simplicity this linear problem is solved on the same mesh on which the primal solution has been obtained. The corresponding computational cost is equivalent to just one additional Newton step in solving the primal problem. The obtained error estimator is

$$|J(e)| \approx \eta = \sum_K \eta_K \,, \quad \eta_K = \widetilde{\omega}_K \rho_K \,.$$

The chosen stabilization S_h according to (4) leads to the fact that the bilinear form associated to the dual problem (5) is exactly the stabilized bilinear form of $(a')^*(u_h; \cdot, \cdot)$. That means, taking the adjoint operator and stabilization commutates.

The entire process leads to an alternating solution of primal and dual problem on a sequence of successively improved meshes and is called weighted-residual feed-back error control. For more details, see [3].

5   Numerical Results

We present numerical results for a combustion model describing an ozone decomposition flame with three species: ozone O_3, oxygen molecules O_2 and oxygen atoms O. The underlying reaction mechanism consists of six (three bidirectional) elementary reactions [11]:

$$O_3 + M \longleftrightarrow O_2 + O + M$$
$$O + O + M \longleftrightarrow O_2 + M$$
$$O + O_3 \longleftrightarrow O_2 + O_2$$
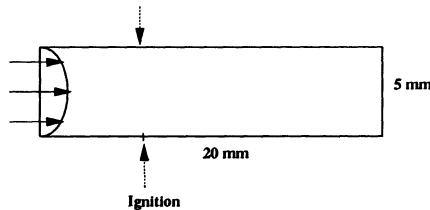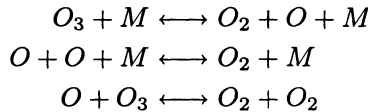
Fig. 1. Geometry for the ozone decomposition

Here, M denotes an arbitrary third body, i.e., one of the three considered species. The formation of the stable O_2 molecules leads to the main part of heat release. Transport coefficients for viscosity, thermal conductivity and diffusion are evaluated using the kinetic models with coefficients based on the data bases of the Sandia National Laboratories [8]. The geometry consists of two flat plates with an inflow of a cold mixture of ozone and oxygen molecules ($w_{O_3} = 0.2$, $w_{O_2} = 0.8$, $T = 298\,K$). The flame is ignited by the hot walls. The hottest point of the wall is indicated by the arrows in Fig. 1. The quantities we wish to control are point values of w_O and the mean value of the temperature. The corresponding functionals are

$$J_1(u) = w_O(x_0) + w_O(x_1) \quad \text{and} \quad J_2(u) = \int_\Omega T\,dx\,.$$

The points $x_{0,1} = (10\,mm, \pm 1.25mm)$ are symmetric to the symmetry axis of the model. For each functional we perform a computation imposing the corresponding error estimator. We get different histories of mesh refinement because the adaptation process is based on η. In Fig. 2, we show the relative error

$$e_{rel} = |J_1(u) - J_1(u_h)|/|J_1(u)|$$

and the estimated relative error of the point values. In Fig. 3, it is shown for the mean value of the temperature. In both cases, we observe an excellent *a posteriori* error estimate over a wide range of mesh size h. The asymptotic behaviour of e_{rel} and η are the same.
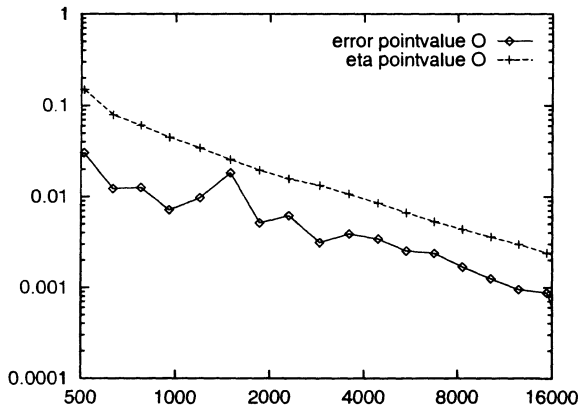
Fig. 2. Relative error e_{rel} and estimator η_{rel} for the control of J_1

Two of the obtained meshes with about 5000 cells are shown in Fig. 4 for the control of J_1 and in Fig. 5 for J_2. In both cases, the flame front is locally refined. However, in the first case, also the neighborhoods of the points x_0 and x_1 are automatically refined. The temperature profile is shown in Fig. 6.
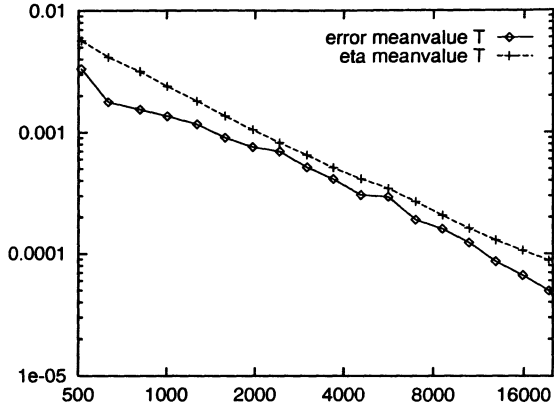
Fig. 3. Relative error e_{rel} and estimator η_{rel} for the control of J_2
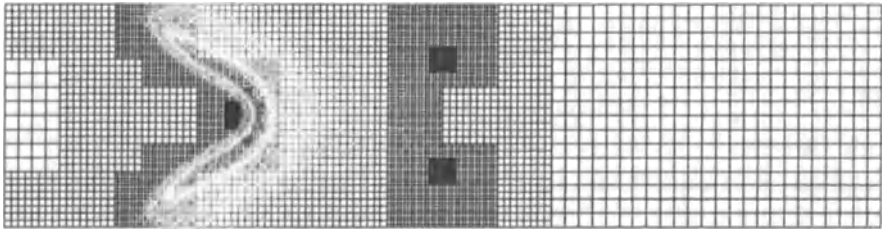
Fig. 4. Obtained mesh for the control of the point values of O
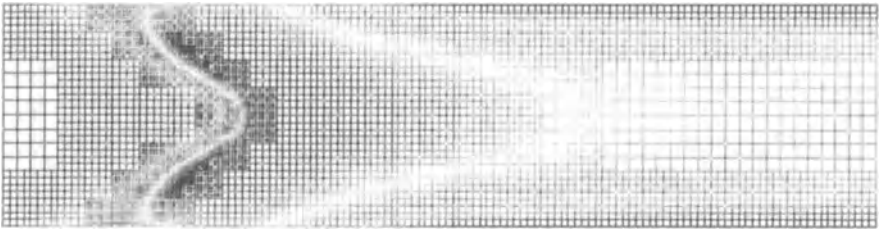
Fig. 5. Obtained mesh for the control of mean value of temperature
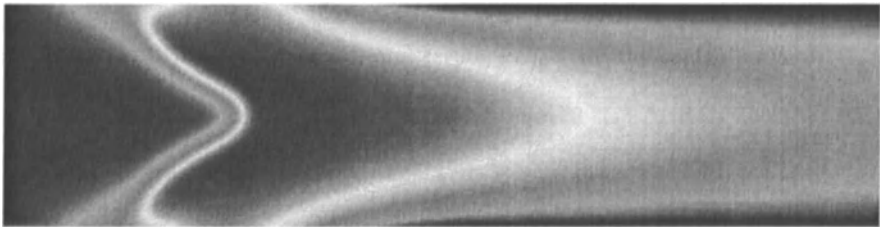
Fig. 6. Temperature profile

References

1. R. Becker. *An Adaptive Finite Element Method for the Incompressible Navier-Stokes Equation on Time-dependent Domains.* Dissertation, Heidelberg University, 1995.
2. R. Becker and R. Rannacher. *A feed-back approach to error control in finite element methods: Basic analysis and examples.* East-West J. Numer. Math., 4(4):237–264, 1996.
3. M. Braack. *An Adaptive Finite Element Method for Reactive Flow Problems.* Dissertation, Heidelberg University, 1998.
4. L. Franca and S. Frey. *Stabilized finite element methods: II. The incompressible Navier-Stokes equations.* Comp. Meth. Appl. Mech. Eng., 99:209–233, 1992.
5. V. Girault and P.-A. Raviart. *Finite Elements for Navier Stokes Equations.* Springer, Berlin, 1986.
6. T. J. R. Hughes, L. P. Franca, and M. Balestra. *A new finite element formulation for computational fluid dynamics: V. Circumvent the Babuska-Brezzi condition: A stable Petrov-Galerkin formulation for the Stokes problem accomodating equal order interpolation.* Comp. Meth. Appl. Mech. Eng., 59:89–99, 1986.
7. C. Johnson. *Numerical Solutions of Partial Differential Equations by the Finite Element Method.* Cambridge University Press, 1987.
8. R. Kee, F. Rupley, and J. Miller. *The Chemkin thermodynamic data base.* Sandia Report, SAND87-8215.UC4, 1987.
9. A. Majda. *Compressible Fluid Flow and Systems of Conservation Laws in Several Space Variables.* Springer, New York, 1984.
10. L. Tobiska and R. Verfürth. *Analysis of a streamline diffusion finite element method for the Stokes and Navier-Stokes equations.* SIAM J. Numer. Anal., 33(1):107–127, 1996.
11. J. Warnatz. *Calculation of the structure of laminar flat flames I: Flame velocity of freely propagating ozone decomposition flames.* Ber. Bunsengemeinschaft. Phys. Chem., 82:193–200, 1978.

Numerical simulation of a silicon floating zone with a free capillary surface

Eberhard Bänsch[1] and Burkhard Höhn[2]

[1] Zentrum für Technomathematik, FB 3, Universität Bremen, Postfach 330440,
    D-28334 Bremen, Germany
[2] Institut für Angewandte Mathematik, Universität Freiburg, Hermann–Herder
    Str. 10, D-79104 Freiburg, Germany

Abstract. In this article we present numerical results concerning the simulation of semiconductor melts with free capillary surfaces , particularly silicon crystal growth by the floating zone method. Considering the solid/liquid interface as fixed such a simulation requires the computation of the moving capillary surface of the melting zone. The mathematical model is a coupled system which consists of a heat equation and the Navier–Stokes equations in the melt with a Marangoni boundary condition. We describe an efficient numerical method for solving this problem and give some results for different physical parameters.

1   Introduction

Fluctuations of the electrical resistivity due to inhomogeneous dopant distribution are still a serious problem for the industrial processing of doped semiconductor crystals. In the case of silicon floating–zone growth, the main source of these inhomogeneities are time–dependent flows in the liquid phase during the growth process. Hence, for optimizing the growth process, it is of great importance to study the influence of thermocapillary and buoyancy convection on macro– and microsegregation, see [4–8]. A very practical experimental setup for these investigations is the floating–zone growth in a mono ellipsoid mirror furnace.

For instance, such a configuration has been successfully used at the Institute for Crystallography, University of Freiburg, for performing silicon floating–zone experiments on earth and also under microgravity, see e.g. [5]. A halogen lamp, positioned in the upper geometrical focus of the ellipsoid, served as a heat source. Fused quartz ampoules containing the starting material were placed in the lower geometrical focus. The parameters of the liquid zone were as follows: $8mm$ zone height and $12mm$ zone diameter. Figure 1 shows both, the surface of the silicon melt and an etched axial cut of the zone showing the solid–liquid interface.

Due to the opaqueness of semiconductor melts, experimental fluid flow observation is extremely difficult and expensive in general. Therefore the numerical simulation of the growth process is an important tool in understanding and predicting the behavior of the system, see e.g. [6].
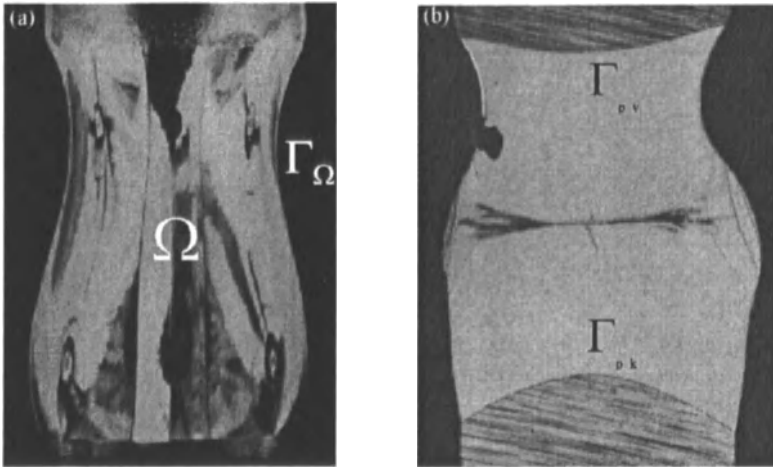
Fig. 1. Silicon floating zone: (a) Surface of the silicon melt, (b) Etched axial cut of the zone showing the solid–liquid interface

2 Mathematical model

Figure 2 gives a schematic diagram of a floating–zone configuration.
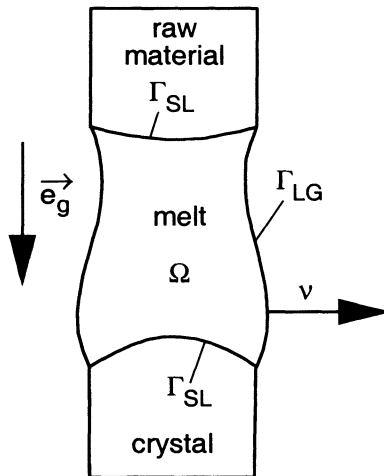
Fig. 2. Geometry of a floating zone

The heat and mass transfer in the liquid zone is governed by the following system of partial differential equations (in dimensionless form):

- Navier–Stokes equations:

$$\partial_t u + (u \cdot \nabla)u - \frac{1}{Re}\Delta u + \nabla p = -\frac{Ra}{Re^2 Pr}Te_g \qquad \text{in } \Omega(t)$$
$$\nabla \cdot u = 0 \qquad \text{in } \Omega(t) \tag{1}$$

- Energy equation:

$$\partial_t T + u \cdot \nabla T - \frac{1}{Re\,Pr}\Delta T = 0 \quad \text{in } \Omega(t) \tag{2}$$

Here $u(t, \cdot) : \Omega(t) \to I\!\!R^d$, $p(t, \cdot) : \Omega(t) \to I\!\!R$ and $T(t, \cdot) : \Omega(t) \to I\!\!R$ denote the flow velocity, the pressure and the temperature, respectively.
The interfaces Γ_{SL} and Γ_{GL} are free boundaries, the first one being subject to a Stefan condition, the latter one determined by a balance of capillary forces versus normal stresses of the flow. We simplify the problem by focusing on the free boundary conditions on Γ_{LG} and prescribing a given solid–liquid interface Γ_{SL} where we impose a homogeneous Dirichlet boundary condition for u and T ($T = 0$ the dimensionless melting temperature):

$$u = 0 \quad \text{on } \Gamma_{SL}, \tag{3}$$
$$T = 0 \quad \text{on } \Gamma_{SL}. \tag{4}$$

Note that prescribing Γ_{SL} implies that also the $d-2$ dimensional *tripleline* (or *triplepoint* for $d = 2$) $\Gamma_{LG} \cap \Gamma_{SL}$ is prescribed and fixed. On the free liquid–gas interface the temperature is prescribed by a given parabolic profile:

$$T = T_D \quad \text{on } \Gamma_{LG}. \tag{5}$$

For the velocity and the motion of the free surface the following conditions hold on Γ_{LG}:

$$u \cdot n = V_\Gamma \quad \text{(slip boundary condition)} \tag{6}$$

$$n \cdot \sigma\tau = -\frac{Ma}{Re^2 Pr}\nabla T \cdot \tau \quad \text{(Marangoni condition)} \tag{7}$$

$$n \cdot \sigma n = \frac{1}{ReCa}\kappa + \frac{Bo}{ReCa}\,\mathrm{id}_\Gamma \cdot e_g \quad \text{(normal stress condition)} \tag{8}$$

with $\sigma := \left(\frac{1}{Re}D(u)_{ij} - p\,\delta_{ij}\right)_{i,j=1}^d$ the stress tensor, $D(u) := \left(\partial_{x_i}u_j + \partial_{x_j}u_i\right)_{i,j=1}^d$ the deformation tensor, κ the sum of the principal curvatures, the unit outer normal vector n, an arbitrary tangential vector τ and the normal velocity V_Γ of the free boundary Γ_{LG}.
The system has to be closed by initial conditions for u, T and Ω. Note that in the continuous case we have conservation of volume since the velocity u is divergence free.
The dimensionless numbers occurring in the above equations are the Reynolds number $Re = \dfrac{U L}{\nu}$, the Prandtl number $Pr = \dfrac{\nu}{k}$, the Rayleigh number

$Ra = \dfrac{g\beta\delta T L^3}{k\nu}$, the Marangoni number $Ma = -\dfrac{(\partial\gamma/\partial T)\delta T L}{k\rho\nu}$, the capillary number $Ca = \dfrac{\nu\rho U}{\gamma}$ and the Bond number $Bo = \dfrac{\rho g L^2}{\gamma}$, with a characteristic velocity U, a characteristic length L, a characteristic temperature difference δT, the density ρ, the surface tension γ, the thermal coefficient $\partial\gamma/\partial T$ of surface tension, the thermal diffusivity k, the kinematic viscosity ν and the gravitational acceleration g.

Stationary, two dimensional numerical methods for the above free boundary problem were studied for instance in [4]. However, even if all data are rotationally symmetric or two dimensional according to the physical setup, the solution may be expected to be 3D and also time–dependent due to symmetry breaking. Thus, it is necessary to define a numerical scheme for the time–dependent case and which works also in 3 space dimensions.

3   Numerical approximation

Discretizing equations (1)–(8), the free boundary conditions (6)–(8) cause several problems, in particular the treatment of the curvature terms and in finding a stable and efficient time discretization.

To resolve these problems we use a variational formulation, where the free boundary conditions are transformed to a boundary integral part of the bilinear forms, see [2] for details. To this end we write the momentum part of the Stokes equations (analogously for the Navier–Stokes equations) in the strong form, multiply by a solenoidal test function φ and integrate by parts. We get

$$\int_{\Omega} \{-\frac{1}{Re}\Delta u + \nabla p\} \cdot \varphi = \frac{1}{2Re}\int_{\Omega} D(u) : D(\varphi) - \int_{\Omega} p\nabla \cdot \varphi - \int_{\Gamma_{LG}} n \cdot \sigma\varphi.$$

Taking into account the boundary conditions (7,8) yields

$$\int_{\Gamma_{LG}} n \cdot \sigma\varphi = -\frac{Ma}{Re^2 Pr}\sum_{i=1}^{d-1}\int_{\Gamma_{LG}} \nabla T \cdot \tau_i\,\varphi \cdot \tau_i + \frac{Bo}{ReCa}\int_{\Gamma_{LG}} \mathrm{id}_{\Gamma_{LG}} \cdot \boldsymbol{e}_g\varphi \cdot n$$

$$+ \frac{1}{ReCa}\int_{\Gamma_{LG}} \kappa\,n \cdot \varphi. \tag{9}$$

Now we make use of the identity

$$\underline{\Delta}\,\mathrm{id}_{\Gamma_{LG}} = \kappa\,n, \tag{10}$$

where $\underline{\Delta}$ denotes the Laplace Beltrami operator on Γ_{LG}. Recalling that $\underline{\Delta} = \underline{\nabla} \cdot \underline{\nabla}$ with $\underline{\nabla}$ the tangential derivatives, the last term in (9) can be written

as

$$\int_{\Gamma_{LG}} \kappa\, n \cdot \varphi = \int_{\Gamma_{LG}} \underline{\Delta}\mathrm{id}_{\Gamma_{LG}} \cdot \varphi = - \int_{\Gamma_{LG}} \underline{\nabla}\mathrm{id}_{\Gamma_{LG}} \cdot \underline{\nabla}\varphi. \tag{11}$$

Summarizing we get

$$\int_{\Omega} \{-\frac{1}{Re}\Delta u + \nabla p\} \cdot \varphi = \frac{1}{2Re} \int_{\Omega} D(u) : D(\varphi) - \int_{\Omega} p\, \nabla \cdot \varphi$$
$$+ \frac{1}{ReCa} \int_{\Gamma_{LG}} \underline{\nabla}\mathrm{id}_{\Gamma_{LG}} \cdot \underline{\nabla}\varphi$$
$$+ \frac{Ma}{Re^2 Pr} \sum_{i=1}^{d-1} \int_{\Gamma_{LG}} \nabla T \cdot \tau_i \varphi \cdot \tau_i$$
$$- \frac{Bo}{ReCa} \int_{\Gamma_{LG}} \mathrm{id}_{\Gamma_{LG}} \cdot e_g \varphi \cdot n \tag{12}$$

Time discretization To discretize in time a semi–implicit coupling of the unknowns for temperature T, geometry Ω and the flow variables u, p is used. More precisely, giving the values at the discrete time instant t_{k-1} we compute

Step 1: T^k by solving (2) on Ω^{k-1} with u^{k-1}

Step 2: u^k, p^k by solving (1) with boundary conditions (7,8) on Ω^{k-1} and using T^k on the right hand side

Step 3: Γ_{LG}^k by $\Gamma_{LG}^k := \Gamma_{LG}^{k-1} + (t_k - t_{k-1})\, u^k \cdot n\, n$

In **Step 2** the boundary conditions (7,8) are incorporated into the variational formulation according to (12). The curvature terms are treated in a semi–implicit way:

$$\int_{\Gamma_{LG}^{k-1}} \underline{\nabla}\mathrm{id}_{\Gamma_{LG}^k} \cdot \underline{\nabla}\varphi = \int_{\Gamma_{LG}^{k-1}} \underline{\nabla}\mathrm{id}_{\Gamma_{LG}^{k-1}} \cdot \underline{\nabla}\varphi + (t_k - t_{k-1}) \int_{\Gamma_{LG}^{k-1}} \underline{\nabla}u^k \cdot \underline{\nabla}\varphi,$$

thus decoupling the flow computation from the determination of the geometry. This leads to a stable and efficient treatment of the free boundary conditions, see [2].

The computation of u^k, p^k is based on the fractional step θ–scheme in a variant as an operator splitting, which decouples two major numerical difficulties, the solenoidal condition and the nonlinearity, see [1,3].

Spatial discretization To discretize in space piecewise quadratic, globally continuous elements for u and T and piecewise linear, globally continuous elements for p are used on a tetrahedral grid.

4 Numerical results

The following two examples show the influence of the hydrostatic pressure on the shape of a floating zone with aspect ratio $h/d = 1.5$. Here $g_E = 9.81m\,s^{-2}$ denotes the gravitational acceleration on earth.

Example 1 First we consider a 2D–floating zone with buoyancy convection and no thermocapillary convection, i.e. $Ma = 0$. The dimensionless parameters are chosen as follows: $Re = 500$, $Pr = 0.02$, $Ca = 0.0016$, $Ra = 400 * |g|$, $Bo = 0.18 * |g|$ with $g \in \{0.5 * g_E, 2.0 * g_E, 3.5 * g_E\}$. Figures $3 - 5$ show both the velocity field together with the temperature distribution in the melt and the corresponding triangulation of the domain Ω.
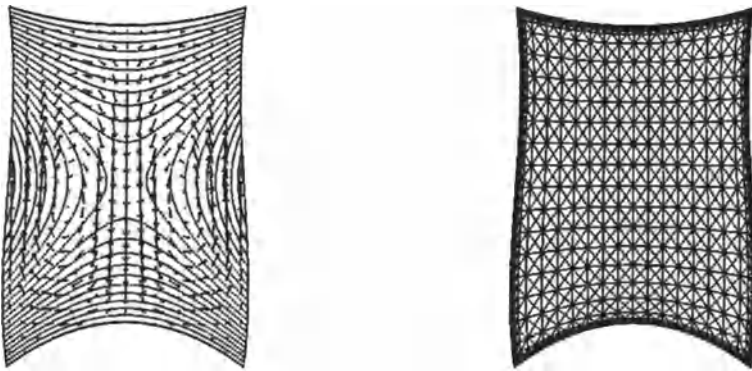
Fig. 3. Velocity field, temperature distribution and triangulation for $g = 0.5 * g_E$
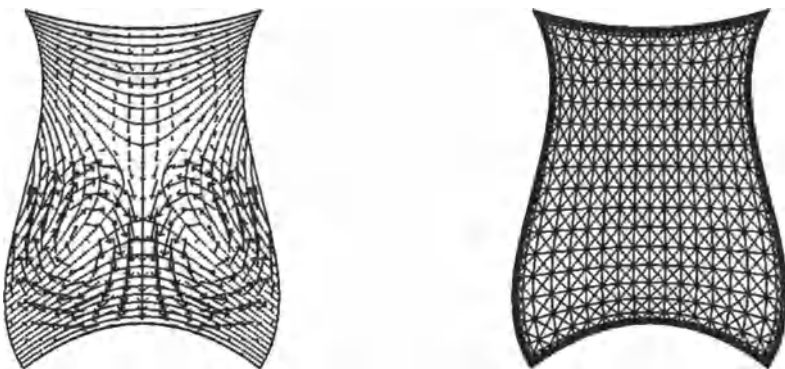
Fig. 4. Velocity field, temperature distribution and triangulation for $g = 2.0 * g_E$
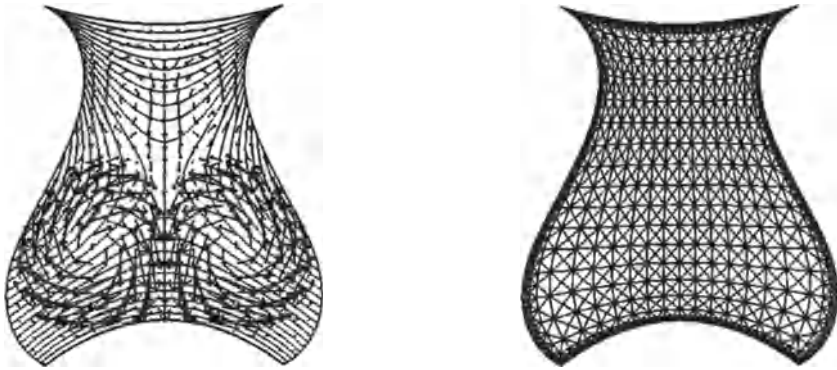
Fig. 5. Velocity field, temperature distribution and triangulation for $g = 3.5 * g_E$

Example 2 Now let us consider a 3D–floating zone with Marangoni convection and no buoyancy convection, i.e. $Ra = 0$. The other dimensionless parameters are: $Re = 50$, $Pr = 2$, $Ma = 150$, $Ca = 0.016$, $Bo = 0.18 * |g|$ with $g \in \{0, 1.0 * g_E, 2.0 * g_E\}$. Figures 6 – 8 show both the velocity field together with the temperature distribution in the melt and the corresponding triangulation of the domain Ω.
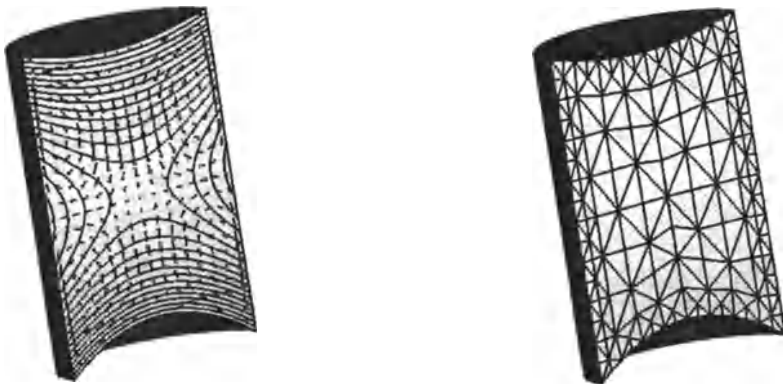
Fig. 6. Velocity field, temperature distribution and triangulation for $g = 0$

References

1. E. BÄNSCH, *Simulation of instationary, incompressible flows*, Acta Math. Univ. Comenianæ LXVII, no. 1, 101–114 (1998)
2. E. BÄNSCH, *Numerical methods for the instationary Navier–Stokes equations with a free capillary surface*, Habilitation thesis, Univ. Freiburg (1998).
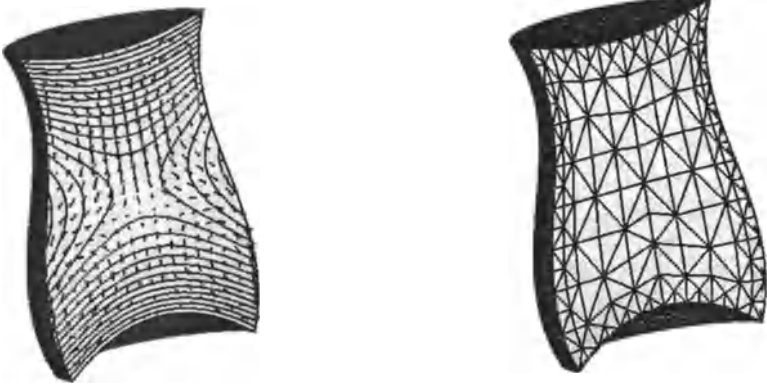
Fig. 7. Velocity field, temperature distribution and triangulation for $g = 1.0 * g_E$
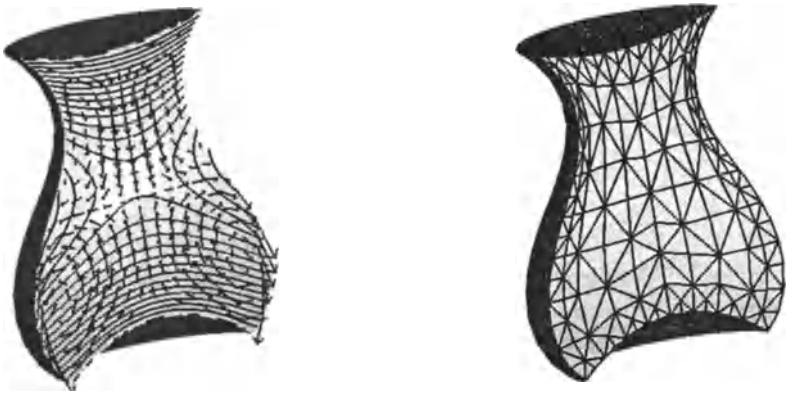
Fig. 8. Velocity field, temperature distribution and triangulation for $g = 2.0 * g_E$

3. M. O. Bristeau, R. Glowinski and J. Periaux, *Numerical methods for the Navier–Stokes equations. Application to the simulation of compressible and incompressible flows*, Computer Physics Report, 6 (1987), pp. 73–188.
4. C. Cuvelier and J. M. Driessen, *Thermocapillary free boundaries in crystal growth*, J. Fluid mech., vol. 169 (1986), pp. 1–26.
5. P. Dold and A. Cröll and K. W. Benz, *Floating–zone growth of silicon in magnetic fields, Part I: Weak static axial fields*, J. Crystal Growth, 183 (1998), pp. 545–553.
6. T. Kaiser and K. W. Benz, *Floating–zone growth of silicon in magnetic fields, Part III: Numerical simulation*, J. Crystal Growth, 191 (1998), pp. 365–376.
7. G. Müller and A. Ostrogorsky, *Convection in Melt Growth*, in Handbook of Crystal Growth 2B, D. T. J. Hurle, eds., Elsevier Science Publishers, North-Holland, 1994, pp. 709–819.
8. D. Schwabe, *Surface–Tension–Driven Flow in Crystal Growth Melts*, in Crystal Growth, Properties and Applications 11, Springer, Berlin, 1988.

Prediction of Pressure Losses in Porous Media Using the Lattice Boltzmann Method

Jörg Bernsdorf, Francis Delhopital, Gunther Brenner, and Franz Durst

Institute of Fluid Mechanics (LSTM), University of Erlangen - Nürnberg, Cauerstr. 4, D – 91058 Erlangen, Germany

Abstract. We used the lattice Boltzmann technique for a detailed study of the pressure drop in porous media flow. In accordance with the experimental results it is shown that the Kozeny-Darcy equation underestimates pressure loss in porous media flow owing to a significant error which is made when only shear forces are taken into account. As an application to engineering problems, we present a 3-D flow simulation through a porous SiC structure which was digitized using the computer tomography technique.

1   Pressure Drop in Porous Media Flow

The exact determination of hydrodynamic data in the flow through complex geometries such as porous media (in filters, catalysts) is of increasing importance for the design of many devices in chemical engineering. Usually, these data are obtained from semi-empirical models such as the Kozeny-Darcy equation for the pressure loss as a function of the Reynolds number and parameters of a geometrically simplified structure. As a consequence, significant errors may result in engineering applications when these correlations are used outside their range of validity. Hence a better understanding of the underlying phenomena is required, allowing more general formulation of flow models. The numerical simulation of the flow in porous media allows one on the one hand, to investigate in detail these phenomena, e.g. by analysing the elongational deformation and the resulting shear rates in the flow and their effect on the bulk hydrodynamic properties. On the other hand, semi-empirical parameters entering in the above models can be easily obtained in a 'numerical' experiment.

   This paper presents a short overview of the hydrodynamic phenomena and some modelling aspects.

1.1   The Kozeny-Darcy Equation

The derivation of the Kozeny-Darcy equation is based on the assumption that porous media flow can be modelled as a flow through a bundle of channels with not strongly changing cross-sections The generalized equation for the cross-sectional mean velocity $\tilde{U}_z$ of a flow through a capillary with hydraulic radius R_h holds (see, e.g., [1]):

$$\tilde{U}_z = -\frac{1}{2\mu} \left(\frac{dP}{dz}\right) R_h^2 \,, \tag{1}$$

where P is the pressure, μ the fluid viscosity and z the mean flow coordinate. The hydraulic radius R_h can be derived from the radius R of the pipe by

$$R_h = \frac{\pi R^2}{2\pi R} = \frac{R}{2} \,. \tag{2}$$

Assuming a bundle of tubes with an average hydraulic radius $\tilde{R}_h$ and length l, (1) can be rewritten as

$$\tilde{U}_z = -\frac{1}{2\mu} \frac{\Delta P}{\Delta l} \tilde{R}_h^2 \,. \tag{3}$$

If the porous medium is built up of spheres of diameter D_p, the quantity R_h can be written as a function of D_p and its porosity ε:

$$R_h = \frac{D_p}{6} \frac{\varepsilon}{(1-\varepsilon)} \,. \tag{4}$$

Introducing an effective velocity $U_0 = \varepsilon \tilde{U}_z$ and substituting in (3) the hydraulic radius as defined in (4), one obtains

$$\tilde{U}_z = \frac{1}{\varepsilon} U_0 = \frac{1}{2\mu} \frac{\Delta P}{\Delta l} \frac{D_p^2}{36} \frac{\varepsilon}{(1-\varepsilon)} \,. \tag{5}$$

This equation can be rewritten in Ergun [3] coordinates:

$$72 = \left[\frac{\Delta P}{\Delta l} \frac{D_p}{\varrho U_0^2} \frac{\varepsilon^3}{(1-\varepsilon)}\right] \left[\frac{U_0 D_p \varrho}{\mu (1-\varepsilon)}\right] \,. \tag{6}$$

Introducing the dimensionless quantities Reynolds number Re and friction factor f as defined by

$$f = \frac{\Delta P}{\Delta l} \frac{D_p}{\varrho U_0^2} \frac{\varepsilon^3}{(1-\varepsilon)} \,, \tag{7}$$

$$Re = \frac{U_0 D_p \varrho}{\mu (1-\varepsilon)} \,, \tag{8}$$

equation (5) can be written in the compact form

$$f = \frac{\Lambda_{\text{th}}}{Re} \tag{9}$$

with $\Lambda_{\text{th}} = 72$.

Most experimental data show a friction coefficient with a factor two or three times higher than this theoretical Λ_{th}. Anyway, for an experimentally found constant Λ_{exp}, the friction factor times Reynolds number relationship appears to be valid.

One attempt to resolve this contradiction between theory and experiment is the introduction of a *tortuosity factor* τ, which is defined as the ratio of the macroscopic length scale of the porous media and the average length of the particle paths in the medium. Thus, the model assumes that the fluid particles move along a highly wrinkled path (fluid channels) owing to their deflection in this highly irregular structure, resulting in a higher pressure drop.

Recent investigations by Durst et al. [2] show that a second and – compared with the tortuosity – much more important physical effect has been neglected in the derivation of the Kozeny-Darcy equation, namely effect of an additional pressure drop due to *elongational strain* of the fluid. In addition to this argument, it might be doubted that a tortuosity factor of $\tau = 2 - 3$ is a realistic assumption, because this would imply that the length of the fluid channels is up to three times longer than the length of the porous media.

One way to get some insight into the nature of these problems is to perform detailed numerical simulations of porous media flow. Three aspects could be dealt with by this simulation:

- The reliability of experimental friction factors Λ_{exp} for both synthetic and natural porous geometries with exactly known properties.
- The tortuosity τ by integrating the streamlines (for stationary flow).
- The contribution of the elongation of fluid elements to the pressure drop by computing this elongation numerically.

In this paper, we will restrict ourselves to the first point by presenting numerical results for the friction factor Λ_{num} for randomly distributed rectangles in three dimensions. A method to compute three-dimensional flows through natural geometries is described by the simulation of flow through computer tomographic data for an SiC structure.

2   Numerical Method

For a detailed numerical simulation of highly complex geometry flow, the Navier-Stokes equation – based finite volume (FV) and finite element (FE) techniques are hardly applicable. The new lattice gas/Boltzmann (LGA/LBA) methods [4] treat the fluid on a statistical level, simulating the movement and interaction of single particles or ensemble-averaged particle density distributions by solving a velocity discrete Boltzmann-type equation.

The lattice Boltzmann method could be shown to be a very efficient tool for flow simulation in highly complex geometries (discretized by up to several million grid points) [5–8]. All numerical simulations presented in this paper were performed with an implementation of the lattice Boltzmann method proposed by Quian [9], which will be briefly described in the following section.

2.1   Lattice − Boltzmann (BGK) Automata

For simplicity, an equidistant orthogonal lattice is chosen for common LBA computations. This could be done without significant loss of memory and performance, since the LBA method requires much less memory and CPU time than conventional FV/FE methods.

On every lattice node r_*, a set of i real numbers, the particle density distributions N_i, is stored. The updating of the lattice consists of basically two steps: a streaming process, where the particle densities are shifted in discrete time steps t_* through the lattice along the connection lines in direction c_i to their next neighbouring nodes $r_* + c_i$, and a relaxation step, where locally a new particle distribution is computed by evaluating an equivalent to the Boltzmann collision integrals ($\triangle_i^{Boltz}$).

For every time step, all quantities appearing in the Navier-Stokes equations (velocity, density, pressure gradient and viscosity) can locally be computed in terms of simple functions of this density distribution and (for the viscosity) of the relaxation parameter ω.

For the present computations, a 3-D nineteen-speed (D3Q19) lattice Boltzmann automata with single time Bhatnager-Gross-Krook (BGK) relaxation collision operator $\triangle_i^{Boltz}$ proposed by Qian [9] is used

$$N_i(t_* + 1, r_* + c_i) = N_i(t_*, r_*) + \triangle_i^{Boltz} , \tag{10}$$

$$\triangle_i^{Boltz} = \omega \left(N_i - N_i^{eq} \right) , \tag{11}$$

with a local equilibrium distribution function N_i^{eq}

$$N_i^{eq} = t_p \, \varrho \left\{ 1 + \frac{c_{i\alpha} \, u_\alpha}{c_s^2} + \frac{u_\alpha \, u_\beta}{2c_s^2} \left(\frac{c_{i\alpha} \, c_{i\beta}}{c_s^2} - \delta_{\alpha\beta} \right) \right\} . \tag{12}$$

This local equilibrium distribution function N_i^{eq} has to be computed every time step for every node from the components of the local flow velocity u_α, the fluid density ϱ, a lattice geometry weighting factor t_p and the speed of sound c_s. It is chosen to recover the incompressible time-dependent Navier-Stokes equations [9]:

$$\partial_t \varrho + \partial_\alpha \left(\varrho u_\alpha \right) = 0 , \tag{13}$$

$$\partial_t (\varrho u_\alpha) + \partial_\beta (\varrho u_\alpha u_\beta) = -\partial_\alpha p + \mu \, \partial_\beta \left(\partial_\beta u_\alpha + \partial_\alpha u_\beta \right) . \tag{14}$$

2.2   Introducing Complex Geometries

As already mentioned, the LBA method allows the application of simple orthogonal equidistant lattices. This lattice type makes (semi-automatic) integration of arbitrary complex geometries very easy: single lattice nodes are either *occupied* by an elementary obstacle, or they are *free* (marker and cell

approach) . Particle densities N_i, which are shifted on an occupied node owing to the streaming process, are simply bounced back to their original location during the next iteration, but with opposite velocity (indicated by the index i). This results in the desired no-slip (zero velocity) wall boundary condition.

2.3   Inlet and Outlet Boundary Conditions

To achieve a well defined Reynolds number, the average flow velocity was fixed at the inlet and the pressure was extrapolated upstream. At the outlet, a fixed pressure was imposed with downstream extrapolated velocity.

3   Numerical Simulations

3.1   Randomly Distributed Rectangles

To check the theoretically derived and experimentally proved relationship between Reynolds number and friction factor (9), and to compute numerically the friction factors Λ_{num}, the pressure drop for flows through various sets of randomly distributed rectangles was determined for different Reynolds numbers.

Problem Definition Inside an $lx \times ly \times lz = 198 \times 100 \times 100$ sized computational domain, non-overlapping square obstacles of size 14^3 lattice units were distributed randomly. A porosity of $\varepsilon \approx 0.8$ was achieved for three different samples with up to 156 cubes. Periodic boundary conditions were applied in y- and z-directions (rectangular to the main flow direction). At the inlet, a uniform velocity profile was imposed, and an additional $lx \times ly \times lz = 50 \times 100 \times 100$ domain was added at both sides of the obstacle area.

Numerical Results For Reynolds numbers over five orders of magnitude (up to ≈ 50), the pressure drop was computed from the numerically achieved flow data for each of the five obstacle samples. An average friction coefficient was computed from these data and compared with the experimental results from Durst et al. (Fig. 1). These experimental data could be very well described by the function $\Lambda_{\text{exp}} = 182 + 1.75\,Re$.

Discussion For low Reynolds numbers, the numerical data fit the experimental results very well. The averaged friction coefficient for $Re < 10$ is $\Lambda_{\text{num}} = 186.3 \pm 11.6$. This indicates that lattice Boltzmann computations are a suitable method for investigating the pressure drop in highly complex geometries.
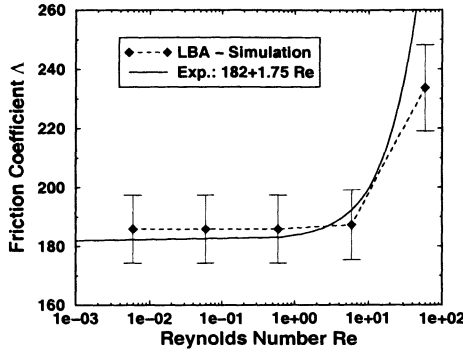
Fig. 1. Friction factor Λ as a function of Reynolds number Re. The numerical results of the LBA simulations (*dashed line*) are compared with the experimental data from Durst et al. [2] (*straight line*)

3.2   Flow Simulation through Computer Tomographic Data for Porous Media

The ability of the lattice Boltzmann method to simulate flow in highly complex geometries opens up the possibility of achieving detailed information about flow properties inside porous structures, which could not be measured by means of experimental devices.

3.3   Geometry Preprocessing

A necessary requirement for the numerical simulation is to digitize the three-dimensional complex structure. With 3-D computer tomography (3D CT), one is able to produce this kind of data, which, after one preprocessing step to a set of voxel data, could automatically be integrated in the LBA software. This procedure omits the time-consuming – and for the present geometries nearly impossible – procedure of grid generation.

3.4   Example: Flow Simulation through an SiC Structure

To illustrate the above-described procedure, low-Reynolds flow was simulated with LBA through a porous SiC 'sponge-like' structure.

Problem Definition A cylindrical probe with a height of 30 mm and a diameter of 82 mm was scanned with 3D CT with an average resolution of 0.5 mm. This leads to a discretization of $lx \times ly \times lz = 44 \times 147 \times 147$ voxels. This resolution, although still rather coarse, leads to a qualitatively good reproduction of the basic features of the original porous geometry, as can be seen from the visualization of these data in Fig. 2.
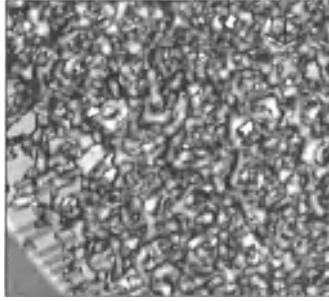
Fig. 2. Section of the digitized SiC structure for the LBA flow simulation

The complex geometry data were centred inside an $lx \times ly \times lz = 100 \times 149 \times 149$ sized channel, and a flow for a Reynolds number of about $Re \approx 1$ was simulated using velocity inlet and pressure outlet boundary conditions.

Computational Efforts The simulation was performed on one processor of a VPP 700 at the Leibniz-Rechenzentrum in Munich; 10 000 iterations were necessary for this set-up, which took about 5760 CPU seconds, and 800 Mb of computer memory were necessary for the storage of the $\approx 2.2 \times 10^6$ voxels.

Numerical Results As a result of the LBA simulation, at each of the $\approx 2.2 \times 10^6$ lattice nodes, the pressure, the three components of the flow velocity and the geometry information are known. It is now possible to obtain local or averaged information from this data set. As an illustration, the flow velocity in two orthogonal cuts through the geometry is shown in Fig. 3. On can see there the huge amount of interconnected flow channels.
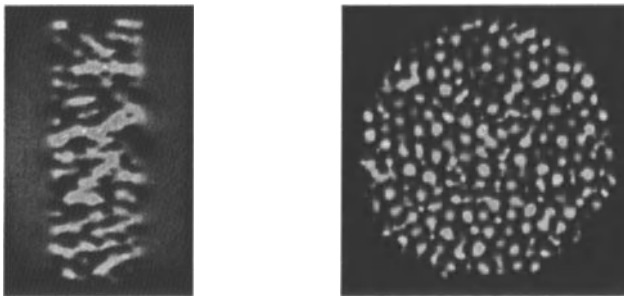
Fig. 3. Flow velocity in rectangular cross-sections of the porous sample

The pressure drop in the same cross-section as in Fig. 3 is shown in Fig. 4 (left), and an isosurface of the overall flow velocity is coloured by the pressure, in Fig. 4 (right), to give a three-dimensional impression of the flow properties.
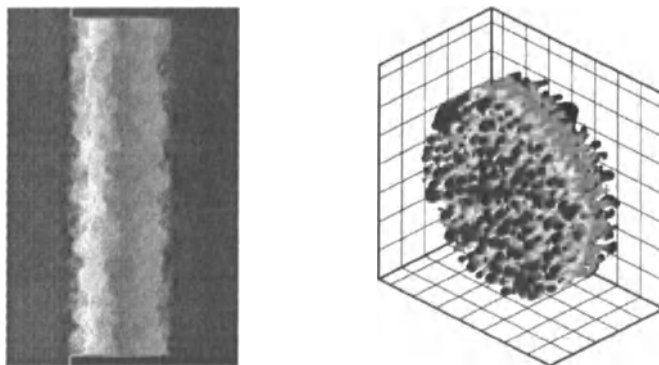
Fig. 4. Pressure drop: in a cross-section (*left*) and on an isosurface of the flow velocity (*right*)

4   Conclusion

We were able to demonstrate that the lattice Boltzmann automata are an efficient method for predicting the correct pressure drop in three-dimensional complex geometry flows. A friction coefficient in very good agreement with experimental data from Durst et al. was achieved for randomnly distributed square obstacles. As an illustration of industrial applications of this method, we demonstrated, how three-dimensional computer tomographic data for porous media could be used as geometry input for LBA simulations.

References

1. Bird R.B., Stewart W.E. and Lightfood E.N. (1960) Transport Phenomena, J. Wiley and Sons, New York
2. Durst F., Haas R. and Interthal W. (1987) Journal of Non–Newtonian Fluid Mechanics **22**: 169–189
3. Ergun S. (1952) Chem. Eng. Prog. **48(2)**: 84–89
4. Frisch U., d'Humières D., Hasslacher B., Lallemand P., Pomeau Y. and Rivet J.-P. (1987) Complex Systems **1**: 649–707
5. Bernsdorf J. and Schäfer M. (1996) ERCOFTAC Bulletin **28**: 24–27
6. Bernsdorf J. and Schäfer M. (1997) Notes on Numerical Fluid Mechanics, Volume **59**: 61–71
7. Bernsdorf J., Durst F. and Schäfer M. (1998) Int. J. Numer. Met. Fluids, *in press*
8. Bernsdorf J., Zeiser Th., Brenner G. and Durst F. (1998) Int. J. Mod. Phys. **C**, *submitted*
9. Qian Y.H. (1992) Europhys.Lett. **17(6)**: 479-484

Simulation and Analysis of Mixing in Two-Dimensional Turbulent Flows Using Fourier and Wavelet Techniques

Henning Bockhorn, Wolfgang Gerlinger, Kai Schneider, and Jörg Ziuber

Institut für Chemische Technik, Universität Karlsruhe (TH), Kaiserstraße 12, D-76128 Karlsruhe

Abstract. This paper presents direct numerical simulations of mixing of passive and reactive scalars in two–dimensional flows. By means of pseudo–spectral methods the governing equations are numerically integrated. As an application we study a temporally growing mixing layer where we focus on the role of coherent vortices. Wavelet techniques are applied to obtain local spectral information about vorticity and scalars. We show that the local generation of fine scales in shear zones is strongly correlated with locally enhanced mixing. Furthermore, we examine the influence of chemical reactions.

1   Introduction

Enhanced transport and mixing of scalars in turbulent flows are important features of turbulent motion. Numerous examples for such mixing processes are found in engineering applications, in particular it plays a prominent role when chemical time scales are smaller or of the same order as the the mixing time. For reasons of optimization and control of technical devices a profound understanding of turbulence, chemical reactions and their interaction is of fundamental interest.

Recent studies have shown the significance of coherent vortices for the dynamics of turbulent flows. We previously studied [1] the influence of different vortex configurations on the mixing of passive and reactive species in two dimensions. In the present paper we investigate the mixing properties in the practically relevant and well–studied case of a planar shear layer [6]. The analyzed flow stems from direct numerical simulations (DNS) performed by means of a Fourier–Galerkin pseudo–spectral method. The advantage with respect to laboratory experiments is that all information about the flow is accessible. We study the mixing of passive scalars by determining global time scales for different Schmidt numbers. Moreover, we show the influence of chemical reactions on the formation of fine scales in scalar fields. Employing Fourier techniques we obtain the global scaling information of the analyzed flow.

Wavelets techniques have been developed in the last decade for analyzing, modelling and computing turbulent flows. For a review we refer to [5]. In contrast to classical Fourier methods the simultaneous localization of wavelets

in space and frequency allows a quantification of the local formation of fine scales, e.g. using local wavelet spectra. Therewith, we show a correlation between the spatially different scaling behaviour of the flow, e.g. the generation of fine scales in shear zones, and the locally enhanced mixing of reactive scalars, leading to increased chemical reaction rates.

2   Physical Problem and Method of Analysis

In this section we present the governing equations with a brief sketch of the numerical scheme and introduce the employed analysis techniques.

2.1   Numerical Scheme

A two–dimensional incompressible viscous flow is described by the Navier–Stokes equations. In primitive variables the equations read:

$$\partial_t \mathbf{v} + \mathbf{v} \cdot \nabla \mathbf{v} - \nu \nabla^2 \mathbf{v} + \nabla p = 0 \tag{1}$$

$$\nabla \cdot \mathbf{v} = 0 \tag{2}$$

with the velocity $\mathbf{v}$, the pressure p, and where ν denotes the kinematic viscosity which is assumed to be constant. For flow visualization we employ the vorticity $\omega = \nabla \times \mathbf{v}$ which is a pseudo–scalar in two dimensions.

The convection–diffusion–reaction equations describe the transport of the species, represented by their concentration,

$$\partial_t C_i + \mathbf{v} \cdot \nabla C_i - D \nabla^2 C_i = -k_2 C_A C_B \tag{3}$$

where C_i denotes the concentration of species $i = A, B$, k_2 the reaction rate coefficient for an isothermal second order reaction, and D the diffusion coefficient.

The above equations are completed by periodic boundary conditions. The initial conditions are described in Sect. 3.1. We discretize (1–3) with a classical Fourier–Galerkin pseudo–spectral method [2] using a semi–implicit time discretization. The equations are solved directly without any subgrid–scale model. For further details on the numerical scheme we refer to [1]. As dimensionless parameters we introduce the Reynolds number $Re = UL/\nu$ using a characteristic velocity U and length L and the Schmidt number $Sc = \nu/D$.

2.2   Fourier and Wavelet Spectra

The global spectral behaviour of the flow is obtained from Fourier–spectra. We define the enstrophy spectrum

$$Z(k) = \frac{1}{2} \sum_{k-\frac{1}{2} < |\mathbf{k}| \leq k+\frac{1}{2}} |\widehat{\omega}(\mathbf{k})|^2 \tag{4}$$

with the Fourier transform $\widehat{\omega}(\mathbf{k}) = 1/(2\pi)^2 \int \omega(\mathbf{x}) \exp(-\mathrm{i}(\mathbf{k} \cdot \mathbf{x})) \mathrm{d}\mathbf{x}$ where $\mathbf{k} = (k_x, k_y)$ and $\mathbf{x} = (x, y)$. It measures the amount of enstrophy in a ring of wave numbers with radius k and gives a global scaling information of ω. For the total enstrophy we have $Z = 1/2 \int |\omega(\mathbf{x})|^2 \mathrm{d}\mathbf{x} = \sum_{k \geq 0} Z(k)$.

To obtain local information in space and scale, we use a two–dimensional multi–resolution analysis (MRA) [4] and develop ω into an orthogonal wavelet series:

$$\omega(\mathbf{x}) = \bar{\omega}_{0,0,0}\, \phi_{0,0,0}(\mathbf{x}) \quad + \sum_{j \geq 0} \sum_{i_x=0}^{2^j-1} \sum_{i_y=0}^{2^j-1} \sum_{\mu=1}^{3} \tilde{\omega}^\mu_{j,i_x,i_y}\, \psi^\mu_{j,i_x,i_y}(\mathbf{x}) \quad , \quad (5)$$

where $\phi_{j,i_x,i_y}(\mathbf{x})$ and $\psi^\mu_{j,i_x,i_y}(\mathbf{x})$ are the two–dimensional scaling functions and the wavelets, respectively. Due to the orthogonality the scaling coefficient is given by $\bar{\omega}_{0,0,0} = \langle \omega, \phi_{0,0,0} \rangle$ and the wavelet coefficients are given by $\tilde{\omega}^\mu_{j,i_x,i_y} = \langle \omega, \psi^\mu_{j,i_x,i_y} \rangle$ where $\langle \cdot, \cdot \rangle$ denotes the inner product. The coefficient $\bar{\omega}_{0,0,0}$ denotes the mean value of vorticity and the coefficients $\tilde{\omega}^\mu_{j,i_x,i_y}$ give the magnitude of oscillation of ω with wave number $k = 2^j$ near the point $(i_x/2^j, j_y/2^j)$ in the horizontal, vertical or diagonal direction ($\mu = 1, 2, 3$, respectively). Therewith, the local enstrophy spectrum can be defined [3]:

$$Z(\mathbf{x}, k) = \frac{1}{2} \left\{ \frac{1}{2} \left(\tilde{\omega}^1_{j,i_x,i_y} + \tilde{\omega}^1_{j,i_x+1,i_y} \right)^2 + \frac{1}{2} \left(\tilde{\omega}^2_{j,i_x,i_y} + \tilde{\omega}^2_{j,i_x,i_y+1} \right)^2 \right.$$
$$\left. + \left(\tilde{\omega}^3_{j,i_x,i_y} \right)^2 \right\} \frac{2^{2j}}{\Delta k_j} \qquad (6)$$

with $\Delta k_j = (k_{j+1}k_j)^{1/2} - (k_{j-1}k_j)^{1/2}$ describing the spectral behaviour of ω for wave numbers $(k_{j-1}k_j)^{1/2} < k < (k_{j+1}k_j)^{1/2}$ at the point $\mathbf{x} = ((2i_x + 1)/2^{j+1}, (2i_y + 1)/2^{j+1})$, and where k_j are the wave numbers around which the wavelets are localized in Fourier space [3].

The global wavelet spectrum is obtained by averaging the local spectra

$$Z(k) = \sum_{i_x=0}^{2^j-1} \sum_{i_y=0}^{2^j-1} Z(\mathbf{x}, k) 2^{-2j} \qquad (7)$$

and constitutes a smoothed version of the Fourier spectrum. Due to orthogonality of the decomposition we also have $Z = \sum_{k_j} Z(k_j)$. In Sect. 3 we use cubic spline wavelets of Battle–Lemarié type [3].

Replacing the vorticity ω by the concentration C we analogously get the Fourier and wavelet scalar spectra, denoted as $E_c(k)$.

3 Results and Discussion

Turbulent flows typically exhibit coherent vortices created in boundary or shear layers or they are emerging from random initial conditions. Their formation and interaction plays an important role for turbulent mixing of scalars

in non–reactive and reactive flows. In two and three–dimensional rotational fluids different characteristics are observed, e.g. rotation of single vortices, merging of co–rotating vortices, and translation of counter–rotating vortices, completed by vortex stretching as an effect in three dimensional turbulence. The strongest nonlinear interaction in two–dimensional turbulence is the merging of two co–rotating vortices. We exemplarily depict in Fig. 1 such a pairing process and illustrate its influence on the mixing of a passive scalar. The vortices are situated in between two initially segregated layers of non–
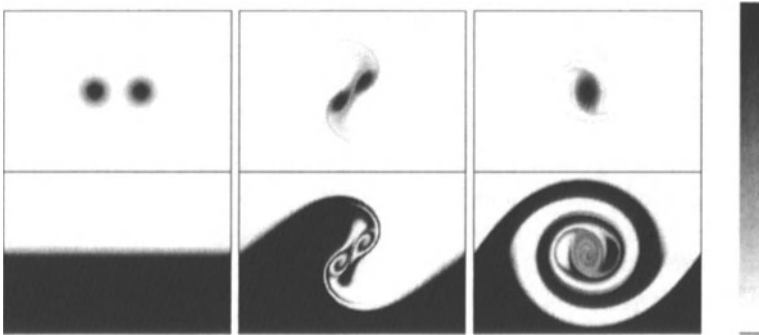
Fig. 1. Evolution of co–rotating vortices in two dimensions at t=0, 2.5 and 10 initial eddy turnover times. *Top*: vorticity. *Bottom*: Concentration of initially segregated non-reactive species. The gray scale is adjusted to data minimum and maximum

reactive fluids and rotate clockwise round each other. The species interface is rolled up and consequently elongated. The rotation and the merging of the vortices generate steep gradients in the concentration field and hence give rise to enhanced diffusion. The efficiency of mixing strongly depends on the initial arrangement of vortices and concentration [1].

3.1   Initial Conditions

As a model of a free shear layer encountered in many practical applications, we consider a temporally growing mixing layer. From the coherent structure point of view we study its mixing properties for passive and reactive scalars. Figure 2 schematically illustrates the initial configuration. As mean initial velocity profile we choose $u(y) = U \tanh(2y/\delta_i)$ with the initial vorticity thickness $\delta_i = 2U/(\mathrm{d}\bar{u}/\mathrm{d}y)_{y=0}$. From linear stability analysis the mixing layer is known to be inviscidly unstable [6]. A perturbation leads to the formation of Kelvin–Helmholtz vortices of longitudinal wavelength $\lambda_a = 7\delta_i$, corresponding to the most amplified wave number. Hence, we superimpose in the vortical region of the initial flow both, a white–noise and a sinusoidal perturbation, the latter with a frequency according to the most unstable wave number to ensure the creation of regularly distributed vortices. The longitudinal extend of the domain is $L = 2\pi$ and corresponds to $8\lambda_a$. In the normal
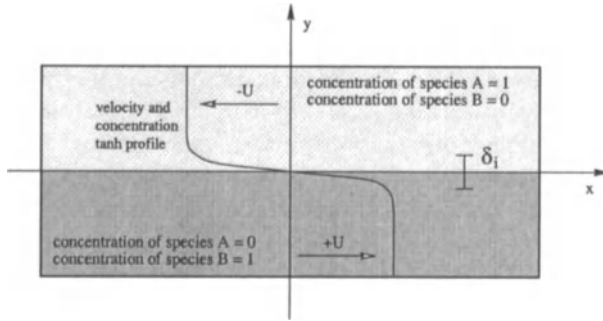
Fig. 2. Scheme of initial configuration for the mixing layer

direction we choose the same box length, which was checked to be sufficiently large to avoid effects of periodicity. The calculations are carried out with a resolution of 256^2 Fourier modes for $Re = 3148$. As initial profile of the concentration we take a smoothed step function to avoid Gibbs–phenomena. The subsequent visualizations refer to a zoom of the longitudinal region between $L/4$ and $3L/4$. The time scale is normalized by δ_i/U.

3.2   Non–reactive Mixing

First we consider the mixing layer for non–reactive scalars, i.e. with $k_2 = 0$ in (3). Figure 3 presents the evolution of vorticity together with the passive scalar. At $t = 18$ we observe the formation of 8 fundamental eddies according
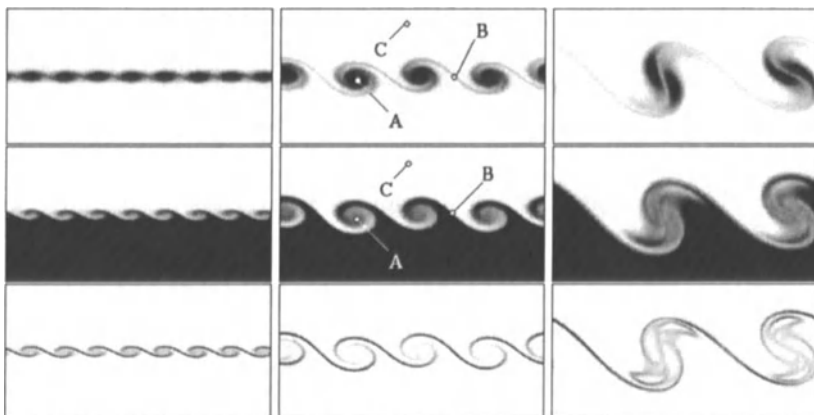
Fig. 3. Flow evolution at $t = 18$, 45 and 72. Vorticity (*top*). Concentration for a non–reactive species with $Sc = 1$ (*middle*). Reaction rate for a second order reaction with $k_2 = 1$ (*bottom*). For gray scale see Fig. 1

to theory. The co–rotating vortices undergo successive pairings, i.e. at $t = 45$

the first merging is completed while at $t = 72$ the second merging process is initiated. The corresponding concentration fields show how the coherent structures elongate the interface and therefore enhance the mixing of the two scalars. To quantify the efficiency of the mixing process for different Sc, we determine global time scales t_0 by fitting the evolution of the concentration variance assuming an exponential decay, valid for pure diffusion. Comparing the obtained time scales for the shear flow with pure diffusion (Table 1) we observe that the vortex interaction strongly enhances mixing, particularly with increasing Sc.

Table 1. Global mixing time scales t_0 for different Sc compared to t_0 for pure diffusion.

Sc	$t_{0,\text{mixing layer}}$	$t_{0,\text{pure diffusion}}$	$t_{0,\text{pd}}/t_{0,\text{ml}}$
0.3	601	2674	4.4
1.0	908	8913	9.8
3.0	1285	26738	20.8

The Fourier spectra of vorticity and concentration in Fig. 4 are very similar and show a large range of active scales. A comparison with the global wavelet spectra shows in both cases a very good agreement, conforming the fact that the latter are smoothed Fourier spectra, where the averaging is increasing with scale. By means of local wavelet spectra the scaling behaviour of flow regions with typical characteristica can be identified and locations of mixing activity can be quantified. Exemplarily, we choose three typical points in the vorticity field at $t = 45$ (see Fig. 3), located in the centre of a vortex (**A**), in a narrow vortex filament (**B**), and outside the active vorticity region (**C**). For the local enstrophy spectra (Fig.4 a) we find consistent results as
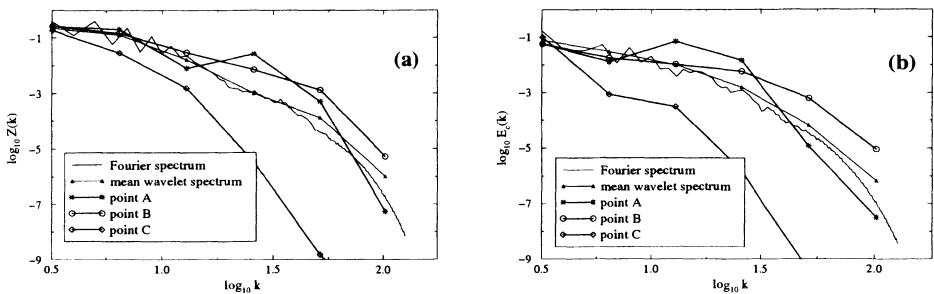
Fig. 4. Global Fourier and wavelet spectra compared with local wavelet spectra for three points in the vorticity (a) and concentration (b) fields in Fig. 3

in [3]. Additionally, we consider the local spectra of the scalar at the corresponding points (Fig.4 b). In large scales all local wavelet spectra coincide by construction with the global one. At fine scales we observe different scaling behaviour for the three points, which is very similar for the enstrophy and scalar spectra. Fine scales are most active in the strain field between the vortices (**B**), i.e. the steep gradients in the shear zones of the vortices also generate small scales in the concentration field leading to enhanced diffusion. The spectrum for the vortex centre (**A**), i.e. at locations where the vorticity is maximal, contains more enstrophy at medium scales but less at finer scales. Corresponding to the scalar spectrum the mixing is less efficient. Outside the active vorticity region (**C**) the two spectra decay rapidly in scale which is equivalent to an almost dynamically inactive region and where no mixing takes place. We conclude that both the Fourier and the global wavelet spectra, and also the local spectra are highly correlated for the flow and the scalars.

3.3 Mixing of Reactive Species

In [1] we have shown that chemical reactions in mixing processes lead to the formation of fine scales, resulting in a reduced decay of the Fourier spectra. Motivated by the results of the previous section we investigate the local spectral properties in a reactive case. Therefore, we perform a simulation for $Sc = 1$ and $k_2 = 1$. As molecular mixing is a prerequisite for chemical reaction, the reaction rate, shown in Fig. 3, directly reflects locations of efficient mixing. The maxima are located in the shear zone where the species
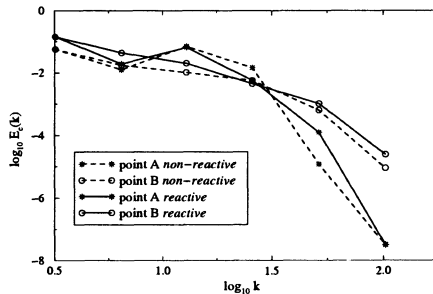
Fig. 5. Comparison of local wavelet spectra for the points **A** and **B** of a concentration field in the reactive and the non–reactive case at $t = 45$

are being efficiently mixed against which the rate is considerably reduced inside the vortices. To quantify the local increase of fine scales we compare in Fig. 5 the local wavelet spectra of the species for the reactive with that of the non–reactive case in the vortex centre (point **A**) and in the shear zone (point **B**). For both points we find in the reactive case a slight increase of smaller

scales. In the vortex this primarily affects medium wave numbers whereas in the shear zone medium and fine scales are enhanced. Hence, we conclude that the global steepening of concentration gradients by chemical reactions in the scalars' Fourier spectra is mainly produced in the shear zone, and therefore is correlated with small scale structures identified in the flow field.

4   Conclusions

We have presented DNS of a temporally developing mixing layer and studied the mixing properties of passive and reactive scalars using Fourier and wavelet techniques. The observed enhanced mixing is due to two mechanisms, the rolling–up of species interface into spirals leading to the generation of fine scales, and the merging of vortices implying an increased stirring. The local spectral analysis by using wavelets shows a spatially varying scaling behaviour of the flow which is strongly correlated with that of the concentration field. This implies that the mixing is most efficient in shear zones where fine scales are produced whereas in the centres of the vortices the mixing activity is reduced by the smoothed gradients. In the reactive case enhanced mixing of the scalars is directly reflected by the chemical reaction, i.e. the reaction rate is locally increased.

Future work is concerned with studying of mixing in more complex geometries, like channel flows with bluff bodies using a penalization method.

References

1. Gerlinger W., Bockhorn H., Falk L., Schneider K. (1999) Numerical Simulation of the Mixing of Passive and Reactive Scalars in Two–Dimensional Flows Dominated by Coherent Vortices. Submitted
2. Canuto C., Hussaini M., Quarteroni A., Zang T. (1988) Spectral Methods in Fluid Dynamics. Springer, New York
3. Do-Khac M., Basedevant C., Perrier V., Dang-Tran K. (1994) Wavelet analysis of 2D turbulent fields. Physica D **76**, 252–277
4. Farge M. (1992) Wavelet transforms and their application to turbulence. Ann. Rev. Fluid Mech. **24**, 395–457
5. Farge M., Kevlahan N., Perrier V., and Schneider K., Turbulence analysis, modelling and computing using wavelets. In *Wavelets and Physics* (Ed. J.C. van den Berg), Cambridge University Press, to appear 1999.
6. Lesieur M. (1997) *Turbulence in Fluids.* 3rd Edition. Kluwer, Dordrecht

Direct numerical simulation of Marangoni convection in a two-fluid system

Thomas Boeck[1] and André Thess[1,2]

[1] Center for Physical Fluid Dynamics, Dept. of Mechanical Engineering,
   Dresden University of Technology, 01062 Dresden, Germany.
[2] Dept. of Mechanical Engineering, Ilmenau University of Technology,
   P.O. Box 100565, 98684 Ilmenau, Germany.

Abstract. We present a three-dimensional pseudospectral numerical scheme for Bénard-Marangoni convection in a two-fluid system based on the full set of hydrodynamic equations. Performance measurements demonstrate good parallel speedup for our implementation. The code provides an efficient tool for high-resolution numerical studies of heat and mass transfer across interfaces .

1 Introduction

Gradients of interfacial tension between liquid phases produce shear stresses driving fluid motion. This so-called Marangoni effect is of importance in extraction processes in chemical engineering [1], in Marangoni drying [2], in electron beam evaporation of liquid metals [3], and other applications. Moreover, Marangoni flows are of interest in the context of structure formation in spatially extended systems. One important example is Bénard-Marangoni convection in an oil layer heated from below with an air layer on top, which has received significant attention in recent years [4,5]. However, numerical simulations have so far mostly been conducted for a reduced system, in which only the flow in the oil layer is computed. The flow in the air layer is ignored. Only recently the flow in both layers was simulated in the two-dimensional case [5]. In this paper, we shall treat the same problem in the full three-dimensional case. After presentation of the basic equations we describe a pseudospectral numerical algorithm for the computation of the flow in both the liquid and the gas phase. Next, we demonstrate that the method can be efficiently parallelized. Finally, we compare the results of a full two-layer simulation with the corresponding one-layer simulation.

2 Two-layer equations

We consider a liquid overlaid with either another liquid or a gas. Both fluids are bounded by parallel rigid walls located at $z = 0$ and $z = d_l + d_g$. The interface between the fluids is assumed parallel to these walls. The symbols d_l and d_g denote the height of the lower and upper layer, where the subscripts

l and g stand for liquid and gas. The liquid-gas interface is located at $z = d_l$. The rigid walls are kept at constant temperatures with a positive difference $\Delta T = T_b - T_t$ between bottom and top. In the horizontal directions x and y we assume periodic boundary conditions with periodicity lengths L_x and L_y.

The relevant material properties of the fluids are the kinematic viscosities ν_j, the densities ρ_j, the heat conductivities λ_j and the thermal diffusivities κ_j, where $j \in \{l, g\}$. The interfacial tension σ acting on the fluid interface depends on the temperature according to $\sigma = \sigma_0 - \gamma T$. We choose d_l as unit of length, ν_l/d_l as unit of velocity, d_l^2/ν_l as unit of time, $\rho_l \nu_l^2/d_l^2$ as unit of pressure, and ΔT as unit of temperature. In the basic state of pure heat conduction, the temperature depends linearly on the vertical coordinate in each layer. Because of the different thermal conductivities, the slope changes at the interface. The conductive profile reads

$$T_c(z) = \begin{cases} (R_\lambda (1 - z) + R_d) / (R_\lambda + R_d) & : \quad 0 \le z < 1, \\ (1 - z + R_d) / (R_\lambda + R_d) & : \quad 1 < z \le 1 + R_d, \end{cases} \tag{1}$$

where $R_x = x_g/x_l$ denotes the ratio between gas and liquid layer for the quantity x. We can now introduce the temperature perturbation $\theta = T - T_c(z)$ as deviation from the distribution in the quiescent state. The velocity fields $\boldsymbol{v}_j = (u_j, v_j, w_j)$ and the temperature perturbations θ_j in each of the incompressible fluid layers are governed by the dimensionless Navier-Stokes and energy equations

$$\Lambda_j \left(\partial_t \boldsymbol{v}_j + (\boldsymbol{v}_j \cdot \nabla) \boldsymbol{v}_j \right) = -\Lambda_j \nabla p_j + \nabla^2 \boldsymbol{v}_j, \tag{2a}$$

$$\nabla \cdot \boldsymbol{v}_j = 0, \tag{2b}$$

$$\Sigma_j \left(\partial_t \theta_j + (\boldsymbol{v}_j \cdot \nabla) \theta_j \right) = \nabla^2 \theta_j + \chi_j w_j. \tag{2c}$$

The separation of the linear conductive profile gives rise to the linear terms $\chi_j w_j$ in the latter equation. The parameters Λ_j, Σ_j and χ_j are given by

$$\Lambda_l = 1, \ \Lambda_g = 1/R_\nu, \tag{3a}$$

$$\Sigma_l = P_l, \ \Sigma_g = P_g/R_\nu, \tag{3b}$$

$$P_l = \nu_l/\kappa_l, \ P_g = \nu_g/\kappa_g, \tag{3c}$$

$$\chi_l = P_l R_\lambda / (R_\lambda + R_d), \ \chi_g = P_g / (R_\nu (R_\lambda + R_d)), \tag{3d}$$

where P_j denote the Prandtl numbers of the fluids.

The boundary conditions complementing the above equations read

$$\theta_l(z = 0) = \boldsymbol{v}_l(z = 0) = 0, \tag{4}$$

$$\theta_g(1 + R_d) = \boldsymbol{v}_g(1 + R_d) = 0 \tag{5}$$

at bottom and top walls. At the liquid-gas interface $z = 1$ the following conditions hold:

$$\theta_l = \theta_g, \tag{6a}$$

$$\partial_z \theta_l = R_\lambda \partial_z \theta_g, \tag{6b}$$

$$u_l = u_g, \; v_l = v_g, \; w_l = w_g = 0, \tag{6c}$$

$$\partial_z u_l - R_{\rho\nu} \partial_z u_g = -M \partial_x \theta_l, \tag{6d}$$

$$\partial_z v_l - R_{\rho\nu} \partial_z v_g = -M \partial_y \theta_l. \tag{6e}$$

Condition (6b) implies the continuity of heat flux. The last two conditions reflect the balance of the surface shear components. The terms on the right hand sides are the Marangoni forces. The parameter

$$M = \frac{\gamma \Delta T d_l}{\rho_l \nu_l^2} \tag{7}$$

is called the Marangoni number.

3   Numerical scheme

3.1   Poloidal-toroidal decomposition

The numerical algorithm is based on the poloidal-toroidal decomposition

$$\boldsymbol{v}_j(x,y,z,t) = \nabla \times (\nabla \times \boldsymbol{e}_z \Phi_j(x,y,z,t)) + \nabla \times \boldsymbol{e}_z \Psi_j(x,y,z,t) \tag{8}$$

of the velocity fields in both layers. By that, the incompressibility constraint is satisfied automatically. The evolution equations for Φ_j and Ψ_j are derived by taking the curl and twice the curl of the Navier-Stokes equation and projection onto the vertical direction. We obtain the equations

$$\Lambda_j \left(\partial_t \zeta_j + N_1 \left(\boldsymbol{v}_j \right) \right) = \nabla^2 \zeta_j, \tag{9a}$$

$$\Lambda_j \left(\partial_t \nabla^2 w_j + N_2 \left(\boldsymbol{v}_j \right) \right) = \nabla^4 w_j, \tag{9b}$$

for the vertical velocity component $w_j = -\Delta_h \Phi_j$ and the vertical vorticity component $\zeta_j = -\Delta_h \Psi_j$, where $\Delta_h = \partial_x^2 + \partial_y^2$ denotes the horizontal Laplace operator. The vorticity is defined by $\boldsymbol{\omega}_j = \nabla \times \boldsymbol{v}_j$. The nonlinear terms N_1, N_2 read

$$N_1 \left(\boldsymbol{v} \right) = -\boldsymbol{e}_z \cdot \nabla \times \left(\boldsymbol{v} \times \left(\nabla \times \boldsymbol{v} \right) \right), \tag{10a}$$

$$N_2 \left(\boldsymbol{v} \right) = \partial_z \nabla \cdot \left(\boldsymbol{v} \times \left(\nabla \times \boldsymbol{v} \right) \right) - \boldsymbol{e}_z \cdot \nabla^2 \left(\boldsymbol{v} \times \left(\nabla \times \boldsymbol{v} \right) \right). \tag{10b}$$

The velocity components u_j and v_j are related to w_j and ζ_j by

$$\Delta_h u_j = -\partial_x \partial_z w_j - \partial_y \zeta_j, \tag{11a}$$

$$\Delta_h v_j = -\partial_y \partial_z w_j + \partial_x \zeta_j, \tag{11b}$$

where the continuity equation and the definition $\zeta_j = \partial_x v_j - \partial_y u_j$ have been used. Obviously, w_j and ζ_j determine the velocity field up to a mean flow $U_j(z) \boldsymbol{e}_x + V_j(z) \boldsymbol{e}_y$. Equations for U_j and V_j are obtained by averaging

the Navier-Stokes equation over horizontal cross-sections of the periodicity domain. From the Navier-Stokes equations in each layer we find that

$$\Lambda_j \left(\partial_t U_j + \partial_z \langle u_j w_j \rangle \right) = \partial_z^2 U_j, \tag{12a}$$

$$\Lambda_j \left(\partial_t V_j + \partial_z \langle v_j w_j \rangle \right) = \partial_z^2 V_j, \tag{12b}$$

where the angular brackets $\langle \rangle$ denote horizontal averages over the periodicity domain. The remaining problem in the reformulation of the evolution equations in terms of w_j, ζ_j, θ_j, U_j and V_j consists in the derivation of appropriate boundary conditions. At the rigid walls $z = 0$ and $z = 1 + R_d$ we have

$$w_j = \partial_z w_j = \zeta_j = U_j = V_j = \theta_j = 0. \tag{13}$$

The condition $\partial_z w_j = 0$ is a consequence of the continuity equation and the no-slip condition $v_j = 0$ at the walls. The conditions at the liquid-gas interface $z = 1$ become

$$\theta_l = \theta_g, \ \partial_z \theta_l = R_\lambda \partial_z \theta_g, \tag{14a}$$

$$w_l = 0, \ w_g = 0, \tag{14b}$$

$$\partial_z w_l = \partial_z w_g, \ \partial_z^2 w_l - R_{\rho\nu} \partial_z^2 w_g = M \Delta_h \theta_l, \tag{14c}$$

$$\zeta_l = \zeta_g, \ \partial_z \zeta_l = R_{\rho\nu} \partial_z \zeta_g, \tag{14d}$$

$$U_l = U_g, \ \partial_z U_l = R_{\rho\nu} U_g, \tag{14e}$$

$$V_l = V_g, \ \partial_z V_l = R_{\rho\nu} V_g, \tag{14f}$$

where the continuity equation has again been used in deriving (14c).

3.2   Pseudospectral discretization

The discretization in each layer is based on an expansion in Fourier modes with respect to x and y and in Chebyshev polynomials in z. In each layer, the same number of Fourier modes is used. The discretization in time employs a finite difference method with fixed time step δt. A hydrodynamic variable η at timelevel $n\delta t$ is represented as

$$\eta(x, y, z, n\delta t) = \sum_{\boldsymbol{k}} \eta_{\boldsymbol{k}}^n(z) \exp(i \left(k_x x + k_y y \right)) \tag{15}$$

with $\boldsymbol{k} = (k_x, k_y)$ as wavevector. Here the expansion coefficients $\eta_{\boldsymbol{k}}^n(z)$ are still functions of the continuous variable z. We now substitute (15) in each of the evolution equations (9a,9b, 2c) and apply the backward Euler method for the linear terms and the Adams-Bashforth method for the nonlinear terms. Using the definitions $\xi = \Delta w$, $D = d/dz$ and $\mathrm{AB}\{f\}^n = (3f^n - f^{n-1})/2$ from the Adams-Bashforth formula we find the system

$$\left(D^2 - \boldsymbol{k}^2 - \frac{\Lambda_j}{\delta t} \right) \zeta_{j,\boldsymbol{k}}^{n+1} = \Lambda_j \left(\frac{\zeta_{j,\boldsymbol{k}}^n}{\delta t} - \mathrm{AB}\left\{ [N_1 \left(v_j \right)]_{\boldsymbol{k}} \right\}^n \right), \tag{16a}$$

$$\left(D^2 - k^2 - \frac{\Lambda_j}{\delta t}\right) \xi_{j,k}^{n+1} = \Lambda_j \left(\frac{\xi_{j,k}^n}{\delta t} - AB \left\{[N_2(v_j)]_k\right\}^n\right), \tag{16b}$$

$$\left(D^2 - k^2\right) w_{j,k}^{n+1} - \xi_{j,k}^{n+1} = 0, \tag{16c}$$

$$\left(D^2 - k^2 - \frac{\Sigma_j}{\delta t}\right) \theta_{j,k}^{n+1} + \chi_j w_{j,k}^{n+1} = \Sigma_j \left(\frac{\theta_{j,k}^n}{\delta t} + AB \left\{[v_j \cdot \nabla \theta_j]_k\right\}^n\right), \tag{16d}$$

$$\left(D^2 - \frac{\Lambda_j}{\delta t}\right) U_j^{n+1} = \Lambda_j \left(\frac{U_j^n}{\delta t} - AB \left\{\frac{\partial}{\partial z}\langle u_j w_j\rangle\right\}^n\right), \tag{16e}$$

$$\left(D^2 - \frac{\Lambda_j}{\delta t}\right) V_j^{n+1} = \Lambda_j \left(\frac{V_j^n}{\delta t} - AB \left\{\frac{\partial}{\partial z}\langle v_j w_j\rangle\right\}^n\right) \tag{16f}$$

of equations for the expansion coefficients for the wavevector k and for the mean flow components at timelevel $(n+1)\delta t$. Each of the above equations is of the form $\left(D^2 - \mu\right) f = g$, i.e. it represents a one-dimensional Helmholtz equation. Discretization by means of the Chebyshev-tau method yields a tridiagonal system of linear equations for the expansion coefficients of f, which can be solved very efficiently [6]. The equations for the lower and upper layer are coupled via the interface boundary conditions. Moreover, the equations for ξ_j, w_j and θ_j are coupled because of the Marangoni boundary condition (14c). Because of the coupling we employ a Green function technique as in [7]. Dropping the indices k and n for the moment, the solution for the coupled equations (16b,16c,16d) reads

$$\xi_j = \xi_j^{(p)} + \alpha_j \xi_j^{(1)} + \beta_j \xi_j^{(2)}, \tag{17a}$$

$$w_j = w_j^{(p)} + \alpha_j w_j^{(1)} + \beta_j w_j^{(2)}, \tag{17b}$$

$$\theta_j = \theta_j^{(p)} + \alpha_j \theta_j^{(1)} + \beta_j \theta_j^{(2)} + \gamma_j \theta_j^{(3)}. \tag{17c}$$

The functions $\xi_j^{(p)}$, $w_j^{(p)}$ and $\theta_j^{(p)}$ are particular solutions of the inhomogeneous equations (16b,16c,16d) with zero boundary values of the function itself. The unknown coefficients α_j, β_j and γ_j multiply the Green functions, which satisfy

$$\left(D^2 - k^2 - \frac{\Lambda_j}{\delta t}\right) \xi_j^{(m)} = 0, \quad \xi_j^{(m)}(1) = 1, \quad \xi_j^{(m)}(z_j) = (-1)^m, \tag{18a}$$

$$\left(D^2 - k^2\right) w_j^{(m)} = \xi_j^{(m)}, \quad w_j^{(m)}(1) = w_j^{(m)}(z_j) = 0, \tag{18b}$$

$$\left(D^2 - k^2 - \frac{\Sigma_j}{\delta t}\right) \theta_j^{(m)} = -\chi_j w_j^{(m)}, \quad \theta_j^{(m)}(1) = \theta_j^{(m)}(z_j) = 0, \tag{18c}$$

$$\left(D^2 - k^2 - \frac{\Sigma_j}{\delta t}\right) \theta_j^{(3)} = 0, \quad \theta_j^{(3)}(1) = 1, \quad \theta_j^{(3)}(z_j) = 0, \tag{18d}$$

where $m = 1, 2$. Here we have used z_j to denote the position of the rigid wall in layer j, i.e. $z_l = 0$ and $z_g = 1 + R_d$. The coefficients $\alpha_l, \alpha_g, \beta_l, \beta_g, \gamma_l, \gamma_g$ are computed by inserting the representation (17a-17c) in the boundary conditions (13,14a-14c) and solving the resulting 6×6 system of linear equations.

Since the Green functions are constant, they need only be computed once at the start of the time integration. We apply the same technique for the solution of the equations for ζ_j and the mean flow components U_j and V_j.

4   Results

4.1   Parallel speedup

The computation of the nonlinear terms requires the largest share of computational cost per time step. We compute these terms by transformation into physical space using fast Fourier and fast Chebyshev transforms. The communication bandwidth available on current parallel architectures allows for an effective parallelization of the algorithm. Each processor is assigned a slice of the wavevector array. The wavevectors assigned to an individual processor cover some x-wavenumber range and the entire range of y-wavenumbers. By that, only the Fourier transforms require inter-process communication. It is implemented by means of global cross-processor transposition [7]. The program can be executed on a number of processors which is a power of two and which is not larger than the number of collocation points with respect to both the x-direction and the y-direction. The number of collocation points are also powers of two since only base two Fourier transforms are used.

The program has been implemented in C and parallelized using MPI . Performance data have been obtained on the Cray T3E-256 at the HLRZ Jülich using up to 64 processors. We have measured the execution time for 50 timesteps at two different resolutions using the MPI function `Wtime()`. Table I contains the time per step for two cases as well as the execution speed. The latter has been obtained with the Performance Analysis Tool PAT. The almost linear increase in speed levels off when the problem size per processor becomes too small. With the larger problem of case 2 this happens at a larger number of processors than for case 1. We remark but cannot explain at the moment that the execution speed increases somewhat faster than the inverse execution time per step.

4.2   Comparison with one-layer simulations

The two-layer code provides a means to access the validity of previous simulations of Bénard-Marangoni convection, which have almost exclusively focused on a one-layer approximation . In the framework of the one-layer approximation, convection in the gas layer is ignored. Moreover, the thermal boundary condition at the liquid-gas interface is commonly approximated by Newton's law of cooling [5]

$$\partial_z \theta_l + B\theta_l = 0, \qquad B = R_\lambda/R_d, \tag{19}$$

where B is called the Biot number. The applicability of this simplified model has only recently been tested numerically for the two-dimensional case. We

Table 1. Efficiency of parallelization for two different cases. Case 1 uses a resolution of 64 Fourier modes in x and y and 17 Chebyshev polynomials in each layer. Case 2 uses 128 modes in x and y. Time per step given in seconds, execution speed in MFlop/s.

number of processors	time per step (case 1)	execution speed (case 1)	time per step (case 2)	execution speed (case 2)
1	3.05	45		
2	1.56	88	6.53	89
4	0.80	173	3.31	178
8	0.39	353	1.68	349
16	0.21	696	0.87	680
32	0.16	1045	0.47	1310
64			0.34	1950

have obtained a first example of good quantitative agreement in the three-dimensional case for an air-silicone oil system. Figure 1 shows isotherms at the liquid-gas interface for the set of parameters given in Table 2. The result of this simulation was used as initial condition for a one-layer simulation corresponding to the same physical situation. No visible difference is found in the isotherms. The Nusselt numbers characterizing convective heat transport are 1.287 for two-layer model and 1.289 for the one-layer model. However, differences are expected for strong convection with $M \gg 1$.
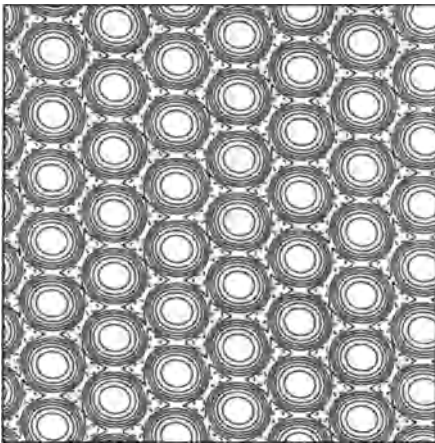
Fig. 1. Isotherms on the liquid-gas interface for a layer of silicon oil with an air layer on top. Notice the hexagonal cell structure. Dashed lines correspond to negative values of the temperature perturbation θ. Hot silicon oil rises in the cell centers, which accounts for the elevated temperature there.

Table 2. Material properties and other parameters of the simulation. N_x, N_y and N_z denote the number of collocation points in the respective directions in each layer.

M	R_d	R_λ	R_ν	R_ρ	P_l	P_g	L_x/d_l	L_y/d_l	N_x	N_y	N_z
4.8	0.33	0.19	1.62	0.0013	100	0.6	20	20	128	128	17

5   Conclusions

We have presented a numerical scheme for the computation of Bénard-Marangoni convection in both the liquid and gas layer. The only significant approximation in the model consists in the neglect of interface deformations. The scheme can be efficiently parallelized. A first simulation for realistic experimental parameters indicates that the full two-layer and the reduced one-layer model give good quantitative agreement. Future investigations will address this question systematically. Another application of the code could be the analysis of defect dynamics in imperfect hexagonal patterns [5]. Incorporation of additional effects such as chemical species and reactions is also possible.

References

1. Scriven, C. V., Sternling, L. E. (1959) Interfacial Turbulence: Hydrodynamic Instability and the Marangoni Effect. A.I.Ch.E. Journal **5**, 514–523.
2. Mara, J., Huethorst, J. A. M. (1991) Physical Principles of Marangoni Drying. Langmuir **7**, 2748–2755.
3. Pumir, A., Blumenfeld, L. (1996) Heat transport in a liquid layer locally heated on its free surface. Phys. Rev. E **54**, R4528–R4531.
4. VanHook, S. et al. (1997) Long-wavelength surface-tension-driven Bénard convection : experiment and theory. J. Fluid Mech. **345**, 45–78.
5. Eckert, K., Bestehorn, M., Thess, A. (1998) Square cells in surface-tension-driven Bénard convection: experiment and theory. J. Fluid Mech. **356**, 155–197.
6. Canuto, C. et al. (1988) Spectral Methods in Fluid Dynamics. Springer.
7. Borue, V., Orszag, S. A., Staroselsky, I. (1995) Interaction of surface waves with turbulence: direct numerical simulations of turbulent open channel flow. J. Fluid Mech. **286**, 1–23.

Computation of Flows with Free Surfaces

Ismet Demirdžić[1], Samir Muzaferija[2], Milovan Perić[3], Eberhard Schreck[2], and Volker Seidl[2]

[1] Faculty of Mechanical Engineering, University of Sarajevo, BIH-71000 Sarajevo, Bosnia and Hercegowina
[2] ICCM Institute of Computational Continuum Mechanics GmbH, Bramfelder Straße 164, D-22305 Hamburg, Germany
[3] Fluid Dynamics and Ship Theory Section, Technical University of Hamburg-Harburg, Lämmersieth 90, D-22305 Hamburg, Germany

Abstract. The paper presents two methods for comuting flows with free surfaces: an interface-tracking and an interface-capturing method. The former computes the liquid flow only, using a numerical grid which adapts itself to the shape and position of the free surface; the kinematic and dynamic boundary conditions are applied there. The second method considers both fluids as a single effective fluid with variable properties; the interface is captured as a region of a sudden change in fluid properties. An additional transport equation is solved to determine the volume fraction of one of the fluids. Advantages and disadvantages of the two methods are discussed and several application examples are presented.

1 Introduction

Many processes in chemical and process engineering involve flows of either Newtonian or non-Newtonian fluids with free surfaces, e.g. coating and mixing processes. In some cases only the flow of the liquid phase is of interest, but very often both gas and liquid flows need to be considered in a coupled manner, e.g. when gas pockets are enclosed by liquid or vice versa.

The computation of such flows is difficult because the shape and the position of the interface between gas and liquid is not known a priori; on the contrary, it often changes both its location and shape in time and may involve merging and fragmentation processes. Yet it is very important to be able to predict the shape of the free surface: first of all, in order to be able to predict the flow of both fluids on either side of it, but also because the free surface itself (its shape, area, velocity etc.) plays an important role in many chemical and bio-chemical processes which may take place e.g. in the liquid phase. Another important aspect in such flows is the determination of the wetted wall surface, which affects the drag, lift, power entrainment, energy dissipation etc.

There are basically two approaches to computing flows with free surfaces: interface-tracking and interface-capturing methods. The former compute the liquid flow only, using a numerical grid which adapts itself to the shape and position of the free surface. The free surface is treated as a boundary

of the computational domain, where the kinematic and dynamic boundary conditions are applied.

On the other hand, interface-capturing methods consider both fluids as a single effective fluid with variable properties; the interface is captured as a region of a sudden change in fluid properties – just like shocks in compressible flows. An additional transport equation needs to be solved to determine the volume fraction of one of the constituent fluids.

Both kinds of methods have their advantages and disadvantages; these are discussed below, after one representative of each kind is described.

2   Interface-Tracking Method

There are various methods of this type, but due to space limitations, only one approach will be described; more details are available in [1].

Approaches of this kind can be used when the free surface is smooth and does not undergo severe deformation; otherwise, the grid may deform too much and prevent further computation without re-gridding. Also, if the free surface is in contact with a solid wall of a complicated shape, it may be difficult to adapt the grid to both free surface and the solid boundary.

The *dynamic condition*, which implies that the forces acting on the fluid at the free surface are in equilibrium, is implemented in the solution method through prescribing the pressure at the free surface. If viscous and surface tension forces are also appreciable, an iterative procedure with an adequate extrapolation of velocities to the free surface must be used.

The *kinematic condition*, which implies that the free surface is an interface between two fluids with no flow through it, can then be used to find the new location of the free surface. Namely, treating the free surface as a boundary with prescribed pressure leads to non-zero mass fluxes through it, thus violating the kinematic condition. These fluxes are used to determine in which direction and by how much the interface needs to be displaced in order to prevent fluid from crossing it. The solution process is iterative and fits within the framework of the standard SIMPLE-type pressure-correction methods usually used to compute incompressible flows. A typical finite-volume method proceeds as follows:

1. Solve the momentum equations using the geometry defined by the current shape of the free surface and the prescribed pressure at it.
2. Enforce local mass conservation in each control volume (CV) by solving the pressure-correction equation, using the prescribed pressure boundary condition at the current free surface. Mass is conserved both globally and in each CV, but the non-zero mass fluxes through the free surface may result.
3. Correct the position of the free surface so that the volume defined by its corrected and previous position compensates the mass fluxes through the free surface obtained in the preceding step.

4. Return to step 1 and repeat until all equations and boundary conditions are satisfied (i.e. until all corrections become negligibly small).
5. Advance to the next time step.

An interface-tracking method of this kind can be implemented in almost any CFD-algorithm. There are many possibilities for adaptation and optimization of the method, which will not be dealt with here; see [1] for more details.

3   Interface-Capturing Method

In this type of methods, a fixed grid is used which covers the space occupied by both the liquid and the gas phase. Since the grid does not follow the deformation of the free surface, the grid movement is only necessary if the shape or location of the solution domain changes.

In addition to the conservation equations for mass and momentum, one introduces and solves an equation for the volume fraction of one phase, c. One sets e.g. $c = 1$ for CVs filled by liquid and $c = 0$ in CVs filled by gas. The change of c is governed by the transport equation:

$$\frac{\mathrm{d}}{\mathrm{d}t} \int_V c \, \mathrm{d}V + \int_S c(\mathbf{v} - \mathbf{v}_\mathrm{b}) \cdot \mathbf{n} \, \mathrm{d}S = 0 \, , \tag{1}$$

where V is the CV-volume bounded by a closed surface S with a unit normal vector $\mathbf{n}$ directed outwards, $\mathbf{v}$ is the fluid velocity vector and $\mathbf{v}_\mathrm{b}$ is the velocity of the CV surface in the case of a moving grid.

The properties of the effective fluid vary in space according to the volume fraction of each phase, i.e.:

$$\rho = \rho_1 c + \rho_2 (1 - c) \, , \quad \mu = \mu_1 c + \mu_2 (1 - c) \, , \tag{2}$$

where subscripts 1 and 2 denote the two fluids (e.g. liquid and gas). If one CV is partially filled with one and partially with the other fluid (i.e. $0 \le c \le 1$), it is assumed that both fluids have the same velocity and pressure. The free surface does not represent a boundary and no boundary conditions need to be prescribed at it. If surface tension is significant at the free surface, this can also be taken into account by transforming the resulting force into a body force [2]. These methods can also deal with merging and fragmentation in multiphase flows [3].

Equation (1) contains only convective fluxes and the unsteady term. If only a steady solution is sought or slowly-varying flows are considered, the fully-implicit Euler method is appropriate for integration in time. For flows in which time evolution of the free surface is important, second-order schemes such as Crank-Nicolson, implicit three-time-levels scheme etc. should be used.

The choice of approximations for convective fluxes is less obvious. The only scheme which unconditionally satisfies the monotonicity criterion is

the first-order upwind scheme; however, it can not be used due to excessive numerical diffusion, which smeares the interface and causes the two fluids to mix over a wide region. On the other hand, any of the higher-order schemes tends to produce over- and undershoots in the vicinity of discontinuities, so special care is needed. One can resort to a wide range of special variation-bounded schemes developed for applications in aerodynamics, like total-variation-diminishing (TVD) and essentially non-oscillatory (ENO) schemes; see [4] for examples. However, the interface-capturing in free-surface flows has some specialities which need to be considered.
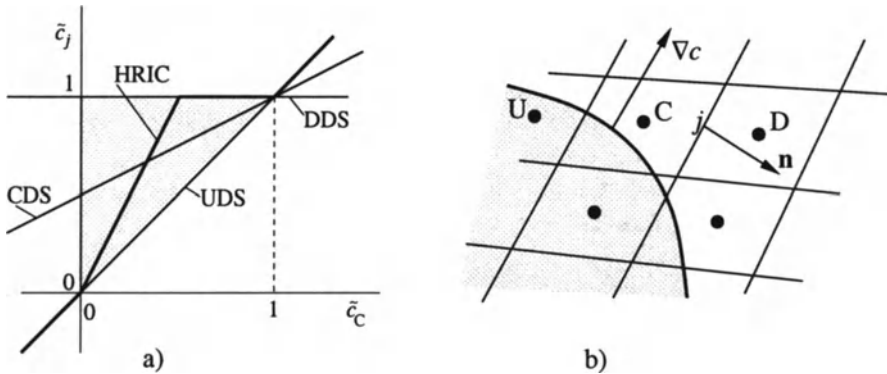
Fig. 1. The normalized variable diagram (**a**) and the definition of free-surface orientation (**b**)

The sharpness of the interface without over- and undershoots can be achieved by limiting the approximation of the cell-face value to lie in the shaded area of the so-called *normalized variable diagram* (NVD) shown in Fig. 1 [5]. The local normalized variable $\tilde{c}$ in the vicinity of the cell-center C is defined as:

$$\tilde{c}(\mathbf{r}) = \frac{c(\mathbf{r}) - c_U}{c_D - c_U} , \qquad (3)$$

where subscripts 'U' and 'D' denote nodes upstream and downstream of the cell-center C. Should the cell-center value $\tilde{c}_C$ turn out to be smaller than zero or larger than unity, this means that the profile of c is not monotone and we need numerical diffusion to get rid of oscillations; for values of $\tilde{c}_C$ between zero and unity, one can choose any dependency from the shaded region of the NVD-diagram. The particular choice made here is indicated in Fig. 1 as HRIC (high-resolution interface capturing) scheme. The reasoning for such a choice is as follows: if the cell around node C is almost empty, only the fluid present at the downstream cell will be convected through the cell face, so it is appropriate to use the downwind scheme (DDS). However, this applies only if the interface is parallel to the cell face and moves in the direction of the cell-face normal; if the interface is perpendicular to the cell

face, it is likely that the convected fluid would be of the same composition as in the donor cell center, so the upwind scheme (UDS) is appropriate. Also, downwind approximation must not drain more fluid than is available in the cell, which depends on the local Courant number,

$$\text{Co} = \frac{\mathbf{v} \cdot \mathbf{n} \, S_j \Delta t}{\Delta V_\text{C}} \; , \tag{4}$$

where S_j is the area of the cell-face j, ΔV_C is the volume of the cell centered around node C, and Δt is the time step. There is no obvious way how to vary the approximation of c_j depending on the Courant number and interface orientation. Generally, for small Courant numbers (≤ 0.5) the value according to HRIC should be used. If the Courant number is large (order of unity or larger), upwind scheme should be used since all fluid from the cell will flow out of it; in the intermediate range, blending of UDS and HRIC should be used. Also, if the angle between the interface normal and cell-face normal is large, UDS should be used.

Finally, the cell-face value of c can be expressed as:

$$c_j = \gamma c_\text{C} + (1 - \gamma) c_\text{D} \; , \tag{5}$$

where γ is a non-linear function of the profile of c, Courant number, and the orientation of the interface. Many choices are possible; some are demonstrated in [1] and [6].

Since the interface is not sharp but is rather smeared over one to three cells (like shocks in compressible flows), local grid refinement is important for an accurate resolution of the free surface. The refinement criterion is, however, simple: cells with $0 < c < 1$ need to be refined.

The discretized equation for c has the same form as all other equations and can be solved using the same linear equation solver. The iteration loop within one time step is extended for solving the equation for c after the pressure-correction equation is solved; the rest of the sequential solution algorithm remains the same.

4   Application examples

Several examples of application of the two methods described above can be found in [1] and [7] (sloshing, slamming, flow around ships); there, the accuracy of the methods was also analysed by performing a systematic grid refinement. It was shown that, when both methods are applicable, they are of nearly the same accuracy. We present here briefly results from some computations of flows relevant to process engineering which can only be computed by an interface-capturing method.

4.1 Flow in an Open Reservoir

In the first example we consider a plane (2D) reservoir which is initially full of water at rest. The width of the reservoir is 0.2 m and the height is 0.1 m. The water starts suddenly flowing in through a bottom opening whose width is 10% of the reservoir width; the upward inlet velocity is 1 m/s. Computation is performed using time steps of 0.2 ms.

(a)   (b)

(c)   (d)
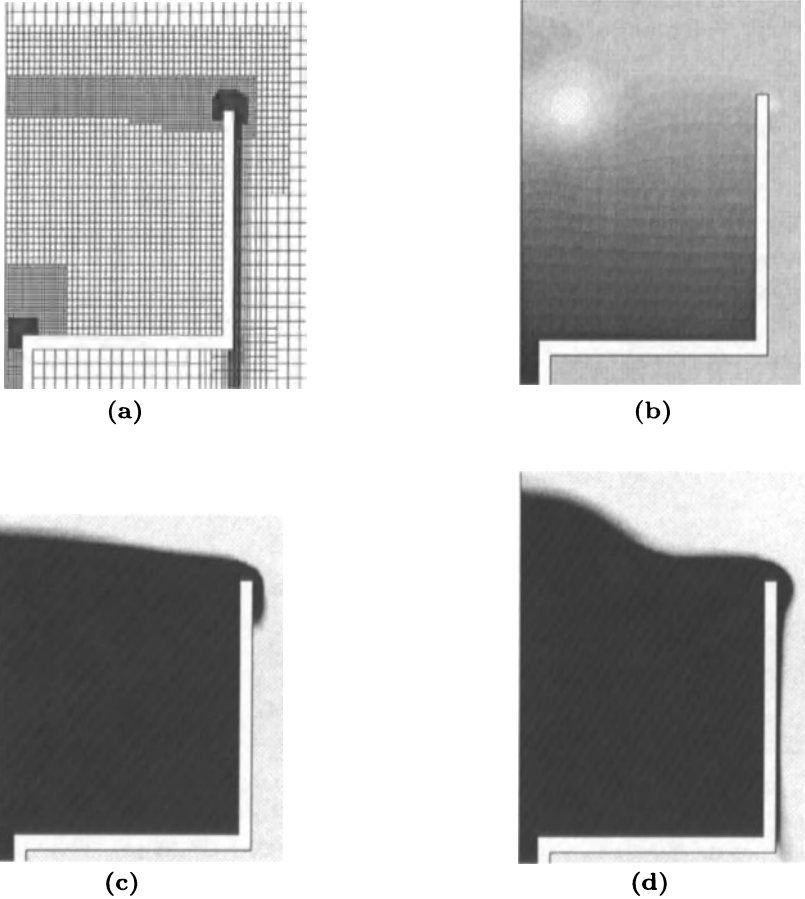
Fig. 2. Computation of flow in an open reservoir. **(a)** Part of the numerical grid. **(b)** Pressure distribution after 0.3 s. **(c)** Volume fraction after 0.2 s. **(d)** Volume fraction after 0.3 s (water is dark)

The inflow causes water to flow over the edge of the reservoir. The incoming jet creates a strong vortex at the sudden expansion, which travels upward towards the free surface; it can be seen in Fig. 2 as a low-pressure

region. The free surface rises substantially above the jet as the time goes on. The liquid film falling down the outer reservoir wall is accelerated due to gravity and becomes thinner. Space does not allow for a detailed analysis of this time-dependent flow; Fig. 2 is meant to indicate the capability of the interface-capturing method to handle this relatively difficult problem.

4.2   Sloshing in a Tank

In this example we demonstrate the possibility to compute flows involving more than two fluids with free surfaces using interface-capturing methods. At the initial time instant all fluids are at rest and occupy the space indicated in Fig. 3 (a); black indicates the heaviest and white the lightest fluid. This initial composition can not be preserved due to different fluid densities (1000 kg/m^3 the heaviest, 1 kg/m^3 the lightest), so they start moving. Figure 3 (b) shows the distribution of fluids shortly after the beginning of the simulation: the heaviest fluid tends to settle at the bottom of the tank, pushing other fluids up. After a while all motions die out and the fluids settle according to the stable stratification (heaviest at the bottom, lightest at the top; Fig. 3 (d)). This is a rather hard test for the discretization of the transport equation for volume fraction c: common differencing schemes lead to a substantial mixing of the species, while HRIC managed to keep them separated all the time, in spite of vigorous sloshing.
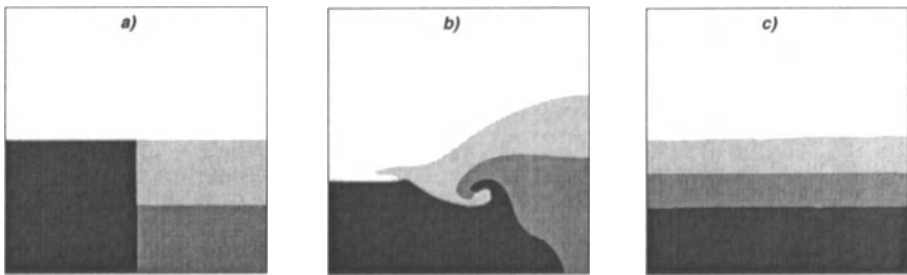
Fig. 3. Computation of sloshing with four fluids in a tank. **(a)** Initial distribution of fluids (black: heaviest, white: lightest). **(b)** Distribution of fluids shortly after the start of the simulation. **(c)** Distribution of fluids at the end of simulation

4.3   Curtain Coating

Coating is an important area of engineering activity in which multicomponent flows with free surfaces occur. We show below an example of computing curtain coating flow at Reynolds-number Re = 2 and capillary number Ca = 10. The substrate is moving with 1 m/s and the film thickness is 0.1 mm. The liquid is issuing from a slot 0.1 mm wide and located 1 mm above

the substrate; its exit velocity is also 1 m/s. After a while a steady flow is established, as shown in Fig. 4 (a). When the Reynolds-number is increased, the liquid begins to accumulate at the upstream side, flowing partly against the substrate movement. For Reynolds-numbers above five, the flow becomes unsteady and three-dimensional. Figure 4 (b) shows the shape of the liquid curtain and film at one instant of time for Re = 10, Ca = 10. Other kinds of coating flows (roll-coating, slot-coating etc.) can also be computed using interface-capturing methods.

(a)   (b)
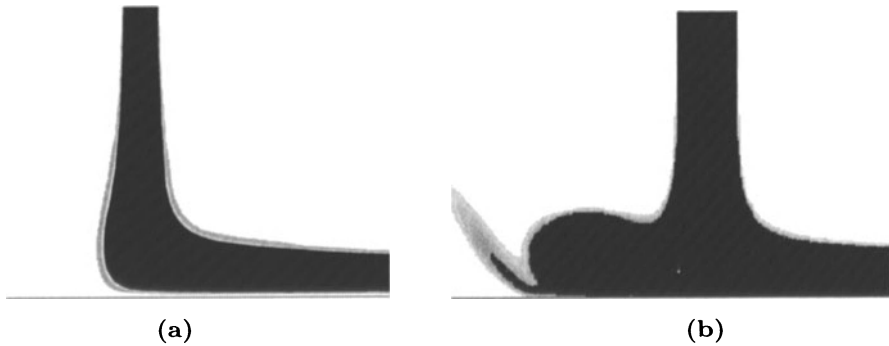
Fig. 4. Computation of curtain coating flow. **(a)** Liquid distribution at Ra = 2, Ca = 10. **(b)** Liquid distribution at Ra = 10, Ca = 10

References

1. Muzaferija, S., Perić M. (1998) Computation of Free Surface Flows Using Interface-Tracking and Interface-Capturing Methods. In: Mahrenholtz O., Markiewicz M. (Eds.) Nonlinear Water Wave Interaction. Computational Mechanics Publications, Southampton, Chap. 2
2. Brackbill, J.U., Kothe, D.B., Zemaach, C. (1992) A Continuum Method for Modelling Surface Tension. J. Comput. Phys. **100**, 335–354
3. Lafaurie, B., Nardone, C., Scardovelli, R., Zaleski, S., Zanetti, G. (1994) Modelling Merging and Fragmentation in Multiphase Flows with SURFER. J. Comput. Phys. **113**, 134–147
4. Hirsch, C. (1991) Numerical Computation of Internal and External Flows. Vols. I & II, Wiley, New York
5. Leonard, B.P. (1997) Bounded Higher-Order Upwind Multidimensional Finite-Volume Convection-Diffusion Algorithms. In: Minkowycz W.J., Sparrow E.M. (Eds.) Advances in Numerical Heat Transfer. Taylor and Francis, New York, 1–57
6. Ubbink, O. (1997) Numerical Prediction of Two Fluid Systems with Sharp Interfaces. PhD Thesis, University of London
7. Muzaferija, S., Perić, M. (1997) Computation of free-surface flows using finite volume method and moving grids. Numer. Heat Transfer, Part B **32**, 369–384

Simulation of Reactive Flow in a Partial Oxidation Reactor with Detailed Gas Phase and Surface Chemistry Models

Olaf Deutschmann[1], Lanny D. Schmidt[2], and Jürgen Warnatz[1]

[1] Interdisciplinary Center for Scientific Computing, University of Heidelberg, Im Neuenheimer Feld 368, D-69120 Heidelberg, Germany
[2] Department of Chemical Engineering and Materials Science, University of Minnesota, 421 Washington Ave. SE, Minneapolis, MN 55455, USA

Abstract. The formation of syngas (H_2 and CO) from methane in a rhodium coated monolith is studied as an example for the simulation of reactive flow in a partial oxidation reactor. A tube wall catalytic reactor, which serves as a model for a single pore of the monolithic catalyst, is simulated. The simulation is carried out using a two-dimensional flow field description coupled with detailed reaction mechanisms for surface and gas phase chemistry. The reactor is characterized by competition between complete and partial oxidation of methane. At atmospheric pressure, the complete oxidation products CO_2 and H_2O are formed on the catalytic surface in the entrance region of the catalytic reactor. At higher pressure, gas phase chemistry becomes important, resulting in an additional formation of these complete oxidation products further downstream and a decrease in syngas selectivity.

1 Introduction

The partial oxidation of methane, the main component of natural gas, in short contact time reactors has recently been shown to offer a promising route to convert natural gas into syngas (H_2 and CO) which subsequently can be converted to higher alkanes or methanol [1,2]. The catalytic reactors such as foam or extruded monoliths, wire gauzes, or sintered spheres, are coated with noble metals such as platinum and rhodium and can be run almost adiabatically with a residence time of approximately one millisecond. The short contact time guarantees a very high throughput using a small amount of catalyst and low energy and capital costs. The combustion products, CO_2 and H_2O, are formed beside of syngas. This highly exothermic combustion reaction provides the heat to operate the reactor auto-thermally at over 1000 K. Aside from this heat release effect, CO_2 and H_2O however are waste products of the process.

The industrial application needs the reactor to operate at elevated pressure, but high pressure experiments in conventional laboratories are expensive and dangerous because the very reactive mixture may explode. Hence,

detailed modeling and simulation will help to understand the complex inter-
actions between reactive flow and catalytic surface and can also be used to
explore reactor conditions which are beyond available experimental facilities.

In this study, the partial oxidation of methane in a tubular reactor with
a rhodium catalytic surface is studied at atmospheric and elevated pressure.
We use detailed models for the transport and both the gas phase and surface
reactions. The competition between partial oxidation, forming the desired
products H_2 and CO, and complete oxidation, forming CO_2 and H_2O, are
discussed. In contrast to a former study [4], the adsorption of H, O, and OH
radicals on the catalyst is taken into account in the present work.

2   Numerical Model

The numerical simulation is based on the CFD code FLUENT [3]. The code
is well established and can easily be used to set up fluid flow problems and
to solve them. However, modeling of detailed chemistry in current versions is
limited because of a maximum number of reactions and difficulties to handle
stiff chemistry. Furthermore, FLUENT's surface reaction model does not take
the surface coverage into account. Therefore, we coupled the FLUENT code to
external subroutines that model detailed gas phase and surface chemistry [4].
In this model, the state of the catalytic surface is described by its temperature
and the coverages of adsorbed species which vary in the flow direction.

Sketches of laboratory-scale short contact time reactor and tubular reac-
tor model are shown in Fig. 1. This tubular reactor serves as a model for
a single pore of the monolithic catalyst. Typical pore diameter varies be-
tween 0.25 and 1 mm, while the length of the catalytic part of the reactor
is typically 1 cm. In these small diameter channels the flow field is always
laminar. Experimental measurements indicate only small temperature gradi-
ents over the catalyst for situations studied in this work. In the simulation,
the catalytic wall is assumed to have a constant temperature. An adiabatic,
chemically inert wall, 1 cm in length, is used in the model to simulate the
experimentally used heat shields in front of and behind the catalytic section.

The tube wall catalytic reactor is described by the two-dimensional con-
servation equations using cylindrical geometry where the axial direction, z,
and the radial direction, r, are the independent variables. At the tube center-
line, a symmetry boundary condition is applied at which all variables have a
zero normal gradient, except the velocity component normal to the bound-
ary. This normal velocity vanishes at the symmetry boundary. A structured
grid is used for the simulation; the grid must be very fine around the cata-
lyst entrance to resolve the flow field. The total number of grid points varied
between 10^3 and 10^4 depending on reactor diameter and external conditions
such as temperature. The number of computational cells with surface reaction
boundaries varied between 30 and 100.
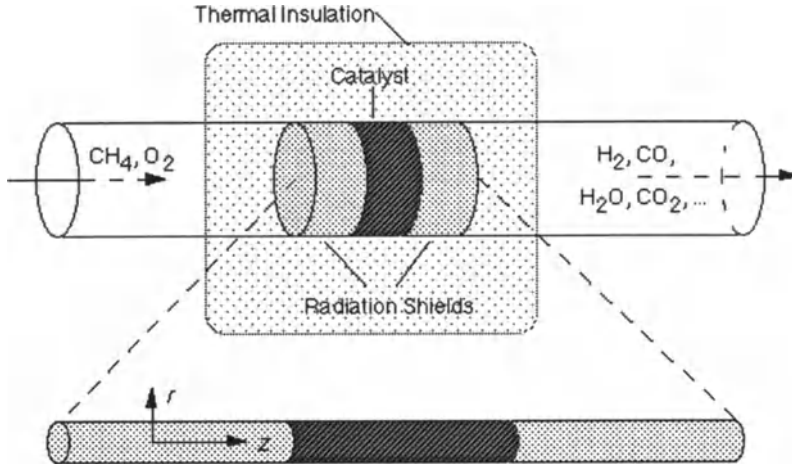
Fig. 1. Sketches of a laboratory-scale reactor (top) and the tubular reactor model representing a single pore of the monolith (bottom).

3   Chemical Reaction System

The formation of syngas from methane/oxygen mixtures on noble metal catalysts is characterized by the competition between a complete oxidation channel globally written as

$$CH_4 + 2\ O_2 \rightarrow CO_2 + 2\ H_2O \qquad \varDelta\,H_R = -\ 890\ kJ/mol$$
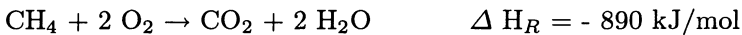
and a partial oxidation channel written as

$$CH_4 + 1/2\ O_2 \rightarrow CO + 2\ H_2 \qquad \varDelta\,H_R = -\ 36\ kJ/mol\ .$$
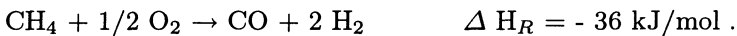
Appropriate catalytic material and residence time must be chosen to achieve high syngas selectivity. Rhodium coated foam catalysts with a residence time of approximately one millisecond are capable of producing high syngas selectivity ($\geq$90%) with a high methane conversion ($\geq$90%) [2].

The oxidation of methane can occur both on the surface and in the gas phase. It is generally assumed that the influence of gas phase chemistry on the overall conversion can be neglected at atmospheric pressure because the residence time is on the order of one millisecond, a time which is too short to ignite the mixture homogeneously. Furthermore, the radicals formed in the gas phase may recombine on the surface of the small diameter channel inhibiting a chain branching reaction. However, an increasing role of gas phase chemistry is expected with increasing pressure.

The gas phase reaction scheme is based on an elementary-step mechanism developed for hydrocarbon oxidation by Warnatz et al. [5]. This mechanism

is reduced by calculation of a homogeneous reactor under given conditions in order to keep the 2-D simulation tractable. The reduction results in a mechanism containing 164 reactions among 22 chemical species. The kinetic data of the pressure dependent reactions are chosen according to the reactor pressure. The crucial steps of the gas phase conversion of methane under given conditions are as follows: Hydrogen abstraction from the methane molecule, mainly by H, O, and OH radicals, which leads to CH_3 radicals. These radicals will either be oxidized to CO and CO_2 via intermediates or they can recombine to C_2H_6. Ethane can subsequently be dehydrogenated to ethylene. A radical pool must be established before gas phase conversion is fast enough to compete with catalytic conversion. Because of the fast complete oxidation channels, gas phase reactions are expected to decrease syngas selectivity. Aside from this decrease in reactor performance, gas phase chemistry has the potential of flames and explosions and must be understood from a reactor safety point of view.

The surface chemistry model is based on the reaction mechanism developed by Hickman and Schmidt [1] for high-temperature partial oxidation of methane in a short contact time reactor with a Rh coated foam monolith. This mechanism assumes dissociative methane and oxygen adsorption, formation of CO, CO_2, H_2, and H_2O via OH, and desorption of products. All reaction steps are reversible except methane adsorption and CO_2 desorption. It is assumed that oxygen is adsorbed non-competitively with other species whereas all other species are adsorbed competitively. More details such as reaction order can be found in the original work [1]. We extended this mechanism by three reactions being the adsorption of H, O, and OH radicals. The sticking coefficients for these steps are assumed to be unity.

4   Results and Discussion

The simulation of the following case will be discussed as an example of catalytic syngas formation in a partial oxidation reactor: a methane/oxygen mixture (volumetric ratio 1.8, 30% nitrogen dilution) flows at a uniform inlet velocity of 1 m/s and at 298 K into a cylindrical tube 3 cm in length with a diameter of 0.5 mm as sketched in Fig. 1. The 1 cm long catalytic wall has no temperature gradient in the axial direction. The catalyst is assumed to be a film on the wall. The wall is assumed to be adiabatic and chemically inert before and after the catalytic section. The conditions are close to experiments carried out by Bodke and Schmidt [2], in which a 65 ppi Rh/α-Al_2O_3 foam monolith was used as catalyst. An auto-thermal reactor temperature of 1073 K was measured by a Pt/Pt-13%Rh thermocouple with an accuracy of 150 K and no axial temperature gradients are reported. The total pressure now is 1.4 bar.

Figure 2 shows the calculated mass fractions of the reactants CH_4 and O_2 and the main products CO_2, H_2O, CO, and H_2 as a function of position in
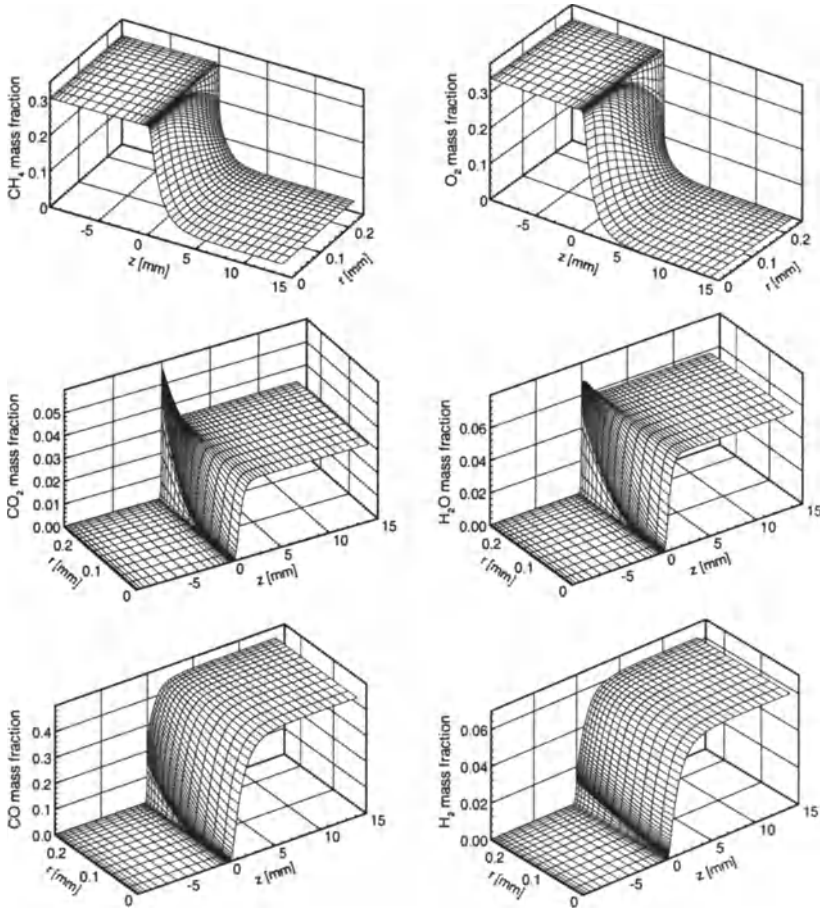
Fig. 2. Mass fraction of CH_4, O_2, CO_2, H_2O, CO, and H_2 as a function of position in the reactor.

the reactor. The catalytic part of the tubular reactor is between 0 and 10 mm axial position (z) and the radial position (r) is set to zero at the tube axis so that the catalytic wall is at r = 0.25 mm. The flow direction is from left to right. Methane oxidation starts directly at the catalyst entrance where large radial and axial gradients are formed. At the catalyst exit, however, there is still some methane left, the methane conversion being 90.1%. In contrast to methane, oxygen is completely (99.96%) consumed in the catalytic reactor.

The formation of hydrogen and carbon monoxide as the desired products and the formation of water and carbon dioxide as the undesired products compete at the catalyst entrance. The strong radial profiles indicate that methane is almost completely oxidized by surface reactions. In the beginning the oxygen concentration is large enough to quickly produce a significant amount of CO_2 and H_2O leading to steep radial concentration gradients of

these species. One millimeter downstream from the catalyst entrance, the complete oxidation channels practically extinguishes, although there is still a considerable oxygen in the gas phase. In this region oxygen is completely used for CO formation. It should be mentioned that the formation of syngas exceeds the formation of the combustion products even in the first part of the catalytic monolith. The higher diffusion coefficient of hydrogen compared to that of carbon monoxide leads to smaller radial gradients of H_2.
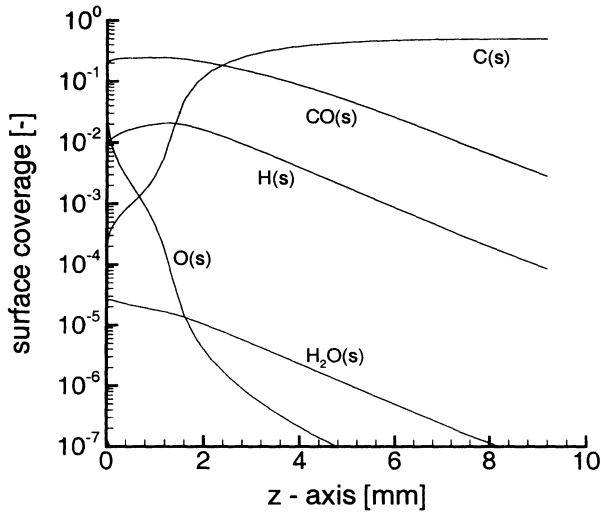
Fig. 3. Surface coverage as a function of the axial position (z) in the reactor. The axial position is zero at the catalyst entrance.

The role of gas phase chemistry in the overall conversion at atmospheric pressure, 1.4 bar, is revealed by a comparison of a simulation with only surface chemistry and a simulation with both surface and gas phase chemistry. Both simulations do not show any significant differences in total conversion and selectivity or in species concentration profiles. The number of radicals such as OH being 10^{-10} is too low to initiate gas phase conversion. Hence, gas phase chemistry does not play a significant role for syngas formation on Rh in the reactor at atmospheric pressure in the present model.

The calculation of surface coverage as a function of the axial position in the reactor is shown in Fig. 3. In the catalyst entrance region, the major surface species are CO(s), H(s), and O(s). In this region, the oxygen concentration is still large, explaining the CO_2 and H_2O formation. CO(s) is formed very fast from C(s) after dissociative methane adsorption. The rate-limiting step for water production is the OH(s) formation because OH(s) immediately leads to water due to the high hydrogen coverage, H(s). This fast OH(s) con-

sumption also results in a OH(s) coverage being lower than 10^{-7}. The activation energy for CO_2 formation is similar to that of OH formation which results in the production of CO_2. Farther downstream, the oxygen coverage rapidly decreases, and therefore, any adsorbed oxygen is consumed by CO(s) formation which desorbs before it can be completely oxidized.

The straight channel geometry is obviously a simplification of a foam monolith where the pores vary in diameter and length and may be connected. Furthermore, the surface reaction mechanism was established by fitting the experimental results to a one-dimensional model which neglects transport effects [1]. However, the calculated selectivities (C and H atom based, respectively) and conversion agree quite well with the experimental data: CH_4 conversion is 90.1% (experiment: 88.9%), O_2 conversion 99.96% (100%), H_2 selectivity 90.6% (91.0%), CO selectivity 95.5% (93.5%). The calculated temperature of the catalytic part of the reactor wall is 1070 K, which is determined from conversion and selectivity assuming a global adiabatic process.

The industrial application of short contact time reactors depends on the possibility of running the reaction at higher pressures. In laboratory experiments, measurements of the pressure dependence are limited due to safety and costs. Hence, the following simulation explores pressure conditions which are beyond available experimental facilities. Now, the reactor pressure is 10 bar, all other conditions are taken from the atmospheric pressure simulation as discussed above. The temperature of the catalytic wall is kept constant at 1070 K. Figure 4 exhibits gas phase profiles of CH_4, CO_2, CO, and OH mass fraction, all of them occur in surface and gas phase reactions as well. The reactor is not long enough for complete conversion of methane. There also is still a radial gradient of CO near the exit of the catalytic part of the reactor ($z = 10$ mm). In the catalyst entrance region, the complete oxidation takes place on the surface as already shown for atmospheric pressure. However, the formation of the combustion products continues behind this entrance region mainly due to gas phase reactions as shown for CO_2. The influence of the gas phase chemistry can also clearly be seen from the fact that the CO_2 formation continues behind the catalytic section of the reactor ($z \geq 10$ mm). OH radicals are an important precursor of complete oxidation of methane. They can not only be formed on the surface and consequently desorb into the gas phase, but also adsorb on the surface and recombine there. Figure 4 reveals that the catalytic surface (0 mm $\leq z \geq 10$ mm) acts as a sink for OH radicals which partly suppressed gas phase reactions. In comparison to the former study [4], where adsorption of O, H, and OH were not taken into account, the present model decreases the influence of gas phase chemistry.

Summarizing, gas phase reactions lead to an increase of undesired complete oxidation products at a pressure of 10 bar. A comparison between the full (surface plus gas phase reactions) simulation and one, which neglects gas phase reactions, reveals a decrease of syngas selectivity of only 1% to 3%. However, homogeneous reactions are expected to become more

and more significant at even higher pressure of 20 - 30 bar at which an industrial application should be operated. The surface chemistry of radicals, adsorption/recombination versus formation/desorption, plays an important role. Therefore, more reliable kinetics data of radical surface reactions are necessary to quantitatively understand reactor performance at high pressure.
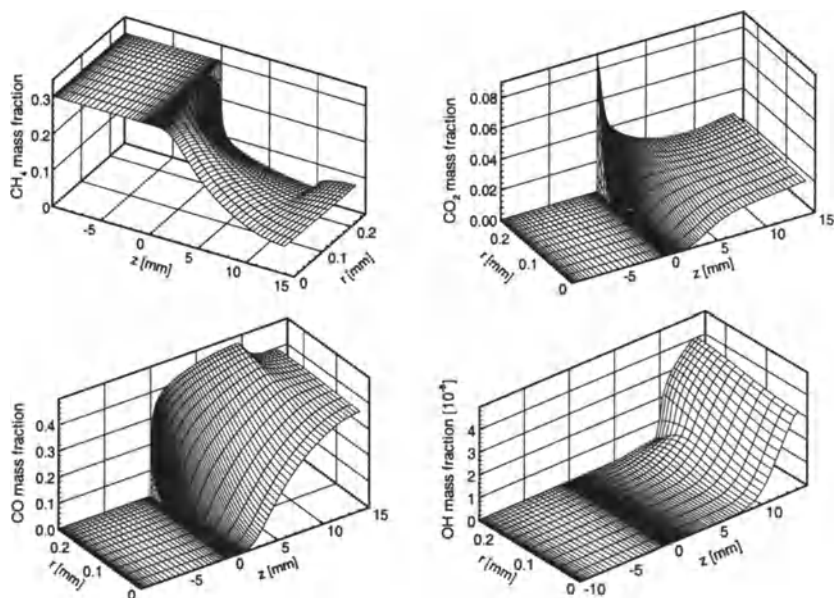
Fig. 4. Mass fraction of CH_4, CO_2, CO, and OH as a function of position in the reactor at 10 bar.

References

1. D. A. Hickman and L. D. Schmidt: Steps in CH_4 Oxidation on Pt and Rh Surfaces: High-Temperature Reactor Simulations, AIChE J. **39**, 1164 (1993)
2. A. Bodke and L. D. Schmidt: The Effect of Ceramic Supports on Partial Oxidation of Hydrocarbons over Noble Metal Coated Monoliths, J. Catalysis **179**, 138 (1998)
3. FLUENT 4.4, copyright FLUENT Inc., Lebanon, NH, 1997
4. O. Deutschmann and L. D. Schmidt: Modeling the Partial Oxidation of Methane in a Short Contact Time Reactor, AIChE J. **44**, 2465 (1998)
5. V. Karbach and J. Warnatz: publication in preparation.

Generalized Multiresolution Analysis on Unstructured Grids

Oliver Friedrich , Friederike Schröder-Pander and Thomas Sonar

Institut für Angewandte Mathematik, Bundesstraße 55, D-20146 Hamburg, Germany

Abstract. Efficiency of high-order essentially non-oscillatory (ENO) approximations of conservation laws may be drastically improved if ideas of multiresolution analysis are taken into account. These methods of data compression not only reduce the necessary amount of discrete data but can also serve as tools in detecting local low-dimensional features in the numerical solution. We describe the mathematical background of the generalized multiresolution analysis as developed by Abgrall and Harten in [2,5,6]. The functional analytic background is ultimately reduced to matrix-vector operations of linear algebra. We consider the important case of multiresolution analysis of cell average data which is used in finite volume approximations.

1   Introduction

One of the most important tasks of Computational Fluid Dynamics (CFD) is the design of highly accurate, robust and efficient numerical methods for the simulation of compressible fluid flow.

The most sophisticated numerical methods combining accuracy with robustness are finite volume approximations based on ENO recovery procedures, see for example [1,7,8]. These methods are a priori not very efficient since all of the flow field is treated with the same expensive algorithm: stencil selection, ENO recovery, solution of local Riemann problems, although this is only required across and close to shocks and contact discontinuities. Here the idea of the generalized multiresolution analysis (MRA) starts: The function or the discrete data is analyzed by decomposing it into different scale components. If some of the scale coefficients fall below a certain tolerance they are neglected which corresponds to data compression. The main advantage in comparison with wavelets is the ability to handle unstructured grids.

The mathematical background of the generalized multiresolution analysis can be found in [4]. Section 2 is concerned with the main body of this work, the description of MRA for cell averages on unstructured grids. Numerical results computed with the tools of section 2 are presented in section 3. More detailed information about the work and more numerical results can be found in [4].

2   Multiresolution of cell averages on unstructured grids

2.1   Volume agglomeration and multiresolution

We consider a triangulation Ω^k of a bounded domain $\Omega \subset \mathbb{R}^2$ where we assume the elements $\Omega_i^k \in \Omega^k$ to be bounded by polygons and furthermore that

$$\Omega = \bigcup_{i=1}^{N_k} \Omega_i^k,$$

i.e. $\partial\Omega$ is also assumed to be polygonal. We call the elements Ω_i^k the cells of the triangulation Ω^k.

On each of the cells we consider linear functionals

$$u \longmapsto\, <\lambda(\Omega_i^k), u> := \frac{1}{|\Omega_i^k|} \int_{\Omega_i^k} u(x)\, dx =: \overline{u}_i^k \in \mathbb{R}$$

which are referred to as cell averages. A sequence of triangulations $\{\Omega^k\}_{k=0}^L$ is defined by volume agglomeration following the algorithm described in [4]. In general two to four cells are agglomerated. The algorithm makes sure that the form of the cells is close to a circle.

We end up with a sequence $\{\Omega^k\}_{k=0}^L$ in which Ω^0 is the finest and Ω^L the coarsest triangulation, i.e. $N_{k+1} < N_k$. We now localize our point of view: The multiresolution analysis on the whole triangulation can be entirely described if we look on the local problem of the agglomeration of q fine cells $\Omega_i^k \in \Omega^k, i = 1, \ldots, q$, into one coarse cell $\Omega_j^{k+1} \in \Omega^{k+1}$.

2.2   Restriction and prolongation

The (nested) discretization $\mathcal{D}_k$ on the q cells Ω_i^k is described by

$$\mathcal{D}_k u := (\overline{u}_1^k, \ldots, \overline{u}_q^k)^T =: v^k \in \mathbb{R}^q =: V^k.$$

The representation D_k^{k+1} of the local restriction operator is defined by

$$D_k^{k+1} v^k := \frac{1}{|\Omega_j^{k+1}|} \sum_{i=1}^q |\Omega_i^k| \overline{u}_i^k = \overline{u}_j^{k+1} =: v^{k+1} \in \mathbb{R} =: V^{k+1}.$$

Since the prolongation is the right inverse of the restriction we are looking for a mapping $P_{k+1}^k : \mathbb{R} \longrightarrow \mathbb{R}^q$, such that the right inversity of the prolongation to the restriction operator

$$D_k^{k+1} P_{k+1}^k = 1$$

holds true.

Lemma 1. *A necessary and sufficient condition for $P_{k+1}^k := (\pi_1^k, \ldots, \pi_q^k)^T$ to be the representation of a prolongation operator is*

$$\sum_{i=1}^{q} |\Omega_i^k| \pi_i^k = |\Omega_j^{k+1}|.$$

From this observation it is easy to construct a variety of recovery operators $\mathcal{R}_{k+1}$.

2.3   Sophisticated recovery operators

More sophisticated classes of recovery operators can be found in polynomial recovery procedures used in ENO methods, see [1,7,8].
Here, a polynomial π_j of certain degree is computed on the coarse grid such that the recovery condition

$$< \lambda(\Omega_j^{k+1}), \pi_j >= \frac{1}{|\Omega_j^{k+1}|} \int_{\Omega_j^{k+1}} \pi_j(x)\, dx \stackrel{!}{=} \overline{u}_j \qquad (1)$$

holds. For the sake of simplicity the superscripts 'k' and 'k + 1' for π_j and $\overline{u}_j$, respectively, are neglected.
Now a recovery operator can be defined by means of

$$\mathcal{R}_{k+1} v^{k+1} = \pi_j.$$

It is shown in [4] that the property of Lemma 1 is fulfilled.
At no point reference was made to the polynomial structure of π_j. Thus, any recovery function π_j on Ω_j^{k+1} respecting the recovery condition defines a valid prolongation operator. For example polynomial recovery algorithms described in [1,7,8] belong to this category.
However, in this work polynomial recovery is implemented as follows. If $\alpha := (\alpha_1, \alpha_2)$ denotes a multiindex we want to compute quadratic polynomials on the coarse grid. Let ν denote the number of neighboring cells of Ω_j^{k+1} and their neighboring cells. We then require

$$\begin{aligned} < \lambda(\Omega_j^{k+1}), \pi_j > &= \overline{u}_j \\ < \lambda(\Omega_i^{k+1}), \pi_j > &= \overline{u}_i \qquad , i = 1, \ldots, \nu. \end{aligned} \qquad (2)$$

to hold for a second degree polynomial $\pi_j(x) = \sum_{|\alpha| \le n} a_\alpha (x - b_j)^\alpha$. Note that b_j denotes the barycenter of Ω_j^{k+1}. We always try to compute a quadratic polynomial. However, if ν is too small (this may happen at a few places at the boundary of the domain) we confine ourselves to a linear polynomial.
In general, the system (2) will be overdetermined since ν is larger than six almost everywhere. Solving (2) with a least squares approach results in a polynomial with $< \lambda(\Omega_i^{k+1}), \pi_j > \neq \overline{u}_i, i = j, 1, \ldots, \nu$, in general. Thus, we

have to enforce the conservation of the cell average on Ω_j^{k+1} by solving instead the system

$$< \lambda(\Omega_j^{k+1}), \tilde{\pi}_j > = 0$$
$$< \lambda(\Omega_i^{k+1}), \tilde{\pi}_j > = \overline{u}_i - \overline{u}_j \qquad , i = 1, \ldots, \nu$$

for a polynomial $\tilde{\pi}_j$ sligthly modified to ensure the recovery condition (1). A detailed description can be found in [4].

3   Numerical results

The test case presented here was carried out using the numerical solution of the double Mach reflection on a wedge by the WENO (weighted ENO) scheme; for a complete description see [3]. The sequence of coarser grids was computed using the agglomeration algorithm described in [4]. Further tests were analyzed in [4].

By storing the coefficients of the prediction errors that do not fall below a certain tolerance ε we restricted the discrete cell data from the finest to the coarsest grid. Thus, only the data on the coarsest grid and the remaining coefficients of the prediction errors after restriction had to be stored. We reconstructed the data from the coarsest to the finest grid in consideration of the remaining prediction error coefficients.

Note that not the scale coefficients, but rather the prediction errors were calculated and truncated. The computation of the scale coefficients is only of theoretical interest in the case of data compression:

- For computing the scale coefficients, a system of linear equations has to be solved for each coarse cell with sums of fine cell areas as matrix entries. This leads to a $1/h^2$ scaling that can hardly be handled on unstructured grids. This results in scale coefficients of different order of magnitude than the prediction errors. Thus, it is not recommendable to truncate the scale coefficients, because in this way the prediction errors cannot be sufficiently controlled.
- The computation of the scale coefficients does not reduce the required memory in all cases: Consider a coarse cell and its four fine cells. The calculation leads to a presentation of the errors with three scale coefficients. However, if there are only one or two prediction errors, more memory can be saved without operating with the scale coefficients.

Two different compression rates were calculated. These rates indicate the percentage storage saved in comparison to the storage of all coefficients of the prediction errors and the data on the coarsest grid (1. rate) and the storage of the data on the finest grid (2. rate), respectively:

1. Compression rate:

$$100 - \frac{100 \cdot (|\{\text{all cells of all grids}\}| - |\{\text{pred. errors} < \varepsilon\}|)}{|\{\text{all cells of all grids}\}|}$$

2. Compression rate:

$$100 - \frac{100 \cdot (|\{\text{all cells of all grids}\}| - |\{\text{pred. errors} < \varepsilon\}|)}{|\{\text{all cells of the finest grid}\}|}$$

In addition, the L_1- and L_∞-errors were calculated, as given in table 1. Inspection of the table also reveals that a sequence of five and nine grid levels was used, respectively, with ε being $\varepsilon = 10^{-2}, 10^{-3}$ and 10^{-4}. The level dependent ε_k are defined in [4].

Test case: Numerical solution of a WENO scheme

The finest grid on the wedge contains 63497 cells which corresponds to $h = 1/120$, the fifth 1607, and the ninth 39 cells.

In this test case many prediction errors had to be stored even on the finest grid which is clearly seen in figure 1. The first column of the figure shows the isolines of the cell data reconstructed locally on each cell. The errors shown right of the isolines refer to the transition from the function on the left to the one plotted below. Nevertheless this yields rather good compression rates of 75.67% and 60.27%, respectively, with $\varepsilon = 10^{-2}$. With decreasing ε the compression rates decrease dramatically: Setting $\varepsilon = 10^{-4}$ the 2. rate amounts to 0.97%. Thus, in this case the effort of the multiresolution algorithm does not remunerate. The comparison of the compression rates indicates that application of all nine grids is not recommendable. In all cases the usage of five grids leads to similar compression rates as application of nine grids.

# level	ε-var	L_1-error	L_∞-error	1. cpr.-rate	2. cpr.-rate
	10^{-2}	2.22e-03	2.93e-02	75.67%	60.27%
5	10^{-3}	1.37e-04	2.47e-03	53.17%	23.53%
	10^{-4}	3.96e-06	2.10e-04	39.36%	0.97%
	10^{-2}	2.80e-03	3.00e-02	75.89%	60.25%
9	10^{-3}	1.68e-04	3.04e-03	53.27%	22.96%
	10^{-4}	4.86e-06	2.12e-04	39.49%	0.23%

Table 1. Numerical solution of a WENO scheme: errors and compression rates

4   Conclusions

We have presented a fairly general theory of generalized multiresolution analysis based on the work of Harten and Abgrall. Our central interest is in the analysis of discrete data from Computational Fluid Dynamics and hence the multiresolution of cell averages appears to be the main topic. All operations can be broken down to simple matrix-vector arithmetic.

In particular, the representation of the scale coefficients is done with the help of basis matrices (not presented here, see [4]). A generally applicable agglomeration algorithm for arbitrary triangulations was given and a reliable and robust prolongation procedure on unstructured grids was developed. Numerical experiments document the ability of the algorithms described to accurately detect discontinuities and to allow massive data compression.

References

1. R. Abgrall. On Essentially Non-Oscillatory Schemes on Unstructured Meshes: Analysis and Implementation. *J.Comp.Phys.*, 114:45–58, 1994
2. R. Abgrall and A. Harten. Multiresolution Representation in Unstructured Meshes: I. Preliminary Report. *CAM Report 94-20, University of California, Los Angeles*, 1994
3. O. Friedrich. Weighted Essentially Non-oscillatory Schemes for the Interpolation of Mean Values on Unstructured Grids. *J.Comp.Phys.*, 144:194–212, 1998
4. O. Friedrich and F. Schröder-Pander and T. Sonar. Generalized Multiresolution Analysis on Unstructured Grids. *Hamburger Beiträge zur Angewandten Mathematik, Internal Report, University of Hamburg*, 1998
5. A. Harten. Multiresolution Representation of Data. *CAM Report 93-13, University of California, Los Angeles*, 1993
6. A. Harten. Multiresolution Representation of Data: II. General Framework. *CAM Report 94-10, University of California, Los Angeles*, 1994
7. A. Harten and S.R. Chakravarthy. Multi-Dimensional ENO Schemes for General Geometries. *ICASE Report No. 91-76*, 1991
8. T. Sonar. *Mehrdimensionale ENO-Verfahren*. B.G.Teubner, Stuttgart, 1997

Computational fluid dynamics applied to chemical reaction engineering

J.A.M. Kuipers and W.P.M. van Swaaij

Twente University of Technology, Department of Chemical Engineering
PO Box 217, 7500 AE Enschede, The Netherlands

Abstract. In this paper a brief review will be presented on the application of Computational Fluid Dynamics (CFD) to the field of Chemical Reaction Engineering (CRE) with emphasis on multiphase flow due to its practical importance. The theoretical framework will be briefly discussed together with available computational strategies for dispersed multiphase flows. Finally some typical results will be presented for one particular class of mutiphase flow.

1 Introduction

In the last few decades Computational Fluid Dynamics (CFD) has become a very powerful and versatile tool for the analysis and solution of problems which are of considerable interest to the chemical engineer. Due to ongoing developments in both numerical algorithms for fluid flow and computer hardware it can be anticipated that this tool will become increasingly important for the analysis and improvement of existing process equipment and design of new process equipment.

2 Theoretical framework

For each continuous phase k present in a multiphase system consisting of N phases, in principle the set of conservation equations for mass, momentum and thermal energy can be applied. If one or more of the N phases consists of solid particles, the Newtonian conservation laws for linear and angular momentum should be used instead. The resulting formulation of a multiphase system will be termed the local instant formulation. Through the specification of the proper initial and boundary conditions and appropriate constitutive laws for the viscous stress tensor the hydrodynamics of a multiphase system can in principle be obtained from the solution of the governing equations. However, for most systems of practical interest the analysis of multiphase systems on basis of the local instant formulation is intractable, even for existing and near-future super-computers, and consequently some kind of simplification must be made.

2.1   Eulerian approach

The aforementioned simplification can be achieved through a continuum mathematical description of the multiphase system. The derivation of the continuum equations is usually based on spatial averaging techniques where the point-hydrodynamic variables are replaced by local averaged variables. For non-reactive multiphase isothermal systems involving laminar flow the conservation equations for mass and momentum are respectively given by:

$$\frac{\partial}{\partial t}(\rho_k) + (\nabla \cdot \rho_k \overline{u}_k) = 0 \tag{1}$$

$$\frac{\partial}{\partial t}(\rho_k \overline{u}_k) + (\nabla \cdot \rho_k \overline{u}_k \overline{u}_k) = -\varepsilon_k \nabla p - (\nabla \cdot \varepsilon_k \tau_k) + \sum_{l=1}^{N} \overline{M}_{kl} + \rho_k \overline{g} \tag{2}$$

where ρ_k, $\overline{u}_k$, ε_k and τ_k represent respectively the macroscopic density, velocity, volume fraction and viscous stress tensor of the kth phase, p the pressure, $\overline{M}_{kl}$ the interphase momentum exchange term between phase k and phase l.

2.2   Eulerian-Lagrangian approach

In multiphase systems involving one or more dispersed phases an alternative to the aforementioned complete continuum representation is possible by adopting a Lagrangian description for these phases. The advantages of this mixed Eulerian-Lagrangian approach are its greater generality and flexibility with respect to the incorporation of microscopic transport phenomena whereas its relatively high (compared to completely Eulerian approaches) computational load constitutes its most important disadvantage. Sokolichin et al. (1997) have compared the Euler-Euler versus the Euler-Lagrange approach for dispersed gas-liquid two-phase flow and found only identical results in case proper numerical schemes for the convective transport terms were employed in their Euler-Euler model. If a Lagrangian description is adopted to represent the dispersed phase, for each individual particle (or bubble or droplet) an equation of motion is solved:

$$\frac{d}{dt}(m_i \overline{v}_i) = \sum \overline{F}_i \tag{3}$$

where m_i, $\overline{v}_i$ represent respectively the mass and velocity of the ith particle and $\sum \overline{F}_i$ the sum of the forces acting on the ith particle. Forces due to gravity, drag, virtual mass, vorticity in the continuous phases and electrical forces can be included in this term. The particle position vector is calculated from:

$$\frac{d}{dt}\overline{x}_i = \overline{v}_i \tag{4}$$

The solution of differential equations (3) and (4) can be obtained with standard numerical integration techniques. Depending on the volume fraction

of the dispersed phase one-way coupling or two-way coupling between the dispersed phase and the continuous phase prevails. In systems involving (turbulent) multiphase flow at very small volume fraction of the dispersed phase, say smaller than 10^{-6}, one-way coupling may be assumed. At such low volume fractions the effect of the particles on the turbulence structure in the continuous phase is negligible while particle-particle interactions (i.e. collisions) do not play a role. For systems with higher volume fractions (10^{-6} to 10^{-3}) the turbulence structure of the continuous phase is influenced by the dispersed phase while particle-particle interaction can still be neglected and two-way coupling between the phases has to be accounted for. With respect to the effect of the dispersed phase on the turbulence structure it can be mentioned that the ratio of the particle response time τ_p and the Kolmogorov time scale τ_K determines whether the particles will enhance the production rate of turbulence energy ($\tau_p/\tau_K > 100$) or increase the dissipation rate of turbulence energy ($\tau_p/\tau_K < 100$). For still higher volume fractions of the dispersed phase particle-particle interaction (i.e. collisions) becomes important and four-way coupling has to be accounted for. In this case an integrated modelling approach is required combining features of Molecular Dynamics (MD), to effectively deal with the huge number of particle-particle and/or particle-wall collisions, and Computational Fluid Dynamics (CFD) to obtain the velocity distribution in the continuous phase (see section 4).

3   Computational strategies for the Eulerian Lagrangian approach

For dispersed multiphase flow roughly speaking three different situations and corresponding computational strategies can be distinguished (also see Figure 1):

case a   case b   case c
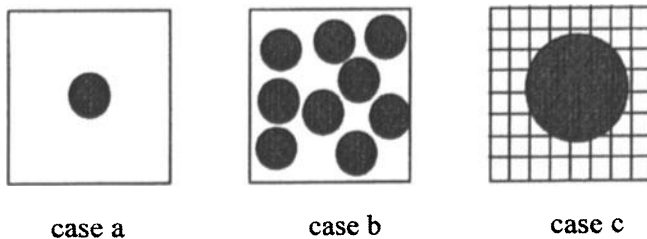
Fig. 1. Different situations that can be distinguished in modeling dispersed multiphase flow.

a) dilute flows where on the average less than one particle is present in a computational cell.

b) dense flows where a relatively high number of particles are present in a computational cell.
c) dilute or dense flows where a particle contains a large number of computational cells.

where it should be mentioned that the dispersed phase could also consist of drops or bubbles which could, in principle, be deformable. The situation for case a) arises when suspensions are relatively dilute and the particles are small. Depending on the exact value of the volume fraction of the dispersed phase one-way coupling or two-way coupling prevails (Pan and Banerjee (1996a)). With one-way coupling particles are being moved in response to the fluid motion without feeding bac effects to the continuous phase whereas in two-way coupling feedback effects are taken into account. As discussed in detail by Pan and Banerjee (1996a) care must be taken to correctly implement two-way coupling. For two-way coupling, different computational strategies are used depending on the fact whether there is only one particle in a computational cell or many. In case b) we deal with dense flows and in our computational strategy four-way coupling has to be accounted for since there is not only mutual interaction between the suspended particles and the continuous phase but also particle-particle interactions (i.e. collisions). The example presented in section 4 belongs to this class of multiphase flow. In case c) the relative size of the particles (with respect to the computational cells) is large enough that they contain many hundreds or even thousands of computational cells. It should be noted that the geometry of the particles is not exactly represented by the computational mesh and special, approximate techniques (i.e. body force methods) have to be used to satisfy the appropriate boundary conditions for the continuous phase at the particle surface (see Pan and Banerjee (1996b)). Despite this approximate method, the empirically known dependence of the drag coefficient versus Reynolds number for an isolated sphere could be correctly reproduced using the body force method. Although these computations are at present limited to a relatively low number of particles they clearly have their utility because they can provide detailed information on fluid-particle interaction phenomena (i.e. wake interactions) in turbulent flows.

4   Results

In this section a few illustrative computational results will be presented which have been obtained for dispersed gas-liquid two-phase flow. For this type of two-phase flow Delnoij et al. (1997) developed a detailed hydrodynamic model based on a mixed Eulerian-Lagrangian approach. Their model describes the time-dependent motion of small, spherical gas bubbles in a bubble column operating in the homogeneous regime where all relevant forces acting on the bubble (drag, virtual mass, lift and gravity forces) were accounted for. Direct bubble-bubble interactions were accounted for via an interaction model

which resembles the collision approach followed by Hoomans et al. (1996) to model gas-fluidized beds. Delnoij et al. investigated the effect of the bubble column aspect ratio on the prevailing flow structure and compared their computational results with experimental data reported by Chen et al. (1989). In Table 1 the important parameters used in their numerical simulations are summarized. Chen et al. reported a transition in the gas-liquid flow pattern in case the aspect ratio of the column changed from two to four. For an aspect ratio of two the Gulfstream type of liquid circulation was predicted whereas for an aspect ratio of four a highly dynamic liquid flow pattern with multiple vortices was computed. From computer animations Delnoij et al. could observe that these vortices were generated at the free surface. Furthermore these vortices were found to be positioned staggered with respect to each other in the column. In part these computational results were supported by Chen's findings. The only major difference with the experimental observations of Chen et al. was the fact that the aforementioned transition already occurred at an aspect ratio of one. This discrepancy is most likely due to the two-dimensional nature of the model developed by Delnoij et al. As an illustration in Figure 2 a few plots of instantaneous bubble configurations and liquid phase velocity fields are shown for bubble columns with an aspect ratio of 2.0 (top) and 7.7 (bottom). From this figure it can be clearly seen that the flow structure is significantly affected by the column aspect ratio.

5   Conclusions and future research

The variety and degree of complexity of systems encountered in industrial practice demands for an integrated modelling approach where models with increasing degree of sophistication should be used to feed models which invoke sub-models with a strong empirical base. For dispersed multiphase flows mixed Eulerian-Lagrangian models offer the possibility to develope closure laws which can subsequently be used in a multi-fluid framework suited for the simulation of macroscopic systems of interest. In this connection also the Lattice Boltzmann method and Stokesian dynamics should be mentioned which offer great potential for simulation of concentrated suspensions in which hydrodynamic interaction has to be accounted for. Turbulence modelling of multiphase flow systems requires major attention in the near future. Also the development of closure laws for phenomena taking place in the vicinity of interfaces such as coalescence, break-up and accumulation of impurities should be considered in more detail. Once these requirements have been met, in principle it would be possible to predict a.o. flow regime transition and the spatial distribution of the phases with confidence which is of utmost importance to the chemical engineer dealing with the design of (novel) multiphase reactors.
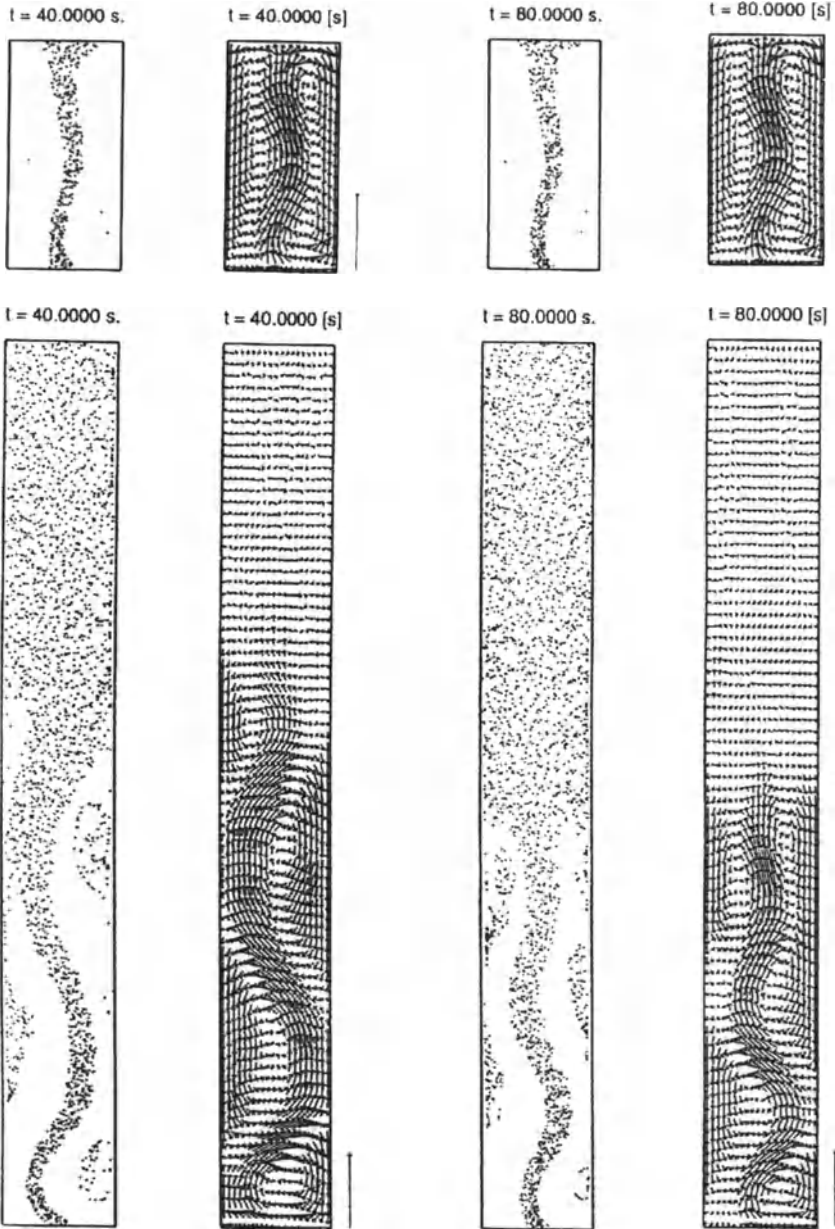
Fig. 2. Effect of bubble column aspect ratio L/D on the flow structure (top: L/D = 2.0, Bottom L/D = 7.7). The reference vector corresponds to a liquid phase velocity of 1.0 m/s.

Table 1. Parameter values used in the numerical simulations of [2].

Column dimensions		
Width	0.1750	m
Height		
- L/D = 1.0	0.1750	m
- L/D = 2.0	0.3500	m
- L/D = 4.8	0.8400	m
- L/D = 7.7	1.3475	m
- L/D = 11.4	1.9950	m
Superficial gas velocity	0.035	m/s
Physical properties (air-water)		
- Density liquid	1000	kg/m^3
- Viscosity liquid	0.001	$kg/(m.s)$
- Density Gas	1.2	kg/m^3
- Bubble diameter	0.002	m
Number of computational cells in lateral direction	20	
Number of computational cells in vertical direction		
- L/D = 1.0	20	
- L/D = 2.0	40	
- L/D = 4.8	96	
- L/D = 7.7	154	
- L/D = 11.4	228	
Time step	0.005	s

Notation

D	Lateral dimension,m	$\overline{F}_i$	Force acting on i^{th} particle, $kg.m/s^2$
$\overline{g}$	Gravitational force per unit mass, m/s^2	L	Vertical dimension, m
m_i	Mass of ith particle, kg	$\overline{M}_{kl}$	Momentum source term due to interaction between phase k and phase l, $kg/(m^2.s^2)$
p	Pressure, Pa	t	Time, s
$\overline{u}$	Velocity, m/s	$\overline{v}_i$	Velocity of ith particle, m/s

Greek symbols

ε	Volume fraction	ρ	Density, kg/m^3
τ	Stress tensor, Pa	τ_p	Particle response time, s
τ_K	Kolmogorov time scale, s		

Subscripts

i	Particle index number	k	Referring to k^{th} phase in multiphase system
K	Kolmogorov	p	Particle

Superscripts

T	Transpose	-	Vector quantity

Operator

∇	Gradient	$\nabla.$	Divergence

References

1. Chen, J.J.J., Jamialahmadi, M. and Li, S.M., 1989, Effect of Liquid Depth on Circulation in Bubble Columns: A Visual Study, Chem. Eng. Res. Des., **67**, 203–207.
2. Delnoij, E., Lammers, F.A., Kuipers, J.A.M. and van Swaaij, W.P.M., 1997, Dynamic Simulation of Dispersed Gas-Liquid Two-Phase Flow Using a Discrete Bubble Model, Chem. Engng. Sci., **52**, 1429–1458.
3. Hoomans, B.P.B., Kuipers, J.A.M., Briels, W.J. and van Swaaij, W.P.M., Discrete Particle Simulation of Bubble and Slug Formation in a Two-Dimensional Gas-Fluidised Bed: A Hard Sphere Approach, 1996, Chem. Engng. Sci., **51**(1), 99–118.
4. Pan, Y. and Banerjee, S., 1996a, Numerical Simulation of Particle Interactions wit Wall Turbulence, Phys. Fluids, **8**(10), 2733–2755.
5. Pan, Y. and Banerjee, S., 1996b, Numerical Investigation of the Effects of Large Particles on Wall-Turbulence, submitted to Phys. Fluids.
6. Sokolichin, A., Eigenberger, G., Lapin, A. and Lübbert, A., 1997, Dynamic Numerical Simulation of Gas-Liquid Two-Phase Flows. Euler-Euler versus Euler-Lagrange, Chem. Engng. Sci., **52**, 611–626.

CFD simulation tool for the systematic examination of effects on band spreading in large radial columns

M. Lisso[1], G. Wozny[1], Y. Beste[2], and W. Arlt[2]

[1] TU Berlin; Institut für Prozeß und Anlagentechnik; Sekr. KWT 9; Str. des 17. Juni 135; 10623 Berlin

[2] Tu Berlin; Institut für Verfahrenstechnik; Sekr. TK 7; Str. des 17. Juni 135; 10623 Berlin

Abstract. Especially the scale up of analytical chromatographic columns for preparative purposes in combination with complex separation conditions leads to non-trivial problems. CFD-Simulation together with basic experiments is an efficient tool to clear up and to optimise the multiple coherent processes in fixed bed columns. For detailed examinations of the inner column effects a three dimensional model for a fixed bed chromatographic column was developed by using the commercial CFD software package FLUENT^{TM}. Based on the results of the CFD-Simulation we want to present the interdependence between the column diameter and the height of a theoretical plate [HETP]. Furthermore we will specify the effect of the inlet and outlet distributors (frits) on the HETP. In our simulations we could show the possibility to optimize the separation performance of the column by subcooling the feed below the temperature of the column wall.

1 Introduction

When using large-diameter high-performance liquid chromatography columns, factors such as fluid dynamic effects at the inlets and outlets [1,2], temperature distribution effects [2-6] and heterogeneity of the packed bed [7-9] play an important role. Because of these reasons the scale up becomes a non-trivial process [9,10]. In this paper the results of the distribution simulation of a non retarded substance will be shown by using a Computational Fluid Dynamics (CFD) software package. This model is based on following assumptions: isothermal conditions and a homogenous fixed bed. Under the above, columns with length of 25 cm and diameter of 1 cm, 5 cm and 10 cm were simulated. Further, the frit quality was defined and the results of varying it were examined. As the second step, the energy balance including the pressure loss as a source term and a temperature dependent viscosity were taken into consideration. Like in a real column it could be shown that a temperature difference between the column wall and the inlet stream leads to a change of the radial and axial distribution of the tracer. Based on this effect it's possible to predict an optimal process temperature difference to maximise the separation performance of the column. Based on the simulation data the separation performance was analysed by using the method of moments [2,9].

As a numerical expression of the separation performance, the number of theoretical separation units (NTU) of the integral tracer profiles at the outlet just beyond the column were compared.

2   Modelling and Simulation

The simulations were conducted under the following assumptions:

- Laminar Flow
- No adsorption
- Homogenous distribution of the fixed bed inside of the column
- Axially symmetrical features of the fixed bed

The Momentum Balance was solved to calculate the velocity field inside of the column. For this matter the Navier Stokes Equation was extended in the radial and axial directions by a pressure loss term Eq. (1) (Darcy's law).

$$\frac{\partial p}{\partial z} = -\frac{v}{\alpha}W \tag{1}$$

Earlier experiments have proved the validity of Eq.(1) that states that the pressure loss is a linear function of the viscosity and velocity in a fixed bed. Further the viscosity was implemented as a second order function of the Temperature to depict the interaction between the Energy Balance and the Momentum Balance. The degree of freedom α in Eq. (1) was used to adapt the special features of the considered fixed bed. To determine α experimental data of the pressure loss of a 6 cm x 21.7 cm column were used [11]. The model of the frit was also based on the extended Navier Stokes equation. The axial value of α for the frit was determined by experimental data too. For this the pressure loss at the same column like above, with frits, but without fixed bed was measured [11]. The frit quality Q Eq. (2) was changed by varying the ratio of the radial to the axial α-value in the range of 2 to 400.

$$Q = \frac{\alpha_{ax}}{\alpha_{rad}} \tag{2}$$

First experimental results showed that the range of technical frits is between 20 and 300. The quality Q of metal web frits was up to 10 times higher compared to sintered frits. The thickness of the frit remained constant at 5 mm in all simulations. This model aims to examine the effect of varying the boundary conditions (BC) at the column wall on the simulated tracer profiles. Here the different BCs are defined by Eq. (3) and (4) which were implemented and the results compared.

$$\left.\frac{\partial w}{\partial r}\right|_{r=R} = 0 \tag{3}$$

$$w|_{r=R} = 0 \tag{4}$$

Other effects on the band spreading like microscopic velocity distributions, the eddy-diffusion and so on were considered in the component balance equation by using axial and radial dispersion coefficients besides the convection term. Similar to the component balance the energy balance considered the convection term, the conductivity term and the pressure loss over the column as a source term. To calculate the fluid dynamic transportation process the commercial software package FLUENT[1] was used. A structured grid was generated to simulate the columns of sizes 1 cm x 25cm; 5 cm x 25 cm and 10 cm x 25 cm. The lengths of the inlet pipe and the outlet pipe were kept constant at 1 cm, at the two ends of the column. The following parameter studies were used to examine the effect on the macroscopic velocity field, on the tracer distribution and on the separation performance:

1. Different column diameters with a constant frit quality for an isothermal column
2. Different frit qualities with a constant column diameter for an isothermal column.
3. Effect of the temperature difference between the inlet stream and the column wall on the separation performance.

The procedure of simulation was as following:

1. Calculate the stationary solution of the momentum balance. The velocity was set to zero as an initial condition.
2. Calculate the stationary solution of the energy balance. The temperature inside the column was set to the same temperature of the column wall as an initial condition.
3. Dynamic simulation of the tracer transportation inside of the column. The unleaded column was used as an initial condition for the component balance equation

To validate the simulation results the radial tracer distributions were qualitatively compared with tracer profiles in a real column.

3   The Velocity Field

The stationary solution of the Momentum balance leads to the velocity distribution of the column. As a result the columns can be subdivided into three zones: an inlet zone, an outlet zone and a central zone fig. (1), which is not influenced by the effects of the

Fig. (1) Simulation results of velocity zones in HPLC-Columns

in- and outlet. For this zone the result of the calculation was a plug flow profile of the axial velocity across the whole cross section of the column. The

---

[1] Trademark of FLUENT INC.

difference between the theoretical average velocity and the plug-flow velocity was observed to be below 0.1the velocity profile is a function of the axial and radial co-ordinate in the inlet and outlet zone.

A very important factor for the separation performance of a column is the length of the inlet and outlet zone. It effects the curvature of the tracer profile in the column. In conclusion it leads to a remixture near the outlet and to a decrease in the separation performance.

The following criterion was defined to determine the end of the inlet zone:
- The whole axial velocity field had to be situated in a small stripe of ±0.5% around the average axial velocity.

The effect of the column diameter on the length of the inlet zone is shown in the Fig. (2).

Effect of the column diameter on the length of the inlet zone with a constant frit quality at Q = 40

The increase in the length of the inlet zone was much more, when the column diameter was changed from 5cm to 10 cm than from 1cm to 5cm. As a consequence the curvature of the radial tracer distribution profiles increased non linearly too.
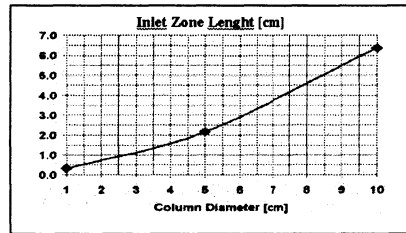
Fig. (2) Effect of the column diameter on the length of the inlet zone with a constant frit quality at Q = 40

4   Influence of the BC at the Column Wall on the Velocity Field

The effect of changing the BCs defined by the Eqs. (3) and (4) on the simulated tracer profiles was examined. Henceforth two simulations with the same numeric and fluid dynamic parameters but different BCs were carried out. Based on the simulation results the retention time and the HETP distribution at different locations inside and at the outlet just beyond the column were calculated to examine the effect of changing BCs. It was observed that the retention times arrived at by using Eq. (3) were always marginally higher. The above is the result of smaller cross flow area and the resultant higher axial velocity achieved by applying Eq. (4). Since HETP is a function of the retention Time, similar differences in the values of the HETP were also observed. In conclusion it can be said that the effect of changing BCs at the column wall on simulated tracer profile can be ignored provided there are enough grid points in the radial direction. For the following calculations we used 4 grid points per mm in the radial direction, 2.8 grid points per mm for the frit and 1.46 grid point per mm for the fixed bed in the axial direction.

5   Qualitative Validation of the Simulation Results

The qualitative judgements of the simulation results are based on [2] which used actual experiments. Fig. (3) illustrates the experimental results of four tracers profiles passed through an isothermal column with a diameter of 6 cm.
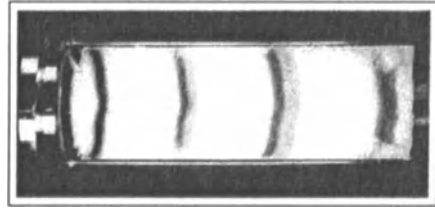
Fig. (3) Distribution of four tracers passing through a real column [2]

The direction of the velocity field in Fig. (3) goes from left towards right. The following qualitative features are to be observed:

1. The tracer profiles are parabolic.

2. The band spread increases as it passes through the column.

3. At the end of the column first the core of the tracer breaks through the outlet pipe, followed by the outer radial zones.

4. The change of the curvature of the profile is negligible as it passes through the column.

5. Near the column wall no increase in the band spread was observed in comparison to the band spread along the radial axis of the column.

A. Brandt's paper also concluded that the effect of the heating of the column core by flow friction on the tracer profile is several times less than the inlet and outlet effects [2]. Based on the observations 1 to 5, a few more criteria for simulation modelling and the validation of the simulation results may be derived. As mentioned in point 5, the column wall doesn't have any effect on the curvature of the tracer profile inside of the column. Further there is no maldistribution near the wall because of unequal packing like in fixed beds with bigger particle diameters. It may be concluded that the simulation results are independent of the BC at the column wall. Based on point 4, the assumption of a homogenised fixed bed and an axially symmetrical distribution in the model is in agreement with the reality. The covered axial way of the tracer inside the column can be calculated as a integral of the local axial velocity. In a parabolic velocity field the differences between covered axial distance would increase for different radial co-ordinates wich increase with time. As a result the curvature of the profile would increase also. This reflection contradicts point 4 of the observations. But the same reflection with a plug flow profile of the axial velocity fulfils point 4. So it can be concluded that the plug flow profile obtained as a result of the simulation inside the column corresponds with a real chromatography column.

6   Simulation Results by Varying the Column Diameter

In the following section the simulated tracer profiles which were obtained by columns of different diameters namely 1 cm, 5 cm, and 10 cm will be discussed.

In Fig. (4) the simulated tracer profiles inside the columns with diameters of 1 cm, 5 cm and 10 cm are shown. The flow direction is again from left to right. The frit quality Q remained constant at 40. The tracer profiles have been recorded at a normalized retention time of 0.17, 0.5 and 1.0 after the injection of the tracer. For all simulated tracer profiles the points 1 to 5 were observed to have met. A comparison of the simulation results leads to the following conclusions:
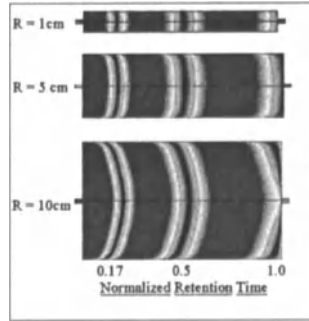
Fig. (4) Simulated tracer profiles of a column with diameters of 1 cm, 5cm and 10cm

- The curvature of the profiles increased as the diameter of the column increased because of the increase of the inlet zone length in the bigger columns.
- At the outlet, the depth of the curvature of the profiles in the bigger columns and the larger frit diameter leads to a bigger band spreading and a longer tailing in the integral tracer profile behind the column. This phenomena is represented in Fig. (5).

Fig. (5) Effect of the column diameter on the integral tracer profiles in the outlet of the column Based on the integral tracer profiles the NTU were calculated. The percentage change of NTU was related to the results of the 1 cm column and can be seen in Fig. (6).
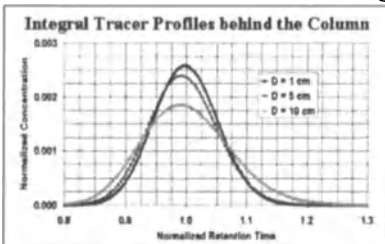
Fig. (5) Effect of the column diameter on the integral tracer profiles in the outlet of the column
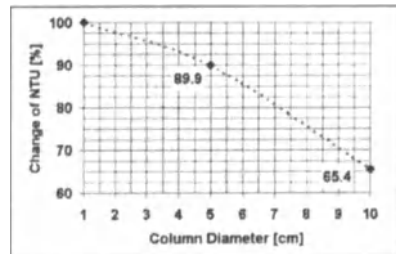
Fig. (6) Change of the NTU by different Diameters

As the diameter increased from 1cm to 5cm, the NTU decreased by 10% and by 35% when the diameter increased from 1 cm to 10 cm. Moreover the

increase in the depth of the curvature of the peak profiles in bigger columns leads to a larger tailing of the integral tracer profile and a decrease in NTU

7   The effect of the frit quality on the performance of the column

Simulation studies were made to examine how the changes in the frit quality effected the performance of the column.

The ratio of the radial to the axial pressure loss factor Q Eq. (2) is one of the important factors to examine the distribution characteristics of the frit. This ratio Q was changed in the range of 400 to 2 to examine the influence of the frit quality on the performance of a 5 cm x 25 cm column. Based on experiments the ratio Q of real frits varies between 30 and 400 depending on the kind of frits.

Fig. (7) show the effects of the frit quality on simulated tracer profiles for a Q of 400, of 40, of 4 and of 2.

In general the decrease of Q leads to a stronger parabolic tracer profile with a deeper curvature. This effect is strongly non linear and in the lower range of Q the tracer profiles are dominated by the frit. The effect on the frit quality on the percentage change of the NTU is shown in Fig. (8).

To calculate the percantage differences all values were compared to the results of the simulation with a Q of 400. Further it shows that Q in the range of 40 and 4 has a much stronger influence on the overall NTU and asymmetry of the integral tracer profile at the outlet pipe just beyond the column than the Q in the range of 400 and 40.
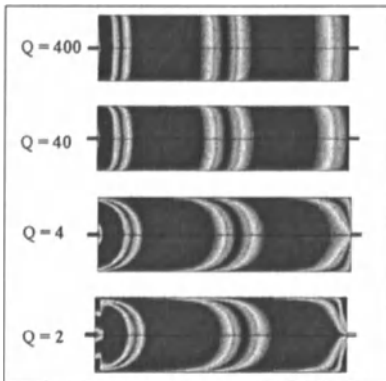
Fig. (7) Effect on the frit quality Q of simulated tracer profiles in a 5cm x 25 cm column
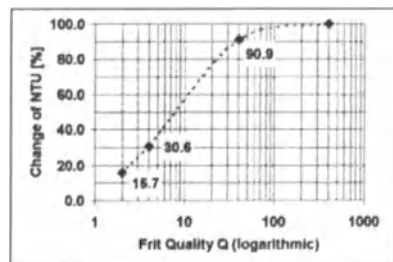
Fig. (8) Effect of the frit quality on the NTU

8   Maximisation of the Separation Performance of a Column by using an Optimal Temperature Difference between the Inlet Stream and the Column Wall

Since 1956 [12,13] it is well known, that the temperature field effects the velocity field and the concentration distribution in a HPLC-Column, because of interactions between the temperature and the viscosity. It was prooven, that these interactions can be used to influence the curvature of the radial tracer profiles and thus to maximize the separation performance. The velocity profiles by subcooling the feedstream of the columns for different temperatures DT is shown in Fig. (9).
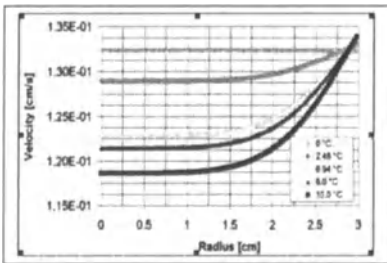
Fig. (9) Effect of cooling the feedstream on the radial velocity profile in the middle of the column
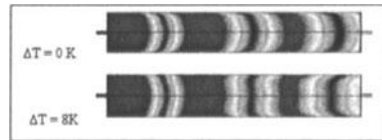
Fig. (10) Comparision of tracer profiles as they pass through the column of an isothermal column and of a cooled inlet stream

These marginal velocity differences lead to changes in the curvaturs of the radial tracer profiles as they pass through the column Fig. (10).

Depending on the temperature difference, this effect led to a slow down of the core and an acceleration of the margins of the radial tracer profile. As a result, the remixing decreased and the performance of the column could be maximised Fig. (11).

As can be seen in Fig. (11), the NTU can be improved by approximately 20%. To predict the optimal temperature difference it is also necessary to consider the adsorptive interaction of the components.
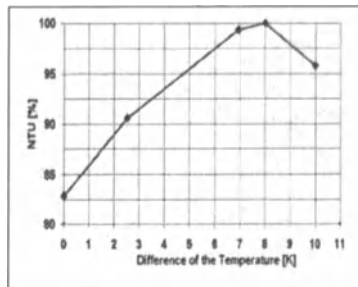
Fig. (11) Effect of the Temperature Difference on the NTU

9   Summary and Outlook

Based on CFD simulations, the effect of the column diameter and the frit quality on the performance of a chromatographic column was examined. To evaluate the influence of the parameter variations, the NTU of the integral tracer profile in the outlet tube just beyond the column were calculated. Based on experiments qualitative features were derived to validate the simulation results.

The results showed that the axial velocity profile in the central zone of an isothermal column almost corresponds to the plug flow profile. The velocity distribution in the inlet and outlet zones of the column is a function of the column diameter and the frit quality.

An increase in the column diameter leads to a decrease of the NTU. Especially here the transition from a column diameter of 5 cm to 10 cm leads to a higher reduction than the transition from 1 cm to 5 cm. So the scale up behaves non linear.

To judge the effect of the frit quality on the column performance, the ratio of radial to axial pressure loss factor was changed. As a result this ratio emerged as an important specification for the distribution and collection quality of the frit. Significantly in the high radial pressure range, the small changes in the pressure loss factor have a strong influence on the performance of the column.

CFD-simulations can be used to predict optimal process conditions for preparative columns for example by changing the temperature differences between the column wall and the inlet stream. In the above case the optimal temperature difference led to an approximate 20% improvement of the separation performance.

In conclusion CFD simulation is a highly efficient tool to carry out parameter studies and to develop strategies for the scale up and optimisation of preparative chromatography.

References

1. B. Coq, G. Cretier, J. L. Rocca: " End-Effects and Band Spreading in Liquid Column Chromatography"; Jour. of Chrom.; 178 (1979); 41 – 46
2. Dr.-Ing. A. Brandt: "Untersuchung der Temperaturabhängigkeit der Trennleistung in der Flüssig-Chromatographie mit präparativer Zielsetzung"; PhD-Thesis at the TU Berlin 1997
3. O. Dapremont, G.B. Cox, M. Martin, P. Hilaireau, H. Colin: "Effect of radial gradient of temperature on the Performance of large-diameter high-performance liquid chromatography columns I. Analytical conditions", J Jour. of Chrom A; 796 (1998); 81–99

Symbols			
D	Dispersion	m_i	Mass of the component
p	Pressure	Q	Factor to define the frit quality
r	Radial coordinate	R	Column radius
t	Time	T	Temperature
[2mm] ΔT	Temperature difference between Feed and Column wall	v	Dynamic viscosity
w	Velocity	z	Axial coordinate
Greek Letters			
α	Pressure loss factor	α_{rad}	Pressure loss factor in the radial direction
α_{ax}	Pressure loss factor in the axial direction	ρ	density
Abbreviations			
[2mm] BC	Boundary Conditions	HETP	Height Equal of a Theoretical Plate
NTU	Number of Theoretical Plates		

4. T. Yun, P. Sajonz, Z. Bensetiti, G. Guiochon: "Influence of the heat of adsortion on elution band profiles in nonlinear liquid chromatography"; Jour. of Chrom A; 760 (1997); 3–16
5. A. Brandt, G. Mann, W. Arlt: "Temperature Gradients in Preparative high-performance liquid chromatography columns"; Jour. of Chrom A, 769 (1997); 109–117
6. A. Brandt, G. Mann, W. Arlt: "Enhancement of the separation efficiency in preparative high-performance liquid chromatography columns"; Jour. of Chrom A, 796 (1998); 223–228
7. T. Yun, G. Guiochon: "Visualisation of the heterogeneity of column beds"; Jour. of Chrom A, 760 (1997); 17–24
8. T. Farkas, J. Q. Chambers, G. Guiochon: "Column effecncy and radial homogeneity in liquid chromatography"; Jour. of Chrom A, 679 (1994); 231–245
9. F. G. Lode, A. Rosefeld, Q. S. Yuan, T. W. Root, E. N. Lightfoot: "Refining the scale-up of chromatographic separations"; Jour. of Chrom A, 796 (1998); 3–14
10. Ch. Heuer, P. Hugo, G. Mann, A. Seidel-Morgenstern: "Scale up in preparative chromatography", Jour. of Chrom. A, 752 (1996); 19–29
11. A. Brandt, Schering AG: " Personal correspondence"
12. H. L. Toor: Ind. And Eng. Chemistry, 48(5) (1956)
13. I. Halász, R. Endele, K. Unger: "Jour. of Chrom.", 112 (1975); 37

On Projection-Based Time-Splitting Schemes for Computing Chemically Reacting Flows

Andreas Prohl

Mathematisches Seminar, Christian-Albrechts-Universität Kiel,
Ludewig-Meyn-Str. 4, D–24098 Kiel, Germany
e-mail: apr@numerik.uni-kiel.de

Abstract. The simulation of chemically reacting flows in specific situations is a basic instrument to predict and understand complex flow phenomena that arise in natural sciences (e.g., salt distributions in oceans and related flow structures) as well as in engineering sciences (e.g., the optimization of crystal growth processes in semiconductor industries).

Due to the huge computational effort that is needed in implicit algorithms, this motivates to develop new, less expensive algorithms which can even be implemented on workstations, while giving reasonably accurate solutions. In this contribution, a combination of the well-known projection methods of Chorin and Van Kan with a semi-explicit time-discretization strategy is proposed. A convergence analysis is given to justify this approach.

1   Introduction

Chemically reacting flows are described by means of the conservation principles for momentum, mass and energy. If we consider a bounded domain $\Omega \subset \mathbb{R}^d$, $d = 2, 3$ where the incompressible reacting fluid is in and observe its behavior for a period of time $[0, t_{M+1}]$, the dynamics can be described by the following system of equations,

$$u_t - Pr\Delta u + (u \cdot \nabla)u + \nabla p = f_0(T), \qquad \operatorname{div} u = 0,$$

$$T_t - \Delta T + (u \cdot \nabla)T = -\sum_{i=1}^{N} h_i W_i(\{Y_i\}_{i=1}^{N}, T), \tag{1}$$

$$Y_{i,t} - \frac{1}{Le}\Delta Y_i + (u \cdot \nabla)Y_i = W_i(\{Y_i\}_{i=1}^{N}, T), \qquad i = 1, ..., N.$$

Here, the reacting incompressible flow is modeled by coupling the Navier-Stokes equations for the fluid flow with reaction-diffusion equations for chemical reactions, using Boussinesq approximation, see [5]. This model is widely used in the control of manufacturing processes, like chemical vapor deposition process modeling for semiconductor materials, and we refer to [4] for an abundant list of references in engineering literature. – For simplicity, we impose the following initial and boundary value data for the problem under

consideration, for $i = 1, .., N$,

$$u(t)\big|_{\partial\Omega} = 0, \qquad T(t)\big|_{\partial\Omega} = 0, \qquad Y_i(t)\big|_{\partial\Omega} = 0, \qquad \forall\, t \in [0, t_{M+1}],$$
$$u(0) = u_0, \qquad T(0) = T_0, \qquad Y_i(0) = Y_{i,0}, \tag{2}$$

In the presented model, Pr is the Prandl number, and Le the Lewis number, which both scale different diffusive and the convective characters of the quantities in the equations. $p = p(x,t)$ is the scalar pressure and $u = u(x,t) \in \mathbb{R}^d$ the solenoidal velocity field. According to the Boussinesq model, the flow is driven by the buoyant forcing term $f_0(T)$, which is an affine function of the temperature $T = T(x,t)$. Finally, the N-tuple $\{Y_i\}_{i=1}^N$ determines the mass fractions $Y_i = Y_i(x,t)$ of N species indexed by i that constitute the chemically reacting fluid flow. Because of the mass conservation principle, there holds $0 \le Y_i \le 1$, and

$$\sum_{i=1}^N Y_i = 1, \qquad \sum_{i=1}^N W_i = 0, \qquad \forall\, (x,t) \in \Omega \times [0, t_{M+1}],$$

where W_i denotes the net production/removal rates of species i, for $1 \le i \le N$. The value h_i is the enthalpy of the species i divided by its molecular weight, i.e., a measure of the amount of heat that is contained in species i.

Chemical reactions between the diverse species are described by means of the Arrhenius model, in which the W_i takes the form

$$W_i(\{Y_i\}_{i=1}^N, T) = \sum_{j=1}^{m_i} A_j e^{-E_j/R_0 T} \prod_{k=1}^N C_j^{\nu_{j,k}}. \tag{3}$$

Some parameters are involved in this relation: the frequency factors A_j, the activation energies E_j, and the universal gas constant R_0. C_i denotes the concentration of the i-th species, i.e., the mass fraction Y_i divided by the molecular weight. The $\nu_{j,k}$ are nonegative integers, where at least one of the $\nu_{j,k}$ is nonzero, for $k = 1, ..., N$, and each j.

The goal of this paper is to propose time-splitting schemes in order to reduce the computational effort that is necessary for a fully implicit time-discretization. In the latter case, the coupling of the diverse functions in the 'flow part' and the 'chemical part' finally leads to large discretization matrices that limit the flexibility of a fully implicit discretization approach, due to restricted computational resources. Second, in order to make sure that the discretization is stable, the finite element discretization pairing for the velocity and pressure fields has to satisfy the LBB-condition of Ladyszhenskaya, Babuska and Brezzi, cf. [1]. In addition to these difficulties, the nonlinear parts that are given by the reaction terms and the convective terms have to

be properly discretized.

Apart from standard notation for Sobolev spaces and norms, we make frequent use of the shorthand notations $d_t\phi^{m+1} := \frac{1}{k}\{\phi^{m+1} - \phi^m\}$, $\overline{\phi}^{m+1/2} := \frac{1}{2}\{\phi^{m+1} + \phi^m\}$, $\overline{\overline{\phi}}^m := \frac{1}{2}\{\overline{\phi}^{m+1/2} + \overline{\phi}^{m-1/2}\}$ and $\tau_{m+1} := \min\{1, t_{m+1}\}$ in the remainder of the work. In the following, C denotes a generic constant that depends on the given data of the problem but is independent on the time-step $k > 0$.

2   A first order time-splitting scheme based on Chorin's projection method

In order to reduce the computational effort in a significant way, a splitting scheme is proposed subsequently that decouples the computation of iterates of velocity field and pressure function, temperature and N mass fraction functions at each iteration step. For the present iteration step, stiffness matrices can then be constructed from the knowledge of the velocity field, temperature and mass fractions from the previous step, and the new iterates for these quantities can then be calculated in parallel. Moreover, velocity field and pressure iterates can be computed in a decoupled manner through the projection method of Chorin, see [2,3]. The scheme $\mathcal{S}^1$ then reads:

Given $\{u^m, T^m, \{Y_i^m\}_{i=1}^N\}$, determine $\{\tilde{u}^{m+1}, p^{m+1}, T^{m+1}, \{Y_i^{m+1}\}_{i=1}^N\} \in (\mathbf{H}_0^1 \cap \mathbf{H}^2) \times H^1/\mathbb{R} \times (H_0^1 \cap H^2) \times \prod_{i=1}^N (H_0^1 \cap H^2)$ in the following way:

1. Start with $u^0 = u_0$, $T^0 = T_0$, $\{Y_i^0\}_{i=1}^N = \{Y_{i,0}\}_{i=1}^N$. Then, the following steps determine the iterates for $m \geq 0$.
2. Find $\tilde{u}^{m+1}$ that solves

$$\frac{1}{k}\{\tilde{u}^{m+1} - u^m\} - Pr\Delta\tilde{u}^{m+1} + (u^m \cdot \nabla)\tilde{u}^{m+1} = f_0(T^m),$$

3. Determine the tuple $\{u^{m+1}, p^{m+1}\}$ that solves the system

$$\frac{1}{k}\{u^{m+1} - \tilde{u}^{m+1}\} + \nabla p^{m+1} = 0$$

$$\operatorname{div} u^{m+1} = 0, \qquad u^{m+1}\big|_{\partial\Omega} \cdot n = 0,$$

4. Compute T^{m+1} that is the solution of

$$\frac{1}{k}\{T^{m+1} - T^m\} - \Delta T^{m+1} + (u^m \cdot \nabla)T^{m+1} = -\sum_{i=1}^N h_i W_i(\{Y_i^m\}_{i=1}^N, T^{m+1}),$$

5. The N-tuple $\{Y_i^{m+1}\}_{i=1}^N$ is governed by

$$\frac{1}{k}\{Y_i^{m+1} - Y_i^m\} - \frac{1}{Le}\Delta Y_i^{m+1} + (u^m \cdot \nabla)Y_i^{m+1} = W_i(\{Y_i^{m+1}\}_{i=1}^N, T^m),$$

with $k > 0$ being the time-step. — Note that all iterates at each time-step can be computed in a fully decoupled manner. Furthermore, we can benefit from this approach by parallelizing the computation at each iteration step. step 3. projects the guess $\tilde{u}^{m+1}$ into the space of solenoidal functions, $\mathbf{J}_0$, $u^{m+1} := P_{\mathbf{J}_0}\tilde{u}^{m+1}$, and can be reformulated in the following way. Applying the div-operator amounts to solving a Laplace-Neumann problem for the pressure iterate,

$$-\Delta p^{m+1} = -\frac{1}{k}\mathrm{div}\,\tilde{u}^{m+1}, \qquad \partial_n p^{m+1}\big|_{\partial\Omega} = 0, \qquad (4)$$

followed by an algebraic update for the present solenoidal velocity field,

$$u^{m+1} = \tilde{u}^{m+1} - k\nabla p^{m+1}.$$

This decoupling strategy in the computation of the velocity field and pressure iterates has been proposed by Chorin and is known as a first order projection scheme for solving the incompressible Navier-Stokes equations, see [2,3]. Now, owing to (4), scheme $\mathcal{S}^1$ implies a pressure-stabilization effect which allows to apply even finite element pairings (for a wide range of parameters $\{k, h\}$ corresponding to time and spatial discretization) that do not satisfy the LBB-constraint, see [1]. — Subsequently, we are interested in approximation properties of this scheme. The following convergence results have been verified in [7].

Theorem 1. *Suppose that the given data of the problem* (1), (2) *are sufficiently smooth. For sufficiently small time-steps* $k \le k_0(t_{M+1})$, *the solution* $\{u^m, p^m, T^m, \{Y_i^m\}_{i=1}^N\}$ *of scheme* $\mathcal{S}^1$ *then satisfies*

$$\max_{0\le m\le M+1}\Big\{\|u(t_m) - \tilde{u}^m\| + \tau_m\|p(t_m) - p^m\|_{-1} + \|T(t_m) - T^m\|$$

$$+ \sum_{i=1}^N \|Y_i(t_m) - Y_i^{m+1}\| + \sqrt{k}\Big(\|u(t_m) - \tilde{u}^m\|_1 + \sqrt{\tau_m}\|p(t_m) - p^m\|$$

$$+ \|T(t_m) - T^m\|_1 + \sum_{i=1}^N \|Y_i(t_m) - Y_i^m\|_1\Big)\Big\} \le Ck,$$

for sufficiently small time-steps $k \le k_0(t_{M+1})$.

Note that the error statements for the pressure iterates in the norm $\ell^\infty(0, t_{M+1}; L^2)$ show lower order of convergence, compared to those for the remaining quantities. This reflects arising boundary layers in the structure of the error function $t_m \mapsto \{p(t_m) - p^m\}$ that are due to the prescription of unphysical, homogeneous pressure data in (4) for the iterates p^m. This fact is well-understood in the context of the Navier-Stokes equations, see [9,6] for further details on this. In particular, optimal convergence behavior for

iterates of the pressure function in the scheme can be recovered on compact subdomains ω of Ω, i.e., for each $\omega \subset\subset \Omega$, there holds

$$\max_{1 \leq m \leq M} \|p(t_m) - p^m\|_\omega \leq Ck, \tag{5}$$

provided $\text{dist}(\partial\omega, \partial\Omega) = \mathcal{O}(1)$, see [9,6].

However, this perturbation of iterates for the pressure function also affects those for the *gradients of the velocity field*, and the question is whether there is also a crucial impact from the projection step 3. on gradients for the iterates that represent concentration and temperature. These quantities are expected to be of interest in applications when studying chemical reactions, and we therefore address this question here. Surprisingly, it turns out that the answer depends on the dimension d of the problem in a crucial way. In fact, in the case $d = 3$ there is a significant impact on the temperature approximation and the mass fractions, that is caused by the projection step 3., whereas it is negligible in the $2D$ case.

Corollary 1. (see [7]) Suppose that the conditions of Theorem 1 are valid. Then, the iterates $\{T^m, \{Y_i^m\}_{i=1}^N\}$ satisfy the improved estimates
  1. in two space dimensions (i.e., $d = 2$), for all $\gamma > 0$, and $\lim_{\gamma \to 0} C_\gamma = \infty$:

$$\max_{0 \leq m \leq M} \sqrt{\tau_m}\Big\{ \|T(t_m) - T^m\|_1 + \sum_{i=1}^N \|Y_i(t_m) - Y_i^m\|_1 \Big\} \leq C_\gamma k^{1-\gamma},$$

2. in three space dimensions (i.e., $d = 3$):

$$\max_{0 \leq m \leq M} \sqrt{\tau_m}\Big\{ \|T(t_m) - T^m\|_1 + \sum_{i=1}^N \|Y_i(t_m) - Y_i^m\|_1 \Big\} \leq Ck^{3/4}.$$

3   A second order time-splitting scheme based on the Van Kan method

In the previous section, we discussed a projection method of first order for chemically reacting flows. Although slight deficiencies are detected in Corollary 1, this projection-based time-splitting scheme seems to be a good compromise of computational effort and desired accuracy, see Theorem 1.

In order to improve the accuracy of the method, a higher order projection based time-splitting scheme can be designed in a way that the basic discretization via Crank-Nicolson is combined with the second order projection method of Van Kan, [10]. The scheme $\mathcal{S}^2$ then reads as follows:

Given approximations $\{\tilde{u}^{m-1}, \tilde{u}^m, u^{m-1}, u^m, p^{m-1}, p^m, T^{m-1}, T^m, \{Y_i^{m-1}\}_{i=1}^N, \{Y_i^m\}_{i=1}^N\}$ of velocity, pressure, temperature and mass fraction functions, which are evaluated at time $t = t_{m-1}$ and $t = t_m$, determine $\{\tilde{u}^{m+1}, u^{m+1}, p^{m+1}, T^{m+1}, \{Y_i^{m+1}\}_{i=1}^N\}$ which is the solution of the following system, for a parameter $\beta > \frac{1}{2}$:

1. Start with $u^0 = u_0$, $T^0 = T_0$, $Y_i^0 = Y_{i,0}$, $1 \leq i \leq N$, and $\|p^0 - p(0)\|_1 \leq Ck$. Then, the following steps determine iterates, for $m \geq 0$.

2. Find $\tilde{u}^{m+1}$ that solves

$$\frac{1}{k}\{\tilde{u}^{m+1} - u^m\} - \frac{1}{2}Pr\Delta\{\tilde{u}^{m+1} + \tilde{u}^m\} + \tilde{\mathcal{N}}_1\left(\{\tilde{u}^{m-\ell}\}_{\ell=0}^1, \{\tilde{u}^{m+1-\ell}\}_{\ell=0}^1\right)$$
$$+ (\frac{3}{2} - \beta)\nabla p^m + (\beta - \frac{1}{2})\nabla p^{m-1} = f_0(\frac{3}{2}T^m - \frac{1}{2}T^{m-1}).$$

3. Determine $\{u^{m+1}, p^{m+1}\}$ that solves the system

$$\frac{1}{k}\{u^{m+1} - \tilde{u}^{m+1}\} + \beta\nabla\{p^{m+1} - p^m\} = 0,$$
$$\text{div}\, u^{m+1} = 0, \qquad u^{m+1}|_{\partial\Omega}\cdot n = 0.$$

4. Compute T^{m+1} that is the solution of

$$\frac{1}{k}\{T^{m+1} - T^m\} - \frac{1}{2}\Delta\{T^{m+1} + T^m\} + \tilde{\mathcal{N}}_2\left(\{\tilde{u}^{m-\ell}\}_{\ell=0}^1, \{T^{m+1-\ell}\}_{\ell=0}^1\right)$$
$$= -\sum_{i=1}^N h_i W_i\left(\frac{3}{2}\{Y_i^m\}_{i=1}^N - \frac{1}{2}\{Y_i^{m-1}\}_{i=1}^N, \overline{T}^{m+1/2}\right).$$

5. The N-tuple $Y^{m+1} := \{Y_i^{m+1}\}_{i=1}^N$ is governed by

$$\frac{1}{k}\{Y_i^{m+1} - Y_i^m\} - \frac{1}{2Le}\Delta\{Y_i^{m+1} + Y_i^m\} + \tilde{\mathcal{N}}_3\left(\{\tilde{u}^{m-\ell}\}_{\ell=0}^1, \{Y_i^{m+1-\ell}\}_{\ell=0}^1\right)$$
$$= W_i\left(\{\overline{Y}_i^{m+1/2}\}_{i=1}^N, \frac{3}{2}T^m - \frac{1}{2}T^{m-1}\right).$$

In this formulation, the nonlinear mappings $\tilde{\mathcal{N}}_j(\cdot, \cdot)$, for $j = 1, 2, 3$, stand for a second order discretization of the nonlinear convective terms, with the possibility of varying explicit or implicit discretizations in the leading first part. The first argument in $\tilde{\mathcal{N}}_j(\cdot, \cdot)$ has to be divergence free in order to assure the stability of the method. Thus, iterates enter into the first argument that are already computed from the projection step 3. before. This is stated in the way $\tilde{\mathcal{N}}_j(\cdot, \cdot) = \mathcal{N}_j(P_{\mathbf{J}_0}\cdot, \cdot)$. — For the purpose of this presentation, we set $\tilde{\mathcal{N}}(\cdot, \cdot) = \tilde{\mathcal{N}}_j(\cdot, \cdot)$, for $j = 1, 2, 3$, with

$$\mathcal{N}\left(\{\phi^{m-\ell}\}_{\ell=0}^1, \{\psi^{m+1-\ell}\}_{\ell=0}^1\right) = [\{\frac{3}{2}\phi^m - \frac{1}{2}\phi^{m-1}\}\cdot\nabla]\overline{\psi}^{m+1/2}. \qquad (6)$$

The application of this mapping in the algorithm allows for the possibility to compute iterates in each iteration cycle *in parallel*.

Remark 1. The scheme needs to be modified for the case $m = 0$. For this case, the convective term is once shifted to its implicit form, $(\overline{\tilde{u}}^{1/2}\cdot\nabla)\overline{\tilde{u}}^{1/2} + \frac{1}{2}(\text{div}\,\overline{\tilde{u}}^{1/2})\overline{\tilde{u}}^{1/2}$, and the choice $\beta = 0$ suppresses the second pressure term in

the momentum equation. To preserve second order of convergence, the right hand side in step 2. has to be replaced by $f_0(\overline{T}^{1/2})$, and correspondingly the right hand sides of the steps 4. and 5. by their implicit forms. This amounts to a coupling of the total scheme $\mathcal{S}^2$ in the first step.

As it is known from the studies of the Van Kan method in [6], this method only performs in an optimal way in case certain (regularity) conditions are satisfied by the solution; on the other hand, there exist modifications of this projection method that can even handle general flow constellations with optimal approximation properties, see [6] on this matter. The following theorem is verified in [8].

Theorem 2. *Suppose that the given data of (1), (2) as well as its solution (compatibility condition) are sufficiently smooth and that the initial step is modified according to Remark 1. Then, the following error bounds are valid for the solution $\{u^{m+1}, p^{m+1}, T^{m+1}, Y^{m+1}\}$ of scheme $\mathcal{S}^2$, for sufficiently small time-steps $k \leq k_0(t_{M+1})$,*

$$\max_{1 \leq m \leq M} \left\{ \tau_{m-1/2}^{1/2} \| u(t_{m+1/2}) - \overline{u}^{m+1/2} \| + \| T(t_{m+1/2}) - \overline{T}^{m+1/2} \| \right.$$

$$+ \sum_{i=1}^{N} \| Y_i(t_{m+1/2}) - \overline{Y}_i^{m+1/2} \|$$

$$+ k \left(\| u(t_{m+1/2}) - \overline{\overline{u}}_1^m \|_1 + \tau_{m-1/2}^{1/2} \| p(t_{m+1/2}) - \overline{\overline{p}}^m \| \right.$$

$$\left. + \| T(t_{m+1/2}) - \overline{\overline{T}}^m \|_1 + \sum_{i=1}^{N} \| Y_i(t_{m+1/2}) - \overline{\overline{Y}}_i^m \|_1 \right) \right\} \leq Ck^2 \left(1 + \log \frac{1}{k} \right),$$

Remark 2. In fact, to prove that the compatibility condition for given initial and boundary data as well as right hand sides in (1) is valid for a given fluid flow problem is a delicate problem in general, and we refer the interested reader to [6], e.g., for further details on this.

As we already know from the discussion of the first order projection-based scheme in section 2, the character of the time-splitting scheme $\mathcal{S}^1$ as a projection method is the reason for slightly suboptimal convergence results for gradients of temperature distribution and gradients of mass fraction functions. The same phenomenon can be observed for scheme $\mathcal{S}^2$.

Corollary 2. *(see [8]) Suppose that the conditions of Theorem 2 are valid. Then, the iterates $\{T^{m+1}, \{Y_i^{m+1}\}_{i=1}^{N}\}$ satisfy the improved estimates*
   1. in two space dimensions (i.e., $d = 2$), for all $\gamma > 0$, and $\lim_{\gamma \to 0} C_\gamma = \infty$:

$$\max_{1 \leq m \leq M} \sqrt{\tau_{m+1}} \left\{ \| T(t_{m+1/2}) - \overline{\overline{T}}^m \|_1 + \sum_{i=1}^{N} \| Y_i(t_{m+1/2}) - \overline{\overline{Y}}_i^m \|_1 \right\} \leq C_\gamma k^{2-\gamma},$$

2. *in three space dimensions (i.e., $d = 3$):*

$$\max_{1 \leq m \leq M} \sqrt{\tau_{m+1}} \Big\{ \|T(t_{m+1/2}) - \overline{\overline{T}}^m\|_1 + \sum_{i=1}^{N} \|Y_i(t_{m+1/2}) - \overline{\overline{Y}}_i^m\|_1 \Big\} \leq Ck^{3/2}.$$

4   Conclusion and Outlook

Two time-splitting schemes have been proposed in this contribution that are based on projection schemes. These methods are suitable for parallelization and allow for an easy implementation and low computational storage requirements. The presented results show optimal behavior of convergence for quantities of interest. As it turns out, the projection methods that are in use in both schemes cause a slight perturbation to the scheme that is only significant in the $3D$ case. This negative effect can be avoided if modified projection methods are used like the Chorin-Uzawa scheme, instead of Chorin's method, that is exempted from this deficiency, see [6,7].

References

1. Brezzi, F., Fortin, M. (1991) Mixed and Hybrid Finite Element Methods. Springer Series in Computational Mathematics.
2. Chorin, A.J. (1968) Numerical solution of the Navier-Stokes equations. Math. Comp. **22**, 745–762
3. Chorin, A.J. (1969) On the convergence of discrete approximations of the Navier-Stokes equations. Math. Comp. **23**, 341–353
4. Knobloch, P. (1996) Solvability and finite element discretization of a mathematical model related to Czochralski crystal growth. Ph.D. thesis, Preprint **MBI-96-5** (Univ. of Magdeburg).
5. Manley, O., Marion, M. , and Temam, R. (1993) Equations of combustion in the presence of complex chemistry. Ind. Univ. Math. J. **42**, 941–967.
6. Prohl, A. (1997) Projection and quasi-compressibility methods for solving the incompressible Navier-Stokes equations. Teubner.
7. Prohl, A. (1998) A first order projection-based time-splitting scheme for computing chemically reacting flows. IMA Preprint Series no. **1540**.
8. Prohl, A. (1998) A second order projection-based time-splitting scheme for computing chemically reacting flows. IMA Preprint Series no. **1541**.
9. Rannacher, R. (1991) On Chorin's projection method in the incompressible Navier-Stokes Equations. in: *Proceedings of the Oberwolfach Conference: Navier-Stokes Equations. Theory and Numerical Methods.*
10. Van Kan (1986) A second-order accurate pressure-correction scheme for viscous incompressible flow. SIAM J. Sci. Stat. Comp. **7**, 870–891.

Chemical partial equilibrium model in gasdynamics problems

Vladimir I. Sakharov[1] and Elena Fateeva[1]

Institute of Mechanics, Moscow State University, Michurinskiy Pr.1, Moscow, 119899, Russia

Abstract. The dissociated and partially ionized gas flows past the blunt–nosed bodies are considered with the nonequilibrium gas–phase chemical reactions taken into account. Implicit numerical method for such flow problems has been developed to obtain the steady–state solution of the Navier–Stokes equations. The solution could be achieved using the full diffusion statement of the problem (full model) or the chemical partial equilibrium model (simplified model). The model of chemical partial equilibrium has been worked out for the problems when chemical reactions have significantly different rates. Applicability range and efficiency of simplified model are estimated. The comparisons between the results obtained using the full model and the simplified model are analyzed. It is demonstrated that the chemical partial equilibrium model is applicable for simulation of the hypersonic flow fields over blunt bodies with a nose radius of more than several centimeters on the part of the reentry trajectory in the Earth's atmosphere.

1 Introduction

The multicomponent gas flows past blunt–nosed bodies entering planetary (Earth's and Martian) atmospheres at hypersonic velocities are accompanied by reactions whose rates differ widely, i.e. chemical partial equilibrium sets in. For instance, as a reentry vehicle with 1 m characteristic radius enters the Earth's atmosphere at 5–8 km/s velocities and 50–80 km altitudes, the gas–phase exchange reactions proceed quite fast in the disturbed region, while the dissociation rates are finite. The motion of a reentry vehicle with a small blunted nose along a gliding trajectory in the Martian atmosphere is another example. At altitudes exceeding 35 km the ionized mixture flow past a landing module cannot be considered as chemical equilibrium. So the associative ionization reactions are close to equilibrium, while the O_2, N_2 and C_2 molecules dissociate either slowly or with finite rate.

The model of chemical partial equilibrium has been developed for the above–mentioned flows. In this model the part of differential diffusion equations is degenerated into algebraic relations of the chemical equilibrium constraint conditions. The number of such equations is equal to the number of fast independent chemical reactions. The chemical production sources on the right–hand sides of the remaining diffusion equations of new unknown functions ('slow' variables) do not contain terms connected with fast reactions. It permits to overcome the stiffness problem.

2   Numerical Method

The finite–volume implicit numerical method is developed to solve the two–dimensional time–dependent Navier–Stokes (NS) equations in the conservation form. It is assumed that the flux vector could be split into 'viscous' and 'inviscid' parts. The solution of the Riemann problem of heat–conducting gas with frozen chemical composition has been obtained to calculate the 'inviscid' fluxes. The spatial derivatives in the 'viscous' terms are approximated with second–order accuracy. Piecewise–parabolic distribution of the physical variables over the network cells and 'minmod' limiters lead to TVD–scheme of second–order accuracy. Finite–difference equation set is resolved by the sweep method along the lines normal to the surface and the Gauss–Zeidel iteration procedure. Coordinate–oriented differences are introduced in the implicit part of the finite–difference operator in accordance with the signs of eigenvalues of Jacobi matrices in convective terms.

3   Chemical Partial Equilibrium Flows

A chemically reacting gas mixture is considered with N species and R reactions taken into account. Let's carry out an analysis of dimensionless rates (Damköhler numbers) of chemical reactions written in the following form:

$$\sum_{i=1}^{N} \nu'_{ij} A_i = \sum_{i=1}^{N} \nu''_{ij} A_i, \qquad j = 1, \ldots, R$$

$$Dm_j = \frac{1}{\varepsilon_{gj}} = \frac{\tau}{\tau_{gj}} = \tau k_{r_j} \left(\frac{\rho}{m}\right)^{\nu''_j - 1}, \qquad \nu''_j = \sum_{i=1}^{N} \nu''_{ij}$$

Here Dm_j, τ, τ_{gj}, k_{r_j}, ρ, and m are, respectively, the Damköhler number, characteristic gasdynamic and chemical times, reverse reaction rate constant of jth reaction, the density, the average mass. The corresponding mass production rate of species A_i is the following:

$$\omega_i = \frac{\rho m_i}{m} \sum_{j=1}^{R} \Gamma_{ij} \frac{v_j}{\varepsilon_{gj}}, \qquad \Gamma_{ij} = \nu''_{ij} - \nu'_{ij}$$

$$v_j = K_{c_j} m^{\nu''_j} \rho^{\nu'_j - \nu''_j} \prod_{k=1}^{N} \left(\frac{c_k}{m_k}\right)^{\nu'_{kj}} - m^{\nu''_j} \prod_{k=1}^{N} \left(\frac{c_k}{m_k}\right)^{\nu''_{kj}}$$

Here K_{c_j}, m_i are the equilibrium constant of jth reaction and the ith species mass, respectively.

Let's suppose the reactions proceed in a mixture with significantly different rates. Let r_f and r_s be the numbers of fast (corresponding to small ε_{gj}) and slow ($\varepsilon_{gj} \geq 1$) independent reactions ($r_f < r$, $r_f + r_s = r$). R_f and

$R_s = R - R_f$ are the total numbers of fast and slow reactions, respectively. Note that the system of r stoichiometrically independent reactions is chosen in such a manner that the number of fast independent reactions r_f be maximum, and the 'slow reactions' imply the reactions which proceed either slowly or at finite rates.

We present ε_{gj} as $\varepsilon_{gj} = \varepsilon \cdot (\varepsilon_{gj}/\varepsilon)$ for fast reactions ($j \leq R_f$). Here $\varepsilon \ll 1$ and $(\varepsilon_{gj}/\varepsilon) \sim 1$. Then vector of chemical production rates $\mathbf{w} = (\omega_1, \ldots, \omega_r)^T$ has a form:

$$\mathbf{w} = \mathbf{M}°\mathbf{\Gamma}\mathbf{Y}, \qquad \mathbf{Y} = \frac{\rho}{m}\left\{\begin{array}{c} \frac{1}{\varepsilon}\mathbf{Y}^1 \\ \mathbf{Y}^2 \end{array}\right\}, \qquad \mathbf{M}° = diag(m_1, \ldots, m_r)$$

$$Y_j^1 = \frac{\varepsilon}{\varepsilon_{gj}}v_j \ (j = 1, \ldots, R_f), \qquad Y_j^2 = \frac{1}{\varepsilon_{gj}}v_j \ (j = R_f + 1, \ldots, R)$$

The first components in $\mathbf{Y}$ correspond to the fast reactions. Let's construct the matrix of stoichiometric coefficients $\mathbf{\Gamma}$ following the same pattern and divide it into blocks:

$$\mathbf{\Gamma} = \overbrace{\underbrace{\left[\begin{array}{cc} \mathbf{\Gamma}_{11} & \mathbf{\Gamma}_{12} \\ \mathbf{\Gamma}_{21} & \mathbf{\Gamma}_{22} \end{array}\right.}_{R_f}\left.\underbrace{\vphantom{\begin{array}{c}\mathbf{\Gamma}_{12}\\\mathbf{\Gamma}_{22}\end{array}}}_{R_s}\right]\begin{array}{l} \}r_f \\ \}r_s \end{array}}, \qquad rank\,\mathbf{\Gamma} = r$$

The matrix $\mathbf{\Gamma}$ is constructed in such a manner, that the $rank\,\mathbf{\Gamma}_{11} = r_f$. As $r_f < r$ the blocks $\mathbf{\Gamma}_{11}$ and $\mathbf{\Gamma}_{21}$ are linearly dependent. Thus they are related by certain matrix $\mathbf{A}$:

$$\mathbf{\Gamma}_{21} = \mathbf{A}\mathbf{\Gamma}_{11}, \qquad \mathbf{A} = \mathbf{\Gamma}_{21}(\mathbf{\Gamma}_{11})^T\left[\mathbf{\Gamma}_{11}(\mathbf{\Gamma}_{11})^T\right]^{-1}, \qquad det\left[\mathbf{\Gamma}_{11}(\mathbf{\Gamma}_{11})^T\right] \neq 0$$

Let's transform the vector of mass concentrations of reaction products and chemical elements $\mathbf{c} = (c_1, \ldots, c_r, c_{r+1}^*, \ldots, c_{N-2}^*)^T$ using the matrix $\mathbf{A}$:

$$\mathbf{u} = \mathbf{T}\mathbf{M}^{-1}\mathbf{c}, \qquad \mathbf{M} = diag(m_1, \ldots, m_{N-2})$$

$$\mathbf{T} = \left[\begin{array}{ccc} \mathbf{E}_1 & \mathbf{0} & \mathbf{0} \\ -\mathbf{A} & \mathbf{E}_2 & \mathbf{0} \\ \mathbf{0} & \mathbf{0} & \mathbf{E}_3 \end{array}\right], \qquad \mathbf{u} = \left\{\begin{array}{c} \mathbf{u}^f \\ \mathbf{u}^s \\ \mathbf{u}^z \end{array}\right\}\begin{array}{l} \}r_f \\ \}r_s \\ \}N_e - 2 \end{array}$$

Here N_e is the number of chemical elements. Matrix $\mathbf{T}$ has the constant components. The unit matrices $\mathbf{E}_1, \mathbf{E}_2, \mathbf{E}_3$ have dimensions $r_f \times r_f$, $r_s \times r_s$, $(N_e-2) \times (N_e-2)$. The component form of transformation is the following:

$$u_i^f = \frac{c_i}{m_i}, \quad u_l^s = -\sum_{i=1}^{r_f}\alpha_{li}\frac{c_i}{m_i} + \frac{c_l}{m_l}, \quad u_k^z = \frac{c_k^*}{m_k}$$

$$(\alpha_{li}) = \mathbf{A}, \quad i = 1, \ldots, r_f, \quad l = r_f + 1, \ldots, r, \quad k = r + 1, \ldots, N - 2$$

The new variables u_i^s are named 'slow' variables. The diffusion equations for the products and elements could be transformed in the following schematic representation as a results of left multiplication on $\mathbf{TM}^{-1}$:

$$\varepsilon \mathcal{L} \mathbf{u}^f = \mathbf{w}^f, \qquad \mathbf{w}^f = \mathbf{\Gamma}_{11} \mathbf{Y}^1 + \varepsilon \mathbf{\Gamma}_{12} \mathbf{Y}^2 \tag{1}$$

$$\mathcal{L} \mathbf{u}^s = \mathbf{w}^s, \qquad \mathbf{w}^s = (\mathbf{\Gamma}_{22} - \mathbf{A}\mathbf{\Gamma}_{12}) \mathbf{Y}^2 \tag{2}$$

$$\mathcal{L} \mathbf{u}^z = 0 \tag{3}$$

Here $\mathcal{L}$ is the Navier–Stokes differential operator. Note, that $\mathbf{w}^s$ depends on the chemical production rates of 'slow' chemical reactions only.

The fast reactions are considered as equilibrium ones in the model of chemical partial equilibrium. Then the vector equation (1) is degenerated into the algebraic system of equations of the equilibrium constraint conditions for r_f fast independent reactions if $\varepsilon \to 0$:

$$v_i = 0, \qquad i = 1, \dots, r_f \tag{4}$$

The diffusion equations (2) and (3) are unchanged, because they involve no small parameters.

So initial system of diffusion equations is replaced by the diffusion equations for the 'slow' variables (2), the chemical elements (3) and the equilibrium constraint conditions (4). The obtained equation system contains r_f differential equations less then initial one. Moreover it is less stiff due to the new chemical production sources of the diffusion equations for 'slow' variables which don't contain terms connected with fast reactions.

4   Results and Discussion

The model of chemical partial equilibrium was used for the numerical simulation of hypersonic viscous multicomponent gas flows past a blunt bodies in the framework of the boundary layer equations on stagnation streamline [1]. The flow conditions corresponded to proceeding along the part of the reentry trajectory of the 'Space Shuttle' vehicle (5th flight, $H = 50 - 70$ km). 11–species air model with 49 chemical reactions was considered. The preliminary analysis of the Damköhler numbers and the comparison between the obtained numerical solutions of the full diffusion problem and the simplified model demonstrated that it was enough to enter only one 'slow' variable in the considered case:

$$u_1^s = \frac{c_O}{m_O} + \frac{c_N}{m_N} + 2 \left(\frac{c_{NO^+}}{m_{NO^+}} + \frac{c_{O_2^+}}{m_{O_2^+}} + \frac{c_{N_2^+}}{m_{N_2^+}} \right) + 3 \left(\frac{c_{O^+}}{m_{O^+}} + \frac{c_{N^+}}{m_{N^+}} \right) \tag{5}$$

Let's call the approach using one 'slow' variable (5) as the 'first model'.

In the present paper applicability of the chemical partial equilibrium model is analyzed under the similar conditions in the framework of the full

NS equations. Note that the numerical simulation of a hypersonic flow in the framework of the full NS assumes deriving the solution in a whole disturbed region over the body including the shock wave structure. An analysis of the Damköhler numbers for such conditions does not permit to limit by one 'slow' variable. It is connected with the strong chemical nonequilibrium in the relaxation zone near the smeared bow shock wave. In this case the whole group of chemical reactions being fast in the boundary layer passes into category 'slow' ones, and the maximal number of independent fast reactions decreases by unit. Because of this, the second 'slow' variable linearly independent with the first one is introduced:

$$u_2^s = \frac{c_N}{m_N} + \frac{c_{NO}}{m_{NO}} + \frac{c_{NO^+}}{m_{NO^+}} + \frac{c_{N^+}}{m_{N^+}} + 2\left(\frac{c_{O^+}}{m_{O^+}} + \frac{c_{N_2^+}}{m_{N_2^+}}\right) \qquad (6)$$

This approach using two 'slow' variables is named the 'second model'. It means that instead of 8 stiff diffusion equations of reaction products one can use only two nonstiff diffusion equations for the above-proposed 'slow' variables during a numerical simulation.

For a comparison between the results obtained in the framework of the NS equations using the full diffusion model, and the NS equations using the simplified models the calculations of flowfield over a 90–deg spherical segment were carried out.

Here, some trajectory points are chosen from numerous calculation results. The resultant profiles plotted against the dimensionless normal to the surface coordinate y are represented by symbols for the full model, by dashed lines the first model, and by solid lines for the second model.

Figs. 1,2 and Fig. 3 presents the flow calculation results for the 50 cm and 5 cm sphere radii, respectively. Free stream conditions are: $H = 61.9$ km, $\rho_\infty = 0.998 \cdot 10^{-4}$ kg/m^3, $v_\infty = 6.19$ km/s (Figs. 1,2), and $H = 74.9$ km, $\rho_\infty = 0.392 \cdot 10^{-4}$ kg/m^3, and $v_\infty = 7.17$ km/s (Fig. 3). Data in Figs. 1,2 and Fig. 3 correspond respectively to the stagnation streamline ($\Theta = 0°$) and the line with $\Theta = 80°$, respectively. Wall is assumed to be noncatalytic with $T_W = 1350°$K.

Let's remark that the distributions of gasdynamic parameters agree very closely for all considered models. However the first model produces the concentrations of dissociated air components differing from 'exact' ones. The second model provides results with reasonable accuracy. Equilibrium results given by square markers (Fig. 2) show that flow is far from the complete equilibrium.

So with the increase of the sphere radius the solutions obtained using the full model and the approach of the chemical partial equilibrium are brought closer together still further. As size of a body is about several centimeters, the distributions of the gasdynamic parameters remain close to each other for all three models, while in the values of concentrations and heat fluxes distinctions are observed (Fig. 3).
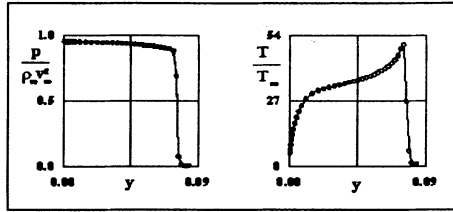
Fig. 1. $H = 61.9$ km, $R = 50$ cm, stagnation streamline
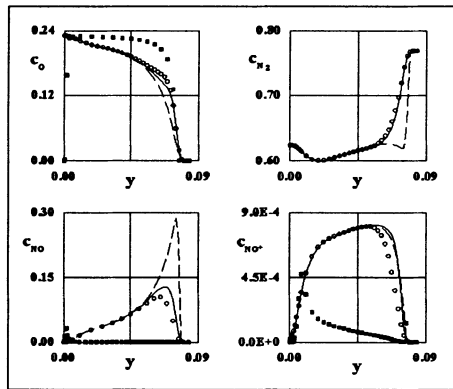
Fig. 2. $H = 61.9$ km, $R = 50$ cm, stagnation streamline
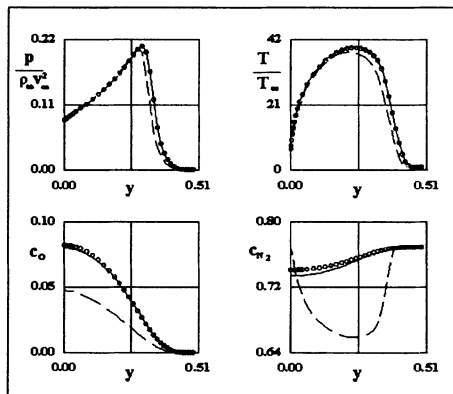
Fig. 3. $H = 74.9$ km, $R = 5$ cm, $\Theta = 80°$

Distributions of the heat fluxes are identical for the 50 cm radius sphere for all considered models (Fig. 4). For the first and full models distinction in the heat fluxes is observed for smaller sphere radius (several centimeters). Note that the skin friction coefficients along body surface agree very closely for all models.
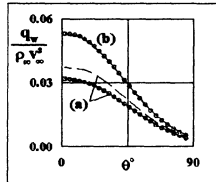
Fig. 4. (a) $H = 74.9$ km, $R = 50$ cm, catalytic surface. **(b)** $H = 54$ km, $R = 5$ cm, noncatalytic surface

Some calculations were carried out using the equilibrium radiative wall conditions. Fig. 5 presents the temperature along the surface at one trajectory point. Results for all models are close to each other.
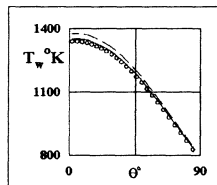
Fig. 5. $H = 85$ km, $R = 50$ cm, noncatalytic surface

5   Conclusions

Finally, it should be stated that the above–proposed efficient numerical method for solution of the supersonic flows past blunted bodies has been developed in the framework of Navier–Stokes equations with nonequilibrium chemical reactions taken into account. The applicability of the chemical partial equilibrium model is shown over wide ranges of free stream parameters, including flows past reentry modules on parts of their reentry trajectories in the Earth's atmosphere.

References

1. Sakharov, V. I., Suslov, O. N., Fateeva, E. I. (1997) Investigation of flows past blunt bodies under conditions of partial chemical equilibrium within the framework of the laminar boundary layer equations. Fluid Dynamics, **32**, 2:233-238.

Modelling Transient Irradiation Intensities of Pool Flames

Steffen Staus and Axel Schönbucher

Gerhard–Mercator–Universität Duisburg, Inst. f. Technische Chemie, Lotharstr. 1, 47048 Duisburg, Germany

Abstract. A new formulation to solve for the barely implicit pressure correction equation of FCT–transport routines by a HOC–scheme will be given. The way it is to be implemented will be presented and the gain will be emphasised. Example calculations on one– and two–dimensional transient flow will be shown with the intention to map the unstable pool flame behaviour. The resulting irradiation intensities on an adjacent body will be depicted.

1 Introduction

Every single day chemical and petrochemical industry is handling a multitude of combustible fluids while large amounts of them have to be safely stored and shipped. During the past, cases of involuntary release occurred repeatedly. Occasionally, the resulting spills or pools did ignite, leading to a unconfined nonpremixed pool flame. As a consequence, pyrolytic and combustion products did disperse, spreading their (toxic) danger to mankind and environment. Also, the thermal radiant impact on the surrounding could provoke major damage to adjacent installations or even lead to further ignition.

Current static empirical models do make use of measured mean radiative intensities and geometric shape assumptions to estimate radiation by a surface emissive power (SEP) of a flame, accounting for different pool diameters and fuels [1] or even not. But this kind of modelling fails to represent the dependence of radiation on the inhomogeneous distribution of temperature and combustion products. Moreover, a dynamic behaviour is an inherent property of a fire plume such that time averaging is an unappropriated approach. Both types of instabilities, the gravity–driven Rayleigh–Taylor as well as the shear–layer dependent Kelvin–Helmholtz one [2], respectively, will always be present leading to a transient spatial development of all field variables of the flame. Thus, transient calculations should be applied.

Usually, flame field models of fire plumes found on the gas dynamic equations including diffusive phenomena and additional sub–models to incorporate source terms. The integration effort to deal with all physical quantities involved, high resolution in multidimensional space and instationary calculation is still to high to work on today's computer architectures. In order

to reduce the computational cost, measurements have to be taken. E. g., instead of primitive variables, some authors employ Zeldovich–properties on species, temperature or specific volume in their calculation [3,4]. But a crucial point in the application to compressible, slow flows is to remove the Courant–Friedrich–Levi–(CFL)–condition on the integral time–step by implicit representation. Patnaik et al. [5] provided a way to preserve the positivity of the nonlinear explicit FCT–algorithm [6] by treating not every quantity implicit, but rather adding just one extra equation to the explicit scheme. A new procedure to solve for this equation is focused here, after radiative transport and its flow field coupling to account for the effects of inhomogeneous absorption ,emission and scattering through VISTA [7] are described. Then, a two–dimensional example calculation is given.

2   Radiation

In VISTA, a one–dimensional radiative transport equation

$$\frac{dI}{ds} = -K_{abs}I + K_{em}I_b - K_{sca}I + \frac{K_{sca}}{4\pi} \int_{\Omega=0}^{4\pi} I(\Omega)d\Omega \tag{1}$$

balances the radiant intensity along a ray's direction ds and provides a basis of the prediction of radiation transmitting a participating media. The terms in (1) stand for (from left to right) weakening due to absorption (index abs), amplification due to (black body) emission (index em), weakening due to scattering (index sca) and amplification due to (coherent) scattering into the ray's direction, respectively. Knowing each coefficient K_{abs}, K_{em}, K_{sca} in (1) as a function of the local position in space enables us to account for inhomogeneous distributions of combustion products and temperature, respectively. A series of rays is emitted from single points on a cylindrical surface area in a certain distance around the centreline of the flame. The ray directions divide the hemispherical angle around each point. Summing up every ray's intensity change at a discrete local control volume yields the energy source due to radiation, $\dot{q}_{ra}'''$, for coupling with the fluid energy balance.

In general, if soot is present in the transmitted media, one will have to distinguish between it's solid body and the radiant characteristics of a gas. Following Kirchhoff's law, $K_{abs} = K_{em}$ is assumed and like in [7] for small soot particles (particle parameter less then 0.4) the relations are applied

$$K_{H_2O+CO_2} = 0.1(X_{H_2O} + X_{CO_2}) \tag{2a}$$

$$K_{soot} = 266 const f_v T \tag{2b}$$

$$K_{overall} = K_{abs,tot} = K_{H_2O+CO_2} + K_{soot} \tag{2c}$$

Finally, irradiation intensities hitting a surface at a specified distance of the flame centre can be computed at any time from radiative data derived as above.

3   Fluid Transport

In flame calculation one may solve for the conservation equations of mass ($\rho \simeq$ density), momentum $\rho\mathbf{v}$, energy E and species n_k of a compressible gaseous mixture under gravity $\mathbf{g}$

$$\frac{\partial \rho}{\partial t} = -\nabla \cdot (\rho\mathbf{v}) \tag{3a}$$

$$\frac{\partial \rho\mathbf{v}}{\partial t} = -\nabla \cdot (\rho\mathbf{v}\mathbf{v}) - \nabla P - \nabla \cdot \tau + \mathbf{g}\,(\rho - \rho_\infty) \tag{3b}$$

$$\frac{\partial E}{\partial t} = -\nabla \cdot ((E+P)\mathbf{v}) - \nabla \cdot \kappa - \sum_{k=1}^{N_{sp}} \nabla \cdot (\phi_k h_k) + \dot{q}_{re}''' + \dot{q}_{ra}''' \tag{3c}$$

$$\frac{\partial n_k}{\partial t} = -\nabla \cdot (n_k\mathbf{v}) - \nabla \cdot \phi_k + \omega_k \tag{3d}$$

where τ, κ, ϕ_k represent the diffusive fluxes of momentum, heat and species, respectively, with volumetric sources of (single step [7]) reaction heat $\dot{q}_{re}'''$, radiative heat $\dot{q}_{ra}'''$ and species production ω_k. Soot is treated according to *Moss* as in [7]. The energy density and ideal gas relations for the internal energy change $de = \rho C_v dT$ and the pressure P read

$$E = e + \frac{1}{2}\rho\mathbf{v} \cdot \mathbf{v} \tag{4}$$

$$dP = (\gamma - 1)de \tag{5}$$

Expressing the time derivatives of (3a)-(3c), once in an explicit and again in an implicit manner, it is possible to render an equation for the pressure correction u_p of the BIC–FCT–algorithm [5] in the form

$$-\nabla \cdot (D\,\nabla u_p) + b\,u_p = f \tag{6}$$

with D, b and f being functions of the flow field variables $P, E, \mathbf{v}, \rho$ at the beginning of and after one explicit time step, respectively. To complete this implicit procedure removing the CFL–restriction on the time increment, after each integral step the e and $\mathbf{v}$ have to be updated by their contribution resulting from u_p.

4   High Order Compact–(HOC)–Pressure Correction

Problems do arise with pressure correction equations in flame calculation where high temperatures T or rather gradients ∇T do appear [3,9]. E. g. for ideal gases D may be seen as depending on T alone. Hence, the inhomogeneous Laplace term renders non–zero first order terms in the convection–diffusion form of (6) which might spoil ellipticity and perturbes the problem. This can lead to unstably growing errors if no measurements are taken. Equation (6) is an inhomogeneous elliptic linear source problem which could be

seen as a convection–diffusion equation with linear source term , too, if the Laplace–term would be differentiated. Doing so and normalising by D, the central discretisation of (6) in two dimensions reads

$$-\delta_x^2 u_{p,ij} - \delta_y^2 u_{p,ij} + c_{ij}\delta_x u_{p,ij} + d_{ij}\delta_y u_{p,ij} + g_{ij}u_{p,ij} - R_{err,ij} = \varphi_{ij} \qquad (7)$$

while δ_x and δ_x^2 symbolize the usual first and second order central differencing operators, respectively. Taylor series expands show, that the truncation error $R_{err,ij}$ for a grid spacing h is given by

$$R_{err,ij} = \frac{h^2}{12}\left[2\left(c\frac{\partial^3 u_p}{\partial x^3} + d\frac{\partial^3 u_p}{\partial y^3}\right) - \left(\frac{\partial^4 u_p}{\partial x^4} + \frac{\partial^4 u_p}{\partial y^4}\right)\right]_{ij} + O(h^4). \qquad (8)$$

Dropping the truncation error in (7) leads to the usual central $O(h^2)$–discretization (CDS) providing a 5–point stencil as a local operator. A box–discretisation of (6) was used in [9] to be solved by MGRID [8], a multigrid method using bilinear or quadratic inter–grid relations, respectively. Again, a 5–point stencil with a $O(h^2)$–representation results. On the other hand, the FCT–routines are designed to be four order accurate in phase errors. Not to disturb the approximation, 4th–order discretisation should be applied to (6). Two additional support points can be used achieve $O(h^4)$. The disadvantage of this 9–point–(5×5)–local operator in two dimensions arises from a greater bandwidth w of the resulting system matrix (and thus w^2 more elimination work as in the 5–point stencil) and difficulties at the boundaries.

A high order compact (HOC) formulation of the local operator, i. e. a 9–point–(3×3)–stencil could avoid this effect. This formulation of (6) will be obtained if the the third and fourth order derivates in leading term of the truncation error (8) can be expressed by $O(h^2)$–representations. Indeed, this is possible through rearranging (6) itself for the second order term in x and again in y and then derivating again. Inserting into (8) and (7) after rearranging finally yields

$$-E_{ij}^1\delta_x^2 u_{p,ij} - E_{ij}^2\delta_y^2 u_{p,ij} + C_{ij}^1\delta_x u_{p,ij} + C_{ij}^2\delta_y u_{ij} + G_{ij}u_{p,ij} \qquad (9)$$

$$-\frac{h^2}{6}\left[\delta_x^2\delta_y^2 u_{p,ij} - c\delta_y^2\delta_x u_{p,ij} - d\delta_x^2\delta_y u_{p,ij} - B_{ij}\delta_y\delta_x u_{p,ij}\right] = F_{i,j} + O(h^4)$$

with

$$E_{ij}^1 = 1 + \frac{h^2}{12}\left[c_{ij}^2 - 2\delta_x c_{ij} - g_{ij}\right] \qquad (10a)$$

$$E_{ij}^2 = 1 + \frac{h^2}{12}\left[d_{ij}^2 - 2\delta_y d_{ij} - g_{ij}\right] \qquad (10b)$$

$$C_{ij}^1 = c_{ij} + \frac{h^2}{12}\left[\delta_x^2 c_{ij} + \delta_y^2 c_{ij} - c_{ij}\delta_x c_{ij} - d_{ij}\delta_y c_{ij} + 2\delta_x g_{ij} - c_{ij}g_{ij}\right] \quad (10c)$$

$$C_{ij}^2 = d_{ij} + \frac{h^2}{12}\left[\delta_x^2 d_{ij} + \delta_y^2 d_{ij} - c_{ij}\delta_x d_{ij} - d_{ij}\delta_y d_{ij} + 2\delta_y g_{ij} - d_{ij}g_{ij}\right] (10d)$$

$$G_{ij} = g_{ij} + \frac{h^2}{12}\left[\delta_x^2 g_{ij} + \delta_y^2 g_{ij} - c_{ij}\delta_x g_{ij} - d_{ij}\delta_y g_{ij}\right] \tag{10e}$$

$$F_{ij} = \varphi_{ij} + \frac{h^2}{12}\left[\delta_x^2 \varphi_{ij} + \delta_y^2 \varphi_{ij} - c_{ij}\delta_x \varphi_{ij} - d_{ij}\delta_y \varphi_{ij}\right] \tag{10f}$$

$$B_{ij} = \delta_x d_{ij} + \delta_y c_{ij} - c_{ij}d_{ij} \quad . \tag{10g}$$

It may be seen from (10f) that the right hand side of (6) has to be utilized in the neighbourhood of the evaluation point as well in order to achieve the high order of approximation. Equations (9) and (10a)–(10g) do reduce to the discrete relations given in [13] if g would identically vanish. In (10e) $\delta_x^2 g_{ij}, \delta_x g_{ij} \geq 0$ even if b in (6) will be a constant. In case of constant coefficients $\mu = ch/2$, $\nu = dh/2$ the equations above read in stencil form

$$\frac{1}{6h^2}\begin{pmatrix} -(1+\mu)(1-\nu) & -2\nu^2 + 4\nu - 4 & -(1-\mu)(1-\nu) \\ -2\mu^2 - 4\mu - 4 & 20 + 4\mu^2 + 4\nu^2 & -2\mu^2 + 4\mu - 4 \\ -(1+\mu)(1+\nu) & -2\nu^2 - 4\nu - 4 & -(1-\mu)(1+\nu) \end{pmatrix} \odot u_p =$$

$$\frac{1}{12}\begin{pmatrix} 0 & 1-\nu & 0 \\ 1+\mu & 8 & 1-\mu \\ 0 & 1+\nu & 0 \end{pmatrix} \odot \varphi \tag{11}$$

which is directly identified with the "Mehrstellen–Verfahren" of Collatz [14] if $\mu = \nu \equiv 0$. Contrasting the central difference way this formulation is unconditionally non–oscillatory [13]. Asymptotic ϵ–stability for $g \equiv 0$ has been analysed by Kouatchou [10].

The given procedure facilitates the employment of the so called "black box" multigrid solver MGD9V (cf. e.g. [11]), which makes use of a discrete (3×3)–molecule. In addition, applying galerkin coarse grid correction and due to it's matrix dependent prolongation and restriction operators it is well suited for systems derived from inhomogeneous elliptic equations, even if dominant convection would be present. Also, it would not violate the local peclet condition on the coarser grid levels. Finally, it is about four times faster in comparison to Bi–CGSTAB [12] on the aquifer problem proposed by van der Vorst [11].

5   Examples

Typically, equation (6) exhibits a convection dominated behaviour at a reaction zone. To examine the phenomenon one may imagine an ideal gas mixture who's coefficient D is proportional to the temperature T. An, indeed, coarse approximation of a flame reactive zone could be obtained by choosing a one–dimensional Gaussian profile from the flame centre outward, e.g. $D(x) = e^{(0.5\,Re\,x^2)}$. In addition, let $b(x) = D(x)$, $\varphi(x) = (2 + Re\,x^2)\,e^x$. Therewith, the one–dimensional equivalent to (6) is given by

$$-u_p^{''} - Re\,x\,u_p^{'} + u_p = \varphi \tag{12}$$
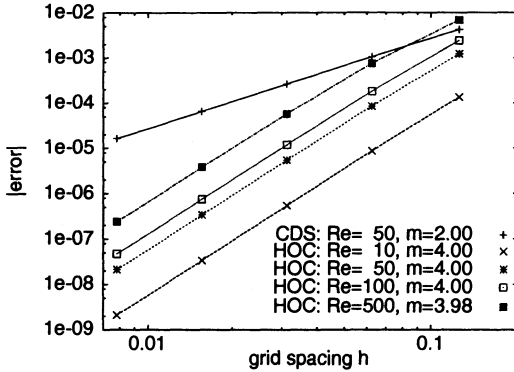
Fig. 1. Convergence comparison of CDS and HOC on problem (12): Absolute error measured at x=0.25 vs. grid-spacing h at different values of the parameter Re. m stands for the convergence rate

Imposing Dirichlet boundaries on (12) $u_p(0) = 1, u_p(1) = 0$, yields the exact solution $u_p(x) = (1 - x)e^x$. Numerical solution shows that the error of CDS is hardly sensitive to increasing convection Re contrasted by HOC (Fig. 1). Nevertheless, a convergence rate $m = 4$ of the HOC–scheme means that it is preserving the $O(h^4)$–approximation even on high convection values for variable coefficients (Fig. 1). This encourages to stop an iterative solution process for a given desired accuracy acc on the same grid already at

$$acc_{HOC} = \sqrt{acc_{CDS}} \tag{13}$$

in case of HOC–approximation. Compared to the $O(h^4)$–5–point discretisation of the one–dimensional advection case posed in [5] the amount of work to compute the system matrix from the coefficients in (6) is about the same (No. of products, ratio: HOC/5–point $=21/20$, No. of sums, ratio: HOC/5–point$=17/16$). Thus, a gain in the HOC case comes from solving a tridiagonal matrix versus a pentadiagonal one. The reduction of the bandwidth w will take more effect in two–dimensional problems, where the bandwidth of a HOC–scheme NxN–system matrix is about s times smaller than that of a non–compact $O(h^4)$–discretisation, where

$$s = \frac{2N + 3}{4N + 1} \tag{14}$$

As a two–dimensional example, an axially symmetric simulation on a part of a sooty nonpremixed flame of $0.1\,m$ in diameter was performed on a 64×64 fixed condensed grid over a puffing cycle (frequency $\simeq 6.2\,s^{-1}$ [15]). Therefore, radial profiles of the density, momentum, energy and species were swept along the flame axis as an initial condition. A potential vortex was imposed to the undisturbed flame structure. As an important species with respect to radiation, Fig. 2 shows the evolution of soot at 4 stages. The resulting instantaneous irradiation a body receives, located at a distance of a pool diameter from the flame axis is shown in Fig. 3. Due to mixing processes, relative displacement of soot and temperature extrema, over– and undershoots do occur in comparison with the undisturbed profile at the beginning (Fig. 3).
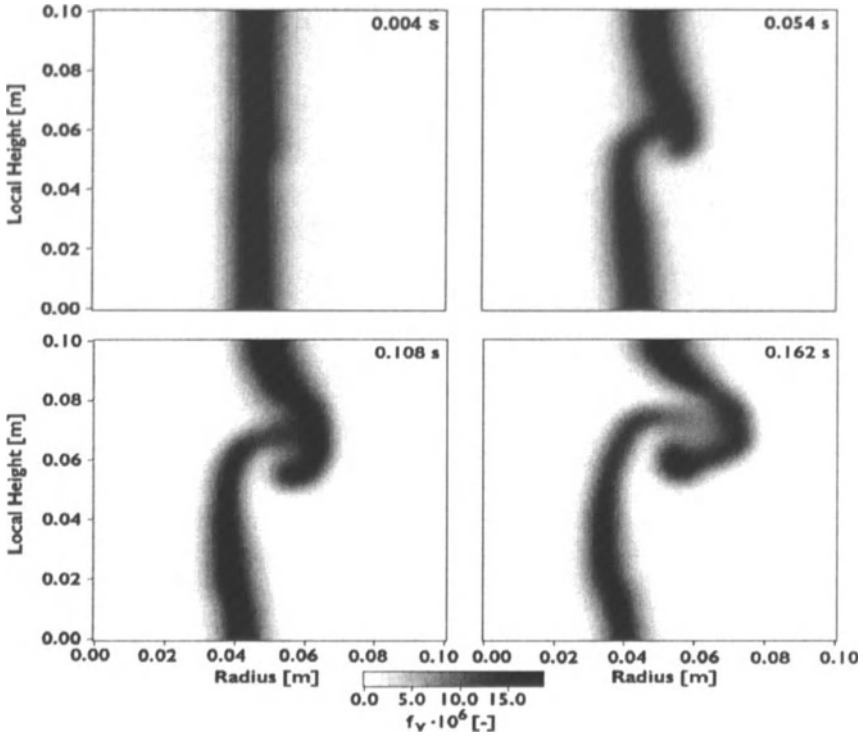
Fig. 2. Soot volume fraction f_v in axial sections at 4 different times
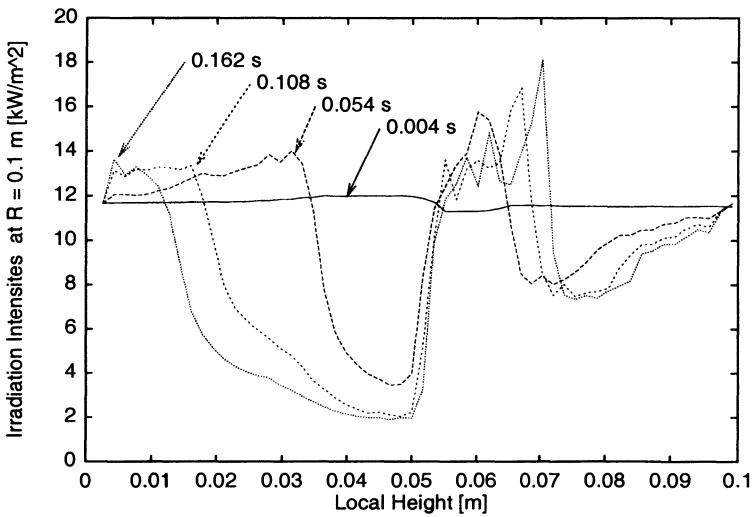
Fig. 3. Irradiation intensities at 0.1 m radial distance vs. height of computational domain

6   Conclusions

The presented HOC–formulation of the pressure correction equation in the BIC–FCT algorithm enables the employment of the problem adapted multigrid method MGD9V. A faster flame code with better resolution of the reaction zone is achieved, providing a tool to analyse transient flame behaviour as well as dynamic radiant environmemenal impact.

References

1. Göck, D.; Fiala, R.; Zhang, X.; Schönbucher, A.: "Das experimentell validierte Ballen–Strahlungsmodell OSRAMO". TÜ 33 (1992), **4**, 137–140 and **6**, 219–233
2. Oertel Jr., H.; Delfs, J.: "Strömungsmechanische Instabilitiäten". Springer, Berlin/Heidelberg, 1996
3. Mell, W. E.; McGrattan, K. B.; Baum, H. R.: "Numerical Simulation of Combustion in Fire Plumes". Twenty–Sixth Symposium (International) on Combustion, The Combustion Institute, 1996, 1523–1530
4. Ghoniem, A. F.; Lakkis, I.; Soteriou, M.: "Numerical Simulation of The Dynamics of Large Fire Plumes and the Phenomenon of Puffing" Twenty–Sixth Symposium (International) on Combustion, The Combustion Institute, 1996, 1531–1539
5. Patnaik, G.; Guiguis, R. H., Boris, J.P.; Oran, E. S.: "A Barely Implicit Correction for Flux Corrected Transport". J. Comput. Phys. **71**, 1–20, 1987
6. Boris, J. P., Landsberg, A. M.; Oran, E. S., Gardner, J. H.: "Flux Corrected Transport Modules for Solving Generalized Continuity Equations". NRL Memorandum Report 7192, Naval Research Laboratories, Washington, D. C., 1993
7. Koch, Th.: "Numerische Simulation einer auftriebsbestimmten, rußenden Diffusionsflamme". Dissertation, Gerhard–Mercator–Universität, Duisburg, 1997
8. DeVore, C. R.: "Vectorisation and Implementation of an Efficient Multigrid Algorithm for the Solution of Elliptic Partial Differential Equations". NRL–Memorandum Report 5504, Naval Research Laboratory, Washington, DC , 1984
9. Patnaik, G.; Laskey, K. J.; Kailasanath, K.; Oran, E. S.; Brun, T. A.: "Flic-A Detailed, Two–Dimensional Flame Model". NRL–Memorandum Report 6555, Naval Research Laboratory, Washington, DC , 1989
10. Kouatchou Ngongang, J. R.: "High–Order Multigrid Techniques for Partial Differential Equations". PhD–Thesis, George Washington University, Washington, DC, 1998
11. de Zeeuw, P. M.: "Acceleration of Iterative Metheods by Coarse Grid Correction". Academisch Proefschrift, Universiteit van Amsterdam, 1997
12. van der Vorst, H. A.: "A fast and smoothly converging variant of Bi–CG for the solution of nonsymmetric linear Systems". SIAM J. Sci. Statist. Comput. **13**, 631–644, 1992
13. Spotz, W. F. : "High Order Compact Finite Difference Schemes for Computational Mecanics". University of Texas, PhD–Thesis, 1995
14. Collatz, L.: "The Numerical Treatment of Differential Equations". Springer, Berlin/ Heidelberg/New York, 3rd. Edition, 1966
15. Schönbucher, A., Göck; D, Kettler A.; Krattenmacher, D.; N., Schieß:"Static and Dynamic Radiance Structures in Pool Fires". Twenty–First Symposium (International) on Combustion, The Combustion Institute, 1988, 92–100

Index

Index of Complementary Volume

Author's Index

Z

Author's Index of Complementary Volume